

ABSTRACT

SCHNEIBLE, JOHN DANIEL. A Material Toolbox for Advanced Therapeutics (Under the direction of Dr. Stefano Menegatti and Dr. Jan Genzer).

Over the last half century, researchers have turned to naturally-inspired products to develop biomaterials that provide solutions to advance diagnostics, pharmaceutical therapy, and regenerative medicine. Two main families of biomaterials have demonstrated translation in the clinic: (*i*) polysaccharides, owing to excellent endogenous biocompatibility and biodegradability, ease of chemical functionalization and processing, commercial abundance, and low cost; and (*ii*) peptide/proteins, equally biocompatible and biodegradable, and amenable to large-scale manufacturing and modification via modular chemical approaches to achieve a wide variety of functionalities.

This doctoral dissertation begins – in **Chapter 1** – with a broad survey of polysaccharides and peptides, and their applications in drug delivery and tissue engineering, especially focusing on materials employed in this work, namely chitosan and synthetic peptides. The chapter ends with a perspective on the future direction of research on biomaterials inspired by polysaccharides and peptides.

Chapters 2, Chapter 3, and Chapter 4 focus on the development of polysaccharide-based (**Chapter 2** and **Chapter 3**) and peptide-based (**Chapter 4**) hydrogels for drug delivery applications. In these chapters, the drug pair doxorubicin (DOX) and gemcitabine (GEM), whose well-known synergism and its dependence on delivery schedule (*i.e.*, sequence of administration) was utilized to develop formulations with superior therapeutic efficacy against triple negative breast cancer model, a highly aggressive form of metastatic cancer. In **Chapter 2**, the interplay betwixt experimental and *in silico* design of a hydrophobically modified-chitosan hydrogel was thoroughly explored. In particular, the diffusion of both drugs – either single or combined –

through chitosan hydrogels was studied using both experimental and *in silico* techniques, the latter providing valuable insight into the physicochemical mechanisms governing drug transport especially in relation with drug-polymer interactions. In **Chapter 3**, an acetylated-chitosan hydrogel was selected from **Chapter 2** and further optimized to deliver GEM and DOX with therapeutically relevant dosages, and with the appropriate delivery kinetics (GEM faster than DOX) and molar ratio. This hydrogel was evaluated in a 2-D (cell monolayer) and 3-D (spheroid) and demonstrated remarkable synergism and tumor volume reduction compared to the free drug pair concurrently administered. In **Chapter 4**, a composite peptide hydrogel, comprising DOX-adsorbed-graphene oxide (GO) particles and a self-assembling MAX8 peptide scaffold loaded with GEM, was developed to deliver an optimized schedule and dose of GEM and DOX. Again, *in silico* simulations were utilized to elucidate the physicochemical parameters underpinning transport properties of the system, with a focus of the adsorption/desorption to/from the modified GO surface. This composite was tested against a 2-D (cell monolayer) model and demonstrated a drastic improvement of therapeutic synergism relative to the concurrent free drug pair.

Chapter 5 and **Chapter 6** shift the focus from drug delivery. **Chapter 5** reports the development of a novel light-responsive cyclic peptide that binds vascular cell adhesion marker 1 (VCAM1), a cell marker implicated in stem cell function, selectively and on-demand. An *in silico* approach was developed to rationally identify potential sequences to achieve selective VCAM1 conformational binding of the cyclic peptide ligand. A novel synthetic route was developed to construct the identified cyclic peptide sequences, which were subsequently characterized and screened for light-controlled binding of VCAM1 as both free protein in solution and displayed on the surface of cells. **Chapter 6** concludes the experimental work and reports on the development and characterization of soft microgels decorated with the peptide AHRPYAAK that mimics fibrin

knob ‘B’ and targets fibrin hole ‘b’ that increase clot density *in vitro* and decrease bleeding in a rodent trauma model *in vivo*.

This work concludes in **Chapter 7** by offering an outlook and future directions in the field of drug delivery and how the work presented here may be relevant to those ends.

© Copyright 2020 by John D. Schneible

All Rights Reserved

A Material Toolbox for Advanced Therapeutics

by
John Daniel Schneible

A dissertation submitted to the Graduate Faculty of
North Carolina State University
in partial fulfillment of the
requirements for the degree of
Doctor of Philosophy

Chemical Engineering

Raleigh, North Carolina
2020

APPROVED BY:

Dr. Stefano Menegatti
Committee Co-Chair

Dr. Michael A. Daniele

Dr. Jan Genzer
Committee Co-Chair

Dr. Orlin Velev

DEDICATION

My journey as a Ph.D. student has been a journey that I am invaluabley grateful for having experienced. This journey allowed me to learn everything I would need to succeed as a scientist; such as: technical knowledge in a vast swathe of topics pertinent to solving the problems that currently afflict society, the right questions to ask to fully probe a scientific hypothesis, the right way to design experiments to address those questions, the relevant keywords to search to find the most pertinent research articles, and several others that, for the sake of brevity, I will not discuss. Far greater than the knowledge I learned to become a successful scientist, however, is the knowledge I learned that cultivated me as a person and has made me a better man, son, boyfriend, friend, employee, and thinker. It takes a certain type of individual to embark on this journey; one that can be best described as replete with high-highs, periods of excitement and fun, and low-lows, periods of dispassion and angst. While the personality of the embarkee on this journey is necessary to ensure success, it is far from sufficient. Without the love and support from the people with whom you are closest, this journey would be impossible.

BIOGRAPHY

John Daniel Schneible was born on April 6th, 1993, in Syracuse, NY. Throughout his childhood he lived in a small town called Lafayette, a town of ~5,000 people that is known throughout Central New York as the home of apples. In high school, John was very passionate about academics, with his favorite subjects being chemistry and world history. Aside from academics, John was heavily involved in athletics throughout high school, receiving varsity letters for baseball, basketball, and golf. In 2011, John graduated high school and began his college career at Onondaga Community College where he studied Engineering Science and maintained jobs as a dishwasher at the golf course and at the town pizza shop. After one year, he transferred to the University at Buffalo, where he majored in Chemical and Biological Engineering. While there, he became so enamored by scientific research that he pursued research adventures in two different laboratories; first with Dr. Sherry Chemler in the Chemistry Department, second with Dr. Haiqing Lin in the Chemical Engineering Department. Through these experiences, he garnered powerful tools that would prove invaluable in graduate school. Aside from scholarly activities at Buffalo, John was a brother of the Alpha Phi Omega Fraternity, where he dedicated a substantial portion of his sophomore and junior year. He graduated *summa cum laude* from Buffalo in 2015 and made his decision to attend graduate school at North Carolina State University on a whim; with an indifference to the research he was aware of and trusting only his gut instincts. John met Dr. Stefano Menegatti in the fall of 2015 and joined his laboratory in the spring of 2016. After four years of intense work, culminating in a patent, a book chapter, and five publications (submitted and/or published), John is defending his doctoral dissertation, after which, he will be joining the United States Patent and Trademark Office as a patent examiner, with plans to pursue law school at George Mason University in 2021 and become a patent attorney thereafter.

ACKNOWLEDGMENTS

The list of people for whom I am extremely thankful for is long. All of these people, in different ways, have helped and supported me through this journey and made this a fulfilling journey. An acknowledgement in my largest accomplishment pales in comparison to the gratitude to which I owe them. The order I have chosen to acknowledge does not reflect, in any way, the priority they hold in my heart and thoughts.

I would first like to thank the faculty members who served in my doctoral committee; Dr. Michael Daniele, Dr. Jan Genzer, and Dr. Orlin Velev. Their input during these projects have helped to steer them in the right direction.

I would also like thank my two undergraduate research advisors, Dr. Sherry Chemler and Dr. Haiqing Lin. By working in their labs, I learned to love research and hone my interests in particular topics. These two labs also equipped me with powerful tools that not only allowed me to hit the ground running when I started, but also, aided me throughout graduate school, such as knowing how to break an emulsion in a separatory funnel.

I like to thank Dr. Saad Khan and Sandra Bailey for their guidance throughout graduate school and making sure things were always done on time and done correctly.

In the lab, the thanks go for and wide. Dr. Billy Kish, my “buffalo bills” brother. I am immensely grateful for the short time we shared together in the lab. Billy showed me the ropes of peptide synthesis and always offered to help me when I started in the lab. Dr. Ashton Lavoie, she made sure the lab was running and she knew HPLC incredibly well. I’m thankful for Ashton teaching me the ins and outs of HPLC and the vent sessions we shared early on in my graduate career. The 1032 squad. Camden the first person in the lab the year after I started, our chats about Andrew Yang and Dave Ramsey, and our “personal” lives always made the lab and the office a

fun environment; though our projects were drastically different, I always enjoyed answering all questions chemistry. The same goes for Srivatsan. I really enjoyed learning about Indian culture, and cricket, and our conversations about American politics, and playing the delivery cooking game at your apartment. Kevin, “Kahvun”, I really appreciated working together and sharing experiences outside the lab, like having a quarantine dinner and watching those Chapel Hill boys beat up on my Orangemen, were finishing at the same time and I’m extremely grateful to have met you and Chelsea. Raphael, “Raphie”, I really enjoyed the late nights we shared together and the conversations we shared, and the acquired addiction to CAVA. Eduardo, “barbie”, always made sure laugh, and thus, more human, and always made sure everything that I needed in the lab was getting ordered on time. Brendan and “the young” Sam made this entire experience more fun; from board game nights, to trivia at Ruckus; these moments were highlights of my week. Ryan, my Minnesota brother from another mother, we worked in different buildings, but our personalities matched. The conversations about football, politics, hanging out with the chemistry grad students, and for flag football kept me grounded to life outside of science. I would like to especially thank all of the undergraduates I had the privilege of mentoring here as they contributed a lot to this work: Radina, Bruce, Jean Marie, Clay (“roger that”), Jonathan and Haofeng. Lastly, I’d like to thank the catalysis crew, Brandyn and Keshav; six hands work better than two. I’m especially thankful to Keshav, “Dr. Sir”, for showing me the ropes with catalysis, and always sharing coffee with me; Danke tschüss!

Aside from the lab, I would be remised to not thank the group that kept me sane during this process and kept me human; Austin, Justin, Christian, Victoria “Vic”, and Ali, the intramural dream team; they are more than friends, they are family. I look forward to reuniting together and seeing everyone succeed.

I would also like to acknowledge the friends from my previous journey, who helped shape me into the person that I am today and have provided reminders of pleasantries from that time. My long-time friend Ken, our daily conversations kept me inspired and going through this process. I'm also thankful for watching the McGregor fight and getting stranded in Houston during Harvey, it taught me the value of solid decision making. Nick, Steve, Nicky Buckets, the Jen, Kelly, Lindz, and Kayleigh have all supported throughout this journey and I am immensely thankful for always going to the Ralph during the winter to watch the bills and catch up. I would also like to thank my roommate from undergraduate, Cheema, who just graduated from medical school; we did it! Thanks for always being up late to chat on the phone and being able to relate to a crazy journey. Lastly, I would like to thank my little, Samuel. Over breaks we always get together and it refreshes the charge on the batteries, after late night chats, spending quality time together during the winter, and, recently, getting quarantine wins in warzone. From home I would like to acknowledge my friends, Connor, Goose, Jeremy, and Vic through phone calls and rounds of golf, I am reminded of my roots and this keeps me humble.

This process would have been impossible without the loved ones who have supported me long before this process started. My parents, and step-parents, who have always been there for me both emotionally and financially here at NC State. I'm immensely appreciative of their support beyond what words can describe, I love them with all my heart, and this work is, largely dedicated to them. I would like to thank my younger brother Ivan, and my "little sister" niece, Jasmine, for their support during this process. Ivan keeps me young and reminds me not to take life so serious, advice that I should probably take more often. He and his fiancée, Jessica, always brighten the holiday season and helps to reset my mindset following winter break. Jasmine has served as my motivation to keep going, she has always, and continues, to inspire me to show her what can be

achieved by a guy from a small, no-name town in Central New York. Lastly, in the family, I would like to thank my girlfriend, Lex, and her parents, Bonnie and John. Her parents have supported me immensely and have been my second set of family, always opened their home to me, and helped make holiday season absent anything work related. Lex has been my rock for the last five years and has showed me unconditional love, support, provided advice when it was most needed, and encouraged me to pursue opportunities that make me the best version of myself for our future together; all of which, I am eternally grateful for, and without which, this journey would not have been possible.

Lastly, I would like to thank my advisor Dr. Stefano Menegatti. Advisor is a formal term, but Stef is far from an advisor, rather he was my mentor and my friend. As such, he commended me when warranted and scolded me when it was deserved. I was one of Stef's first students and, as a result, responsible, in large part, for helping start the lab. This cultivated a trust that afforded flexibility in exploring ideas, or tricky synthetic chemistry routes that were, very often, unrelated to the work presented here. Stef trusted me to synthesize peptides for projects for collaborators, which allowed me to do what I love most in the lab, chemistry, and made me the residential contract peptide chemist. Accordingly, I was responsible for training incoming graduate students and teaching peptide chemistry, this taught me how to teach, an extremely valuable skill. As one of the first students, Stef would occasionally turn to me for advice on incoming students and trust me as his eyes in the lab. Aside from our professional relationship, Stef has always treated me like family, asking me about the personal matters going on in my life and being a crutch, an ear, or an advisor when I needed it most. During my time here, Stef and I shared many dinners, rife with philosophical conversation, and political conversations. These were my one of favorite activities

as a graduate student. Words cannot express how inordinately grateful I am to have worked with him through my career as a graduate student and gotten to know him at a deep level.

†To all of these people, this work is dedicated†

JDS

TABLE OF CONTENTS

LIST OF TABLES.....	xiii
LIST OF FIGURES	xv
Chapter 1: Natural and Synthetic Biopolymers in Drug Delivery and Tissue Engineering	1
Abstract.....	2
1.1. Introduction.....	3
1.2. Synthetic and Natural Substrates	3
1.3. Applications of Natural and Synthetic Polypeptides	5
1.3.1. Drug Delivery Vehicles	5
1.3.1.1. Ultra-small Peptides.....	6
1.3.1.2. β -Scaffolds	6
1.3.1.3. α -Scaffolds	7
1.3.1.4. Peptide Amphiphiles (APs).....	8
1.3.1.5. Elastin-like Polypeptides (ELPs)	10
1.3.1.6. Cyclic Peptides (CPs)	10
1.3.2. Targeting Agents.....	11
1.3.3. Cell-Permeating Peptides.....	13
1.3.4. Peptides in Tissue Engineering and Regenerative Medicine	16
1.3.4.1. Collagen, Gelatin, and Fibrin.....	16
1.3.4.2. Elastin-like Polypeptides (ELPs)	17
1.3.4.3. Synthetic Peptides	19
1.4. Applications of Polysaccharides	22
1.4.1. Drug Delivery	22
1.4.1.1. Hyaluronic Acid (HA)	23
1.4.1.2. Dextran (Dex)	25
1.4.1.3. Chitosan (CN)	26
1.4.2. Tissue Engineering and Regenerative Medicine.....	28
1.4.2.1. Plant and Bacterial Cellulose (BC)	29
1.4.2.2. Chitosan (CN)	30
1.4.2.3. Hyaluronic Acid (HA)	33
1.4.2.4. Alginate.....	36
1.5. Conclusion and Future Outlook	37
References.....	39
Figures.....	118
Chapter 2: Tailoring the Chemical Modification of Chitosan Hydrogels to Fine-Tune the Release of a Synergistic Combination of Chemotherapeutics	124
Abstract.....	125
2.1. Introduction.....	126
2.2. Materials and Methods.....	131
2.2.1. Materials	131
2.2.2. Modification of Chitosan	131
2.2.3. Determination of the Level of Modification	132
2.2.4. Computational Procedure.....	133
2.2.5. Single-Drug Loading and Release Studies	134

2.2.6. Dual-Drug Loading and Release Studies	135
2.2.7. Mathematical Model	135
2.3. Results and Discussion	136
2.3.1. Chitosan Gel Preparation and Selection	136
2.3.2. <i>In silico</i> Modeling of Single and Dual-Drug Diffusion through Modified Chitosan Hydrogels.....	137
2.3.2.1. Drug-Chitosan Interactions at All-Atom Resolution	137
2.3.2.2. Coarse-Grained Simulations of Acyl-Modified Chitosan Hydrogels.....	139
2.3.2.3. Simulation of Single-Drug Migration through Modified Chitosan Hydrogels.....	143
2.3.2.4. Simulation of Dual-Drug Migration through Modified Chitosan Hydrogels	146
2.3.3. Experimental Single-Drug Release	147
2.3.3.1. Kinetic Profiles of Single-Drug Release.....	147
2.3.3.2. Equilibrium Single-Drug Release	149
2.3.3.3. Mathematical Model Fitting	150
2.3.4. Experimental Dual-Drug Release	151
2.4. Conclusions.....	153
References.....	155
Tables	161
Figures.....	166

Chapter 3: Chitosan Hydrogels for Synergistic Delivery of Chemotherapeutics to Triple Negative Breast Cancer Cells and Spheroids..... 185

Abstract.....	186
3.1. Introduction.....	187
3.2. Materials and Methods.....	190
3.2.1. Materials	190
3.2.2. Modification of Chitosan	190
3.2.3. Single-Drug Loading and Release	191
3.2.4. Dual-Drug Loading and Release.....	192
3.2.5. 2-D Cell Culture.....	193
3.2.6. 2-D Cell Viability Assay.....	193
3.2.7. 3-D Spheroid Culture	194
3.2.8. 3-D Spheroid Assay	194
3.2.9. Statistical Analysis.....	195
3.3. Results.....	195
3.3.1. Single-Drug Loading and Release Studies	195
3.3.2. Optimization of Dual-Drug Loading and Release	196
3.3.3. 2-D <i>In vitro</i> Viability Assay	197
3.3.4. 3-D Spheroid Assay	198
3.4. Discussion	201
3.4.1. Single-Drug Loading and Release Studies	201
3.4.2. Dual-Drug Loading and Release Studies.....	201
3.4.3. <i>In vitro</i> 2-D and 3-D Viability Assays.....	202
3.5. Conclusions.....	203
References.....	205
Figures.....	209

Chapter 4: Modified Graphene Oxide (GO) Particles in Peptide Hydrogels: A Hybrid System Enabling Scheduled Delivery of Synergistic Combinations of Chemotherapeutics.....	216
Abstract.....	217
4.1. Introduction.....	218
4.2. Materials and Methods.....	221
4.2.1. Materials	221
4.2.2. Synthesis of GO Particles	222
4.2.3. Surface Modification of GO Particles.....	223
4.2.4. DOX Loading and Release Screening Studies.....	223
4.2.5. Synthesis of (tGO) Particle Library	224
4.2.6. DOX Loading and Release from tGO Particle Library	225
4.2.7. Molecular Dynamics (MD) Simulations of tGO	226
4.2.8. Preparation of Max8 Hydrogel and tGO-Max8 Composite.....	229
4.2.9. Dual-Drug Release from tGO-Max8 Composite	229
4.2.10. Cell Culture.....	230
4.2.11. Cell Viability Assay	230
4.2.12. Statistical Analysis.....	231
4.3. Results and Discussion	231
4.3.1. Synthesis and Characterization of Modified Graphene Oxide (GO) and DOX Loading and Release Screening Studies	231
4.3.2. TREN-modified GO (tGO) Characterization.....	233
4.3.3. Experimental and <i>in silico</i> Evaluation of DOX Adsorption on tGO	234
4.3.4. Evaluation of DOX Release from tGO	237
4.3.5. Release of GEM and DOX from tGO-Max8 Composite.....	240
4.3.6. <i>In vitro</i> Characterization	242
4.4. Conclusions.....	243
References.....	246
Tables.....	256
Figures.....	258

Chapter 5: Inducible Conformation-Controlled Protein-Binding Affinity in Azobenzene-Cyclized Peptides.....	270
Abstract.....	271
5.1. Introduction.....	272
5.2. Materials and Methods.....	275
5.2.1. Materials	275
5.2.2. Peptide Synthesis	276
5.2.3. Peptide Photo-isomerization	277
5.2.4. Circular Dichroism.....	278
5.2.5. Binding Affinity using Surface Plasmon Resonance (SPR)	278
5.2.6. <i>In silico</i> Design of VCAM1-binding Peptides.....	279
5.2.7. Cell Culture and VCAM1 Expression	282
5.2.8. RT-qPCR Quantification of VCAM1 Expression	283
5.2.9. Cell-labeling with cycloAZOB[G-VHAKQHRN-K*].....	283
5.2.10. Cell Imaging.....	284
5.3. Results and Discussion	285

5.3.1. Azobenzene-cyclized Peptide Design.....	285
5.3.2. <i>In silico</i> Design of VCAM1-binding Peptides.....	286
5.3.3. Characterization of Azobenzene-cyclized Peptides.....	289
5.3.4. Binding Affinity by Surface Plasmon Resonance (SPR).....	293
5.3.5. Cell-labeling with cycloAZOB[G-VHAKQHRN-K*].....	293
5.4. Conclusions.....	294
References.....	296
Tables.....	304
Figures.....	308
Chapter 6: Synthetic Platelet Microgels Containing Fibrin knob B Mimetic Motifs	
Enhance Clotting Responses.....	318
Abstract.....	319
6.1. Introduction.....	320
6.2. Materials and Methods.....	322
6.2.1. Ultra-low Crosslinked (ULC) Microgel Synthesis and Characterization	322
6.2.2. Construction of FAMCY Particles by Peptide Conjugation on ULC Microgels.....	324
6.2.3. Evaluation of Fibrin Clot Structure in the presence of FAMCYs	324
6.2.4. Determination of Fibrin Clot Polymerization and Stability in the presence of FAMCYs.....	325
6.2.5. Analysis of FAMCY Hemostatic Ability <i>in vivo</i>	326
6.2.6. Statistical Analysis.....	327
6.3. Results.....	328
6.3.1. FAMCYs Increase Clot Density at Optimal Concentrations	328
6.3.2. Influence of Particle Size and Acrylic Acid Content on Fibrin Clot Density.....	329
6.3.3. Fibrin Clot Stability is Increased in the presence of an Optimal Concentration of FAMCYs.....	332
6.3.4. FAMCYs Decrease Blood Loss and Increase Fibrin Incorporation at Wound Sites in a Liver Laceration Model of Traumatic Injury	333
6.4. Discussion	334
6.5. Conclusions.....	337
References.....	339
Figures.....	341
Chapter 7: Conclusions and Future Work..... 348	
7.1. Summary	349
7.2. Future Work	351
References.....	352

LIST OF TABLES

Table 2.1	Empirical models of drug diffusion used to fit the release profiles for DOX and GEM from acetyl-, butanoyl-, and heptanoyl-chitosan hydrogels	161
Table 2.2	Number and (percentage of total) of non-bonded interactions observed between drug molecules and chitosan chains (backbone and modifications) in the different chitosan networks over the drug molecules trajectories during the simulation; where DOX molecules are treated as a group so that any given chitosan or modification site can only contribute one contact. In the table, low represents $\chi = 16\%$ for both systems, and high represents $\chi = 50\%$ and 32% for acetyl- and butanoyl- modified systems, respectively	161
Table 2.3	Summary of R^2 values obtained by fitting the empirical models of drug diffusion to the data of DOX and GEM release from acetyl-chitosan gels.....	162
Table 2.4	Summary of R^2 values obtained by fitting the empirical models of drug diffusion to the data of DOX and GEM release from butanoyl-chitosan gels	163
Table 2.5	Summary of R^2 values obtained by fitting the empirical models of drug diffusion to the data of DOX and GEM release from heptanoyl-chitosan gels.....	164
Table 2.6	Fitting parameters derived from the Korsmeyer-Peppas model for GEM and DOX released from acetyl-modified chitosan gels.....	165
Table 2.7	Fitting parameters derived from the Korsmeyer-Peppas model for GEM and DOX released from butanoyl-modified chitosan gels	165
Table 4.1	Partial charges for major functional groups	256
Table 4.2	Loading of DOX on GO and tGO particles ($\text{mg DOX mg}^{-1} \text{ GO}$). Error represents 99% C.I. ($n \geq 3$).....	256
Table 4.3	Percent release of DOX from GO and tGO in 10 mM PBS pH 5 after 72 hr and 650 hr, for particles loaded in acidic, neutral, basic and high ionic strength (PBS) conditions. Error represents 99% C.I. ($n \geq 3$).....	257
Table 4.4	Percent release of DOX from GO and tGO in 10 mM PBS pH 7.4 after 72 hr and 650 hr, for particles loaded in acidic, neutral, basic and high ionic strength (PBS) conditions. Error represents 99% C.I. ($n \geq 3$).....	257
Table 5.1	SiteMap parameters for the top five scored potential VCAM1 binding pockets. All scores are unitless unless otherwise noted	304

Table 5.2	Structure of 25 variants of the VHPKQHR precursor in the azobenzene-cyclized form cyclo _{AZOB} [G-VH(X)KQHR(Z)-K]-GSG as both <i>cis</i> and <i>trans</i> isomers, and corresponding values of their hydrodynamic radius (R_h) and the root mean square deviation (RMSD). Note: the GSG spacer is abstracted for clarity	305
Table 5.3	Structure of the peptide-VCAM1 complexes formed by docking azobenzene-cyclized peptide variants 1-4, 6-11, 14, 15, 17-20, 22, and 24 (Table 5.1) onto the putative binding sites S1-S5 of VCAM1	306
Table 5.4	Average thickness of the SAM and SAM-peptide monolayers, and corresponding peptide density determined by ellipsometry	307
Table 5.5	Values of $\Delta G_{B,Trans}$, $\Delta G_{B,Cis}$, and $ \Delta\Delta G_B $ of the interaction between VCAM1 and cyclo _{AZOB} [G-VHAKQHRP-K*], cyclo _{AZOB} [G-VHNKQHRP-K*], cyclo _{AZOB} [G-VHPKQHRS-K*], cyclo _{AZOB} [G-VHAKQHRN-K*], cyclo _{AZOB} [G-VHNKQHRS-K*], cyclo _{AZOB} [G-VHPKQHRP-K*], and VHPKQHR determined by fitting the VCAM1 adsorption data obtained from the SPR sensorgrams to a Langmuir isotherm. The “---” indicates that no accurate SPR reading could be obtained	307

LIST OF FIGURES

- Figure 1.1 Overview of the substrate families, fabrication technologies, and applications of peptides, proteins, and polysaccharides in biomedical engineering 118
- Figure 1.2 Structures of polysaccharides utilized as substrates in drug delivery, tissue engineering and regenerative medicine: **(A)** hyaluronic acid, **(B)** alginic acid, **(C)** pectin, **(D)** chitosan, **(E)** dextran, and **(F)** cellulose. Native functional groups used for modification are highlighted, including carboxyl and primary amine groups 119
- Figure 1.3 Structures of natural polypeptides utilized as substrates in drug delivery, tissue engineering, and regenerative medicine: **(A)** collagen (Protein Data Bank, PDB ID: 1BKV), **(B)** gelatin, **(C)** fibrinogen (PDB ID: 3GHG), **(D)** keratin 1/10 (PDB ID: 4ZRY), **(E)** keratin 5/14 (PDB ID: 3TNU), **(F)** laminin (PBD ID: 5XAU), and **(G)** silk fibroin (PDB ID: 3UAA). The higher-order morphology directly impact functionality, *e.g.*, tertiary helical structure of collagen, especially in tissue growth and regeneration 120
- Figure 1.4 Structures of synthetic polypeptides utilized as substrates in drug delivery, tissue engineering, and regenerative medicine: **(A)** KLD (Lys-Leu-Asp), **(B)** EAK (Glu-Ala-Lys), **(C)** MAX1 (PDB ID: 2NIE), **(D)** R₃(AKALTEL)₃, **(E)** peptide amphiphile [C₁₆]-VVVAAAKKKK, **(F)** ELP (VKV₆F), **(G)** cyclic peptide QDAEDAQDACDA, **(H)** G-RGD-G 121
- Figure 1.5 Self-assembly of monomer peptides (random coil, α -helix, β -sheet, and peptide amphiphile) into ordered assemblies and subsequently into nanostructures (nanosheet, nanotube, micelle, and nanofilament) 122
- Figure 1.6 Fabrication techniques to convert polysaccharides into hydrogel substrates for tissue engineering and regenerative medicine: **(A)** electrostatic interaction, **(B)** solvent removal, **(C)** chemical crosslinking, **(D)** salt-mediated non-covalent crosslinking, **(E)** reaction of an NHS-ester with a primary amine forming an amide bond, **(F)** thiol-ene Michael addition forming a thioether bond, **(G)** alkyne-azide “click” reaction forming a triazole bond, **(H)** reaction of an aldehyde and a primary amine forming a Schiff base (imine bond) followed by “reductive amidation” forming a secondary amide bond, and **(I)** UV-catalyzed reaction of acrylic groups resulting in an aliphatic linkage 123
- Figure 2.1 Comparison of gel fraction for acetyl-, butanoyl-, and heptanoyl-chitosan gels prepared using base chitosan polymers with molecular weights of 15 and 50-190 kDa. Data represent mean \pm 95% C.I. ($n \geq 12$) 166

Figure 2.2 Lennard-Jones and Coulombic contribution to the DOX-modification group interaction energy for (a) acetyl-chitosan and (b) butanoyl-chitosan; and Lennard-Jones and Coulombic contribution to the DOX-backbone interaction energy for (c) acetyl-chitosan and (d) butanoyl chitosans at different χ	167
Figure 2.3 Lennard-Jones and Coulombic contribution to the GEM-modification group interaction energy for (a) acetyl-chitosan and (b) butanoyl-chitosan; and Lennard-Jones and Coulombic contribution to the GEM-backbone interaction energy for (c) acetyl-chitosan and (d) butanoyl chitosans at different χ	168
Figure 2.4 Hydrogen bond contacts between DOX and modification groups in a (a) acetyl-modified and (b) butanoyl-modified chitosan gel; and hydrogen bond contacts between DOX and the backbone in a (c) acetyl-modified and (d) butanoyl-modified chitosan gel at different degrees of modification.	169
Figure 2.5 All-atom simulations depicting the interactions between DOX (cyan) and chitosan (grey and yellow) for (a) acetyl-modified and (b) butanoyl-modified chitosans.....	169
Figure 2.6 All-atom and coarse-grained representations of (a) DOX, (b) GEM, (c) unmodified glucosamine monomer, (d) acetyl-glucosamine, (e) butanoyl-glucosamine, and (f) heptanoyl-glucosamine.....	170
Figure 2.7 Radial distribution functions correspondence between the all-atom simulations and coarse-grained simulations interaction sites for (a) coarse-grained site A with A (Figure 2.6), (b) coarse grained site A with B, (c) coarse-grained site A with modification site M, and (d) coarse-grained site A with water bead.....	171
Figure 2.8 Representative simulation snapshots of chitosan hydrogels with a blocky modification pattern for (a) 16% acetylation, (b) 50% acetylation, (c) 16% butanoation, and (d) 32% butanoation	172
Figure 2.9 Representative simulation snapshots of chitosan hydrogels with evenly-spaced modification pattern for (a) 16% acetylation, (b) 50% acetylation, (c) 16% butanoation, and (d) 32% butanoation	172
Figure 2.10 Schematic cluster/channel structure formed by hydrophobically-modified chitosan, wherein the micellar aggregates (red) comprise chitosan segments with high degree of hydrophobic modification, and the bridges (green) represent chitosan segments with low degree of modification [68]	173

Figure 2.11 Pore size distribution functions for (a) evenly-spaced acetyl-chitosan, (b) blocky acetyl-chitosan, (c) evenly-spaced butanoyl-chitosan, and (d) blocky butanoyl-chitosan	173
Figure 2.12 Drug diffusion constants <i>vs.</i> χ for single-drug migration across different chitosan networks for evenly-spaced (black) and blocky (red) modification patterns for: (a) GEM and (b) DOX in acetyl-chitosan, and (c) GEM and (d) DOX in butanoyl-chitosan.....	174
Figure 2.13 Snapshot of DOX migration through: (a) acetyl-chitosan networks at low χ (16%); (b) acetyl-chitosan networks at high χ (50%); (c) butanoyl-chitosan network at low χ (16%); (d) butanoyl-chitosan networks at high χ (32%), where the chitosan backbone is represented by red beads, modifications are represented by yellow beads, and DOX is represented by black beads	175
Figure 2.14 Mean-squared displacement (MSD) plot <i>vs.</i> time for diffusion of DOX through the blocky-modified chitosan network at $\chi = 32\%$, where DOX-Captured refers to DOX that becomes entrapped within a cluster and DOX-Free refers to DOX that remains in the pores of the cluster/channel morphology during the simulation	175
Figure 2.15 Drug diffusion constants <i>vs.</i> χ for dual-drug migration across different chitosan networks: (a) GEM in acetyl-chitosan, (b) DOX in acetyl-chitosan, (c) GEM in butanoyl-chitosan, and (d) DOX in butanoyl-chitosan	176
Figure 2.16 Radial distribution functions of GEM around the center of mass of DOX in acetyl-chitosan networks with (a) evenly-spaced and (b) blocky modification, and in butanoyl-chitosan networks with (c) evenly-spaced and (d) blocky modification	177
Figure 2.17 Release profiles of DOX (triangles) and GEM (squares) from chitosan hydrogels at $\chi = 25\%$ of (a) acetyl at 72 hr, and (b) butanoyl at 72 hr, (c) acetyl at 1 hr, and (d) butanoyl at 1 hr. Data represent mean \pm 99% C.I. ($n \geq 3$)	178
Figure 2.18 Release profiles of DOX (triangles) and GEM (squares) from heptanoyl-modified chitosan hydrogels at $\chi = 25\%$. Data represent mean \pm 99% C.I. ($n \geq 3$)	179
Figure 2.19 Release profiles of (a) GEM and (b) DOX from acetyl-chitosan hydrogels. Data represent mean \pm 99% C.I. ($n \geq 3$).....	179
Figure 2.20 Release profiles of (a) GEM and (b) DOX from butanoyl-chitosan hydrogels. Data represent mean \pm 99% C.I. ($n \geq 3$)	180

Figure 2.21 Release profiles of (a) GEM and (b) DOX from heptanoyl-chitosan hydrogels. Data represent mean \pm 99% C.I. ($n \geq 3$)	180
Figure 2.22 Equilibrium release percent of DOX (triangles) and GEM (squares), and GEM/DOX molar ratio (red circles) vs. χ for (a) acetyl-chitosan and (b) butanoyl-chitosan. Data represent mean \pm 99% C.I. ($n \geq 3$)	181
Figure 2.23 Equilibrium release percent of DOX (black triangles) and GEM (black squares), and GEM/DOX molar ratio (red circles) vs. χ for heptanoyl-chitosan. Data represent mean \pm 99% C.I. ($n \geq 3$)	181
Figure 2.24 The K values obtained from the Korsmeyer-Peppas model for single GEM (black) and DOX (red) release vs. χ in (a) acetyl-modified chitosan gels and (b) butanoyl-modified chitosan gels. Data represent mean \pm 99% C.I. ($n \geq 3$)	182
Figure 2.25 Molar ratio of GEM to DOX released from dually loaded acetyl-chitosan hydrogels. Data represent mean \pm 99% C.I. ($n \geq 3$)	182
Figure 2.26 Molar ratio of GEM to DOX released from dually loaded butanoyl-chitosan hydrogels. Data represent mean \pm 99% C.I. ($n \geq 3$)	183
Figure 2.27 Molar ratio of GEM to DOX released from dually loaded heptanoyl-chitosan hydrogels. Data represent mean \pm 99% C.I. ($n \geq 3$)	183
Figure 2.28 Equilibrium dual-drug release percent of DOX (triangles) and GEM (squares), and GEM/DOX molar ratio (red circles) vs. χ for (a) acetyl-chitosan and (b) butanoyl-chitosan. Data represent mean \pm 99% C.I. ($n \geq 3$)	184
Figure 2.29 K values obtained from the Korsmeyer-Peppas model for GEM (black) and DOX (red) released vs. χ from (a) acetyl-modified chitosan gels and (b) butanoyl-chitosan gel. Data represent mean \pm 99% C.I. ($n \geq 3$)	184
Figure 3.1 Loading of (A) DOX and (B) GEM as a function of loading concentration utilized. Release profiles for (C) DOX at various loading concentrations: $0.5 \mu\text{g mL}^{-1}$ (squares), $1 \mu\text{g mL}^{-1}$ (circles), and $2 \mu\text{g mL}^{-1}$ (triangles), and (D) GEM at various loading concentrations: $25 \mu\text{g mL}^{-1}$ (squares), $50 \mu\text{g mL}^{-1}$ (circles), and $100 \mu\text{g mL}^{-1}$ (triangles). Data are represented as mean \pm S.D. ($n \geq 3$); ** represents $p < 0.01$, as obtain from the Students t-test.....	209
Figure 3.2 The corresponding doses from release studies for (A) DOX and (B) GEM at 72 hr. Data are represented as mean \pm S.D. ($n \geq 3$); ns and * represent no statistical significance and $p < 0.05$, respectively, as obtained from the Student's t-test.....	210

Figure 3.3 (A) Amounts of DOX and GEM loaded on ACS hydrogels using either diluted drug solutions ($25 \mu\text{g mL}^{-1}$ GEM and $0.5 \mu\text{g mL}^{-1}$ DOX, grey column) or concentrated drug solutions ($50 \mu\text{g mL}^{-1}$ GEM and $1 \mu\text{g mL}^{-1}$, black column). (B) Release profiles of DOX (red) and GEM (black) from the ACS hydrogels loaded with either concentrated (circles) or diluted (squares) drug solutions. Data are represented as mean \pm S.D. ($n \geq 3$); ns and * represent no statistical significance and $p < 0.05$, respectively, as obtained from the Student's t-test	210
Figure 3.4 The corresponding doses from release studies for a low concentration ($25 \mu\text{g mL}^{-1}$ GEM and $0.5 \mu\text{g mL}^{-1}$ DOX) and a high concentration ($50 \mu\text{g mL}^{-1}$ GEM and $1 \mu\text{g mL}^{-1}$ DOX) at 72 hr. Data are represented as mean \pm S.D. ($n \geq 3$); * represents $p < 0.05$, as obtained from the Student's t-test	211
Figure 3.5 (A) Dose-response curves for free DOX (red), free GEM (black), 10:1 molar ratio free drug combination of GEM/DOX (blue), and $\geq 10:1$ molar ratio of DOX and GEM released from the ACS hydrogel; (B) Cytotoxicity of the ACS hydrogel relative to untreated cells (control)	211
Figure 3.6 Change in volume of spheroids corresponding to a selected dose of treatment. The control (black) and ACS hydrogel (grey) represent spheroids receiving no treatments and exposure to 150 mg of unloaded hydrogel, respectively. Treatments were performed using drug concentrations of $1.67 \mu\text{M}$ GEM (green), $2.5 \mu\text{M}$ DOX (red), $20 \mu\text{M} + 2 \mu\text{M}$ DOX as free drugs concurrently administered (blue), and $20.8 \mu\text{M}$ GEM + $2.08 \mu\text{M}$ DOX released from the ACS hydrogel (orange). Data are represented as mean \pm S.D. ($n \geq 3$); ns represents no statistical significance, * and ** represent $p < 0.05$, and $p < 0.01$, respectively, as obtained from the Student's t-test	212
Figure 3.7 Images of spheroids corresponding to the conditions utilized in Figure 3.6; all grey-scale images represent spheroids prior to treatment and all fluorescent images represent spheroids following treatment; green and red, represent viable and non-viable cells, respectively. (A) and (B) are the control, (C) and (D) are the unloaded hydrogel, (E) and (F) represent treatment with $1.67 \mu\text{M}$ GEM, (G) and (H) represent treatment with $2.5 \mu\text{M}$ DOX, (I) and (J) represent treatment with $2.0 \mu\text{M}$ DOX and $20.0 \mu\text{M}$ GEM concurrently administered, and (K) and (L) represent treatment with $2.08 \mu\text{M}$ DOX and $20.8 \mu\text{M}$ GEM released from the ACS gel. The scale bar in all images is $400 \mu\text{M}$	213
Figure 3.8 Tumor organoid volume change observed as a function of drug concentration for free GEM (green), free DOX (red) free GEM:DOX concurrently administered at a molar ratio of 10:1 (blue), and GEM:DOX released from ACS hydrogel at molar ratio $\geq 10:1$. The desired therapeutic	

window is indicated by the black box. Data are represented as mean \pm S.D.
(n \geq 3) 214

Figure 3.9 Dependence of drug concentration of spheroid volume for: (A) GEM (1 – 3.33 μ M; 2 – 6.67 μ M; 3 – 13.3 μ M; 4 – 26.7 μ M; 5 – 53.3 μ M), (B) DOX (1 – 0.156 μ M; 2 – 0.313 μ M; 3 – 0.625 μ M; 4 – 1.25 μ M; 5 – 5.0 μ M), (C) DOX and GEM free in solution (1 – 0.25 μ M DOX + 2.5 μ M GEM; 2 – 0.5 μ M DOX + 5 μ M GEM; 3 – 1.0 μ M DOX + 10.0 μ M GEM; 4 – 2.0 μ M DOX + 20.0 μ M GEM; 5 – 4.0 μ M DOX + 40.0 μ M GEM), (D) DOX and GEM released from the ACS hydrogel (1 – 0.42 μ M DOX + 4.2 μ M GEM; 2 – 0.83 μ M DOX + 8.3 μ M GEM; 3 – 1.25 μ M DOX + 12.5 μ M GEM; 4 – 1.67 μ M DOX + 16.7 μ M GEM; 5 – 2.08 μ M DOX + 20.8 μ M GEM).
The scale bar in all images is 400 μ m 215

Figure 4.1 Design and proposed mechanism of dual release of DOX and GEM from the hybrid system comprising modified GO nanoparticles suspended in a Max8 hydrogel. The combination of drug release at controlled relative molar ratio and kinetics enhances the inherent synergism of DOX and GEM beyond the simple effect of codelivery 258

Figure 4.2 SEM of GO particles with an average size of 800 nm 258

Figure 4.3 Initial screening studies of (A) DOX loading on GO particles with different chemical modifications (listed in the abscissa); (B) DOX release from modified GO particles with 500 hr. Error bars represent mean \pm 99% C.I. (n \geq 3). ** indicates p < 0.01, and *** represents p < 0.001, as obtained from a Student's t-test 259

Figure 4.4 DOX release from modified GO particles with 100 hr. Data represent mean \pm 99% C.I. (n \geq 3) 259

Figure 4.5 The effect of molar ratio TREN used for tGO reactions on ζ potential (black) and the corresponding concentration of amine groups (red). Data represent mean \pm S.D. (n \geq 3) 260

Figure 4.6 FTIR analysis of native GO and tGO particles and corresponding model structure 260

Figure 4.7 (A) Loading of DOX onto tGO particles as a function of ζ potential at different loading conditions: Milli-Q water (titrated with HCl or NaOH) at pH 4 (squares), pH 6 (circles), and pH 9 (triangles) and PBS at pH 7.4 (diamonds), where data represent mean \pm 99% C.I. (n \geq 3); (B) Comparison between the values of DOX loading measured at pH 6 (black) vs. predicted by the MD simulations at pH 6.1 (red). The experimental data is presented as mean \pm 99% C.I. (n \geq 3), while the data from the simulations is

presented as mean \pm S.D. for $n \geq 4$ independent simulations with distinct initial configurations.....	261
Figure 4.8 Snapshots from DOX (red frame) loading on TREN- (blue frame) modified GO (grey frame) and the dispersion of Cl^- ions (cyan balls) on (A) native GO ($\zeta = -36.5$ mV), (B) tGO ($\zeta = -8.9$ mV), (C) tGO ($\zeta = 10.1$ mV), and (D) tGO ($\zeta = 20.7$ mV).....	262
Figure 4.9 Release profiles at pH 5 from DOX/tGO particles loaded at (A) pH 4, (B) pH 6, (C) pH 9, and (D) PBS at pH 7.4. Data represent mean \pm 99% C.I. ($n \geq 3$)	263
Figure 4.10 Release profiles at pH 7.4 from DOX/tGO particles loaded at (A) pH 4, (B) pH 6, (C) pH 9, and (D) PBS at pH 7.4. Data represent mean \pm 99% C.I. ($n \geq 3$)	264
Figure 4.11 Values of DOX percent release at pH 5 after (A) 72 hr and (B) 650 hr from DOX/GO and DOX/tGO particles loaded at neutral pH and low ionic strength (squares) or high ionic strength (circles). Hashed lines are added to guide the visualization of the results. Data represent mean \pm 99% C.I. ($n \geq 3$).....	265
Figure 4.12 Values of DOX percent release at pH 7.4 after (A) 72 hr and (B) 650 hr from DOX/GO and DOX/tGO particles loaded at neutral pH and low ionic strength (squares) or high ionic strength (circles). Hashed lines are added to guide the visualization of the results. Data represent mean \pm 99% C.I. ($n \geq 3$).....	265
Figure 4.13 Snapshots from DOX (red frame) loading on TREN- (blue frame) modified GO (grey frame) and the dispersion of Cl^- ions (cyan balls) on (A) native GO ($\zeta = -36.5$ mV), (B) tGO ($\zeta = -8.9$ mV), (C) tGO ($\zeta = 10.1$ mV), and (D) tGO ($\zeta = 20.7$ mV).....	266
Figure 4.14 Release profiles of GEM from a Max8 hydrogel at 2% (w/w) (squares) and 4% (w/w) (circles). Data represent mean \pm 99% C.I. ($n \geq 3$).....	267
Figure 4.15 Microscopy images of (A) tGO particles, (B) DOX/tGO particles, (C) Max8 hydrogel, (D) tGO particles dispersed in Max8 hydrogel, (E) DOX/tGO particles dispersed in Max8 hydrogel; (1) brightfield, (2) fluorescence (absorption: 590 nm – emission: 617 nm), and (3) combined brightfield-fluorescence overlay. Scale bar represents 20 μM	267
Figure 4.16 (A) Release profiles of GEM from 2% (w/w) GEM/Max8 (black circles), DOX from free DOX/tGO particles (black squares), DOX from DOX/tGO particles embedded in a 2% (w/w) Max8 hydrogel (red squares), GEM from a 2% (w/w) GEM/Max8 hydrogel loaded with tGO particles (blue	

circles), and DOX from DOX/tGO particles embedded in a 2% (w/w) GEM/Max8 hydrogel (blue squares); **(B)** release of DOX from the system listed in panel **(A)**. Data represent mean \pm 99% C.I. ($n \geq 3$) 268

Figure 4.17 **(A)** Dose-response curves for free DOX (red), free GEM (black), DOX/tGO particles (blue), 10:1 molar ratio free drug combination of GEM/DOX (green), 10:1 molar ratio free drug combination of GEM/DOX from composite system with 5 μ L (purple), and 12.5 μ L (yellow) of DOX/tGO-GEM/Max8 composite gel; **(B)** Dose-response curves for DOX (squares), DOX/tGO (triangles), and (tGO) circles); **(C)** Cytotoxicity of Max8 hydrogel (low – 5 μ L and high – 12.5 μ L) and tGO particles (low – 0.2 μ g mL $^{-1}$ and high – 14.6 μ L mL $^{-1}$) relative to untreated cells (control), and **(D)** calculated IC50 values for the various formulations and the corresponding combination index (CI). Data represent mean \pm S.D. ($n \geq 3$). ns indicates no significance and * indicates $p < 0.05$, as obtained from a Student's t-test 269

Figure 5.1 Structure of the proposed azobenzene-cyclized peptides 308

Figure 5.2 Putative peptide binding sites (S1-S5) on VCAM1 identified by performing a druggability analysis of the crystal structure of VCAM1 (PDB ID: 1VCA) using SiteMap 308

Figure 5.3 **(A)** UV-vis absorption spectra for VHGKQHRP-K* (solid), cyclo_{SUCC}[VHGKQHRP-K*] (dot-dash), and cyclo_{AZOB}[VHGKQHRP-K*] (dash); **(B)** Δ absorbance for the *cis*-induced isomer (red) and *trans*-induced isomer (blue); **(C)** *trans*-to-*cis* isomerization upon exposure to UV light (305-390 nm) and **(D)** *cis*-to-*trans* isomerization upon exposure to visible light (> 420 nm). For **(C)** and **(D)** fitted lines are solid (squares), hash (circles), dot-hast (triangles), and data are mean \pm S.D. 309

Figure 5.4 Spectral absorbance changes of 0.38 mM solution of cyclo_{AZOB}[VHGKQHRP-K*] in Milli-Q water upon exposure to UV bandpass filtered light (**A** and **B**) and subsequent LP420 filtered light (**C** and **D**). Spectra are scanned from 500 nm to 250 nm at 10 nm s $^{-1}$ and time indicates light exposure at the start of each scan 310

Figure 5.5 Representative changes of absorbance at 350 nm for 1.5 mM (**A**, **B**, **C**), 0.38 mM (**D**, **E**, **F**), and 0.15 mM (**G**, **H**, **I**) solutions of cyclo_{AZOB}[VHGKQHRP-K*] upon exposure to light filter with UV bandpass (BP 305-390 nm) and LP420 filters at different values of light intensity 311

Figure 5.6 Spectra of Dymax BlueWave 200 curing lamp and corresponding filtered outputs using UV bandpass (BP305-390) and LP420 filters 312

Figure 5.7 Reversible and repeatable <i>trans-cis</i> and <i>cis-trans</i> isomerization cyclo _{AZOB} [VHGKQHRP-K*] dissolved in MilliQ water at the concentration of 0.15 mM	312
Figure 5.8 Thermal <i>cis-to-trans</i> isomerization (relaxation) of cyclo _{AZOB} [VHGKQHRP-K*]. The red curve represents initial induction of the peptide into the <i>cis</i> conformation and the blue curve represents the recovery of the <i>trans</i> configuration. Isomerization was monitored by recording the absorbance at 350 nm of a 0.15 mM solution of peptide in MilliQ water for 48 hr, at 37°C in the dark	313
Figure 5.9 (A) Circulation dichroism (CD) spectra of cyclo _{AZOB} [VHGKQHRP-K*] peptide upon photo-induced isomerization, indication a random coil conformation, (B) CD spectra of peptide variants indicating a random coil conformation for all peptides, (C) Structure of VHPKQHR-GSG and cyclo _{SUCC} [G-VHAKQHRN-K*] peptides with an α -helix segment, and cyclo _{AZOB} [G-VHAKQHRN-K*] with random coil in both <i>trans</i> and <i>cis</i> conformation	314
Figure 5.10 SPR measurements of VCAM1:peptide K _{D,Trans} and K _{D,Cis} for (A) of cyclo _{AZOB} [G-VHAKQHRN-K*]; (B) cyclo _{AZOB} [G-VHPKQHRS-K*]; (C) cyclo _{AZOB} [G-VHAKQHRD-K*]; and (D) VHPKQHR. The data points were obtained as an average of triplicate readings.....	315
Figure 5.11 Confirmation of VCAM1 induction by LPS exposure via immunohistochemical analysis and qRT-PCR characterization. BMEC was demonstrated to express VCAM-1 when treated with IL-4, followed by LPS. LPS treatment alone showed no significant change in VCAM-1 expression. HUVEC and HDFn controls showed no increase in VCAM-1 expression with either treatment condition. Statistical analysis was performed using a 2way ANOVA with Tukey's <i>post hoc</i> comparison test with an alpha value of 0.05 (*) considered statistically significant	316
Figure 5.12 Confirmation of VCAM1 induction in BMECs by synergistic treatment with IL-4 and LPS via immunohistochemical analysis quantification. Relative intensity of tagged VCAM-1 antibody compared across different cell treatment condition aggress with RT-qPCR measurements, showing the most induction of VCAM-1 in BMECs treated with IL-4 followed by LPS. Error bars represent the standard deviation. Statistical analysis was performed using a paired t-test with an alpha value of 0.05 (*) considered statistically significant	316
Figure 5.13 cyclo _{AZOB} [G-VHAKQHRN-K*] in the <i>cis</i> conformation incubated with cells (A) expressing and (B) not expressing VCAM-1, cyclo _{AZOB} [G-VHAKQHRN-K*] in the <i>trans</i> conformation incubated with cells; (C) expressing and (D) not expressing VCAM-1, and (E) the relative intensity	

of biotin-labelled *cis/trans* cyclo_{AZOB}[G-VHAKQHRN-K*] incubated with VCAM-1⁺⁻ induced cells. Statistics were done with a 2-tailed t-test with at p value < 0.05 (*) considered statistically significant 317

Figure 5.14 IL-4/LPS treatment induced VCAM1 expression confirmed with **(A)** antibody staining, **(B)** *cis*-cyclo_{AZOB}[G-VHAKQHRN-K*] peptide, and **(C)** the colocalization of the anti-VCAM1 antibody and *cis*-cyclo_{AZOB}[G-VHAKQHRN-K*] peptide around the nucleus of the cell 317

Figure 6.1 **(1)** Intact circulating fibrinogen; **(2)** Enzymatic cleavage of fibrinopeptides by thrombin activate knobs a and b; **(3)** Activated knobs bind to corresponding holes on adjacent proteins; **(4)** Fibrin network formation 341

Figure 6.2 **(A)** Representative AFM image (top) and height trace (bottom) of 90:10 NIPAm:AAc ULC microgel; **(B)** Confocal microscopy images of clots formed with ~1 μ m, 90:10 NIPAm:AAc FAMCY particles at 1, 2, or 4 mg mL⁻¹ particle concentrations. **(C)** Fiber density, defined as the ratio of black pixels (fiber) to white pixels (negative space), is significantly enhance at a concentration of 2 mg mL⁻¹ relative to control clots formed using higher and lower concentrations of FAMCY particles. n = 3 clots per group. Scale bar = 10 μ m. *p<0.05; **p<0.01 342

Figure 6.3 **(A)** Representative atomic force microscopy dry imaging and **(B)** height traces to confirm the creation of small ~150 nm particles and medium ~450 nm 90:10 NIPAm:AAc particles; **(C)** Confocal microscopy and **(D)** fiber density quantification of clots formed in the presence of small, medium, and large 90:10 NIPAm:AAc FAMCYs at a concentration of 2 mg mL⁻¹. n = 3 clots per group. Scale bar = 10 μ m. *p<0.05 343

Figure 6.4 **(A)** Representative atomic force microscopy dry imaging and **(B)** height traces of 80:20, 85:15, 90:10 NIPAm:AAc particles to determine diameter and height. Particle diameters were measured on ImageJ and particle heights calculated from max values obtained from individual height traces. No statistical difference in diameter or height was observed between particle types of varying acrylic acid content. n ≥ 30 particles/group; **(C)** Confocal microscopy and **(D)** fiber density quantification of clots formed in the presence of ~1 μ m, 80:20, 85:15, 90:10 NIPAm:AAc FAMCYs at a concentration of 2 mg mL⁻¹. n = 3 clots per group. Scale bar = 10 μ m 344

Figure 6.5 Polymerization and degradation curves for clots formed in the presence of 1, 2, or 4 mg mL⁻¹ 1 μ m 90:10 FAMCYs (top). At the previously discovered optimal concentration of 2 mg mL⁻¹, FAMCY clots show significantly greater maximum turbidity and resistance to fibrinolysis than control clots and clots containing control peptide FAMCYs or ULCs, as illustrated by absorbance (A350) curves of clots (top) and by quantification of the area under the curves (bottom). Clots containing control peptide

FAMCYs or ULCs polymerize and degrade at rates very similar to those of control fibrin-only clots. *p < 0.05; n = 3 duplicate experiments 345

Figure 6.6 **(A)** Blood loss over time is decreased after treatment with an optimal dosage of FAMCYs; **(B)** Total blood loss is significantly decreased after treatment with an optimal dosage of FAMCYs relative to saline controls. Large (~1 μm) 90:10 NIPAm:AAc FAMCYs, control peptide FAMCYs, and ULCs were examined *in vivo*. n = 6 in saline group, n = 5 in all other treatment groups; *p<0.05; ***<0.001 346

Figure 6.7 **(A)** Immunohistochemistry of fibrin (red) at wound sites following liver laceration injury; **(B)** Quantification using ImageJ Particle Analysis to determine total area (μm^2) of fibrin-positive stain shows fibrin incorporation at wound sites is increased following treatment with FAMCY particles relative to treatment with saline or control peptide FAMCYs. Scale bar = 400 μm . n = 6 in saline group, n = 5 in all other treatment groups. *p<0.05; **p<0.01 347

CHAPTER 1

Natural and Synthetic Biopolymers in Drug Delivery and Tissue Engineering

John D. Schneible, Michael A. Daniele, and Stefano Menegatti

An adapted version of this chapter has been accepted as a textbook chapter for publication in “Advances in Biopolymers for Biomedical and Biotechnological Applications” Weinheim, Germany: Wiley-VCH; 2020.

Abstract

Natural and synthetic biopolymers represent the most diverse class of engineered biomaterials. The variety of chemical constituents, modification strategies, processing methods, and functionalities, while overwhelming at first glance, are linked by common uses in drug delivery and tissue engineering. This chapter intends to highlight the main features of biopolymers for such use by surveying the last decade of publications on natural and synthetic polypeptides and polysaccharides. Particular focus is devoted to the development of systems for the delivery of anticancer therapeutics, the engineering of tissue grafts, and *in vivo* regeneration. For peptides, we present numerous examples of self-assembling sequences as drug delivery vehicles and tissue scaffolds, as well as cell-binding and tissue-penetrating sequences that promote targeted delivery and tissue integration. We then retrace the same applications, with the leading role being played by polysaccharides, in particular dextran, chitosan, hyaluronate, and cellulose. The similarities in processing and utilizing polypeptides and polysaccharides across these applications bring the “parallel lives” of these materials out of the massive body of literature to the full fruition of the reader.

1.1. Introduction

Through the last three decades, hydrogels for biomedical applications have grown into a vast class of materials, featuring a large variety of ingredients, fabrication techniques, and uses [1-3]. Together with a massive body of literature, the value of hydrogels is illustrated by myriad commercial products, ranging from drug delivery to tissue engineering and regenerative medicine. Key to their success is the high biocompatibility and physicochemical diversity, which enable functional adaptation to many different physiological microenvironments [4, 5]. Herein, we survey the reports on peptides and polysaccharides, in particular focusing on chemical constituency, structure-function relations, and their impact on drug delivery and tissue engineering [6-12].

Peptide and polysaccharide hydrogels have gained popularity as biocompatible and biodegradable drug delivery vectors [13-18], as micro-/nano-particles [19-21], micelles [22-24], and bulk hydrogels (**Figure 1.1**) [25-27]. Peptides have gained popularity for their ability to tune drug loading and release the payload in a stimuli-/environment-controlled manner [15, 17, 18]. Peptides can also provide accumulation and internalization of bioactive ingredients at target sites by acting as site-selective ligands and cell-penetrating vectors [28-34]. Similarly, polysaccharides have been extensively studied as drug delivery systems [35], owing to their wide availability [36-49], physicochemical diversity, and high number of reactive groups per chain, which enable facile chemical modification for tuning drug loading and release [35, 50, 51], stability [52, 53], and tissue adhesion [54].

These materials have also been utilized to engineer scaffolds for tissue engineering and wound healing [55- 60]. A wide variety of fabrication techniques (*e.g.*, phase separation [61-64], 3D printing [65, 66], supercritical fluid technology [67, 68], porogen leaching [64, 69-72], and micro-patterning techniques [64, 73-75]) have been combined with a host of crosslinking and

functionalization chemistries (*e.g.*, mechanical robustness, display and storage of growth factors, and stimuli-responsiveness [76]) to generate hydrogels with biomimetic morphology, mechanical properties, and biochemical functionality. These systems have been demonstrated for tissue engineering and repair *in vivo*, as well as in surgical applications as filling materials and implants [77-82]. While an exhaustive treatment of these topics is not permitted by the vastness of the field, we will nonetheless attempt to provide a portrait of the technologies and applications centered around peptides and polysaccharides that hold promise to improve human health.

1.2. Synthetic and Natural Substrates

Polysaccharides and polypeptides can be derived from renewable resources or be obtained synthetically [83, 84]. The polysaccharides of bioengineering value include plant exudates and algal derivatives (alginate, galactans, carrageenan), animal (chitin, chitosan [CN], glycosaminoglycan, hyaluronic acid [HA]), and microbial (dextran [Dex], gellan gum, pullulan, xanthan gum, and cellulose) polysaccharides (**Figure 1.2**) [85-87]. Their peptide counterparts include collagen, elastin, silk fibroin, fibrin, fibrinogen, fibronectin, gelatin, laminin, vitronectin, keratin, silk, and adhesive proteins (**Figure 1.3**) [88, 89]. The introduction of synthetic routes to produce peptides and oligosaccharides has impressed considerable acceleration to the science and engineering of biomedical materials. Using commercially available reagents and equipment, peptides of up to 50 residues can be routinely prepared with high yield and reproducibility [90]. *De novo* synthesis enables a superior control of chemical identity compared with natural materials, which often lack chemical definition and can contain harmful contaminants that are difficult to define and remove. Further, synthetic biopolymers can introduce non-natural moieties that provide advantageous functionalities, such as conjugation to other biomolecules, adhesion to inorganic

materials (*e.g.*, metal and silica), and radioactivity or fluorescence [91]. The synthesis of polysaccharides [92-94], while conceptually similar to that of peptides, is considerably more challenging, due to the stereospecific linkage of sugar monomers. The introduction of novel orthogonal protection/deprotection schemes [95-98] has enabled the synthesis of oligosaccharides and condensed polysaccharides, which have been successfully utilized in as diagnostics [99, 100], vectors for drug delivery [101, 102] and gene therapy [103-105], and tissue engineering [14].

1.3. Applications of Natural and Synthetic Polypeptides

1.3.1. Drug Delivery Vehicles

Hydrogels for drug delivery generally comprise one or more active ingredients either dispersed into or covalently bound to a polymer [25, 106, 107] whose properties determine the pharmacokinetics of the therapeutic payload [108-113]. The drug is released either by diffusion through the polymer [27], by degradation of the polymer [30, 31], or by loss of the supramolecular structure of the carrier [114, 115]. Peptides have been extensively utilized as building blocks for self-assembling 3D nanostructures (*e.g.*, nanovesicles, nanofibers, nanotubes, nanoribbons) and hydrogels for drug delivery [12, 15, 17, 18, 116-119]. Notably, peptide-based systems are superior to traditional vehicles (*e.g.*, liposomes), as they confer higher drug loading and stabilization, lower leakage, sustained release, and specific targeting and permeation to cells [120]. Further, the behavior of self-assembled peptide structures can be fine-tuned through the amino acid make-up [117, 121-123] or adding polyelectrolytes or templates, [124, 125] to become responsive to pH [126, 127], ionic strength [128, 129], and temperature [130, 131] of the environments. Peptide-based drug delivery vehicles can be classified into (**Figure 1.4**):

1.3.1.1. Ultra-small Peptides

These inexpensive, short peptide sequences are widely utilized to form self-assembled hydrogels. For example, KLD and EAK motifs have been used to construct hydrogels capable of controlled release of anticancer drugs such as doxorubicin (DOX) [132] and ellipticine (EPT) [133]. Environment-responsive small peptides, such as V₆K₂ and L₆K₂, are of particular interest for their ability to self-assemble in structures capable of morphing from nanotubes to nanovesicles [134]. These have been utilized for delivering anticancer drugs (DOX and paclitaxel [(PTX)]) [135] and gene therapeutics [134, 136, 137]. Similar nanovesicles, assembled with dipeptides VE, LE, and G_{n-p}E (G_{n-p}: n-propyl glycine) were utilized to encapsulate DOX and other biomolecules to be released in response to calcium ions within the target cells [138]. Tetrapeptides GAIL and GFIL served as building blocks to construct hydrogels with thermo- and pH-responsive behavior, which were utilized to encapsulate DOX and afforded controlled release with 90% release of DOX after 45 hours [139], showing good therapeutic effect together and non-detectable side effects.

1.3.1.2. β-Scaffolds

β-sheet structures originating from repeated peptide domains have been observed in several natural proteins such as silk fibroin [140-142], egg-shell proteins [143], and adenovirus fiber protein [144]. Synthetic peptides comprising alternated hydrophobic and charged amino acids (*e.g.*, EAK16-II, AEAEAKAKAEAEAKAK) [133] also assemble into β-sheet structures whose properties can be controlled by tuning the ratio of enantiomeric peptides. These materials have been extensively utilized for drug delivery [145, 146], owing to their high loading capacity for hydrophobic drugs and their tissue -penetration ability [147-152]. Notable examples include β-sheet fibrils of FEFQFNFK for sustained release of EPT to MCF-7 and A549 cells [153];

hydrogel-forming β -sheet peptide KRRMKWKKK for sustained release of DOX and Smac-(second mitochondria-derived activator of caspases)-derived pro-apoptotic peptide (SDPP) [132]; β -hairpin peptide VKVKVKV^DPPTKVEVKVKV [154], which self-assembles in response to an increase in the ionic strength of the medium [155], to deliver poorly soluble anti-cancer drugs [156]; or Nap-GFFYGRGD, which was used to encapsulate and release curcumin to HepG2 liver carcinoma cells in a mouse model [157]. Among β -sheet-forming synthetic peptides, the most widely utilized sequences are RADA16-I16 and RADA16-II16. These peptides form nanofibers of 10-60 nm in size and have been utilized for the sustained release of cytotoxic drugs [158, 159], in particular anticancer therapeutics [146, 160, 161], protein therapeutics, and growth factors [10, 162-168]. Prolonged release of growth factors makes RADA16-based substrates ideal for cell culture [164, 169], tissue repair [170], and tissue engineering [171, 172], as will be discussed later.

1.3.1.3. α -Scaffolds

α -helical peptides consist of repeats of the heptad $X_1X_2X_3X_4X_5X_6X_7$, wherein X_1 and X_4 are hydrophobic amino acids, and X_5 and X_7 are charged amino acids [173-175]. The hydrophobic interaction between X_1 and X_4 , and the electrostatic interaction between X_5 and X_7 confer these peptides with the coiled α -helical structure [176-178]. Positions X_2 and X_3 can be replaced with amino acids that provide weaker interactions, resulting in more flexible α -helices that form physical hydrogels, featuring smaller and softer bundles of fibers [179]. This rationale is exemplified by numerous examples, such as the peptides $A_3(LET\text{LAKA})_3$ [180], α FFP (QLAREL)₄ [181], and $R_3(AKALTEL)_3$ [182], the hydrogelating self-assembling fibers (hSAF) peptides [179], the 30-mer GALA peptide [183], and the coiled-coil pentamers (*e.g.*,

QLAREL(QQLAREL)₄) [184-187]. α -helical peptides have been extensively characterized for their ability to form supra-molecular, [18] structures (*e.g.*, nanofibers and nanofilaments), [188-191] but have only minimally been applied for drug delivery with most applications focusing on gene delivery, showing efficient gene loading and transfection in target cells [183, 192, 193].

1.3.1.4. Peptide Amphiphiles (APs)

These di-block biopolymers comprise a hydrophobic peptide tail, rich in A, G, L, and F amino acids, and a hydrophilic bioactive peptide head, rich in D, E, H, and R amino acids. These sequences self-assemble into nanostructured hydrogels that demonstrated great potential in drug delivery [12, 194]. For example, the lipid-like peptides G₄DD, G₆DD, G₈DD, A₆D, A₆K, and KA₄ sequences, self-assemble into nanostructures at their critical aggregation concentration, and have been utilized as drug delivery vectors [134, 194, 195]. When the hydrophobic tail is replaced by one or multiple alkyl chains or an amphiphilic surfactant [12, 196], the resulting APs self-assemble into cylindrical fibrils whose surface displays a high density of peptide antigens [197]. Palmitoyl-GGGAAAR and palmitoyl-GGGAAAKRK, for example, assemble into nanofibers that have been utilized for drug delivery to the brain [198]; while capable of penetrating the neurons, these nanofibers were found to be degraded by plasma enzymes, which limits accumulation in the brain and reduces potential side toxicity; in another example, fibrils of palmitoyl-YDAGFLR encapsulating a dalargin prodrug were utilized for crossing the blood-brain barrier, and controlling the uptake and release into brain tissue of mice models [199]. Other examples include nanofiber-based hydrogel of palmitic acid-GTAGGLIGQRGDS for cisplatin release,; [200] [C₁₂]-PPPPRRRR cell-penetrating nanofibers for delivery of DOX and PTX in MCF-7 cells,; [201], or core-shell micelles of [C₁₆]-VVVAAAKKKK-folate for folate targeted delivery of DOX to MDA-

MB-231 cells [202]. Notably, a number of AP-based vectors have been utilized for controlled delivery of biotherapeutics, such as growth factors and gene therapy products [203-206]. Among the latter, notable examples include a cholesterol-peptide conjugates for DNA delivery into HepG2 and HEK293 cells [207], capable of amino acid sequence-dependent gene expression efficiency [208]; a multiblock peptide comprising a hydrophobic cell membrane-binding sequence linked to a cell-permeating sequence (KKRKV) and capable of high-efficiency complexing and intracellular trafficking of therapeutic small interfering RNA (siRNA) to a variety of cell lines [209-211]; and the peptide Ac-(AF)₆-H₅K₁₅, which self-assemble into a micelle carriers that co-delivered a synergistic combination of DOX and p53 genes into HepG2 human liver carcinoma cells [212]. Another notable application of peptide amphiphiles (PAs) is drug delivery to bones. For example, oligo-aspartates that bind hydroxyapatite have in fact been shown to promote accumulation of small drugs in bones *in vivo* [213, 214]; similarly, peptide nanofibers displaying phosphorylated serine and tyrosine (P(S_{PO4}F)₅S_{PO4}P and P(Y_{PO4}F)₅Y_{PO4}P) were used for surface nucleation of hydroxyapatite [215-217] to improve bone mineralization [218-220]. Finally, PAs have also been utilized to engineer bio-responsive delivery systems. For example, palmitoyl-GTAGLIGQRGDS were used to construct a cisplatin-loaded nanofiber gel decorated with RGD peptides for cancer targeting; the gel matrix was degraded by matrix metalloproteinase-2 (MMP2), thus releasing cisplatin at the tumor site [200]. Similarly, a KRRASVAGK-[C₁₂]-based hydrogel containing a substrate for protein kinase A (PKA) was developed for PKA-responsive delivery of DOX to MDA-MB-231 cancer cells [221].

1.3.1.5. Elastin-like Polypeptides (ELPs)

ELPs are a renowned class of natural polymers that exhibit thermo-responsive behavior. ELPs are constituted by repeats of VPGXG, wherein X is a variable amino acid that dictates the phase transition temperature and the behavior of the resulting peptide-rich phase [222, 223]. This characteristic has been extensively utilized to engineer injectable formulations that, upon exposure to the body temperature, form coacervate structures for sustained local delivery [224-226]. Of particular interest is the ability of ELPs to efficiently encapsulate drugs that present high hydrophobicity or abundant hydrogen bonding groups and are traditionally challenging to formulate [223]. Combinations of ELPs and anticancer drugs (*e.g.*, DOX, PTX, camptothecin [CPT], gemcitabine [GEM]) [226-228] form micellar structures that have been demonstrated for chemotherapeutic treatment both *in vitro* and *in vivo* systems [229, 230]. To facilitate cellular uptake of the therapeutic payload, fusions of ELPs with cell-penetrating peptides (*e.g.*, CPPs-Bac, Tat, and SynB1) have been genetically engineered [226, 230]. Conjugates or aggregates of these peptides with anticancer drugs have shown superior accumulation and penetration into cancer tissues compared with non-targeted systems and free drugs, with remarkable reduction of side - effects [231, 232].

1.3.1.6. Cyclic Peptides (CPs)

Finally, CPs that form self-assembled nanotubes via hydrogen bonding have been also utilized as drug delivery vehicles [233-235]. This is owed to their higher mechanical and biochemical stability, and higher tissue permeability compared with structures formed by their linear counterparts [233-235]. Among the numerous examples, cyclic peptide nanotubes of (WDL)₄QDL afforded a high level of 5-fluorouracil (5-FU) penetration in tumor cells, resulting in

potent anticancer activity [236]; self-assembled cyclic peptide nanotubes, with the sequence Q^DAE^DAQ^DAC^DA loaded with DOX have been shown to increase drug uptake and cytotoxic effect in human breast cancer cells, demonstrating potential to overcome multidrug resistance [237].

1.3.2. Targeting Agents

Targeted drug delivery has been shown to impact pharmacokinetics and improve therapeutic outcomes [238-242]. Peptides are playing a growing role as targeting agents displayed onto a drug carriers for the treatments of lung [243-250], colon [251-255], skin [256-260], and breast cancer [261-268]. Of growing interest are tumor-targeting peptides (TTPs) [269, 270], which provide superior targeting activity compared with naked drug delivery systems by recognizing the proteins expressed by tumor-associated endothelium while showing no affinity for healthy endothelium [243]. Liposomes are a popular drug delivery modality that have benefited from the incorporation of TTPs, and the list of examples is endless. PEGylated liposomes functionalized with PIVO-8 and PIVO-24 afforded a two-fold higher accumulation of DOX in subcutaneous murine lung cancer compared with non-targeted liposomes [243]. Liposomes decorated with BiP-(immunoglobulin heavy-chain binding protein) targeting peptide WIFPWIQL showed a four-fold higher accumulation within neovascular cells compared with prostate and colon cancer cells, indicating potential for blocking tumor invasion by attacking its vascularization [251]. Similarly, liposomes functionalized with peptides GNGRG and APRPG attacked tumor vascularization by targeting the aminopeptidase N (APN) onto tumor-associated endothelial cells [252, 271, 272]; functionalization with GNGRG and APRPG not only affords stronger anti-proliferative effect, but also reduced drug accumulation in the spleen, liver, kidneys, lung, and heart. The disulfide-cyclic variant CNGRCGV and the linear peptide CPRECESA, which target

aminopeptidase A (APA), have also been utilized to functionalize liposomes to target the tumor-associated vasculature [273-275]. Liposomes decorated with peptides targeting APN and APA have been utilized to deliver DOX to endothelial and perivascular cells that support neuroblastoma tumor in a mouse model, showing therapeutic efficacy [276]. Peptides that target hormones and growth factors are also widely utilized TTPs. Among the former, we recognize the somatostatin-binding peptide FCFWKTCT [247], the luteinizing hormone-releasing hormone (LHRH)-binding peptide Pyr-HWSYGLRPG [263], cholecystokinin-binding GDYMGWMDF [260], and neuropeptide Y-targeting RRPYIL [254]. FCYWKTCT-functionalized liposomes incorporating metal chelating lipids were used to deliver radioactive $^{111}\text{InCl}_3$ to AR42J pancreatic cancer cells [250]. Growth factor-binding peptides include VEGF-targeting WHSDMEWWYLLG, neuropilin-1-targeting ATWLPPR, α V integrin-targeting GARYCRGDCFDG, and PDGF receptor-targeting GCRGRRST [258, 259]. Liposomes functionalized with peptide KRFKQDGGSWSHW, which binds and activates tumor growth factor β (TGF- β) [253], have been shown to halt tumor progression in mice compared with non-targeting liposomes. In another example, the peptide TDSILRSYDWTY, which specifically targets non-small cell lung cancer (NSCLC) cells [244], was used to functionalize DOX-loaded liposomes for treating xenografted mice, affording a five-fold higher DOX delivery than free drug, and two-fold higher delivery than traditional liposomes. DOX-loaded liposomes functionalized with a similar NSCLC-targeting peptide, CSNIDARAC, were shown to halt tumor growth and produce minimal accumulation in the liver, lung, spleen, and heart in comparison with free DOX and non-targeting DOX-loaded liposomes [248].

A special place is occupied by integrin-binding peptides, to date the most utilized targeting moieties in the history of drug delivery, first and foremost RGD-based sequences. Innumerable RGD-functionalized systems have been developed as anti-cancer nanomedicines, carrying either

traditional chemotherapeutics [277, 278] or gene drugs [279]. Lately, cyclic variants of RGD have been employed to functionalize liposomes for drug delivery against breast cancer [280-282], colon cancer [261, 283, 284], and melanoma [285], as well as diagnostics against lung tumors [286]. A notable RGD-derivative targeting α 5 β 1 integrin, KSSPHSRNSGSGSGSGRGDSP [287-290], has utilized to confer liposomes and polymersomes with both cell targeting and penetrating activities; these formulations were effective in delivering diverse drugs (5-FU, DOX, tumor necrosis factor- α , siRNA, and plasmid DNA) to colon cancer cells [261, 267, 289], prostate cancer cells [291, 292], and porcine Langerhans islets [293]. It is worth noting that linear and cyclic RGD peptides have been extensively utilized for developing synthetic mimetics of cells, especially platelets. In an early work, RGD-decorated nanoparticles were shown to reduce bleeding time by half after IV administration in a rat model [294]; later, liposomes, albumin particles, latex particles, and PLL-PLGA (poly-L-lysine-poly(lactide-*co*-glycolide) nanoparticles functionalized with RGD peptides were also developed [294-303]. Recently, liposomes functionalized with von Willebrand factor-binding peptides (VBPs), collagen-binding peptides (CBPs), and GRGDS peptides were shown to be highly efficacious in both microfluidic and murine wound models [304]. Lastly, layer-by-layer, discoidal, soft nanoparticles coated with polyamidoamine (PAMAM) dendrimers functionalized with VBP, CBP, or GRGDS peptides have demonstrated a remarkable 65% reduction in bleeding time relative to natural platelets, the highest reported value to date [305].

1.3.3. Cell-Permeating Peptides

Together with cell-targeting peptides, cell-permeating peptides (CPPs) have been extensively integrated with drug delivery systems [34, 238, 306, 307] to promote the internalization of cargoes such as siRNA [308-310], nucleic acids [311, 312], small molecule

therapeutic agents [313, 314], proteins [315, 316], peptides [317, 318], and contrast agents [319]. Recently, novel CPPs have also been developed for nuclear localization [320-324], organelle and cytoplasmic protein targeting [325-331], and stimuli-responsive delivery [227, 232, 332]. Protein-derived sequences were among first CPPs developed. Among these, the most notable are the Tat-derived sequence Tat₄₉₋₅₇ [333, 334], penetratin₄₃₋₅₈ [335, 336], the herpes virus-derived VP22 [337], and the Kaposi FGF signal sequences [338-340], which derive from viral capsid proteins, and have been utilized for intracellular delivery of antibodies [341, 342], peptides [343-348], proteins [349-353], nucleic acids [354-356], peptide nucleic acids (PNAs) [357], and drugs [358, 359]. A plethora of synthetic sequences have also been developed [32, 34], including cationic [360], amphiphilic, and hydrophobic CPPs, and skin-permeating peptides (SPPs). Cationic sequences, such as poly-R and (WR)_n ($n > 4$) [361, 362], are among the first synthetic CPPs [363-367]; these CPPs have been reported to induce a wide variety of side effects, chiefly, cell membrane disruption, which comprises cell viability and leads to severe cell toxicity and tissue irritation [368-370]. Amphiphilic CPPs contain both polar and non-polar residues [371-373]. Some are derived from proteins, such as pVEC, ARF(1-22), BPrPr(1-28), MPG, penetratin, and CADY, while others are synthetic, like proline-rich peptides, and the model amphipathic peptide (MAP) and its derivatives MAP17, MAP12, GALA, and KALA [374, 375]. Amphipathic CPPs can be α -helical, with the coil featuring a hydrophobic side and a charged or polar side, or β -sheet, comprising one hydrophobic and one hydrophilic string of amino acids. Conjugates of Tat, penetratin, CADY, and poly-R peptides with DOX have been developed for treating different cell lines *in vitro* and *in vivo* [358, 376-385]. In other studies, peptides YTA2 and YTA4 have been conjugated to methotrexate (MTX) and fluorescent probes for treatment and imaging of breast cancer cells [313, 386, 387]. Amphiphilic CPPs MPG8 and PEP3 have been utilized for delivering

short regulatory oligonucleotides in both cancer and healthy cell lines to modulate gene expression [320, 388, 389]. Finally, hydrophobic CPPs form a smaller class that includes stapled peptides, prenylated peptides, and pepducins [390-392], the signal sequence for integrin β 3 (VTVLALGALAGVGVG), and Kaposi fibroblast growth factor (AAVALLPAVLLALLAP) [393], whose potential for drug delivery has been marginally studied. Finally, SPPs have been developed, the majority of which has been identified by screening phage-display libraries specifically to achieve transdermal drug delivery. Examples include peptide DRTTLTN, IMT-P8, and SPACETM. Peptide DRTTLTN reaches the epidermis via fluidization of the lipids and extension of the keratin fibers in the stratum corneum (SC), and has been applied for transdermal delivery of unfractionated heparin (UFH), yielding a remarkable increase of UFH permeation compared with UFH alone [394]. IMT-P8, an arginine-rich SPP [395, 396], penetrates the SC, permeates the epidermis, and accumulates hair follicles; fusions of this peptide with green fluorescent protein (GFP) and proapoptotic peptide KLA were evaluated on murine skin *in vivo*, [397] and found to achieve higher skin penetration compared with Tat, inducing localization in mitochondria and cell death.

Finally, the disulfide-cyclic “skin permeating and cell entering” (SPACETM) peptide ACHSALT KHCG has been extensively characterized for dermal delivery of siRNA, small molecules, proteins, and biopolymers. Conjugates of SPACETM and siRNA targeting interleukin-10 and GAPDH have been shown to absorb in skin porcine with a 10-fold increase compared with siRNA solution, achieving effective knockdown (60-80%) of the corresponding proteins both *in vitro* and *in vivo*. Ethosomal carriers constructed with SPACETM-phospholipids conjugates have been utilized to deliver HA across both human and porcine skin *in vitro*, and murine skin *in vivo*, with significant increments compared with aqueous HA [398]. SPACETM was also found effective

in permeating small drugs without covalent conjugation. In one example, a hydro-alcoholic solution of SPACE™ and corticosterone enhanced epidermal permeation compared with Cortisone™ cream, both *in vitro* on porcine skin and in hairless mice models [399]. In another study, SPACE™ was utilized to promote *in vitro* dermal absorption of cyclosporine A (CsA), achieving a nine-fold increase compared with a hydro-alcoholic solution of CsA [400]. Recently, a computational algorithm was developed for the *de novo* identification of disulfide-cyclic peptides that enhance transdermal delivery of CsA. Selected heptameric sequences ACSATLQHSCG, ACSLTWNWNCG, ACTSTGRNACG, and ACSASTNHNCG, and octameric peptide ACNAHQARSTCG were tested *in vitro* and found to afford a CsA permeation comparable with or higher than SPACE™, without triggering any toxic effect on skin keratinocytes, even at high concentration [401].

1.3.4. Peptides in Tissue Engineering and Regenerative Medicine

Hydrogels produced with self-assembling proteins and peptides have been extensively applied as scaffolds for tissue engineering and regenerative medicine (**Figure 1.5**) [10, 162, 402-414]. Among the many building blocks utilized in these efforts, we must mention:

1.3.4.1. Collagen, Gelatin, and Fibrin

These proteins, either produced recombinantly [415-423] or obtained from mammalian sources [424-428], are the most widely utilized biologically -derived substrates for tissue engineering [89]. Collagen, the main component of connective tissue, tendon, skin, and cartilage, is known for its biocompatibility, bioactivity, and wide availability. Collagen is often modified by covalent conjugation or physical adsorption of growth factors to promote regenerative outcomes,

such as neovascularization and angiogenesis, [429-433] or cartilage repair [434, 435], osteogenesis [436-438], and infiltration of human fibroblasts to promote cellularization and vascularization of implants [439-441]. Gelatin, *i.e.*, hydrolyzed and denatured collagen, is also frequently functionalized with growth factors (*e.g.*, TGF- β , bone morphogenetic proteins [(BMPs]), and VEGF) and utilized as substrate for cartilage regeneration [442-445], angiogenesis, and osteogenesis [446, 447]. Fibrin has been frequently utilized as matrix for the immobilization of growth factors FGF and BMP, and the conditioning of platelets, leukocytes, fibroblasts, and endothelial cells for bone tissue engineering and regeneration [448-451].

1.3.4.2. Elastin-like Polypeptides (ELPs)

ELPs have gained great popularity in tissue engineering [452-455], owing to their biocompatibility and facile physicochemical customization. Their sequence can in fact be tailored to enable cross-linking, [456-460] and functionalization with biomolecular cues, [461-463] and to adjust their thermomechanical properties for easy processing into gels [459, 460, 464-467], films [458, 463], foams [467], and fibers [468, 469]. Non-crosslinked ELPs have been shown to be ideal substrates for cartilage engineering [470], as they promote biosynthesis and retention of chondrocyte-associated extracellular matrix (ECM) and long-term phenotype maintenance of chondrocytes and human adipose-derived adult stem (hADAS) cells [471, 472]. Soft, non-crosslinked ELPs are not ideal for load-bearing materials to promote cartilage regeneration. Crosslinked ELPs, on the other hand, form mechanically robust hydrogels that are capable of hosting primary chondrocytes and promote formation of cartilage matrix, [459] and have been used as injectable 3D scaffolds for cartilage regeneration in animal models [457, 460, 462, 473-475]. Crosslinked ELP hydrogels have also been employed in engineering intervertebral discs that

were successfully implanted in animal models [476, 477], where they promoted formation of new cartilage without significant inflammation and local degradation; analogous ELP hydrogels have been developed to engineer load-bearing cartilage tissue for defect filling [475]. Notably, the mechanical properties of ELPs can also be controlled thermally by taking advantage of sequence-dependent thermo-responsive behavior. Upon temperature-induced gelation, in fact, ELP hydrogels present a rheological behavior similar to that of strong collagen and hyaluronan substrates, thereby serving as ideal substrates for cartilage engineering [471, 478, 479] and implants for *in vivo* applications [480]. These ELP hydrogels exhibit high durability and biostability *in vivo*, without triggering inflammatory responses or calcification [481-483]. Being produced by recombinant techniques, ELPs can also be fused with proteins, such as growth factors and cytokines, to better direct cell adhesion, proliferation, and differentiation [484, 485]. For example, an ELP-interleukin-1 receptor antagonist (ELP-IL-1Ra) fusion was developed for intra-articular treatment of osteoarthritis [486, 487]; numerous other examples of ELP-based fusions with growth factors (*e.g.*, soluble tumor necrosis factor receptor II ([sTNFRII]), epidermal growth factor, and oncogene inhibitors) have been developed for anti-inflammatory use, cellularization of surgical implants, or halting the progress of solid tumors [227, 345, 346, 488]. ELPs can also be fused with cell-binding small peptide domains [489]. Numerous examples are reported of crosslinked ELP hydrogels displaying fibronectin-derived REDV, laminin-derived IKVAV, or integrin-binding RGD motifs [463, 485, 489, 490], utilized as mimetics of the ECM. These hydrogels have been utilized as substrates for fibroblasts, platelets, and endothelial cells to engineer small diameter vascular grafts that effectively integrate with host tissues [458, 461-463, 484, 485, 489-492], as well as stem cells and primary chondrocytes for cartilage and intervertebral disc engineering [457-459, 462, 466, 483-485, 489, 490, 493, 494]. Notably, ELPs can also be

mixed with synthetic polymers and formed into processed materials. For example, ELP-based nonwoven nanofiber substrates have been developed for vascular engineering [481, 483] and ocular tissue engineering [495, 496]. Hybrids of ELPs and polyacrylic acid (PAA) and polyethylenimine (PEI) have been processed into substrates for culturing and controlling the differentiation of primary hepatocytes [497]; notably, ELP-PAA and ELP-PEI trigger high production of both urea and albumin in hepatocytes, proving to be ideal substrate to culture hepatocytes for liver regeneration [497, 498].

1.3.4.3. Synthetic Peptides [499]

Synthetic peptides have gathered significant momentum as affordable and tailorabile building blocks for biomimetic hydrogels for tissue engineering and reconstitution [475, 494, 500-503]. A plethora of sequences are known that *(i)* self-assemble into structures with customized physiochemical properties, most notably stimuli-responsiveness to environmental conditions; *(ii)* can be crosslinked *in vitro* and *in vivo* by chemical, enzymatic, or electromagnetic triggers; or *(iii)* can be combined with biopolymers, resulting in ECM-mimetic matrices with controlled morphology, biocompatibility, and biodegradability [459, 466, 494, 499, 500, 502, 504-510]. Among the most studied synthetic peptides are RAD16-I and RAD16-II, which self-assemble into ribbons and fibrils [511] that form highly porous hydrogels with high water content (99-99.5%) [162, 512, 513]. Their high porosity favors migration of nutrients, growth factors, and oxygen [403, 514], making these materials ideal substrates to sustain growth and differentiation of a variety of mammalian cells [166, 170, 402, 514-527]. Primarily, these peptides have been used in cardiovascular engineering applications [166, 514, 519, 522, 526]. Examples include RAD16-I hydrogels functionalized with laminin-derived peptides YIGSR and RYVVLPR to culture aortic

endothelial cells into tubules [528]; a RAD16-I hydrogel functionalized with a VEGF agonist peptide and RGD peptides to grow and differentiate human umbilical vein endothelial cells (HUVECs) toward tubulogenic phenotype [529, 530]; and a RAD16-II scaffold to engineer murine neonatal cardiomyocytes, in combination with endothelial cells, into ventricular tissue [514, 531]. Numerous studies have also demonstrated the potential of these materials for *in vivo* applications. For example, RAD16-II nanofibers loaded with mesenchymal stem cells (MSCs) were injected into a rat model of myocardial infarction, where they promoted proliferation and differentiation of MSCs into cardiomyocytes to reduce ischemic heart tissue and restore cardiac function [519]. In another example, a RAD16-I hydrogel hosting a combination of skeletal myoblasts and adipose-derived MSCs achieved remarkable reduction of necrotic tissue and reformation of functional heart muscle in a murine model of infarcted myocardium [522]. A RAD16-II hydrogel loaded with insulin-like growth factor 1 (IGF-1) [163] was injected in the left ventricle of mouse models, where it became rapidly populated by capillary-forming endothelial cells and smooth muscle cells that formed functional vessel-like structures and arterioles [514], resulting in improved heart functionality within 30 days upon injection. More recently, the RAD16-I and RAD16-II have demonstrated applicability in neural tissue engineering. RAD16-I hydrogels mixed with fibronectin, laminin, collagen, and bone marrow-homing peptides have been utilized as 3D scaffolds for adhesion and differentiation of neural stem cells (NSCs), [513, 532] and engineering neurite outgrowth and synaptic brain tissue [515]. A RAD16-I hydrogel with brain tissue-like softness was functionalized with laminin-derived peptide IKVAV to guide the migration, adhesion, and neuronal differentiation of NSCs to reconstruct injured brain tissues [533]. Further, several reports have illustrated the potential use of injectable cell-loaded RAD-16-based hydrogels for neuronal and brain tissue repair [514, 530, 534, 535]. For example, an NSC-loaded hydrogel

implanted in a rat model of damaged cerebral neocortex yielded a notable regeneration in brain tissue [533]. Similar RAD16-II microporous hydrogels have been utilized to achieve homogeneous encapsulation and growth of neuronal cells for repairing damaged optic nerves [534], spinal cords [517], and brain injuries *in vivo* [155, 402, 534-536]. Many other fibril-forming β -sheet peptides and α -helical peptides have been extensively utilized to engineer 3D substrates for mammalian cells [155, 402, 405, 407, 410, 537]. Among hydrogel-forming β -sheet peptides, P11 sequences are noted for their biocompatibility and non-immunogenicity, and ability to self-assemble under desired conditions of pH and ionic strength [538-541]. For example, an RGD-decorated hydrogel constructed with P11-2 (Ac-QQKFQFQQ) was developed as substrate with adjustable stiffness for HUVECs [542, 543] and human dermal fibroblasts [544]; the peptide/water and RGD-/non-RGD peptide ratios were used as tuning parameters, showing correlation between mechanical properties and phenotypic response. The MAX peptide family is another notable example of β -hairpin peptides, known for cytocompatibility and antibacterial properties, [545, 546] and their ability to self-assemble when combined with cell suspensions in cell culture media, thereby encapsulating the cells without damage [155, 547]. Many of these nanofiber-forming β -sheet peptides have also been assembled into multi-domain peptides (MDPs) in combination with cell-binding and cell-signaling peptides, and sequences, enabling enzymatic crosslinking or digestion. These MDPs have been engineered into scaffolds for vascular grafts, [548] and injectable gels for tissue repair [549, 550]. Similarly, many α -helical peptides have been extensively utilized to engineer 3D hydrogel substrates for endothelial cells, neuronal cells, hepatocytes, chondrocytes, and osteoblasts [194, 403, 515, 528, 529] in combination with proteins for cell differentiation, and formation of vascular or organ structures [9, 410, 513, 530, 549, 551, 552]. PAs have also been utilized as cell culture and tissue engineering substrates, chiefly for their ability to undergo

remodeling by resident cell populations [553, 554]. This is particularly useful in stem cell differentiation, where matrix remodeling is necessary to elicit the desired differentiation response and support the new fully differentiated daughter cell population. Hydrogels obtained by combining PAs with synthetic biopolymers (*e.g.*, polyglycolic acid) were used as 3D scaffolds in cell culture bioreactors to obtain bone and vascular grafts from MSCs [59, 555-558]. *In vivo*, IKVAV AP gels supporting neural progenitor cells promoted neuronal differentiation, and were applied for treating spinal cord injuries in mice models, resulting in axon growth and functional recovery [405, 559]. Analogous PA-based hydrogels loaded with growth factors and cytokines (*e.g.*, TGF- β and BMPs) have been developed for cell growth and differentiation of hMSCs toward chondrogenic [560], osteogenic [557, 561, 562], myogenic, adipogenic, and neurogenic lineages [405, 563]

1.4. Applications of Polysaccharides

1.4.1 Drug Delivery

Like proteins and polypeptides, polysaccharides have been widely utilized as drug delivery vehicles [564-574], owing to their excellent biocompatibility and biodegradability, ease of chemical functionalization and processing, commercial abundance, and low cost. Their versatility enables a multitude of applications, including drug conjugates and drug-loaded self-assembled structures for increasing the solubility and circulation time of otherwise insoluble or rapidly-cleared drugs, and particle coating for targeted delivery or as alternatives to PEGylation for stealth function. Research on polysaccharide-drug conjugates has grown hand in hand with bioconjugation technology [575-583], resulting in new linkers for site-specific conjugation [584, 585], pH-responsive release [582, 586, 587], especially useful in the mildly acidic environment of

tumor cells [575, 588], or enzyme-directed cleavage for intracellular drug release [575, 581, 589-591]. Of recent interest is sustained intestinal release of traditional injectable therapeutics (*e.g.*, insulin and immunotherapies) and drugs for fighting colon cancer, ulcers, Crohn's disease, and gastrointestinal infections. Polysaccharides are ideal for colon targeting, as they resist the gastrointestinal environment but are degraded by the bacterial enzymes in the colon, resulting in release of the therapeutic payload and bioresorbable oligosaccharides [592-595].

1.4.1.1. Hyaluronic Acid (HA) [596]

HA consists of D-gluconic acid-D-N-acetylglucosamine dimer repeats whose hydroxyl and carboxyl groups have been extensively utilized for drug conjugation [597]. HA has gained great popularity as drug delivery vector for its ability to specifically target cell surface marker CD44 [598-604], which is overexpressed in many cancer and cancer stem cells [599, 605]. A great deal of studies have been devoted to optimizing HA-drug conjugates to prevent aggregation [588, 600], improve conjugation [602, 606-608], and understand cell internalization [561, 609-611]. In this role, HA has served as carrier for (*i*) butyric acid to treat Lewis lung, melanoma, and leukemia [612-614]; (*ii*) PTX against ovarian, bladder, breast, and brain cancer [600, 610, 615-619]; (*iii*) CPT for peritoneal cancer [620, 621]; (*iv*) DOX to treat breast cancer [622]; and (*v*) cisplatin for breast cancer, squamous cell cancer of the head and neck (SCCHN), melanoma, sarcoma, and breast cancer [623-628]. In a recent study, DOX and CPT were conjugated to HA at a 4.5 : 1 molar ratio CPT:DOX, which is synergistic against HER2+ BT-474 breast cancer cells [629]. Analogous formulations were prepared by conjugating DOX to HA via a pH-labile hydrazone bond, [630] and PTX via ester bond; the former provided higher anticancer efficacy *in vivo* compared with free DOX [622], while the latter showed targeted toxicity *in vitro* and strong anticancer activity *in vivo*.

in human ovarian carcinoma xenografts, [600] and bladder carcinoma [631, 632]. HA micelles, liposomes, and nanoparticles have also been developed for the delivery of insoluble anticancer drugs. Their PEGylation and functionalization with proteins and peptides results in prolonged circulation and active targeting, while incorporation of thermo-/pH- responsive building blocks enables site-selective release. Examples of HA-based nanoparticulate formulations include:

- (i) Micelles carrying DOX for treatment of breast and prostate cancer, [633, 634] or PTX to treat breast cancer and SSCHN [635-638].
- (ii) Liposomes loaded with mitomycin C (MMC) to treat primary, metastatic cancers, and Lewis lung carcinoma in mice, [639] or GEM against pancreatic cancer [640, 641]; DOX-loaded liposomes against breast cancer [642, 643] were also successfully tested on human breast cancer xenografts in mice [622]; analogous PTX liposomes were developed against hepatocellular carcinoma [644] and CD44+ human ovarian carcinoma, showing antitumor activity *in vivo* [600].
- (iii) Core-shell nanoparticles wherein synthetic polymers (*e.g.*, PLA [polylactic acid] and PLGA) and HA, respectively, populate the inner and outer layers have been developed to carry chemotherapeutic drugs against various breast cancer cell lines; [645-649] Ehrlich ascites tumor, breast cancer, and SSCHN; [650-654] and sarcoma [655]. Similar lipid-HA nanoparticles have been developed to deliver chemotherapeutics to treat breast cancer and carcinoma [650-654, 656-662], colon cancer [663], melanoma [655, 664-666], and lung cancer [667]. Great effort has been devoted into studying the biodistribution, side toxicity, tumor accumulation, and antitumor efficacy *in vitro* and *in vivo* of these lipid-HA systems [645, 647, 648].

1.4.1.2. Dextran (Dex)

Dex is also widely employed as drug carrier either by formation of non-covalent complexes [668-671] as well as conjugates based on either traditional chemistries [672] or innovative linkers enabling environment-controlled release [673-676]. Conjugates with chemotherapeutics are naturally the most widely studied. Among the examples of traditional conjugates, we find a Dex-cytarabine system that greatly improved survival in leukemia murine models [677] and Dex-MTX conjugates that showed therapeutic efficacy in mouse models of brain tumor [678] and leukemia [679, 680]. Short peptide linkers have then gained popularity for drug conjugation to Dex carriers. For example, an oligo-glycine linkers were used to construct Dex-CPT conjugates that showed significant antitumor activity *in vivo* against an ensemble of human tumor xenografts, [673, 674, 676, 681, 682] and colon cancer [587, 683]; using the same GGGF linker, a conjugate of Dex and exatecan, a CPT analog, was prepared, which exhibited strong therapeutic activity against a panel of human xenografts and murine solid tumors [675, 684, 685]. The linker Jeffamine-PVGLIG, which is cleaved by matrix metalloproteinase enzymes, was used to link MTX to Dex; the resulting conjugate showed improved efficacy against human tumor xenograft models compared with the free drug [586, 590, 591]. To facilitate the conjugation of the drug payload through cleavable bonds, modified versions of Dex, such as oxidized (Ox) or carboxymethyl (CM) Dex, have been developed. PTX-CM-Dex ester conjugates showed significant antitumor activity against multiple colon cancer cell lines *in vivo* [587, 683]; similarly, an imine conjugate of DOX to Ox-Dex showed higher therapeutic activity and lower heart accumulation and acute toxicity compared with free DOX in a Lewis lung carcinoma rat model [686]. Notably, a CM-Dex conjugate with deliomotecan, a CPT analog, has entered clinical trial; two cancer patients responded to therapy, but showed adverse effects [676]. Other clinical studies were performed with a CM-Dex-CPT conjugate,

which showed stabilization of the disease in 50% of patients affected by advanced solid tumors [685], and an Ox-Dex-DOX conjugate administered through IV infusion, which led to stabilization of the disease in 90% of patients, although toxic side effects were reported [687]. Worthy of notice are also the PEGylated Dex nanogels utilized for gene therapy, in particular for IV administration of small -interfering RNA (siRNA) and microRNA [688-691], which have successfully achieved gene knockdown in human hepatoma and glioblastoma [692, 693]. Among others, it is worth reporting a series of studies employing Dex nanogels for delivering siRNA that silences the genes responsible for multi-drug resistance in drug-resistant cancer cell lines [694-696]; the cells were sensitized to drug treatment, which resulted in effective suppression of cell growth *in vitro* and tumor growth *in vivo*.

1.4.1.3. Chitosan (CN)

CN is the most widely utilized cationic biopolymer as drug carrier [697-699]. CN owes its success to the amino groups displayed on the glucosamine monomers, which enable fine-tuning of its gelation behavior and mechanical properties by chemical modification and conjugation of anticancer drugs. Direct drug conjugates with CN have been developed as injectable macromolecular drug carriers. A number of conjugates with MMC, for example, have showed good antitumor activity against murine leukemias, melanoma, sarcoma, metastatic liver cancer, and hepatic cell carcinoma *in vitro* [700] and comparable efficacy but reduced systemic toxicity against sarcoma *in vivo* [700-702]. DOX-CN conjugates, which formed micelles in solution comprising a DOX-rich core and a CN-rich shell, were shown to suppress tumor growth without systemic toxicity *in vivo* against breast cancer [703], melanoma [699], and mesothelioma cells [704]. Other micelle-forming PTX-CN conjugates developed for oral administration showed

significant inhibition of murine melanoma [601], and similar DTX-CN conjugates provided increased bioavailability, lower acute toxicity, and effective antitumor efficacy *in vivo* [705]. Conjugates with insulin for oral administration have also been developed, which released the payload in the intestine, increasing its bioavailability and controlling blood glucose levels effectively for several hours in diabetic rats [706]. Because of its insolubility at physiological pH, CN has been mostly utilized in the form of bulk and particulate hydrogels [670, 671, 707-710]. Numerous methods have been developed to fabricate CN micro- and nano-particles for sustained drug release, including crosslinking, solvent exchange, ionic gelation, spray drying, emulsion polymerization, and precipitation/reconstitution [35, 711-728]. Notably, DOX-loaded nanoparticles were shown to circulate systemically without drug leaching and accumulate into tumor tissue, where they delivered the payload intracellularly by pH-triggered release [704]; analogous DOX-loaded nanospheres functionalized with HER2-targeting antibodies showed great promise for target delivery against HER2+ breast and ovarian cancers [671]. Being positively charged, NC nanoparticles make attractive vectors for oligonucleotide conjugations and gene delivery [729-731]. In one study, CN particles crosslinked with deoxycholic acid and loaded with plasmid DNA were shown to effectively transfect COS-1 cells [732-737]. CN nanoparticles co-delivering tumor-suppressing IL17RB siRNA and DOX induced apoptosis and inhibited migration of breast cancer cells, owing to siRNA-induced sensitization of cells to DOX [738-744]. PEGylated RGD-functionalized CN nanoparticles loaded with siRNA targeting the lactate transporter MCT1 and the glutamine transporter ASCT2 showed strong antiproliferative effect both *in vitro* and *in vivo*. In another study, CN nanoparticles were developed to deliver siRNA that silences galectin-1 (Gal-1), a lectin associated with brain tumor progression; the particles were delivered to the central nervous system upon intranasal administration and showed significant

reduction of Gal-1 expression in tumor-bearing mice. Like nanoparticles, CN nanofibers also show great potential for drug and gene delivery [745-748]. Their high specific surface and porosity improve drug loading and cell binding, [749] and enable high integration of optically and magnetically active materials for cancer imaging [750-774]. Examples include CN thin films loaded with mesoporous aluminosilicate to fine-tune the delivery rate of metformin [774] or DOX [756, 768]; CN nanoparticles modified with magnetic iron oxide nanoparticles to control the delivery of DOX while concurrently enabling cell imaging [773]; particles loaded with magnetic nanocrystals for MR (magnetic resonance) cancer imaging and pH-controlled release of DOX [760]; and iron oxide nanoparticles coating CN for concurrent cancer imaging and treatment by delivery of MTX [765, 769] or MTX and GEM [759, 765, 769]. To complete the list of uses revolving around CN's cationic nature, it is worth mentioning complexation with negatively charged polyelectrolytes, which has been utilized as a method for constructing robust drug delivery systems such as particles, tablets, gels, and films [775]. CN-alginate constructs, for example, have been utilized to deliver anti-cancer [776-778], ocular [779], asthma and pulmonary [780], and anti-inflammatory drugs [781]. Similarly, CN-HA systems have been developed for ocular applications, [782-784] and non-viral gene delivery for treating asthma and osteoarthritis [785, 786]. Tablets of CN and xanthan gum also show great promise for sustained drug release in the intestine [787, 788].

1.4.2. Tissue Engineering and Regenerative Medicine

The qualities that make polysaccharides ideal as drug delivery vectors – hydrophilicity, biocompatibility, controlled water uptake and degradation kinetics, and tailorabile biochemical functionalization – make them attractive substrates for tissue engineering [8, 789-800] and

regeneration [54, 570, 694, 801-808]. A multitude of methods have been implemented to adapt polysaccharides for tissue engineering applications, including enzymatic and photo-induced crosslinking, chemical crosslinking by Schiff base reaction, Michaelis addition, and click chemistry, and physical methods like ion-, pH-, and temperature-induced gelation (**Figure 1.6**) [809-817]. Let us peruse some examples:

1.4.2.1. Plant and Bacterial Cellulose (BC)

A plethora of 3D porous structures, such as sponges, hydrogels, and nanofiber matrices, have been developed using plant cellulose and its blends with other polymers for tissue engineering [818-820]. Particular attention has been devoted toward osteogenic and chondrogenic tissue scaffolds, since the porosity and mechanical strength of cellulose are ideal for osteoblast and chondrocyte infiltration and proliferation. In one study, cellulose microparticles were sintered into a 3D scaffold with mechanical properties similar to those of native bone and functionalized with collagen to support adhesion, spreading, and maturation of human osteoblasts, with consequent mineralization of the substrate [803, 821]. Similar scaffolds have been utilized to produce porous bone grafts and non-porous screws and plates for orthopedic applications [822, 823]. Cellulose has also been electrospun into fiber matrices and coated with BMP proteins for osteogenic differentiation of bone marrow stromal cells into bone tissue after implantation [824]. Cellulose scaffolds coated with calcium phosphates have also been developed to sustain proliferation and phenotype development of human chondrocytes cells and have been widely utilized for cartilage engineering [818]. More recently, bacterial BC has been introduced, which combines the biocompatibility of its plant cognate with higher water content and tensile strength, thus making a better substrate for cartilage and bone tissues [825-828], as has been shown in clinical trials [829].

BC is obtained from bacterial cultures of *Acetobacter xylinum* as a highly crystalline nanofibrous material similar to collagen, [825-827, 830] and, like all other polysaccharide substrates, can be functionalized with biochemical cues to be employed as a cell culture substrate. In one study, BC functionalized with osteogenic growth peptide supported osteoblast development *in vitro*, promoting high levels of alkaline phosphatase expression and mineralization, while showing no cytotoxicity and genotoxicity *in vitro* [831]. In another example, BC scaffolds coated with BMP-2 were utilized for adhesion and proliferation of fibroblast-like cells and were subsequently implanted subcutaneously in mice, resulting in ectopic bone formation [832].

1.4.2.2. Chitosan (CN)

Crosslinked CN hydrogels and composites play a leading role as scaffolds for soft and hard tissue engineering and injectable systems for tissue regeneration. The amine groups on CN enable fine-tuning of the elastic modulus [833] and conjugation of ECM proteins and bioactive ingredients to support a variety of resident cell populations [834, 835]. To sample the versatility of CN composites, one can consider case studies where CN has been combined with other biopolymers (*e.g.*, HA, alginate, aloe vera, etc.) to produce fibers and films for engineering ligaments [836], muscle tissue, skin [837], cartilage [838, 839], and even salivary glands [840]. Electrospinning of nanofiber composites has gained popularity as a processing technology for CN in combination with natural and synthetic biopolymers. For example, polycaprolactone (PCL)-CN coated nanofibers were electrospun with collagen to serve as osteogenic and chondrogenic cell scaffolds. Similarly, nanofibrous CN membranes were developed to support the adhesion and proliferation of Schwann cells, which play a crucial role in axonal regeneration in the peripheral nervous system [841], as well as cells from mouse neuroblastoma that produce the nerve growth

factors (NGFs) implicated in the reconstruction of peripheral nerve lesions [842]. Among synthetic complements to CN, a notable role is played by stimuli-responsive polymers, which have been integrated with CN to enable on-demand cell entrapment or detachment. A multilayer UV-curable CN-methacrylate was developed to encapsulate cells upon UV exposure and showed cell protection after crosslinking [843]. A thermo-responsive CN-pNIPAAm hydrogel [844] promoted cell adhesion and spreading upon heating, where pNIPAAm hydrophobically collapses, and allowed detachment of cell sheets upon cooling, where pNIPAAm regains hydrophilic character. Other composites based on CN and biopolymers such as gelatin, collagen, and starch have also been developed as 3D porous scaffolds for cartilage engineering [798, 845-847], tubular scaffolds for vascular grafts [846, 848, 849], asymmetric porous scaffolds for skin grafts [850-852], and membranes for constructing adipose tissue grafts [853]. Ceramic materials have also been integrated with CN to create composites with fine-tuned 3D morphology. Examples include CN crosslinked with silica particles for skin engineering and regeneration [854] and a CN-nanohydroxyapatite framework for growing bone tissue using stem cell cells extracted from human periodontal ligament tissues [855]. By combining their bioactive properties and tunable mechanics, CN composites have shown promise as injectable systems to promote tissue regeneration. An illustrative list of case studies includes: coated CN tubules for engineering adipose stem cells into neurosphere cells to repair transected sciatic nerve in Sprague-Dawley rats [856]; a rigid CN hydrogel to promote skin regeneration in third-degree burns inflicted to female minipigs [857]; a thin film of CN and silk fibroin to repair ventral hernia in guinea pigs [858]; a blended hydrogel of CN and hydroxyethyl cellulose to repair of articular cartilage defects in sheep [859]; an in situ gelling mixture of CN and sodium alginate dialdehyde loaded with corneal endothelial cells for corneal regeneration [860]; and CN microspheres dispersed in a calcium phosphate paste for bone

regeneration of damaged femur in rabbits [861]. In all these examples, CN scaffolds promotes 3D tissue remodeling, with integration of the new tissue with the native one, deposition of new ECM, uniform vascularization, and cellular infiltration in repair sites, which contributed to ensuring mechanical and functional stability of the regenerated tissue. Owing to their ability to rapidly exchange gas and adsorb fluids, CN-based porous constructs are ideal materials for wound dressing [862]. CN hemostatic bandages and fillings have been reported to stop bleeding from deadly wounds in large animals much more rapidly than gauze dressings and increase the rate of survival [863]. The positive charges on CN chains, in fact, bridge erythrocytes by binding their negatively charged cell membrane and stimulates platelet intervention and rapid clotting. CN hemostats are frequently blended with biodegradable organic acids (*e.g.*, succinic or lactic acid), to increase sponginess and make these materials bioresorbable. A number of hemostatic dressings are now commercial, such as the HemCon® bandage [862, 864], and are utilized by the United States and European armed forces. The abundance of amine groups on CN has also been utilized to develop materials for treating peptic ulcers by neutralizing gastric acids and form a protective layer in the stomach [865, 866]. CN-based composites have also been developed to retain moisture and enable easy peeling for treatment of skin injuries and have been loaded with antibiotics to ensure a sterile environment for the healing of burns. Examples include blends of CN, poly(vinyl alcohol), and alginate, loaded with broad-spectrum antibacterials (*e.g.*, ciprofloxacin, minocycline, and ornidazole) and cast into moist films [867, 868] that form flexible and elastic membranes on wounds, and provide superior healing activity compared with conventional gauzes. To further facilitate dressing removal from critical wounds, thermo-responsive pNIPAAm has been combined with CN into films that can be easily peeled from the wound upon cooling [869]. Further,

in place of common antibiotics, silver and zinc oxide nanoparticles have been integrated CN films to avoid microorganism proliferation in infection-prone wounds [869-876].

1.4.2.3. Hyaluronic Acid (HA)

As a major component of the ECM in soft connective tissues, HA regulates lubrication, inter- and intra-cellular communication, exchange of nutrients and metabolic waste, and rheological properties and shock absorption [877, 878]. Its biocompatibility, biodegradability, and ease of functionalization make HA an ideal material for tissue engineering [879, 880]. Echoing its biological role, HA is mostly applied as a substrate for cartilage and bone tissue engineering and regeneration. HA, in fact, induces cartilage stem and progenitor cells to differentiate into chondrocytes [881, 882] and stimulate the deposition of ECM [883-887], thus promoting a microenvironment that is conducive to cartilage production and *in situ* regeneration [885, 888-890]. Similarly, HA also supports the adhesion, differentiation, and growth of MSCs and BMSCs for osteochondral tissue formation [891, 892] and bone formation and regeneration [893]. Thus, countless HA blends with natural and synthetic biopolymers [885-887, 894] and chemically modified, photopolymerizable, and thermo-responsive, [895- 901] HA gels have been developed to encapsulate chondrocytes, supporting excellent cellular viability and proliferation and secretion of cartilaginous ECM compounds (aggrecan, collagen type I and type II) [885, 902]. The materials have been utilized to construct and regenerate cartilage [902, 903], intervertebral disc [904] and nucleus pulposus [905], human meniscus [906], and vocal cords [907]. Analogous HA ingredients, loaded with growth factors (*e.g.*, BMP-2), and functionalized with complementary reactive groups or UV-reactive moieties (*e.g.*, acrylate and benzophenone) for *in situ* formation of strong hydrogels, have been developed for bone tissue engineering and regeneration [893, 908-915].

Notably, HA hydrogels are degraded by hyaluronidase at a rate dictated by the type and degree of modification, crosslinking, and blending with other materials. HA degradation enables the diffusion of growth factors, migration of cells, and distribution of ECM, ultimately promoting integration with the native tissues [916]. While high molecular weight HA is a known anti-inflammatory and inhibitor of cell proliferation [917, 918], low molecular weight HA has been found to promote cell migration and angiogenesis [917, 919, 920]. Functionalized hyaluronic acid oligomers (HAOs), *per se* [917, 921], or displayed on other biomaterials [922-924] promote vessel sprouting and outgrowth by driving cell migration through ECM and have been utilized to develop scaffolds for vascular grafts. HAO release by hyaluronidases from a gellan gum-HA hydrogel has been shown to promote the proliferation of HUVECs [925]. In another study, conductive thin films of HA were used to develop electrically-responsive systems that induce angiogenesis on demand *in vivo* [926]. HA porous hydrogels have also proven effective in the engineering and regeneration of neuronal tissue in animal models [927, 928]. Early work conducted with localized injections of HA in animal models of nerve damage showed axonal regeneration and improved conduction, together with a decrease of perineural scar tissue [929, 930]. Soft HA hydrogels, in fact, possess brain tissue-like modulus (< 1 kPa) and are ideal substrates for differentiating MSCs into neurogenic lineages and NSCs into neuronal lineages [931-933]. As biochemical functionalization became recognized as critical to ensure high regenerative outcomes, HA hydrogels functionalized with RGD peptides and growth factors multiplied. A RGD-decorated HA matrix with tunable stiffness and peptide density was developed to guide neural progenitor cells and promote neurite outgrowth [934]; while neurite extension was noted in HA matrices without cell-binding peptides, RGD-HA with optimized peptide density showed superior neurite outgrowth; similarly, the elasticity of the HA matrix showed a strong influence over the behavior of hippocampal neural

progenitor cells, with an optimum of outgrowth and density of neurites at a storage modulus of 400 Pa. Porous RGD-HA hydrogels were effectively employed in healing of cortex defects [935] and spinal cord injury (SCI) *in vivo*, [936] by improving vascularization and neurite extension while reducing scar formation in the defect area. A set of studies focused on HA-ephrinB2 conjugates that promote *in vivo* formation and differentiation of new neurons in areas of the brain that are in a prolonged state of inactivity through sustained delivery of ephrinB2 [937-939]. More recently, structural anisotropy (*e.g.*, uniaxial fibrils and nano-/micro-tubular constructs, matrices with gradient porosity) has been combined with biochemical functionalization (*e.g.*, NGF, neurotrophin-3 [NT-3], brain-derived neurotrophin neurotrophic factor ([BDNF]), glial cell line-derived neurotrophic factor [GDNF], and ciliary neurotrophic factor [CNTF]) to better guide the migration of cells toward lesion sites and promote growth and functional regeneration [940-944]. A number of studies have focused on the use of HA pre-filled with pluripotent stem cells to sustain survival, differentiation, and proliferation of stem cells into neuroblasts, thereby achieving better repair of nerve injuries [945-947]. This work has led to biomimetic cell-filled HA gels being utilized as inks for 3D bioprinting of neural replacement tissues [948]. The HA component of the bio-ink contains the biomolecular cues that drive cell differentiation into specific neural types upon printing. Bio-printed neuronal constructs feature precise control of the 3D spatial distribution of cell types and scaffold properties and therefore superior biomimetic and restorative behavior. Other studies on HA scaffolds have been focused on constructing adipose grafts or promoting proliferation and retention of adipose tissue *in vivo* [949]. HYAFF® 11 scaffolds, which consist of porous, bioresorbable foams of HA esters [950, 951], possess the physical and biochemical properties that are suitable for the development of functional adipose tissue. *In vitro* tests with HYAFF® 11 scaffolds have demonstrated adhesion and proliferation of adipocytes through the 3D

scaffolds; furthermore, *in vivo* studies with patients with small tissue deficit showed that implants produced by incubating adipose stromal cells into HYAFF® 11 scaffolds and implanted as subcutaneous pocket promoted the reconstruction of an adipose layer without triggering any toxicity or inflammation [952, 953]. Notably, these HA scaffolds have been also utilized for inducing human adipose stem cells into forming cornea-like structures [954].

1.4.2.4. Alginate

Easy to form, non-immunogenic, and non-toxic, alginate has become widely applied as injectable hydrogel, sponge, and fiber [955-960]. Like HA, alginate has been utilized to support vascular grafts and cardiac tissue repair, as well as cartilage, bone, neuronal, and adipose tissues. Examples of injectable hydrogels of alginate blends with HA and gelatin have shown excellent performance in encapsulating and maintaining the viability of primary chondrocytes, supporting their proliferation and migration within the polymer matrix, and integrating well with the ECM and the resulting cartilage with negligible inflammatory and oxidative stress responses [961, 962]. On the front of bone tissue engineering, porous structures of alginate and CN are produced by coacervation, which supported adhesion, proliferation, and production of calcified matrix by osteoblasts, resulting in excellent *in vivo* biocompatibility [963]. Recent studies have presented blends of alginate and calcium salts [964], micro- and nano-particles [965-969], and photo-crosslinkable polymers [970, 971] in the form of injectable pastes and cements preloaded with MSCs and biochemical cues for stimulating differentiation toward the osteogenic lineage; these formulations exhibited osteo-differentiation and secretion of bone minerals both *in vitro* and *in vivo* and promoted bone repair and in small and large animal models [972, 973]. Alginate patches functionalized with biochemical cues (*e.g.*, RGD peptides and growth factors) [974] have also

been utilized as scaffolds for cardiac tissue engineering. In several studies functionalized alginate patches supported adhesion and proliferation of neonatal rat cardiac cells and increased cardiac tissue regeneration compared with control alginate patches [974]; shortly after the application, micro-fibrous bundles of cardiomyocytes were noted, which showed integration with native tissue and regeneration of functional tissue in scar or necrotic areas [960, 975, 976].

1.5. Conclusion and Future Outlook

Three decades of research and preclinical development of peptide- and polysaccharide-based biomaterials for drug delivery and tissue engineering have brought a prodigious wealth of fundamental knowledge and technological capabilities to fruition of the scientific, pharmaceutical, and medical community. Having established the correlations between the physicochemical and biomolecular properties of these materials with their biological outcome *in vitro* and *in vivo*, a new epoch has recently begun, centered on the integration of these materials with modern design and fabrication techniques, devices for real-time monitoring, and cutting-edge biochemical and biological discoveries that can morph the human body into its own therapy manufacturer. The latest advancements in computational tools, in fact, enable accurate *in silico* modeling of complex supramolecular systems for extended simulation times that were unthinkable a handful of years ago and will soon extend modeling to the interactions between these systems and cells. In parallel, the development of new fabrication technologies, such as high-throughput 3D printing, and optical instrumentation enables precise assembly of truly biomimetic systems and accurate spatiotemporal control of their performance. Biopolymer materials are also undergoing integration with miniaturized implantable systems that collect biochemical data and control in real time the behavior of the implanted material and the release of the therapeutic or cellular payload and

communicate data with medical personnel. Finally, capitalizing on their ability as delivery agents, these biomaterials will enable next-generation therapeutic approaches, such as gene therapy, that harness the bio-machinery of the body to produce target-specific therapeutics

REFERENCES

- [1] Van Tomme, S.R., G. Storm, and W.E. Hennink, In situ gelling hydrogels for pharmaceutical and biomedical applications. *International Journal of Pharmaceutics*, 2008. 355(1): p. 1-18.
- [2] Huang, R., W. Qi, L. Fan, et al., Self-assembling peptide-polysaccharide hybrid hydrogel as a potential carrier for drug delivery. *Soft Matter*, 2011. 7(13): p. 6222-6230.
- [3] Hoffman, A.S., Hydrogels for biomedical applications. *Advanced Drug Delivery Reviews*, 2012. 64: p. 18-23.
- [4] Drury, J.L. and D.J. Mooney, Hydrogels for tissue engineering: scaffold design variables and applications. *Biomaterials*, 2003. 24(24): p. 4337-4351.
- [5] Seliktar, D., Designing cell-compatible hydrogels for biomedical applications. *Science*, 2012. 336(6085): p. 1124-1128.
- [6] Mahler, A., M. Reches, M. Rechter, et al., Rigid, Self-assembled hydrogel composed of a modified aromatic dipeptide. *Advanced Materials*, 2006. 18(11): p. 1365-1370.
- [7] Sui, Z., W.J. King, and W.L. Murphy, Protein-based hydrogels with tunable dynamic responses. *Advanced Functional Materials*, 2008. 18(12): p. 1824-1831.
- [8] Jin R., L.S. Moreira Teixeira, P.J. Dijkstra, et al., Injectable chitosan-based hydrogels for cartilage tissue engineering. *Biomaterials*, 2009. 30(13): p. 2544-2551.
- [9] Koutsopoulos, S., L.D. Unsworth, Y. Nagai, and S. Zhang, Controlled release of functional proteins through designer self-assembling peptide nanofiber hydrogel scaffold. *Proceedings of the National Academy of Sciences of the United States of America*, 2009. 106(12): p. 4623-4628.
- [10] Yanlian, Y., K. Ulung, W. Xiumei, et al., Designer self-assembling peptide nanomaterials. *Nano Today*, 2009. 4(2): p. 193-210.
- [11] Zhou, M., A.M. Smith, A.K. Das, et al., Self-assembled peptide-based hydrogels as scaffolds for anchorage-dependent cells. *Biomaterials*, 2009. 30(13): p. 2523-2530.
- [12] Cui, H., M.J. Webber, and S.I. Stupp, Self-assembly of peptide amphiphiles: from molecules to nanostructures to biomaterials. *Peptide Science*, 2010. 94(1): p. 1-18.
- [13] Covello, T., P. Matricardi, C. Marianelli, and F. Alhaique, Polysaccharide hydrogels for modified release formulations. *Journal of Controlled Release*, 2007. 119(1): p. 5-24.
- [14] Chawla, K., T.-B. Yu, S.W. Liao, and Z. Guan, Biodegradable and biocompatible synthetic saccharide-peptide hydrogels for three-dimensional stem cell culture. *Biomacromolecules*, 2011. 12(3): p. 560-567.

- [15] Altunbas, A. and D.J. Pochan, Peptide-based and polypeptide-based hydrogels for drug delivery and tissue engineering. *Topics in Current Chemistry*, 2012. 310: p. 135-167.
- [16] Jonker, A.M., D.W.P.M. Löwik, and J.C.M. van Hest, Peptide- and protein-based hydrogels. *Chemistry of Materials*, 2012. 24(5): p. 759-773.
- [17] Panda, J.J. and V. Singh Chauhan, Short peptide based self-assembled nanostructures: implications in drug delivery and tissue engineering. *Polymer Chemistry*, 2014. 5(15): p. 4418-4436.
- [18] Habibi, N., N. Kamaly, A. Memic, and H. Shafiee, Self-assembled peptide-based nanostructures: smart nanomaterials toward targeted drug delivery. *Nano Today*, 2016. 11(1): p. 41-60.
- [19] De Jong, W.H. and P.J.A. Borm, Drug delivery and nanoparticles: applications and hazards. *International Journal of Nanomedicine*, 2008. 3(2): p. 133-149.
- [20] Hu, Q., W. Sun, C. Wang, and Z. Gu, Recent advances of cocktail chemotherapy by combination drug delivery systems. *Advanced Drug Delivery Reviews*, 2016. 98: p. 19-34.
- [21] Rizvi, S.A.A. and A.M. Saleh, Applications of nanoparticle systems in drug delivery technology. *Saudi Pharmaceutical Journal*, 2018. 26(1): p. 64-70.
- [22] Croy, S.R. and G.S. Kwon, Polymeric micelles for drug delivery. *Current Pharmaceutical Design*, 2006. 12(36): p. 4669-4684.
- [23] Kedar, U., P. Phutane, S. Shidhaye, and V. Kadam, Advances in polymeric micelles for drug delivery and tumor targeting. *Nanomedicine: Nanotechnology, Biology and Medicine*, 2010. 6(6): p. 714-729.
- [24] Zhang, Y., Y. Huang, and S. Li, Polymeric micelles: nanocarriers for cancer-targeted drug delivery. *AAPS PharmSciTech*, 2014. 15(4): p. 862-871.
- [25] Hoare, T.R. and D.S. Kohane, Hydrogels in drug delivery: progress and challenges. *Polymer*, 2008. 49(8): p. 1993-2007.
- [26] Park, H., K. Park, and W.S.W. Shalaby, *Biodegradable Hydrogels for Drug Delivery*. 2011: CRC Press 272.
- [27] Li, J. and D.J. Mooney, Designing hydrogels for controlled drug delivery. *Nature Reviews Materials*, 2016. 1(12): p. 1-17.
- [28] Snyder, E.L. and S.F. Dowdy, Cell penetrating peptides in drug delivery. *Pharmaceutical Research*, 2004. 21(3): p. 389-393.

- [29] Temsamani, J. and P. Vidal, The use of cell-penetrating peptides for drug delivery. *Drug Discovery Today*, 2004. 9(23): p. 1012-1019.
- [30] Tréhin, R. and H.P. Merkle, Chances and pitfalls of cell penetrating peptides for cellular drug delivery. *European Journal of Pharmaceutics and Biopharmaceutics*, 2004. 58(2): p. 209-223.
- [31] Foged, C. and H.M. Nielsen, Cell-penetrating peptides for drug delivery across membrane barriers. *Expert Opinion on Drug Delivery*, 2008. 5(1): p. 105-117.
- [32] Vivès, E., J. Schmidt, and A. Pèlegrein, Cell-penetrating and cell-targeting peptides in drug delivery. *Biochimica et Biophysica Acta (BBA) - Reviews on Cancer*, 2008. 1786(2): p. 126-138.
- [33] Regberg, J., A. Srimanee, and Ü. Langel, Applications of cell-penetrating peptides for tumor targeting and future cancer therapies. *Pharmaceuticals*, 2012. 5(9): p. 991-1007.
- [34] Wang, F., Y. Wang, X. Zhang, et al., Recent progress of cell-penetrating peptides as new carriers for intracellular cargo delivery. *Journal of Controlled Release*, 2014. 174: p. 126-136.
- [35] Liu, Z., Y. Jiao, Y. Wang, et al., Polysaccharides-based nanoparticles as drug delivery systems. *Advanced Drug Delivery Reviews*, 2008. 60(15): p. 1650-1662.
- [36] Maia, J., L. Ferreira, R. Carvalho, et al., Synthesis and characterization of new injectable and degradable dextran-based hydrogels. *Polymer*, 2005. 46(23): p. 9604-9614.
- [37] Augst, A.D., H.J. Kong, and D.J. Mooney, Alginate hydrogels as biomaterials. *Macromolecular Bioscience*, 2006. 6(8): p. 623-633.
- [38] Dhaneshwar, S.S., M. Kandpal, N. Gairola, and S.S. Kadam, Dextran: a promising macromolecular drug carrier. *Indian Journal of Pharmaceutical Sciences*, 2006. 68(6): p. 705.
- [39] Bhattarai, N., J. Gunn, and M. Zhang, Chitosan-based hydrogels for controlled, localized drug delivery. *Advanced Drug Delivery Reviews*, 2010. 62(1): p. 83-99.
- [40] Kar, R., S. Mohapatra, S. Bhanja, et al., Formulation and in vitro characterization of xanthan gum-based sustained release matrix tablets of isosorbide-5-mononitrate. *Iranian Journal of Pharmaceutical Research : IJPR*, 2010. 9(1): p. 13-19.
- [41] Prabaharan, M., Prospective of guar gum and its derivatives as controlled drug delivery systems. *International Journal of Biological Macromolecules*, 2011. 49(2): p. 117-124.
- [42] Lee, K.Y. and D.J. Mooney, Alginate: properties and biomedical applications. *Progress in Polymer Science*, 2012. 37(1): p. 106-126.

- [43] Opera, A.-M., L. Profire, C.E. Lupusoru, et al., Synthesis and characterization of some cellulose/chondroitin sulphate hydrogels and their evaluation as carriers for drug delivery. *Carbohydrate Polymers*, 2012. 87(1): p. 721-729.
- [44] Varshosaz, J., Dextran conjugates in drug delivery. *Expert Opinion on Drug Delivery*, 2012. 9(5): p. 509-523.
- [45] Badwaik, H.R., T.K. Giri, K.T. Nakhate, et al., Xanthan gum and its derivatives as a potential bio-polymeric carrier for drug delivery system. *Current Drug Delivery*, 2013. 10(5): p. 587-600.
- [46] Kono, H., F. Otaka, and M. Ozaki, Preparation and characterization of guar gum hydrogels as carrier materials for controlled protein drug delivery. *Carbohydrate Polymers*, 2014. 111: p. 830-840.
- [47] Ahmadi, F., Z. Oveis, S. Mohammadi Samani, and Z. Amoozgar, Chitosan based hydrogels: characteristics and pharmaceutical applications. *Research in Pharmaceutical Sciences*, 2015. 10(1): p. 1-16.
- [48] Neves, S.C., D.B. Gomes, A. Sousa, et al., Biofunctionalized pectin hydrogels as 3D cellular microenvironments. *Journal of Materials Chemistry B*, 2015. 3(10): p. 2096-2108.
- [49] Hamedi, H., S. Moradi, S.M. Hudson, and A.E. Tonelli, Chitosan based hydrogels and their applications for drug delivery in wound dressings: a review. *Carbohydrate Polymers*, 2018. 199: p. 445-460.
- [50] Matricardi, P., C. Di Meo, T. Covello, et al., Interpenetrating polymer networks polysaccharide hydrogels for drug delivery and tissue engineering. *Advanced Drug Delivery Reviews*, 2013. 65(9): p. 1172-1187.
- [51] Li, S., Q. Xiong, X. Lai, et al., Molecular modification of polysaccharides and resulting bioactivities. *Comprehensive Reviews in Food Science and Food Safety*, 2016. 15(2): p. 237-250.
- [52] Ahmed, E.M., Hydrogel: preparation, characterization, and applications: a review. *Journal of Advanced Research*, 2015. 6(2): p. 105-121.
- [53] Kumar, D., J. Pandey, V. Raj, and P. Kumar, A review on the modification of polysaccharide through graft copolymerization for various potential applications. *The Open Medicinal Chemistry Journal*, 2017. 11: p. 109-126.
- [54] Lee, J.W., J.H. Park, and J.R. Robinson, Bioadhesive-based dosage forms: the next generation. *Journal of Pharmaceutical Sciences*, 2000. 89(7): p. 850-866.
- [55] Ma, T., Y. Li, S.T. Yang, and D.A. Kniss, Effects of pore size in 3-D fibrous matrix on human trophoblast tissue development. *Biotechnology and Bioengineering*, 2000. 70(6): p. 606-618.

- [56] Xie, Y., S.T. Yang, and D.A. Kniss, Three-dimensional cell-scaffold constructs promote efficient gene transfection: implications for cell-based gene therapy. *Tissue Engineering*, 2001. 7(5): p. 585-598.
- [57] Shimaoka, H., Y. Dohi, H. Ohgushi, et al., Recombinant growth/differentiation factor-5 (GDF-5) stimulates osteogenic differentiation of marrow mesenchymal stem cells in porous hydroxyapatite ceramic. *Journal of Biomedical Materials Research Part A*, 2004. 68A(1): p. 168-176.
- [58] Hosseinkhani, H., T. Azzam, H. Kobayashi, et al., Combination of 3D tissue engineered scaffold and non-viral gene carrier enhance in vitro DNA expression of mesenchymal stem cells. *Biomaterials*, 2006. 27(23): p. 4269-4278.
- [59] Hosseinkhani, H., M. Yamamoto, Y. Inatsugu, et al., Enhanced ectopic bone formation using a combination of plasmid DNA impregnation into 3-D scaffold and bioreactor perfusion culture. *Biomaterials*, 2006. 27(8): p. 1387-1398.
- [60] Collins, M.N. and C. Birkinshaw, Hyaluronic acid based scaffolds for tissue engineering—a review. *Carbohydrate Polymers*, 2013. 92(2): p. 1262-1279.
- [61] Schugens, C., V. Maquet, C. Grandfils, et al., Polylactide macroporous biodegradable implants for cell transplantation. II. Preparation of polylactide foams by liquid-liquid phase separation. *Journal of Biomedical Materials Research*, 1996. 30(4): p. 449-461.
- [62] Schugens, C., V. Maquet, C. Grandfils, et al., Biodegradable and macroporous polylactide implants for cell transplantation: 1. Preparation of macroporous polylactide supports by solid-liquid phase separation. *Polymer*, 1996. 37(6): p. 1027-1038.
- [63] Nam, Y.S. and T.G. Park, Porous biodegradable polymeric scaffolds prepared by thermally induced phase separation. *Journal of Biomedical Materials Research*, 1999. 47(1): p. 8-17.
- [64] Taboas, J.M., R.D. Maddox, P.H. Krebsbach, and S.J Hollister, Indirect solid free form fabrication of local and global porous, biomimetic and composite 3D polymer-ceramic scaffolds. *Biomaterials*, 2003. 24(1): p. 181-194.
- [65] Zein, I., D.W. Hutmacher, K.C. Tan, and S.H Teoh, Fused deposition modeling of novel scaffold architectures for tissue engineering applications. *Biomaterials*, 2002. 23(4): p. 1169-1185.
- [66] Hutmacher, D.W., K.W. Ng, C. Kaps, et al., Elastic cartilage engineering using novel scaffold architectures in combination with a biomimetic cell carrier. *Biomaterials*, 2003. 24(24): p. 4445-4458.
- [67] Mooney, D.J., D.F. Baldwin, N.P. Suh, et al., Novel approach to fabricate porous sponges of poly(D,L-lactic-co-glycolic acid) without the use of organic solvents. *Biomaterials*, 1996. 17(14): p. 1417-1422.

- [68] Harris, L.D., B.S. Kim, and D.J. Mooney, Open pore biodegradable matrices formed with gas foaming. *Journal of Biomedical Materials Research*, 1998. 42(3): p. 396-402.
- [69] Oxley, H.R., P.H. Corkhill, J.H. Fitton, and B.J. Tighe, Macroporous hydrogels for biomedical applications: methodology and morphology. *Biomaterials*, 1993. 14(14): p. 1064-1072.
- [70] Nikpour, M., H. Chaouk, A. Mau, et al., Porous conducting membranes based on polypyrrole-PMMA composites. *Synthetic Metals*, 1999. 99(2): p. 121-126.
- [71] Chen, G., T. Ushida, and T. Tateishi, Preparation of poly(L-lactic acid) and poly(DL-lactic-coglycolic acid) foams by use of ice microparticulates. *Biomaterials*, 2001. 22(18): p. 2563-2567.
- [72] Lin, A.S.P., T.H. Barrows, S.H. Cartmell, and R.E. Guldberg, Microarchitectural and mechanical characterization of oriented porous polymer scaffolds. *Biomaterials*, 2003. 24(3): p. 481-489.
- [73] Chirila, T.V., I.J. Constable, G.J. Crawford, et al., Poly(2-hydroxyethyl methacrylate) sponges as implant materials: in vivo and in vitro evaluation of cellular invasion. *Biomaterials*, 1993. 14(1): p. 26-38.
- [74] Kane, R.S., S. Takayama, E. Ostuni, et al., Patterning proteins and cells using soft lithography. *Biomaterials*, 1999. 20(23): p. 2363-2376.
- [75] Zhang, X., X.N. Jiang, and C. Sun, Micro-stereolithography of polymeric and ceramic microstructures. *Sensors and Actuators A: Physical*, 1999. 77(2): p. 149-156.
- [76] Balakrishnan, B. and R. Banerjee, Biopolymer-based hydrogels for cartilage tissue engineering. *Chemical Reviews*, 2011. 111(8): p. 4453-4474.
- [77] Bent, A.E., J. Foote, S. Siegel, et al., Collagen implant for treating stress urinary incontinence in women with urethral hypermobility. *Journal of Urology*, 2001. 166(4): p. 1354-1357.
- [78] Kogan, G., L. Soltés, R. Stern, and P. Gemeiner, Hyaluronic acid: a natural biopolymer with a broad range of biomedical and industrial applications. *Biotechnology Letters*, 2007. 29(1): p. 17-25.
- [79] Kim, I.L., R.L. Mauck, and J.A. Burdick, Hydrogel design for cartilage tissue engineering: a case study with hyaluronic acid. *Biomaterials*, 2011. 32(34): p. 8771-8782.
- [80] Chang, S.J., Y.-T. Huang, S.-C. Yang, et al., In vitro properties of gellan gum sponge as the dental filling to maintain alveolar space. *Carbohydrate Polymers*, 2012. 88(2): p. 684-689.

- [81] Fagien, S. and D. Cassuto, Reconstituted injectable hyaluronic acid: expanded applications in facial aesthetics and additional thoughts on the mechanism of action in cosmetic medicine. *Plastic and Reconstructive Surgery*, 2012. 130(1): p. 208-217.
- [82] Mossaad, B.M. and J.D. Frame, Correction of breast contour deformities using polyurethane breast implant capsule in revisional breast surgery. *Journal of Plastic, Reconstructive and Aesthetic Surgery : JPRASJournal of plastic, reconstructive and aesthetic surgery: JPRAS*, 2012. 65(10): p. 1425-1429.
- [83] Chan, W. and P. White, *Fmoc Solid Phase Peptide Synthesis: A Practical Approach*. 1999: Oxford University Press. 371.
- [84] Xiao, R. and M.W. Grinstaff, Chemical synthesis of polysaccharides and polysaccharide mimetics. *Progress in Polymer Science*, 2017. 74: p. 78-116.
- [85] Mano, J.F., G.A. Silva, H.S. Azevedo, et al., Natural origin biodegradable systems in tissue engineering and regenerative medicine: present status and some moving trends. *Journal of the Royal Society, Interface*, 2007. 4(17): p. 999-1030.
- [86] Pawar, R., W. Jadhav, S.R. Bhusare, et al., Polysaccharides as carriers of bioactive agents for medical applications, in *Natural-Based Polymers for Biomedical Applications*, (ed. R.L. Reis, N.M. Neves, J.F. Mano, et al.), 2008, Woodhead Publishing: Cambridge, United Kingdom. p. 3-53.
- [87] Senni, K., J. Pereira, F. Gueniche, et al., Marine polysaccharides: a source of bioactive molecules for cell therapy and tissue engineering. *Marine Drugs*, 2011. 9(9): p. 1664-1681.
- [88] Malafaya, P.B., G.A. Silva, and R.L. Reis, Natural-origin polymers as carriers and scaffolds for biomolecules and cell delivery in tissue engineering applications. *Advanced Drug Delivery Reviews*, 2007. 59(4): p. 207-233.
- [89] Gomes, S., I.B. Leonor, J.F. Mano, et al., Natural and genetically engineered proteins for tissue engineering. *Progress in Polymer Science*, 2012. 37(1): p. 1-17.
- [90] Cemazar, M. and D.J. Craik, Microwave-assisted Boc-solid phase peptide synthesis of cyclic cysteine-rich peptides. *Journal of Peptide Science*, 2008. 14(6): p. 683-689.
- [91] Collier, J.H. and T. Segura, Evolving the use of peptides as biomaterials components. *Biomaterials*, 2011. 32(18): p. 4198-4204.
- [92] Ito, Y. and S. Manabe, Solid-phase oligosaccharide synthesis and related technologies. *Current Opinion in Chemical Biology*, 1998. 2(6): p. 701-708.
- [93] Andrade, R.B., O.J. Plante, L.G. Melean, and P.H. Seeberger, Solid-phase oligosaccharide synthesis: preparation of complex structures using a novel linker and different glycosylating agents. *Organic Letters*, 1999. 1(11): p. 1811-1814.

- [94] Seeberger, P.H. and W.-C. Haase, Solid-phase oligosaccharide synthesis and combinatorial carbohydrate libraries. *Chemical Reviews*, 2000. 100(12): p. 4349-4394.
- [95] Zhu, T. and G.-J. Boons, A new set of orthogonal-protecting groups for oligosaccharide synthesis on a polymeric support. *Tetrahedron: Asymmetry*, 2000. 11(1): p. 199-205.
- [96] Wang, Q., J.S. Dordick, and R.J. Linhardt, Synthesis and application of carbohydrate containing polymers. *Chemistry of Materials*, 2002. 14(8): p. 3232-3244.
- [97] Rauter, A.P., T. Lindhorst, and Y. Queneau, *Carbohydrate Chemistry*. 2014: Royal Society of Chemistry. 671.
- [98] Polyakova, S.M., A.V. Nizovtsev, R.A. Kunetskiy, and N.V. Bovin, New protecting groups in the synthesis of oligosaccharides. *Russian Chemical Bulletin*, 2015. 64(5): p. 973-989.
- [99] Bouchet-Spinelli, A., B. Reuillard, L. Coche-Guérente, et al., Oligosaccharide biosensor for direct monitoring of enzymatic activities using QCM-D. *Biosensors and Bioelectronics*, 2013. 49: p. 290-296.
- [100] Sun, Y.-S. and X.D. Zhu, Real-time, label-free characterization of oligosaccharide-binding proteins using carbohydrate microarrays and an ellipsometry-based biosensor. *Instrumentation Science and Technology*, 2017. 45(5): p. 506-524
- [101] Boltje, T.J., T. Buskas, and G.-J. Boons, Opportunities and challenges in synthetic oligosaccharide and glycoconjugate research. *Nature Chemistry*, 2009. 1(8): p. 611-622.
- [102] Ravichandran, V., G.P. Kothandaraman, C. Bories, et al, Synthetic polysaccharides as drug carriers: synthesis of polyglucose-amphotericin B conjugates and in vitro evaluation of their anti-fungal and anti-leishmanial activities, *Journal of Nanoscience and Nanotechnology*, 2018. 18(4): p. 2405-2414.
- [103] Nair, J.K., J.L. Willoughby, A. Chan, et al., Multivalent N-acetylgalactosamine-conjugated siRNA localizes in hepatocytes and elicits robust RNAi-mediated gene silencing. *Journal of the American Chemical Society*, 2014. 136(49): p. 16958-16961.
- [104] Huang, Y., Preclinical and clinical advances of GalNAc-decorated nucleic acid therapeutics. *Molecular Therapy. Nucleic Acids*, 2017. 6: p. 116-132.
- [105] Springer, A.D. and S.F. Dowdy, GalNAc-siRNA conjugates: leading the way for delivery of RNAi therapeutics. *Nucleic Acid Therapeutics*, 2018. 28(3): p. 109-118.
- [106] Bouhadir, K.H., Sustained and controlled release of daunomycin from cross-linked poly(aldehyde guluronate) hydrogels. *Journal of Pharmaceutical Sciences*, 2000. 89(7): p. 10.

- [107] Rodríguez, R.A., C. Alvarez-Lorenzo, and A. Concheiro, Interactions of ibuprofen with cationic polysaccharides in aqueous dispersions and hydrogels. European Journal of Pharmaceutical Sciences, 2003. 20(4-5): p. 429-438.
- [108] Zhang, L., A.F. Radovic-Moreno, F. Alexis, et al., Co-delivery of hydrophobic and hydrophilic drugs from nanoparticle-aptamer bioconjugates. ChemMedChem, 2007. 2(9): p. 1268-1271.
- [109] Li, S.-D. and L. Huang, Pharmacokinetics and biodistribution of nanoparticles. Molecular Pharmaceutics, 2008. 5(4): p. 496-504.
- [110] Farokhzad, O.C. and R. Langer, Impact of nanotechnology on drug delivery. ACS Nano, 2009. 3(1): p. 16-20.
- [111] Li, S.-D. and L. Huang, Stealth nanoparticles: high density but sheddable PEG is a key for tumor targeting. Journal of Controlled Release, 2010. 145(3): p. 178-181.
- [112] Liu, D., L.M. Bimbo, E. Mäkilä, et al., Co-delivery of a hydrophobic small molecule and a hydrophilic peptide by porous silicon nanoparticles. Journal of Controlled Release, 2013. 170(2): p. 268-278.
- [113] Guo, S. and L. Huang, Nanoparticles containing insoluble drug for cancer therapy. Biotechnology Advances, 2014. 32(4): p. 778-788.
- [114] Yui, N., Supramolecular Design for Biological Applications. 2002: CRC Press 424.
- [115] Webber, M.J. and R. Langer, Drug delivery by supramolecular design. Chemical Society Reviews, 2017. 46(21): p. 6600-6620.
- [116] de Bruyn Ouboter, D., Rational design of purely peptidic amphiphiles for drug delivery applications. 2011, University of Basel. p. 133 S.
- [117] Mandal, D., A.N. Shirazi, and K. Parang, Self-assembly of peptides to nanostructures. Organic and Biomolecular Chemistry, 2014. 12(22): p. 3544-3561.
- [118] Eskandari, S., et al., Recent advances in self-assembled peptides: implications for targeted drug delivery and vaccine engineering. Advanced Drug Delivery Reviews, 2017. 110-111: p. 169-187.
- [119] Fan, T., X. Yu, B. Shen, and L. Sun, Peptide self-assembled nanostructures for drug delivery applications. Journal of Nanomaterials, 2017. 9: p. 1-16.
- [120] Kumar, P., V. Pillay, G. Modi, et al., Self-assembling peptides: implications for patenting in drug delivery and tissue engineering. Recent Patents on Drug Delivery and Formulation, 2011. 5(1): p. 24-51.

- [121] Hong, Y., R.L. Legge, S. Zhang, and P. Chen, Effect of amino acid sequence and pH on nanofiber formation of self-assembling peptides EAK16-II and EAK16-IV. *Biomacromolecules*, 2003. 4(5): p. 1433-1442.
- [122] Larsen, T.H., M.C. Branco, K. Rajagopal, et al., Sequence-dependent gelation kinetics of β -hairpin peptide hydrogels. *Macromolecules*, 2009. 42(21): p. 8443-8450.
- [123] Bowerman, C.J., W. Liyanage, A.J. Federation, and B.L. Nilsson, Tuning β -sheet peptide self-assembly and hydrogelation behavior by modification of sequence hydrophobicity and aromaticity. *Biomacromolecules*, 2011. 12(7): p. 2735-2745.
- [124] Pu, K.-Y., K. Li, and B. Liu, Multicolor conjugate polyelectrolyte/peptide complexes as self-assembled nanoparticles for receptor-targeted cellular imaging. *Chemistry of Materials*, 2010. 22(24): p. 6736-6741.
- [125] Wang, W. and Y. Chau, Self-assembly mediated platform for rapid and facile preparation of peptide-functionalized nanoparticles with high stability. *Chemistry of Materials*, 2012. 24(5): p. 946-953.
- [126] Jin, Y., Y. Huang, H. Yang, et al., A peptide-based pH-sensitive drug delivery system for targeted ablation of cancer cells. *Chemical Communications*, 2015. 51(77): p. 14454-14457.
- [127] Chang, C., P. Liang, L. Chen, et al., pH-responsive nanoparticle assembly from peptide amphiphiles for tumor targeting drug delivery. *Journal of Biomaterials Science. Polymer Edition*, 2017. 28(13): p. 1338-1350.
- [128] Feng, Y., M. Taraban, and Y.B. Yu, The effect of ionic strength on the mechanical, structural and transport properties of peptide hydrogels. *Soft Matter*, 2012. 8(46): p. 11723-11731.
- [129] Li, R., C.C. Horgan, B. Long, et al., Tuning the mechanical and morphological properties of self-assembled peptide hydrogels via control over the gelation mechanism through regulation of ionic strength and the rate of pH change. *RSC Advances*, 2015. 5(1): p. 301-307.
- [130] Mackay, J.A. and A. Chilkoti, Temperature sensitive peptides: engineering hyperthermia-directed therapeutics. *International Journal of Hyperthermia*, 2008. 24(6): p. 483-495.
- [131] Aladini, F., C. Araman, and C.F.W. Becker, Chemical synthesis and characterization of elastin-like polypeptides (ELPs) with variable guest residues. *Journal of Peptide Science*, 2016. 22(5): p. 334-342.
- [132] Yishay-Safranchik, E., M. Golan, and A. David, Controlled release of doxorubicin and Smac-derived pro-apoptotic peptide from self-assembled KLD-based peptide hydrogels. *Polymers for Advanced Technologies*, 2014. 25(5): p. 539-544.

- [133] Lu, S., H. Wang, Y. Sheng, et al., Molecular binding of self-assembling peptide EAK16-II with anticancer agent EPT and its implication in cancer cell inhibition. *Journal of Controlled Release*, 2012. 160(1): p. 33-40.
- [134] Von Malzahn, G., S. Vauthey, S. Santoso, and S. Zhang, Positively charged surfactant-like peptides self-assemble into nanostructures. *Langmuir*, 2003. 19(10): p. 4332-4337.
- [135] Jabbari, E., et al., Drug release kinetics, cell uptake, and tumor toxicity of hybrid VVVVVVKK peptide-assembled polylactide nanoparticles. *European Journal of Pharmaceutics and Biopharmaceutics*, 2013. 84(1): p. 49-62.
- [136] Yan, X., Q. He, K. Wang, et al., Transition of cationic dipeptide nanotubes into vesicles and oligonucleotide delivery. *Angewandte Chemie*, 2007. 46(14): p. 2431-2434.
- [137] McCarthy, H.O., J. McCafferty, C.M. McCrudden, et al, Development and characterization of self-assembling nanoparticles using a bio-inspired amphipathic peptide for gene delivery. *Journal of Controlled Release*, 2014. 189: p. 141-149.
- [138] Naskar, J., S. Roy, A. Joardar, et al., Self-assembling dipeptide-based nontoxic vesicles as carriers for drugs and other biologically important molecules. *Organic and Biomolecular Chemistry*, 2011. 9(19): p. 6610-6615.
- [139] Naskar, J., G. Palui, and A. Banerjee, Tetrapeptide-based hydrogels: for encapsulation and slow release of an anticancer drug at physiological pH. *Journal of Physical Chemistry B*, 2009. 113(35): p. 11787-11792.
- [140] Hayashi, C.Y., N.H. Shipley, and R.V. Lewis, Hypotheses that correlate the sequence, structure, and mechanical properties of spider silk proteins. *International Journal of Biological Macromolecules*, 1999. 24(2-3): p. 271-275.
- [141] Matsumoto, A., J. Chen, A.L. Collette, et al., Mechanisms of silk fibroin sol-gel transitions. *Journal of Physical Chemistry B*, 2006. 110(43): p. 21630-21638.
- [142] Slotta, U., S. Hess, K. Spiess, et al., Spider silk and amyloid fibrils: a structural comparison. *Macromolecular Bioscience*, 2007. 7(2): p. 183-188.
- [143] Aggeli, A., S.J. Hamodrakas, K. Komitopoulou, and M. Konsolaki, Tandemly repeating peptide motifs and their secondary structure in *Ceratitis capitata* eggshell proteins Ccs36 and Ccs38. *International Journal of Biological Macromolecules*, 1991. 13(5): p. 307-315.
- [144] Green, N.M., N.G. Wrigley, W.C. Russell, et al., Evidence for a repeating cross-beta sheet structure in the adenovirus fibre. *The EMBO Journal*, 1983. 2(8): p. 1357-1365.
- [145] Gelain, F., A. Horii, and S. Zhang, Designer self-assembling peptide scaffolds for 3-D tissue cell cultures and regenerative medicine. *Macromolecular Bioscience*, 2007. 7(5): p. 544-551.

- [146] Fung, S.Y., H. Yang, and P. Chen, Sequence effect of self-assembling peptides on the complexation and in vitro delivery of the hydrophobic anticancer drug ellipticine. *PLoS One*, 2008. 3(4): p. e1956.
- [147] Mastrobattista, E., M.A. van der Aa, W.E. Hennink, and D.J. Crommelin, Artificial viruses: a nanotechnological approach to gene delivery. *Nature Reviews Drug Discovery*, 2006. 5(2): p. 115-121.
- [148] Henricus, M.M., K.T. Johnson, and I.A. Banerjee, Investigation of insulin loaded self-assembled microtubules for drug release. *Bioconjugate Chemistry*, 2008. 19(12): p. 2394-2400.
- [149] Lim, Y.-B., K.-S. Moon, and M. Lee, Recent advances in functional supramolecular nanostructures assembled from bioactive building blocks. *Chemical Society Reviews*, 2009. 38(4): p. 925-934.
- [150] Chung, E.K., E. Lee, Y.B. Kim, and M. Lee, Cyclic peptide facial amphiphile preprogrammed to self-assemble into bioactive peptide capsules. *Chemistry – A European Journal*, 2010. 16(18): p. 5305-5309.
- [151] Zhang, J., R. Hao, L. Huang, et al., Self-assembly of a peptide amphiphile based on hydrolyzed *Bombyx mori* silk fibroin. *Chemical Communications*, 2011. 47(37): p. 10296-10298.
- [152] Wang, Q., X. Zhang, J. Zheng, and D. Liu, Self-assembled peptide nanotubes as potential nanocarriers for drug delivery. *RSC Advances*, 2014. 4(48): p. 25461-25469.
- [153] Sadatmousavi, Parisa. "Peptide-mediated anticancer drug delivery." Master's thesis, University of Waterloo, 2009.
- [154] Leonard, S.R., A.R. Cormier, X. Pang, et al., Solid-state NMR evidence for β -hairpin structure within MAX8 designer peptide nanofibers. *Biophysical Journal*, 2013. 105(1): p. 222-230.
- [155] Haines-Butterick, L., K. Rajagopal, M. Branco, et al., Controlling hydrogelation kinetics by peptide design for three-dimensional encapsulation and injectable delivery of cells. *Proceedings of the National Academy of Sciences of the United States of America*, 2007. 104(19): p. 7791-7796.
- [156] Altunbas, A., S.J. Lee, S.A. Rajasekeran, et al., Encapsulation of curcumin in self-assembling peptide hydrogels as injectable drug delivery vehicles. *Biomaterials*, 2011. 32(25): p. 5906-5914.
- [157] Liu, J., J. Liu, H. Xu, et al., Novel tumor-targeting, self-assembling peptide nanofiber as a carrier for effective curcumin delivery. *International Journal of Nanomedicine*, 2014. 9: p. 197-207.

- [158] Zarzhitsky, S. and H. Rapaport, The interactions between doxorubicin and amphiphilic and acidic β -sheet peptides towards drug delivery hydrogels. *Journal of Colloid and Interface Science*, 2011. 360(2): p. 525-531.
- [159] Wu, H., T. Zhou, L. Tian, et al., Self-assembling RADA16-I peptide hydrogel scaffold loaded with tamoxifen for breast reconstruction. *BioMed Research International*, 2017. 3656193: p. 1-10.
- [160] Fung, S.Y., H. Yang, and P. Chen, Formation of colloidal suspension of hydrophobic compounds with an amphiphilic self-assembling peptide. *Colloids and Surfaces B: Biointerfaces*, 2007. 55(2): p. 200-211.
- [161] Fung, S.Y., H. Yang, P.T. Bhola, et al., Self-assembling peptide as a potential carrier for hydrophobic anticancer drug ellipticine: complexation, release and in vitro delivery. *Advanced Functional Materials*, 2009. 19(1): p. 74-83.
- [162] Zhang, S., Emerging biological materials through molecular self-assembly. *Biotechnology Advances*, 2002. 20(5): p. 321-339.
- [163] Davis, M.E., P.C.H. Hsieh, T. Takahashi, et al., Local myocardial insulin-like growth factor 1 (IGF-1) delivery with biotinylated peptide nanofibers improves cell therapy for myocardial infarction. *Proceedings of the National Academy of Sciences of the United States of America*, 2006. 103(21): p. 8155-8160.
- [164] Hsieh, P.C.H., C. MacGillivray, J. Gannon, et al., Local controlled intramyocardial delivery of platelet-derived growth factor improves postinfarction ventricular function without pulmonary toxicity. *Circulation*, 2006. 114(7): p. 637-644.
- [165] Segers, V.F., T. Tokunou, L.J. Higgins, et al., Local delivery of protease-resistant stromal cell derived factor-1 for stem cell recruitment after myocardial infarction. *Circulation*, 2007. 116(15): p. 1683-1692.
- [166] Padin-Iruegas, M.E., Y. Misao, M.E. Davis, et al., Cardiac progenitor cells and biotinylated insulin-like growth factor-1 nanofibers improve endogenous and exogenous myocardial regeneration after infarction. *Circulation*, 2009. 120(10): p. 876-887.
- [167] Guo, H.-D., G.-H. Cui, J.-J. Yang, et al., Sustained delivery of VEGF from designer self-assembling peptides improves cardiac function after myocardial infarction. *Biochemical and Biophysical Research Communications*, 2012. 424(1): p. 105-111.
- [168] Zhou, A., S. Chen, B. He, et al., Controlled release of TGF-beta 1 from RADA self-assembling peptide hydrogel scaffolds. *Drug Design, Development and Therapy*, 2016. 10: p. 3043-3051.

- [169] Hsieh, P.C.H., M.E. Davis, J. Gannon, et al., Controlled delivery of PDGF-BB for myocardial protection using injectable self-assembling peptide nanofibers. *Journal of Clinical Investigation*, 2006. 116(1): p. 237-248.
- [170] Kim, J.H., Y. Jung, S.-H. Kim, et al., The enhancement of mature vessel formation and cardiac function in infarcted hearts using dual growth factor delivery with self-assembling peptides. *Biomaterials*, 2011. 32(26): p. 6080-6088.
- [171] Xu, F.-F., Y.-C. Wang, S. Sun, et al., Comparison between self-assembling peptide nanofiber scaffold (SAPNS) and fibrin sealant in neurosurgical hemostasis. *Clinical and Translational Science*, 2015. 8(5): p. 490-494.
- [172] Wu, X., L. He, W. Li, et al., Functional self-assembling peptide nanofiber hydrogel for peripheral nerve regeneration. *Regenerative Biomaterials*, 2017. 4(1): p. 21-30.
- [173] Liu, W., L.M. Jawerth, E.A. Sparks, et al., Fibrin fibers have extraordinary extensibility and elasticity. *Science*, 2006. 313(5787): p. 634.
- [174] Brown, A.E.X., R.I. Litvinov, D.E. Discher, and J.W. Weisel, Forced unfolding of coiled-coils in fibrinogen by single-molecule AFM. *Biophysical Journal*, 2007. 92(5): p. L39-L41.
- [175] Piechocka, I.K., R.G. Bacabac, M. Potters, et al., Structural hierarchy governs fibrin gel mechanics. *Biophysical Journal*, 2010. 98(10): p. 2281-2289.
- [176] Yu, Y.B., Coiled-coils: stability, specificity, and drug delivery potential. *Advanced Drug Delivery Reviews*, 2002. 54(8): p. 1113-1129.
- [177] Ulijn, R.V. and A.M. Smith, Designing peptide based nanomaterials. *Chemical Society Reviews*, 2008. 37(4): p. 664-675.
- [178] Fletcher, N.L., C.V. Lockett, and A.F. Dexter, A pH-responsive coiled-coil peptide hydrogel. *Soft Matter*, 2011. 7(21): p. 10210-10218.
- [179] Banwell, E.F., E.S. Abelardo, D.J. Adams, et al., Rational design and application of responsive α -helical peptide hydrogels. *Nature Materials*, 2009. 8(7): p. 596-600.
- [180] Kojima, S., Y. Kuriki, T. Yoshida, et al., Fibril formation by an amphipathic α -helix-forming polypeptide produced by gene engineering. *Proceedings of the Japan Academy, Series B*, 1997. 73(1): p. 7-11.
- [181] Zimenkov, Y., V.P. Conticello, L. Guo, and P. Thiagarajan, Rational design of a nanoscale helical scaffold derived from self-assembly of a dimeric coiled coil motif. *Tetrahedron*, 2004. 60(34): p. 7237-7246.

- [182] Kojima, S., Y. Kuriki, K. Yazaki, and K. Miura, Stabilization of the fibrous structure of an α -helix-forming peptide by sequence reversal. *Biochemical and Biophysical Research Communications*, 2005. 331(2): p. 577-582.
- [183] Li, W., F. Nicol, and F.C. Szoka, GALA: a designed synthetic pH-responsive amphipathic peptide with applications in drug and gene delivery. *Advanced Drug Delivery Reviews*, 2004. 56(7): p. 967-985.
- [184] Melnik, T.N., V. Villard, V. Vasiliev, et al., Shift of fibril-forming ability of the designed α -helical coiled-coil peptides into the physiological pH region. *Protein Engineering, Design and Selection*, 2003. 16(12): p. 1125-1130.
- [185] Kajava, A.V., S.A. Potekhin, G. Corradin, and R.D. Leapman, Organization of designed nanofibrils assembled from α -helical peptides as determined by electron microscopy. *Journal of Peptide Science*, 2004. 10(5): p. 291-297.
- [186] Villard, V., O. Kalyuzhniy, O. Riccio, et al., Synthetic RGD-containing α -helical coiled coil peptides promote integrin-dependent cell adhesion. *Journal of Peptide Science*, 2006. 12(3): p. 206-212.
- [187] Zimenkov, Y., S.N. Dublin, R. Ni, et al., Rational design of a reversible pH-responsive switch for peptide self-assembly. *Journal of the American Chemical Society*, 2006. 128(21): p. 6770-6771.
- [188] Wagner, D.E., C.L. Phillips, W.M. Ali, et al., Toward the development of peptide nanofilaments and nanoropes as smart materials. *Proceedings of the National Academy of Sciences of the United States of America*, 2005. 102(36): p. 12656.
- [189] Gribbon, C., K.J. Channon, W. Zhang, et al., MagicWand: a single, designed peptide that assembles to stable, ordered α -helical fibers. *Biochemistry*, 2008. 47(39): p. 10365-10371.
- [190] Yan, C. and D.J. Pochan, Rheological properties of peptide-based hydrogels for biomedical and other applications. *Chemical Society Reviews*, 2010. 39(9): p. 3528-3540.
- [191] Wu, Y. and J.H. Collier, α -Helical coiled-coil peptide materials for biomedical applications. *Wiley Interdisciplinary Reviews: Nanomedicine and Nanobiotechnology*, 2017. 9(2): p. e1424.
- [192] Gabrielson, N.P., H. Lu, L. Yin, et al., Reactive and bioactive cationic α -helical polypeptide template for nonviral gene delivery. *Angewandte Chemie*, 2012. 51(5): p. 1143-1147.
- [193] Lee, D., Y.M. Li, J. Kim, et al., Enhanced tumor-targeted gene delivery by bioreducible polyethylenimine tethering EGFR divalent ligands. *Biomaterials Science*, 2015. 3(7): p. 1096-1104.

- [194] Caplan, M.R., E.M. Schwartzfarb, S. Zhang, et al., Control of self-assembling oligopeptide matrix formation through systematic variation of amino acid sequence. *Biomaterials*, 2002. 23(1): p. 219-227.
- [195] Vauthhey, S., S. Santoso, H. Gong, et al., Molecular self-assembly of surfactant-like peptides to form nanotubes and nanovesicles. *Proceedings of the National Academy of Sciences of the United States of America*, 2002. 99(8): p. 5355-5360.
- [196] Hamley, I.W., Self-assembly of amphiphilic peptides. *Soft Matter*, 2011. 7(9): p. 4122-4138.
- [197] Krogstad, D.V., Investigating the Structure-property Relationships of Aqueous Self-assembled Materials. 2012: University of California, Santa Barbara, CA. 262.
- [198] Mazza, M., A. Patel, R. Pons, et al., Peptide nanofibres as molecular transporters: from self-assembly to in vivo degradation. *Faraday Discussions*, 2014. 166(0): p. 181-194.
- [199] Mazza, M., R. Norman, J. Anwar, et al., Nanofiber-based delivery of therapeutic peptides to the brain. *ACS Nano*, 2013. 7(2): p. 1016-1026.
- [200] Kim, J.-K., J. Anderson, H.-W. Jun, et al., Self-assembling peptide amphiphile-based nanofiber gel for bioresponsive cisplatin delivery. *Molecular Pharmaceutics*, 2009. 6(3): p. 978-985.
- [201] Sardan, M., M. Kilinc, R. Genc, et al., Cell penetrating peptide amphiphile integrated liposomal systems for enhanced delivery of anticancer drugs to tumor cells. *Faraday Discussions*, 2014. 166(0): p. 269-283.
- [202] Boekhoven, J., R.H. Zha, F. Tantakitti, et al., Alginate-peptide amphiphile core-shell microparticles as a targeted drug delivery system. *RSC Advances*, 2015. 5(12): p. 8753-8756.
- [203] Ghanaati, S., M.J. Webber, R.E. Unger, et al., Dynamic in vivo biocompatibility of angiogenic peptide amphiphile nanofibers. *Biomaterials*, 2009. 30(31): p. 6202-6212.
- [204] Chow, L.W., L.J. Wang, D.B. Kaufman, and S.I. Stupp, Self-assembling nanostructures to deliver angiogenic factors to pancreatic islets. *Biomaterials*, 2010. 31(24): p. 6154-6161.
- [205] Angeloni, N.L., C.W. Bond, Y. Tang, et al., Regeneration of the cavernous nerve by sonic hedgehog using aligned peptide amphiphile nanofibers. *Biomaterials*, 2011. 32(4): p. 1091-1101.
- [206] Preslar, A.T., G. Parigi, M.T. McClendon, et al., Gd(III)-labeled peptide nanofibers for reporting on biomaterial localization in vivo. *ACS Nano*, 2014. 8(7): p. 7325-7332.
- [207] Kim, H.-J., T. Kim, and M. Lee, Responsive nanostructures from aqueous assembly of rigid-flexible block molecules. *Accounts of Chemical Research*, 2011. 44(1): p. 72-82.

- [208] Guo, X.D., F. Tandiono, N. Wiradharma, et al., Cationic micelles self-assembled from cholesterol-conjugated oligopeptides as an efficient gene delivery vector. *Biomaterials*, 2008. 29(36): p. 4838-4846.
- [209] Morris, M.C., P. Vidal, L. Chaloin, et al., A new peptide vector for efficient delivery of oligonucleotides into mammalian cells. *Nucleic Acids Research*, 1997. 25(14): p. 2730-2736.
- [210] Simeoni, F., M.C. Morris, F. Heitz, and G. Divita, Insight into the mechanism of the peptide-based gene delivery system MPG: implications for delivery of siRNA into mammalian cells. *Nucleic Acids Research*, 2003. 31(11): p. 2717-2724.
- [211] Crombez, L., M.C. Morris, S. Deshayes, et al., Peptide-based nanoparticle for ex vivo and in vivo drug delivery. *Current Pharmaceutical Design*, 2008. 14(34): p. 3656-3665.
- [212] Wiradharma, N., Y.W. Tong, and Y.-Y. Yang, Self-assembled oligopeptide nanostructures for co-delivery of drug and gene with synergistic therapeutic effect. *Biomaterials*, 2009. 30(17): p. 3100-3109.
- [213] Ouyang, L., W. Huang, G. He, and L. Guo, Bone targeting prodrugs based on peptide dendrimers, synthesis and hydroxyapatite binding in vitro. *Letters in Organic Chemistry*, 2009. 6(4): p. 272-277.
- [214] Jiang, T., X. Yu, E.J. Carbone, et al., Poly aspartic acid peptide-linked PLGA based nanoscale particles: potential for bone-targeting drug delivery applications. *International Journal of Pharmaceutics*, 2014. 475(1-2): p. 547-557.
- [215] Sone, E.D. and S.I. Stupp, Semiconductor-encapsulated peptide–amphiphile nanofibers. *Journal of the American Chemical Society*, 2004. 126(40): p. 12756-12757.
- [216] Palmer, L.C., C.J. Newcomb, S.R. Kaltz, et al., Biomimetic systems for hydroxyapatite mineralization inspired by bone and enamel. *Chemical Reviews*, 2008. 108(11): p. 4754-4783.
- [217] Spoerke, E.D., S.G. Anthony, and S. Stupp, Enzyme directed templating of artificial bone mineral. *Advanced Materials*, 2009. 21(4): p. 425-430.
- [218] Sutton, S., N.L. Campbell, A.I. Cooper, et al., Controlled release from modified amino acid hydrogels governed by molecular size or network dynamics. *Langmuir*, 2009. 25(17): p. 10285-10291.
- [219] Polo-Corrales, L., M. Latorre-Esteves, and J.E. Ramirez-Vick, Scaffold design for bone regeneration. *Journal of Nanoscience and Nanotechnology*, 2014. 14(1): p. 15-56.
- [220] Rapaport H, inventor; Ben Gurion University of Negev Research, Development Authority Ltd, assignee. Amphiphilic peptides and hydrogel matrices thereof for bone repair. United States patent US 8,658,763. 2014 Feb 25.

- [221] Webber, M.J., C.J. Newcomb, R. Bitton, and S.I. Stupp, Switching of self-assembly in a peptide nanostructure with a specific enzyme. *Soft Matter*, 2011. 7(20): p. 9665-9672.
- [222] Deming, T., Peptide-Based Materials, Topics in Current Chemistry., (ed. T. Deming), 2012, Springer: Berlin Heidelberg-Verlag.
- [223] Shi, P., J.A. Gustafson, and J.A. MacKay, Genetically engineered nanocarriers for drug delivery. *International Journal of Nanomedicine*, 2014. 9: p. 1617-1626.
- [224] McDaniel, J.R., D.J. Callahan, and A. Chilkoti, Drug delivery to solid tumors by elastin-like polypeptides. *Advanced Drug Delivery Reviews*, 2010. 62(15): p. 1456-1467.
- [225] Amiram, M., K.M. Luginbuhl, X. Li, et al., Injectable protease-operated depots of glucagon-like peptide-1 provide extended and tunable glucose control. *Proceedings of the National Academy of Sciences of the United States of America*, 2013. 110(8): p. 2792-2797.
- [226] MacEwan, S.R. and A. Chilkoti, Applications of elastin-like polypeptides in drug delivery. *Journal of Controlled Release*, 2014. 190: p. 314-330.
- [227] Bidwell, G.L. and D. Raucher, Cell penetrating elastin-like polypeptides for therapeutic peptide delivery. *Advanced Drug Delivery Reviews*, 2010. 62(15): p. 1486-1496.
- [228] Ryu, J.S. and D. Raucher, Anti-tumor efficacy of a therapeutic peptide based on thermo-responsive elastin-like polypeptide in combination with gemcitabine. *Cancer Letters*, 2014. 348(1): p. 177-184.
- [229] McDaniel, J.R., S.R. Macewan, M. Dewhirst, and A. Chilkoti, Doxorubicin-conjugated chimeric polypeptide nanoparticles that respond to mild hyperthermia. *Journal of Controlled Release*, 2012. 159(3): p. 362-367.
- [230] Moktan, S., E. Perkins, F. Kratz, and D. Raucher, Thermal targeting of an acid-sensitive doxorubicin conjugate of elastin-like polypeptide enhances the therapeutic efficacy compared with the parent compound *in vivo*. *Molecular Cancer Therapeutics*, 2012. 11(7): p. 1547-1556.
- [231] Bidwell III, G.L., I. Fokt, W. Priebe, and D. Raucher, Development of elastin-like polypeptide for thermally targeted delivery of doxorubicin. *Biochemical Pharmacology*, 2007. 73(5): p. 620-631.
- [232] Walker, L., E. Perkins, F. Kratz, and D. Raucher, Cell penetrating peptides fused to a thermally targeted biopolymer drug carrier improve the delivery and antitumor efficacy of an acid-sensitive doxorubicin derivative. *International Journal of Pharmaceutics*, 2012. 436(1-2): p. 825-832.
- [233] Horne, W.S., C.D. Stout, and M.R. Ghadiri, A heterocyclic peptide nanotube. *Journal of the American Chemical Society*, 2003. 125(31): p. 9372-9376.

- [234] Ashkenasy, N., W.S. Horne, and M.R. Ghadiri, Design of self-assembling peptide nanotubes with delocalized electronic states. *Small*, 2006. 2(1): p. 99-102.
- [235] Brea, R.J., C. Reiriz, and J.R. Granja, Towards functional bionanomaterials based on self-assembling cyclic peptide nanotubes. *Chemical Society Reviews*, 2010. 39(5): p. 1448-1456.
- [236] Liu, H., J. Chen, Q. Shen, et al., Molecular insights on the cyclic peptide nanotube-mediated transportation of antitumor drug 5-fluorouracil. *Molecular Pharmaceutics*, 2010. 7(6): p. 1985-1994.
- [237] Wang, Y., S. Yi, L. Sun, et al., Doxorubicin-loaded cyclic peptide nanotube bundles overcome chemoresistance in breast cancer cells. *Journal of Biomedical Nanotechnology*, 2014. 10(3): p. 445-454.
- [238] Heitz, F., M.C. Morris, and G. Divita, Twenty years of cell-penetrating peptides: from molecular mechanisms to therapeutics. *British Journal of Pharmacology*, 2009. 157(2): p. 195-206.
- [239] Pangburn, T.O., M.A. Petersen, B. Waybrant, et al., Peptide- and aptamer-functionalized nanovectors for targeted delivery of therapeutics. *Journal of Biomechanical Engineering*, 2009. 131(7): p. 074005.
- [240] Blanco, E., A. Hsiao, A.P. Mann, et al., Nanomedicine in cancer therapy: innovative trends and prospects. *Cancer Science*, 2011. 102(7): p. 1247-1252.
- [241] Muro, S., Challenges in design and characterization of ligand-targeted drug delivery systems. *Journal of Controlled Release*, 2012. 164(2): p. 125-137.
- [242] Pearce, T.R., K. Shroff, and E. Kokkoli, Peptide targeted lipid nanoparticles for anticancer drug delivery. *Advanced Materials*, 2012. 24(28): p. 3803-3822.
- [243] Chang, D.-K., C.-Y. Chiu, S.-Y. Kuo, et al., Antiangiogenic targeting liposomes increase therapeutic efficacy for solid tumors. *Journal of Biological Chemistry*, 2009. 284(19): p. 12905-12916.
- [244] Chang, D.-K., C.-T. Lin, C.-H. Wu, and H.-C. Wu, A novel peptide enhances therapeutic efficacy of liposomal anti-cancer drugs in mice models of human lung cancer. *PLoS One*, 2009. 4(1): p. e4171.
- [245] Mai, J., S. Song, M. Rui, et al., A synthetic peptide mediated active targeting of cisplatin liposomes to Tie2 expressing cells. *Journal of Controlled Release*, 2009. 139(3): p. 174-181.
- [246] Meng, S., B. Su, W. Li, et al., Enhanced antitumor effect of novel dual-targeted paclitaxel liposomes. *Nanotechnology*, 2010. 21(41): p. 415103.

- [247] Zhang, J., W. Jin, X. Wang, et al., A novel octreotide modified lipid vesicle improved the anticancer efficacy of doxorubicin in somatostatin receptor 2 positive tumor models. *Molecular Pharmaceutics*, 2010. 7(4): p. 1159-1168.
- [248] He, X., M.-H. Na, J.-S. Kim, et al., A novel peptide probe for imaging and targeted delivery of liposomal doxorubicin to lung tumor. *Molecular Pharmaceutics*, 2011. 8(2): p. 430-438.
- [249] Lowery, A., H. Onishko, D.E. Hallahan, and Z. Han, Tumor-targeted delivery of liposome-encapsulated doxorubicin by use of a peptide that selectively binds to irradiated tumors. *Journal of Controlled Release*, 2011. 150(1): p. 117-124.
- [250] Helbok, A., C. Rangger, E. von Guggenberg, et al., Targeting properties of peptide-modified radiolabeled liposomal nanoparticles. *Nanomedicine: Nanotechnology, Biology, and Medicine*, 2012. 8(1): p. 112-118.
- [251] Katanasaka, Y., T. Ishii, T. Asai, et al., Cancer antineovascular therapy with liposome drug delivery systems targeted to BiP/GRP78. *International Journal of Cancer*, 2010. 127(11): p. 2685-2698.
- [252] Murase, Y., T. Asai, Y. Katanasaka, et al., A novel DDS strategy, "dual-targeting", and its application for antineovascular therapy. *Cancer Letters*, 2010. 287(2): p. 165-171.
- [253] Rivera-Fillat, M.P., F. Reig, E.M. Martínez, and M.R. Grau-Oliete, Improved therapeutic responses for liposomal doxorubicin targeted via thrombospondin peptidomimetics versus untargeted doxorubicin. *Journal of Peptide Science*, 2010. 16(7): p. 315-321.
- [254] Falciani, C., A. Accardo, J. Brunetti, et al., Target-selective drug delivery through liposomes labeled with oligobranched neurotensin peptides. *ChemMedChem*, 2011. 6(4): p. 678-685.
- [255] Kuai, R., W. Yuan, W. Li, et al., Targeted delivery of cargoes into a murine solid tumor by a cell-penetrating peptide and cleavable poly(ethylene glycol) comodified liposomal delivery system via systemic administration. *Molecular Pharmaceutics*, 2011. 8(6): p. 2151-2161.
- [256] Dubey, P.K., D. Singodia, and S.P. Vyas, Liposomes modified with YIGSR peptide for tumor targeting. *Journal of Drug Targeting*, 2010. 18(5): p. 373-380.
- [257] Takara, K., H. Hatakeyama, N. Ohga, et al., Design of a dual-ligand system using a specific ligand and cell penetrating peptide, resulting in a synergistic effect on selectivity and cellular uptake. *International Journal of Pharmaceutics*, 2010. 396(1-2): p. 143-148.
- [258] Herrington, T.P. and J.G. Altin, Effective tumor targeting and enhanced anti-tumor effect of liposomes engrafted with peptides specific for tumor lymphatics and vasculature. *International Journal of Pharmaceutics*, 2011. 411(1-2): p. 206-214.

- [259] Herrington, T.P. and J.G. Altin, Increasing the antitumor efficacy of doxorubicin-loaded liposomes with peptides anchored via a chelator lipid. *Journal of Drug Targeting*, 2011. 19(8): p. 681-689.
- [260] Morisco, A., A. Accardo, D. Tesauro, et al., Peptide-labeled supramolecular aggregates as selective doxorubicin carriers for delivery to tumor cells. *Biopolymers*, 2011. 96(1): p. 88-96.
- [261] Garg, A., A.W. Tisdale, E. Haidari, and E. Kokkoli, Targeting colon cancer cells using PEGylated liposomes modified with a fibronectin-mimetic peptide. *International Journal of Pharmaceutics*, 2009. 366(1-2): p. 201-210.
- [262] Dai, W., T. Yang, X. Wang, et al., PHSCNK-modified and doxorubicin-loaded liposomes as a dual targeting system to integrin-overexpressing tumor neovasculature and tumor cells. *Journal of Drug Targeting*, 2010. 18(4): p. 254-263.
- [263] He, Y., L. Zhang, and C. Song, Luteinizing hormone-releasing hormone receptor-mediated delivery of mitoxantrone using LHRH analogs modified with PEGylated liposomes. *International Journal of Nanomedicine*, 2010. 5: p. 697-705.
- [264] Negussie, A.H., J.L. Miller, G. Reddy, et al., Synthesis and in vitro evaluation of cyclic NGR peptide targeted thermally sensitive liposome. *Journal of Controlled Release*, 2010. 143(2): p. 265-273.
- [265] Wang, T., G.G. D'Souza, D. Bedi, et al., Enhanced binding and killing of target tumor cells by drug-loaded liposomes modified with tumor-specific phage fusion coat protein. *Nanomedicine*, 2010. 5(4): p. 563-574.
- [266] Wang, T., S. Yang, V.A. Petrenko, and V.P. Torchilin, Cytoplasmic delivery of liposomes into MCF-7 breast cancer cells mediated by cell-specific phage fusion coat protein. *Molecular Pharmaceutics*, 2010. 7(4): p. 1149-1158.
- [267] Garg, A. and E. Kokkoli, pH-sensitive PEGylated liposomes functionalized with a fibronectin-mimetic peptide show enhanced intracellular delivery to colon cancer cell. *Current Pharmaceutical Biotechnology*, 2011. 12(8): p. 1135-1143.
- [268] Kang, M.J., S. Lee, B.K. Kim, et al., Pep-1 peptide-modified liposomal carriers for intracellular delivery of gold nanoparticles. *Chemical and Pharmaceutical Bulletin*, 2011. 59(1): p. 109-112.
- [269] Kuil, J., A.H. Velders, and F.W.B. van Leeuwen, Multimodal tumor-targeting peptides functionalized with both a radio- and a fluorescent label. *Bioconjugate Chemistry*, 2010. 21(10): p. 1709-1719.
- [270] Dissanayake, S., W.A. Denny, S. Gamage, and V. Sarojini, Recent developments in anticancer drug delivery using cell penetrating and tumor targeting peptides. *Journal of Controlled Release*, 2017. 250: p. 62-76.

- [271] Pasqualini, R., E. Koivunen, R. Kain, et al., Aminopeptidase N is a receptor for tumor-homing peptides and a target for inhibiting angiogenesis. *Cancer Research*, 2000. 60(3): p. 722-727.
- [272] Oku, N., T. Asai, K. Watanabe, et al., Anti-neovascular therapy using novel peptides homing to angiogenic vessels. *Oncogene*, 2002. 21(17): p. 2662-2669.
- [273] Colombo, G., F. Curnis, G.M.S. De Mori, et al., Structure-activity relationships of linear and cyclic peptides containing the NGR tumor-homing motif. *Journal of Biological Chemistry*, 2002. 277(49): p. 47891-47897.
- [274] Marchiò, S., J. Lahdenranta, R.O. Schlingemann, et al., Aminopeptidase AA is a functional target in angiogenic blood vessels. *Cancer Cell*, 2004. 5(2): p. 151-162.
- [275] Loi, M., D. Di Paolo, M. Soster, et al., Novel phage display-derived neuroblastoma-targeting peptides potentiate the effect of drug nanocarriers in preclinical settings. *Journal of Controlled Release*, 2013. 170(2): p. 233-241.
- [276] Loi, M., S. Marchiò, P. Becherini, et al., Combined targeting of perivascular and endothelial tumor cells enhances anti-tumor efficacy of liposomal chemotherapy in neuroblastoma. *Journal of Controlled Release*, 2010. 145(1): p. 66-73.
- [277] Zhao, H., J.-C. Wang, Q.-S. Sun, et al., RGD-based strategies for improving antitumor activity of paclitaxel-loaded liposomes in nude mice xenografted with human ovarian cancer. *Journal of Drug Targeting*, 2009. 17(1): p. 10-18.
- [278] Du, H., C. Cui, L. Wang, et al., Novel tetrapeptide, RGDF, mediated tumor specific liposomal doxorubicin (DOX) preparations. *Molecular Pharmaceutics*, 2011. 8(4): p. 1224-1232.
- [279] Jiang, J., S.-J. Yang, J.-C. Wang, et al., Sequential treatment of drug-resistant tumors with RGD-modified liposomes containing siRNA or doxorubicin. *European Journal of Pharmaceutics and Biopharmaceutics*, 2010. 76(2): p. 170-178.
- [280] Naik, S., D. Patel, K. Chuttani, et al., In vitro mechanistic study of cell death and in vivo performance evaluation of RGD grafted PEGylated docetaxel liposomes in breast cancer. *Nanomedicine: Nanotechnology, Biology and Medicine*, 2012. 8(6): p. 951-962.
- [281] Veneti, E., R.S. Tu, and D.T. Auguste, RGD-targeted liposome binding and uptake on breast cancer cells is dependent on elastin linker secondary structure. *Bioconjugate Chemistry*, 2016. 27(8): p. 1813-1821.
- [282] Wen, X., J. Li, D. Cai, et al., Anticancer efficacy of targeted shikonin liposomes modified with RGD in breast cancer cells. *Molecules*, 2018. 23(2): p. 268.

- [283] Amin, M., M. Mansourian, G.A. Koning, et al., Development of a novel cyclic RGD peptide for multiple targeting approaches of liposomes to tumor region. *Journal of Controlled Release*, 2015. 220: p. 308-315.
- [284] Cheng, Y. and Y. Ji, RGD-modified polymer and liposome nanovehicles: recent research progress for drug delivery in cancer therapeutics. *European Journal of Pharmaceutical Sciences*, 2019. 128: p. 8-17.
- [285] Liu, X.-Y., L.-M. Ruan, W.-W. Mao, et al., Preparation of RGD-modified long circulating liposome loading matrine, and its in vitro anti-cancer effects. *International Journal of Medical Sciences*, 2010. 7(4): p. 197-208.
- [286] Li, W., B. Su, S. Meng, et al., RGD-targeted paramagnetic liposomes for early detection of tumor: in vitro and in vivo studies. *European Journal of Radiology*, 2011. 80(2): p. 598-606.
- [287] Kokkoli, E., A. Mardilovich, A. Wedekind, et al., Self-assembly and applications of biomimetic and bioactive peptide-amphiphiles. *Soft Matter*, 2006. 2(12): p. 1015-1024.
- [288] Mardilovich, A., J.A. Craig, M.Q. McCammon, et al., Design of a novel fibronectin-mimetic peptide-amphiphile for functionalized biomaterials. *Langmuir*, 2006. 22(7): p. 3259-3264.
- [289] Pangburn, T.O., F.S. Bates, and E. Kokkoli, Polymersomes functionalized via “click” chemistry with the fibronectin mimetic peptides PR_b and GRGDSP for targeted delivery to cells with different levels of $\alpha 5\beta 1$ expression. *Soft Matter*, 2012. 8(16): p. 4449-4461.
- [290] Shroff, K., T.R. Pearce, and E. Kokkoli, Enhanced integrin mediated signaling and cell cycle progression on fibronectin mimetic peptide amphiphile monolayers. *Langmuir*, 2012. 28(3): p. 1858-1865.
- [291] Demirgöz, D., A. Garg, and E. Kokkoli, PR_b-targeted PEGylated liposomes for prostate cancer therapy. *Langmuir*, 2008. 24(23): p. 13518-13524.
- [292] Demirgöz, D., T.O. Pangburn, K.P. Davis, et al., PR_b-targeted delivery of tumor necrosis factor- α by polymersomes for the treatment of prostate cancer. *Soft Matter*, 2009. 5(10): p. 2011-2019.
- [293] Atchison, N.A., W. Fan, K.K Papas, et al., Binding of the fibronectin-mimetic peptide, PR_b, to $\alpha 5\beta 1$ on pig islet cells increases fibronectin production and facilitates internalization of PR_b functionalized liposomes. *Langmuir*, 2010. 26(17): p. 14081-14088.
- [294] Bertram, J.P., C.A. Williams, R. Robinson, et al., Intravenous hemostat: nanotechnology to halt bleeding. *Science Translational Medicine*, 2009. 1(11): p. 11ra22.

- [295] Nishiya, T., M. Kainoh, M. Murata, et al., Platelet interactions with liposomes carrying recombinant platelet membrane glycoproteins or fibrinogen: approach to platelet substitutes. *Artificial Cells, Blood Substitutes, and Immobilization Biotechnology*, 2001. 29(6): p. 453-464.
- [296] Nishiya, T., M. Kainoh, M. Murata, et al., Reconstitution of adhesive properties of human platelets in liposomes carrying both recombinant glycoproteins Ia/IIa and Ib α alpha under flow conditions: specific synergy of receptor-ligand interactions. *Blood*, 2002. 100(1): p. 136-142.
- [297] Takeoka, S., Y. Teramura, Y. Okamura, et al., Rolling properties of rGPIb α -conjugated phospholipid vesicles with different membrane flexibilities on vWF surface under flow conditions. *Biochemical and Biophysical Research Communications*, 2002. 296(3): p. 765-770.
- [298] Takeoka, S., Y. Okamura, Y. Teramura, et al., Function of fibrinogen gamma-chain dodecapeptide-conjugated latex beads under flow. *Biochemical and Biophysical Research Communications*, 2003. 312(3): p. 773-779.
- [299] Okamura, Y., I. Maekawa, Y. Teramura, et al., Hemostatic effects of phospholipid vesicles carrying fibrinogen γ chain dodecapeptide in vitro and in vivo. *Bioconjugate Chemistry*, 2005. 16(6): p. 1589-1596.
- [300] Okamura, Y., S. Takeoka, Y. Teramura, et al., Hemostatic effects of fibrinogen gamma-chain dodecapeptide-conjugated polymerized albumin particles in vitro and in vivo. *Transfusion*, 2005. 45(7): p. 1221-1228.
- [301] Okamura, Y., T. Fujie, H. Maruyama, et al., Prolonged hemostatic ability of polyethylene glycol-modified polymerized albumin particles carrying fibrinogen gamma-chain dodecapeptide. *Transfusion*, 2007. 47(7): p. 1254-1262.
- [302] Okamura, Y., T. Fujie, M. Nogawa, et al., Haemostatic effects of polymerized albumin particles carrying fibrinogen gamma-chain dodecapeptide as platelet substitutes in severely thrombocytopenic rabbits. *Transfusion Medicine*, 2008. 18(3): p. 158-166.
- [303] Okamura, Y., S. Takeoka, K. Eto, et al., Development of fibrinogen gamma-chain peptide-coated, adenosine diphosphate-encapsulated liposomes as a synthetic platelet substitute. *Journal of Thrombosis and Haemostasis*, 2009. 7(3): p. 470-477.
- [304] Ravikumar, M., C.L. Modery, T.L. Wong, and A.S. Gupta, Peptide-decorated liposomes promote arrest and aggregation of activated platelets under flow on vascular injury relevant protein surfaces in vitro. *Biomacromolecules*, 2012. 13(5): p. 1495-1502.
- [305] Anselmo, A.C., C.L. Modery-Pawlowski, S. Menegatti, et al., Platelet-like nanoparticles: mimicking shape, flexibility, and surface biology of platelets to target vascular injuries. *ACS Nano*, 2014. 8(11): p. 11243-11253.

- [306] Snyder, E.L. and S.F. Dowdy, Recent advances in the use of protein transduction domains for the delivery of peptides, proteins and nucleic acids *in vivo*. *Expert Opinion on Drug Delivery*, 2005. 2(1): p. 43-51.
- [307] Munyendo, W.L.L., H. Lv, H. Benza-Ingoula, et al., Cell penetrating peptides in the delivery of biopharmaceuticals. *Biomolecules*, 2012. 2(2): p. 187-202.
- [308] Cheng, C.J. and W.M. Saltzman, Enhanced siRNA delivery into cells by exploiting the synergy between targeting ligands and cell-penetrating peptides. *Biomaterials*, 2011. 32(26): p. 6194-6203.
- [309] Ezzat, K., E.M. Zaghloul, S. El Andaloussi, et al., Solid formulation of cell-penetrating peptide nanocomplexes with siRNA and their stability in simulated gastric conditions. *Journal of Controlled Release*, 2012. 162(1): p. 1-8.
- [310] Nakase, I., G. Tanaka, and S. Futaki, Cell-penetrating peptides (CPPs) as a vector for the delivery of siRNAs into cells. *Molecular Biosystems*, 2013. 9(5): p. 855-861.
- [311] H. Bai, Y. You, H. Yan, et al., Antisense inhibition of gene expression and growth in gram-negative bacteria by cell-penetrating peptide conjugates of peptide nucleic acids targeted to rpoD gene. *Biomaterials*, 2012. 33(2): p. 659-667.
- [312] Nakase, I., H. Akita, K. Kogure, et al., Efficient intracellular delivery of nucleic acid pharmaceuticals using cell-penetrating peptides. *Accounts of Chemical Research*, 2012. 45(7): p. 1132-1139.
- [313] Lindgren, M., K. Rosenthal-Aizman, K. Saar, et al., Overcoming methotrexate resistance in breast cancer tumour cells by the use of a new cell-penetrating peptide. *Biochemical Pharmacology*, 2006. 71(4): p. 416-425.
- [314] Lee, J.Y., K.H. Bae, J.S. Kim, et al., Intracellular delivery of paclitaxel using oil-free, shell cross-linked HSA-multi-armed PEG nanocapsules. *Biomaterials*, 2011. 32(33): p. 8635-8644.
- [315] Liu, B.R., Y.-W. Huang, and H.-J. Lee, Mechanistic studies of intracellular delivery of proteins by cell-penetrating peptides in cyanobacteria. *BMC Microbiology*, 2013. 13: p. 57.
- [316] Liu, B.R., J.-S. Liou, Y.-J. Chen, et al., Delivery of nucleic acids, proteins, and nanoparticles by arginine-rich cell-penetrating peptides in rotifers. *Marine Biotechnology*, 2013. 15(5): p. 584-595.
- [317] Mäe, M. and Ü. Langel, Cell-penetrating peptides as vectors for peptide, protein and oligonucleotide delivery. *Current Opinion in Pharmacology*, 2006. 6(5): p. 509-514.
- [318] Järver, P., I. Mäger, and Ü. Langel, In vivo biodistribution and efficacy of peptide mediated delivery. *Trends in Pharmacological Sciences*, 2010. 31(11): p. 528-535.

- [319] Lewin, M., N. Carlesso, C.H. Tung, et al., Tat peptide-derivatized magnetic nanoparticles allow in vivo tracking and recovery of progenitor cells. *Nature Biotechnology*, 2000. 18(4): p. 410-414.
- [320] Bolhassani, A., Potential efficacy of cell-penetrating peptides for nucleic acid and drug delivery in cancer. *Biochimica et Biophysica Acta (BBA) - Reviews on Cancer*, 2011. 1816(2): p. 232-246.
- [321] Chen, H.-C.G., S.-T. Chiou, J.-Y. Zheng, et al., The nuclear localization signal sequence of porcine circovirus type 2 ORF2 enhances intracellular delivery of plasmid DNA. *Archives of Virology*, 2011. 156(5): p. 803-815.
- [322] Wang, H.-Y., J.-X. Chen, Y.-X. Sun, et al., Construction of cell penetrating peptide vectors with N-terminal stearylated nuclear localization signal for targeted delivery of DNA into the cell nuclei. *Journal of Controlled Release*, 2011. 155(1): p. 26-33.
- [323] Kim, B.-K., H. Kang, K.-O. Doh, et al., Homodimeric SV40 NLS peptide formed by disulfide bond as enhancer for gene delivery. *Bioorganic and Medicinal Chemistry Letters*, 2012. 22(17): p. 5415-5418.
- [324] Yin, J., X. Meng, S. Zhang, et al., The effect of a nuclear localization sequence on transfection efficacy of genes delivered by cobalt(II)-polybenzimidazole complexes. *Biomaterials*, 2012. 33(31): p. 7884-7894.
- [325] Barnett, E.M., X. Zhang, D. Maxwell, et al., Single-cell imaging of retinal ganglion cell apoptosis with a cell-penetrating, activatable peptide probe in an in vivo glaucoma model. *Proceedings of the National Academy of Sciences of the United States of America*, 2009. 106(23): p. 9391-9396.
- [326] Kamei, N., M. Morishita, Y. Kanayama, et al., Molecular imaging analysis of intestinal insulin absorption boosted by cell-penetrating peptides by using positron emission tomography. *Journal of Controlled Release*, 2010. 146(1): p. 16-22.
- [327] Nguyen, Q.T., E.S. Olson, T.A. Aguilera, et al., Surgery with molecular fluorescence imaging using activatable cell-penetrating peptides decreases residual cancer and improves survival. *Proceedings of the National Academy of Sciences of the United States of America*, 2010. 107(9): p. 4317-4322.
- [328] Olson, E.S., T. Jiang, T.A. Aguilera, et al., Activatable cell penetrating peptides linked to nanoparticles as dual probes for in vivo fluorescence and MR imaging of proteases. *Proceedings of the National Academy of Sciences of the United States of America*, 2010. 107(9): p. 4311-4316.
- [329] Huang, C.-W., Z. Li, and P.S. Conti, In vivo near-infrared fluorescence imaging of integrin $\alpha 2\beta 1$ in prostate cancer with cell-penetrating-peptide-conjugated DGEA probe. *Journal of Nuclear Medicine*, 2011. 52(12): p. 1979-1986.

- [330] Zhai, X.-H., M. Liu, X.-J. Guo, et al., SKOV-3 cell imaging by paramagnetic particles labeled with hairpin cell-penetrating peptides. Chinese Medical Journal, 2011. 124(1): p. 111-117.
- [331] Olson, E.S., M.A. Whitney, B. Friedman, et al., In vivo fluorescence imaging of atherosclerotic plaques with activatable cell-penetrating peptides targeting thrombin activity. Integrative Biology: Quantitative Biosciences from Nano to Macro, 2012. 4(6): p. 595-605.
- [332] Koren, E., A. Apte, A. Jani, and V.P. Torchilin, Multifunctional PEGylated 2C5-immunoliposomes containing pH-sensitive bonds and TAT peptide for enhanced tumor cell internalization and cytotoxicity. Journal of Controlled Release, 2012. 160(2): p. 264-273.
- [333] Virès, E., C. Granier, P. Prevot, and B. Lebleu, Structure-activity relationship study of the plasma membrane translocating potential of a short peptide from HIV-1 Tat protein. Letters in Peptide Science, 1997. 4(4): p. 429-436.
- [334] Koren, E., A. Apte, R.R. Sawant, et al., Cell-penetrating TAT peptide in drug delivery systems: proteolytic stability requirements. Drug Delivery, 2011. 18(5): p. 377-384.
- [335] Derossi, D., S. Calvet, A. Trembleau, et al., Cell internalization of the third helix of the antennapedia homeodomain is receptor-independent. Journal of Biological Chemistry, 1996. 271(30): p. 18188-18193.
- [336] Fischer, P.M., N.Z. Zhelev, S. Wang, et al., Structure-activity relationship of truncated and substituted analogues of the intracellular delivery vector Penetratin. Journal of Peptide Research, 2000. 55(2): p. 163-172.
- [337] Elliott, G. and P. O'Hare, Intercellular trafficking and protein delivery by a herpesvirus structural protein. Cell, 1997. 88(2): p. 223-233.
- [338] Lin, Y.Z., S.Y. Yao, R.A. Veach, et al., Inhibition of nuclear translocation of transcription factor NF-KBNF-kappa B by a synthetic peptide containing a cell membrane-permeable motif and nuclear localization sequence. Journal of Biological Chemistry, 1995. 270(24): p. 14255-14258.
- [339] Lin, Y.Z., S.Y. Yao, and J. Hawiger, Role of the nuclear localization sequence in fibroblast growth factor-1-stimulated mitogenic pathways. Journal of Biological Chemistry, 1996. 271(10): p. 5305-5308.
- [340] Rojas, M., J.P. Donahue, Z. Tan, and Y.-Z. Lin, Genetic engineering of proteins with cell membrane permeability. Nature Biotechnology, 1998. 16(4): p. 370-375.
- [341] Anderson, D.C., R. Manger, J. Schroeder, et al., Enhanced in vitro tumor cell retention and internalization of antibody derivatized with synthetic peptides. Bioconjugate Chemistry, 1993. 4(1): p. 10-18.

- [342] Anderson, D.C., E. Nichols, R. Manger, et al., Tumor cell retention of antibody Fab fragments is enhanced by an attached HIV TAT protein-derived peptide. *Biochemical and Biophysical Research Communications*, 1993. 194(2): p. 876-884.
- [343] Vives, E., P. Charneau, J. van Rietschoten, et al., Effects of the Tat basic domain on human immunodeficiency virus type 1 transactivation, using chemically synthesized Tat protein and Tat peptides. *Journal of Virology*, 1994. 68(5): p. 3343-3353.
- [344] Bidwell, G.L. and D. Raucher, Application of thermally responsive polypeptides directed against c-Myc transcriptional function for cancer therapy. *Molecular Cancer Therapeutics*, 2005. 4(7): p. 1076-1085.
- [345] Massodi, I., G.L. Bidwell, and D. Raucher, Evaluation of cell penetrating peptides fused to elastin-like polypeptide for drug delivery. *Journal of Controlled Release*, 2005. 108(2-3): p. 396-408.
- [346] Bidwell, G.L., A.N. Davis, and D. Raucher, Targeting a c-Myc inhibitory polypeptide to specific intracellular compartments using cell penetrating peptides. *Journal of Controlled Release*, 2009. 135(1): p. 2-10.
- [347] Massodi, I., E. Thomas, and D. Raucher, Application of thermally responsive elastin-like polypeptide fused to a lactoferrin-derived peptide for treatment of pancreatic cancer. *Molecules*, 2009. 14(6): p. 1999-2015.
- [348] Massodi, I., S. Moktan, A. Rawat, et al., Inhibition of ovarian cancer cell proliferation by a cell cycle inhibitory peptide fused to a thermally responsive polypeptide carrier. *International Journal of Cancer*, 2010. 126(2): p. 533-544.
- [349] Stauber, R.H. and G.N. Pavlakis, Intracellular trafficking and interactions of the HIV-1 Tat protein. *Virology*, 1998. 252(1): p. 126-136.
- [350] Schwarze, S.R., A. Ho, A. Vocero-Akbani, and S.F. Dowdy, In vivo protein transduction: delivery of a biologically active protein into the mouse. *Science*, 1999. 285(5433): p. 1569-1572.
- [351] Vocero-Akbani, A., N. Vader Heyden, N.A. Lissy, et al., Killing HIV-infected cells by transduction with an HIV protease-activated caspase-3 protein. *Nature Medicine*, 1999. 5(1): p. 29-33.
- [352] Caron, N.J., Y. Torrente, G. Camirand, et al., Intracellular delivery of a Tat-eGFP fusion protein into muscle cells. *Molecular Therapy*, 2001. 3(3): p. 310-318.
- [353] Shamji, M.F., J. Chen, A.H. Friedman, et al., Synthesis and characterization of a thermally-responsive tumor necrosis factor antagonist. *Journal of Controlled Release*, 2008. 129(3): p. 179-186.

- [354] Astriab-Fisher, A., D.S. Sergueev, M. Fisher, et al. Antisense inhibition of P-glycoprotein expression using peptide-oligonucleotide conjugates. *Biochemical Pharmacology*, 2000. 60(1): p. 83-90.
- [355] Tung, C.-H., S. Mueller, and R. Weissleder, Novel branching membrane translocational peptide as gene delivery vector. *Bioorganic and Medicinal Chemistry*, 2002. 10(11): p. 3609-3614.
- [356] Chen, T.-H.H., Y. Bae, and D.Y. Furgeson, Intelligent biosynthetic nanobiomaterials (IBNs) for hyperthermic gene delivery. *Pharmaceutical Research*, 2008. 25(3): p. 683-691.
- [357] Pooga, M., U. Soomets, M. Hällbrink, et al., Cell penetrating PNA constructs regulate galanin receptor levels and modify pain transmission in vivo. *Nature Biotechnology*, 1998. 16(9): p. 857-861.
- [358] Rousselle, C., P. Clair, J.M. Lefauconnier, et al., New advances in the transport of doxorubicin through the blood-brain barrier by a peptide vector-mediated strategy. *Molecular Pharmacology*, 2000. 57(4): p. 679-686.
- [359] Mazel, M., P. Clair, C. Rousselle, et al., Doxorubicin-peptide conjugates overcome multidrug resistance. *Anti-Cancer Drugs*, 2001. 12(2): p. 107-116.
- [360] El-Sayed, A., S. Futaki, and H. Harashima, Delivery of macromolecules using arginine-rich cell-penetrating peptides: ways to overcome endosomal entrapment. *The AAPS Journal*, 2009. 11(1): p. 13-22.
- [361] Mitchell, D.J., D.T. Kim, L. Steinman, et al., Polyarginine enters cells more efficiently than other polycationic homopolymers. *Journal of Peptide Research*, 2000. 56(5): p. 318-325.
- [362] Futaki, S., T. Suzuki, W. Ohashi, et al., Arginine-rich peptides. An abundant source of membrane-permeable peptides having potential as carriers for intracellular protein delivery. *Journal of Biological Chemistry*, 2001. 276(8): p. 5836-5840.
- [363] Maiolo, J.R., M. Ferrer, and E.A. Ottinger, Effects of cargo molecules on the cellular uptake of arginine-rich cell-penetrating peptides. *Biochimica et Biophysica Acta (BBA) - Biomembranes*, 2005. 1712(2): p. 161-172.
- [364] Kale, A.A. and V.P. Torchilin, Enhanced transfection of tumor cells in vivo using "smart" pH-sensitive TAT-modified pegylated liposomes. *Journal of Drug Targeting*, 2007. 15(7-8): p. 538-545.
- [365] Kale, A.A. and V.P. Torchilin, "Smart" drug carriers: PEGylated TATp-modified pH-sensitive liposomes. *Journal of Liposome Research*, 2007. 17(3-4): p. 197-203.

- [366] Abes, R., H.M. Moulton, P. Clair, et al., Delivery of steric block morpholino oligomers by (R-X-R)₄ peptides: structure-activity studies. *Nucleic Acids Research*, 2008. 36(20): p. 6343-6354.
- [367] Verdurmen, W.P.R. and R. Brock, Biological responses towards cationic peptides and drug carriers. *Trends in Pharmacological Sciences*, 2011. 32(2): p. 116-124.
- [368] Pooga, M., A. Elmquist, and Ü. Langel, Toxicity and side effects of cell-penetrating peptides. *Cell-Penetrating Peptides*, 2002: p. 245.
- [369] Saar, K., M. Lindgren, M. Hansen, et al., Cell-penetrating peptides: a comparative membrane toxicity study. *Analytical Biochemistry*, 2005. 345(1): p. 55-65.
- [370] Nasrollahi, S.A., C. Taghibiglou, E. Azizi, and E.S. Farboud, Cell-penetrating peptides as a novel transdermal drug delivery system. *Chemical Biology and Drug Design*, 2012. 80(5): p. 639-646.
- [371] Lundberg, P., M. Magzoub, M. Lindberg, et al., Cell membrane translocation of the N-terminal (1-28) part of the prion protein. *Biochemical and Biophysical Research Communications*, 2002. 299(1): p. 85-90.
- [372] Deshayes, S., T. Plénat, G. Aldrian-Herrada, et al., Primary amphipathic cell-penetrating peptides: structural requirements and interactions with model membranes. *Biochemistry*, 2004. 43(24): p. 7698-7706.
- [373] Rydström, A., S. Deshayes, K. Konate, et al., Direct translocation as major cellular uptake for CADY self-assembling peptide-based nanoparticles. *PLoS One*, 2011. 6(10): p. e25924.
- [374] Oehlke, J., A. Scheller, B. Wiesner, et al., Cellular uptake of an α -helical amphipathic model peptide with the potential to deliver polar compounds into the cell interior non-endocytically. *Biochimica et Biophysica Acta (BBA) - Biomembranes*, 1998. 1414(1): p. 127-139.
- [375] Milletti, F., Cell-penetrating peptides: classes, origin, and current landscape. *Drug Discovery Today*, 2012. 17(15): p. 850-860.
- [376] Wender, P.A., D.J. Mitchell, K. Pattabiraman, et al., The design, synthesis, and evaluation of molecules that enable or enhance cellular uptake: peptoid molecular transporters. *Proceedings of the National Academy of Sciences of the United States of America*, 2000. 97(24): p. 13003.
- [377] Rousselle, C., M. Smirnova, P. Clair, et al., Enhanced delivery of doxorubicin into the brain via a peptide-vector-mediated strategy: saturation kinetics and specificity. *Journal of Pharmacology and Experimental Therapeutics*, 2001. 296(1): p. 124-131.

- [378] Aroui, S., N. Ram, F. Appaix, et al., Maurocalcine as a non-toxic drug carrier overcomes doxorubicin resistance in the cancer cell line MDA-MB 231. *Pharmaceutical Research*, 2009. 26(4): p. 836-845.
- [379] Chen, J., S. Li, and Q. Shen, Folic acid and cell-penetrating peptide conjugated PLGA-PEG bifunctional nanoparticles for vincristine sulfate delivery. *European Journal of Pharmaceutical Sciences*, 2012. 47(2): p. 430-443.
- [380] Kondo, E., K. Saito, Y. Tashiro, et al., Tumour lineage-homing cell-penetrating peptides as anticancer molecular delivery systems. *Nature Communications*, 2012. 3: p. 951.
- [381] Li, Y., X. Zheng, Z. Cao, et al., Self-assembled peptide (CADY-1) improved the clinical application of doxorubicin. *International Journal of Pharmaceutics*, 2012. 434(1-2): p. 209-214.
- [382] Nakase, I., Y. Konishi, M. Ueda, et al., Accumulation of arginine-rich cell-penetrating peptides in tumors and the potential for anticancer drug delivery in vivo. *Journal of Controlled Release*, 2012. 159(2): p. 181-188.
- [383] Shi, N.-Q., W. Gao, B. Xiang, and X.-R. Qi, Enhancing cellular uptake of activable cell-penetrating peptide-doxorubicin conjugate by enzymatic cleavage. *International Journal of Nanomedicine*, 2012. 7: p. 1613-1621.
- [384] Uchida, Y., D. Raina, S. Kharbanda, and D. Kufe, Inhibition of the MUC1-C oncoprotein is synergistic with cytotoxic agents in the treatment of breast cancer cells. *Cancer Biology and Therapy*, 2013. 14(2): p. 127-134.
- [385] Komin, A., L.M. Russell, K.A. Hristova, and P.C. Searson, Peptide-based strategies for enhanced cell uptake, transcellular transport, and circulation: mechanisms and challenges. *Advanced Drug Delivery Reviews*, 2017. 110-111: p. 52-64.
- [386] Patel, L.N., J.L. Zaro, and W.-C. Shen, Cell penetrating peptides: intracellular pathways and pharmaceutical perspectives. *Pharmaceutical Research*, 2007. 24(11): p. 1977-1992.
- [387] Mäe, M., O. Rautsi, J. Enbäck, et al., Tumour targeting with rationally modified cell-penetrating peptides. *International Journal of Peptide Research and Therapeutics*, 2012. 18(4): p. 361-371.
- [388] Crombez, L., M.C. Morris, F. Heitz, and G. Divita, A non-covalent peptide-based strategy for ex vivo and in vivo oligonucleotide delivery. *Methods in Molecular Biology*, 2011. 764: p. 59-73.
- [389] Margus, H., K. Padari, and M. Pooga, Cell-penetrating peptides as versatile vehicles for oligonucleotide delivery. *Molecular Therapy*, 2012. 20(3): p. 525-533.

- [390] Schafmeister, C.E., J. Po, and G.L. Verdine, An all-hydrocarbon cross-linking system for enhancing the helicity and metabolic stability of peptides. *Journal of the American Chemical Society*, 2000. 122(24): p. 5891-5892.
- [391] Covic, L., A.L. Gresser, J. Talavera, et al., Activation and inhibition of G protein-coupled receptors by cell-penetrating membrane-tethered peptides. *Proceedings of the National Academy of Sciences of the United States of America*, 2002. 99(2): p. 643-648.
- [392] Ochocki, J.D., D.G. Mullen, E.V. Wattenberg, and M.D. Distefano, Evaluation of a cell penetrating prenylated peptide lacking an intrinsic fluorophore via in situ click reaction. *Bioorganic and Medicinal Chemistry Letters*, 2011. 21(17): p. 4998-5001.
- [393] Watkins, C.L., P. Brennan, C. Fegan, et al., Cellular uptake, distribution and cytotoxicity of the hydrophobic cell penetrating peptide sequence PFVYLI linked to the proapoptotic domain peptide PAD. *Journal of Controlled Release*, 2009. 140(3): p. 237-244.
- [394] Gennari, C.G.M., S. Franzè, S. Pellegrino, et al., Skin penetrating peptide as a tool to enhance the permeation of heparin through human epidermis. *Biomacromolecules*, 2016. 17(1): p. 46-55.
- [395] Gautam, A., K. Chaudhary, R. Kumar, et al., In silico approaches for designing highly effective cell penetrating peptides. *Journal of Translational Medicine*, 2013. 11: p. 74.
- [396] Gautam, A., M. Sharma, P. Vir, et al., Identification and characterization of novel protein-derived arginine-rich cell-penetrating peptides. *European Journal of Pharmaceutics and Biopharmaceutics*, 2015. 89: p. 93-106.
- [397] Gautam, A., J.S. Nanda, J.S. Samuel, et al., Topical delivery of protein and peptide using novel cell penetrating peptide IMT-P8. *Scientific Reports*, 2016. 6: p. 26278.
- [398] Chen, M., V. Gupta, A.C. Anselmo, et al., Topical delivery of hyaluronic acid into skin using SPACE-peptide carriers. *Journal of Controlled Release*, 2014. 173: p. 67-74.
- [399] Kumar, S., M. Chen, A.C. Anselmo, et al., Enhanced epidermal localization of topically applied steroids using SPACETM peptide. *Drug Delivery and Translational Research*, 2015. 5(5): p. 523-530.
- [400] Chen, M., S. Kumar, A.C. Anselmo, et al., Topical delivery of cyclosporine AA into the skin using SPACE-peptide. *Journal of Controlled Release*, 2015. 199: p. 190-197.
- [401] Menegatti, S., M. Zakrewsky, S. Kumar, et al., De novo design of skin-penetrating peptides for enhanced transdermal delivery of peptide drugs. *Advanced Healthcare Materials*, 2016. 5(5): p. 602-609.
- [402] Zhang, S., T.C. Holmes, C.M. DiPersio, et al., Self-complementary oligopeptide matrices support mammalian cell attachment. *Biomaterials*, 1995. 16(18): p. 1385-1393.

- [403] Kisiday, J., M. Jin, B. Kurz, et al., Self-assembling peptide hydrogel fosters chondrocyte extracellular matrix production and cell division: implications for cartilage tissue repair. *Proceedings of the National Academy of Sciences of the United States of America*, 2002. 99(15): p. 9996-10001.
- [404] Zhang, S., Fabrication of novel biomaterials through molecular self-assembly. *Nature Biotechnology*, 2003. 21(10): p. 1171-1178.
- [405] Silva, G.A., C. Czeisler, K.L. Niece, et al., Selective differentiation of neural progenitor cells by high-epitope density nanofibers. *Science*, 2004. 303(5662): p. 1352-1355.
- [406] Law, B., R. Weissleder, and C.-H. Tung, Peptide-based biomaterials for protease-enhanced drug delivery. *Biomacromolecules*, 2006. 7(4): p. 1261-1265.
- [407] Ramachandran, S. and Y.B. Yu, Peptide-based viscoelastic matrices for drug delivery and tissue repair. *BioDrugs: Clinical Immunotherapeutics, Biopharmaceuticals and Gene Therapy*, 2006. 20(5): p. 263-269.
- [408] Zhao, X. and S. Zhang, Molecular designer self-assembling peptides. *Chemical Society Reviews*, 2006. 35(11): p. 1105-1110.
- [409] Zhao, X. and S. Zhang, Self-assembling nanopeptides become a new type of biomaterial, in *Polymers for Regenerative Medicine*, (ed. C. Werner), 2006, Springer: Berlin Heidelberg-Verlag. p. 145-170.
- [410] Horii, A., X. Wang, F. Gelain, and S. Zhang, Biological designer self-assembling peptide nanofiber scaffolds significantly enhance osteoblast proliferation, differentiation and 3-D migration. *PLoS One*, 2007. 2(2): p. 1-9.
- [411] Segers, V.F.M. and R.T. Lee, Local delivery of proteins and the use of self-assembling peptides. *Drug Discovery Today*, 2007. 12(13-14): p. 561-568.
- [412] Branco, M.C. and J.P. Schneider, Self-assembling materials for therapeutic delivery. *Acta Biomaterialia*, 2009. 5(3): p. 817-831.
- [413] Loo, Y., S. Zhang, and C.A.E. Hauser, From short peptides to nanofibers to macromolecular assemblies in biomedicine. *Biotechnology Advances*, 2012. 30(3): p. 593-603.
- [414] Luo, Z. and S. Zhang, Designer nanomaterials using chiral self-assembling peptide systems and their emerging benefit for society. *Chemical Society Reviews*, 2012. 41(13): p. 4736-4754.
- [415] Vuorela, A., J. Myllyharju, R. Nissi, et al., Assembly of human prolyl 4-hydroxylase and type III collagen in the yeast *Pichia pastoris*: formation of a stable enzyme tetramer requires coexpression with collagen and assembly of a stable collagen requires coexpression with prolyl 4-hydroxylase. *The EMBO Journal*, 1997. 16(22): p. 6702-6712.

- [416] Vaughn, P.R., M. Galanis, K.M. Richards, et al., Production of recombinant hydroxylated human type III collagen fragment in *Saccharomyces cerevisiae*. *DNA and Cell Biology*, 1998. 17(6): p. 511-518.
- [417] Myllyharju, J., M. Nokelainen, A. Vuorela, and K.I. Kivirikko, Expression of recombinant human type I-III collagens in the yeast *Pichia pastoris*. *Biochemical Society Transactions*, 2000. 28(4): p. 353-357.
- [418] Toman, P.D., G. Chisholm, H. McMullin, et al., Production of recombinant human type I procollagen trimers using a four-gene expression system in the yeast *Saccharomyces cerevisiae*. *Journal of Biological Chemistry*, 2000. 275(30): p. 23303-23309.
- [419] Nokelainen, M., H. Tu, A. Vuorela, et al., High-level production of human type I collagen in the yeast *Pichia pastoris*. *Yeast*, 2001. 18(9): p. 797-806.
- [420] Olsen, D.R., S.D. Leigh, R. Chang, et al., Production of human type I collagen in yeast reveals unexpected new insights into the molecular assembly of collagen trimers. *Journal of Biological Chemistry*, 2001. 276(26): p. 24038-24043.
- [421] Liu, W., K. Merrett, M. Griffith, et al., Recombinant human collagen for tissue engineered corneal substitutes. *Biomaterials*, 2008. 29(9): p. 1147-1158.
- [422] Tojo, N., I. Miyagi, M. Miura, and H. Ohi, Recombinant human fibrinogen expressed in the yeast *Pichia pastoris* was assembled and biologically active. *Protein Expression and Purification*, 2008. 59(2): p. 289-296.
- [423] Sallach, R.E., V.P. Conticello, and E.L. Chaikof, Expression of a recombinant elastin-like protein in *Pichia pastoris*. *Biotechnology Progress*, 2009. 25(6): p. 1810-1818.
- [424] Tillet, E., H. Wiedemann, R. Golbik, et al., Recombinant expression and structural and binding properties of $\alpha 1(VI)$ and $\alpha 2(VI)$ chains of human collagen type VI. *European Journal of Biochemistry*, 1994. 221(1): p. 177-187.
- [425] Fichard, A., E. Tillet, F. Delacoux, et al., Human recombinant $\alpha 1(V)$ collagen chain homotrimeric assembly and subsequent processing. *Journal of Biological Chemistry*, 1997. 272(48): p. 30083-30087.
- [426] Frischholz, S., F. Beier, I. Girkontaite, et al., Characterization of human type X procollagen and its NC-1 domain expressed as recombinant proteins in HEK293 cells. *Journal of Biological Chemistry*, 1998. 273(8): p. 4547-4555.
- [427] Chen, M., F.K. Costa, C.R. Lindvay, et al., The recombinant expression of full-length type VII collagen and characterization of molecular mechanisms underlying dystrophic epidermolysis bullosa. *Journal of Biological Chemistry*, 2002. 277(3): p. 2118-2124.

- [428] Butler, S.P., T.K. O'Sickey, S.T. Lord, et al., Secretion of recombinant human fibrinogen by the murine mammary gland. *Transgenic Research*, 2004. 13(5): p. 437-450.
- [429] Nillesen, S.T.M., P.J. Geutjes, R. Wismans, et al., Increased angiogenesis and blood vessel maturation in acellular collagen-heparin scaffolds containing both FGF2 and VEGF. *Biomaterials*, 2007. 28(6): p. 1123-1131.
- [430] Shen, Y.H., M.S. Shoichet, and M. Radisic, Vascular endothelial growth factor immobilized in collagen scaffold promotes penetration and proliferation of endothelial cells. *Acta Biomaterialia*, 2008. 4(3): p. 477-489.
- [431] Borselli, C., F. Ungaro, O. Oliviero, et al., Bioactivation of collagen matrices through sustained VEGF release from PLGA microspheres. *Journal of Biomedical Materials Research. Part A*, 2010. 92(1): p. 94-102.
- [432] He, Q., Y. Zhao, B. Chen, et al., Improved cellularization and angiogenesis using collagen scaffolds chemically conjugated with vascular endothelial growth factor. *Acta Biomaterialia*, 2011. 7(3): p. 1084-1093.
- [433] Miyagi, Y., L.L.Y. Chiu, M. Cimini, et al., Biodegradable collagen patch with covalently immobilized VEGF for myocardial repair. *Biomaterials*, 2011. 32(5): p. 1280-1290.
- [434] Côté, M.-F., G. Laroche, E. Gagnon, et al., Denatured collagen as support for a FGF-2 delivery system: physicochemical characterizations and in vitro release kinetics and bioactivity. *Biomaterials*, 2004. 25(17): p. 3761-3772.
- [435] Maehara, H., S. Sotome, T. Yoshii, et al., Repair of large osteochondral defects in rabbits using porous hydroxyapatite/collagen (HAp/CCol) and fibroblast growth factor-2 (FGF-2). *Journal of Orthopaedic Research*, 2010. 28(5): p. 677-686.
- [436] Takeda, Y., H. Tsujigawa, H. Nagatsuka, et al., Regeneration of rat auditory ossicles using recombinant human BMP-2/collagen composites. *Journal of Biomedical Materials Research. Part A*, 2005. 73(2): p. 133-141.
- [437] Gavénis, K., D. Klee, R.M. Pereira-Paz, et al., BMP-7 loaded microspheres as a new delivery system for the cultivation of human chondrocytes in a collagen type-I gel. *Journal of Biomedical Materials Research. Part B, Applied Biomaterials*, 2007. 82(2): p. 275-283.
- [438] Zhao, Y., J. Zhang, X. Wang, et al., The osteogenic effect of bone morphogenetic protein-2 on the collagen scaffold conjugated with antibodies. *Journal of Controlled Release*, 2010. 141(1): p. 30-37.
- [439] Sun, B., B. Chen, Y. Zhao, et al., Crosslinking heparin to collagen scaffolds for the delivery of human platelet-derived growth factor. *Journal of Biomedical Materials Research. Part B, Applied Biomaterials*, 2009. 91(1): p. 366-372.

- [440] Teixeira, S., L. Yang, P.J.Dijkstra, et al., Heparinized hydroxyapatite/collagen three-dimensional scaffolds for tissue engineering. *Journal of Materials Science. Materials in Medicine*, 2010. 21(8): p. 2385-2392.
- [441] Wu, J.M., Y.Y. Xu, Z.H. Li, et al., Heparin-functionalized collagen matrices with controlled release of basic fibroblast growth factor. *Journal of Materials Science. Materials in Medicine*, 2011. 22(1): p. 107-114.
- [442] Srouji, S., A. Rachmiel, I. Blumenfeld, and E. Livne, Mandibular defect repair by TGF-beta and IGF-1 released from a biodegradable osteoconductive hydrogel. *Journal of Cranio-Maxillo-Facial Surgery. Journal of Cranio-Maxillo-Facial Surgery*, 2005. 33(2): p. 79-84.
- [443] Chou, C.-H., W.T.K. Cheng, C.-C. Lin, et al., TGF-beta1 immobilized tri-co-polymer for articular cartilage tissue engineering. *Journal of Biomedical Materials Research. Part B, Applied Biomaterials*, 2006. 77(2): p. 338-348.
- [444] Fan, H., Y. Hu, X. Li, et al., Ectopic cartilage formation induced by mesenchymal stem cells on porous gelatin-chondroitin-hyaluronate scaffold containing microspheres loaded with TGF-beta1. *International Journal of Artificial Organs*, 2006. 29(6): p. 602-611.
- [445] Ogawa, T., T. Akazawa, and Y. Tabata, In vitro proliferation and chondrogenic differentiation of rat bone marrow stem cells cultured with gelatin hydrogel microspheres for TGF-beta1 release. *Journal of Biomaterials Science. Polymer Edition*, 2010. 21(5): p. 609-621.
- [446] Kempen, D.H.R., L. Lu, T.E. Hefferan, et al., Retention of in vitro and in vivo BMP-2 bioactivities in sustained delivery vehicles for bone tissue engineering. *Biomaterials*, 2008. 29(22): p. 3245-3252.
- [447] Kempen, D.H.R., L. Lu, A. Heijink, et al., Effect of local sequential VEGF and BMP-2 delivery on ectopic and orthotopic bone regeneration. *Biomaterials*, 2009. 30(14): p. 2816-2825.
- [448] Royce, S.M., M. Askari, and K.G. Marra, Incorporation of polymer microspheres within fibrin scaffolds for the controlled delivery of FGF-1. *Journal of Biomaterials Science. Polymer Edition*, 2004. 15(10): p. 1327-1336.
- [449] Campbell, P.G., E.D. Miller, G.W. Fisher, et al., Engineered spatial patterns of FGF-2 immobilized on fibrin direct cell organization. *Biomaterials*, 2005. 26(33): p. 6762-6770.
- [450] Chung, Y.-I., K.-M. Ahn, S.-H. Jeon, et al, Enhanced bone regeneration with BMP-2 loaded functional nanoparticle-hydrogel complex. *Journal of Controlled Release*, 2007. 121(1-2): p. 91-99.
- [451] Park, K.-H., H. Kim, S. Moon, and K. Na, Bone morphogenic protein-2 (BMP-2) loaded nanoparticles mixed with human mesenchymal stem cell in fibrin hydrogel for bone tissue engineering. *Journal of Bioscience and Bioengineering*, 2009. 108(6): p. 530-537.

- [452] Urry, D.W., Physical chemistry of biological free energy transduction as demonstrated by elastic protein-based polymers. *Journal of Physical Chemistry B*, 1997. 101(51): p. 11007-11028.
- [453] Urry, D.W., Five axioms for the functional design of peptide-based polymers as molecular machines and materials: principle for macromolecular assemblies. *Peptide Science*, 1998. 47(2): p. 167-178.
- [454] Meyer, D.E. and A. Chilkoti, Quantification of the effects of chain length and concentration on the thermal behavior of elastin-like polypeptides. *Biomacromolecules*, 2004. 5(3): p. 846-851.
- [455] Lim, D.W., K. Trabbic-Carlson, J.A. Mackay, and A. Chilkoti, Improved non-chromatographic purification of a recombinant protein by cationic elastin-like polypeptides. *Biomacromolecules*, 2007. 8(5): p. 1417-1424.
- [456] Lee, J., C.W. Macosko, and D.W. Urry, Mechanical properties of cross-linked synthetic elastomeric polypentapeptides. *Macromolecules*, 2001. 34(17): p. 5968-5974.
- [457] Trabbic-Carlson, K., L.A. Setton, and A. Chilkoti, Swelling and mechanical behaviors of chemically cross-linked hydrogels of elastin-like polypeptides. *Biomacromolecules*, 2003. 4(3): p. 572-580.
- [458] Nowatzki, P.J. and D.A. Tirrell, Physical properties of artificial extracellular matrix protein films prepared by isocyanate crosslinking. *Biomaterials*, 2004. 25(7): p. 1261-1267.
- [459] McHale, M.K., L.A. Setton, and A. Chilkoti, Synthesis and in vitro evaluation of enzymatically cross-linked elastin-like polypeptide gels for cartilaginous tissue repair. *Tissue Engineering*, 2005. 11(11-12): p. 1768-1779.
- [460] Lim, D.W., D.L. Nettles, L.A. Setton, and A. Chilkoti, Rapid cross-linking of elastin-like polypeptides with (hydroxymethyl)phosphines in aqueous solution. *Biomacromolecules*, 2007. 8(5): p. 1463-1470.
- [461] Nicol, A., D.C. Gowda, and D.W. Urry, Cell adhesion and growth on synthetic elastomeric matrices containing Arg-Gly-AAsp-Ser3. *Journal of Biomedical Materials Research*, 1992. 26(3): p. 393-413.
- [462] Welsh, E.R. and D.A. Tirrell, Engineering the extracellular matrix: a novel approach to polymeric biomaterials. I. Control of the physical properties of artificial protein matrices designed to support adhesion of vascular endothelial cells. *Biomacromolecules*, 2000. 1(1): p. 23-30.
- [463] Liu, J.C. and D.A. Tirrell, Cell response to RGD density in cross-linked artificial extracellular matrix protein films. *Biomacromolecules*, 2008. 9(11): p. 2984-2988.

- [464] Urry, D.W., T.M. Parker, M.C. Reid, and C. Gowda, Biocompatibility of the bioelastic materials, poly(GVGVP) and its γ -irradiation cross-linked matrix: summary of generic biological test results. *Journal of Bioactive and Compatible Polymers*, 1991. 6(3): p. 263-282.
- [465] Lee, J., C.W. Macosko, and D.W. Urry, Swelling behavior of γ -irradiation cross-linked elastomeric polypentapeptide-based hydrogels. *Macromolecules*, 2001. 34(12): p. 4114-4123.
- [466] Nagapudi, K., W.T. Brinkman, J.E. Leisen, et al., Photomediated solid-state cross-linking of an elastin-mimetic recombinant protein polymer. *Macromolecules*, 2002. 35(5): p. 1730-1737.
- [467] Srokowski, E.M. and K.A. Woodhouse, Development and characterization of novel cross-linked bio-elastomeric materials. *Journal of Biomaterials Science. Polymer Edition*, 2008. 19(6): p. 785-799.
- [468] Huang, L., R.A. McMillan, R.P. Apkarian, et al., Generation of synthetic elastin-mimetic small diameter fibers and fiber networks. *Macromolecules*, 2000. 33(8): p. 2989-2997.
- [469] Lee, J., C.W. Macosko, and D.W. Urry, Elastomeric polypentapeptides cross-linked into matrixes and fibers. *Biomacromolecules*, 2001. 2(1): p. 170-179.
- [470] Betre, H., Chilkoti, A., and Setton, L.A. (2002). A two-step chondrocyte recovery system based on thermally sensitive elastin-like polypeptide scaffolds for cartilage tissue engineering. in Proceedings of the Second 2nd Joint 24th Annual Conference and the Annual Fall Meeting of the Biomedical Engineering Society [Engineering in Medicine and Biology].
- [471] Betre, H., L.A. Setton, D.E. Meyer, and A. Chilkoti, Characterization of a genetically engineered elastin-like polypeptide for cartilaginous tissue repair. *Biomacromolecules*, 2002. 3(5): p. 910-916.
- [472] Betre, H., S.R. Ong, F. Guilak, et al., Chondrocytic differentiation of human adipose-derived adult stem cells in elastin-like polypeptide. *Biomaterials*, 2006. 27(1): p. 91-99.
- [473] Nettles, D.L., K. Kitaoka, N.A. Hanson, et al., In situ crosslinking elastin-like polypeptide gels for application to articular cartilage repair in a goat osteochondral defect model. *Tissue Engineering. Part A*, 2008. 14(7): p. 1133-1140.
- [474] Hrabchak, C., J. Rouleau, I. Moss, et al., Assessment of biocompatibility and initial evaluation of genipin cross-linked elastin-like polypeptides in the treatment of an osteochondral knee defect in rabbits. *Acta Biomaterialia*, 2010. 6(6): p. 2108-2115.
- [475] Nettles, D.L., A. Chilkoti, and L.A. Setton, Applications of elastin-like polypeptides in tissue engineering. *Advanced Drug Delivery Reviews*, 2010. 62(15): p. 1479-1485.
- [476] Moss, I.L., L. Gordon, K.A. Woodhouse, et al., A novel thiol-modified hyaluronan and elastin-like polypeptide composite material for tissue engineering of the nucleus pulposus of the intervertebral disc. *Spine*, 2011. 36(13): p. 1022-1029.

- [477] Muiznieks, L.D., Genipin cross-linking of elastin and elastin-based proteins, in Protein Scaffolds: Design, Synthesis, and Applications, (ed. A.K. Udit), 2018, Springer New York: New York, NY. p. 213-221.
- [478] Nicol, A., C. Gowda, and D.W. Urry, Elastic protein-based polymers as cell attachment matrices. *Journal of Vascular Surgery*, 1991. 13(5): p. 746-748.
- [479] Urry, D.W., A. Pattanaik, J. Xu, et al., Elastic protein-based polymers in soft tissue augmentation and generation. *Journal of Biomaterials Science. Polymer Edition*, 1998. 9(10): p. 1015-1048.
- [480] Betre, H., W. Liu, M.R. Zalutsky, et al., A thermally responsive biopolymer for intra-articular drug delivery. *Journal of Controlled Release*, 2006. 115(2): p. 175-182.
- [481] Caves, J.M., V.A. Kumar, A.W. Martinez, et al., The use of microfiber composites of elastin-like protein matrix reinforced with synthetic collagen in the design of vascular grafts. *Biomaterials*, 2010. 31(27): p. 7175-7182.
- [482] Ravi, S. and E.L. Chaikof, Biomaterials for vascular tissue engineering. *Regenerative Medicine*, 2010. 5(1): p. 107-120.
- [483] Sallach, R.E., W. Cui, F. Balderrama, et al., Long-term biostability of self-assembling protein polymers in the absence of covalent crosslinking. *Biomaterials*, 2010. 31(4): p. 779-791.
- [484] Di Zio, K. and D.A. Tirrell, Mechanical properties of artificial protein matrices engineered for control of cell and tissue behavior. *Macromolecules*, 2003. 36(5): p. 1553-1558.
- [485] Heilshorn, S.C., K.A. DiZio, E.R. Welsh, and D.A. Tirrell, Endothelial cell adhesion to the fibronectin CS5 domain in artificial extracellular matrix proteins. *Biomaterials*, 2003. 24(23): p. 4245-4252.
- [486] Trabbic-Carlson, K., L. Liu, B. Kim, and A. Chilkoti, Expression and purification of recombinant proteins from Escherichia coli: comparison of an elastin-like polypeptide fusion with an oligohistidine fusion. *Protein Science*, 2004. 13(12): p. 3274-3284.
- [487] Shamji, M.F., L. Whitlatch, A.H. Friedman, et al., An injectable and in situ-gelling biopolymer for sustained drug release following perineural administration. *Spine*, 2008. 33(7): p. 748-754.
- [488] Massodi, I., G.L. Bidwell III, A. Davis, et al., Inhibition of ovarian cancer cell metastasis by a fusion polypeptide Tat-ELP. *Clinical and Experimental Metastasis*, 2009. 26(3): p. 251-260.
- [489] Heilshorn, S.C., J.C. Liu, and D.A. Tirrell, Cell-binding domain context affects cell behavior on engineered proteins. *Biomacromolecules*, 2005. 6(1): p. 318-323.

- [490] Liu, J.C., S.C. Heilshorn, and D.A. Tirrell, Comparative cell response to artificial extracellular matrix proteins containing the RGD and CS5 cell-binding domains. *Biomacromolecules*, 2004. 5(2): p. 497-504.
- [491] Lin, H.-B., C. García-Echeverría, S. Asakura, et al., Endothelial cell adhesion on polyurethanes containing covalently attached RGD-peptides. *Biomaterials*, 1992. 13(13): p. 905-914.
- [492] Panitch, A., T. Yamaoka, M.J. Fournier, et al., Design and biosynthesis of elastin-like artificial extracellular matrix proteins containing periodically spaced fibronectin CS5 domains. *Macromolecules*, 1999. 32(5): p. 1701-1703.
- [493] Almine, J.F., D.V. Bax, S.M. Mithieux, et al., Elastin-based materials. *Chemical Society Reviews*, 2010. 39(9): p. 3371-3379.
- [494] Kim, W. and E.L. Chaikof, Recombinant elastin-mimetic biomaterials: emerging applications in medicine. *Advanced Drug Delivery Reviews*, 2010. 62(15): p. 1468-1478.
- [495] Girotti, A., J. Reguera, J.C. Rodríguez-Cabello, et al., Design and bioproduction of a recombinant multi(bio)functional elastin-like protein polymer containing cell adhesion sequences for tissue engineering purposes. *Journal of Materials Science. Materials in Medicine*, 2004. 15(4): p. 479-484.
- [496] Martínez-Osorio, H., M. Juárez-Campo, Y. Diebold, et al. Genetically engineered elastin-like polymer as a substratum to culture cells from the ocular surface. *Current Eye Research*, 2009. 34(1): p. 48-56.
- [497] Janorkar, A.V., P. Rajagopalan, M.L. Yarmush, and Z. Megeed, The use of elastin-like polypeptide-polyelectrolyte complexes to control hepatocyte morphology and function in vitro. *Biomaterials*, 2008. 29(6): p. 625-632.
- [498] Swierczewska, M., C.S. Hajicharalambous, A.V. Janorkar, et al., Cellular response to nanoscale elastin-like polypeptide polyelectrolyte multilayers. *Acta Biomaterialia*, 2008. 4(4): p. 827-837.
- [499] Maude, S., E. Ingham, and A. Aggeli, Biomimetic self-assembling peptides as scaffolds for soft tissue engineering. *Nanomedicine*, 2013. 8(5): p. 823-847.
- [500] Nagapudi, K., W.T. Brinkman, B.S. Thomas, et al., Viscoelastic and mechanical behavior of recombinant protein elastomers. *Biomaterials*, 2005. 26(23): p. 4695-4706.
- [501] Chow, D., M.L. Nunalee, D.W. Lim, et al., Peptide-based biopolymers in biomedicine and biotechnology .Materials Science and Engineering. : R, : Reports: A Review Journal, 2008. 62(4): p. 125-155.

- [502] Sallach, R.E., W. Cui, J. Wen, et al., Elastin-mimetic protein polymers capable of physical and chemical crosslinking. *Biomaterials*, 2009. 30(3): p. 409-422.
- [503] MacEwan, S.R. and A. Chilkoti, Elastin-like polypeptides: biomedical applications of tunable biopolymers. *Biopolymers*, 2010. 94(1): p. 60-77.
- [504] Hecht, M.H., De novo design of beta-sheet proteins. *Proceedings of the National Academy of Sciences of the United States of America*, 1994. 91(19): p. 8729-8730.
- [505] Xiong, H., B.L. Buckwater, H.M. Shieh, and M.H. Hecht, Periodicity of polar and nonpolar amino acids is the major determinant of secondary structure in self-assembling oligomeric peptides. *Proceedings of the National Academy of Sciences of the United States of America*, 1995. 92(14): p. 6349-6353.
- [506] Dobson, C.M., Protein misfolding, evolution and disease. *Trends in Biochemical Sciences*, 1999. 24(9): p. 329-332.
- [507] MacPhee, C.E. and D.N. Woolfson, Engineered and designed peptide-based fibrous biomaterials. *Current Opinion in Solid State and Materials Science*, 2004. 8(2): p. 141-149.
- [508] Wu, X., R.E. Sallach, J.M. Caves, et al., Deformation responses of a physically crosslinked high molecular weight elastin-like protein polymer. *Biomacromolecules*, 2008. 9(7): p. 1787-1794.
- [509] Gustafson, J.A. and H. Ghandehari, Silk-elastin like protein polymers for matrix-mediated cancer gene therapy. *Advanced Drug Delivery Reviews*, 2010. 62(15): p. 1509-1523.
- [510] Numata, K. and D.L. Kaplan, Silk-based delivery systems of bioactive molecules. *Advanced Drug Delivery Reviews*, 2010. 62(15): p. 1497-1508.
- [511] Zhang, S., T. Holmes, C. Lockshin, and A. Rich, Spontaneous assembly of a self-complementary oligopeptide to form a stable macroscopic membrane. *Proceedings of the National Academy of Sciences of the United States of America*, 1993. 90(8): p. 3334-3338.
- [512] Yokoi, H., T. Kinoshita, and S. Zhang, Dynamic reassembly of peptide RADA16 nanofiber scaffold. *Proceedings of the National Academy of Sciences of the United States of America*, 2005. 102(24): p. 8414-8419.
- [513] Gelain, F., D. Bottai, A. Vescovi, and S. Zhang, Designer self-assembling peptide nanofiber scaffolds for adult mouse neural stem cell 3-dimensional cultures. *PLoS One*, 2006. 1: p. e119.
- [514] Davis, M.E., J.P. Motion, D.A. Narmoneva, et al., Injectable self-assembling peptide nanofibers create intramyocardial microenvironments for endothelial cells. *Circulation*, 2005. 111(4): p. 442-450.

- [515] Holmes, T.C., S. de Lacalle, X. Su, et al., Extensive neurite outgrowth and active synapse formation on self-assembling peptide scaffolds. *Proceedings of the National Academy of Sciences of the United States of America*, 2000. 97(12): p. 6728-6733.
- [516] Engel, F.B., P.C.H. Hsieh, R.T. Lee, and M.T. Keating, FGF1/p38 MAP kinase inhibitor therapy induces cardiomyocyte mitosis, reduces scarring, and rescues function after myocardial infarction. *Proceedings of the National Academy of Sciences of the United States of America*, 2006. 103(42): p. 15546-15551.
- [517] Guo, J., H. Su, Y. Zeng, et al., Reknitting the injured spinal cord by self-assembling peptide nanofiber scaffold. *Nanomedicine: Nanotechnology, Biology, and Medicine*, 2007. 3(4): p. 311-321.
- [518] Sieminski, A.L., C.E. Semino, H. Gong, and R.D. Kamm, Primary sequence of ionic self-assembling peptide gels affects endothelial cell adhesion and capillary morphogenesis. *Journal of Biomedical Materials Research. Part A*, 2008. 87(2): p. 494-504.
- [519] Cui, X.-J., H. Xie, H.-J. Wang, et al., Transplantation of mesenchymal stem cells with self-assembling polypeptide scaffolds is conducive to treating myocardial infarction in rats. *Tohoku Journal of Experimental Medicine*, 2010. 222(4): p. 281-289.
- [520] Guo, H.-D., G.-H. Cui, H.-J. Wang, and Y.-Z. Tan, Transplantation of marrow-derived cardiac stem cells carried in designer self-assembling peptide nanofibers improves cardiac function after myocardial infarction. *Biochemical and Biophysical Research Communications*, 2010. 399(1): p. 42-48.
- [521] Lin, Y.-D., M.-L. Yeh, Y.-J. Yang, et al., Intramyocardial peptide nanofiber injection improves postinfarction ventricular remodeling and efficacy of bone marrow cell therapy in pigs. *Circulation*, 2010. 122(11 Suppl): p. S132-141.
- [522] Tokunaga, M., M.-L. Liu, T. Nagai, et al., Implantation of cardiac progenitor cells using self-assembling peptide improves cardiac function after myocardial infarction. *Journal of Molecular and Cellular Cardiology*, 2010. 49(6): p. 972-983.
- [523] Cho, H., S. Balaji, A.Q. Sheikh, et al., Regulation of endothelial cell activation and angiogenesis by injectable peptide nanofibers. *Acta Biomaterialia*, 2012. 8(1): p. 154-164.
- [524] Lin, Y.-D., C.-Y. Luo, Y.-N. Hu, et al., Instructive nanofiber scaffolds with VEGF create a microenvironment for arteriogenesis and cardiac repair. *Science Translational Medicine*, 2012. 4(146): p. 146ra109.
- [525] Kim, J.H., Y. Jung, B.-S. Kim, and S.H. Kim, Stem cell recruitment and angiogenesis of neuropeptide substance P coupled with self-assembling peptide nanofiber in a mouse hind limb ischemia model. *Biomaterials*, 2013. 34(6): p. 1657-1668.

- [526] Boopathy, A.V., P.L. Che, I. Somasuntharam, et al., The modulation of cardiac progenitor cell function by hydrogel-dependent Notch1 activation. *Biomaterials*, 2014. 35(28): p. 8103-8112.
- [527] Prat-Vidal, C., C. Gálvez-Montón, V. Puig-Sanvicenç, et al., Online monitoring of myocardial bioprostheses for cardiac repair. *International Journal of Cardiology*, 2014. 174(3): p. 654-661.
- [528] Genové, E., C. Shen, S. Zhang, and C.E. Semino, The effect of functionalized self-assembling peptide scaffolds on human aortic endothelial cell function. *Biomaterials*, 2005. 26(16): p. 3341-3351.
- [529] Narmoneva, D.A., O. Oni, A.L. Sieminski, et al., Self-assembling short oligopeptides and the promotion of angiogenesis. *Biomaterials*, 2005. 26(23): p. 4837-4846.
- [530] Wang, X., A. Horii, and S. Zhang, Designer functionalized self-assembling peptide nanofiber scaffolds for growth, migration, and tubulogenesis of human umbilical vein endothelial cells. *Soft Matter*, 2008. 4(12): p. 2388-2395.
- [531] Narmoneva, D.A., R. Vukmirovic, M.E. Davis, et al., Endothelial cells promote cardiac myocyte survival and spatial reorganization. *Circulation*, 2004. 110(8): p. 962-968.
- [532] Cunha, C., S. Panseri, O. Villa, et al., 3D culture of adult mouse neural stem cells within functionalized self-assembling peptide scaffolds. *International Journal of Nanomedicine*, 2011. 6: p. 943.
- [533] Cheng, T.-Y., M.-H. Chen, W.-H. Chang, et al., Neural stem cells encapsulated in a functionalized self-assembling peptide hydrogel for brain tissue engineering. *Biomaterials*, 2013. 34(8): p. 2005-2016.
- [534] Ellis-Behnke, R.G., Y.-X. Liang, S.-W. You, et al., Nano neuro knitting: peptide nanofiber scaffold for brain repair and axon regeneration with functional return of vision. *Proceedings of the National Academy of Sciences of the United States of America*, 2006. 103(13): p. 5054-5059.
- [535] Guo, J., K.K.G. Leung, H. Su, et al., Self-assembling peptide nanofiber scaffold promotes the reconstruction of acutely injured brain. *Nanomedicine: Nanotechnology, Biology, and Medicine*, 2009. 5(3): p. 345-351.
- [536] Song, H., L. Zhang, and X. Zhao, Hemostatic efficacy of biological self-assembling peptide nanofibers in a rat kidney model. *Macromolecular Bioscience*, 2010. 10(1): p. 33-39.
- [537] Gras, S.L., A.K. Tickler, A.M. Squires, et al., Functionalized amyloid fibrils for roles in cell adhesion. *Biomaterials*, 2008. 29(11): p. 1553-1562.

- [538] Aggeli, A., M. Bell L.M. Carrick, et al., pH as a trigger of peptide β -sheet self-assembly and reversible switching between nematic and isotropic phases. *Journal of the American Chemical Society*, 2003. 125(32): p. 9619-9628.
- [539] Davies, R.P.W., A. Aggeli, A.J. Beevers, et al., Self-assembling β -sheet tape forming peptides. *Supramolecular Chemistry*, 2006. 18(5): p. 435-443.
- [540] Carrick, L.M., A. Aggeli, N. Boden, et al., Effect of ionic strength on the self-assembly, morphology and gelation of pH responsive β -sheet tape-forming peptides. *Tetrahedron*, 2007. 63(31): p. 7457-7467.
- [541] Silvertown, J.D., B.P.Y. Wong, K.S. Sivagurunathan, et al., Remineralization of natural early caries lesions in vitro by P11-4 monitored with photothermal radiometry and luminescence. *Journal of Investigative and Clinical Dentistry*, 2017. 8(4): p. 1-8.
- [542] Jung, J.P., J.L Jones, S.A. Cronier, and J.H. Collier, Modulating the mechanical properties of self-assembled peptide hydrogels via native chemical ligation. *Biomaterials*, 2008. 29(13): p. 2143-2151.
- [543] Jung, J.P., A.K. Nagaraj, E.K. Fox, et al., Co-assembling peptides as defined matrices for endothelial cells. *Biomaterials*, 2009. 30(12): p. 2400-2410.
- [544] Kyle, S.,A. Aggeli, E. Ingham, and M.J. McPherson, Recombinant self-assembling peptides as biomaterials for tissue engineering. *Biomaterials*, 2010. 31(36): p. 9395-9405.
- [545] Salick, D.A., J.K. Kretsinger, D.J. Pochan, and J.P. Schneider, Inherent antibacterial activity of a peptide-based beta-hairpin hydrogel. *Journal of the American Chemical Society*, 2007. 129(47): p. 14793-14799.
- [546] Worthington, P., D.J. Pochan, and S.A. Langhans, Peptide hydrogels – versatile matrices for 3D cell culture in cancer medicine. *Frontiers in Oncology*, 2015. 5: p. 1-10.
- [547] Schneider, J.P., D.J. Pochan, B. Ozbas, et al., Responsive hydrogels from the intramolecular folding and self-assembly of a designed peptide. *Journal of the American Chemical Society*, 2002. 124(50): p. 15030-15037.
- [548] Kumar, V.A., N.L. Taylor, S. Shi, et al., Highly angiogenic peptide nanofibers. *ACS Nano*, 2015. 9(1): p. 860-868.
- [549] Galler, K.M., J.D. Hartgerink, A.C. Cavendar, et al., A customized self-assembling peptide hydrogel for dental pulp tissue engineering. *Tissue Engineering. Part A*, 2012. 18(1-2): p. 176-184.
- [550] Kang, M.K., J.S. Colombo, R.N. D'Souza, and J.D. Hartgerink, Sequence effects of self-assembling multidomain peptide hydrogels on encapsulated SHED cells. *Biomacromolecules*, 2014. 15(6): p. 2004-2011.

- [551] Collier, J.H., J.S. Rudra, J.Z. Gasiorowski, and J.P. Jung, Multi-component extracellular matrices based on peptide self-assembly. *Chemical Society Reviews*, 2010. 39(9): p. 3413-3424.
- [552] Hauser, C.A.E. and S. Zhang, Designer self-assembling peptide nanofiber biological materials. *Chemical Society Reviews*, 2010. 39(8): p. 2780-2790.
- [553] Beniash, E., J.D. Hartgerink, H. Storrie, et al., Self-assembling peptide amphiphile nanofiber matrices for cell entrapment. *Acta Biomaterialia*, 2005. 1(4): p. 387-397.
- [554] Storrie, H., M.O. Guler, S.N. Abu-Amara, et al., Supramolecular crafting of cell adhesion. *Biomaterials*, 2007. 28(31): p. 4608-4618.
- [555] Hosseinkhani, H., M. Hosseinkhani, and H. Kobayashi, Proliferation and differentiation of mesenchymal stem cells using self-assembled peptide amphiphile nanofibers. *Biomedical Materials*, 2006. 1(1): p. 8-15.
- [556] Hosseinkhani, H., M. Hosseinkhani, and H. Kobayashi, Design of tissue-engineered nanoscaffold through self-assembly of peptide amphiphile. *Journal of Bioactive and Compatible Polymers*, 2006. 21(4): p. 277-296.
- [557] Hosseinkhani, H., M. Hosseinkhani, and H. Kobayashi, Osteogenic differentiation of mesenchymal stem cells in self-assembled peptide-amphiphile nanofibers. *Biomaterials*, 2006. 27(22): p. 4079-4086.
- [558] Hosseinkhani, H., M. Hosseinkhani, F. Tian, et al., Ectopic bone formation in collagen sponge self-assembled peptide-amphiphile nanofibers hybrid scaffold in a perfusion culture bioreactor. *Biomaterials*, 2006. 27(29): p. 5089-5098.
- [559] Tysseling-Mattiace, V.M., V. Sahni, K.L. Niece, et al., Self-assembling nanofibers inhibit glial scar formation and promote axon elongation after spinal cord injury. *Journal of Neuroscience*, 2008. 28(14): p. 3814-3823.
- [560] Shah, R.N., N.A. Shah, M.M.D.R. Lim, et al., Supramolecular design of self-assembling nanofibers for cartilage regeneration. *Proceedings of the National Academy of Sciences of the United States of America*, 2010. 107(8): p. 3293-3298.
- [561] Cai, S., Y. Liu, X.Z. Shu, and G.D. Prestwich, Injectable glycosaminoglycan hydrogels for controlled release of human basic fibroblast growth factor. *Biomaterials*, 2005. 26(30): p. 6054-6067.
- [562] Hosseinkhani, H., M. Hosseinkhani, A. Khademhosseini, and H. Kobayashi, Bone regeneration through controlled release of bone morphogenetic protein-2 from 3-D tissue engineered nano-scaffold. *Journal of Controlled Release*, 2007. 117(3): p. 380-386.

- [563] Hartgerink, J.D., E. Beniash, and S.I. Stupp, Self-assembly and mineralization of peptide-amphiphile nanofibers. *Science*, 2001. 294(5547): p. 1684-1688.
- [564] Morimoto, K., H. Yamaguchi, Y. Iwakura, et al., Effects of viscous hyaluronate-sodium solutions on the nasal absorption of vasopressin and an analogue. *Pharmaceutical Research*, 1991. 8(4): p. 471-474.
- [565] Cascone, M.G., B. Sim, and S. Downes, Blends of synthetic and natural polymers as drug delivery systems for growth hormone. *Biomaterials*, 1995. 16(7): p. 569-574.
- [566] Moore, A.R. and D.A. Willoughby, Hyaluronan as a drug delivery system for diclofenac: a hypothesis for mode of action. *International Journal of Tissue Reactions*, 1995. 17(4): p. 153-156.
- [567] Gowland, G., A.R. Moore, D. Willis, and D.A. Willoughby, Marked enhanced efficacy of cyclosporin when combined with hyaluronic acid. *Clinical Drug Investigation*, 1996. 11(4): p. 245-250.
- [568] Miller, J.A., R.L. Ferguson, D.L. Powers, et al., Efficacy of hyaluronic acid/nonsteroidal anti-inflammatory drug systems in preventing postsurgical tendon adhesions. *Journal of Biomedical Materials Research*, 1997. 38(1): p. 25-33.
- [569] Luo, Y., K.R. Kirker, and G.D. Prestwich, Cross-linked hyaluronic acid hydrogel films: new biomaterials for drug delivery. *Journal of Controlled Release*, 2000. 69(1): p. 169-184.
- [570] Sinha, V.R. and R. Kumria, Polysaccharides in colon-specific drug delivery. *International Journal of Pharmaceutics*, 2001. 224(1): p. 19-38.
- [571] Chourasia, M.K. and S.K. Jain, Polysaccharides for colon targeted drug delivery. *Drug Delivery*, 2004. 11(2): p. 129-148.
- [572] Goodarzi, N., R. Varshochian, G. Kamalinia, et al., A review of polysaccharide cytotoxic drug conjugates for cancer therapy. *Carbohydrate Polymers*, 2013. 92(2): p. 1280-1293.
- [573] Basu, A., K.R. Kundru, E. Abtew, and A.J. Domb, Polysaccharide-based conjugates for biomedical applications. *Bioconjugate Chemistry*, 2015. 26(8): p. 1396-1412.
- [574] Yang, J., S. Han, H. Zheng, et al., Preparation and application of micro/nanoparticles based on natural polysaccharides. *Carbohydrate Polymers*, 2015. 123: p. 53-66.
- [575] Garnett, M.C., Targeted drug conjugates: principles and progress. *Advanced Drug Delivery Reviews*, 2001. 53(2): p. 171-216.
- [576] Ojima, I., X. Geng, X. Wu, et al., Tumor-specific novel taxoid–monoclonal antibody conjugates. *Journal of Medicinal Chemistry*, 2002. 45(26): p. 5620-5623.

- [577] Haag, R. and F. Kratz, Polymer therapeutics: concepts and applications. *Angewandte Chemie*, 2006. 45(8): p. 1198-1215.
- [578] Khandare, J. and T. Minko, Polymer-drug conjugates: progress in polymeric prodrugs. *Progress in Polymer Science*, 2006. 31(4): p. 359-397.
- [579] Yeh, C.-C., M.-F. Hou, S.-H. Wu, et al., A study of glutathione status in the blood and tissues of patients with breast cancer. *Cell Biochemistry and Function*, 2006. 24(6): p. 555-559.
- [580] Pasut, G. and F.M. Veronese, Polymer-drug conjugation, recent achievements and general strategies. *Progress in Polymer Science*, 2007. 32(8): p. 933-961.
- [581] Warnecke, A., I. Fichtner, G. Sass, and F. Kratz, Synthesis, cleavage profile, and antitumor efficacy of an albumin-binding prodrug of methotrexate that is cleaved by plasmin and cathepsin B. *Archiv der Pharmazie*, 2007. 340(8): p. 389-395.
- [582] Homma, A., H. Sato, T. Tamura, et al., Synthesis and optimization of hyaluronic acid-methotrexate conjugates to maximize benefit in the treatment of osteoarthritis. *Bioorganic and Medicinal Chemistry*, 2010. 18(3): p. 1062-1075.
- [583] Bildstein, L., C. Dubernet, and P. Couvreur, Prodrug-based intracellular delivery of anticancer agents. *Advanced Drug Delivery Reviews*, 2011. 63(1-2): p. 3-23.
- [584] Hou, L., Y. Fan, J. Yao, et al., Low molecular weight heparin-all-trans-retinoid acid conjugate as a drug carrier for combination cancer chemotherapy of paclitaxel and all-trans-retinoid acid. *Carbohydrate Polymers*, 2011. 86(3): p. 1157-1166.
- [585] Luo, Q., P. Wang, Y. Miao, et al., A novel 5-fluorouracil prodrug using hydroxyethyl starch as a macromolecular carrier for sustained release. *Carbohydrate Polymers*, 2012. 87(4): p. 2642-2647.
- [586] Chau, Y., F.E. Tan, and R. Langer, Synthesis and characterization of dextran-peptide-methotrexate conjugates for tumor targeting via mediation by matrix metalloproteinase II and matrix metalloproteinase IX. *Bioconjugate Chemistry*, 2004. 15(4): p. 931-941.
- [587] Sugahara, S.-I., M. Kajiki, H. Kuriyama, and T.-R. Kobayashi, Carrier effects on antitumor activity and neurotoxicity of AZ10992, a paclitaxel-carboxymethyl dextran conjugate, in a mouse model. *Biological and Pharmaceutical Bulletin*, 2008. 31(2): p. 223-230.
- [588] Luo, Y., M.R. Ziebell, and G.D. Prestwich, A hyaluronic acid-taxol antitumor bioconjugate targeted to cancer cells. *Biomacromolecules*, 2000. 1(2): p. 208-218.
- [589] Dubowchik, G.M., S. Radia, H. Mastalerz, et al., Doxorubicin immunoconjugates containing bivalent, lysosomally-cleavable dipeptide linkages. *Bioorganic and Medicinal Chemistry Letters*, 2002. 12(11): p. 1529-1532.

- [590] Chau, Y., N.M. Dang, F.E. Tan, and R. Langer, Investigation of targeting mechanism of new dextran-peptide-methotrexate conjugates using biodistribution study in matrix-metalloproteinase-overexpressing tumor xenograft model. *Journal of Pharmaceutical Sciences*, 2006. 95(3): p. 542-551.
- [591] Chau, Y., R.F. Padera, N.M. Dang, and R. Langer, Antitumor efficacy of a novel polymer-peptide-drug conjugate in human tumor xenograft models. *International Journal of Cancer*, 2006. 118(6): p. 1519-1526.
- [592] Zhou, W., Y. Wang, J. Jian, and S. Song, Self-aggregated nanoparticles based on amphiphilic poly(lactic acid)-grafted-chitosan copolymer for ocular delivery of amphotericin B. *International Journal of Nanomedicine*, 2013. 8: p. 3715-3728.
- [593] Lautenschläger, C., C. Schmidt, K. Lange, and A. Stallmach, Drug delivery strategies for targeted treatment of inflammatory bowel disease. *Zeitschrift Fur Gastroenterologie*, 2015. 53(3): p. 226-234.
- [594] Lautenschläger, C., J. Sendker, S. Hüwel, et al., Intestinal formation of trans-crocetin from saffron extract (*Crocus sativus L.*) and in vitro permeation through intestinal and blood brain barrier. *Phytomedicine*, 2015. 22(1): p. 36-44.
- [595] Pitobeira, N.A.O., J.G. Veras Neto, D.A. Silva, et al., Self-assembled nanoparticles of acetylated cashew gum: characterization and evaluation as potential drug carrier. *Carbohydrate Polymers*, 2015. 117: p. 610-615.
- [596] Dosio, F., S. Arpicco, B. Stella, and E. Fattal, Hyaluronic acid for anticancer drug and nucleic acid delivery. *Advanced Drug Delivery Reviews*, 2016. 97: p. 204-236.
- [597] Luo, Y. and G.D. Prestwich, Synthesis and selective cytotoxicity of a hyaluronic acid-antitumor bioconjugate. *Bioconjugate Chemistry*, 1999. 10(5): p. 755-763.
- [598] Götte, M. and G.W. Yip, Heparanase, hyaluronan, and CD44 in cancers: a breast carcinoma perspective. *Cancer Research*, 2006. 66(21): p. 10233-10237.
- [599] Schätzlein, A.G., Delivering cancer stem cell therapies - a role for nanomedicines? *European Journal of Cancer*, 2006. 42(9): p. 1309-1315.
- [600] Auzenne, E., S.C. Ghosh, M. Khodadadian, et al., Hyaluronic acid-paclitaxel: antitumor efficacy against CD44(+) human ovarian carcinoma xenografts. *Neoplasia*, 2007. 9(6): p. 479-486.
- [601] Lee, E., J. Lee, I.-H. Lee, et al., Conjugated chitosan as a novel platform for oral delivery of paclitaxel. *Journal of Medicinal Chemistry*, 2008. 51(20): p. 6442-6449.
- [602] Lee, H., K. Lee, and T.G. Park, Hyaluronic acid-paclitaxel conjugate micelles: synthesis, characterization, and antitumor activity. *Bioconjugate Chemistry*, 2008. 19(6): p. 1319-1325.

- [603] Oh, E.J., K. Park, K.S. Kim, et al., Target specific and long-acting delivery of protein, peptide, and nucleotide therapeutics using hyaluronic acid derivatives. *Journal of Controlled Release*, 2010. 141(1): p. 2-12.
- [604] Pedrosa, S.S., P. Pereira, A. Correia, and F.M. Gama, Targetability of hyaluronic acid nanogel to cancer cells: in vitro and in vivo studies. *European Journal of Pharmaceutical Sciences*, 2017. 104: p. 102-113.
- [605] Dalerba, P., R.W. Cho, and M.F. Clarke, Cancer stem cells: models and concepts. *Annual Review of Medicine*, 2007. 58: p. 267-284.
- [606] Zhang, M. and S.P. James, Synthesis and properties of melt-processable hyaluronan esters. *Journal of Materials Science. Materials in Medicine*, 2005. 16(6): p. 587-593.
- [607] Zhang, M. and S.P. James, Silylation of hyaluronan to improve hydrophobicity and reactivity for improved processing and derivatization. *Polymer*, 2005. 46(11): p. 3639-3648.
- [608] Norbedo, S., F. Dinon, M. Bergamin, et al., Synthesis of 6-amino-6-deoxyhyaluronan as an intermediate for conjugation with carboxylate-containing compounds: application to hyaluronan-camptothecin conjugates. *Carbohydrate Research*, 2009. 344(1): p. 98-104.
- [609] Leonelli, F., A. La Bella, A. Francescangeli, et al., A new and simply available class of hydrosoluble bioconjugates by coupling paclitaxel to hyaluronic acid through a 4-hydroxybutanoic acid derived linker. *Helvetica Chimica Acta*, 2005. 88(1): p. 154-159.
- [610] Rosato, A., A. Banzato, G. De Luca, et al., HYTAD1-p20: a new paclitaxel-hyaluronic acid hydrosoluble bioconjugate for treatment of superficial bladder cancer. *Urologic Oncology*, 2006. 24(3): p. 207-215.
- [611] Manju, S. and K. Sreenivasan, Conjugation of curcumin onto hyaluronic acid enhances its aqueous solubility and stability. *Journal of Colloid and Interface Science*, 2011. 359(1): p. 318-325.
- [612] Coradini, D., C. Pellizzaro, G. Abolafio, et al., Hyaluronic-acid butyric esters as promising antineoplastic agents in human lung carcinoma: a preclinical study. *Investigational New Drugs*, 2004. 22(3): p. 207-217.
- [613] Speranza, A., C. Pellizzaro, and D. Coradini, Hyaluronic acid butyric esters in cancer therapy. *Anti-Cancer Drugs*, 2005. 16(4): p. 373-379.
- [614] Coradini, D., C. Pellizzaro, I. Scarlata, et al., A novel retinoic/butyric hyaluronan ester for the treatment of acute promyelocytic leukemia: preliminary preclinical results. *Leukemia*, 2006. 20(5): p. 785-792.

- [615] Banzato, A., S. Bobisse, M. Rondina, et al., A paclitaxel-hyaluronan bioconjugate targeting ovarian cancer affords a potent in vivo therapeutic activity. *Clinical Cancer Research*, 2008. 14(11): p. 3598-3606.
- [616] De Stefano, I., A. Battaglia, G.F. Zannoni, et al., Hyaluronic acid-paclitaxel: effects of intraperitoneal administration against CD44(+) human ovarian cancer xenografts. *Cancer Chemotherapy and Pharmacology*, 2011. 68(1): p. 107-116.
- [617] Galer, C.E., D. Sano, S.C. Ghosh, et al., Hyaluronic acid-paclitaxel conjugate inhibits growth of human squamous cell carcinomas of the head and neck via a hyaluronic acid-mediated mechanism. *Oral Oncology*, 2011. 47(11): p. 1039-1047.
- [618] Lee, S.J., S.C. Ghosh, H.D. Han, et al., Metronomic activity of CD44-targeted hyaluronic acid-paclitaxel in ovarian carcinoma. *Clinical Cancer Research*, 2012. 18(15): p. 4114-4121.
- [619] Mittapalli, R.K., X. Liu, C.E. Adkins, et al., Paclitaxel-hyaluronic nanoconjugates prolong overall survival in a preclinical brain metastases of breast cancer model. *Molecular Cancer Therapeutics*, 2013. 12(11): p. 2389-2399.
- [620] Serafino, A., M. Zonfrillo, F. Andreola, et al., CD44-targeting for antitumor drug delivery: a new SN-38-hyaluronan bioconjugate for locoregional treatment of peritoneal carcinomatosis. *Current Cancer Drug Targets*, 2011. 11(5): p. 572-585.
- [621] Montagner, I.M., A. Merlo, G. Zuccolotto, et al., Peritoneal tumor carcinomatosis: pharmacological targeting with hyaluronan-based bioconjugates overcomes therapeutic indications of current drugs. *PLoS One*, 2014. 9(11): p. e112240.
- [622] Cai, S., S. Thati, T.R. Bagby, et al., Localized doxorubicin chemotherapy with a biopolymeric nanocarrier improves survival and reduces toxicity in xenografts of human breast cancer. *Journal of Controlled Release*, 2010. 146(2): p. 212-218.
- [623] Cai, S., Y. Xie, T.R. Bagby, et al., Intralymphatic chemotherapy using a hyaluronan-cisplatin conjugate. *Journal of Surgical Research*, 2008. 147(2): p. 247-252.
- [624] Cohen, S.M., R. Mukerji, S. Cai, et al., Subcutaneous delivery of nanoconjugated doxorubicin and cisplatin for locally advanced breast cancer demonstrates improved efficacy and decreased toxicity at lower doses than standard systemic combination therapy in vivo. *American Journal of Surgery*, 2011. 202 (6): 646-652; discussion 652-653.
- [625] Venable, R.O., D.R. Worley, D.L. Gustafson, et al., Effects of intratumoral administration of a hyaluronan-cisplatin nanoconjugate to five dogs with soft tissue sarcomas. *American Journal of Veterinary Research*, 2012. 73(12): p. 1969-1976.
- [626] Cohen, S.M., N. Rockefeller, R. Mukerji, et al., Efficacy and toxicity of peritumoral delivery of nanoconjugated cisplatin in an in vivo murine model of head and neck squamous cell carcinoma. *JAMA Otolaryngology–Head and Neck Surgery*, 2013. 139(4): p. 382-387.

- [627] Yang, Q., D.J. Aires, S. Cai, et al., In vivo efficacy of nano hyaluronan-conjugated cisplatin for treatment of murine melanoma. *Journal of Drugs in Dermatology*, 2014. 13(3): p. 283-287.
- [628] Ling, X., Y. Shen, R. Sun, et al., Tumor-targeting delivery of hyaluronic acid-platinum(IV) nanoconjugate to reduce toxicity and improve survival. *Polymer Chemistry*, 2015. 6(9): p. 1541-1552.
- [629] Camacho, K.M., S. Menegatti, and S. Mitragotri, Low-molecular-weight polymer-drug conjugates for synergistic anticancer activity of camptothecin and doxorubicin combinations. *Nanomedicine*, 2016. 11(9): p. 1139-1151.
- [630] Luo, Y., N.J. Bernshaw, Z.-R. Lu, et al., Targeted delivery of doxorubicin by HPMA copolymer-hyaluronan bioconjugates. *Pharmaceutical Research*, 2002. 19(4): p. 396-402.
- [631] Bassi, P.F., A. Volpe, D. D'Agostino, et al., Paclitaxel-hyaluronic acid for intravesical therapy of *Bacillus Calmette-Guérin* refractory carcinoma *in situ* of the bladder: results of a phase I study. *Journal of Urology*, 2011. 185(2): p. 445-449.
- [632] Montagner, I.M., A. Banzato, G. Zuccolotto, et al., Paclitaxel-hyaluronan hydrosoluble bioconjugate: mechanism of action in human bladder cancer cell lines. *Urologic Oncology: Seminars and Original Investigations*, 2013. 31(7): p. 1261-1269.
- [633] Qiu, L., M. Qiao, Q. Chen, et al., Enhanced effect of pH-sensitive mixed copolymer micelles for overcoming multidrug resistance of doxorubicin. *Biomaterials*, 2014. 35(37): p. 9877-9887.
- [634] Li, K., H. Liu, W. Gao, et al., Mulberry-like dual-drug complicated nanocarriers assembled with apogossypolone amphiphilic starch micelles and doxorubicin hyaluronic acid nanoparticles for tumor combination and targeted therapy. *Biomaterials*, 2015. 39: p. 131-144.
- [635] Li, J., M. Huo, J. Wang, et al., Redox-sensitive micelles self-assembled from amphiphilic hyaluronic acid-deoxycholic acid conjugates for targeted intracellular delivery of paclitaxel. *Biomaterials*, 2012. 33(7): p. 2310-2320.
- [636] Liu, Y., J. Sun, H. Lian, et al., Folate and CD44 receptors dual-targeting hydrophobized hyaluronic acid paclitaxel-loaded polymeric micelles for overcoming multidrug resistance and improving tumor distribution. *Journal of Pharmaceutical Sciences*, 2014. 103(5): p. 1538-1547.
- [637] Thomas, R.G., M. Moon, S. Lee, and Y.Y. Jeong, Paclitaxel loaded hyaluronic acid nanoparticles for targeted cancer therapy: *in vitro* and *in vivo* analysis. *International Journal of Biological Macromolecules*, 2015. 72: p. 510-518.
- [638] Yin, T., L. Wang, L. Yin, et al., Co-delivery of hydrophobic paclitaxel and hydrophilic AURKA specific siRNA by redox-sensitive micelles for effective treatment of breast cancer. *Biomaterials*, 2015. 61: p. 10-25.

- [639] Peer, D. and R. Margalit, Loading mitomycin C inside long circulating hyaluronan targeted nano-liposomes increases its antitumor activity in three mice tumor models. International Journal of Cancer, 2004. 108(5): p. 780-789.
- [640] Arpicco, S., C. Lerda, E. Dalla Pozza, et al., Hyaluronic acid-coated liposomes for active targeting of gemcitabine. European Journal of Pharmaceutics and Biopharmaceutics, 2013. 85(3 Pt. A): p. 373-380.
- [641] Dalla Pozza, E., C. Lerda, C. Costanzo, et al., Targeting gemcitabine containing liposomes to CD44 expressing pancreatic adenocarcinoma cells causes an increase in the antitumoral activity. Biochimica et Biophysica Acta (BBA) - Biomembranes, 2013. 1828(5): p. 1396-1404.
- [642] Peer, D. and R. Margalit, Tumor-targeted hyaluronan nanoliposomes increase the antitumor activity of liposomal doxorubicin in syngeneic and human xenograft mouse tumor models. Neoplasia, 2004. 6(4): p. 343-353.
- [643] Park, J.-H., H.-J. Cho, H.Y. Yoon, et al., Hyaluronic acid derivative-coated nanohybrid liposomes for cancer imaging and drug delivery. Journal of Controlled Release, 2014. 174: p. 98-108.
- [644] Jiang, T., Z. Zhang, Y. Zhang, et al., Dual-functional liposomes based on pH-responsive cell-penetrating peptide and hyaluronic acid for tumor-targeted anticancer drug delivery. Biomaterials, 2012. 33(36): p. 9246-9258.
- [645] Cho, H.-J., H.Y. Yoon, H. Koo, et al., Self-assembled nanoparticles based on hyaluronic acid-ceramide (HA-CE) and Pluronic® for tumor-targeted delivery of docetaxel. Biomaterials, 2011. 32(29): p. 7181-7190.
- [646] Huang, J., H. Zhang, Y. Yu, et al., Biodegradable self-assembled nanoparticles of poly (D,L-lactide-co-glycolide)/hyaluronic acid block copolymers for target delivery of docetaxel to breast cancer. Biomaterials, 2014. 35(1): p. 550-566.
- [647] Song, S., F. Chen, H. Qi, et al., Multifunctional tumor-targeting nanocarriers based on hyaluronic acid-mediated and pH-sensitive properties for efficient delivery of docetaxel. Pharmaceutical Research, 2014. 31(4): p. 1032-1045.
- [648] Song, S., H. Qi, J. Xu, et al., Hyaluronan-based nanocarriers with CD44-overexpressed cancer cell targeting. Pharmaceutical Research, 2014. 31(11): p. 2988-3005.
- [649] Liang, D., A.-T. Wang, Z.-Z. Yang, et al., Enhance cancer cell recognition and overcome drug resistance using hyaluronic acid and α -tocopheryl succinate based multifunctional nanoparticles. Molecular Pharmaceutics, 2015. 12(6): p. 2189-2202.
- [650] Yadav, A.K., P. Mishra, A.K. Mishra, et al., Development and characterization of hyaluronic acid-anchored PLGA nanoparticulate carriers of doxorubicin. Nanomedicine: Nanotechnology, Biology, and Medicine, 2007. 3(4): p. 246-257.

- [651] Yadav, A.K., P. Mishra, S. Jain, et al., Preparation and characterization of HA-PEG-PCL intelligent core-corona nanoparticles for delivery of doxorubicin. *Journal of Drug Targeting*, 2008. 16(6): p. 464-478.
- [652] Han, H.S., T. Thambi, K.Y. Choi, et al., Bioreducible shell-cross-linked hyaluronic acid nanoparticles for tumor-targeted drug delivery. *Biomacromolecules*, 2015. 16(2): p. 447-456.
- [653] Hu, K., H. Zhou, Y. Liu, et al., Hyaluronic acid functional amphipathic and redox-responsive polymer particles for the co-delivery of doxorubicin and cyclopamine to eradicate breast cancer cells and cancer stem cells. *Nanoscale*, 2015. 7(18): p. 8607-8618.
- [654] Park, H.-K., S.J. Lee, J.-S. Oh, et al., Smart nanoparticles based on hyaluronic acid for redox-responsive and CD44 receptor-mediated targeting of tumor. *Nanoscale Research Letters*, 2015. 10(1): p. 981.
- [655] He, M., Z. Zhao, L. Yin, et al., Hyaluronic acid coated poly(butyl cyanoacrylate) nanoparticles as anticancer drug carriers. *International Journal of Pharmaceutics*, 2009. 373(1-2): p. 165-173.
- [656] Choi, K.Y., H.Y. Yoon, J.-H. Kim, et al., Smart nanocarrier based on PEGylated hyaluronic acid for cancer therapy. *ACS Nano*, 2011. 5(11): p. 8591-8599.
- [657] Cho, H.-J., I.-S. Yoon, H.Y. Yoon, et al., Polyethylene glycol-conjugated hyaluronic acid-ceramide self-assembled nanoparticles for targeted delivery of doxorubicin. *Biomaterials*, 2012. 33(4): p. 1190-1200.
- [658] Jin, Y.-J., U. Termsarasab, S.-H. Ko, et al., Hyaluronic acid derivative-based self-assembled nanoparticles for the treatment of melanoma. *Pharmaceutical Research*, 2012. 29(12): p. 3443-3454.
- [659] Han, H.S., J. Lee, H.R. Kim, et al., Robust PEGylated hyaluronic acid nanoparticles as the carrier of doxorubicin: mineralization and its effect on tumor targetability *in vivo*. *Journal of Controlled Release*, 2013. 168(2): p. 105-114.
- [660] Lee, C.-S. and K. Na, Photochemically triggered cytosolic drug delivery using pH-responsive hyaluronic acid nanoparticles for light-induced cancer therapy. *Biomacromolecules*, 2014. 15(11): p. 4228-4238.
- [661] Mezghrani, O., Y. Tang, X. Ke, et al., Hepatocellular carcinoma dually-targeted nanoparticles for reduction triggered intracellular delivery of doxorubicin. *International Journal of Pharmaceutics*, 2015. 478(2): p. 553-568.
- [662] Zhong, Y., J. Zhang, R. Cheng, et al., Reversibly crosslinked hyaluronic acid nanoparticles for active targeting and intelligent delivery of doxorubicin to drug resistant CD44⁺ human breast tumor xenografts. *Journal of Controlled Release*, 2015. 205: p. 144-154.

- [663] Choi, K.Y., E.J. Jeon, H.Y. Yoon, et al., Theranostic nanoparticles based on PEGylated hyaluronic acid for the diagnosis, therapy and monitoring of colon cancer. *Biomaterials*, 2012. 33(26): p. 6186-6193.
- [664] Yao, J., L. Zhang, J. Zhou, et al., Efficient simultaneous tumor targeting delivery of all-trans retinoid acid and paclitaxel based on hyaluronic acid-based multifunctional nanocarrier. *Molecular Pharmaceutics*, 2013. 10(3): p. 1080-1091.
- [665] Yoon, H.Y., H. Koo, K.Y. Choi, et al., Photo-crosslinked hyaluronic acid nanoparticles with improved stability for in vivo tumor-targeted drug delivery. *Biomaterials*, 2013. 34(21): p. 5273-5280.
- [666] Wang, W., M. Xi, X. Duan, et al., Delivery of baicalein and paclitaxel using self-assembled nanoparticles: synergistic antitumor effect in vitro and in vivo. *International Journal of Nanomedicine*, 2015. 10: p. 3737-3750.
- [667] Ganesh, S., A.K. Iyer, F. Gattaccea, et al., In vivo biodistribution of siRNA and cisplatin administered using CD44-targeted hyaluronic acid nanoparticles. *Journal of Controlled Release*, 2013. 172(3): p. 699-706.
- [668] Nakashima, M., K. Ichinose, T. Kanematsu, et al., In vitro characteristics and in vivo plasma disposition of cisplatin conjugated with oxidized and dicarboxymethylated dextrans. *Biological and Pharmaceutical Bulletin*, 1999. 22(7): p. 756-761.
- [669] Tan, M.L., A.M. Friedhuber, D.E. Dunstan, et al., The performance of doxorubicin encapsulated in chitosan—dextran sulphate microparticles in an osteosarcoma model. *Biomaterials*, 2010. 31(3): p. 541-551.
- [670] Yousefpour, P., F. Atyabi, E.V. Farahani, et al., Polyanionic carbohydrate doxorubicin-dextran nanocomplex as a delivery system for anticancer drugs: in vitro analysis and evaluations. *International Journal of Nanomedicine*, 2011. 6: p. 1487-1496.
- [671] Yousefpour, P., F. Atyabi, E.V. Farahani, et al., Targeted delivery of doxorubicin-utilizing chitosan nanoparticles surface-functionalized with anti-Her2 trastuzumab. *International Journal of Nanomedicine*, 2011. 6: p. 1977-1990.
- [672] Mehvar, R., Dextrans for targeted and sustained delivery of therapeutic and imaging agents. *Journal of Controlled Release*, 2000. 69(1): p. 1-25.
- [673] Harada, M., J. Imai, S. Okuno, and T. Suzuki, Macrophage-mediated activation of camptothecin analogue T-2513-carboxymethyl dextran conjugate (T-0128): possible cellular mechanism for antitumor activity. *Journal of Controlled Release*, 2000. 69(3): p. 389-397.
- [674] Harada, M., H. Sakakibara, T. Yano, et al., Determinants for the drug release from T-0128, camptothecin analogue-carboxymethyl dextran conjugate. *Journal of Controlled Release*, 2000. 69(3): p. 399-412.

- [675] Ochi, Y., Y. Shiose, H. Kuga, and E. Kumazawa, A possible mechanism for the long-lasting antitumor effect of the macromolecular conjugate DE-310: mediation by cellular uptake and drug release of its active camptothecin analog DX-8951. *Cancer Chemotherapy and Pharmacology*, 2005. 55(4): p. 323-332.
- [676] Veltkamp, S.A., E.O. Witteveen, E. Capriati, et al., Clinical and pharmacologic study of the novel prodrug deliomotecan (MEN 4901/T-0128) in patients with solid tumors. *Clinical Cancer Research*, 2008. 14(22): p. 7535-7544.
- [677] Onishi, H., Y. Seno, P. Pithayanukul, and T. Nagai, Conjugate of N4-(4-carboxybutyryl)-ara-C and ethylenediamine-introduced dextran. Drug release profiles and further in vivo study of its antitumor effects. *Drug Design and Delivery*, 1991. 7(2): p. 139-145.
- [678] Dang, W., O.M. Colvin, H. Brem, and W.M. Saltzman, Covalent coupling of methotrexate to dextran enhances the penetration of cytotoxicity into a tissue-like matrix. *Cancer Research*, 1994. 54(7): p. 1729-1735.
- [679] Nevozhay, D., R. Budzynska, M. Jagiello, et al., The effect of the substitution level of some dextran-methotrexate conjugates on their antitumor activity in experimental cancer models. *Anticancer Research*, 2006. 26(3A): p. 2179-2186.
- [680] Nevozhay, D., R. Budzynska, U. Kanska, et al., Antitumor properties and toxicity of dextran-methotrexate conjugates are dependent on the molecular weight of the carrier. *Anticancer Research*, 2006. 26(2A): p. 1135-1143.
- [681] Okuno, S., M. Harada, T. Yano, et al., Complete regression of xenografted human carcinomas by camptothecin analogue-carboxymethyl dextran conjugate (T-0128). *Cancer Research*, 2000. 60(11): p. 2988-2995.
- [682] Harada, M., J. Murata, Y. Sakamura, et al., Carrier and dose effects on the pharmacokinetics of T-0128, a camptothecin analogue-carboxymethyl dextran conjugate, in non-tumor- and tumor-bearing rats. *Journal of Controlled Release*, 2001. 71(1): p. 71-86.
- [683] Sugahara, S.-I., M. Kajiki, H. Kuriyama, and T.-R. Kobayashi, Complete regression of xenografted human carcinomas by a paclitaxel-carboxymethyl dextran conjugate (AZ10992). *Journal of Controlled Release*, 2007. 117(1): p. 40-50.
- [684] Inoue, K., E. Kumazawa, H. Kuga, et al., CM-dextran-polyalcohol-camptothecin conjugate: DE-310 with a novel carrier system and its preclinical data. *Advances in Experimental Medicine and Biology*, 2003. 519: p. 145-153.
- [685] Soopenberg, O., M.J.A. de Jonge, A. Sparreboom, et al., Phase I and pharmacokinetic study of DE-310 in patients with advanced solid tumors. *Clinical Cancer Research*, 2005. 11(2 Pt. 1): p. 703-711.

- [686] Munechika, K., Y. Sogame, N. Kishi, et al., Tissue distribution of macromolecular conjugate, adriamycin linked to oxidized dextran, in rat and mouse bearing tumor cells. *Biological and Pharmaceutical Bulletin*, 1994. 17(9): p. 1193-1198.
- [687] Danhauser-Riedl, S., E. Hausmann, H.D. Schick, et al., Phase I clinical and pharmacokinetic trial of dextran conjugated doxorubicin (AD-70, DOX-OXD). *Investigational New Drugs*, 1993. 11(2-3): p. 187-195.
- [688] Naeye, B., K. Raemdonck, K. Remaut, et al., PEGylation of biodegradable dextran nanogels for siRNA delivery. *European Journal of Pharmaceutical Sciences*, 2010. 40(4): p. 342-351.
- [689] Naeye, B., H. Deschout, M. Röding, et al., Hemocompatibility of siRNA loaded dextran nanogels. *Biomaterials*, 2011. 32(34): p. 9120-9127.
- [690] Tripathi, S.K., R. Goyal, and K.C. Gupta, Surface modification of crosslinked dextran nanoparticles influences transfection efficiency of dextran-polyethylenimine nanocomposites. *Soft Matter*, 2011. 7(24): p. 11360-11371.
- [691] De Backer, L., T. Naessens, S. De Koker, et al., Hybrid pulmonary surfactant-coated nanogels mediate efficient in vivo delivery of siRNA to murine alveolar macrophages. *Journal of Controlled Release*, 2015. 217: p. 53-63.
- [692] Shatsberg, Z., X. Zhang, P. Ofek, et al., Functionalized nanogels carrying an anticancer microRNA for glioblastoma therapy. *Journal of Controlled Release*, 2016. 239: p. 159-168.
- [693] Dutta, R. and R.I. Mahato, Recent advances in hepatocellular carcinoma therapy. *Pharmacology and Therapeutics*, 2017. 173: p. 106-117.
- [694] Raemdonck, K., B. Naeye, A. Högset, et al., Prolonged gene silencing by combining siRNA nanogels and photochemical internalization. *Journal of Controlled Release*, 2010. 145(3): p. 281-288.
- [695] Choi, K.Y., O.F. Silvestre, X. Huang, et al., Versatile RNA interference nanoplatform for systemic delivery of RNAs. *ACS Nano*, 2014. 8(5): p. 4559-4570.
- [696] Kang, L., Z. Gao, W. Huang, et al., Nanocarrier-mediated co-delivery of chemotherapeutic drugs and gene agents for cancer treatment. *Acta Pharmaceutica Sinica B*, 2015. 5(3): p. 169-175.
- [697] Kim, Y.H., S.H. Gihm, C.R. Park, et al., Structural characteristics of size-controlled self-aggregates of deoxycholic acid-modified chitosan and their application as a DNA delivery carrier. *Bioconjugate Chemistry*, 2001. 12(6): p. 932-938.
- [698] Park, J.H., Y.W. Cho, H. Chung, et al., Synthesis and characterization of sugar-bearing chitosan derivatives: aqueous solubility and biodegradability. *Biomacromolecules*, 2003. 4(4): p. 1087-1091.

- [699] Park, J.H., S. Kwon, M. Lee, et al., Self-assembled nanoparticles based on glycol chitosan bearing hydrophobic moieties as carriers for doxorubicin: in vivo biodistribution and anti-tumor activity. *Biomaterials*, 2006. 27(1): p. 119-126.
- [700] Kato, Y., H. Onishi, and Y. Machida, N-succinyl-chitosan as a drug carrier: water-insoluble and water-soluble conjugates. *Biomaterials*, 2004. 25(5): p. 907-915.
- [701] Sato, M., H. Onishi, M. Kitano, et al., Preparation and drug release characteristics of the conjugates of mitomycin C with glycol-chitosan and N-succinyl-chitosan. *Biological and Pharmaceutical Bulletin*, 1996. 19(2): p. 241-245.
- [702] Sato, M., H. Onishi, J. Takahara, et al., In vivo drug release and antitumor characteristics of water-soluble conjugates of mitomycin C with glycol-chitosan and N-succinyl-chitosan. *Biological and Pharmaceutical Bulletin*, 1996. 19(9): p. 1170-1177.
- [703] Hu, F.-Q., L.-N. Liu, Y.-Z. Du, and H. Yuan, Synthesis and antitumor activity of doxorubicin conjugated stearic acid-g-chitosan oligosaccharide polymeric micelles. *Biomaterials*, 2009. 30(36): p. 6955-6963.
- [704] Son, Y.J., J.-S. Jang, Y.W. Cho, et al., Biodistribution and anti-tumor efficacy of doxorubicin loaded glycol-chitosan nanoaggregates by EPR effect. *Journal of Controlled Release*, 2003. 91(1-2): p. 135-145.
- [705] Lee, E., H. Kim, I.-H. Lee, and S. Jon, In vivo antitumor effects of chitosan-conjugated docetaxel after oral administration. *Journal of Controlled Release*, 2009. 140(2): p. 79-85.
- [706] Lee, E., J. Lee, and S. Jon, A novel approach to oral delivery of insulin by conjugating with low molecular weight chitosan. *Bioconjugate Chemistry*, 2010. 21(10): p. 1720-1723.
- [707] Atyabi, F., F.A. Moghaddam, R. Dinarvand, et al., Thiolated chitosan coated poly hydroxyethyl methacrylate nanoparticles: synthesis and characterization. *Carbohydrate Polymers*, 2008. 74(1): p. 59-67.
- [708] Anitha, A., N. Deepa, K.P. Chennazhi, et al., Development of mucoadhesive thiolated chitosan nanoparticles for biomedical applications. *Carbohydrate Polymers*, 2011. 83(1): p. 66-73.
- [709] Quiñones, J.P., H. Peniche, and C Peniche, Self-assembled nanoparticles of glycol chitosan – Ergocalciferol succinate conjugate, for controlled release. *Carbohydrate Polymers*, 2012. 88(4): p. 1373-1377.
- [710] Rajitha, P., D. Gopinath, R. Biswas, et al., Chitosan nanoparticles in drug therapy of infectious and inflammatory diseases. *Expert Opinion on Drug Delivery*, 2016. 13(8): p. 1177-1194.

- [711] Jameela, S.R. and A. Jayakrishnan, Glutaraldehyde cross-linked chitosan microspheres as a long acting biodegradable drug delivery vehicle: studies on the in vitro release of mitoxantrone and in vivo degradation of microspheres in rat muscle. *Biomaterials*, 1995. 16(10): p. 769-775.
- [712] He, P., S.S. Davis, and L. Illum, Chitosan microspheres prepared by spray drying. *International Journal of Pharmaceutics*, 1999. 187(1): p. 53-65.
- [713] Mitra, S., U. Gaur, P.C. Ghosh, and A.N. Maitra, Tumour targeted delivery of encapsulated dextran-doxorubicin conjugate using chitosan nanoparticles as carrier. *Journal of Controlled Release*, 2001. 74(1-3): p. 317-323.
- [714] Denkbaş, E.B., E. Kılıçay, C. Birlikseven, and E. Öztürk, Magnetic chitosan microspheres: preparation and characterization. *Reactive and Functional Polymers*, 2002. 50(3): p. 225-232.
- [715] Thanou, M., B.I. Florea, M. Geldof, et al., Quaternized chitosan oligomers as novel gene delivery vectors in epithelial cell lines. *Biomaterials*, 2002. 23(1): p. 153-159.
- [716] Agnihotri, S.A., N.N. Mallikarjuna, and T.M. Aminabhavi, Recent advances on chitosan-based micro- and nanoparticles in drug delivery. *Journal of Controlled Release*, 2004. 100(1): p. 5-28.
- [717] Qi, L., Z. Xu, X. Jiang, et al., Preparation and antibacterial activity of chitosan nanoparticles. *Carbohydrate Research*, 2004. 339(16): p. 2693-2700.
- [718] Sinha, V.R., A.K. Singla, S. Wadhawan, et al., Chitosan microspheres as a potential carrier for drugs. *International Journal of Pharmaceutics*, 2004. 274(1-2): p. 1-33.
- [719] Kim, K., S. Kwon, J.H. Park, et al., Physicochemical characterizations of self-assembled nanoparticles of glycol chitosan-deoxycholic acid conjugates. *Biomacromolecules*, 2005. 6(2): p. 1154-1158.
- [720] Amidi, M., S.G. Romeijn, G. Borchard, et al., Preparation and characterization of protein-loaded N-trimethyl chitosan nanoparticles as nasal delivery system. *Journal of Controlled Release*, 2006. 111(1-2): p. 107-116.
- [721] Liu, C., Y. Tan, C. Liu, et al., Preparations, characterizations and applications of chitosan-based nanoparticles. *Journal of Ocean University of China*, 2007. 6(3): p. 237-243.
- [722] Park, K., J.-H. Kim, Y.S. Nam, et al., Effect of polymer molecular weight on the tumor targeting characteristics of self-assembled glycol chitosan nanoparticles. *Journal of Controlled Release*, 2007. 122(3): p. 305-314.
- [723] Kim, J.-H., Y.-S. Kim, K. Park, et al., Self-assembled glycol chitosan nanoparticles for the sustained and prolonged delivery of antiangiogenic small peptide drugs in cancer therapy. *Biomaterials*, 2008. 29(12): p. 1920-1930.

- [724] Kim, J.-H., Y.-S. Kim, K. Park, et al., Antitumor efficacy of cisplatin-loaded glycol chitosan nanoparticles in tumor-bearing mice. *Journal of Controlled Release*, 2008. 127(1): p. 41-49.
- [725] Wang, Y.-S., Q. Jiang, R.-S. Li, et al., Self-assembled nanoparticles of cholesterol-modified O-carboxymethyl chitosan as a novel carrier for paclitaxel. *Nanotechnology*, 2008. 19(14): p. 145101.
- [726] Ganguly, K., A.R. Kulkarni, and T.M. Aminabhavi, In vitro cytotoxicity and in vivo efficacy of 5-fluorouracil-loaded enteric-coated PEG-crosslinked chitosan microspheres in colorectal cancer therapy in rats. *Drug Delivery*, 2015. 23(8): p. 1-14.
- [727] Luque-Alcaraz, A.G., J. Lizardi-Mendoza, F.M. Goycoolea, et al., Preparation of chitosan nanoparticles by nanoprecipitation and their ability as a drug nanocarrier. *RSC Advances*, 2016. 6(64): p. 59250-59256.
- [728] Chitosan Based Biomaterials, Volume 1, (ed. J.A. Jennings, and J.D. Bumgardner), 2017, Elsevier: Amsterdam, Netherlands.
- [729] Mao, H.Q., K. Roy, V.L. Troung-Le, et al., Chitosan-DNA nanoparticles as gene carriers: synthesis, characterization and transfection efficiency. *Journal of Controlled Release*, 2001. 70(3): p. 399-421.
- [730] Mansouri, S., P. Lavigne, K. Corsi, et al., Chitosan-DNA nanoparticles as non-viral vectors in gene therapy: strategies to improve transfection efficacy. *European Journal of Pharmaceutics and Biopharmaceutics*, 2004. 57(1): p. 1-8.
- [731] Xue, W.-J., Y. Feng, F. Wang, et al., Asialoglycoprotein receptor-magnetic dual targeting nanoparticles for delivery of RASSF1A to hepatocellular carcinoma. *Scientific Reports*, 2016. 6: p. 22149.
- [732] Azzam, T., H. Eliyahu, E. Makovitzki, et al., Hydrophobized dextran-spermine conjugate as potential vector for in vitro gene transfection. *Journal of Controlled Release*, 2004. 96(2): p. 309-323.
- [733] Mao, S., W. Sun, and T. Kissel, Chitosan-based formulations for delivery of DNA and siRNA. *Advanced Drug Delivery Reviews*, 2010. 62(1): p. 12-27.
- [734] Rudzinski, W.E. and T.M. Aminabhavi, Chitosan as a carrier for targeted delivery of small interfering RNA. *International Journal of Pharmaceutics*, 2010. 399(1-2): p. 1-11.
- [735] Jiang, H.-L., H.-T. Lim, Y.-K. Kim, et al., Chitosan-graft-spermine as a gene carrier in vitro and in vivo. *European Journal of Pharmaceutics and Biopharmaceutics*, 2011. 77(1): p. 36-42.
- [736] Saboktakin, M.R., N.A. Tabar, R.M. Tabatabaie, et al., Intelligent drug delivery systems based on modified chitosan nanoparticles. *Letters in Organic Chemistry*, 2012. 9(1): p. 56-70.

- [737] Ragelle, H., G. Vandermeulen, and V. Préat, Chitosan-based siRNA delivery systems. *Journal of Controlled Release*, 2013. 172(1): p. 207-218.
- [738] Lee, D.W., K.-S. Yun, H.-S. Ban, et al., Preparation and characterization of chitosan/polyguluronate nanoparticles for siRNA delivery. *Journal of Controlled Release*, 2009. 139(2): p. 146-152.
- [739] Huh, M.S., S.-Y. Lee, S. Park, et al., Tumor-homing glycol chitosan/polyethylenimine nanoparticles for the systemic delivery of siRNA in tumor-bearing mice. *Journal of Controlled Release*, 2010. 144(2): p. 134-143.
- [740] Jeong, E.J., M. Choi, J. Lee, et al., The spacer arm length in cell-penetrating peptides influences chitosan/siRNA nanoparticle delivery for pulmonary inflammation treatment. *Nanoscale*, 2015. 7(47): p. 20095-20104.
- [741] Alinejad, V., M. Hossein Somi, B. Baradaran, et al., Co-delivery of IL17RB siRNA and doxorubicin by chitosan-based nanoparticles for enhanced anticancer efficacy in breast cancer cells. *Biomedicine and Pharmacotherapy*, 2016. 83: p. 229-240.
- [742] Corbet, C., H. Ragelle, V. Pourcelle, et al., Delivery of siRNA targeting tumor metabolism using non-covalent PEGylated chitosan nanoparticles: identification of an optimal combination of ligand structure, linker and grafting method. *Journal of Controlled Release*, 2016. 223: p. 53-63.
- [743] Van Woensel, M., N. Wauthoz, R. Rosière, et al., Development of siRNA-loaded chitosan nanoparticles targeting Galectin-1 for the treatment of glioblastoma multiforme via intranasal administration. *Journal of Controlled Release*, 2016. 227: p. 71-81.
- [744] Wang, H., M. Pan, J. Ni, et al., ClC-7 deficiency impairs tooth development and eruption. *Scientific Reports*, 2016. 6: p. 19971.
- [745] Yoo, H.S., T.G. Kim, and T.G. Park, Surface-functionalized electrospun nanofibers for tissue engineering and drug delivery. *Advanced Drug Delivery Reviews*, 2009. 61(12): p. 1033-1042.
- [746] Pillay, V., C. Dott, Y.E. Choonara, et al., A review of the effect of processing variables on the fabrication of electrospun nanofibers for drug delivery applications. *Journal of Nanomaterials*, 2013. 2013(1): p. 1-22
- [747] Hu, X., S. Liu, G. Zhou, et al., Electrospinning of polymeric nanofibers for drug delivery applications. *Journal of Controlled Release*, 2014. 185: p. 12-21.
- [748] Sridhar, R., R. Lakshminarayanan, K. Madhaiyan, et al., Electrosprayed nanoparticles and electrospun nanofibers based on natural materials: applications in tissue regeneration, drug delivery and pharmaceuticals. *Chemical Society Reviews*, 2015. 44(3): p. 790-814.

- [749] Lim, E.-K. and B.H. Chung, Preparation of pyrenyl-based multifunctional nanocomposites for biomedical applications. *Nature Protocols*, 2016. 11(2): p. 236-251.
- [750] Wang, X., Y. Du, J. Luo, et al., Chitosan/organic rectorite nanocomposite films: structure, characteristic and drug delivery behaviour. *Carbohydrate Polymers*, 2007. 69(1): p. 41-49.
- [751] Liu, K.-H., T.-Y. Liu, S.-Y. Chen, and D.-M. Liu, Drug release behavior of chitosan-montmorillonite nanocomposite hydrogels following electrostimulation. *Acta Biomaterialia*, 2008. 4(4): p. 1038-1045.
- [752] Depan, D., A.P. Kumar, and R.P. Singh, Cell proliferation and controlled drug release studies of nanohybrids based on chitosan-g-lactic acid and montmorillonite. *Acta Biomaterialia*, 2009. 5(1): p. 93-100.
- [753] Sun, Y., Z.-L. Chen, X.-X Yang, et al., Magnetic chitosan nanoparticles as a drug delivery system for targeting photodynamic therapy. *Nanotechnology*, 2009. 20(13): p. 135102.
- [754] Aguzzi, C., P. Capra, C. Bonferoni, et al., Chitosan-silicate biocomposites to be used in modified drug release of 5-aminosalicylic acid (5-ASA). *Applied Clay Science*, 2010. 50(1): p. 106-111.
- [755] Hua, S., H. Yang, W. Wang, and A. Wang, Controlled release of ofloxacin from chitosan-montmorillonite hydrogel. *Applied Clay Science*, 2010. 50(1): p. 112-117.
- [756] Yuan, Q., J. Shah, S. Hein, and R.D.K. Misra, Controlled and extended drug release behavior of chitosan-based nanoparticle carrier. *Acta Biomaterialia*, 2010. 6(3): p. 1140-1148.
- [757] Bao, H., Y. Pan, Y. Ping, et al., Chitosan-functionalized graphene oxide as a nanocarrier for drug and gene delivery. *Small*, 2011. 7(11): p. 1569-1578.
- [758] Nanda, R., A. Sasmal, and P.L. Nayak, Preparation and characterization of chitosan-polylactide composites blended with Cloisite 30B for control release of the anticancer drug paclitaxel. *Carbohydrate Polymers*, 2011. 83(2): p. 988-994.
- [759] Arias, J.L., L.H. Reddy, and P. Couvreur, Fe₃O₄/chitosan nanocomposite for magnetic drug targeting to cancer. *Journal of Materials Chemistry*, 2012. 22(15): p. 7622-7632.
- [760] Lim, E.-K., W. Sajomsang, Y. Choi, et al., Chitosan-based intelligent theragnosis nanocomposites enable pH-sensitive drug release with MR-guided imaging for cancer therapy. *Nanoscale Research Letters*, 2013. 8(1): p. 467.
- [761] Sun, L., Y. Wang, T. Jiang, et al., Novel chitosan-functionalized spherical nanosilica matrix as an oral sustained drug delivery system for poorly water-soluble drug carvedilol. *ACS Applied Materials and Interfaces*, 2013. 5(1): p. 103-113.

- [762] Zhang, D., P. Sun, P. Li, et al., A magnetic chitosan hydrogel for sustained and prolonged delivery of *Bacillus Calmette-Guérin* in the treatment of bladder cancer. *Biomaterials*, 2013. 34(38): p. 10258-10266.
- [763] Chandran, P.R. and N. Sandhyarani, An electric field responsive drug delivery system based on chitosan-gold nanocomposites for site specific and controlled delivery of 5-fluorouracil. *RSC Advances*, 2014. 4(85): p. 44922-44929.
- [764] Farshi Azhar, F.F. and AA. Olad, AA study on sustained release formulations for oral delivery of 5-fluorouracil based on alginate-chitosan/montmorillonite nanocomposite systems. *Applied Clay Science*, 2014. 101: p. 288-296.
- [765] Jia, M., Y. Li, X. Yang, et al., Development of both methotrexate and mitomycin C loaded PEGylated chitosan nanoparticles for targeted drug codelivery and synergistic anticancer effect. *ACS Applied Materials and Interfaces*, 2014. 6(14): p. 11413-11423.
- [766] Justin, R. and B. Chen, Characterization and drug release performance of biodegradable chitosan-graphene oxide nanocomposites. *Carbohydrate Polymers*, 2014. 103: p. 70-80.
- [767] Vasile, B.S., O. Oprea, G. Voicu, et al., Synthesis and characterization of a novel controlled release zinc oxide/gentamicin-chitosan composite with potential applications in wounds care. *International Journal of Pharmaceutics*, 2014. 463(2): p. 161-169.
- [768] Abou Taleb, M.F.A., A. Alkahtani, and S.K. Mohamed, Radiation synthesis and characterization of sodium alginate/chitosan/hydroxyapatite nanocomposite hydrogels: a drug delivery system for liver cancer. *Polymer Bulletin*, 2015. 72(4): p. 725-742.
- [769] Lin, J., Y. Li, Y. Li, et al., Drug/dye-loaded, multifunctional PEG-chitosan-iron oxide nanocomposites for methotrexate synergistically self-targeted cancer therapy and dual model imaging. *ACS Applied Materials and Interfaces*, 2015. 7(22): p. 11908-11920.
- [770] Yadollahi, M., S. Farhoudian, and H. Namazi, One-pot synthesis of antibacterial chitosan/silver bio-nanocomposite hydrogel beads as drug delivery systems. *International Journal of Biological Macromolecules*, 2015. 79: p. 37-43.
- [771] Prabha, G. and V. Raj, Preparation and characterization of polymer nanocomposites coated magnetic nanoparticles for drug delivery applications. *Journal of Magnetism and Magnetic Materials*, 2016. 408: p. 26-34.
- [772] Yadollahi, M., S. Farhoudian, S. Barkhordari, et al. Facile synthesis of chitosan/ZnO bio-nanocomposite hydrogel beads as drug delivery systems. *International Journal of Biological Macromolecules*, 2016. 82: p. 273-278.
- [773] Ding, Y., H. Yin, S. Shen, et al., Chitosan-based magnetic/fluorescent nanocomposites for cell labelling and controlled drug release. *New Journal of Chemistry*, 2017. 41(4): p. 1736-1743.

- [774] Shariatinia, Z. and Z. Zahraee, Controlled release of metformin from chitosan-based nanocomposite films containing mesoporous MCM-41 nanoparticles as novel drug delivery systems. *Journal of Colloid and Interface Science*, 2017. 501: p. 60-76.
- [775] Luo, Y. and Q. Wang, Recent development of chitosan-based polyelectrolyte complexes with natural polysaccharides for drug delivery. *International Journal of Biological Macromolecules*, 2014. 64: p. 353-367.
- [776] Anal, A.K. and W.F. Stevens, Chitosan-alginate multilayer beads for controlled release of ampicillin. *International Journal of Pharmaceutics*, 2005. 290(1-2): p. 45-54.
- [777] Zhao, Q.S., Q.X. Ji, X.J. Cheng, et al., Preparation of alginate coated chitosan hydrogel beads by thermosensitive internal gelation technique. *Journal of Sol-Gel Science and Technology*, 2010. 54(2): p. 232-237.
- [778] Tavakol, M., E. Vasheghani-Farahani, and S. Hashemi-Najafabadi, The effect of polymer and CaCl₂ concentrations on the sulfasalazine release from alginate-N,O-carboxymethyl chitosan beads. *Progress in Biomaterials*, 2013. 2: p. 1-8.
- [779] Motwani, S.K., S. Chopra, S. Talegaonkar, et al., Chitosan-sodium alginate nanoparticles as submicroscopic reservoirs for ocular delivery: formulation, optimisation and in vitro characterisation. *European Journal of Pharmaceutics and Biopharmaceutics*, 2008. 68(3): p. 513-525.
- [780] Elzatahry, A.A., M.S. Mohy Eldin, E.A. Soliman, and E.A. Hassan, Evaluation of alginate-chitosan bioadhesive beads as a drug delivery system for the controlled release of theophylline. *Journal of Applied Polymer Science*, 2009. 111(5): p. 2452-2459.
- [781] Wong, T.W., L.W. Chan, S.B. Kho, and P.W.S. Heng, Design of controlled-release solid dosage forms of alginate and chitosan using microwave. *Journal of Controlled Release*, 2002. 84(3): p. 99-114.
- [782] de la Fuente, M., B. Seijo, and M.J. Alonso, Bioadhesive hyaluronan-chitosan nanoparticles can transport genes across the ocular mucosa and transfect ocular tissue. *Gene Therapy*, 2008. 15(9): p. 668-676.
- [783] de la Fuente, M., B. Seijo, and M.J. Alonso, Novel hyaluronic acid-chitosan nanoparticles for ocular gene therapy. *Investigative Ophthalmology and Visual Science*, 2008. 49(5): p. 2016-2024.
- [784] Contreras-Ruiz, L., M. de la Fuente, C. García-Vázquez, et al., Ocular tolerance to a topical formulation of hyaluronic acid and chitosan-based nanoparticles. *Cornea*, 2010. 29(5): p. 550-558.

- [785] Oyarzun-Ampuero, F.A., J. Brea, M.I. Loza, et al., Chitosan-hyaluronic acid nanoparticles loaded with heparin for the treatment of asthma. *International Journal of Pharmaceutics*, 2009. 381(2): p. 122-129.
- [786] Lu, H.-D., H.-Q. Zhao, K. Wang, and L.-L. Lv, Novel hyaluronic acid-chitosan nanoparticles as non-viral gene delivery vectors targeting osteoarthritis. *International Journal of Pharmaceutics*, 2011. 420(2): p. 358-365.
- [787] Fukuda, M., N.A. Peppas, and J.W. McGinity, Properties of sustained release hot-melt extruded tablets containing chitosan and xanthan gum. *International Journal of Pharmaceutics*, 2006. 310(1-2): p. 90-100.
- [788] Phaechamud, T. and G.C. Ritthidej, Sustained-release from layered matrix system comprising chitosan and xanthan gum. *Drug Development and Industrial Pharmacy*, 2007. 33(6): p. 595-605.
- [789] Hong, Y., Y. Gong, C. Gao, and J. Shen, Collagen-coated polylactide microcarriers/chitosan hydrogel composite: injectable scaffold for cartilage regeneration. *Journal of Biomedical Materials Research Part A*, 2008. 85(3): p. 628-637.
- [790] Wang, F., Z. Li, M. Khan, et al., Injectable, rapid gelling and highly flexible hydrogel composites as growth factor and cell carriers. *Acta Biomaterialia*, 2010. 6(6): p. 1978-1991.
- [791] Shelke, N.B., R. Kadam, P. Tyagi, et al. Intravitreal poly(L-lactide) microparticles sustain retinal and choroidal delivery of TG-0054, a hydrophilic drug intended for neovascular diseases. *Drug Delivery and Translational Research*, 2011. 1(1): p. 76-90.
- [792] Verma, S., A.J. Domb, and N. Kumar, Nanomaterials for regenerative medicine. *Nanomedicine*, 2011. 6(1): p. 157-181.
- [793] Verma, S., K. Garkhal, A. Mittal, and N. Kumar, Biodegradable polymers for emerging clinical use in tissue engineering, in *Biodegradable Polymers in Clinical Use and Clinical Development* (ed. A.J. Domb, N. Kumar, and A. Ezra), 2011, John Wiley and Sons, Ltd.: Oxford, United Kingdom. p. 565-629.
- [794] Tian, H., Z. Tang, X. Zhuang, et al., Biodegradable synthetic polymers: preparation, functionalization and biomedical application. *Progress in Polymer Science*, 2012. 37(2): p. 237-280.
- [795] Oh, S.H. and J.H. Lee, Hydrophilization of synthetic biodegradable polymer scaffolds for improved cell/tissue compatibility. *Biomedical Materials*, 2013. 8(1): p. 014101.
- [796] Bidarra, S.J., C.C. Barrias, and P.L. Granja, Injectable alginate hydrogels for cell delivery in tissue engineering. *Acta Biomaterialia*, 2014. 10(4): p. 1646-1662.

- [797] Dorsey, S.M., J.R. McGarvey, H. Wang, et al., MRI evaluation of injectable hyaluronic acid-based hydrogel therapy to limit ventricular remodeling after myocardial infarction. *Biomaterials*, 2015. 69: p. 65-75.
- [798] Shen, Z.-S., X. Cui, R.-X. Hou, et al., Tough biodegradable chitosan-gelatin hydrogels via in situ precipitation for potential cartilage tissue engineering. *RSC Advances*, 2015. 5(69): p. 55640-55647.
- [799] Sim, H.J., T. Thambi, and D.S. Lee, Heparin-based temperature-sensitive injectable hydrogels for protein delivery. *Journal of Materials Chemistry B*, 2015. 3(45): p. 8892-8901.
- [800] Liu, M., X. Zeng, C. Ma, et al., Injectable hydrogels for cartilage and bone tissue engineering. *Bone Research*, 2017. 5: p. 17014.
- [801] Sokolsky-Papkov, M., K. Agashi, A. Olaye, et al., Polymer carriers for drug delivery in tissue engineering. *Advanced Drug Delivery Reviews*, 2007. 59(4-5): p. 187-206.
- [802] Lee, K.Y., L. Jeong, Y.O. Kang, et al., Electrospinning of polysaccharides for regenerative medicine. *Advanced Drug Delivery Reviews*, 2009. 61(12): p. 1020-1032.
- [803] Aravamudhan, A., D.M. Ramos, J. Nip, et al., Cellulose and collagen derived micro-nano structured scaffolds for bone tissue engineering. *Journal of Biomedical Nanotechnology*, 2013. 9(4): p. 719-731.
- [804] Wang, Y. and P.G. Wang, Polysaccharide-based systems in drug and gene delivery. *Advanced Drug Delivery Reviews*, 2013. 65(9): p. 1121-1122.
- [805] Chadha, R. and S. Bhandari, Drug-excipient compatibility screening-role of thermoanalytical and spectroscopic techniques. *Journal of Pharmaceutical and Biomedical Analysis*, 2014. 87: p. 82-97.
- [806] Cheng, Y., D. Ramos, P. Lee, et al., Collagen functionalized bioactive nanofiber matrices for osteogenic differentiation of mesenchymal stem cells: bone tissue engineering. *Journal of Biomedical Nanotechnology*, 2014. 10(2): p. 287-298.
- [807] Lautenschläger, C., C. Schmidt, D. Fischer, and A. Stallmach, Drug delivery strategies in the therapy of inflammatory bowel disease. *Advanced Drug Delivery Reviews*, 2014. 71: p. 58-76.
- [808] Rokstad, A.M.A., I. Lacík, P. de Vos, and B.L. Strand, Advances in biocompatibility and physico-chemical characterization of microspheres for cell encapsulation. *Advanced Drug Delivery Reviews*, 2014. 67-68: p. 111-130.
- [809] Chiu, Y.-L., S.-C. Chen, C.-J. Su, et al., pH-triggered injectable hydrogels prepared from aqueous N-palmitoyl chitosan: in vitro characteristics and in vivo biocompatibility. *Biomaterials*, 2009. 30(28): p. 4877-4888.

- [810] Jin, R., L.S. Moreira-Teixeira, P.J. Dijkstra, et al., Enzymatically-crosslinked injectable hydrogels based on biomimetic dextran-hyaluronic acid conjugates for cartilage tissue engineering. *Biomaterials*, 2010. 31(11): p. 3103-3113.
- [811] Tan, H. and K.G. Marra, Injectable, biodegradable hydrogels for tissue engineering applications. *Materials*, 2010. 3(3): p. 1746-1767.
- [812] Choi, B.G., M.H. Park, S.-H. Cho, et al., Thermal gelling polyalanine-poloxamine-polyalanine aqueous solution for chondrocytes 3D culture: initial concentration effect. *Soft Matter*, 2011. 7(2): p. 456-462.
- [813] Li, Y., J. Rodrigues, and H. Tomás, Injectable and biodegradable hydrogels: gelation, biodegradation and biomedical applications. *Chemical Society Reviews*, 2012. 41(6): p. 2193-2221.
- [814] Ko, D.Y., U.P. Shinde, and B. Yeon, Recent progress of in situ formed gels for biomedical applications. *Progress in Polymer Science*, 2013. 38(3): p. 672-701.
- [815] Yeon, B., M.H. Park, H.J. Moon, et al., 3D culture of adipose-tissue-derived stem cells mainly leads to chondrogenesis in poly(ethylene glycol)-poly(L-alanine) diblock copolymer thermogel. *Biomacromolecules*, 2013. 14(9): p. 3256-3266.
- [816] Park, H., E.K. Woo, and K.Y. Lee, Ionically cross-linkable hyaluronate-based hydrogels for injectable cell delivery. *Journal of Controlled Release*, 2014. 196: p. 146-153.
- [817] Lin, C.-C., C.S. Ki, and H. Shih, Thiol-norbornene photo-click hydrogels for tissue engineering applications. *Journal of Applied Polymer Science*, 2015. 132(8): p. 1-11.
- [818] Müller, F.A., L. Müller, I. Hofmann, et al., Cellulose-based scaffold materials for cartilage tissue engineering. *Biomaterials*, 2006. 27(21): p. 3955-3963.
- [819] Domingues, R.M.A., M.E. Gomes, and R.L. Reis, The potential of cellulose nanocrystals in tissue engineering strategies. *Biomacromolecules*, 2014. 15(7): p. 2327-2346.
- [820] Courtenay, J.C., M.A. Johns, F. Galembbeck, et al., Surface modified cellulose scaffolds for tissue engineering. *Cellulose*, 2017. 24(1): p. 253-267.
- [821] Kumbar, S.G., U.S. Toti, M. Deng, et al., Novel mechanically competent polysaccharide scaffolds for bone tissue engineering. *Biomedical Materials*, 2011. 6(6): p. 065005.
- [822] Laurencin CT, Kumbar SG, Nukavarapu SP, James R, inventors; University of Connecticut, University of Virginia, assignee. Mechanically competent natural polymer based porous grafts for bone repair and regeneration. United States patent application US 12/710,637. 2010 Sep 30.

- [823] Kumbar SG, Laurencin CT, inventors; University of Connecticut, assignee. Natural Polymer-Based Porous Orthopedic Fixation Screw for Bone Repair and Regeneration. United States patent application US 13/033,094. 2011 Aug 25.
- [824] Filion, T.M., A. Kutikov, and J. Song, Chemically modified cellulose fibrous meshes for use as tissue engineering scaffolds. *Bioorganic and Medicinal Chemistry Letters*, 2011. 21(17): p. 5067-5070.
- [825] Czaja, W., D. Romanowicz, and R. Malcolm Brown, Structural investigations of microbial cellulose produced in stationary and agitated culture. *Cellulose*, 2004. 11(3): p. 403-411.
- [826] Bodhibukkana, C., T. Srichana, S. Kaewnopparat, et al., Composite membrane of bacterially-derived cellulose and molecularly imprinted polymer for use as a transdermal enantioselective controlled-release system of racemic propranolol. *Journal of Controlled Release*, 2006. 113(1): p. 43-56.
- [827] Fu, L., Y. Zhang, C. Li, et al., Skin tissue repair materials from bacterial cellulose by a multilayer fermentation method. *Journal of Materials Chemistry*, 2012. 22(24): p. 12349-12357.
- [828] Aravamudhan, A., D.M. Ramos, A.A. Ahmed Nada, and S.G. Kumbar Natural polymers: polysaccharides and their derivatives for biomedical applications, in *Natural and Synthetic Biomedical Polymers*, (ed. S.G. Kumbar, C.T. Laurencin, and M. Deng), 2014, Elsevier: Oxford, United Kingdom. p. 67-89.
- [829] Almeida, I.F., T. Pereira, N.H.C.S. Silva, et al., Bacterial cellulose membranes as drug delivery systems: an *in vivo* skin compatibility study. *European Journal of Pharmaceutics and Biopharmaceutics*, 2014. 86(3): p. 332-336.
- [830] Klemm, D., B. Heublein, H.-P. Fink, and A. Bohn, Cellulose: fascinating biopolymer and sustainable raw material. *Angewandte Chemie*, 2005. 44(22): p. 3358-3393.
- [831] Takada, T., T. Katagiri, M. Ifuku, et al., Sulfated polysaccharides enhance the biological activities of bone morphogenetic proteins. *Journal of Biological Chemistry*, 2003. 278(44): p. 43229-43235.
- [832] Shi, Q., Y. Li, J. Sun, et al., The osteogenesis of bacterial cellulose scaffold loaded with bone morphogenetic protein-2. *Biomaterials*, 2012. 33(28): p. 6644-6649.
- [833] Hajiabbas, M., S. Mashayekhan, A. Nazaripouya, et al., Chitosan-gelatin sheets as scaffolds for muscle tissue engineering. *Artificial Cells, Nanomedicine, and Biotechnology*, 2015. 43(2): p. 124-132.
- [834] Nair, L.S., T. Starnes, J.-W.K. Ko, and C.T. Laurencin, Development of injectable thermogelling chitosan-inorganic phosphate solutions for biomedical applications. *Biomacromolecules*, 2007. 8(12): p. 3779-3785.

- [835] Cheng, Y., A. Nada, C.M. Valmikinathan, et al., In situ gelling polysaccharide-based hydrogel for cell and drug delivery in tissue engineering. *Journal of Applied Polymer Science*, 2014. 131(4): p. 39934-39943.
- [836] Funakoshi, T., T. Majima, N. Iwasaki, et al., Novel chitosan-based hyaluronan hybrid polymer fibers as a scaffold in ligament tissue engineering. *Journal of Biomedical Materials Research. Part A*, 2005. 74(3): p. 338-346.
- [837] Silva, S.S., S.G. Caridade, J.F. Mano, and R.L. Reis, Effect of crosslinking in chitosan/aloe vera-based membranes for biomedical applications. *Carbohydrate Polymers*, 2013. 98(1): p. 581-588.
- [838] da Silva, M.L.A., A. Crawford, J.M. Mundy, et al., Chitosan/polyester-based scaffolds for cartilage tissue engineering: assessment of extracellular matrix formation. *Acta Biomaterialia*, 2010. 6(3): p. 1149-1157.
- [839] Silva, J.M., N. Georgi, R. Costa, et al. Nanostructured 3D constructs based on chitosan and chondroitin sulphate multilayers for cartilage tissue engineering. *PLoS One*, 2013. 8(2): p. e55451.
- [840] Yang, T.-L. and T.-H. Young, The enhancement of submandibular gland branch formation on chitosan membranes. *Biomaterials*, 2008. 29(16): p. 2501-2508.
- [841] Yuan, Y., P. Zhang, Y. Yang, et al., The interaction of Schwann cells with chitosan membranes and fibers in vitro. *Biomaterials*, 2004. 25(18): p. 4273-4278.
- [842] Simões, M.J., A. Gärtner, Y. Shiroasaki, et al., In vitro and in vivo chitosan membranes testing for peripheral nerve reconstruction. *Acta Médica Portuguesa*, 2011. 24(1): p. 43-52.
- [843] Poon, Y.F., Y. Cao, Y. Liu, et al. Hydrogels based on dual curable chitosan-graft-polyethylene glycol-graft-methacrylate: application to layer-by-layer cell encapsulation. *ACS Applied Materials and Interfaces*, 2010. 2(7): p. 2012-2025.
- [844] Wang, J., L. Chen, Y. Zhao, et al., Cell adhesion and accelerated detachment on the surface of temperature-sensitive chitosan and poly(N-isopropylacrylamide) hydrogels. *Journal of Materials Science. Materials in Medicine*, 2009. 20(2): p. 583-590.
- [845] Sá-Lima, H., S.G. Caridade, J.F. Mano, and R.L. Reis, Stimuli-responsive chitosan-starch injectable hydrogels combined with encapsulated adipose-derived stromal cells for articular cartilage regeneration. *Soft Matter*, 2010. 6(20): p. 5184-5195.
- [846] Yan, L.-P., Y.-J. Wang, L. Ren, et al., Genipin-cross-linked collagen/chitosan biomimetic scaffolds for articular cartilage tissue engineering applications. *Journal of Biomedical Materials Research Part A*, 2010. 95(2): p. 465-475.

- [847] Moreira, C.D.F., S.M. Carvalho, H.S. Mansur, and M.M. Pereira, Thermogelling chitosan-collagen-bioactive glass nanoparticle hybrids as potential injectable systems for tissue engineering. *Materials Science and Engineering. C, Materials for Biological Applications*, 2016. 58: p. 1207-1216.
- [848] Zhang, L., Q. Ao, A. Wang, et al., A sandwich tubular scaffold derived from chitosan for blood vessel tissue engineering. *Journal of Biomedical Materials Research. Part A*, 2006. 77(2): p. 277-284.
- [849] Shi, H., C. Han, Z. Mao, et al., Enhanced angiogenesis in porous collagen-chitosan scaffolds loaded with angiogenin. *Tissue Engineering. Part A*, 2008. 14(11): p. 1775-1785.
- [850] Chen, Y.-H., I.J. Wang, and T.-H. Young, Formation of keratocyte spheroids on chitosan-coated surface can maintain keratocyte phenotypes. *Tissue Engineering. Part A*, 2009. 15(8): p. 2001-2013.
- [851] Choi, J.S. and H.S. Yoo, Pluronic/chitosan hydrogels containing epidermal growth factor with wound-adhesive and photo-crosslinkable properties. *Journal of Biomedical Materials Research. Part A*, 2010. 95(2): p. 564-573.
- [852] Han, C.-M., L.-P. Zhang, J.-Z. Sun, et al., Application of collagen-chitosan/fibrin glue asymmetric scaffolds in skin tissue engineering. *Journal of Zhejiang University. Science. B*, 2010. 11(7): p. 524-530.
- [853] Wu, X., L. Black, G. Santacana-Laffitte, and C.W. Patrick Jr., Preparation and assessment of glutaraldehyde-crosslinked collagen-chitosan hydrogels for adipose tissue engineering. *Journal of Biomedical Materials Research. Part A*, 2007. 81(1): p. 59-65.
- [854] Mei, L., D. Hu, J. Ma, et al., Preparation, characterization and evaluation of chitosan macroporous for potential application in skin tissue engineering. *International Journal of Biological Macromolecules*, 2012. 51(5): p. 992-997.
- [855] Ge, S., N. Zhao, L. Wang, et al., Bone repair by periodontal ligament stem cell seeded nanohydroxyapatite-chitosan scaffold. *International Journal of Nanomedicine*, 2012. 7: p. 5405-5414.
- [856] Hsueh, Y.-Y., Y.-J. Chang, T.-C. Huang, et al., Functional recoveries of sciatic nerve regeneration by combining chitosan-coated conduit and neurosphere cells induced from adipose-derived stem cells. *Biomaterials*, 2014. 35(7): p. 2234-2244.
- [857] Boucard, N., C. Viton, D. Agay, et al. The use of physical hydrogels of chitosan for skin regeneration following third-degree burns. *Biomaterials*, 2007. 28(24): p. 3478-3488.
- [858] Gobin, A.S., C.E. Butler, and A.B. Mathur, Repair and regeneration of the abdominal wall musculofascial defect using silk fibroin-chitosan blend. *Tissue Engineering*, 2006. 12(12): p. 3383-3394.

- [859] Hao, T., N. Wen, J.-K. Cao, et al. The support of matrix accumulation and the promotion of sheep articular cartilage defects repair in vivo by chitosan hydrogels. *Osteoarthritis and Cartilage*, 2010. 18(2): p. 257-265.
- [860] Liang, Y., W. Liu, B. Han, et al., An in situ formed biodegradable hydrogel for reconstruction of the corneal endothelium. *Colloids and Surfaces B: Biointerfaces*, 2011. 82(1): p. 1-7.
- [861] Meng, D., L. Dong, Y. Wen, and Q. Xie, Effects of adding resorbable chitosan microspheres to calcium phosphate cements for bone regeneration. *Materials Science and Engineering. C, Materials for Biological Applications*, 2015. 47: p. 266-272.
- [862] Jayakumar, R., M. Prabaharan, P.T. Sudheesh Kumar, et al. Biomaterials based on chitin and chitosan in wound dressing applications. *Biotechnology Advances*, 2011. 29(3): p. 322-337.
- [863] Kozen, B.G., S.J. Kircher, J. Henao, et al., An alternative hemostatic dressing: comparison of CELOX, HemCon, and QuikClot. *Academic Emergency Medicine*, 2008. 15(1): p. 74-81.
- [864] Peh, K., T. Khan, and H. Ch'ng, Mechanical, bioadhesive strength and biological evaluations of chitosan films for wound dressing. *Societe Canadienne Des Sciences Pharmaceutiques*, 2000. 3(3): p. 303-311.
- [865] Anandan, R., P.G.V. Nair, and S. Mathew, Anti-ulcerogenic effect of chitin and chitosan on mucosal antioxidant defence system in HCl-ethanol-induced ulcer in rats. *Journal of Pharmacy and Pharmacology*, 2004. 56(2): p. 265-269.
- [866] Tavarria, F.K., M.P. Jorge, A.L.T.G. Ruiz, et al., Anti-proliferative, anti-inflammatory, anti-ulcerogenic and wound healing properties of chitosan. Vol. 12. 2016. 114-122.
- [867] Pei, H.N., X.G. Chen, Y. Li, and H.Y. Zhou, Characterization and ornidazole release in vitro of a novel composite film prepared with chitosan/poly(vinyl alcohol)/alginate. *Journal of Biomedical Materials Research. Part A*, 2008. 85(2): p. 566-572.
- [868] Sung, J.H., M.-R. Hwang, J.O. Kim, et al., Gel characterisation and in vivo evaluation of minocycline-loaded wound dressing with enhanced wound healing using polyvinyl alcohol and chitosan. *International Journal of Pharmaceutics*, 2010. 392(1-2): p. 232-240.
- [869] Radhakumary, C., M. Antony, and K. Sreenivasan, Drug loaded thermoresponsive and cytocompatible chitosan based hydrogel as a potential wound dressing. *Carbohydrate Polymers*, 2011. 83(2): p. 705-713.
- [870] Cohen, M.L., The theory of real materials. *Annual Review of Materials Science*, 2000. 30(1): p. 1-26.

- [871] Mi, F.-L., Y.-B. Wu, S.-S. Shyu, et al., Asymmetric chitosan membranes prepared by dry/wet phase separation: a new type of wound dressing for controlled antibacterial release. *Journal of Membrane Science*, 2003. 212(1): p. 237-254.
- [872] Lu, S., W. Gao, and H.Y. Gu, Construction, application and biosafety of silver nanocrystalline chitosan wound dressing. *Burns: Journal of the International Society for Burn Injuries*, 2008. 34(5): p. 623-628.
- [873] Ong, S.-Y., J. Wu, S.M. Moothala, et al., Development of a chitosan-based wound dressing with improved hemostatic and antimicrobial properties. *Biomaterials*, 2008. 29(32): p. 4323-4332.
- [874] Thomas, V., M.M. Yallapu, B. Sreedhar, and S.K. Bajpai, Fabrication, characterization of chitosan/nanosilver film and its potential antibacterial application. *Journal of Biomaterials Science. Polymer Edition*, 2009. 20(14): p. 2129-2144.
- [875] Li, L.-H., J.-C. Deng, H.-R. Deng, et al., Preparation, characterization and antimicrobial activities of chitosan/Ag/ZnO blend films. *Chemical Engineering Journal*, 2010. 160(1): p. 378-382.
- [876] Vimala, K., Y.M. Mohan, K.S. Sivudu, et al., Fabrication of porous chitosan films impregnated with silver nanoparticles: a facile approach for superior antibacterial application. *Colloids and Surfaces B: Biointerfaces*, 2010. 76(1): p. 248-258.
- [877] Nishinari, K. and R. Takahashi, Interaction in polysaccharide solutions and gels. *Current Opinion in Colloid and Interface Science*, 2003. 8(4): p. 396-400.
- [878] Liao, Y.-H. S.A. Jones, B. Forbes, et al., Hyaluronan: pharmaceutical characterization and drug delivery. *Drug Delivery*, 2005. 12(6): p. 327-342.
- [879] Hunt, N.C. and L.M. Grover, Cell encapsulation using biopolymer gels for regenerative medicine. *Biotechnology Letters*, 2010. 32(6): p. 733-742.
- [880] Li, L., Z.-Y. He, X.-W. Wei, and Y.-Q. Wei, Recent advances of biomaterials in biotherapy. *Regenerative Biomaterials*, 2016. 3(2): p. 99-105.
- [881] Carney, S.L. and H. Muir, The structure and function of cartilage proteoglycans. *Physiological Reviews*, 1988. 68(3): p. 858-910.
- [882] Kim D.H., J.T. Martin, D.M. Elliott, et al. Phenotypic stability, matrix elaboration and functional maturation of nucleus pulposus cells encapsulated in photocrosslinkable hyaluronic acid hydrogels. *Acta Biomaterialia*, 2015. 12: p. 21-29.
- [883] Hwang, H.-D., H.-J. Cho, P. Balakrishnan, et al. Cross-linked hyaluronic acid-based flexible cell delivery system: application for chondrogenic differentiation. *Colloids and Surfaces B: Biointerfaces*, 2012. 91: p. 106-113.

- [884] Toh, W.S., T.C. Lim, M. Kurisawa, and M. Spector, Modulation of mesenchymal stem cell chondrogenesis in a tunable hyaluronic acid hydrogel microenvironment. *Biomaterials*, 2012. 33(15): p. 3835-3845.
- [885] Park, H., B. Choi, J. Hu, and M. Lee, Injectable chitosan hyaluronic acid hydrogels for cartilage tissue engineering. *Acta Biomaterialia*, 2013. 9(1): p. 4779-4786.
- [886] Yu, Y., M.J. Brouillette, D. Seol, et al., Use of recombinant human stromal cell-derived factor 1 α -loaded fibrin/hyaluronic acid hydrogel networks to achieve functional repair of full-thickness bovine articular cartilage via homing of chondrogenic progenitor cells. *Arthritis and Rheumatology*, 2015. 67(5): p. 1274-1285.
- [887] Amann, E., P. Wolff, E. Breel, et al., Hyaluronic acid facilitates chondrogenesis and matrix deposition of human adipose derived mesenchymal stem cells and human chondrocytes co-cultures. *Acta Biomaterialia*, 2017. 52: p. 130-144.
- [888] Khademhosseini, A., G. Eng, J. Yeh, et al., Micromolding of photocrosslinkable hyaluronic acid for cell encapsulation and entrapment. *Journal of Biomedical Materials Research. Part A*, 2006. 79(3): p. 522-532.
- [889] Chung, C. and J.A. Burdick, Influence of three-dimensional hyaluronic acid microenvironments on mesenchymal stem cell chondrogenesis. *Tissue Engineering. Part A*, 2009. 15(2): p. 243-254.
- [890] Skaalure, S.C., S.O. Dimson, A.M. Pennington, and S.J. Bryant, Semi-interpenetrating networks of hyaluronic acid in degradable PEG hydrogels for cartilage tissue engineering. *Acta Biomaterialia*, 2014. 10(8): p. 3409-3420.
- [891] Kayakabe, M., S. Tsutsumi, H. Watanabe, et al., Transplantation of autologous rabbit BM-derived mesenchymal stromal cells embedded in hyaluronic acid gel sponge into osteochondral defects of the knee. *Cytotherapy*, 2006. 8(4): p. 343-353.
- [892] Park, J.Y., J.-C. Choi, J.-H. Shim, et al., A comparative study on collagen type I and hyaluronic acid dependent cell behavior for osteochondral tissue bioprinting. *Biofabrication*, 2014. 6(3): p. 035004.
- [893] Kim, J., I.S. Kim, T.H. Cho, et al., Bone regeneration using hyaluronic acid-based hydrogel with bone morphogenic protein-2 and human mesenchymal stem cells. *Biomaterials*, 2007. 28(10): p. 1830-1837.
- [894] Chen, W.-H., W.-C. Lo, W.-C. Hsu, et al., Synergistic anabolic actions of hyaluronic acid and platelet-rich plasma on cartilage regeneration in osteoarthritis therapy. *Biomaterials*, 2014. 35(36): p. 9599-9607.

- [895] Liu, Y., X.Z. Shu, and G.D. Prestwich, Osteochondral defect repair with autologous bone marrow-derived mesenchymal stem cells in an injectable, *in situ*, cross-linked synthetic extracellular matrix. *Tissue Engineering*, 2006. 12(12): p. 3405-3416.
- [896] Tan, H., C.R. Chu, K.A. Payne, and K.G. Marra, Injectable *in situ* forming biodegradable chitosan-hyaluronic acid based hydrogels for cartilage tissue engineering. *Biomaterials*, 2009. 30(13): p. 2499-2506.
- [897] Zhang, L., Y. Xiao, B. Jiang, et al., Effect of adipic dihydrazide modification on the performance of collagen/hyaluronic acid scaffold. *Journal of Biomedical Materials Research. Part B, Applied Biomaterials*, 2010. 92(2): p. 307-316.
- [898] Erickson, I.E., S.R. Kestle, K.H. Zellars, et al., High mesenchymal stem cell seeding densities in hyaluronic acid hydrogels produce engineered cartilage with native tissue properties. *Acta Biomaterialia*, 2012. 8(8): p. 3027-3034.
- [899] Kim, H.J., K.K. Kim, I.K. Park, et al., Hybrid scaffolds composed of hyaluronic acid and collagen for cartilage regeneration. *Tissue Engineering and Regenerative Medicine*, 2012. 9(2): p. 57-62.
- [900] Kim, M., S. Garrity, I.E. Erickson, et al. (2012). Optimization of macromer density in human MSC-laden hyaluronic acid (HA) hydrogels. in 2012 38th Annual Northeast Bioengineering Conference (NEBEC). .
- [901] Yu, F., X. Cao, Y. Li, et al., An injectable hyaluronic acid/PEG hydrogel for cartilage tissue engineering formed by integrating enzymatic crosslinking and Diels-Alder “click chemistry”. *Polymer Chemistry*, 2013. 5(3): p. 1082-1090.
- [902] Palumbo, F.S., C. Fiorica, M. Di Stefano, et al., In *situ* forming hydrogels of hyaluronic acid and inulin derivatives for cartilage regeneration. *Carbohydrate Polymers*, 2015. 122: p. 408-416.
- [903] Ha, C.-W., Y.-B. Park, J.-Y. Chung, and Y.-G. Park, Cartilage repair using composites of human umbilical cord blood-derived mesenchymal stem cells and hyaluronic acid hydrogel in a minipig model. *Stem Cells Translational Medicine*, 2015. 4(9): p. 1044-1051.
- [904] Frith, J.E., D.J. Menzies, A.R. Cameron, et al., Effects of bound versus soluble pentosan polysulphate in PEG/HA-based hydrogels tailored for intervertebral disc regeneration. *Biomaterials*, 2014. 35(4): p. 1150-1162.
- [905] Chen, Y.-C., W.-Y. Su, S.-H. Yang, et al., In *situ* forming hydrogels composed of oxidized high molecular weight hyaluronic acid and gelatin for nucleus pulposus regeneration. *Acta Biomaterialia*, 2013. 9(2): p. 5181-5193.

- [906] Freymann, U., M. Endres, K. Neumann, et al., Expanded human meniscus-derived cells in 3-D polymer-hyaluronan scaffolds for meniscus repair. *Acta Biomaterialia*, 2012. 8(2): p. 677-685.
- [907] Kim, Y.-M., S.H. Oh, J.-S. Choi, et al., Adipose-derived stem cell-containing hyaluronic acid/alginate hydrogel improves vocal fold wound healing. *The Laryngoscope*, 2014. 124(3): p. E64-72.
- [908] Oberlender, S.A. and R.S. Tuan, Spatiotemporal profile of N-cadherin expression in the developing limb mesenchyme. *Cell Adhesion and Communication*, 1994. 2(6): p. 521-537.
- [909] Zou, L., X. Zou, L. Chen, et al., Effect of hyaluronan on osteogenic differentiation of porcine bone marrow stromal cells in vitro. *Journal of Orthopaedic Research*, 2008. 26(5): p. 713-720.
- [910] Patterson, J., R. Siew, S.W. Herring, et al., Hyaluronic acid hydrogels with controlled degradation properties for oriented bone regeneration. *Biomaterials*, 2010. 31(26): p. 6772-6781.
- [911] Bhakta, G., B. Rai, Z.X.H. Lim, et al., Hyaluronic acid-based hydrogels functionalized with heparin that support controlled release of bioactive BMP-2. *Biomaterials*, 2012. 33(26): p. 6113-6122.
- [912] Bhakta, G., Z.X.H. Lim, B. Rai, et al., The influence of collagen and hyaluronan matrices on the delivery and bioactivity of bone morphogenetic protein-2 and ectopic bone formation. *Acta Biomaterialia*, 2013. 9(11): p. 9098-9106.
- [913] Park, H.-J., Y. Jin, J. Shin, et al., Catechol-functionalized hyaluronic acid hydrogels enhance angiogenesis and osteogenesis of human adipose-derived stem cells in critical tissue defects. *Biomacromolecules*, 2016. 17(6): p. 1939-1948.
- [914] Subramaniam, S., Y.-H. Fang, S. Sivasubramanian, et al., Hydroxyapatite-calcium sulfate-hyaluronic acid composite encapsulated with collagenase as bone substitute for alveolar bone regeneration. *Biomaterials*, 2016. 74: p. 99-108.
- [915] Zhu, M., S. Lin, Y. Sun, et al., Hydrogels functionalized with N-cadherin mimetic peptide enhance osteogenesis of hMSCs by emulating the osteogenic niche. *Biomaterials*, 2016. 77: p. 44-52.
- [916] Sahoo, S., C. Chung, S. Khetan, and J.A. Burdick, Hydrolytically degradable hyaluronic acid hydrogels with controlled temporal structures. *Biomacromolecules*, 2008. 9(4): p. 1088-1092.
- [917] West, D.C., I.N. Hampson, F. Arnold, and S. Kumar, Angiogenesis induced by degradation products of hyaluronic acid. *Science*, 1985. 228(4705): p. 1324-1326.

- [918] Day, A.J. and C.A. de la Motte, Hyaluronan cross-linking: a protective mechanism in inflammation? *Trends in Immunology*, 2005. 26(12): p. 637-643.
- [919] Noble, P.W., F.R. Lake, P.M. Henson, and D.W. Riches, Hyaluronate activation of CD44 induces insulin-like growth factor-1 expression by a tumor necrosis factor-alpha-dependent mechanism in murine macrophages. *Journal of Clinical Investigation*, 1993. 91(6): p. 2368-2377.
- [920] Park, D., Y. Kim, H. Kim, et al., Hyaluronic acid promotes angiogenesis by inducing RHAMM-TGF β receptor interaction via CD44-PKC δ . *Molecules and Cells*, 2012. 33(6): p. 563-574.
- [921] Rooney, P., S. Kumar, J. Ponting, and M. Wang, The role of hyaluronan in tumour neovascularization (review). *International Journal of Cancer*, 1995. 60(5): p. 632-636.
- [922] Perng, C.-K., Y.-J. Wang, C.-H. Tsi, and H. Ma, In vivo angiogenesis effect of porous collagen scaffold with hyaluronic acid oligosaccharides. *Journal of Surgical Research*, 2011. 168(1): p. 9-15.
- [923] Seidlits, S.K., C.T. Drinnan, R.R. Petersen, et al., Fibronectin-hyaluronic acid composite hydrogels for three-dimensional endothelial cell culture. *Acta Biomaterialia*, 2011. 7(6): p. 2401-2409.
- [924] Mohandas, A., B.S. Anisha, K.P. Chennazhi, and R. Jayakumar, Chitosan-hyaluronic acid/VEGF loaded fibrin nanoparticles composite sponges for enhancing angiogenesis in wounds. *Colloids and Surfaces B: Biointerfaces*, 2015. 127: p. 105-113.
- [925] da Silva, L.P., R.P. Pirraco, T.C. Santos, et al., Neovascularization induced by the hyaluronic acid-based spongy-like hydrogels degradation products. *ACS Applied Materials and Interfaces*, 2016. 8(49): p. 33464-33474.
- [926] Collier, J.H., J.P. Camp, T.W. Hudson, and C.E. Schmidt, Synthesis and characterization of polypyrrole-hyaluronic acid composite biomaterials for tissue engineering applications. *Journal of Biomedical Materials Research*, 2000. 50(4): p. 574-584.
- [927] Wang, X., J. He, Y. Wang, and F.-Z. Cui, Hyaluronic acid-based scaffold for central neural tissue engineering. *Interface Focus*, 2012. 2(3): p. 278-291.
- [928] Hemshekhar, M., R.M. Thushara, S. Chandranayaka, et al., Emerging roles of hyaluronic acid bioscaffolds in tissue engineering and regenerative medicine. *International Journal of Biological Macromolecules*, 2016. 86: p. 917-928.
- [929] Wang, K.K., I.R. Nemeth, B.R. Seckel, et al., Hyaluronic acid enhances peripheral nerve regeneration in vivo. *Microsurgery*, 1998. 18(4): p. 270-275.

- [930] Ozgenel, G.Y., Effects of hyaluronic acid on peripheral nerve scarring and regeneration in rats. *Microsurgery*, 2003. 23(6): p. 575-581.
- [931] Engler, A.J., S. Sen, H.L. Sweeney, and D.E. Discher, Matrix elasticity directs stem cell lineage specification. *Cell*, 2006. 126(4): p. 677-689.
- [932] Hynes, S.R., M.F. Rauch, J.P. Bertram, and E.B. Lavik, A library of tunable poly(ethylene glycol)/poly(L-lysine) hydrogels to investigate the material cues that influence neural stem cell differentiation. *Journal of Biomedical Materials Research Part A*, 2009. 89(2): p. 499-509.
- [933] Leipzig, N.D. and M.S. Shoichet, The effect of substrate stiffness on adult neural stem cell behavior. *Biomaterials*, 2009. 30(36): p. 6867-6878.
- [934] Tarus, D., L. Hamard, F. Caraguel, et al., Design of hyaluronic acid hydrogels to promote neurite outgrowth in three dimensions. *ACS Applied Materials and Interfaces*, 2016. 8(38): p. 25051-25059.
- [935] Cui, F.Z., W.M. Tian, S.P. Hou, et al., Hyaluronic acid hydrogel immobilized with RGD peptides for brain tissue engineering. *Journal of Materials Science: Materials in Medicine*, 2006. 17(12): p. 1393-1401.
- [936] Zaviskova, K., D. Tukmachev, J. Dubisova, et al., Injectable hydroxyphenyl derivative of hyaluronic acid hydrogel modified with RGD as scaffold for spinal cord injury repair. *Journal of Biomedical Materials Research Part A*, 2018. 106(4): p. 1129-1140.
- [937] Ashton, R.S., A. Conway, C. Pangarkar, et al., Astrocytes regulate adult hippocampal neurogenesis through ephrin-B signaling. *Nature Neuroscience*, 2012. 15(10): p. 1399-1406.
- [938] Conway, A., T. Vazin, D.P. Spelke, et al., Multivalent ligands control stem cell behaviour in vitro and in vivo. *Nature Nanotechnology*, 2013. 8(11): p. 831-838.
- [939] Conway, A. and D.V. Schaffer, Biomaterial microenvironments to support the generation of new neurons in the adult brain. *Stem Cells*, 2014. 32(5): p. 1220-1229.
- [940] Krewson, C.E., M.L. Klarman, and W.M. Saltzman, Distribution of nerve growth factor following direct delivery to brain interstitium. *Brain Research*, 1995. 680(1-2): p. 196-206.
- [941] Burdick, J.A., M. Ward, E. Liang, et al., Stimulation of neurite outgrowth by neurotrophins delivered from degradable hydrogels. *Biomaterials*, 2006. 27(3): p. 452-459.
- [942] Jain, A., Y.-T. Kim, R.J. McKeon, and R.V. Bellamkonda, In situ gelling hydrogels for conformal repair of spinal cord defects, and local delivery of BDNF after spinal cord injury. *Biomaterials*, 2006. 27(3): p. 497-504.

- [943] Wang, Y.-C., Y.-T. Wu, H.-Y. Huang, et al., Sustained intraspinal delivery of neurotrophic factor encapsulated in biodegradable nanoparticles following contusive spinal cord injury. *Biomaterials*, 2008. 29(34): p. 4546-4553.
- [944] Mo, L., Z. Yang, A. Zhang, and X. Li, The repair of the injured adult rat hippocampus with NT-3-chitosan carriers. *Biomaterials*, 2010. 31(8): p. 2184-2192.
- [945] Lam, J., W.E. Lowry, S.T. Carmichael, and T. Segura, Delivery of iPS-NPCs to the stroke cavity within a hyaluronic acid matrix promotes the differentiation of transplanted cells. *Advanced Functional Materials*, 2014. 24(44): p. 7053-7062.
- [946] Him, H.J., T.H. Perera, T.S. Wilems, et al., Response to di-functionalized hyaluronic acid with orthogonal chemistry grafting at independent modification sites in rodent models of neural differentiation and spinal cord injury. *Journal of Materials Chemistry B*, 2016. 4(42): p. 6865-6875.
- [947] Nih, L.R., S.T. Carmichael, and T. Segura, Hydrogels for brain repair after stroke: an emerging treatment option. *Current Opinion in Biotechnology*, 2016. 40: p. 155-163.
- [948] Knowlton, S., S. Anand, T. Shah, and S. Tasoglu, Bioprinting for neural tissue engineering. *Trends in Neurosciences*, 2018. 41(1): p. 31-46.
- [949] Alghoul, M., A. Mendiola, R. Seth, et al., The effect of hyaluronan hydrogel on fat graft survival. *Aesthetic Surgery Journal*, 2012. 32(5): p. 622-633.
- [950] Cortivo, R., P. Brun, A. Rastrelli, and G. Abatangelo, In vitro studies on biocompatibility of hyaluronic acid esters. *Biomaterials*, 1991. 12(8): p. 727-730.
- [951] Benedetti, L., R. Cortivo, T. Berti, et al., Biocompatibility and biodegradation of different hyaluronan derivatives (Hyaff) implanted in rats. *Biomaterials*, 1993. 14(15): p. 1154-1160.
- [952] Halbleib, L., T. Skurk, C. de Luca, et al., Tissue engineering of white adipose tissue using hyaluronic acid-based scaffolds. I: in vitro differentiation of human adipocyte precursor cells on scaffolds. *Biomaterials*, 2003. 24(18): p. 3125-3132.
- [953] Stilliaert, F.B., C. Di Bartolo, J.A. Hunt, et al., Human clinical experience with adipose precursor cells seeded on hyaluronic acid-based spongy scaffolds. *Biomaterials*, 2008. 29(29): p. 3953-3959.
- [954] Espandar, L., B. Bunnell, G.Y. Wang, et al., Adipose-derived stem cells on hyaluronic acid-derived scaffold: a new horizon in bioengineered cornea. *Archives of Ophthalmology*, 2012. 130(2): p. 202-208.
- [955] Otterlei, M., K. Ostgaard, G. Skjåk-Braek, et al., Induction of cytokine production from human monocytes stimulated with alginate. *Journal of Immunotherapy*, 1991. 10(4): p. 286-291.

- [956] Iwamoto, M., M. Kurachi, T. Nakashima, et al., Structure-activity relationship of alginate oligosaccharides in the induction of cytokine production from RAW264.7 cells. *FEBS Letters*, 2005. 579(20): p. 4423-4429.
- [957] Park, H., S.-W. Kang, B.-S. Kim, et al., Shear-reversibly crosslinked alginate hydrogels for tissue engineering. *Macromolecular Bioscience*, 2009. 9(9): p. 895-901.
- [958] Follin, B., M. Juhl, S. Cohen, et al., Human adipose-derived stromal cells in a clinically applicable injectable alginate hydrogel: phenotypic and immunomodulatory evaluation. *Cyotherapy*, 2015. 17(8): p. 1104-1118.
- [959] Venkatesan, J., I. Bhatnagar, P. Manivasagan, et al., Alginate composites for bone tissue engineering: a review. *International Journal of Biological Macromolecules*, 2015. 72: p. 269-281.
- [960] Ruvinov, E. and S. Cohen, Alginate biomaterial for the treatment of myocardial infarction: progress, translational strategies, and clinical outlook: from ocean algae to patient bedside. *Advanced Drug Delivery Reviews*, 2016. 96: p. 54-76.
- [961] Balakrishnan, B., N. Joshi, A. Jayakrishnan, and R. Banerjee, Self-crosslinked oxidized alginate/gelatin hydrogel as injectable, adhesive biomimetic scaffolds for cartilage regeneration. *Acta Biomaterialia*, 2014. 10(8): p. 3650-3663.
- [962] Park, H. and K.Y. Lee, Cartilage regeneration using biodegradable oxidized alginate/hyaluronate hydrogels. *Journal of Biomedical Materials Research. Part A*, 2014. 102(12): p. 4519-4525.
- [963] Li, Z., H.R. Ramay, K.D. Hauch, et al., Chitosan-alginate hybrid scaffolds for bone tissue engineering. *Biomaterials*, 2005. 26(18): p. 3919-3928.
- [964] Zhao, L., M.D. Weir, and H.H.K. Xu, An injectable calcium phosphate-alginate hydrogel-umbilical cord mesenchymal stem cell paste for bone tissue engineering. *Biomaterials*, 2010. 31(25): p. 6502-6510.
- [965] Park, D.-J., B.-H. Choi, S.-J. Zhu, et al., Injectable bone using chitosan-alginate gel/mesenchymal stem cells/BMP-2 composites. *Journal of Cranio-Maxillofacial Surgery*, 2005. 33(1): p. 50-54.
- [966] Yu, J., K.T. Du, Q. Fang, et al., The use of human mesenchymal stem cells encapsulated in RGD modified alginate microspheres in the repair of myocardial infarction in the rat. *Biomaterials*, 2010. 31(27): p. 7012-7020.
- [967] Wang, Q., S. Jamal, M.S. Detamore, and C. Berkland, PLGA-chitosan/PLGA-alginate nanoparticle blends as biodegradable colloidal gels for seeding human umbilical cord mesenchymal stem cells. *Journal of Biomedical Materials Research Part A*, 2011. 96(3): p. 520-527.

- [968] Zhou, H. and H.H.K. Xu, The fast release of stem cells from alginate-fibrin microbeads in injectable scaffolds for bone tissue engineering. *Biomaterials*, 2011. 32(30): p. 7503-7513.
- [969] He, X., R. Dziak, K. Mao, et al., Integration of a novel injectable nano calcium sulfate/alginate scaffold and BMP2 gene-modified mesenchymal stem cells for bone regeneration. *Tissue Engineering Part A*, 2012. 19(3-4): p. 508-518.
- [970] Lewandowska-Łańcucka, J., K. Mystek, A. Mignon, et al., Alginate- and gelatin-based bioactive photocross-linkable hybrid materials for bone tissue engineering. *Carbohydrate Polymers*, 2017. 157: p. 1714-1722.
- [971] Chen, G., N. Kawazoe, and Y. Ito, Photo-crosslinkable hydrogels for tissue engineering applications, in *Photochemistry for Biomedical Applications: From Device Fabrication to Diagnosis and Therapy*, (ed. Y. Ito) 2018, Springer: Singapore, Singapore. p. 277-300.
- [972] Pina, S., J.M. Oliveira, and R.L. Reis, Natural-based nanocomposites for bone tissue engineering and regenerative medicine: a review. *Advanced Materials*, 2015. 27(7): p. 1143-1169.
- [973] Filardo, G., F. Perdisa, M. Gelinsky, et al., Novel alginate biphasic scaffold for osteochondral regeneration: an in vivo evaluation in rabbit and sheep models. *Journal of Materials Science: Materials in Medicine*, 2018. 29(6): p. 74.
- [974] Shachar, M., O. Tsur-Gang, T. Dvir, et al., The effect of immobilized RGD peptide in alginate scaffolds on cardiac tissue engineering. *Acta Biomaterialia*, 2011. 7(1): p. 152-162.
- [975] Sapir, Y., O. Kryukov, and S. Cohen, Integration of multiple cell-matrix interactions into alginate scaffolds for promoting cardiac tissue regeneration. *Biomaterials*, 2011. 32(7): p. 1838-1847.
- [976] Xu, Z. and M.T. Lam, Alginate application for heart and cardiovascular diseases, in *Alginates and their Biomedical Applications*, (ed. B.H.A. Rehm and M.F. Moradali). 2018, Springer: Singapore, Singapore. p. 185-212.

Figures

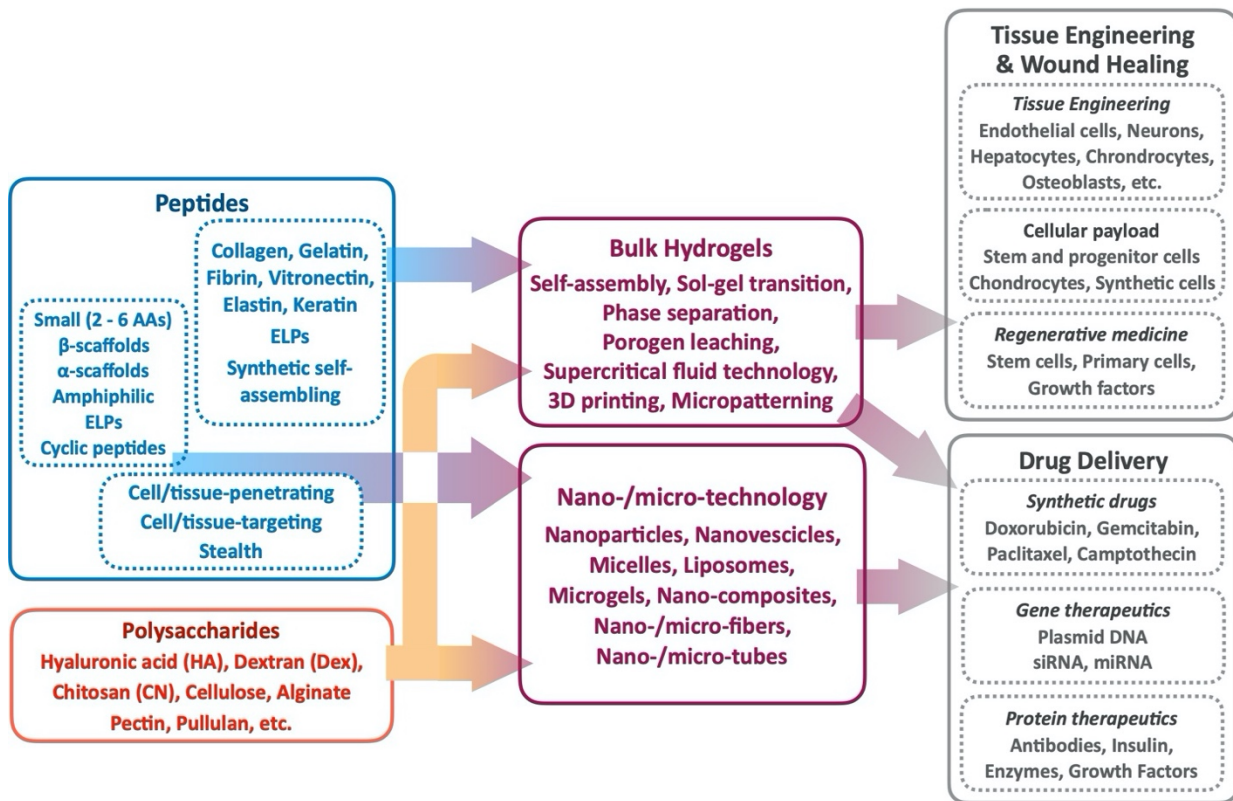


Figure 1.1 Overview of the substrate families, fabrication technologies, and applications of peptides, proteins, and polysaccharides in biomedical engineering.

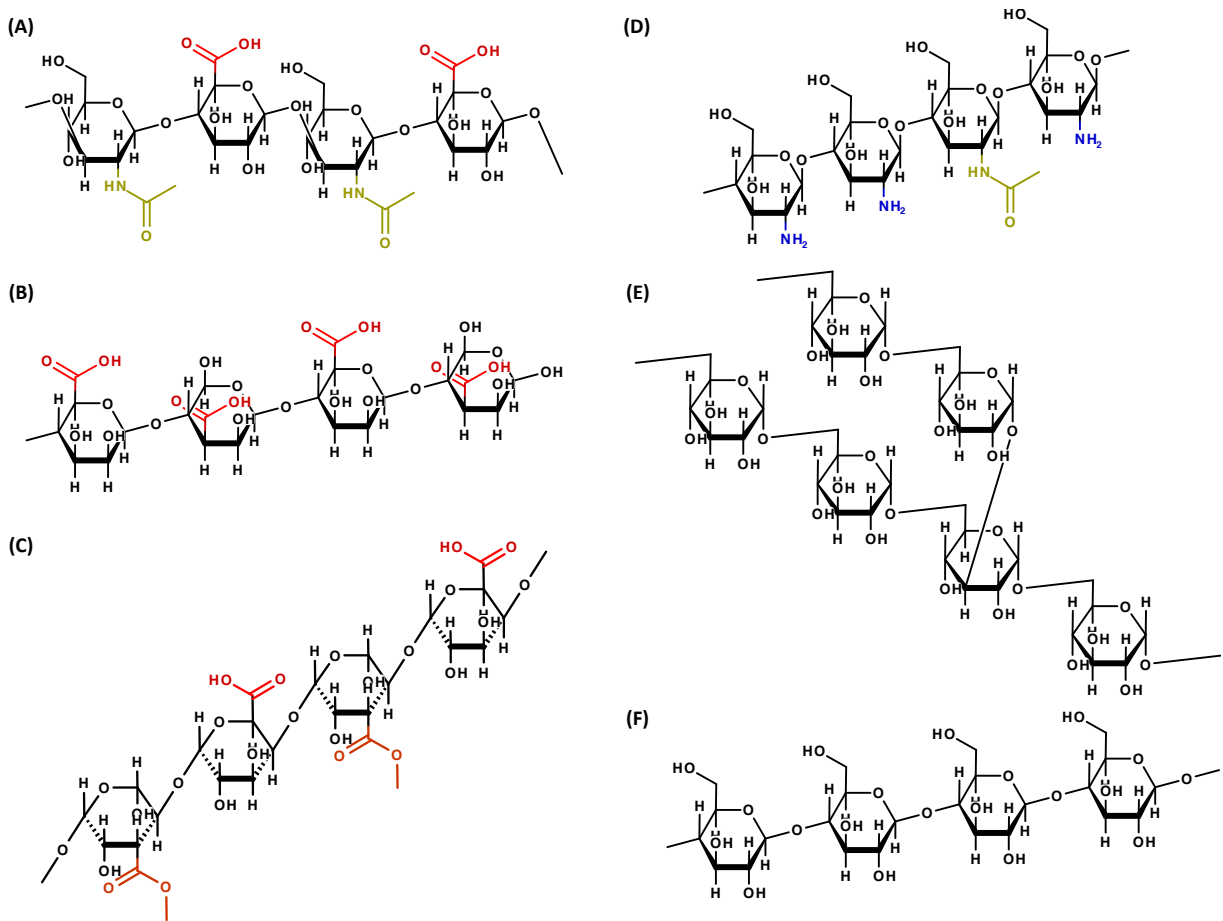


Figure 1.2 Structures of polysaccharides utilized as substrates in drug delivery, tissue engineering, and regenerative medicine: (A) hyaluronic acid, (B) alginic acid, (C) pectin, (D) chitosan, (E) dextran, and (F) cellulose. Native functional groups used for modification are highlighted, including carboxyl and primary amine groups.

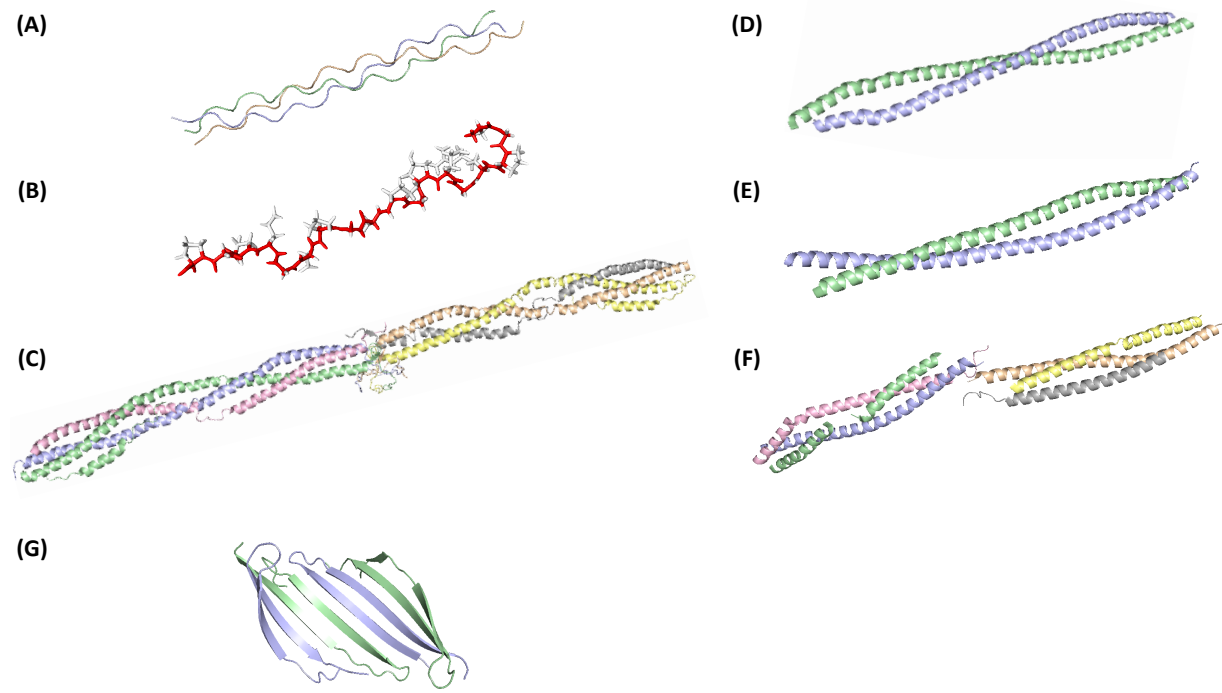


Figure 1.3 Structures of natural polypeptides utilized as substrates in drug delivery, tissue engineering, and regenerative medicine: **(A)** collagen (Protein Data Bank, PDB ID: 1BKV), **(B)** gelatin, **(C)** fibrinogen (PDB ID: 3GHG), **(D)** keratin 1/10 (PDB ID: 4ZRY), **(E)** keratin 5/14 (PDB ID: 3TNU), **(F)** laminin (PDB ID: 5XAU), and **(G)** silk fibroin (PDB ID: 3UA0). The higher-order morphology directly impact functionality, *e.g.*, tertiary helical structure of collagen, especially in tissue growth and regeneration.

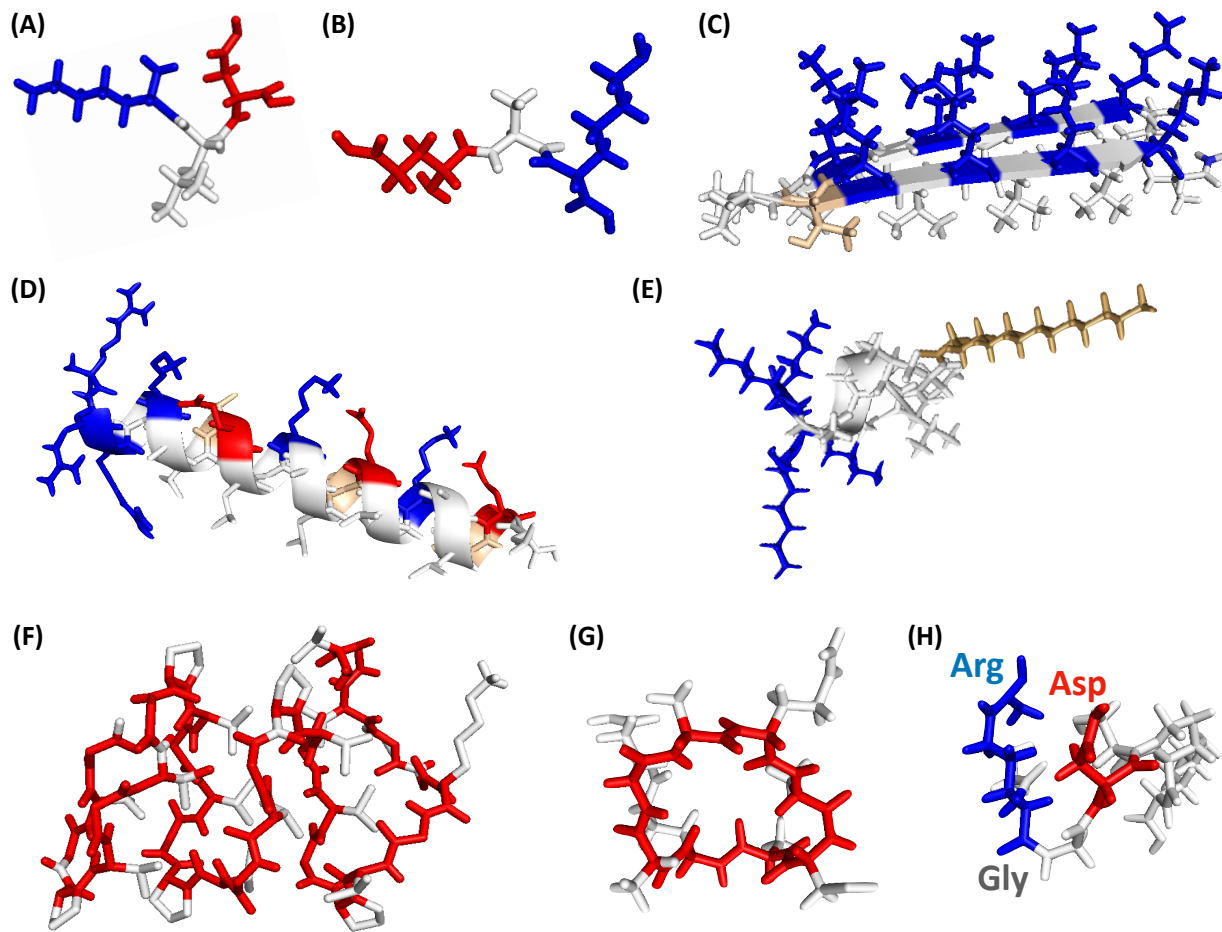


Figure 1.4 Structures of synthetic polypeptides utilized as substrates in drug delivery, tissue engineering, and regenerative medicine: (A) KLD (Lys-Leu-Asp), (B) EAK (Glu-Ala-Lys), (C) MAX1 (PDB ID: 2N1E), (D) R₃(AKALTEL)₃, (E) peptide amphiphile [C₁₆]-VVVAAAKKKK, (F) ELP (VKV₆F), (G) cyclic peptide QDAEDAQDACDA, (H) G-RGD-S.

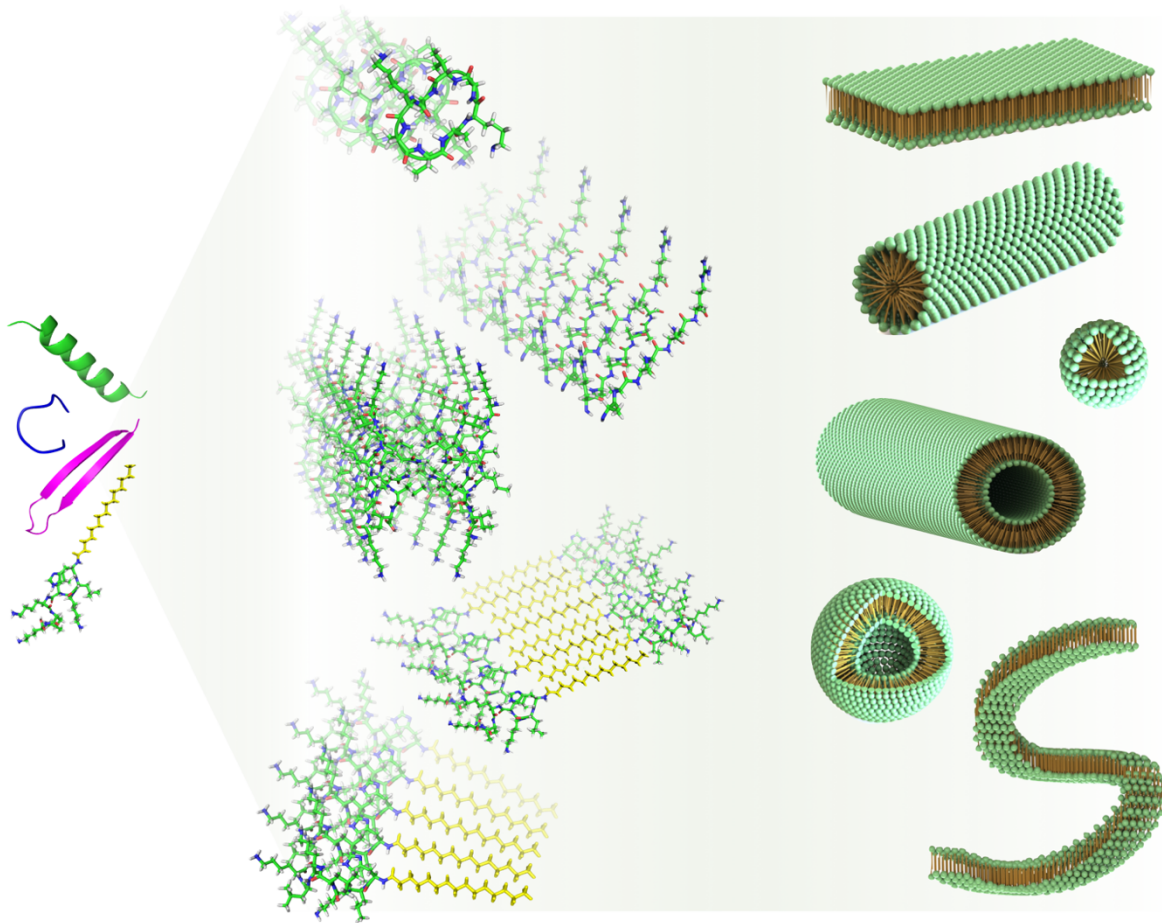


Figure 1.5 Self-assembly of monomer peptides (random coil, α -helix, β -sheet, and peptide amphiphile) into ordered assemblies and subsequently into nanostructures (nanosheet, nanotube, micelle, and nanofilament).

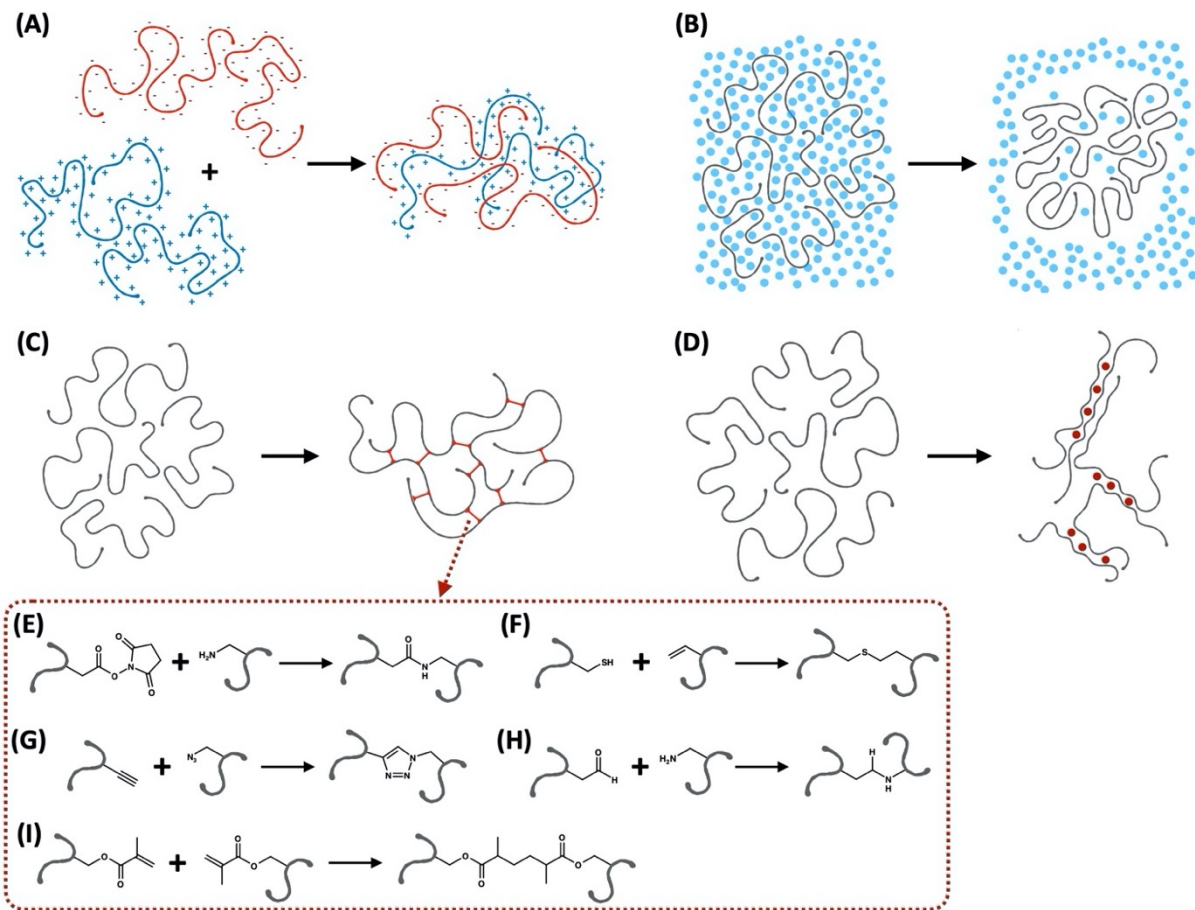


Figure 1.6 Fabrication techniques to convert polysaccharides into hydrogel substrates for tissue engineering and regenerative medicine: (A) electrostatic interaction, (B) solvent removal, (C) chemical crosslinking, (D) salt-mediated non-covalent crosslinking, (E) reaction of an NHS-ester with a primary amine forming an amide bond, (F) thiol-ene Michael addition forming a thioether bond, (G) alkyne-azide “click” reaction forming a triazole bond, (H) reaction of an aldehyde and a primary amine forming a Schiff base (imine bond) followed by “reductive amination” forming a secondary amine bond, and (I) UV-catalyzed reaction of acrylic groups resulting in an aliphatic linkage.

CHAPTER 2

Tailoring the Chemical Modification of Chitosan Hydrogels to Fine-Tune the Release of a Synergistic Combination of Chemotherapeutics

John D. Schneible, Ankush Singhal, Radina L. Lilova, Carol K. Hall, Andrea Grafmüller, and Stefano Menegatti

A version of this chapter has been published in Biomacromolecules 2019, 20(8), 3126-3141.

Abstract

Combination chemotherapy with a defined ratio and sequence of drug release is a clinically established and effective route to treat advanced solid tumors. In this context, a growing body of literature demonstrates the potential of hydrogels constructed with chemically modified polysaccharides as depots for controlled release of chemotherapeutics. Identifying the appropriate modification in terms of physicochemical properties of the functional group and its degree of substitution (χ) to achieve the desired release profile for multiple drugs is, however, a complex multivariate problem. To address this issue, we have developed a computational toolbox that models the migration of a drug pair through a hydrated network of polysaccharide chains modified with hydrophobic moieties. In this study, we chose doxorubicin (DOX) and Gemcitabine (GEM) as model drugs, as their synergistic effect against breast cancer has been thoroughly investigated, and chitosan as the model polymer. Our model describes how the modification of chitosan chains with acetyl, butanoyl, and heptanoyl moieties at different values χ governs both the structure of the hydrogel network and drug migration through it. Our experimental data confirm the *in silico* predictions for both single- and dual-drug release and, most notably, the counterintuitive inversion of release *vs.* χ that occurs when switching from a single- to a dual-drug system. Consensus between predicted and experimental data indicates that acetyl modifications ($\chi = 32\text{-}42\%$) and butanoyl modifications ($\chi = 19\text{-}24\%$) provide synergistic GEM/DOX release molar ratios (*i.e.*, 5-10). Collectively, these results demonstrate the potential of this model in guiding the design of chemotherapeutic hydrogels to combat cancer.

2.1. Introduction

Combination therapy with synergistic chemotherapeutics has become of increasing interest owing to its ability to overcome the main limitations of the single-drug approach: acquired drug resistance [1-3] and heavy dosage of highly cytotoxic drugs [4, 5]. Multidrug chemotherapy operates by simultaneously disrupting various metabolic pathways in cancer cells and has been shown to overcome drug resistance and reduce side effects considerably [6]. The complementary action of drugs targeting different metabolic pathways, in fact, provides enhanced therapeutic activity while requiring a significantly lower dosage. Recent work in this field has demonstrated that the therapeutic outcome depends not only on the molar ratio of the drugs in the cocktail but also on the schedule of administration, that is, the sequence at which the various drugs reach the target cells [7, 8]. Optimizing both ratio and sequence in a combined chemotherapy regimen is therefore essential to further lower the dosage relative to single-drug therapy needed to obtain a satisfactory therapeutic outcome [7, 9, 10]. This reduction of required therapeutic dosing (IC₅₀ values) using drug combinations relative to single-drug chemotherapy has been recently demonstrated *in vivo* using various combination chemotherapy regimens and tumor models [11-13].

To implement synergistic delivery schemes, researchers have investigated the use of nanoparticles [8, 11, 14], liposomes [15, 16], micelles [17, 18], polymer–drug conjugates (PDCs) [12, 19], and hydrogels [20, 21]. Among these systems, hydrogels possess unique advantages. Owing to the flexible microstructure of hydrogels, release kinetics can be tuned by varying the gel fraction in physical hydrogels and the cross-linking density in chemically cross-linked gels [22, 23]. In addition, hydrogels act as drug “depots” that afford sustained release and maintain a high local drug concentration in the surrounding tissues over an extended period, thereby circumventing

the pharmacokinetic limitations of most chemotherapeutic agents [24]. Further, the loading and release rates of the therapeutic payload in and out of hydrogels are mostly governed by diffusion, which depend on the molecular interactions between the polymer chains and the drugs, as well as the network morphology. These features have been harnessed for tuning the release kinetics and the scheduling of drugs, especially through chemical modification of the polymer backbone [25].

A polymer of major interest to researchers and clinicians for developing therapeutic hydrogels is chitosan. Chitosan, which is derived from naturally abundant chitin, is a biocompatible, nontoxic polymer that is degradable by human enzymes [26]. In addition, the presence of primary amine groups on the glucosamine monomer provides a site for chemical modification, which has been extensively exploited to tailor the kinetics of drug release [27, 28]. Interestingly, owing to their relatively short half-life in physiological media (*i.e.*, days-month(s)), physical chitosan hydrogels are ideal for short-term delivery and do not release any toxic degradation byproducts [29]. As a result, a variety of chitosan-based formulations have been developed for oral, ophthalmic, and transdermal applications [26, 30-32], several of which have received FDA approval, demonstrating clear feasibility of these materials toward clinical translation.

Customizing the chemical modification of chitosan hydrogels to achieve a precise, synergistic ratio and kinetics of drug release, however, is a complex multivariate problem that depends on the physicochemical properties of the drugs, the composition and level of functional moieties, and the gel fraction. Collectively, these factors determine the hydrogel structure as well as the interactions between the drugs and the polymer backbone, thereby governing the release outcome. Such a large design space makes the optimization of hydrogels for the controlled release of specific combinations of chemotherapeutics extremely laborious. A toolbox capable of guiding

the developmental phase would be of great assistance to pharmaceutical chemists in streamlining preclinical studies, thus realizing the full potential of these materials.

To this end, we have developed a method for guiding the chemical modification of chitosan chains to be utilized for designing hydrogels that afford the delivery for any desired drug combination with a synergistic molar ratio and kinetics. Our method comprises a computational modeling phase and an experimental validation phase. The computational phase comprises both all-atom and coarse-grained molecular dynamic (MD) simulations that model networks constructed with modified chitosan chains; its goal is to understand the microstructure/morphology, polymer–drug interactions, and the resulting diffusion of one or multiple drugs. The input design parameters input by the operator include (*i*) the chemical identity and distribution of the modifications across each chitosan chain, (*ii*) the ratios of the numbers of water molecules to polymer chains and of drug molecules to polymer chains, and (*iii*) the loading of the single drugs. While atomistic molecular dynamics can provide detailed insights into the effect of chemical modifications on the drugs' local interactions with the polymer chains, coarse-grained simulations enable rapid modeling of larger systems, containing a high number of polymer chains, water molecules, and drug molecules, for longer simulation times. Since the modeling of chemically modified, drug-loaded hydrogels, requires simulations with sufficient spatio-temporal width to provide reliable guidance for design, we resolved to develop an *ad hoc* coarse-grained model [33-35]. Specifically, our model returns predicted diffusion coefficients of every drug species. The design parameters affording the most favorable diffusion coefficients toward synergistic molar ratio and kinetics of drug release were utilized in the experimental validation phase to construct the drug-loaded hydrogels.

To demonstrate our method, we selected doxorubicin (DOX) and Gemcitabine (GEM) as a model drug pair and three N-acyl groups (acetyl, butanoyl, and heptanoyl) as model modification moieties. The combination of DOX, a topoisomerase II inhibitor, and GEM, an antimetabolite, has been proven to be a highly effective drug regimen. Both are FDA-approved chemotherapeutics and have been studied in a variety of drug delivery vehicles, such as micellar nanoparticles, PDCs, polymersomes, mesoporous silica nanoparticles, and nanostructured lipid carriers [15, 36-40]. Their synergistic combination has been demonstrated with multiple breast cancer cell lines, such as MCF7 and MDA-MB-231 [7, 41]. While extensive research has focused on their synergistic molar ratio, much less work has focused on the effect of scheduling on their therapeutic outcome. Vogus *et al.* have reported a strong effect of the scheduling of GEM and DOX release on MDA-MB-231 cells, by showing that simultaneous treatment with both drugs and incubation with GEM prior to DOX induced more toxicity than treatment with DOX prior to GEM, for the same concentrations. Furthermore, they showed that treatment with GEM prior to DOX (combination index, CI = 0.16 ± 0.03) afforded higher synergy than treating simultaneously with GEM and DOX (CI = 0.76 ± 0.10). They also found that the earlier the cells are exposed to GEM prior to DOX, the higher the resulting amount of synergy (lowest CI) [7]. In a follow-up work, Vogus *et al.* studied the effect of the GEM:DOX molar ratio on MDA-MB-231 cells, and MCF-10a cells, non-tumorigenic breast epithelial cells, demonstrating that synergism on the cancer cells is fairly independent of molar ratio, whereas maximum antagonism to healthy cells occurs at the higher values of the molar ratio [41]. These studies provide evidence that an efficacious GEM/DOX delivery system should be able to stagger the release of the two drugs, such that GEM impacts the cells prior to DOX, and release a molar ratio of GEM:DOX > 1.

Acetyl, butanoyl, and heptanoyl moieties were chosen for chitosan modification as they represent similar but increasingly hydrophobic modifications and therefore allow us to study systematically the kinetics of drug release. Specifically, they enable two mechanisms of modulating the molar ratio and relative kinetics of drug release: the first based on the molecular interaction between modified chitosan chains and the drug molecules, and the second based on the formation of microscopic channels within the hydrogel network resulting from the hydrophobically driven aggregation of modified chitosan chains. The first mechanism applies mostly to hydrophobic drugs (*e.g.*, DOX) resulting in slower release kinetics and becomes more prominent when the polymer is modified with longer aliphatic chains or with a higher degree of modification. The second mechanism, instead, impacts all drugs and depends not only on the composition and degree of modification but also on its distribution along the chitosan chain (*e.g.*, random *vs.* blocky). Both phenomena were captured by our coarse-grained molecular dynamics simulation and were observed experimentally with butanoyl- and heptanoyl-chitosan hydrogels.

The systems modeled and tested in this study feature chitosan hydrogels prepared with different degrees of modification (χ) (*i.e.*, 0-50% molar acetyl, 5-40% molar butanoyl, and 5-30% molar heptanoyl on chitosan) and loaded either with a single-drug (DOX or GEM) or with a double-drug (DOX and GEM) payload. We compared the predicted trends of drug diffusion coefficients with those obtained from experimental measures fitted on the Korsmeyer-Peppas equation [42]. Furthermore, we report the development of hydrogels that are capable of delivering the GEM/DOX combination with the desired kinetics and dose ratio of the pair. With dual-drug-loaded systems, acetyl-chitosan gels with $\chi = 32\text{-}42\%$ delivered a GEM/DOX molar ratio of 7.5-10.5, whereas butanoyl-chitosan gels with $\chi = 19\text{-}24\%$ delivered a molar ratio of 10-7.5. Further, the GEM/DOX ratio of release exponents calculated using the Korsmeyer-Peppas equation, which

is a measure of release kinetics, was 3.7-8.9 for acetyl-chitosan gels and 5.6-6.3 for butanoyl-chitosan gels, indicative of faster GEM release than DOX. Both of these measures agree with computational results. Because the acetyl-modified gels display favorable release kinetics of GEM/DOX and a wider working range of modification, future work will further develop and test acetyl-modified gels for efficacy *in vitro*. Collectively, these results demonstrate the potential of the proposed strategy to guide the rapid, successful development of hydrogels – including, but not limited to, chitosan – for controlled release of synergistic combinations of anticancer drugs.

2.2. Materials and Methods

2.2.1. Materials

Low-molecular-weight chitosan (85% maximum degree of deacetylation, 15 kDa) was obtained from Polysciences Inc. (Warrington, PA). Low-molecular-weight chitosan (75-85% degree of deacetylation, 50-190 kDa), acetic anhydride, phosphate-buffered saline (PBS), and the Kaiser Test kit were obtained from Sigma Aldrich (St. Louis, MO). Butyric and heptanoic anhydride were obtained from TCI Chemicals (Portland, OR). Doxorubicin hydrochloride (DOX) and Gemcitabine hydrochloride (GEM) were obtained from LC Laboratories (Woburn, MA). All other chemicals were of reagent grade or higher.

2.2.2. Modification of Chitosan

The protocol of chemical modification of chitosan was adapted from Kubota *et al.* [43]. Briefly, chitosan was dissolved in 1% acetic acid (w/w) at a concentration of 6 mg mL⁻¹ and filtered to remove insoluble components. A stoichiometric amount of chosen anhydride (acetic, butyric, or heptanoic) was added to the chitosan solution and allowed to react at room temperature

overnight. The solution was then precipitated by dropwise addition in a 3× reaction volume of 5 M methanolic potassium hydroxide. The precipitate was then collected and washed to neutral pH with methanol and copiously washed with water to yield a physical hydrogel. The gel was weighed, and subsequently lyophilized and weighed, to determine the gel fraction as the ratio of the mass pre- and post- lyophilization.

2.2.3. Determination of the Level of Modification

The level of acyl modification of the chitosan polymer chains was measured using a modified version of the Ninhydrin assay developed by Kaiser *et al.* [44]. Briefly, lyophilized samples of modified chitosan were dissolved in 1% acetic acid (w/w) at 3 mg mL⁻¹, and native chitosan (used to generate a standard curve) was dissolved at varying concentrations (0.5-7.5 mg mL⁻¹). Chitosan solutions were then combined with 30 µL of potassium cyanide in water/pyridine and ninhydrin and 6% in ethanol. The solutions were then incubated at 100 °C for 5 min. The solution was then diluted to 200×, and absorbance at 570 nm was measured by UV-vis spectroscopy. The level of modification was determined through the derived Equation 1:

$$(1) \quad \chi = \frac{\left(1 - \frac{D \cdot M \cdot C^*}{C}\right)}{\left(1 - \frac{D \cdot M_{mod} \cdot C^*}{C}\right)}$$

where χ is the degree of modification, C^* is the molar concentration of amine groups on a chitosan chain, D is the dilution factor, C is the mass concentration used for the Kaiser test, M is the molecular weight of the glucosamine monomer, and M_{mod} is the molecular weight of the modification.

2.2.4. Computational Procedure

The simulations were performed utilizing the GROMACS 4.6.4 package [45]. All-atom molecular dynamics (MD) simulations were performed using the GLYCAM_{OSMO14}^{TIP5P} force field [46, 47]. The parameters for the butanoyl and heptanoyl modifications, as well as for GEM and DOX were obtained from the gaff force field [48], whereas the partial charges were derived following the GLYCAM06 protocol [46]. All all-atom chitosan systems contained 10 chitosan chains with degree of polymerization (DP, number of monosaccharides per chain) of 16, and 200 water molecules per chain. Separate simulations were performed using 50 DOX, 50 GEM, or 50 DOX and 50 GEM molecules, with 10 water molecules per drug molecule, to derive the interaction potentials for the drug-drug and drug-water interactions. Similarly, additional systems containing 10 DOX or 10 GEM molecules together with 10 chitosan chains with DP = 16 and 200 water molecules per chain were simulated to derive the drug-polymer interaction. The particle mesh Ewald method [49] was used to calculate the long-range electrostatic interaction using a Lennard-Jones (LJ) and electrostatic interaction with a cutoff of 1.4 nm. The system was equilibrated in the NPT ensemble for 50 ns using a Parinello-Rahman barostat with additional pressure dispersion correction [50] and subsequently equilibrated for 400 ns in the NVT ensemble. A final 100 ns NVT MD simulation was performed to derive the coarse-grained interaction potentials.

In the coarse-grained model, each monosaccharide was mapped onto three coarse-grained interaction sites. The modifications were represented by one, two, and three additional sites for the acetyl, butanoyl, and heptanoyl groups, respectively. Water molecules were represented as a single coarse-grained site. DOX and GEM were represented by 11 and 4 coarse-grained sites, respectively. The interaction potentials between these sites were generated using Boltzmann inversion [51] for the bonded interactions and the MSCG method [52] for nonbonded interactions,

following the procedure described by Sauter *et al.* [53]. Coarse-grained systems containing 20 chitosan chains with DP of 50, and 100,000 water beads (5,000 water molecules per chains), were equilibrated for 100 ns using the Nosé–Hoover thermostat [54–56]. The drug diffusion simulations were performed by randomly loading the chitosan networks with either 10 DOX or 10 GEM for single-drug release or 10 DOX and 10 GEM molecules for dual-drug release. The diffusion coefficients of the drugs were obtained from the slope of their mean square displacement (MSD) as a function of time. Pore distributions were calculated using the procedure described by Bhattacharya and Gubbins [57] with the SOLVOPT routine for constrained nonlinear optimization [58]. The procedure finds the largest sphere that can be placed in the network while containing randomly chosen points.

2.2.5. Single-Drug Loading and Release Studies

Initial single-drug loading and release studies were performed using low-molecular-weight chitosan (Polysciences Inc). Drug loading experiments were performed by incubating 150 mg of chitosan hydrogel with 1 mL of a 1 mg mL^{-1} aqueous drug solution for 48 hr. After loading, the drug-depleted supernatant was collected for drug quantification by UV-vis spectroscopy. The loaded hydrogel was then combined with 1 mL of 0.01 M PBS pH 7.4 and placed in a 37 °C orbital shaker at 50 rpm. At selected time points, 200 μL of the sample was withdrawn and replenished with fresh PBS. After the release studies, all samples (loading supernatant and time point collections) were analyzed by UV-vis on Bioteck Synergy at 480 and 290 nm to determine the amounts released of DOX and GEM, respectively.

2.2.6. Dual-Drug Loading and Release Studies

Dual-drug loading and release studies were performed on the low-molecular-weight chitosan gels Polysciences Inc. Samples of 150 mg of hydrogel were incubated with 1 mL of a 1 mg mL⁻¹ aqueous DOX/GEM solution, 50/50 molar ratio, for 48 hr. The supernatant was collected, and the loaded hydrogel was then combined with 1 mL of 0.01 M PBS pH 7.4 and placed in a 37 °C orbital shaker at 50 rpm. At selected time points, 200 µL of the aqueous supernatant was withdrawn and replenished with fresh PBS. Samples were then passed through a Waters 2690 Separation reversed-phase high-performance liquid chromatography system equipped with an Aeris 3.6 µm C18 column (150 × 4.6 mm). The gradient utilized 0.1% formic acid (A) and acetonitrile with 0.1% formic acid (B) from 5-100% B over 10 min. The column eluate was monitored at wavelengths of 290 and 480 nm, wavelengths corresponding to the GEM and DOX. The concentrations of GEM and DOX were determined by peak-area integration of the resulting 290 and 480 nm chromatograms relative to the respective standard curves.

2.2.7. Mathematical Drug Release Models

Several models are used to describe drug diffusion profiles [59] or the quantity of drug released from the modified chitosan hydrogels over time (**Table 2.1**): *(i)* the zero-order model, which describes drug dissolution from pharmaceutical dosage forms that do not disaggregate and release the drug slowly; *(ii)* the first-order model, which describes drug dissolution that occurs from porous matrices and water-soluble drugs; *(iii)* the Hixson–Crowell model [60], which describes release that occurs in planes that are parallel to the drug surface if the tablet dimensions diminish proportionally, meaning that the initial geometrical form keeps constant all the time; *(iv)* the Higuchi model [61], which describes the release of water-soluble and low-solubility drugs

incorporated in semisolid and/or solid matrixes; and (*v*) the Korsmeyer–Peppas model [42], which characterizes release from hydrophilic matrices and is presented in Equation 2:

$$(2) \quad \frac{Q_t}{Q_\infty} = K_k t^n$$

where Q_t is the amount of drug released at time t , Q_∞ is the maximum possible amount, and the ratio of Q_t to Q_∞ is the percent release. K_k is the release rate constant, which is correlated to the diffusion coefficient, and n is the release exponent, where $n \sim 0.5$ denotes Fick-type drug diffusion, and $n > 0.5$ indicates that spatial rearrangement of the polymer chains also contributes to drug transport. The release exponent, n , is a metric for characterizing the mechanism of release. To determine n , only the portion of the release curve where $Q_t/Q_\infty < 0.6$ was used. The in vitro drug release data was analyzed by fitting it to all models listed in **Table 2.5.1**.

2.3. Results

2.3.1. Chitosan Gel Preparation and Selection

Initial studies were performed using two chitosan starting materials to evaluate the properties of the resulting gels, namely, the consistency in gel fraction across different acyl modifications and different degrees of modification and to select a polymer for further optimization. **Figure 2.1** illustrates the polymer gel fraction (*i.e.*, the mass of polymer contained in a given mass of hydrogel) obtained with either 15 or 50–190 kDa chitosan using acetyl, butanoyl, and heptanoyl moieties, spanning a wide array of modification levels, ranging from native chitosan (0% modified) to 50% modified. Interestingly, the gel fraction was found to depend only on the acyl moiety used to modify the polymer but not on the chitosan molecular weight. The mean gel fractions (percent ratio of polymer weight vs. total hydrogel weight) obtained with 15 kDa chitosan (~90 monomers), in fact, were 2.02 ± 0.5 , 2.59 ± 0.3 , and 3.31 ± 0.4 for the acetyl-, butanoyl-, and

heptanoyl- modifications, respectively, whereas the corresponding values obtained with 50-190 kDa chitosan (~300-1200 monomers) were 2.14 ± 0.6 , 2.63 ± 0.2 , and 3.29 ± 0.5 , across all modification levels. This consistency in gel fraction across a vastly different length of polymer suggests that the physical behavior of the gels depends mainly on the type and degree of the modification groups. Thus, to maintain consistency between the experimental and *in silico* studies, which are limited to 50 monomer-long chitosan chains to limit computational costs, 15 kDa chitosan was utilized in all subsequent studies. With the drug transport through the hydrogels being dependent on both gel fraction and modification on the polymer backbone, consistency in gel fraction values is critical to study the correlation between drug release and the type and degree of modification. Since the gel fraction for heptanoyl-modified gels was statistically different from acetyl-modified gels, and the average gel fraction values for acetyl- and butanoyl-modified gels were closer than those of butanoyl- and heptanoyl-modified gels with both 15 and 50-190 kDa chitosan, drug release from heptanoyl-modified hydrogels was not computationally modeled.

2.3.2. *In Silico* Modeling of Single and Dual-Drug Diffusion through Modified Chitosan Hydrogels

2.3.2.1. Drug-Chitosan Interactions at All-Atom Resolution

All-atom simulations of the drug-loaded chitosan hydrogels were analyzed to obtain a molecular-level understanding of (*i*) the interactions between the drug molecules and the modified chitosan chains and (*ii*) the dependence of these interactions on the type and degree (χ) of modification. Atomistic systems feature a high density of saccharide monomers (chitosan) and low water content, which is necessary to obtain a sufficient sampling of the forces needed to implement the coarse-grained procedure. This high density, however, results in many nonbonded interactions

between the polymer and drug molecules. It must be also noted that the frequency of these interactions in real hydrogels, where the water content is much higher, is much lower. Nonetheless, the atomistic analysis of these interactions provides insight into their relative contribution toward determining drug diffusion through the network. The interaction energies among the drug molecules, the chitosan backbone, and the modification groups were separated into electrostatic and Lennard-Jones (LJ) contributions and the ability to form hydrogen-bond contacts. The resulting interactions between DOX and modification groups and between DOX and the chitosan backbone as a function of χ are reported in **Figure 2.2**. The analogous results for GEM are reported in **Figure 2.3**. The hydrogen-bond interactions for DOX modification and DOX backbone as a function of χ are reported in **Figure 2.4**.

We observed that the interactions between drug molecules and modified chitosan chains were consistently of the LJ type, particularly for DOX, which interacts both with the chitosan backbone and with the modification groups. The daunosamine moiety in DOX aligns with the pyranose rings in the chitosan backbone, resulting in the formation of multiple hydrogen bonds (**Figure 2.5**). As χ increases, the number of contacts (nonbonded interactions) between DOX and the modification groups (both acetyl and butanoyl) increases, resulting in higher interaction energy as shown in **Figure 2.2**. On the other hand, the dependence of the backbone interactions with χ is less clear, as the number of nonbonded interactions decreases with χ for acetyl modifications and increases slightly for butanoyl modifications. It should be noted, however, that DOX molecules tend to aggregate into clusters, thereby reducing their ability to form interactions with the backbone, especially within the time scale of the all-atom simulations, where equilibration of the aggregate size is not accessible. GEM shows overall weaker interactions with the modified chitosan chains compared with DOX. The LJ contribution to the interaction energy, in fact, is

about 50% of that observed with DOX, whereas the electrostatic contribution is approximately the same for the two drugs.

2.3.2.2. Coarse-Grained Simulations of Acyl-Modified Chitosan Hydrogels

The all-atom simulations described in the last section were performed to evaluate the molecular-level interactions and elucidate the thermodynamic mechanisms by which the drugs interact with the chitosan backbone and the modification groups. However, to understand how the chemical modifications govern the morphology of the hydrogel and the transport of the drugs therein, it is necessary to model drug-loaded hydrogels across a large spatio-temporal scale, where a high number of elements (long polymer chains, drug molecules, and water molecules) and their dynamic interplay can be simulated, thereby rendering a physically accurate representation of these systems. This, however, is not possible with all-atom simulations. We therefore resolved to adopt a coarse-grained modeling procedure that was informed by the results of the all-atom simulations and that has been shown to capture the behavior of the polysaccharide-based hydrogel [47].

The coarse-grained models for the base glucosamine and the modified (acetyl, butanoyl, and heptanoyl) glucosamine monomers, as well as the drug molecules were constructed as routinely done by grouping four heavy atoms into one coarse-grained interaction site while preserving the overall ring topology of the molecule. Water molecules were represented by one coarse-grained interaction site. The coarse-grained mapping of DOX and GEM is shown in **Figure 2.6a** and **Figure 2.6b**, respectively, whereas that of the monosaccharides with zero, one, two, and three interaction sites corresponding to unmodified and acetyl, butanoyl, and heptanoyl modifications is reported in **Figure 2.6c – Figure 2.6f**.

The coarse-grained interaction potentials of the drug molecules and the chitosan chains were obtained from all-atom molecular dynamics (MD) simulations following the force matching

method [62-64] and a procedure outlined in our prior work [53]. The radial distribution functions between all interaction sites of the coarse-grained model showed excellent agreement with their equivalent obtained from all-atom simulations as shown in **Figure 2.7**. The transferability to systems with different degrees of modification was explicitly confirmed so that the coarse-grained model was expected to accurately reflect the interactions of the underlying atomistic force field.

The hydrogel models were set to comprise 20 chitosan chains, each of 50 monomers (polymerization degree, DP = 50), and modified using the same values of χ utilized in the follow-up experimental work: χ of 0, 16, 32, and 50% for acetyl-chitosan, and χ of 0, 16, 24, and 32% for butanoyl-chitosan.

We considered the use of chitosan chains with DP > 50 unnecessary, given the lack of correlation between the gel fraction and the molecular weight of chitosan (**Figure 2.1**) and the resulting higher computational cost. Furthermore, the modification pattern, that is, the distribution of the acetyl-, butanoyl-, and heptanoyl- groups on the chitosan chains, was also considered. In real hydrogels, both χ and the modification patterns are governed by the monomers and the reagents utilized for chemical modification, as well as the structure of the polymer chain in solution as it evolves through the course of the chemical modification. Whereas χ can be easily measured, evaluating the modification patterns is much more challenging, and it is often assumed to be random. However, other distributions of the modification groups resembling either an evenly spaced or a blocky pattern can also be envisioned, and their presence can be inferred based on indirect measurements derived from macroscopic behaviors of the polymer. A consideration for the modified chitosan molecules is that the hydrophobic tails (acetic, butanoic, and heptanoic) of the anhydrides utilized for modifying the chitosan chains dissolved in an acidic aqueous

environment are likely to aggregate around the modified monomers that are initially formed and promote localized modification thereupon, resulting in a block-type pattern.

Both χ and the modification pattern, in fact, govern the aggregation of polymer chains in solution; in particular, chain aggregation is promoted by blocky modification patterns as opposed to a random distribution along the polymer chain [65-67]. To evaluate the effect of the modification pattern on the network structure and molecular interactions, chitosan chains modified with two different patterns, namely, evenly spaced (*i.e.*, two neighbor modification groups are separated by a number of unmodified monomers equal to $[PD \times (1 - \chi)]/[(PD \times \chi) - 1]$) and blocky (*i.e.*, clusters of MM modified monomers separated by a number of unmodified monomers equal to $[MM \times (1 - \chi)]/\chi$), were constructed to be simulated. A random modification pattern, where blocks of different sizes are assigned to every chain, would render the derivation of structure *vs.* χ correlations particularly challenging and was not considered in this work. The hydrogels were constructed with 100,000 water molecules in total, corresponding to a gel fraction value of 8.2%. While this is higher than the experimental values (2 – 2.5 % (w/w)), increasing the number of water molecules per polymer chain would escalate the computational costs and prevent the possibility of scanning over a range of conditions for system optimization. The resulting equilibrated structures of acetyl- and butanoyl-chitosan featuring blocky modification pattern are presented in **Figure 2.8**, whereas the corresponding structures with an evenly spaced modification pattern are reported in **Figure 2.9**.

The coarse-grained simulation of these systems indicates that increasing χ consistently promotes aggregation of the chitosan chains, morphing the microstructure of the gel from a homogeneous network of contacting chains to a heterogeneous system featuring hydrophobic-rich domains (clusters) surrounding large pores (channels). This transition is evident with butanoyl-

chitosan, which shows a strong dependence of aggregation upon the modification pattern (see **Figure 2.8c** and **Figure 2.8d**) for a blocky modification pattern with $\chi = 16$ and 32%, respectively, and **Figure 2.9c** and **Figure 2.9d** for an evenly spaced pattern with $\chi = 16$ and 32%, respectively), and a less pronounced dependence upon the modification pattern for acetyl-chitosan, for which both the modification pattern and the value of χ seem to have little or no influence (see **Figure 2.8a** and **Figure 2.8b** for the blocky modification pattern with $\chi = 16$ and 50%, respectively, and **Figure 2.9a** and **Figure 2.9b** for the evenly spaced pattern with $\chi = 16$ and 50%, respectively). The clusters formed at high values of χ feature a hydrophobic core, which comprises the segments of chitosan chains carrying the modification, and a hydrophilic shell; polymer bridges connecting the clusters are formed by the chitosan segments carrying low or no modification. These types of structures (**Figure 2.10**) have been extensively studied in prior literature and have been comprehensively reviewed by Philippova and Korchagina [68].

To obtain a more quantitative measure of network homogeneity, the structures derived from the coarse-grained simulations were analyzed by calculating the distribution of pore sizes (**Figure 2.11**). The pore size distribution in the acetyl-chitosan network remains essentially unchanged over the entire range of χ for both evenly spaced and blocky modification patterns (**Figure 2.11a** and **Figure 2.11b**); this corresponds to the homogeneous network structure featuring relatively small pores shown in the simulation snapshots in **Figure 2.8a** and **Figure 2.8b**. In butanoyl-chitosan, on the other hand, the pore size distribution shifts to markedly larger pore diameters at higher χ , indicating the appearance of large channels resulting from the formation of hydrophobic clusters for both modification patterns. The comparison between pore size distributions further indicates that the transition of butanoyl-chitosan from a homogeneous network to cluster/channel morphology occurs at lower χ with a blocky modification pattern than

with an evenly spaced pattern (**Figure 2.11c** and **Figure 2.11d**). The large difference in the hydrogel morphology between acetyl and butanoyl modifications likely plays a significant role in determining the migration of drug molecules.

2.3.2.3. Simulation of Single-Drug Migration through Modified Chitosan Hydrogels

After equilibrating the chitosan hydrogel structure, the coarse-grained hydrogels were loaded with 10 drug molecules of either DOX or GEM initially placed at random positions. The number of drug molecules was chosen to match the loading (ratio of drug molecules *vs.* polymer chains) featured by the experimental systems. In choosing the number of drug molecules, we also considered the tradeoff between ensuring reproducible simulations (higher drug loading) and avoiding the formation of aggregates (lower drug loading). While, in fact, an insufficient number of drug molecules can lead to poor statistical significance, especially when diffusing through structurally nonhomogeneous systems, excessive drug loading results in the formation of aggregates, which would distort drug migration through the polymer network. Regarding the choice of distributing the drug molecules randomly across the network, we note that the diffusion constants obtained by arranging the drug molecules into different initial distributions showed the same trends and, in most cases, agree within the fitting error.

Coarse-grained simulations of 10 ns were performed, and the migration of the drug molecules through the networks was monitored. The diffusion constants were calculated from the slope of the mean-squared displacement (MSD) of the drug molecules with respect to time and are reported in **Figure 2.12**; it should be noted that the diffusion constants did not significantly change with simulations performed at longer time scales. The error bars correspond to the fitting error due to the nonlinearity of MSD fitting.

As anticipated, the differences in hydrogel morphology (homogeneous vs. clusters/channels) and physicochemical properties of the drugs and the modification groups result in different trends of drug diffusion *vs.* χ . GEM migrates through all networks with a diffusion constant similar to that of free GEM in water, indicating that there is no effect of the polymer on its diffusion (**Figure 2.12a** and **Figure 2.12c**). GEM molecules, which are small and hydrophilic, form a relatively low number of nonbonded interactions with the chitosan chains, irrespective of the type of modification and χ , as listed in **Table 2.2**. Owing to the limited interaction with the polymer chains, GEM travels easily through the water-filled channels in both homogeneous and cluster/channel hydrogel morphologies. Only a slight reduction in GEM diffusion is observed in butanoyl-chitosan at higher χ .

On the other hand, DOX molecules, which are larger and more hydrophobic than GEM, show markedly different values of the diffusion coefficient and, most notably, an inversion in the diffusion trends with χ between acetyl and butanoyl modifications. In acetylated-chitosan networks, DOX diffusion decreases as χ increases, independent of the modification pattern (**Figure 2.12b**). However, the network structure and pore size distributions between acetylated-chitosan networks with evenly spaced and blocky modification were the same (**Figure 2.11a** and **Figure 2.11b**), ruling out a role of network morphology on decreasing the mobility of DOX as χ increases. Rather, the lower diffusion coefficient of DOX at higher χ is due to a higher number of nonbonded interactions between DOX and the acetyl groups on the chitosan chains. As reported in **Table 2.2**, in fact, the number of nonbonded interactions between DOX and the acetyl moieties increases with χ for both modification patterns, although the number of nonbonded interactions with the backbone remains constant; for example, a DOX molecule forms an average of 15 ± 2 interactions with acetyl-chitosan at $\chi = 16\%$ and up to 60 ± 4 interactions with acetyl-chitosan at $\chi = 50\%$ with an

evenly spaced pattern. This indicates that hydrophobic nonbonded interactions are the main cause of the slowed diffusion.

DOX diffusion through butanoyl-chitosan gels, on the other hand, increases with χ independent of modification patterns (**Figure 2.12d**). As χ increases, the butanoyl-chitosan network undergoes a transition from homogeneous (**Figure 2.8c**) to cluster/channel morphology (**Figure 2.8d**). Coarse-grained simulations of DOX migration through butanoyl-chitosan networks showed sharp differences in the migration of DOX molecules across chitosan networks with different morphologies. Specifically, the migration of DOX through the homogeneous butanoyl-chitosan network (low χ , **Figure 2.13c**) is identical to that of DOX through the homogeneous acetyl-chitosan network (low and high χ , **Figure 2.13a** and **Figure 2.13b**). In clustered butanoyl-chitosan, instead, DOX molecules either adsorb onto/within the chitosan clusters or travel freely through the large pores (**Figure 2.13d**). This indicates that, as in acetyl-chitosan systems, a high number of interactions occur between DOX and butanoyl-chitosan at high χ (**Table 2.2**); at the same time, the DOX molecules freely migrating through the large pore determine a strong increase in the overall diffusion coefficients, as indicated by the comparison in mean-squared displacement (MSD) *vs.* time for both adsorbed and freely migrating DOX molecules (**Figure 2.14**). It is also crucial to note that the chitosan *vs.* water ratio and – consequently – the channel *vs.* cluster ratio is much higher in the experimental systems than in the simulated networks. We therefore expect the actual hydrogel to mirror the increase in the diffusion coefficient with χ observed in the coarse-grained simulations.

The faster dynamics enabled by the smoother energy landscapes featured in coarse-grained simulations may introduce some error in the calculation of the diffusion constants; however, the comparison among the migration of drug molecules in different networks provides a reliable

evaluation of the influence of the network morphology and physicochemical properties on drug transport. In the cluster/channel morphology, in particular, the difference between diffusional pathways of single-drug molecules becomes very pronounced, with drug molecules experiencing sharper differences in the morphology of the medium through which they diffuse. Collectively, these single-drug simulations indicate that the hydrophobicity driven morphing of the hydrogel structure affects drug diffusion by two opposing mechanisms: first, the larger pores favor the migration of the drug molecules; and second, the nesting of the modification groups within the core of the clusters is responsible for strong adsorption of the drug molecules that collide with the chitosan clusters; notably, our simulations indicate that while both DOX and GEM are affected by the first mechanism, only DOX undergoes the second mechanism. We anticipate that the high water/polymer ratio of the real chitosan hydrogels makes the first mechanism dominant over the second.

2.3.2.4. Simulation of Dual-Drug Migration through Modified Chitosan Hydrogels

We finally sought to understand how the combination of multiple drugs affects the molecular interactions and diffusion through the networks for different types and degrees of modification. Such understanding is needed to gain control over the kinetics and molar ratio of release when using synergistic drug combinations. While numerous *in silico* models have been developed to simulate the migration of single drugs through polymer hydrogel networks [69, 70], models for multiple drugs are much less common. Combining drugs, especially with different physicochemical properties, in fact, introduces considerable complexity related to drug-drug interactions and their effect on drug-polymer interactions.

Following the procedure outlined above, we performed coarse-grained simulations of equimolar GEM and DOX migration through the different chitosan networks and calculated the

diffusion constants for both drugs. Notably, the values derived from dual-drug release (**Figure 2.15**) show rather different trends from those obtained with single drugs (**Figure 2.12**). In particular, the diffusion of DOX remains almost constant across the entire range of χ for both acetyl- and butanoyl-chitosan. The diffusion of GEM is also markedly different. With an evenly spaced modification pattern, GEM diffusion decreases with χ through both acetyl- and butanoyl-chitosan. With the blocky modification pattern, instead, GEM diffusion increases with χ through acetyl-chitosan and is almost constant with χ through butanoyl-chitosan. These differences are actually the result of drug-drug interactions, which significantly affect drug-polymer interactions. This is confirmed by the radial distribution functions for GEM around DOX molecules, which indicate a strong tendency of the two drug molecules to aggregate. As can be seen from the double-peak shape of the curves in **Figure 2.16**, in fact, clusters comprising one DOX, and two GEM molecules are frequently formed.

2.3.3. Experimental Single-Drug Release

2.3.3.1. Kinetic Profiles of Single-Drug Release

Single-drug release experiments were performed by contacting 150 mg of drug-loaded hydrogel with PBS at pH 7.4 to simulate physiological conditions. The drug release profiles presented in **Figure 2.17** were obtained using acetyl- and butanoyl-chitosan gels with χ of 25%, which is comparable to the lowest modification investigated in the MD simulations. The analogous plot for heptanoyl-chitosan is reported in **Figure 2.18**, and all of the other release profiles for different modification types and degree are reported in **Figure 2.19 – Figure 2.21**. Collectively, these data indicate that the choice of modification has a profound impact on the kinetics of drug release.

In the acetyl-chitosan gel (**Figure 2.17a** and **Figure 2.17c**), GEM is released slightly more rapidly than DOX, achieving 20% release in about 1 h, compared with 6.5 h for DOX. Notably, the two drugs are released at different doses; in particular, the hydrogels released ~40% of the GEM payload (100 µg) and ~25% of the loaded DOX (32 µg) over 72 h, corresponding to a molar ratio of 6.3 of GEM/DOX. The difference in both release kinetics and dose can be related to the physicochemical properties of the two drugs, DOX being moderately hydrophobic and GEM being very hydrophilic. These results agree with the simulations of single-drug diffusion through acetyl-chitosan, wherein the hydrophobic interactions between DOX and the acetyl moieties displayed throughout the homogeneous network decrease its migration compared with GEM, which exhibits no change in the diffusion coefficient as modification prevalence increases in the acetyl-chitosan network (**Figure 2.12a** and **Figure 2.12b**).

The butanoyl-chitosan hydrogel shows a markedly different behavior (**Figure 2.17b** and **Figure 2.17d**), with DOX being released more rapidly than GEM, reaching 20% release instantaneously compared with 1 h for GEM. Additionally, the hydrogels released ~45% of the GEM payload (98 µg) and ~60% of the DOX payload (78 µg) over a 72 h period, corresponding to a molar ratio of 2.6 of GEM/DOX. These results corroborate the single-drug diffusion simulations through the butanoyl-chitosan networks (**Figure 2.12c** and **Figure 2.12d**), which indicated that the release of DOX is not affected by LJ-type interactions with the modified chitosan chains, but is rather governed by rapid migration through the large channels produced by the hydrophobic clustering of the butanoyl-chitosan chains. The release of GEM, on the other hand, is unaffected by the transition of a homogenous to heterogeneous structure. Both the computational (**Figure 2.12a** and **Figure 2.12c**) and experimental (**Figure 2.16a** and **Figure 2.16b**) results of drug diffusion indicate that there is no dependence of GEM diffusion on modification type and

pattern. The release profiles of DOX and GEM obtained from chitosan hydrogels constructed with different degrees of acetylation (15–55%) (**Figure 2.19**) and butanoation (15–40%) (**Figure 2.20**) consistently align with the *in silico* results, corroborating the correlation between drug release kinetics and hydrophobicity driven morphing of the hydrogel microstructure provided by our coarse-grained model. Drug release from heptanoyl-chitosan gels across a range of χ between 15 and 35% (**Figure 2.21**) showed strong similarity with that from butanoyl-chitosan gels. These results were anticipated, given than heptanoyl moieties, owing to their higher hydrophobicity, are expected to trigger the formation of the cluster-channels microstructure at low degrees of modification.

2.3.3.2. Equilibrium Single-Drug Release

The values of equilibrium release, defined to be the asymptotic values of drug release ($t > 30$ h), and the corresponding GEM/DOX molar ratio from the different acetyl- and butanoyl-modified gels are collated in **Figure 2.22**, where they are plotted against the degree of acetyl and butanoyl modification (χ_A and χ_B). Analogous plots obtained with heptanoyl-modified gels are reported in **Figure 2.23**.

For acetyl-modified gels (**Figure 2.22a**), a downward trend in DOX release is observed as χ increases, from a 36% release (native chitosan, $\chi_A = 0.150$) to a 7% release ($\chi_A = 0.592$). This is indicative of DOX retention in the hydrogel network by hydrophobic adsorption of the drug on the acetyl modifications (**Table 2.2**), as the hydrogel maintains a homogenous structure. The release of GEM fluctuates between 35% release ($\chi_A = 0.150$) and 46% release ($\chi_A = 0.531$), indicating a quasi-constant release within experimental error. The hydrophilic character of GEM minimized its nonbonded interaction with the acetyl moieties (**Table 2.2**), rendering its diffusion independent of χ . In butanoyl-chitosan gels (**Figure 2.22b**), the amount of DOX released increases significantly

with χ , from a 36% release ($\chi_B = 0.150$) to a 92% release ($\chi_B = 0.384$), whereas GEM release remains relatively constant, varying from a 35% release ($\chi_B = 0.150$) to a 36% release ($\chi_B = 0.411$) with no statistically significant difference across all modifications.

These trends fully agree with the results obtained from the single-drug diffusion simulations (**Figure 2.12**), indicating that the migration of DOX is controlled by the hydrophobic interactions with the acetyl-chitosan chains arranged in a homogeneous gel and by pure diffusion across the cluster/channels structure of butanoyl-chitosan gels. The migration of GEM, instead, is effectively independent of gel modification and microstructure, likely a result of GEM's hydrophilicity. As discussed above, the trend of DOX release seems to corroborate the hypothesis of a blocky modification pattern, wherein the clusters feature a micellar structure comprising a hydrophobic core rich in butanoyl-chitosan segments and a hydrophilic shell formed by unmodified chitosan segments. In this scenario, in fact, DOX migrates more rapidly than in the case of chitosan modified by evenly spaced modification, where the surface of clusters may display butanoyl groups that would adsorb DOX, thereby hindering its migration.

2.3.3.3. Mathematical Model Fitting

Drug release data from acetyl-, butanoyl-, and heptanoyl-modified gels loaded with either GEM or DOX were fitted to several empirical models, listed in **Table 2.1**. The fitting results summarized in **Table 2.3 – Table 2.5** indicate that the Korsmeyer-Peppas model provided the best fit for the release of both DOX and GEM from the hydrogels utilized in this study. In the Korsmeyer-Peppas model, the values of the diffusion (or release) exponent, n , and the kinetic constant, K , are correlated to the mechanism of release and the diffusion coefficient, respectively [42]. In particular, $n \leq 0.45$ indicates a classical Fickian diffusion mechanism from cylindrical matrices. The fitted values of these parameters for acetyl- and butanoyl-chitosan gels are reported

in **Table 2.6** and **Table 2.7**, respectively. For all of the gels, release of DOX and GEM followed the Fickian mechanism.

Notably, the data indicate a clear trend for the kinetic constant K (**Figure 2.24**), which is linked to the diffusion coefficient. In acetyl-modified gels (**Figure 2.24a**), the K values for GEM fluctuate between 11.4 and 19.5, without a strong correlation to χ . The K values for DOX, on the other hand, drastically decrease from 16.6 to 2.3 with increasing χ . This translates in a decrease of the effective diffusion coefficient of DOX with χ , due to the increasing number of nonbonded interactions between DOX and the modified chitosan chains at higher χ_A as predicted by our *in silico* model (**Table 2.2**).

The butanoyl-modified gels also showed values of $n \leq 0.45$ for both drugs, indicating a purely Fickian diffusion mechanism of migration through the hydrogel. As with acetyl-modified gels, the values of K for GEM release from butanoyl-modified gels fluctuate between 15.8 and 18.8, showing no correlation with χ (**Figure 2.24b**). In contrast, the value of K for DOX doubles over the range of χ , going from 20.9 to 50.8. As χ increases, in fact, the butanoyl moieties morph the hydrogel structure from a homogeneous network to a heterogeneous cluster/channel structure. Once again, as hypothesized for the blocky modification pattern, the large channels and the concealment of the hydrophobic modifications within the clusters result in a doubling of the effective diffusion coefficient of DOX.

2.3.4. Experimental Dual-Drug Release

The final goal of this study is to develop a delivery system that releases multiple chemotherapeutics with precise kinetics and a molar ratio conducive to synergistic therapeutic effects. We therefore performed a number of dual-drug release studies aimed at correlating the release kinetics and doses of GEM and DOX with the type and degree of modification of the

chitosan hydrogel. As in the single-drug studies, dual-drug release was performed using acetyl-, butanoyl-, and heptanoyl-modified gels spanning a range of modification levels comparable to those utilized in the dual-drug *in silico* modeling. Specifically, acetyl-chitosan gels covered the range of χ values between 0.249 and 0.592, whereas butanoyl-chitosan gels covered a range between 0.189 and 0.334. The resulting release profiles (percent release *vs.* time) are reported in **Figure 2.25 – Figure 2.27**.

In all dual-drug release studies, the asymptotic release was obtained within 24 h, resulting in wide ranges of equilibrium GEM/DOX molar ratios for both acetyl-chitosan and butanoyl-chitosan gels, as shown in **Figure 2.28**. In acetyl-chitosan gels, the equilibrium GEM/DOX molar ratio increases with χ from 2.2 at $\chi_A = 0.264$ to 14.3 at $\chi_A = 0.592$. In butanoyl-chitosan gels, the GEM/DOX ratio decreases with χ , from 10.0 at $\chi_B = 0.189$ to 5.2 at $\chi_B = 0.334$. These trends show some similarity with single-drug release data, although the GEM/DOX ratios are considerably higher for dual-drug release than for the single-drug release.

In addition to equilibrium data, kinetic release properties were determined by fitting the GEM and DOX release data to the Korsmeyer-Peppas model, reported for both acetyl- and butanoyl-chitosan in **Figure 2.29**. It is important to notice that the diffusion rate for DOX is nearly constant across the entire range of χ for both acetyl- and butanoyl-chitosan, whereas the GEM diffusion rate slightly increases with χ through acetyl-chitosan and is almost constant with χ through butanoyl-chitosan. These results match the dual-drug release profile predicted by our MD simulations (**Figure 2.15**) for chitosan modified with a blocky pattern, thereby corroborating the hypothesis of blocky modification. For both acetyl- and butanoyl- modified gels, the K values for GEM and DOX do not show a strong correlation with χ , likely due to the drug-drug interactions within the chitosan matrix, which are also predicted by the MD simulations (**Figure 2.16**).

Nonetheless, as observed in single-drug release studies, the releases of GEM and DOX were characterized by markedly different values of K , indicating that GEM is released more rapidly than DOX.

These dual-drug studies demonstrate the efficacy of modified chitosan gels for combined chemotherapeutic treatment. First, the formulations studied herein afford the desired schedule, with GEM being released prior to DOX; in all dual-drug studies, in fact, the ratio of K values (GEM/DOX) ranges from 2.0 to 9.0, with a mean of 5.4, indicating release of GEM much faster than DOX. Second, the desired molar ratio (dose), namely, the molar ratio yielding the highest synergy (GEM/DOX = ~10), is present from 32 to 42% modification in acetyl-modified gels and from 19 to 24% modification in butanoyl-modified gels. These findings are consistent with the current literature demonstrating that the combination of GEM and DOX can be administered such that a synergistic efficacy may be observed *in vitro* or *in vivo* when the aforementioned kinetics and dose are present [7, 41].

2.4. Conclusions

Hydrogels constructed with native or modified polysaccharides and loaded with chemotherapeutic drugs have been extensively studied, and a number of them have entered the clinical pipeline through the last decade [71-74]. A growing body of literature focuses on polymer conjugates and hydrogels that deliver synergistic combinations of drugs. In developing these systems for a given drug combination, the choice of the modification groups, degree of modification, and initial drug loading are crucial to ensure the therapeutic efficacy of the formulation. Empirical exploration of such a wide design space, however, is cumbersome and hinders the preclinical stages. This study focuses on developing a computationally designed and

experimentally validated system that could serve as a powerful guide to pharmaceutical chemists in the identification of the design parameters that afford a schedule and a ratio of drug release that ensure a successful therapeutic outcome. Specifically, the proposed model has managed to accurately portray complex phenomena, such as the different microscale morphologies present in hydrogels constructed with different types and degrees of modification, and the migration of not only one but also two drugs through these modified polymer networks. The experimental data validate the behaviors predicted by the molecular dynamics simulations and indicate specific formulations that afford synergistic combinations for the specific drug pair considered in this study (DOX and GEM) within the scope of the current literature. While focusing on hydrophobically modified chitosan hydrogels and the GEM-DOX drug pair, this method is applicable to any other polymer substrates, whether natural or synthetic, modification moiety, and therapeutic payload. The results presented in this work fully demonstrate the potential of this approach to accelerate the translation of drug-loaded hydrogels for cancer therapy.

REFERENCES

- [1] Zhang, D., and D. Fan, New Insights into the Mechanisms of Gastric Cancer Multidrug Resistance and Future Perspectives. *Future Oncology*, 2010. 6: p. 527-537.
- [2] Saeki, T., T. Tsuruo, W. Sato, and K. Nishikawa, Drug Resistance in Chemotherapy for Breast Cancer. *Cancer Chemotherapy and Pharmacology*, 2005. 56: p. 84-89.
- [3] Frączek, N., I. Bronisz, M. Pietryka, et al., An Outline of Main Factors of Drug Resistance Influencing Cancer Therapy. *Journal of Chemotherapy*, 2016. 28: p. 457-464.
- [4] Lotfi-Jam, K., M. Carey, M. Jefford, et al., Nonpharmacologic Strategies for Managing Common Chemotherapy Adverse Effects: A Systematic Review. *Journal of Clinical Oncology*, 2008. 26: p. 5618-5629.
- [5] Genre, D., C. Protière, G. Macquart-Moulin, et al., Quality of Life of Breast Cancer Patients Receiving High-Dose-Intensity Chemotherapy: Impact of Length of Cycles. *Supportive Care in Cancer*, 2002. 10: p. 222-230.
- [6] Chou, T.-C., Drug Combination Studies and Their Synergy Quantification Using the Chou-Talalay Method. *Cancer Research*, 2010. 70: p. 440-446.
- [7] Vogus, D.R., M.A. Evans, A. Pusuluri, et al., A Hyaluronic Acid Conjugate Engineered to Synergistically and Sequentially Deliver Gemcitabine and Doxorubicin to Treat Triple Negative Breast Cancer. *Journal of Controlled Release*, 2017. 267: p. 191-202.
- [8] Rui, M., Y. Xin, R. Li, et al., Targeted Biomimetic Nanoparticles for Synergistic Combination Chemotherapy of Paclitaxel and Doxorubicin. *Molecular Pharmaceutics*, 2017. 14: p. 107-123.
- [9] Li, T., Y.-H. Ling, I.D. Goldman, and R. Perez-Soler, Schedule-Dependent Cytotoxic Synergism of Pemetrexed and Erlotinib in Human Non-Small Cell Lung Cancer Cells. *Clinical Cancer Research*, 2007. 13: p. 3413-3422.
- [10] Meczes, E.L., A.D.J. Pearson, C.A. Austin, and M.J. Tilby, Schedule-Dependent Response of Neuroblastoma Cell Lines to Combinations of Etoposide and Cisplatin. *British Journal of Cancer*, 2002. 86: p. 485-489.
- [11] Hu, Q., W. Sun, C. Wang, and Z. Gu, Recent Advances of Cocktail Chemotherapy by Combination Drug Delivery Systems. *Advanced Drug Delivery Reviews*, 2016. 98: p. 19-34.
- [12] Camacho, K.M., S. Menegatti, and S. Mitragotri, Low-Molecular-Weight Polymer-Drug Conjugates for Synergistic Anticancer Activity of Camptothecin and Doxorubicin Combinations. *Nanomedicine*, 2016. 11: p. 1139-1151.

- [13] Zhang, Y., C. Yang, W. Wang, et al., Co-Delivery of Doxorubicin and Curcumin by PH-Sensitive Prodrug Nanoparticle for Combination Therapy of Cancer. *Scientific Reports*, 2016. 6: p. 21225.
- [14] Huang, W.-T., M. Larsson, Y.-C. Lee, et al., Dual Drug-Loaded Biofunctionalized Amphiphilic Chitosan Nanoparticles: Enhanced Synergy between Cisplatin and Demethoxycurcumin against Multidrug-Resistant Stem-like Lung Cancer Cells. *European Journal of Pharmaceutics and Biopharmaceutics*, 2016. 109: p. 165-173.
- [15] Camacho, K.M., S. Menegatti, D.R. Vogus, et al., DAFODIL: A Novel Liposome-Encapsulated Synergistic Combination of Doxorubicin and 5FU for Low Dose Chemotherapy. *Journal of Controlled Release*, 2016. 229: p. 154-162.
- [16] Zhang, B., T. Wang, S. Yang, et al., Development and Evaluation of Oxaliplatin and Irinotecan Co-Loaded Liposomes for Enhanced Colorectal Cancer Therapy. *Journal of Controlled Release*, 2016. 238: p. 10-21.
- [17] Scarano, W., P. de Souza, and M.H. Stenzel, Dual-Drug Delivery of Curcumin and Platinum Drugs in Polymeric Micelles Enhances the Synergistic Effects: A Double Act for the Treatment of Multidrug-Resistant Cancer. *Biomaterials Science*, 2014. 3: p. 163-174.
- [18] Zhang, P., J. Li, M. Ghazwani, et al., Effective Co-Delivery of Doxorubicin and Dasatinib Using a PEG-Fmoc Nanocarrier for Combination Cancer Chemotherapy. *Biomaterials*, 2015. 67: p. 104-114.
- [19] Zhou, D., H. Xiao, F. Meng, et al., A Polymer-(Tandem Drugs) Conjugate for Enhanced Cancer Treatment. *Advanced Healthcare Materials*, 2013. 2: p. 822-827.
- [20] Li, X., R. Fan, Y. Wang, et al., In Situ Gel-Forming Dual Drug Delivery System for Synergistic Combination Therapy of Colorectal Peritoneal Carcinomatosis. *RSC Advances*, 2015. 5: p. 101494-101506.
- [21] Wu, X., C. He, Y. Wu, and X. Chen, Synergistic Therapeutic Effects of Schiff's Base Cross-Linked Injectable Hydrogels for Local Co-Delivery of Metformin and 5-Fluorouracil in a Mouse Colon Carcinoma Model. *Biomaterials*, 2016. 75: p. 148-162.
- [22] Huang, J., W.-J. Wang, B.-G. Li, and S. Zhu, Design and Synthesis of Poly(Butyl Acrylate) Networks through RAFT Polymerization with Crosslinking for Controlled-Release Applications. *Macromolecular Materials and Engineering*, 2013. 298: p. 391-399.
- [23] Hezaveh, H., and I.I. Muhamad, Modification and Swelling Kinetic Study of Kappa-Carrageenan-Based Hydrogel for Controlled Release Study. *Journal of the Taiwan Institute of Chemical Engineers*, 2013. 44: p. 182-191.
- [24] Hoare, T.R., and D.S. Kohane, Hydrogels in Drug Delivery: Progress and Challenges. *Polymer*, 2008. 49: p. 1993-2007.

- [25] Li, J., and D.J. Mooney, Designing Hydrogels for Controlled Drug Delivery. *Nature Reviews Materials*, 2016. 1: p. 16071.
- [26] Bhattacharai, N., J. Gunn, and M. Zhang, Chitosan-Based Hydrogels for Controlled, Localized Drug Delivery. *Advanced Drug Delivery Reviews*, 2010. 62: p. 83-99.
- [27] Hu, L., Y. Sun, and Y. Wu, Advances in Chitosan-Based Drug Delivery Vehicles. *Nanoscale*, 2013. 5: p. 3103-3111.
- [28] Riva, R., H. Ragelle, A. desRieux, et al., Chitosan and Chitosan Derivatives in Drug Delivery and Tissue Engineering, in Chitosan for Biomaterials II (ed. R. Jayakumar, M. Prabaharan, and R.A.A. Muzzarelli), 2011, Springer: Berlin Heidelberg-Verlag. p. 19-44.
- [29] Peppas, N.A., J.Z. Hilt, A. Khademhosseini, and R. Langer, Hydrogels in Biology and Medicine: From Molecular Principles to Bionanotechnology. *Advanced Materials*, 2006. 18: p. 1345-1360
- [30] Nur, M., and T. Vasiljevic, Can Natural Polymers Assist in Delivering Insulin Orally?. *International Journal of Biological Macromolecules*, 2017. 103: p. 889-901.
- [31] Hong, S.-C., S.-Y. Yoo, H. Kim, and J. Lee, Chitosan-Based Multifunctional Platforms for Local Delivery of Therapeutics. *Marine Drugs*, 2017. 15: p. 60.
- [32] Lam, P.L., and R. Gambari, Advanced Progress of Microencapsulation Technologies: In Vivo and in Vitro Models for Studying Oral and Transdermal Drug Deliveries. *Journal of Controlled Release*, 2014. 178: p. 25-45
- [33] Perilla, J.R., B.C. Goh, C.K. Cassidy, et al., Molecular Dynamics Simulations of Large Macromolecular Complexes. *Current Opinions in Structural Biology*, 2015. 31: p. 64-74.
- [34] Katiyar, R.S., and P.K. Jha, Molecular Simulations in Drug Delivery: Opportunities and Challenges. *Wiley Interdisciplinary Reviews: Computational Molecular Science*, 2018. 8: p. e1358
- [35] Albano, J.M.R., E. de Paula, and M. Pickholz, Molecular Dynamics Simulations to Study Drug Delivery Systems, in Molecular Dynamics (ed. A. Vakhrushev), 2018. IntechOpen: London, United Kingdom. p. 74-90.
- [36] Liu, D., Y. Chen, X. Feng, et al., Micellar Nanoparticles Loaded with Gemcitabine and Doxorubicin Showed Synergistic Effect. *Colloids and Surfaces B: Biointerfaces*, 2014. 113: p. 158-168.
- [37] Lammers, T., V. Subr, K. Ulbrich, et al., Simultaneous Delivery of Doxorubicin and Gemcitabine to Tumors in Vivo Using Prototypic Polymeric Drug Carriers. *Biomaterials*, 2009. 30: p. 3466-3475

- [38] Nahire, R., M.K. Haldar, S. Paul, et al., Multifunctional Polymersomes for Cytosolic Delivery of Gemcitabine and Doxorubicin to Cancer Cells. *Biomaterials*, 2014. 35: p. 6482-6497.
- [39] Croissant, J.G., D. Zhang, S. Alsaiari, et al., Protein-Gold Clusters-Capped Mesoporous Silica Nanoparticles for High Drug Loading, Autonomous Gemcitabine/Doxorubicin Co-Delivery, and in-Vivo Tumor Imaging. *Journal of Controlled Release*, 2016. 229: p. 183-191.
- [40] Ni, S., L. Qiu, G. Zhang, et al., Lymph Cancer Chemotherapy: Delivery of Doxorubicin-Gemcitabine Prodrug and Vincristine by Nanostructured Lipid Carriers. *International Journal of Nanomedicine*, 2017. 12: p. 1565-1576.
- [41] Vogus, D.R., A. Pusuluri, R. Chen, and S. Mitragotri, Schedule Dependent Synergy of Gemcitabine and Doxorubicin: Improvement of in Vitro Efficacy and Lack of in Vitro-in Vivo Correlation. *Bioengineering and Translational Medicine*, 2018. 3: p. 49-57.
- [42] Korsmeyer, R.W., R. Gurny, E. Doelker, et al., Mechanisms of Solute Release from Porous Hydrophilic Polymers. *International Journal of Pharmaceutics*, 1983. 15: p. 25-35.
- [43] Kubota, N., N. Tatsumoto, T. Sano, and K. Toya, A Simple Preparation of Half N-Acetylated Chitosan Highly Soluble in Water and Aqueous Organic Solvents. *Carbohydrate Research*, 2000. 324: p. 268-274.
- [44] Kaiser, E., R.L. Colescott, C.D. Bossinger, and P.I. Cook, Color Test for Detection of Free Terminal Amino Groups in the Solid-Phase Synthesis of Peptides. *Analytical Biochemistry*, 1970. 34: p. 595-598.
- [45] Van Der Spoel, D.V.D., E. Lindahl, B. Hess, et al., GROMACS: Fast, Flexible, and Free. *Journal of Computational Chemistry*, 2005. 26: p. 1701-1718.
- [46] Kirschner, K.N., A.B. Yongye, S.M Tschampel, et al., GLYCAM06: A Generalizable Biomolecular Force Field. *Carbohydrates. Journal of Computational Chemistry*, 2008. 29: p. 622-655.
- [47] Sauter, J., and A. Grafmüller, Predicting the Chemical Potential and Osmotic Pressure of Polysaccharide Solutions by Molecular Simulations. *Journal of Chemical Theory and Computation*, 2016. 12: p. 4375-4384.
- [48] Case, D.A, T.A. Darden, T.E. Cheatham III, et al., AMBER 10; University of California: San Francisco, 2008.
- [49] Darden, T., D. York, and L. Pedersen, Particle Mesh Ewald: An $N \cdot \log(N)$ Method for Ewald Sums in Large Systems. *Journal of Chemical Physics*, 1993. 98: p. 10089-10092.
- [50] Parrinello, M., and A. Rahman, Polymorphic Transitions in Single Crystals: A New Molecular Dynamics Method. *Journal of Applied Physics*, 1981. 52: p. 7182-7190.

- [51] Rühle, V., C. Junghans, A. Lukyanov, et al., Versatile Object-Oriented Toolkit for Coarse-Graining Applications. *Journal of Chemical Theory and Computation*, 2009. 5: p. 3211-3223.
- [52] Lu, L., S. Izvekov, A. Das, et al., Efficient, Regularized, and Scalable Algorithms for Multiscale Coarse-Graining. *Journal of Chemical Theory and Computation*, 2010. 6: p. 954-965.
- [53] Sauter, J., and A. Grafmüller, Procedure for Transferable Coarse-Grained Models of Aqueous Polysaccharides. *Journal of Chemical Theory and Computation*, 2017. 13: p. 223-236.
- [54] Patra, P.K., and B.A. Bhattacharya, A Deterministic Thermostat for Controlling Temperature Using All Degrees of Freedom. *Journal of Chemical Physics*, 2014. 140: p. 064106.
- [55] Nosé, S.A., A Unified Formulation of the Constant Temperature Molecular Dynamics Methods. *Journal of Chemical Physics*, 1984. 81: p. 511-519.
- [56] Hoover, W.G., Canonical Dynamics: Equilibrium Phase-Space Distributions. *Physical Review A*, 1985. 31: p. 1695-1697.
- [57] Bhattacharya, S., and K.E. Gubbins, Fast Method for Computing Pore Size Distributions of Model Materials. *Langmuir*, 2006. 22: p. 7726-7731.
- [58] Kappel, F., and A.V. Kuntsevich, An Implementation of Shor's r-Algorithm. *Computational Optimization and Applications*, 2000. 15: p. 193-205.
- [59] Dash, S., P.N. Murthy, L. Nath, and P. Chowdhury, Kinetic Modeling on Drug Release from Controlled Drug Delivery Systems. *Acta Poloniae Pharmaceutica*, 2010. 67: p. 217-223.
- [60] Hixson, A.W., and J.H. Crowell, Dependence of Reaction Velocity upon Surface and Agitation. *Industrial and Engineering Chemistry*, 1931. 23: p. 923-931.
- [61] Higuchi, T., Theoretical Analysis of Rate of Release of Solid Drugs Dispersed in Solid Matrices. *Journal of Pharmaceutical Sciences*, 1963. 52: p. 1145-1149.
- [62] Ercolessi, F., and J.B. Adams, Interatomic Potentials from First-Principles Calculations: The Force-Matching Method. *Europhysics Letters*, 1994. 26: p. 583-588.
- [63] Noid, W.G., J.-W. Chu, G.S. Ayton, et al., The Multiscale Coarse-Graining Method. I. A Rigorous Bridge between Atomistic and Coarse-Grained Models. *Journal of Chemical Physics*, 2008. 128: p. 244114.
- [64] Lu, L., J.F. Dama, and G.A. Voth, Fitting Coarse-Grained Distribution Functions through an Iterative Force-Matching Method. *Journal of Chemical Physics*, 2013. 139: p. 121906.

- [65] Ortona, O., G. D'Errico, G. Mangiapia, and D. Ciccarelli, The Aggregative Behavior of Hydrophobically Modified Chitosans with High Substitution Degree in Aqueous Solution. *Carbohydrate Polymers*, 2008. 74: p. 16-22.
- [66] Jiang, G.-B., D. Quan, K. Liao, and H. Wang, Preparation of Polymeric Micelles Based on Chitosan Bearing a Small Amount of Highly Hydrophobic Groups. *Carbohydrate Polymers*, 2006. 66: p. 514-520.
- [67] Rinaudo, M., R. Auzely, C. Vallin, and I. Mullagaliev, Specific Interactions in Modified Chitosan Systems. *Biomacromolecules*, 2005. 6: p. 2396-2407.
- [68] Philippova, O.E., and E.V. Korchagina, Chitosan and Its Hydrophobic Derivatives: Preparation and Aggregation in Dilute Aqueous Solutions. *Polymer Science, Series A*, 2012. 54: p. 552-572.
- [69] Yeh, P.D., and A. Alexeev, Mesoscale Modelling of Environmentally Responsive Hydrogels: Emerging Applications. *Chemical Communications*, 2015. 51: p. 10083-10095.
- [70] Decuzzi, P., Facilitating the Clinical Integration of Nanomedicines: The Roles of Theoretical and Computational Scientists. *ACS Nano*, 2016. 10: p. 8133-8138.
- [71] Svenson, S., M. Wolfgang, J. Hwang, et al., Preclinical to Clinical Development of the Novel Camptothecin Nanopharmaceutical CRLX101. *Journal of Controlled Release*, 2011. 153: p. 49-55.
- [72] Schluep, T., J. Hwang, I.J. Hildebrandt, et al., Pharmacokinetics and Tumor Dynamics of the Nanoparticle IT-101 from PET Imaging and Tumor Histological Measurements. *Proceedings of the National Academy of Sciences of the United States of America*, 2009. 106: p. 11394-11399.
- [73] Weiss, G.J., J. Chao, J.D. Neidhart, et al., First-in-Human Phase 1/2a Trial of CRLX101, a Cyclodextrin-Containing Polymer-Camptothecin Nanopharmaceutical in Patients with Advanced Solid Tumor Malignancies. *Investigational New Drugs*, 2013. 31: p. 986-1000.
- [74] Clark, A.J., D.T. Wiley, J.E. Zuckerman, et al., CRLX101 Nanoparticles Localize in Human Tumors and Not in Adjacent, Nonneoplastic Tissue after Intravenous Dosing. *Proceedings of the National Academy of Sciences of the United States of America*, 2016. 113: p. 3850-3854.

Tables

Table 2.1 Empirical models of drug diffusion used to fit the release profiles for DOX and GEM from acetyl-, butanoyl-, and heptanoyl-chitosan hydrogels.

Mathematical Model	Form
Zero Order	$Q_t = Q_0 + Kot$
First Order	$\ln Q_t = \ln Q_0 + K_1 t$
Hixson-Crowell	$Q_t^{1/3} - Q_0^{1/3} = K_{st}$
Higuchi	$Q_t = K_H t^{1/2}$
Korsmeyer-Peppas	$Q_t / Q_\infty = K_k t^n$

Table 2.2 Number and (percentage of total) of non-bonded interactions observed between drug molecules and chitosan chains (backbone and modifications) in the different chitosan networks over the drug molecules trajectories during the simulation; where DOX molecules are treated as a group so that any given chitosan or modification site can only contribute one contact. In the table, low represents $\chi = 16\%$ for both systems, and high represents $\chi = 50\%$ and 32% for acetyl- and butanoyl- modified systems, respectively.

drug		Backbone, Low	Mod., Low	Backbone, High	Mod., High
DOX	Acetyl (evenly spaced)	217 ± 14 (93.5%)	15 ± 2 (6.5%)	239 ± 11 (83.9%)	46 ± 4 (16.1%)
	Acetyl (blocky)	225 ± 12 (84.9%)	40 ± 3 (15.1%)	221 ± 11 (79.8%)	56 ± 4 (20.2%)
	Butanoyl (evenly spaced)	219 ± 15 (78.5%)	60 ± 7 (21.5%)	316 ± 23 (83.6%)	62 ± 6 (16.4%)
	Butanoyl (blocky)	276 ± 13 (83.1%)	56 ± 7 (16.9%)	371 ± 18 (88.1%)	50 ± 7 (11.9%)
GEM	Acetyl (evenly spaced)	26 ± 10 (89.7%)	3 ± 1 (10.3%)	33 ± 10 (80.5%)	8 ± 3 (19.5%)
	Acetyl (blocky)	30 ± 9 (88.2%)	4 ± 2 (11.8%)	41 ± 11 (80.4%)	10 ± 4 (19.6%)
	Butanoyl (evenly spaced)	34 ± 10 (89.5%)	4 ± 2 (10.5%)	169 ± 25 (87.6%)	24 ± 7 (12.4%)
	Butanoyl (blocky)	61 ± 11 (81.3%)	14 ± 5 (18.7%)	163 ± 16 (80.3%)	40 ± 6 (19.7%)

Table 2.3 Summary of R^2 values obtained by fitting the empirical models of drug diffusion to the data of DOX and GEM release from acetyl-chitosan gels.

DOX:

<i>Mathematical Model</i>	R^2 ($\chi = 0.150$)	R^2 ($\chi = 0.264$)	R^2 ($\chi = 0.376$)	R^2 ($\chi = 0.408$)	R^2 ($\chi = 0.531$)	R^2 ($\chi = 0.592$)
<i>Zero Order</i>	0.653	0.675	0.700	0.783	0.431	0.789
<i>First Order</i>	0.699	0.708	0.716	0.805	0.439	0.796
<i>Hixson-Crowell</i>	0.312	0.367	0.413	0.409	0.207	0.498
<i>Higuchi</i>	0.882	0.898	0.909	0.956	0.681	0.959
<i>Korsmeyer-Peppas</i>	0.986	0.975	0.976	0.997	0.891	0.984

GEM:

<i>Mathematical Model</i>	R^2 ($\chi = 0.150$)	R^2 ($\chi = 0.264$)	R^2 ($\chi = 0.376$)	R^2 ($\chi = 0.408$)	R^2 ($\chi = 0.531$)
<i>Zero Order</i>	0.612	0.619	0.639	0.707	0.740
<i>First Order</i>	0.651	0.675	0.665	0.766	0.804
<i>Hixson-Crowell</i>	0.380	0.366	0.426	0.444	0.506
<i>Higuchi</i>	0.845	0.843	0.868	0.908	0.929
<i>Korsmeyer-Peppas</i>	0.936	0.954	0.934	0.948	0.935

Table 2.4 Summary of R^2 values obtained by fitting the empirical models of drug diffusion to the data of DOX and GEM release from butanoyl-chitosan gels.

DOX:

<i>Mathematical Model</i>	R^2 ($\chi = 0.189$)	R^2 ($\chi = 0.211$)	R^2 ($\chi = 0.249$)	R^2 ($\chi = 0.301$)	R^2 ($\chi = 0.334$)	R^2 ($\chi = 0.384$)
<i>Zero Order</i>	0.507	0.325	0.337	0.487	0.514	0.581
<i>First Order</i>	0.550	0.384	0.452	0.590	0.658	0.921
<i>Hixson-Crowell</i>	0.290	0.196	0.236	0.308	0.363	0.577
<i>Higuchi</i>	0.753	0.554	0.570	0.729	0.764	0.824
<i>Korsmeyer-Peppas</i>	0.949	0.880	0.999	0.993	0.951	0.996

GEM:

<i>Mathematical Model</i>	R^2 ($\chi = 0.189$)	R^2 ($\chi = 0.211$)	R^2 ($\chi = 0.249$)	R^2 ($\chi = 0.301$)	R^2 ($\chi = 0.334$)	R^2 ($\chi = 0.384$)
<i>Zero Order</i>	0.630	0.667	0.724	0.640	0.600	0.664
<i>First Order</i>	0.686	0.723	0.792	0.678	0.631	0.722
<i>Hixson-Crowell</i>	0.430	0.459	0.465	0.425	0.381	0.385
<i>Higuchi</i>	0.853	0.889	0.910	0.864	0.840	0.873
<i>Korsmeyer-Peppas</i>	0.920	0.971	0.957	0.925	0.954	0.955

Table 2.5 Summary of R^2 values obtained by fitting the empirical models of drug diffusion to the data of DOX and GEM release from heptanoyl-chitosan gels.

DOX:

<i>Mathematical Model</i>	R^2	R^2	R^2
	($\chi = 0.190$)	($\chi = 0.258$)	($\chi = 0.319$)
<i>Zero Order</i>	0.679	0.792	0.649
<i>First Order</i>	0.684	0.812	0.755
<i>Hixson-Crowell</i>	0.406	0.496	0.448
<i>Higuchi</i>	0.905	0.958	0.861
<i>Korsmeyer-Peppas</i>	0.949	0.978	0.918

GEM:

<i>Mathematical Model</i>	R^2	R^2	R^2
	($\chi = 0.190$)	($\chi = 0.258$)	($\chi = 0.319$)
<i>Zero Order</i>	0.749	0.671	0.755
<i>First Order</i>	0.788	0.696	0.792
<i>Hixson-Crowell</i>	0.511	0.468	0.478
<i>Higuchi</i>	0.937	0.888	0.940
<i>Korsmeyer-Peppas</i>	0.952	0.939	0.982

Table 2.6 Fitting parameters derived from the Korsmeyer-Peppas model for GEM and DOX released from acetyl-modified chitosan gels.

Fitting Values	$\chi = 0.150$	$\chi = 0.264$	$\chi = 0.376$	$\chi = 0.304$	$\chi = 0.531$	$\chi = 0.592$
<i>GEM-R²</i>	0.936	0.954	0.934	0.948	0.935	---
<i>GEM-n</i>	0.306	0.256	0.386	0.331	0.445	---
<i>GEM-K</i>	15.5	19.5	11.4	16.9	15.7	---
<i>DOX-R²</i>	0.986	0.975	0.976	0.997	0.891	0.984
<i>DOX-n</i>	0.288	0.373	0.433	0.338	0.193	0.236
<i>DOX-K</i>	16.6	10.8	6.4	5.0	5.4	2.3

Table 2.7 Fitting parameters derived from the Korsmeyer-Peppas model for GEM and DOX released from butanoyl-modified chitosan gels.

Fitting Values	$\chi = 0.189$	$\chi = 0.211$	$\chi = 0.249$	$\chi = 0.301$	$\chi = 0.334$	$\chi = 0.384$
<i>GEM-R²</i>	0.920	0.971	0.957	0.925	0.954	0.955
<i>GEM-n</i>	0.370	0.369	0.322	0.366	0.308	0.264
<i>GEM-K</i>	18.4	19.6	18.8	14.3	15.8	18.0
<i>DOX-R²</i>	0.949	0.880	0.999	0.993	0.951	0.996
<i>DOX-n</i>	0.208	0.126	0.132	0.188	0.212	0.371
<i>DOX-K</i>	20.9	36.7	46.0	39.7	50.8	46.5

Figures

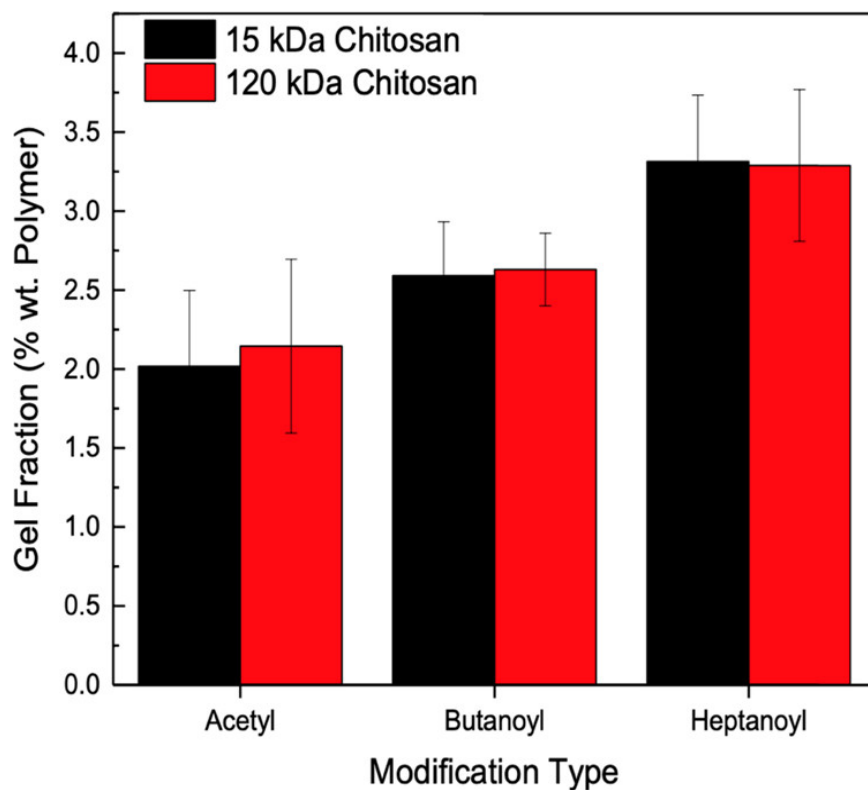


Figure 2.1 Comparison of gel fraction for acetyl-, butanoyl-, and heptanoyl-chitosan gels prepared using base chitosan polymers with molecular weights of 15 and 50-190 kDa. Data represent mean \pm 95% CI ($n \geq 12$).

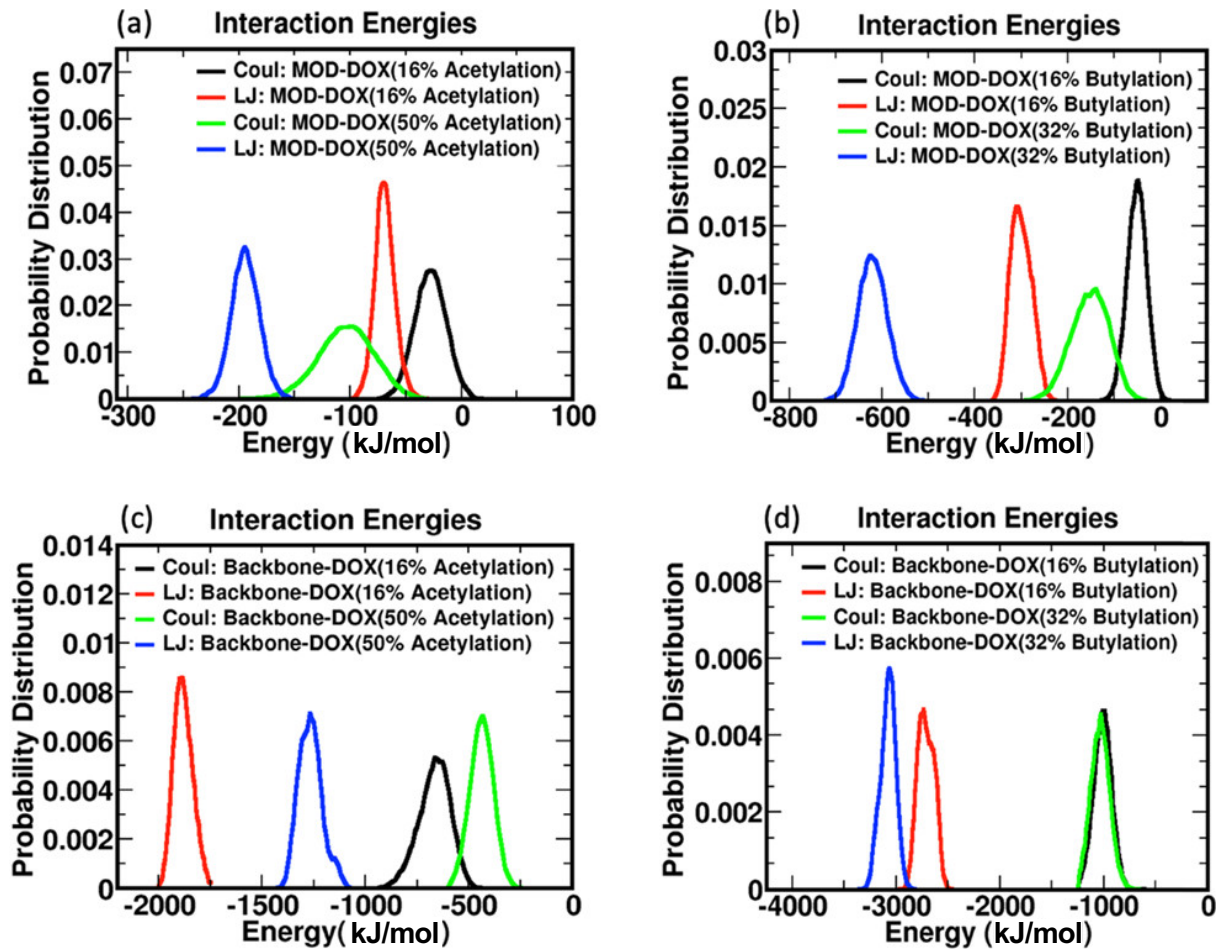


Figure 2.2 Lennard-Jones and Coulombic contribution to the DOX-modification group interaction energy for (a) acetyl-chitosan and (b) butanoyl-chitosan; and Lennard-Jones and Coulombic contribution to the DOX-backbone interaction energy for (c) acetyl-chitosan and (d) butanoyl-chitosans at different χ .

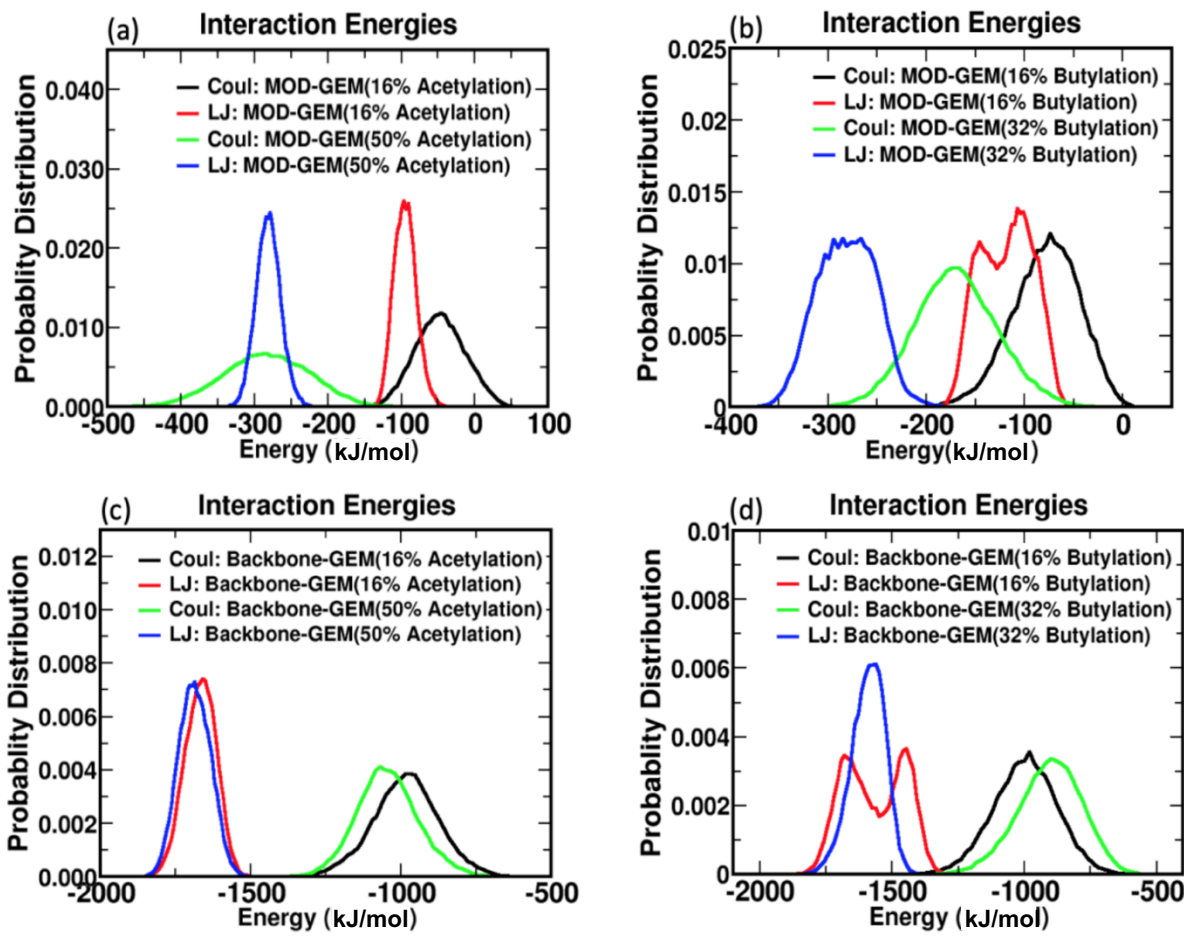


Figure 2.3 Lennard-Jones and coulombic contribution to the GEM-modification group interaction energy for **(a)** acetyl-chitosan and **(b)** butanoyl-chitosan; and Lennard-Jones and coulombic contribution to the GEM-backbone interaction energy for **(c)** acetyl-chitosan and **(d)** butanoyl-chitosans at different χ .

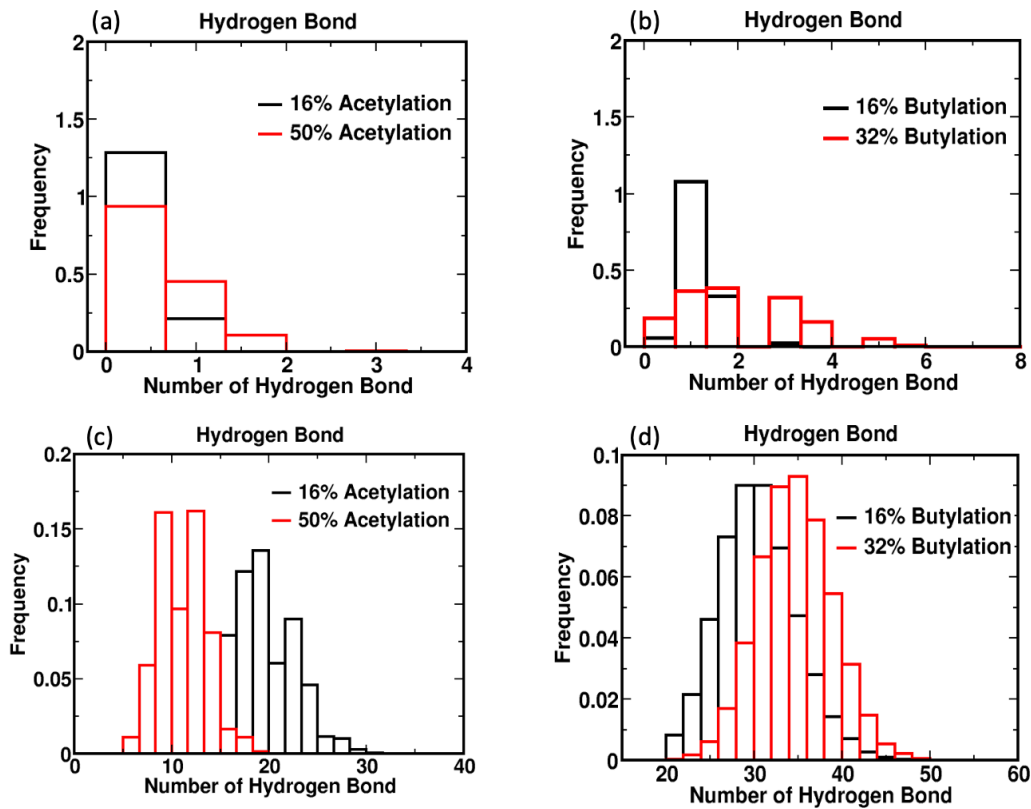


Figure 2.4 Hydrogen bond contacts between DOX and modification groups in a (a) acetyl-modified and (b) butanoyl-modified chitosan gel; and hydrogen bond contacts between DOX and the backbone in a (c) acetyl-modified and (d) butanoyl-modified chitosan gel at different degrees of modification.

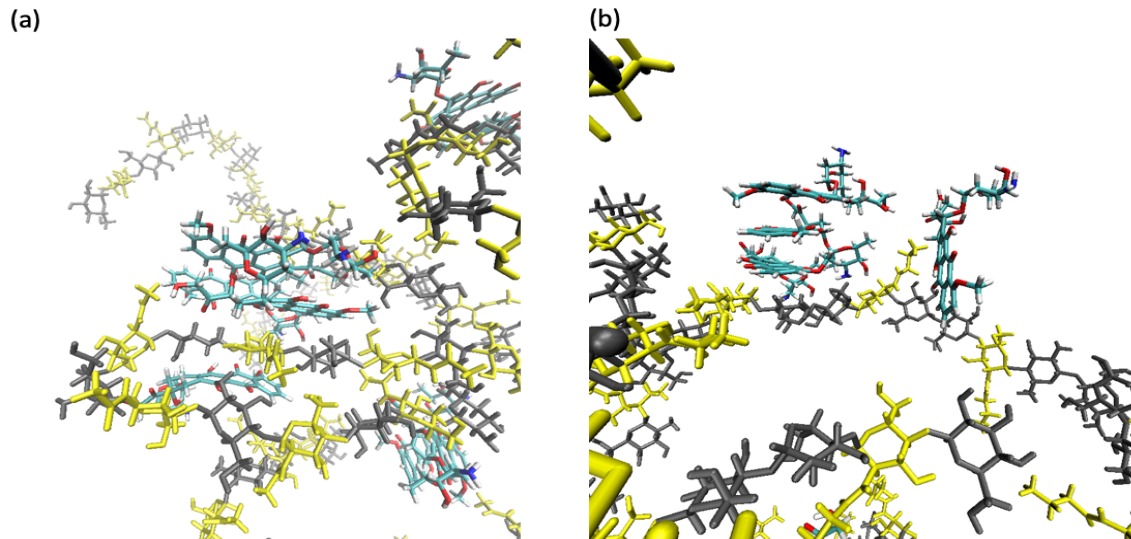


Figure 2.5 All-atom simulations depicting the interactions between DOX (cyan) and chitosan (grey and yellow) for (a) acetyl-modified and (b) butanoyl-modified chitosans.

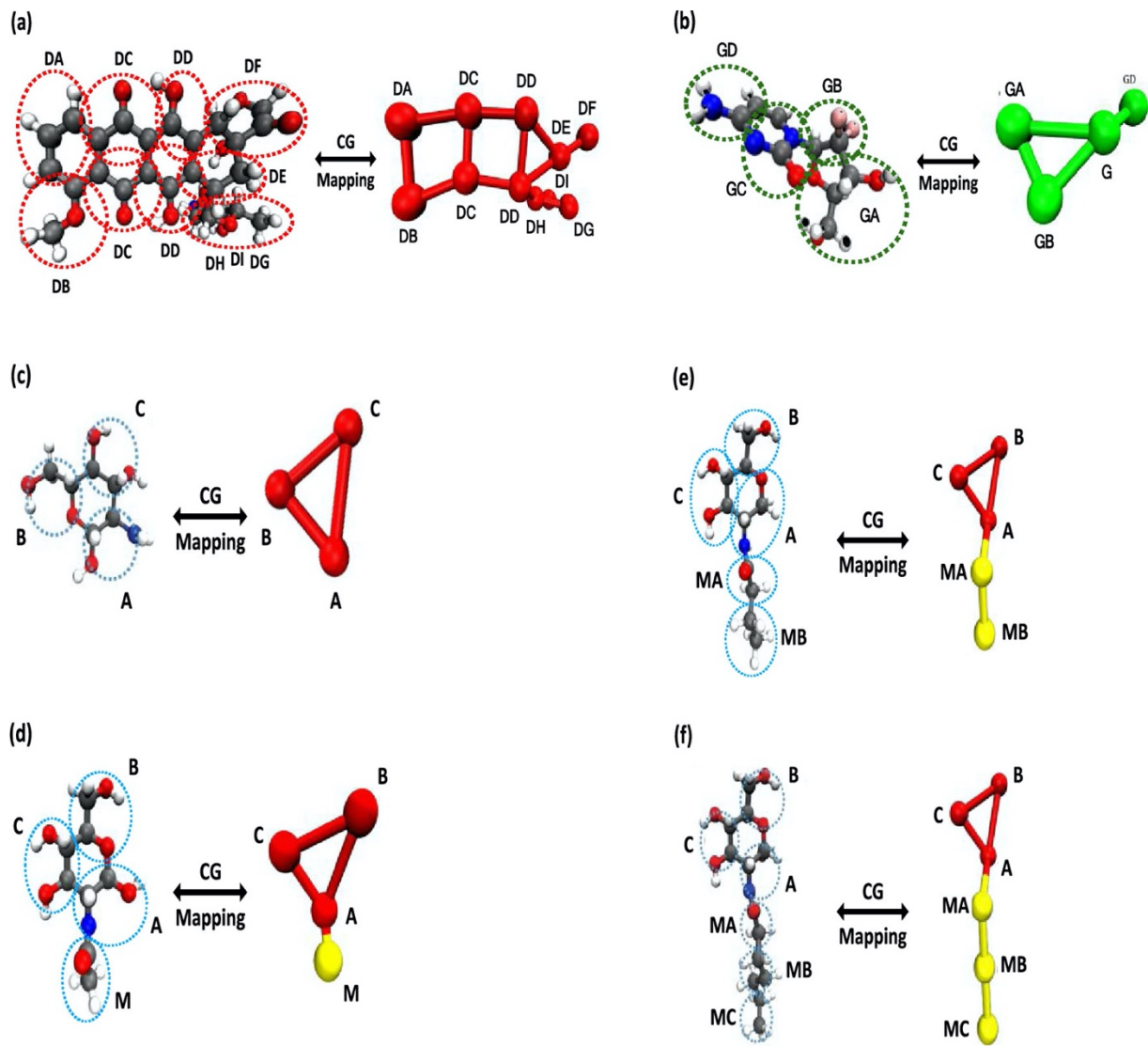


Figure 2.6 All-atom and coarse-grained representations of (a) DOX, (b) GEM, (c) unmodified glucosamine monomer, (d) acetyl-glucosamine, (e) butanoyl-glucosamine, and (f) heptanoyl-glucosamine.

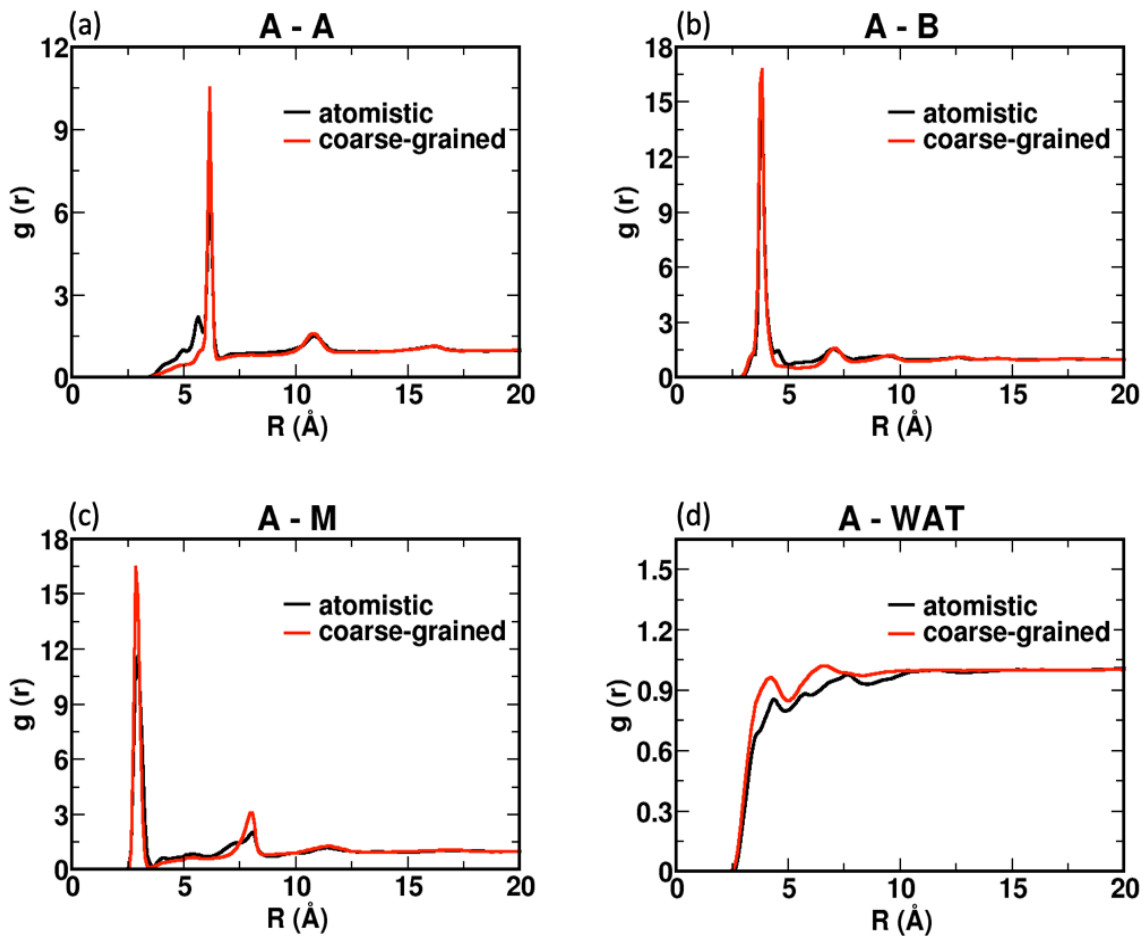


Figure 2.7 Radial distribution functions correspondence between the all-atom simulations and coarse-grained simulations interaction sites for (a) coarse-grained site A with A (Figure 2.6), (b) coarse-grained site A with B, (c) coarse-grained site A with modification site M, and (d) coarse-grained site A with water bead.

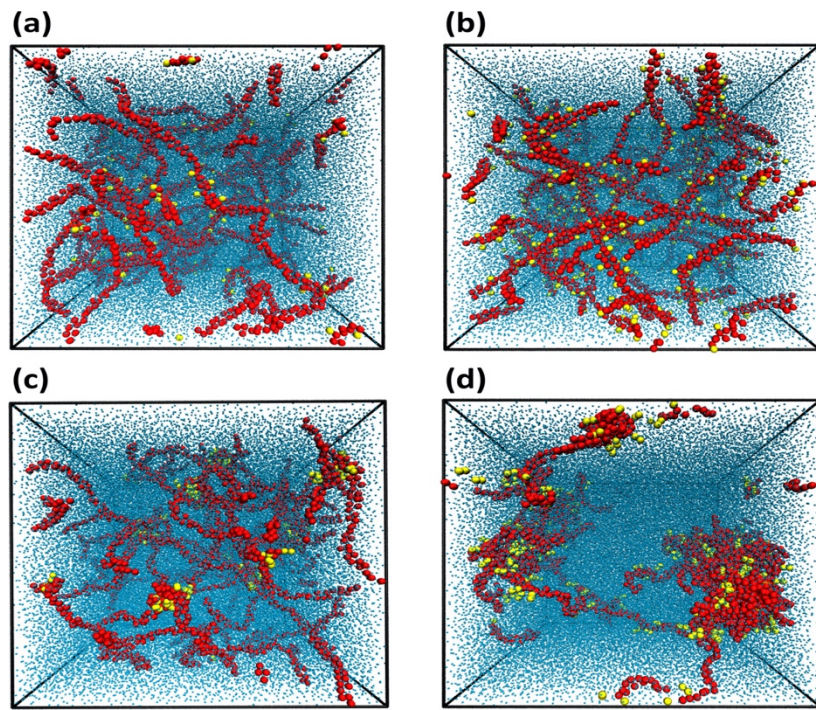


Figure 2.8 Representative simulation snapshots of chitosan hydrogels with a blocky modification pattern for (a) 16% acetylation, (b) 50% acetylation, (c) 16% butanoation, and (d) 32% butanoation.

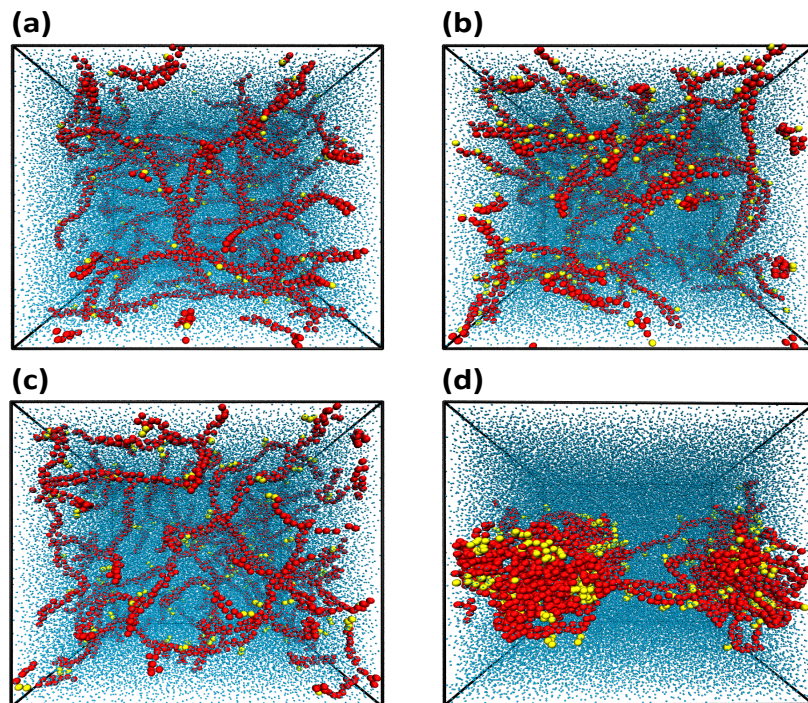


Figure 2.9 Representative simulation snapshots of chitosan hydrogels with evenly-spaced modification pattern for (a) 16% acetylation, (b) 50% acetylation, (c) 16 % butanoation, and (d) 32% butanoation.

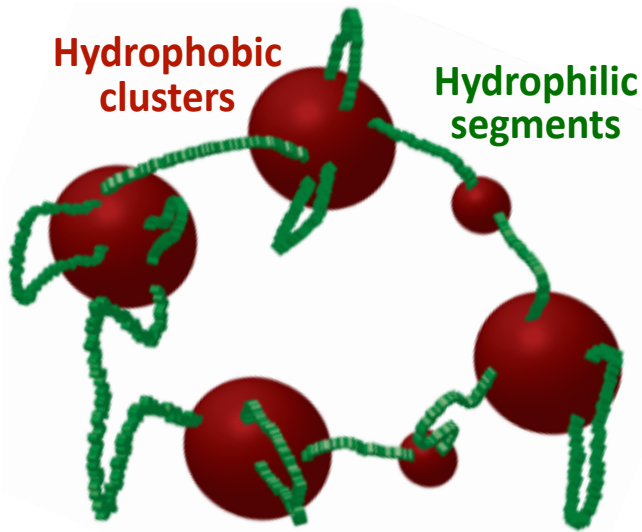


Figure 2.10 Schematic cluster/channel structure formed by hydrophobically-modified chitosan, wherein the micellar aggregates (red) comprise chitosan segments with high degree of hydrophobic modification, and the bridges (green) represent chitosan segments with low degree of modification [68].

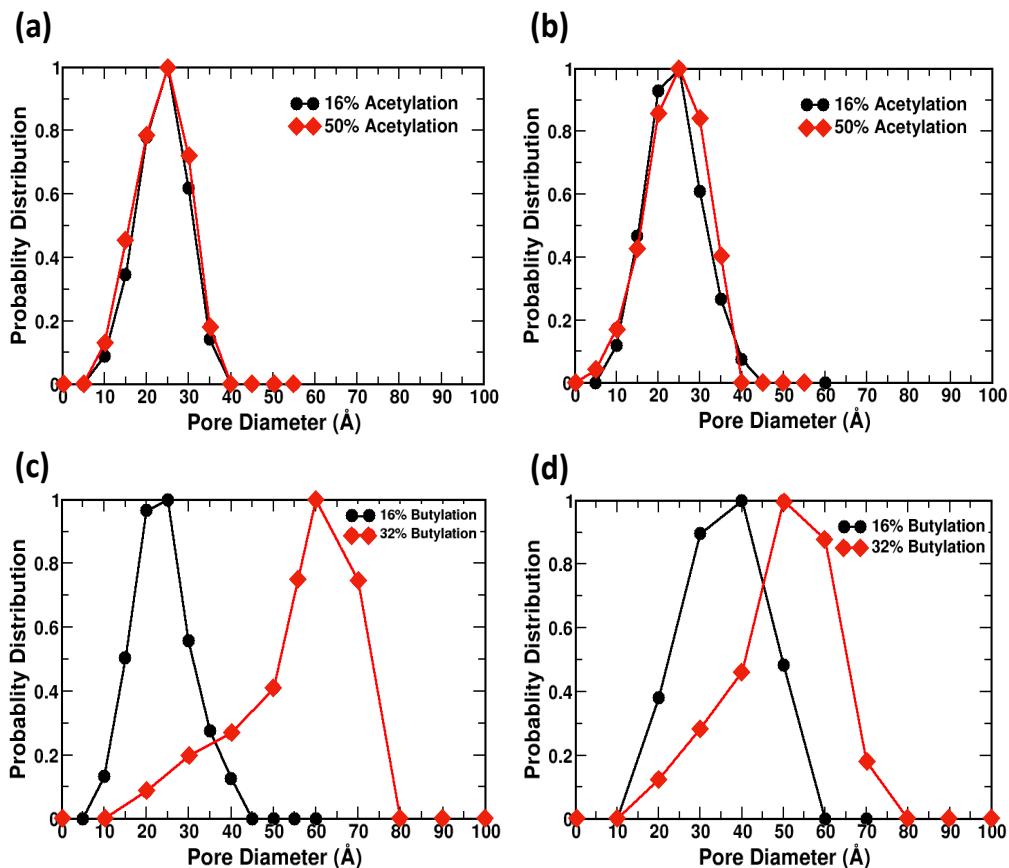


Figure 2.11 Pore size distribution functions for (a) evenly-spaced acetyl-chitosan, (b) blocky acetyl-chitosan, (c) evenly-spaced butanoyl-chitosan, and (d) blocky butanoyl-chitosan.

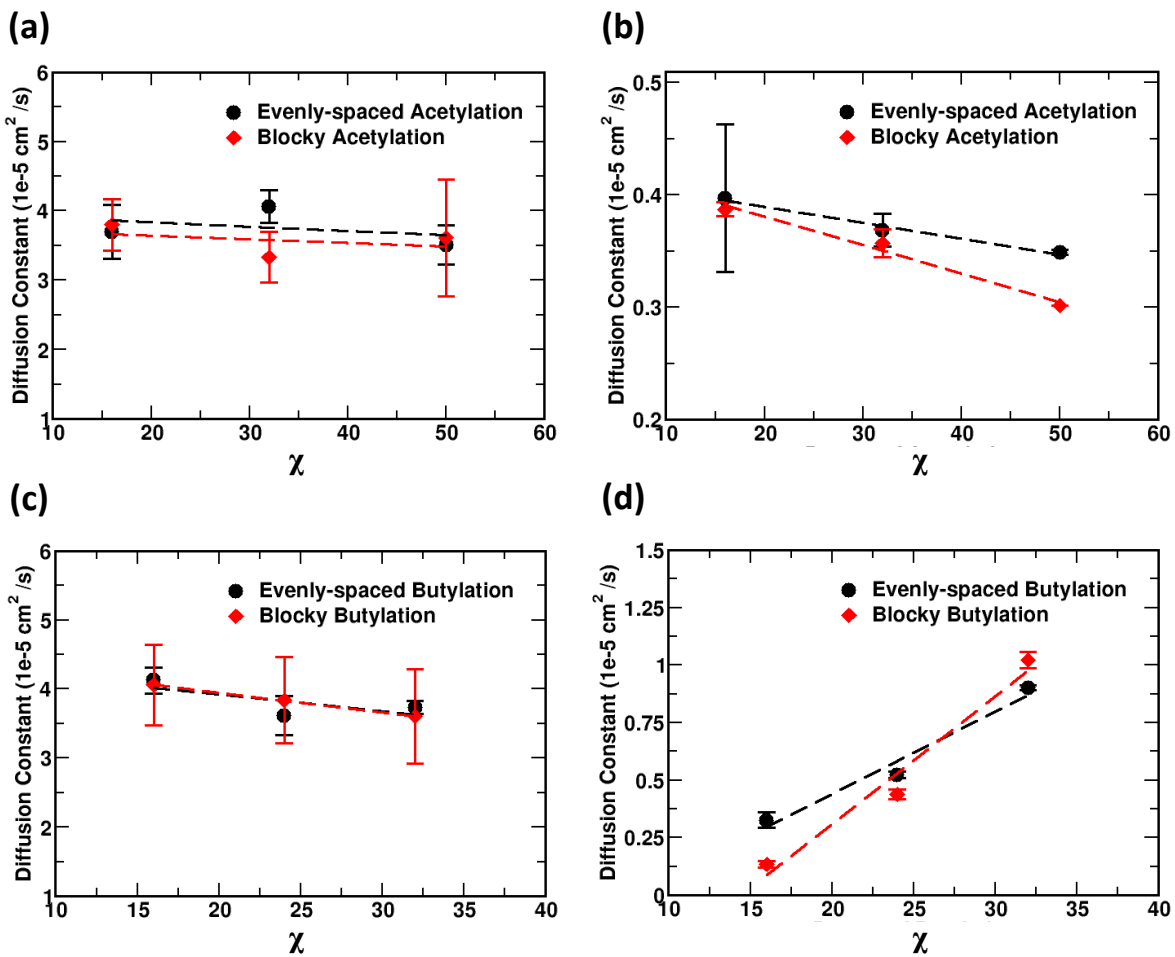


Figure 2.12 Drug diffusion constants *vs.* χ for single-drug migration across different chitosan networks for evenly-spaced (black) and blocky (red) modification patterns: **(a)** GEM and **(b)** DOX in acetyl-chitosan, and **(c)** GEM and **(d)** DOX in butanoyl-chitosan.

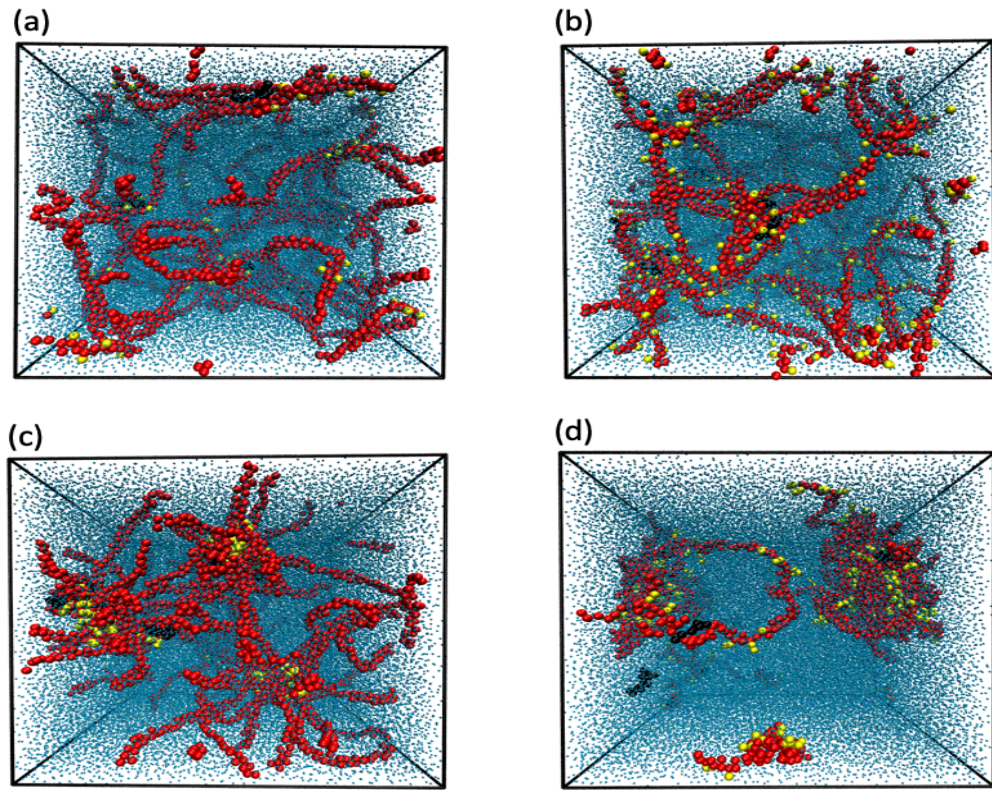


Figure 2.13 Snapshot of DOX migration through: (a) acetyl-chitosan networks at low χ (16%); (b) acetyl-chitosan networks at high χ (50%); (c) butanoyl-chitosan network at low χ (16%); (d) butanoyl-chitosan networks at high χ (32%), where the chitosan backbone is represented by red beads, modifications are represented by yellow beads, and DOX is represented by black beads.

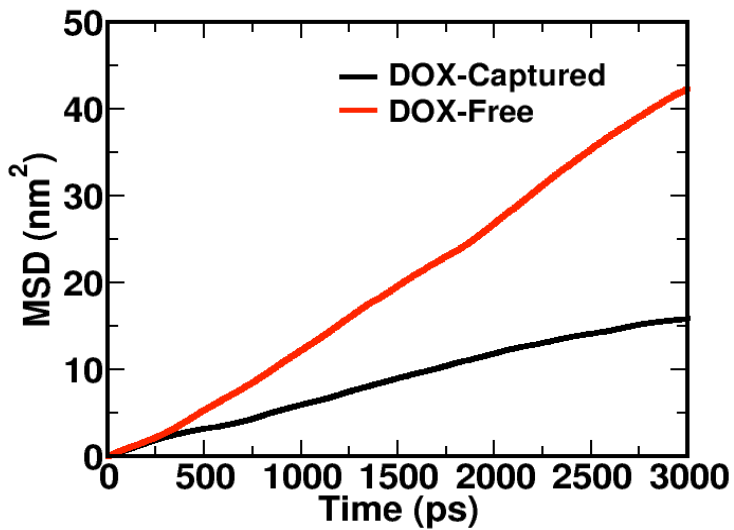


Figure 2.14 Mean-squared displacement (MSD) plot vs. time for diffusion of DOX through the blocky-modified chitosan network at $\chi = 32\%$, where DOX-Captured refers to DOX that becomes entrapped within a cluster and DOX-Free refers to DOX that remains in the pores of the cluster/channel morphology during the simulation.

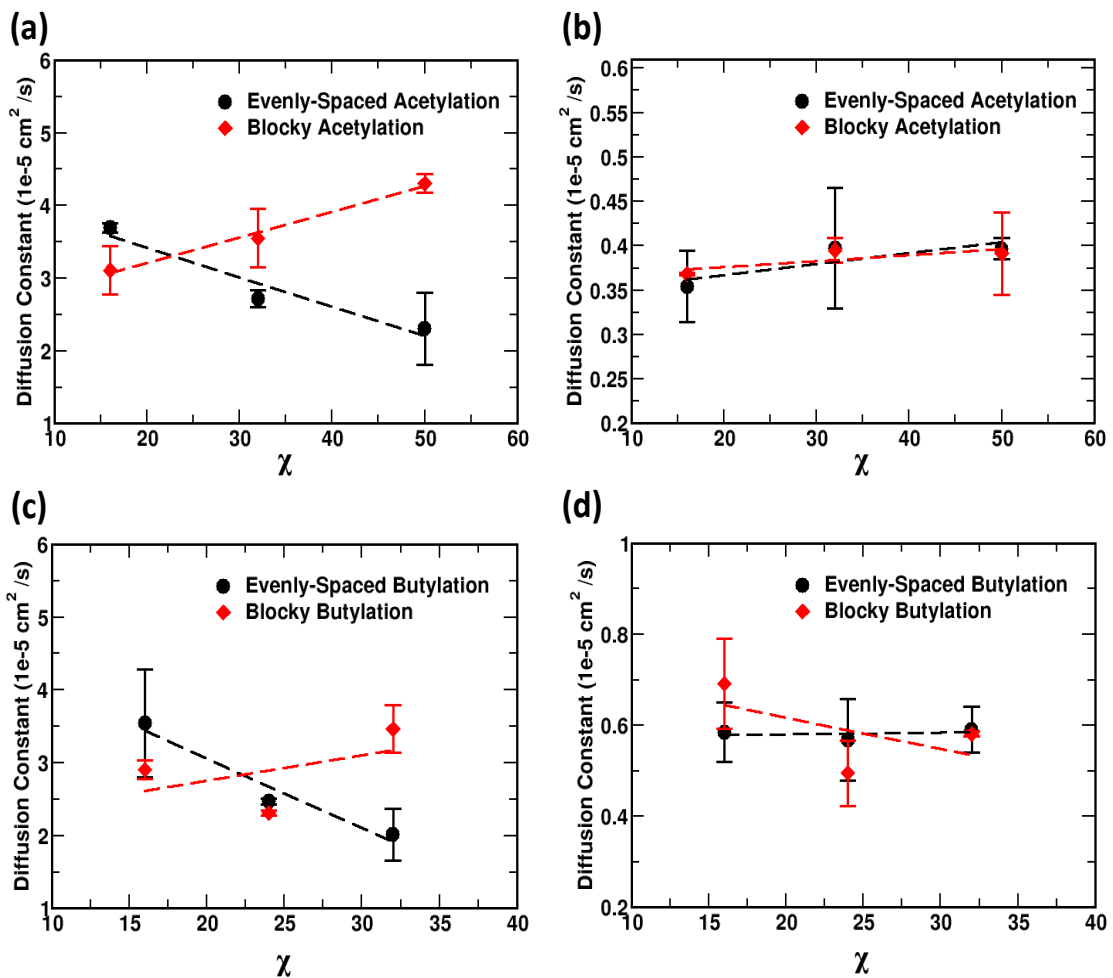


Figure 2.15 Drug diffusion constants $\text{vs. } \chi$ for dual-drug migration across different chitosan networks: **(a)** GEM in acetyl-chitosan, **(b)** DOX in acetyl-chitosan, **(c)** GEM in butanoyl-chitosan, and **(d)** DOX in butanoyl-chitosan.

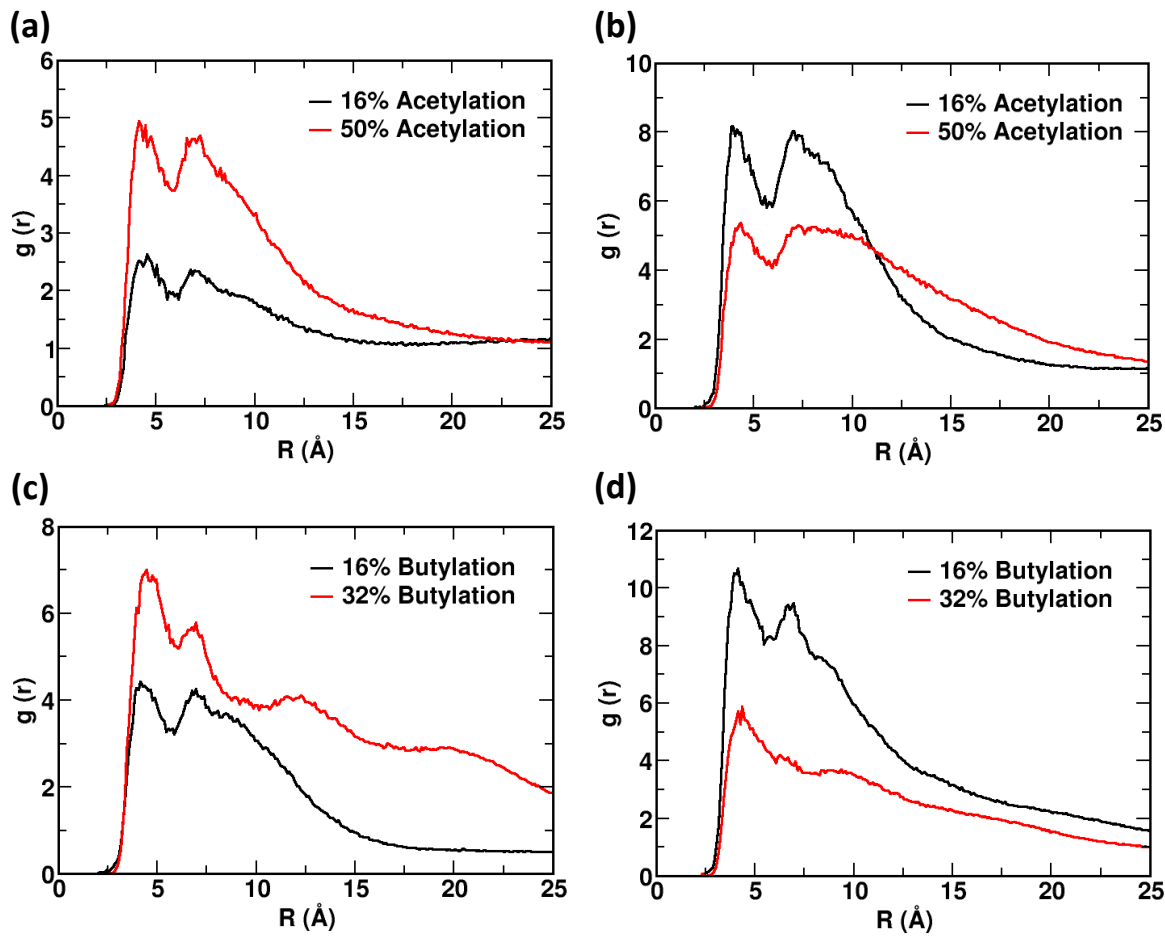


Figure 2.16 Radial distribution functions of GEM around the center of mass of DOX in acetyl-chitosan networks with **(a)** evenly-spaced and **(b)** blocky modification, and in butanoyl-chitosan networks with **(c)** evenly-spaced and **(d)** blocky modification.

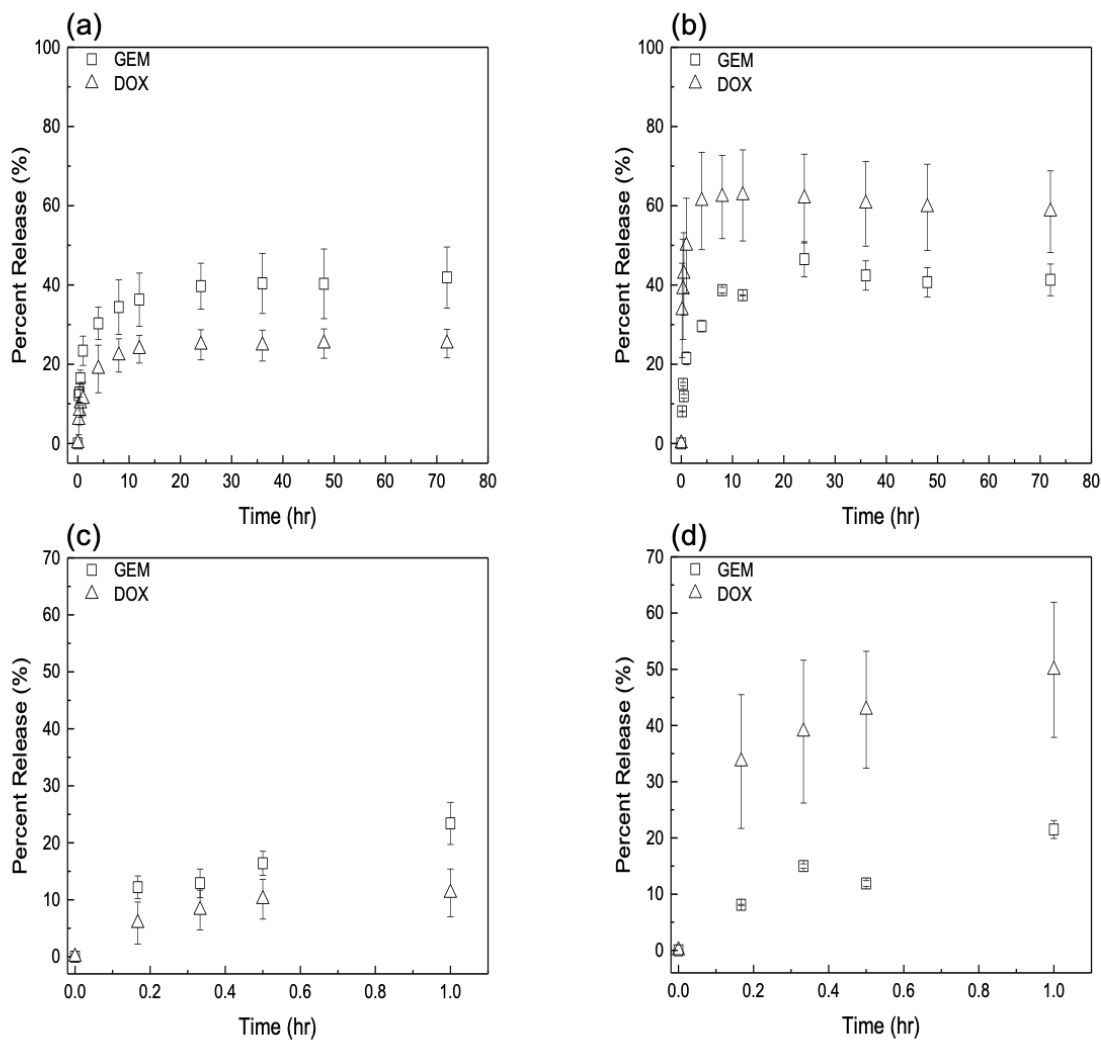


Figure 2.17 Release profiles of DOX (triangles) and GEM (squares) from chitosan hydrogels at $\chi = 25\%$ of **(a)** acetyl at 72 hr, and **(b)** butanoyl at 72 hr, **(c)** acetyl at 1 hr, and **(d)** butanoyl at 1 hr. Data represent mean \pm 99% C.I. ($n \geq 3$).

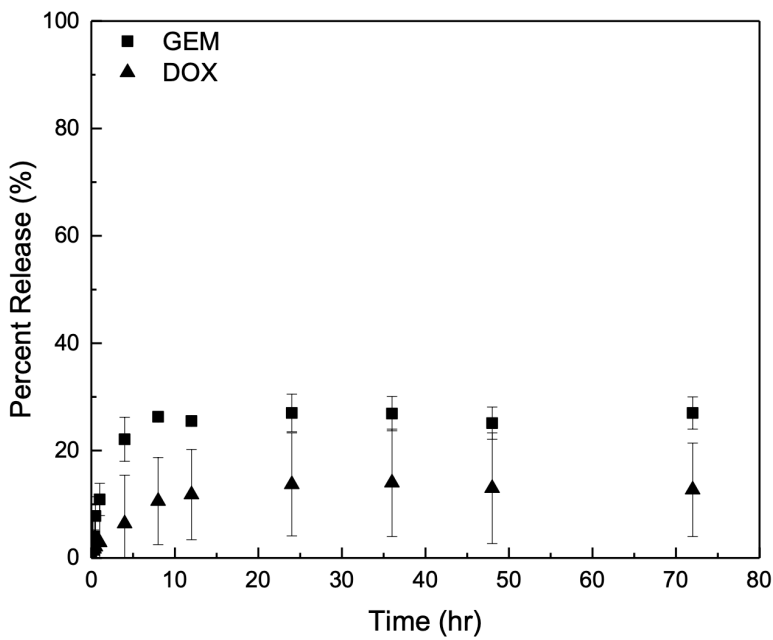


Figure 2.18 Release profiles of DOX (triangles) and GEM (squares) from heptanoyl-modified chitosan hydrogels at $\chi = 25\%$. Data represent mean \pm 99% C.I. ($n \geq 3$).

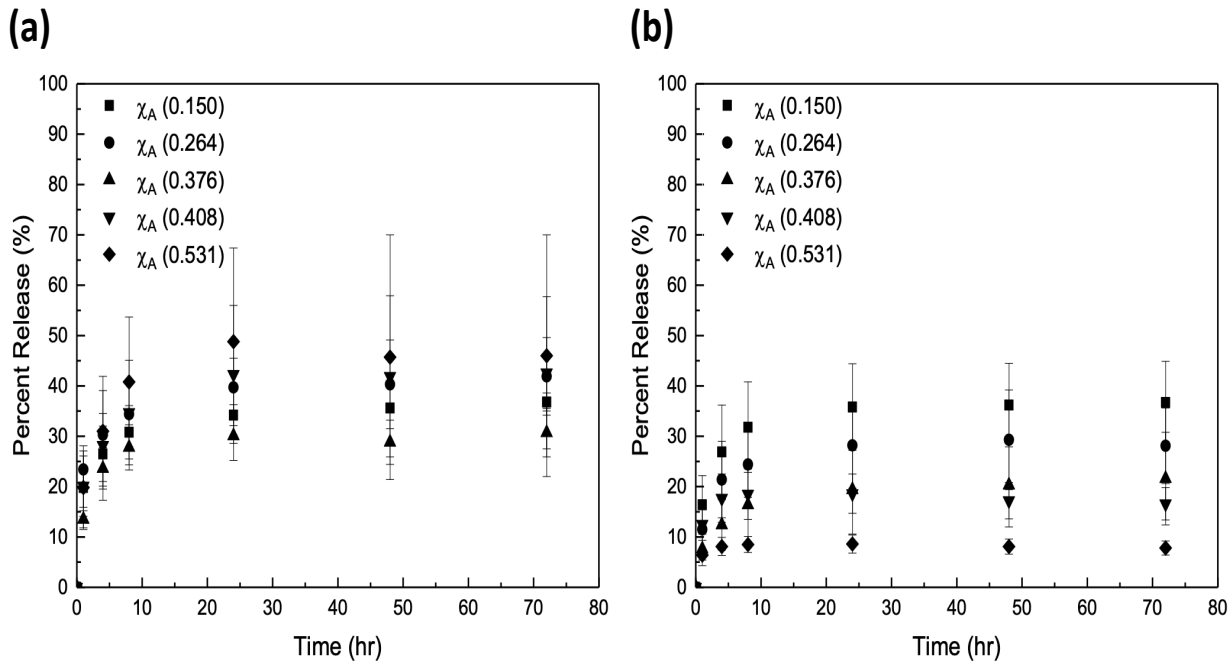


Figure 2.19 Release profiles of (a) GEM and (b) DOX from acetyl-chitosan hydrogels. Data represent mean \pm 99% C.I. ($n \geq 3$).

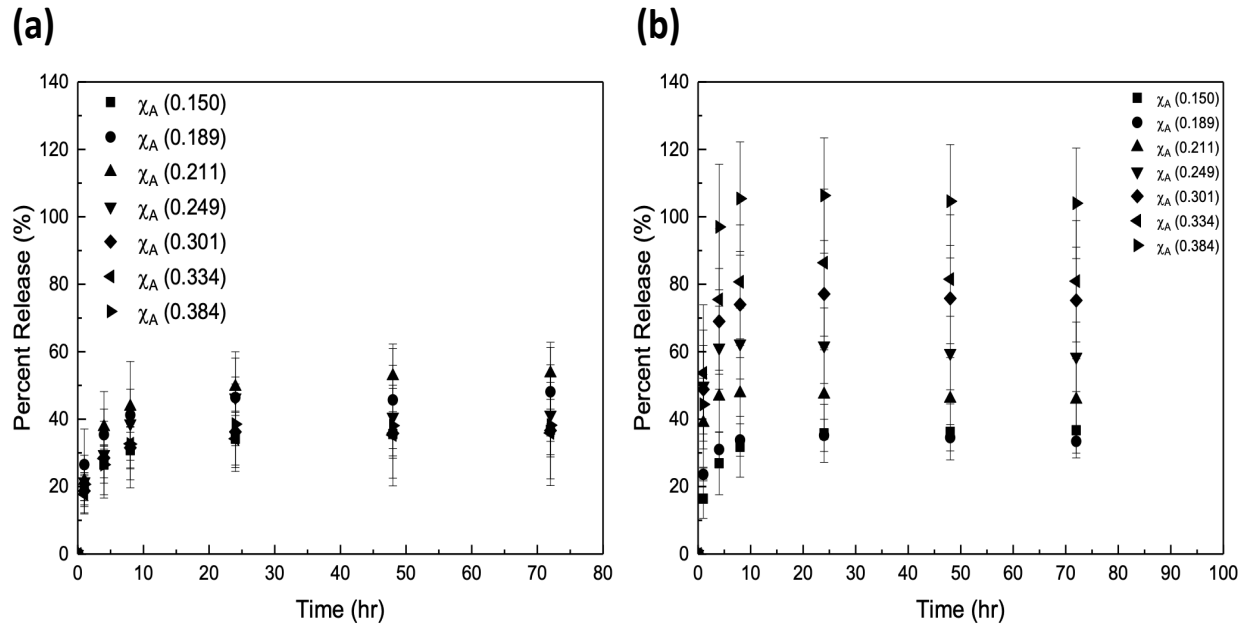


Figure 2.20 Release profiles of (a) GEM and (b) DOX from butanoyl-chitosan hydrogels. Data represent mean \pm 99% C.I. ($n \geq 3$).

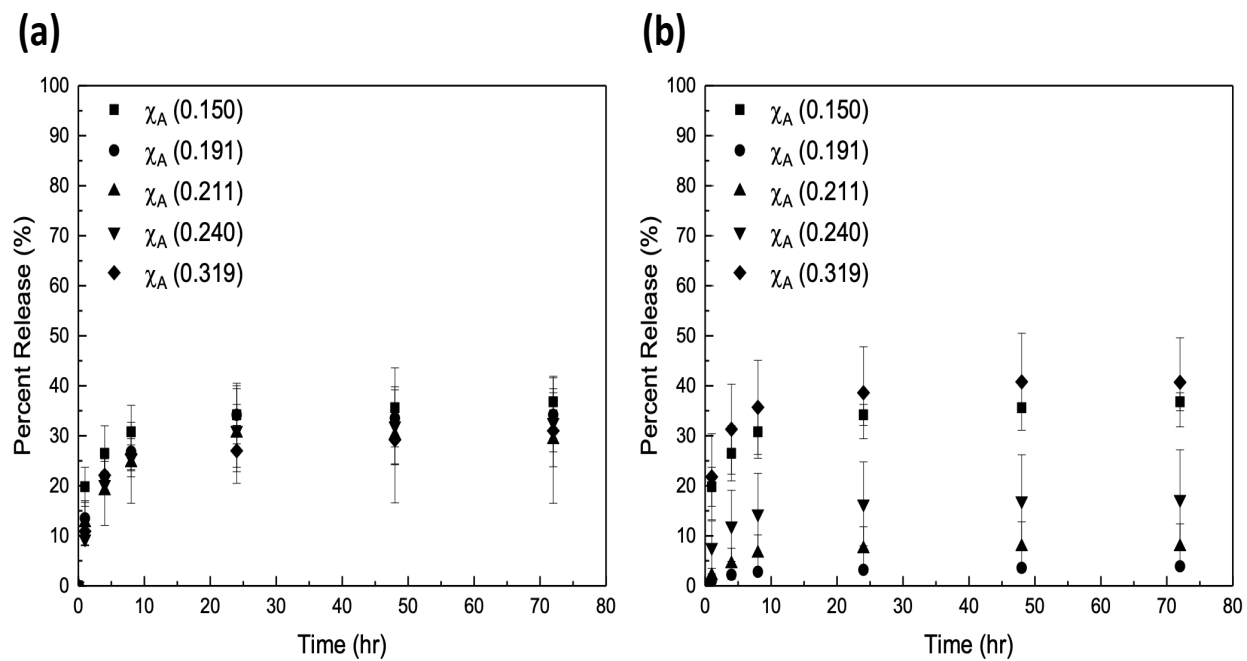


Figure 2.21 Release profiles of (a) GEM and (b) DOX from heptanoyl-chitosan hydrogels. Data represent mean \pm 99% C.I. ($n \geq 3$).

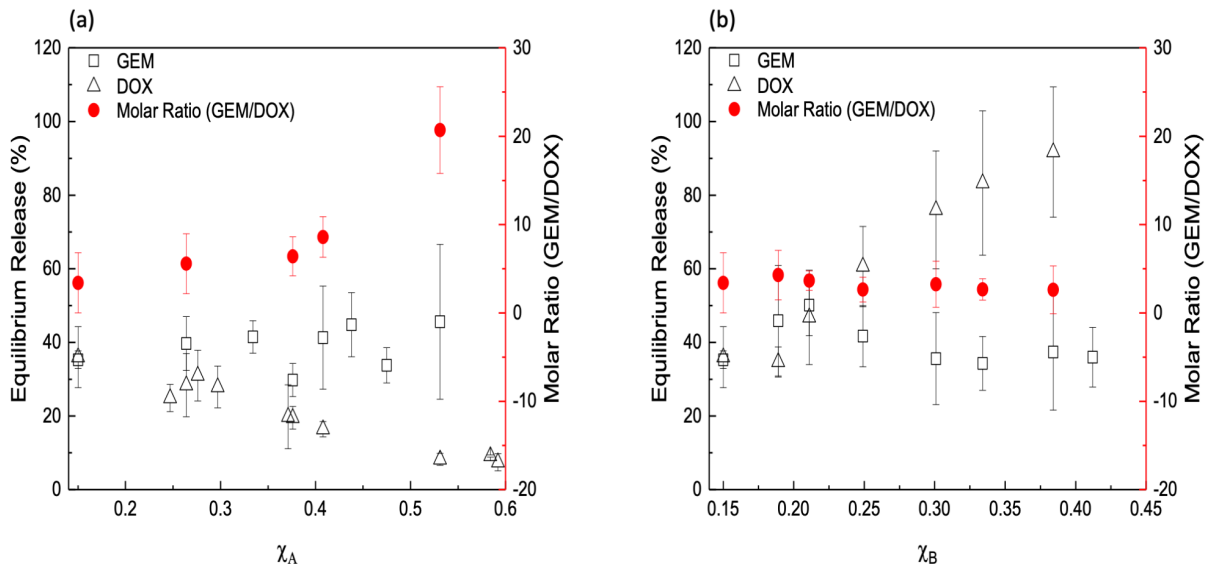


Figure 2.22 Equilibrium release percent of DOX (triangles) and GEM (squares), and GEM/DOX molar ratio (red circles) vs. χ for (a) acetyl-chitosan and (b) butanoyl-chitosan. Data represent mean \pm 99% C.I. ($n \geq 3$).

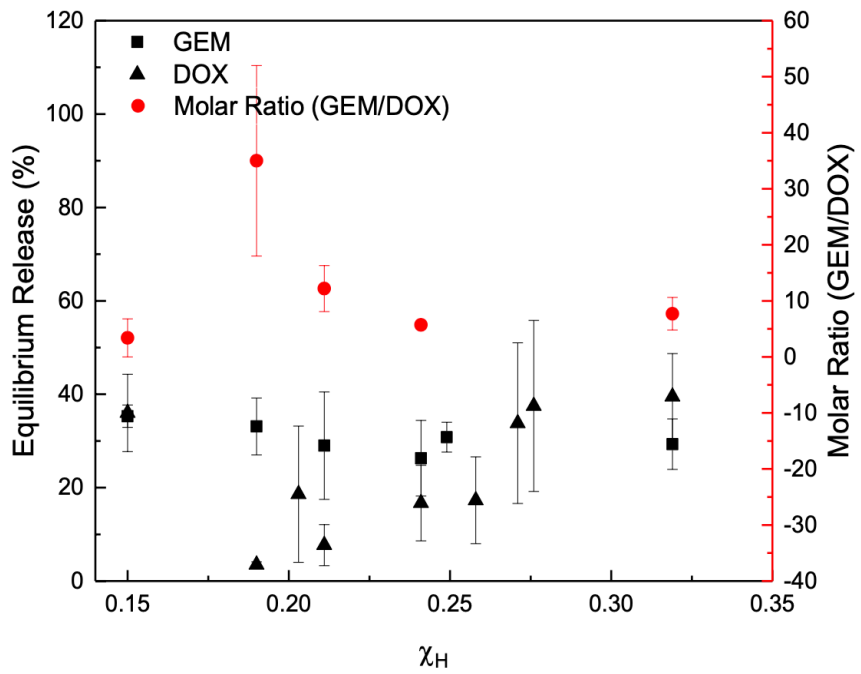


Figure 2.23 Equilibrium release percent of DOX (black triangles) and GEM (black squares) and GEM/DOX molar ratio (red circles) vs. χ for heptanoyl-chitosan. Data represent mean \pm 99% C.I. ($n \geq 3$).

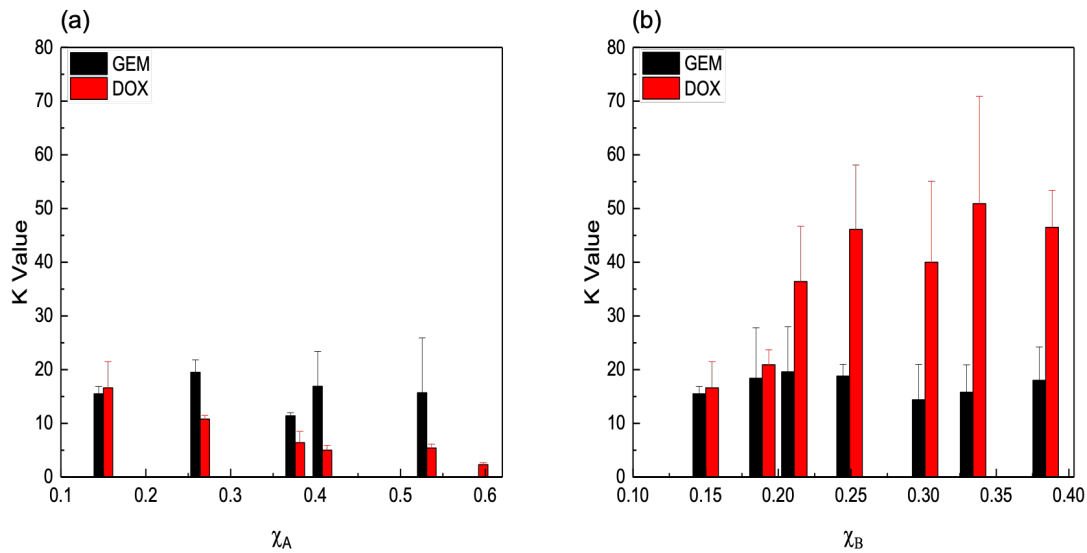


Figure 2.24 The K values obtained from the Korsmeyer-Peppas model for single GEM (black) and DOX (red) release vs. χ in **(a)** acetyl-modified chitosan gels and **(b)** butanoyl-modified chitosan gels. Data represent mean \pm 99% C.I. ($n \geq 3$).

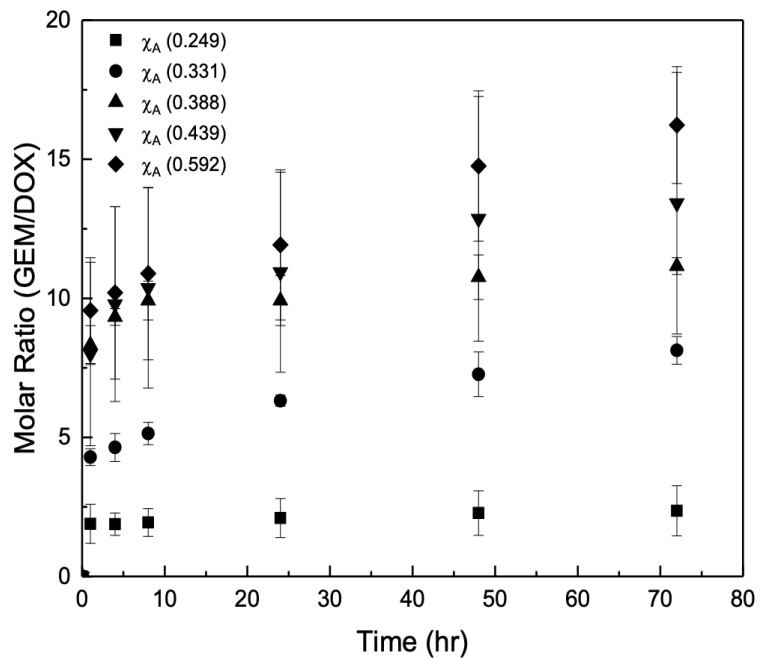


Figure 2.25 Molar ratio of GEM to DOX released from dually loaded acetyl-chitosan hydrogels. Data represent mean \pm 99% C.I. ($n \geq 3$).

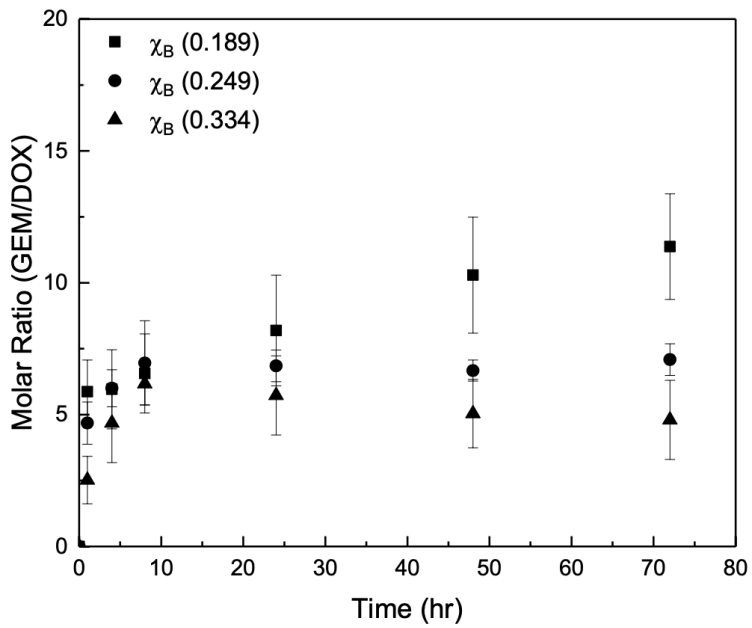


Figure 2.26 Molar ratio of GEM to DOX released from dually loaded butanoyl-chitosan hydrogels. Data represent mean \pm 99% C.I. ($n \geq 3$).

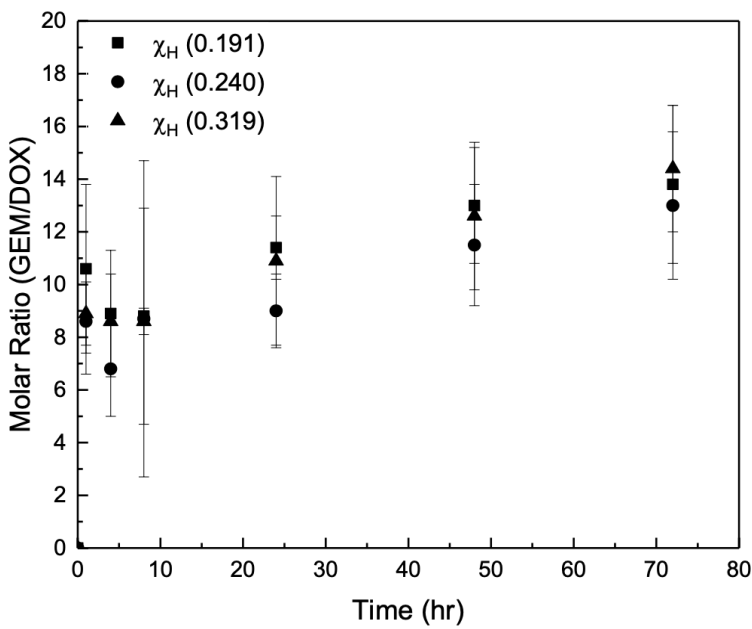


Figure 2.27 Molar ratio of GEM to DOX released from dually loaded heptanoyl-chitosan hydrogels. Data represent mean \pm 99% C.I. ($n \geq 3$).

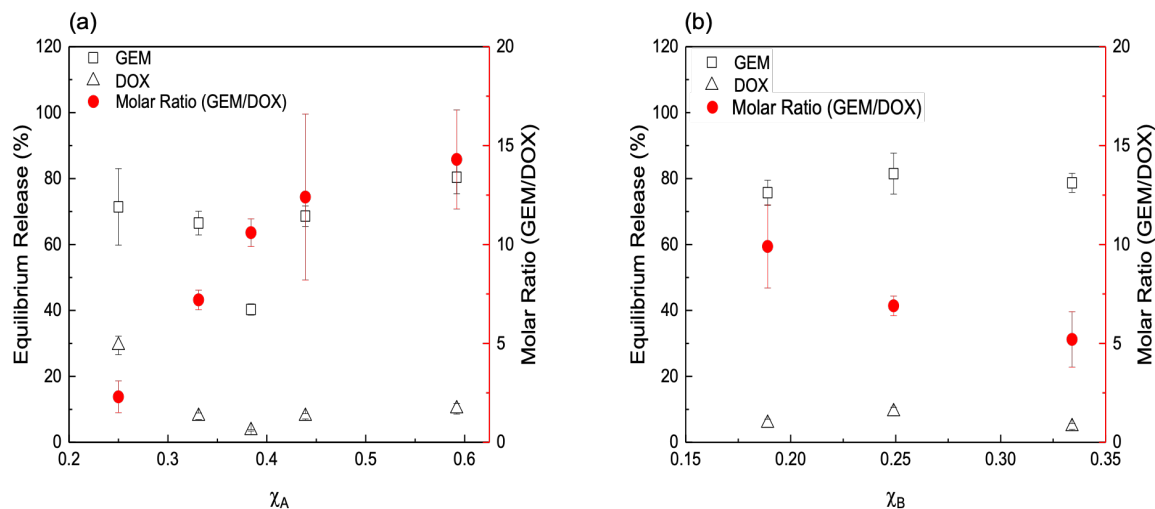


Figure 2.28 Equilibrium dual-drug release percent of DOX (triangles) and GEM (squares), and GEM/DOX molar ratio (red circles) vs. χ for (a) acetyl-chitosan and (b) butanoyl-chitosan. Data represent mean \pm 99% C.I. ($n \geq 3$).

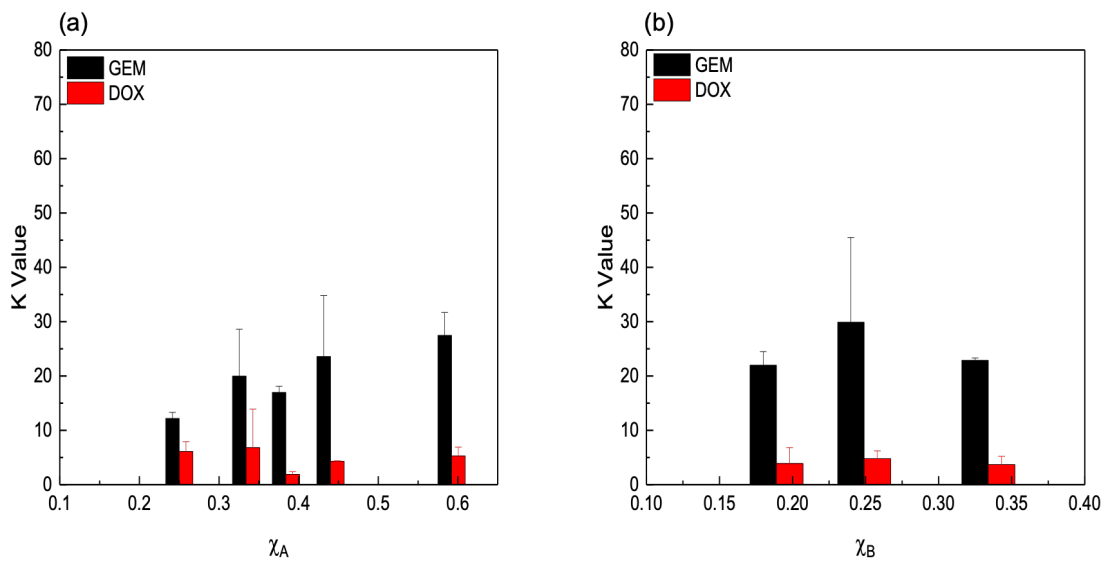


Figure 2.29 K values obtained from the Korsmeyer-Peppas model for GEM (black) and DOX (red) released vs. χ from (a) acetyl-modified chitosan gels and (b) butanoyl-chitosan gels. Data represent mean \pm 99% C.I. ($n \geq 3$).

CHAPTER 3

Chitosan Hydrogels for Synergistic Delivery of Chemotherapeutics to Triple Negative Breast Cancer Cells and Spheroids

John D. Schneible, Ashlyn T. Young, Michael A. Daniele, and Stefano Menegatti

An adapted version of this chapter has been accepted for publication in Pharmaceutical Research.

Abstract

This study aimed to develop a hydrogel system for treating aggressive triple negative breast cancer (TNBC) via kinetically-controlled delivery of the synergistic drug pair doxorubicin (DOX) and gemcitabine (GEM). A 2D cell culture assay was adopted to evaluate therapeutic efficacy by determining combination index (CI), and a novel 3D assay using cancer spheroids was implemented to assess the potential for translation *in vivo*. The hydrogel delivery system was prepared by loading acetylated-chitosan (ACS, with degree of acetylation $\chi_{Ac} = 40 \pm 5\%$) with an aqueous solution of DOX:GEM. The release of DOX and GEM was characterized *in vitro* to identify a combined drug loading that affords release kinetics and final dose that are therapeutically synergistic. The selected DOX/GEM-ACS formulation was evaluated *in vitro* against 2-D (cell culture monolayer) and 3-D (spheroids) models of TNBC to respectively determine the combination index (CI) and the tumor volume reduction. The desired release dosage and kinetics of GEM (4.5 μ M, corresponding to 22.0% of the payload, released in 24 hr) and DOX (0.07 μ M, corresponding to 14.3% of the payload, released in 72 hr), and equilibrium molar ratio ($\geq 10:1$) were achieved. When tested on 2-D model of TNBC, the select dual-drug-loaded hydrogel provided a CI of 0.14, indicating strong synergism; the control concurrent administration of DOX and GEM as free drugs afforded lower therapeutic efficacy, with a CI of 0.23. Finally, the hydrogel delivery system accomplished a notable volume reduction of the cancer spheroids (up to 30% of the initial volume), whereas the corresponding dosage of free drugs only slowed growth. Our studies indicate that the ACS hydrogel delivery system accomplishes a drug release kinetics and ratio that afford strong therapeutically synergism. These results, in combination with the choice of ACS as affordable and highly abundant source material, provide a strong pre-clinical demonstration of the potential of the proposed system for complementing surgical resection of aggressive solid tumors.

3.1. Introduction

Combination chemotherapy has become increasingly ubiquitous in the field of drug delivery owing to its distinct advantages over single-drug therapies [1, 2]. Single-drug therapies cause acquired drug resistance following prolonged administration, leading to non-responsiveness to therapy, the need of increased dosages, and ultimately poor prognosis and quality of life [3-5]. Combination chemotherapy overcomes these limitations by disrupting multiple metabolic pathways simultaneously, resulting in three progressively desirable therapeutic outcomes: additive effect, potentiation, and synergism [2]. Among these, synergism is achieved when the combined efficacy of multiple drugs is remarkably higher than the sum of the individual therapies administered independently and represents the most auspicious therapeutic outcome [2, 6]. In the past, synergy of chemotherapy regimens has been mostly attributed to the properties and molar ratio of the administered drugs; however, recent studies demonstrate that the order by which the drugs are administered, or schedule, is critical towards maximizing the synergistic outcome [7-9], by comparing scheduled regimens with their single-drug therapy counterparts *in vitro*, in animal models, and in the clinical setting [7-17].

Current studies on drug delivery systems (DDSs) that deliver synergistic combination chemotherapy regimens utilize a variety of drug delivery carriers, namely nano/micro-particles and liposomes [2, 18, 19], polymer-drug conjugates [20], and hydrogels [21]. Among these, hydrogels present unique advantages. Owing to their flexible microstructure, hydrogels can be tuned by controlling the gel fraction and crosslinking density to achieve the desired release kinetics, dose, and molar ratio [22, 23]. Notably, hydrogels can serve as “depots” from which sustained release – and thus a local high concentration – is maintained towards the surrounding tissue, thus bypassing the pharmacokinetic limitations of other DDSs and free chemotherapeutics

[24-26]. In hydrogel-based DDSs, drug loading and release depends strongly on molecular interactions between the drug molecules and the polymer chains that form the hydrogel scaffold, as well as the gel morphology, both of which can be tuned through judicious chemical modification of the polymer [24, 26].

One polymer that has captivated researchers for development of DDSs is chitosan [27, 28]. Chitosan, a biopolymer derived from naturally abundant chitin, is biocompatible and biodegradable [29]. Chitosan chains display primary amine groups that enable facile chemical modification and have been utilized to tailor the release kinetics of the therapeutic cargo [23, 30]. Further, because chitosan has an endogenous short physiological half-life (*i.e.*, days – weeks(s)), physical chitosan hydrogels present an optimal short-time DDS and release no toxic degradation byproducts [31]. Consequently, a variety of chitosan-based products have been developed for biomedical applications, such as oral and ocular delivery systems as well as wound dressings, some of which have received FDA approval, demonstrating clinical feasibility [32, 33].

In this work, we utilized the drug pair of gemcitabine (GEM) and doxorubicin (DOX), which were selected for their extensively documented synergism [7, 8, 34, 35]. Previous work has defined the optimum molar ratio (GEM: DOX > 1) and delivery kinetics (GEM prior to DOX) for this drug pair to treat breast cancer [7, 8, 34]. In previous work, we studied the physicochemical factors governing release of GEM and DOX from chitosan hydrogels modified with acetyl, butanoyl, and heptanoyl moieties, using an integrated *in silico* – experimental approach [23]. We demonstrated that acetyl-modified chitosan (ACS) affords the optimum delivery ratio and kinetics for this drug pair, in both single-drug loaded and co-loaded systems. In this work, we selected one particular ACS with degree of modification (χ_{Ac}) of $40 \pm 5\%$, which demonstrated favorable kinetics and molar ratio of GEM/DOX during release. To assess the viability of this system as an

injectable depot, initial release studies were performed with DOX and GEM at different single-drug loadings. Specifically, we optimized this system by examining different loading conditions for the individual drugs to achieve the release of individual DOX and GEM at a therapeutically viable concentration, namely $0.26 \mu\text{M} - 0.64 \mu\text{M}$ for DOX within 72 hr, and $2.8 \mu\text{M} - 19.4 \mu\text{M}$ for GEM within 72 hr. The optimized hydrogel co-loaded with GEM/DOX afforded release doses of $0.07 \mu\text{M} - 0.13 \mu\text{M}$ for DOX and $4.5 \mu\text{M} - 20.7 \mu\text{M}$ for GEM, after 72 hr, which fall within the desired (synergistic) therapeutic window [7, 8, 34]. The ACS hydrogel was evaluated *in vitro* against the TNBC cell line MDA-MB-231 in the form of 2-D (cell monolayer) and 3-D (spheroids) systems. Notably, the select DOX/GEM-loaded ACS afforded a combination index (CI) of 0.142 ± 0.010 in the 2-D assay. This was considerably lower than the CI obtained with the free drug DOX-GEM combination (0.223 ± 0.002) at the same global drug concentration and molar ratio, indicating that the ACS delivery system provides a significant contribution towards achieving therapeutic synergism; for comparison, Vogus *et al.* obtained a comparable CI (0.12) using a complex microfluidic system that provides precise control of the delivery scheduled and dose of DOX and GEM against TNBC cells [8]. In the 3-D assay, the DOX/GEM-loaded ACS gel afforded a significant decrease in tumor volume, reducing the spheroid growth percentage from a $30 \pm 2.9\%$ increase in volume (no treatment) to $-32.7 \pm 2.2\%$; in comparison, the concurrent administration of a GEM:DOX ratio of 10:1 only reduced volume growth to $2.4 \pm 5.2\%$. Collectively, these results demonstrate the efficacy of the proposed ACS delivery system in achieving scheduling-based therapeutic synergism and its translational potential towards future clinical studies.

3.2. Materials and Methods

3.2.1. Materials

Low-molecular-weight chitosan (85% maximum degree of deacetylation, 15 kDa) was obtained from Polysciences Inc. (Warrington, PA). Acetic anhydride, phosphate-buffered saline (PBS), potassium hydroxide, and the Kaiser Test kit were from Sigma Aldrich (St. Louis, MO). Doxorubicin hydrochloride (DOX) and Gemcitabine hydrochloride (GEM) were obtained from LC Laboratories (Woburn, MA). Triple negative breast cancer cells MDA-MB-231 were purchased from ATCC (Manassas, VA). Dulbecco's Modified Eagle Medium (DMEM) and fetal bovine serum (FBS) were obtained from Genesee Scientific (San Diego, CA). Penicillin Streptomycin (Pen Strep) was obtained from Gibco (Gaithersburg, MD). 3-(4,5-dimethylthiazol-2-yl)-2,5-diphenyltetrazolium bromide (MTT), was purchased from Invitrogen (Carlsbad, CA). Corning Matrigel Growth Factor Reduced (GFR) Basement Membrane Matrix was purchased from Fisher Scientific (Hampton, NH). All other reagents were of reagent grade or higher.

3.2.2. Modification of Chitosan

Chitosan modification was performed following an adapted protocol from previous work [23]. Briefly, chitosan was dissolved at 6 mg mL⁻¹ in 1% acetic acid (w/w) and filtered to remove insoluble components. A stoichiometric amount of acetic anhydride was added dropwise, and the mixture was stirred at room temperature for 1 hr. The reaction was stopped by precipitating the chitosan solution dropwise into a 3× volume of 5 M methanolic potassium hydroxide. The precipitate was collected by centrifugation and washed with methanol until neutral pH. The precipitate was then washed copiously with DI water, followed by 10 mM PBS, pH 7.4, to yield a

physical hydrogel; for the experiments performed with cells, all washing steps were carried out aseptically.

The level of acetyl modification (χ_{Ac}) was determined by a modified version of the Ninhydrin assay developed by Kaiser *et al.* [36]. Lyophilized ACS was dissolved in 1% acetic acid (w/w) at 3 mg mL⁻¹, and unmodified chitosan was dissolved at varying concentrations (0.5-6 mg mL⁻¹). Aliquots of 100 µL of chitosan solution were combined with 30 µL of potassium cyanide in water/pyridine and 30 µL of ninhydrin (6% in ethanol). The solutions were then incubated at 100°C for 5 min, diluted 200× and analyzed via UV-vis spectroscopy at 570 nm. The level of modification was determined using Equation 1:

$$(1) \quad \chi = \frac{\left(1 - \frac{D \cdot M \cdot C^*}{C}\right)}{\left(1 - \frac{D \cdot M_{mod} \cdot C^*}{C}\right)}$$

where χ is the degree of modification, C^* is the molar concentration of amine groups on a chitosan chain, D is the dilution factor, C is the mass concentration used for the Kaiser test, M is the molecular weight of the glucosamine monomer, and M_{mod} is the molecular weight of the acetyl modification.

3.2.3. Single-Drug Loading and Release

Single-drug loading measurements were performed by incubating 150 mg of ACS hydrogel with 1.2 mL of drug solutions in PBS at 0.5-2 µg mL⁻¹ for DOX and 25-100 µg mL⁻¹ for GEM, for 48 hr at RT. After loading, the drug-depleted supernatant was collected to quantify the amount of drug absorbed in the hydrogel. An aliquot of 150 mg of loaded hydrogel was then combined with 1 mL of 10 mM PBS, pH 7.4, and placed in an orbital shaker at 50 rpm at 37°C. At selected time points, 200 µL of supernatant was withdrawn and replenished with PBS. After the

release studies, samples containing DOX (loading supernatant and time point collections) were analyzed by fluorescent spectroscopy on a Biotek Synergy H1 Microplate Reader (Agilent, Winooski, VT) at $\lambda_{\text{ex}} = 480$ nm and $\lambda_{\text{em}} = 580$ nm. Samples containing GEM were analyzed using liquid chromatography on a Waters 2690 HPLC system (Waters, Milford, MA) equipped with an Aeris 3.6 μm C18 column (50×4.6 mm). The chromatographic method utilized an isocratic 5% acetonitrile in water (0.1% formic acid (v/v)) for 5 min, while monitoring the effluent via UV spectrophotometry at 290 nm. GEM concentration was determined by integrating the peak area. All experiments were performed in triplicate.

3.2.4. Dual-Drug Loading and Release

Dual-drug loading experiments were performed by incubating 150 mg of ACS hydrogel with 1.2 mL of drug solution at either low ($25 \mu\text{g mL}^{-1}$ GEM and $0.5 \mu\text{g mL}^{-1}$ DOX in PBS) or high concentration ($50 \mu\text{g mL}^{-1}$ GEM and $1 \mu\text{g mL}^{-1}$ DOX in PBS) for 48 hr at RT. After loading, the drug-depleted supernatant was collected to quantify drug loading. Drug loading, supernatant sampling, and quantification of DOX release were performed as described in *Section 3.2.3*. The collected samples were analyzed using a Waters 2690 HPLC system (Waters, Milford, MA) equipped with an Aeris 3.6 μm C18 column (50×4.6 mm). The chromatographic method utilized a 5-100% gradient of acetonitrile (0.1% formic acid (v/v)) in water (0.1% formic acid (v/v)) over 10 min, while monitoring the effluent via UV spectrophotometry at 290 nm. GEM concentration was determined by integrating the peak area. All experiments were performed in triplicate.

3.2.5. 2-D Cell Culture

Triple negative breast cancer cells, MDA-MB-231, were cultured in DMEM supplemented with 10% (v/v) FBS and 1% (v/v) Pen Strep in a humidified incubator at 37°C and 5% CO₂.

3.2.6. 2-D Cell Viability Assay

Cells were seeded at a density of 3×10^4 cells/well in a 24-well plate, corresponding to 5×10^3 cells/well in a 96-well format, and allowed to adhere overnight. Trans-well inserts were added to the plate, and the treatment condition was applied. Treatments with free drug employed 100 µL of drug-infused media, whereas treatments with drug-loaded ACS were performed by adding the gel (25, 50, 75, 100, or 125 mg) followed by 100 µL of media. The 24-well plate was then placed in a humidified incubator at 37°C and 5% CO₂ for 72 hr. The drug-infused media were obtained by diluting stock solutions of DOX and GEM in sterile DMSO with cell culture media (DMEM supplemented with 10% (v/v) FBS and 1% (v/v) Pen-Strep) such that the maximum concentration of DMSO did not exceed 0.5% (v/v). The mass of hydrogel used in the treatments was chosen to achieve a concentration of DOX released after 72 hr equal to that utilized in free drug cell viability experiments. After 72 hr of treatment the media was aspirated, and the cells were incubated with 500 µL of MTT (0.5 mg mL⁻¹ in cell culture media) for 4 hr at 37°C. The MTT solution was aspirated and 500 µL of DMSO was added to the to dissolve formazan crystals. The concentration of formazan was quantified by UV-Vis spectroscopy at 540 nm on a Biotek Synergy H1 Microplate Reader (Agilent, Santa Clara, CA).

3.2.7. 3-D Spheroid Culture

Spheroids constituted by MDA-MB-231 cells were cultured following the protocol established by Froehlich *et al.* [37] using the liquid overlay technique. Briefly, 100 µL of cell suspension, 1×10^4 cells, in cell culture media supplemented in 3.5% Matrigel were seeded in a round bottom Cellstar® cell-repellent surface 96-well plate. Cells were cultured in a 37°C incubator with 5% CO₂ and 100% humidity for 3 days forming spheroids.

3.2.8. 3-D Spheroid Assay

After 72 hr of culture, the 3-D spheroids were imaged to determine initial size prior to treatment using a Nikon Eclipse TE-2000E inverted fluorescence optical microscope with a mechanical stage (Nikon, Tokyo, Japan). Following imaging, the spheroids were treated via incubation for 72 hr with either (i) free drug solution of DOX, (ii) free drug solution of GEM, (iii) free drug solution containing both GEM and DOX at a molar ratio of 10:1, or (iv) a dual-drug-loaded hydrogel releasing a molar ratio of GEM:DOX \geq 10:1. After treatment, the spheroids were imaged via phase contrast microscopy. For treatments using gels, the spheroids were transferred to a 24-well plate and the volume of media was brought to 500 µL. Trans-well inserts were added to the plate, and the drug-loaded gel was added to the trans-well insert and covered with 100 µL of media. The mass of gel added (25, 50, 75, 100, or 125 mg) was chosen to expose the cells to a concentration of DOX/GEM comparable to that utilized in case (iii).

Growth inhibition was adopted as a metric to quantify treatment efficacy against spheroids, as done in the current literature [38, 39]. Following treatment, the spheroids were collected and imaged via optical microscopy. All images of cells were processed using ImageJ (NIH) by removing background and measuring all spheroids as ellipses. The major axis (d_{max}) and minor

axis (d_{\min}) were measured and the volume of the spheroid was calculated as $V = (\pi \times d_{\max} \times d_{\min})/6$. The change in spheroid volume was defined by $(V-V^*)/V^*$, where V is the spheroid volume post-treatment and V^* was the spheroid volume immediately prior to treatment.

In addition to growth inhibition, live-dead staining was performed to visualize cell death within the spheroids. Following treatment, spheroids were incubated with 100 μL of staining solution for a final concentration of 2 μM calcein AM ($\lambda_{\text{excitation}}/\lambda_{\text{emission}}$: 494/517 nm) and 4 μM EthD-1 ($\lambda_{\text{excitation}}/\lambda_{\text{emission}}$: 528/617 nm), for 15 min at 37°C. Following incubation, the spheroids were fluorescently imaged, using FITC and TRITC fluorescence filter cubes.

3.2.9. Statistical Analysis

Statistical significance was determined by evaluation of the Student's t-test using Microsoft Excel. Statistical significance for samples was evaluated against the control test condition, and $p < 0.05$ was considered significant. For analysis *, and ** represent $p < 0.05, 0.01$, respectively.

3.3. Results

3.3.1. Single-Drug Loading and Release Studies

In previous work, we conducted an in-depth study of the transport mechanism of DOX and GEM on ACS hydrogels featuring different levels of acetylation (χ_{Ac}) [23], and selected a value of χ_{Ac} ($40 \pm 5\%$) that grants favorable release properties, namely, faster release of GEM relative to DOX, and a GEM:DOX molar ratio $\geq 10:1$. In this work, we sought to optimize the loading of GEM and DOX on the select ACS hydrogel to obtain the release of a therapeutically-viable and synergistic dose of the drug combination.

Preliminary single-drug loading and release tests with both DOX and GEM were conducted. As anticipated, we observed an increase in loading for both DOX and GEM as the drug concentration in the feedstock increased (**Figure 3.1A** and **Figure 3.1B**, respectively). Specifically, loading of DOX was not significantly affected by loading concentration and ranged from 1.8 ± 0.2 to 3.1 ± 0.04 ng per mg of ACS hydrogel, while the loading of GEM ranged from 55.7 ± 0.7 μg to 214 ± 6.7 ng per mg of ACS hydrogel. Release was performed in PBS at pH 7.4 and 37°C to simulate physiological conditions. We observed that the release of DOX was relatively independent of the loading drug concentration (*i.e.*, no statistically significant correlation was observed, **Figure 3.1C**), varying between 51.3 ± 13.6 % and 65.1 ± 0.7 % at 72 hr. Similarly, GEM release varied between 10.9 ± 1.0 % and 16.3 ± 2.2 % over 72 hr (**Figure 3.1D**).

We finally calculated the corresponding dose of DOX and GEM released from the ACS hydrogels based on the last time point (72 hr) on the temporal release profiles (**Figure 3.2**): DOX released dose ranged between 0.263 ± 0.04 μM and 0.632 ± 0.12 μM , while GEM dose ranged between 2.87 ± 0.3 μM to 19.4 ± 4.3 μM , both of which are expected to be therapeutically efficacious.

3.3.2. Optimization of Dual-Drug Loading and Release

We then sought to optimize the dual-drug loading of ACS hydrogels to achieve the release of DOX and GEM with global kinetics and dosage ratio (1:10) that are conducive to therapeutic synergism [7, 8, 34]. To this end, we utilized the results of single-drug release studies to guide to design of dual-drug release studies. Specifically, two drug solutions were adopted: (*i*) a diluted solution featuring a GEM concentration of $25 \mu\text{g mL}^{-1}$ and DOX concentration of $0.5 \mu\text{g mL}^{-1}$, which granted final (72 hr) doses of 2.87 ± 0.3 μM of GEM and 0.263 ± 0.04 μM of DOX in

single-drug release studies; and (*ii*) a concentrated solution featuring a GEM concentration of 50 $\mu\text{g mL}^{-1}$ GEM and DOX concentration of 1 $\mu\text{g mL}^{-1}$, which granted final (72 hr) doses of $7.43 \pm 0.6 \mu\text{M}$ for GEM and $0.330 \pm 0.13 \mu\text{M}$ for DOX in single-drug release studies. The resulting loading in ACS hydrogel (χ_{Ac} of $40 \pm 5 \%$) was $65.1 \pm 8 \text{ ng}$ of GEM per mg of ACS and $1.71 \pm 0.07 \text{ ng}$ of DOX per mg of ACS when using the diluted loading solution, and $90.7 \pm 15.3 \text{ ng}$ of GEM per mg of ACS and $3.32 \pm 0.3 \text{ ng}$ of DOX per mg of ACS when using the concentrated loading solution (**Figure 3.3A**). Notably, these loading values fall within experimental error relative to the single-drug loading values.

The resulting temporal release profiles indicate that $22.0 \pm 5.0 \%$ of GEM and $14.3 \pm 1.6 \%$ of DOX are released over 72 hr from the ACS hydrogel prepared using diluted loading solution (squares in **Figure 3.3B**), whereas $41.1 \pm 6.8 \%$ of GEM and $13.7 \pm 1.1 \%$ of DOX are released from the ACS hydrogel prepared using concentrated loading solution (circles in **Figure 3.3B**). These correspond to GEM and DOX doses of $4.56 \pm 1.4 \mu\text{M}$ and $0.067 \pm 0.01 \mu\text{M}$ released over 72 hr from the ACS hydrogel loaded with diluted drug solutions, and $20.7 \pm 2.4 \mu\text{M}$ and $0.126 \pm 0.02 \mu\text{M}$ released from the ACS hydrogel loaded with concentrated drug solutions (**Figure 3.4**).

3.3.3. 2-D *In vitro* Viability Assay

We then resolved to evaluate the therapeutically relevance of our DDS against the TNBC cell line MDA-MB-231 in a 2D (cell monolayer) cytotoxicity assay. The dose response curves and the corresponding fit with the median effect equation [40] are presented in **Figure 3.5A**. From these results we derived the IC₅₀ values for the various treatments, namely $23.1 \pm 2.5 \mu\text{M}$ for GEM, $0.641 \pm 0.06 \mu\text{M}$ for DOX, $0.112 \pm 0.01 \mu\text{M}$ for the GEM+DOX free drug combination (10:1 molar ratio), and $0.071 \pm 0.002 \mu\text{M}$ for the GEM+DOX drug combination released from the

ACS hydrogel (we note that the IC₅₀ of DOX is higher than the value that we reported in prior work on ACS hydrogels and found in the literature, namely 0.08 μM – 0.2 μM; in this study, however, we utilized a high seeding cell density to build our 2-D assay, and the resulting high cell density is known to increase the effective IC₅₀ [41]. To evaluate drug synergism, we utilized the IC₅₀ values provided by the combination therapies to calculate the combination index (CI) [42]. For the free drug combination, the CI was found to be 0.223 ± 0.002, indicating a strong synergism, consistent with previous findings [7, 8, 34]. Notably, the DDS afforded a CI of 0.142 ± 0.010, indicating even higher synergism. For comparison, Vogus *et al.* obtained only a slightly lower CI (0.12) using a model microfluidic system capable of precisely controlling the delivery scheduled and dose of the same drug pair (DOX and GEM) against TNBC cells [8]. This indicates that the DDS successfully delivers the desired kinetics and drug dose, demonstrating the effectiveness of the proposed design.

To ensure that the improved treatment resulted solely from the DDS implementing favorable delivery kinetics, we evaluated the biocompatibility of the hydrogel with no drug cargo. The data in **Figure 3.5B**, reporting the comparison in the viability of gel-treated and non-treated cells, demonstrate excellent biocompatibility of ACS hydrogel.

3.3.4. 3-D Spheroid Assay

To further assess the therapeutic efficacy of the proposed DDS, we evaluated the GEM/DOX-loaded ACS hydrogel using a 3-D tumor spheroid assay, which has been shown to reflect the likelihood of successful translation of DDS *in vivo* [38, 39]. With this assay we sought to achieve two goals: demonstrate that the DDS offers a better treatment outcome than the prescribed dual free drug administration and determine the necessary dosing needed to maximize

tumor volume reduction. **Figure 3.6** reports the achieved change in tumor volume following a mid-dose drug treatment ($\sim 2 \mu\text{M}$).

After 72 hr, the untreated spheroid showed a $30 \pm 2.9\%$ increase in volume, nearly identical to that incubated with the unloaded ACS hydrogel ($29.6 \pm 7.3\%$), thus corroborating the claim of biocompatibility of the DDS. The volume increase of spheroids treated with $1.67 \mu\text{M}$ GEM dropped to $20.5 \pm 2.1\%$, yet without showing a statistically significant difference compared to the control. When treated with $2.5 \mu\text{M}$ DOX, the increase in spheroid volume was further reduced to $8.7 \pm 4.5\%$, with statistically significant difference compared to the control ($p < 0.05$). Similarly, the concurrently free drug combination treatment ($2.0 \mu\text{M}$ DOX and $20 \mu\text{M}$ GEM) limited the spheroid growth to $2.4 \pm 5.2\%$, indicating a statistically significant volume reduction ($p < 0.05$). Remarkably, the DDS delivering a dose of $2.08 \mu\text{M}$ DOX and $20.8 \mu\text{M}$ GEM afforded a reduction in spheroid volume of $-32.7 \pm 2.2\%$, which corresponds to a statistically significant volume drop compared to both no treatment and $2.5 \mu\text{M}$ DOX treatment ($p < 0.01$), as well as concurrent free drug combination at a similar dose ($p < 0.05$).

We also utilized fluorescence-based live-dead staining to identify a relationship between volume change in the spheroids upon treatment and the viability of the cells constituting those spheroids (**Figure 3.7**, where green fluorescence and red fluorescence represents viable and non-viable cells, respectively). Notably, the increase in red fluorescence trends in the same direction as volume change, namely substantial decreases in volume change results in increased red fluorescence relative to the control. Although both free and ACS-based combination treatments yield a similar red fluorescence, the spheroids treated with the dual-drug-loaded ACS are visibly smaller (**Figure 3.7K** and **Figure 3.7L**) compared to those treated via concurrent free drug

administration at a similar dosage (**Figure 3.6.7I** and **Figure 3.6.7J**). Collectively, these data demonstrate the efficacy of treatment stemming from the proposed DDS.

To fully elucidate the impact of drug dosage on spheroid volume reduction, we finally explored the effect of concentration of both single and dual-drugs on the spheroid volume change (**Figure 3.8**). Treatment with free GEM lowered the spheroid volume increase from $30.1 \pm 9.2\%$ ($0.21\text{ }\mu\text{M}$ GEM) to $-7.29 \pm 3.0\%$ ($53.3\text{ }\mu\text{M}$); considering the viability in spheroid volume upon treatment (**Figure 3.7F**), it is evident that GEM fails to reduce the viability of the spheroids (**Figure 3.9A1 – Figure 3.9A5**), although it substantially reduces the ability of the spheroid to proliferate and grow as dosing increases . Treatment with DOX, on the other hand, afforded a drastic decrease in spheroid volume, from $19.4 \pm 3.6\%$ ($0.02\text{ }\mu\text{M}$) to $-10.2 \pm 2.4\%$ ($1.25\text{ }\mu\text{M}$). At higher DOX doses, an inverse trend in volume increase is observed (**Figure 3.7H**). This, however, can be attributed to a strong reduction in viability (**Figure 3.9B1 – Figure 3.9B5**) that results in loss of cohesiveness, and ultimately in a high observed volume increase ($51.9 \pm 6.3\%$ at $5\text{ }\mu\text{M}$). Spheroids exposed to the combination of free DOX and GEM showed a trend comparable to that of DOX-only treatment, namely a reduction in volume from $25.6 \pm 0.5\%$ volume change at $0.016\text{ }\mu\text{M}$ DOX ($0.160\text{ }\mu\text{M}$ GEM) to $2.4 \pm 5.2\%$ at $2\text{ }\mu\text{M}$ DOX ($20\text{ }\mu\text{M}$ GEM), followed by a drastic increase in volume change, up to $66.9 \pm 19.3\%$ at $4\text{ }\mu\text{M}$ DOX ($40\text{ }\mu\text{M}$ GEM), and loss of viability at higher doses (**Figure 3.9C1 – Figure 3.9C5**). Finally, the ACS DDS produced an initial volume decrease from $-21.3 \pm 3.8\%$ at $0.42\text{ }\mu\text{M}$ DOX ($4.2\text{ }\mu\text{M}$ GEM) to $-32.7 \pm 2.2\%$ at $2.08\text{ }\mu\text{M}$ DOX ($20.8\text{ }\mu\text{M}$ GEM), which represent the highest reduction among all treatments, and the highest reduction in viability of the spheroid (**Figure 3.7L**). Upon increasing dosage to $4.02\text{ }\mu\text{M}$ DOX ($40.2\text{ }\mu\text{M}$ GEM), the volume change increased to a $-12.7 \pm 3.3\%$, concomitant with a high loss in viability of the spheroid (**Figure 3.9D1 – 3.9D5**).

3.4. Discussion

3.4.1. Single-Drug Loading and Release Studies

Single-drug loading and release studies were initially undertaken to evaluate the transport of DOX and GEM through the ACS hydrogel and to ensure that the loading of both drugs enabled therapeutically efficacious release doses (**Figure 3.2**). Our results demonstrate that *(i)* GEM release represents the first front of drug delivery, with the GEM flux exhausted within a 24 hr time frame (**Figure 3.1D**), whereas *(ii)* DOX is release at ‘steady state’ across the entire 72 hr window (**Figure 3.1C**). This release scheme, where the GEM total dose is released prior to a steady flux of DOX, represents the desired delivery schedule for this drug pair. Notably, the release profiles of both GEM and DOX (**Figure 3.1C** and **Figure 3.1D**) did not show dependence upon the initial drug loading on the ACS hydrogel, indicating that drug transport and release kinetics are controlled by the drug-polymer interactions and that the proposed DDS is efficient and robust. This study of single-drug loading and release are functional to the design and interpretation of the subsequent dual-drug release study and represent a necessary step in the pre-clinical characterization pathway [23].

3.4.2. Dual-Drug Loading and Release Studies

We subsequently utilized the results of single-drug studies to guide dual-drug loading and release studies. Notably, the amounts of GEM and DOX co-loaded on the ACS hydrogel (**Figure 3.3A**) were within experimental error relative to single-drug loading. Whilst seemingly minor, this feature greatly simplifies the screening of the loading conditions, as it enables performing the loading studies in a facile single-payload format and subsequently translating them accurately in a multi-payload format. On the other hand, a deviation from ideality can be observed in the release profile from a co-loaded hydrogel, especially for multimodal drugs like DOX (**Figure 3.3B**) whose

complex amphiphilic character drives complex drug-drug and drug-polymer interactions (28), making their transport mechanism difficult to predict; nonetheless, the release profile is independent of the loading concentration, as observed in the single-drug study. GEM release from the co-loaded hydrogel (**Figure 3.3B**), on the other hand, was consistent with single-drug release at the lower concentration utilized and only deviated at higher loading concentrations (**Figure 3.3D**).

3.4.3. *In vitro* 2-D and 3-D Viability Assays

We finally evaluated the therapeutic efficacy of the proposed DDS against 2-D (cell monolayers) and 3-D (tumor spheroids) models of the TNBC cell line MDA-MB-231. In view of combination chemotherapy, we adopted (*i*) the “combination index” (CI) and (*ii*) the tumor volume reduction as critical performance parameters. For references, when DOX and GEM were concurrently released as free drugs in a 1:10 molar ratio, we observed a synergistic treatment outcome, indicated by a CI of 0.23, consistent with published studies focusing on this drug pair and target cell line [7, 8, 34]. The treatment with dual-drug-loaded ACS hydrogel further reduced the CI to 0.14, providing evidence that the ability of the hydrogel to control the delivery kinetics and ratio improves the therapeutic efficacy. Notably, this result compares well with the CI value obtained by Vogus *et al.* (CI ~ 0.12) [8], who utilized a microfluidic setup to achieve a completely segregated delivery schedule across the same 72 hr window.

The DDS was then evaluated on 3-D tumor spheroids. These models have earned wide popularity in evaluating drug regimens as they accurately predict successful *in vivo* translation [38, 39]. To our knowledge, the present study represents the first report evaluating the GEM+DOX pair against a TNBC spheroid model. When treated with GEM as a free drug in solution, the viability

of the spheroids was hardly impacted (**Figure 3.9A1 – Figure 3.9A5**), although higher doses clearly limit their growth, as shown in **Figure 3.8**. The treatment with free DOX, on the other hand, achieved both reduction of spheroid growth and viability, resulting in the disintegration of the spheroids (**Figure 3.8** and **Figure 3.9B1 – Figure 3.9B5**). The combined treatment with free GEM and DOX in solution offered a trade-off between volume reduction and viability, as reflected in the volume change curve (blue squares in **Figure 3.8**), which appears to be an average of the results of the single free drug treatments (red and green squares in **Figure 3.8**). Furthermore, the combined free drug treatment afforded a decrease in viability at increasing at higher doses comparable to that achieved by DOX alone (**Figure 3.9C1 – Figure 3.9C5**). Spheroids treated with GEM/DOX-loaded ACS hydrogel, on the other hand, showed a more drastic volume decrease (orange squares in **Figure 3.8**), combined with a major loss in viability (**Figure 3.9D1 – Figure 3.9D5**). Collectively, these results demonstrate that hydrogel-mediated scheduling is critical to improve therapeutic efficacy, advocating for the use of the proposed ACS hydrogel for the treatment of TNBC.

3.5. Conclusions

The use of hydrogels constructed from modified polysaccharides and loaded with therapeutics has been extensively studied over the last decade and remains an active area of research. Next-generation therapeutic biomaterials are becoming increasingly focused on integrating the paradigm of scheduled and synergistic combination within the design of drug-delivery systems. These systems, by achieving a precise control of dosages and delivery schedules, provide enhanced drug synergism and enable a drastic reduction of the required therapeutic doses, while maintaining highly efficacious outcomes. This study focuses on the development of an ACS

hydrogel that (*i*) is constructed with scalable chemistry on a naturally abundant material, (*ii*) is capable of delivering a recognized synergistic drug pair (DOX and GEM) with precise dosages and release kinetics, and (*iii*) can be delivered locally at the malignancy site. When evaluated against the MDA-MB-231 (TNBC) cell line, a cancer with notoriously poor prognosis, the proposed dual-drug-loaded ACS hydrogel afforded remarkable results in terms of both combination index a reduction of spheroid growth. This work provides a roadmap for developing naturally-derived hydrogels and evaluating their efficacy, thereby laying the groundwork for the future development of materials targeting aggressive metastatic solid tumors that – to this day – greatly impact the health and quality of life of millions of people worldwide.

REFERENCES

- [1] Mokhtari R.B., T.S. Homayouni, N. Baluch, et al., Combination therapy in combating cancer. *Oncotarget*, 2017. 8(23): p. 38022-38043.
- [2] Hu, Q., W. Sun, C. Wang, and Z. Gu. Recent Advances of Cocktail Chemotherapy by Combination Drug Delivery Systems. *Advanced Drug Delivery Reviews*, 2016. 98: p. 19-34.
- [3] Nikolaou, M., A. Pavlopoulou, A.G. Georgakilas, and E. Kyrodimos, The challenge of drug resistance in cancer treatment: a current overview. *Clinical and Experimental Metastasis*, 2018. 35(4): p. 309-318.
- [4] Palmer, A.C., and P.K Sorger, Combination Cancer Therapy Can Confer Benefit via Patient-to-Patient Variability without Drug Additivity or Synergy. *Cell*, 2017. 171(7): p. 1678-1691.
- [5] Lee, Y.-G., J.H. Lee, S.-H. Kim, et al., Comparative analysis between combination and single-agent chemotherapy for elderly patients with advanced non-small cell lung cancer: A nationwide population-based outcome study. *Lung Cancer*, 2018. 122: p. 88-93.
- [6] Pusuluri, A., V. Krishnan, D. Wu, et al. Role of synergy and immunostimulation in design of chemotherapy combinations: An analysis of doxorubicin and camptothecin. *Bioengineering and Translational Medicine*, 2019. 4(2): p. e10129.
- [7] Vogus, D.R., M.A. Evans, A. Pusuluri, et al., A hyaluronic acid conjugate engineered to synergistically and sequentially deliver gemcitabine and doxorubicin to treat triple negative breast cancer. *Journal of Controlled Release*, 2017. 267: p. 191-202.
- [8] Vogus, D.R., A. Pusuluri, R. Chen, et al., Schedule dependent synergy of gemcitabine and doxorubicin: Improvement of in vitro efficacy and lack of in vitro-in vivo correlation. *Bioengineering and Translational Medicine*, 2018. 3(1): p. 49-57.
- [9] Bao, Y.-X., X.-D. Zhao, H.-B. Deng, et al., Schedule-dependent cytotoxicity of sunitinib and TRAIL in human non-small cell lung cancer cells with or without EGFR and KRAS mutations. *Cellular Oncology*, 2016. 39(4): p. 343-352.
- [10] Zhang, Z., S. Liu, Y. Qi, et al., Time-programmed DCA and oxaliplatin release by multilayered nanofiber mats in prevention of local cancer recurrence following surgery. *Journal of Controlled Release*, 2016. 235: p. 125-133.
- [11] Li, X., Y. He, J. Hou, et al., A Time-Programmed Release of Dual Drugs from an Implantable Trilayer Structured Fiber Device for Synergistic Treatment of Breast Cancer. *Small*, 2020. 16(9): p. e1902262.
- [12] Wei, L., J. Chen, S. Zhao, et al., Thermo-sensitive polypeptide hydrogel for locally sequential delivery of two-pronged antitumor drugs. *Acta Biomaterialia*, 2017. 58: p. 44-53.

- [13] Wang, H., J. Wu, K. Xie, et al., Precise Engineering of Prodrug Cocktails into Single Polymeric Nanoparticles for Combination Cancer Therapy: Extended and Sequentially Controllable Drug Release. *ACS Applied Materials and Interfaces*, 2017. 9(12): p. 10567-10576.
- [14] Wang, T., D. Wang, J. Liu, et al., Acidity-Triggered Ligand-Presenting Nanoparticles To Overcome Sequential Drug Delivery Barriers to Tumors. *Nano Letters*, 2017. 17(9): p. 5429-5436.
- [15] Li, L., W. Sun, Z. Zhang, and Y. Huang, Time-staggered delivery of docetaxel and H1-S6A,F8A peptide for sequential dual-strike chemotherapy through tumor priming and nuclear targeting. *Journal of Controlled Release*, 2016. 232: p. 62-74.
- [16] Simkens, L.H.J., H. van Tinteren, A. May, et al., Maintenance treatment with capecitabine and bevacizumab in metastatic colorectal cancer (CAIRO3): a phase 3 randomised controlled trial of the Dutch Colorectal Cancer Group. *Lancet*, 2015. 385(9980): p. 1843-1852.
- [17] Ducreux, M., D. Malka, J. Mendiboure, et al., Sequential versus combination chemotherapy for the treatment of advanced colorectal cancer (FFCD 2000-05): an open-label, randomised, phase 3 trial. *Lancet Oncology*, 2011. 12(11): p. 1032-1044.
- [18] Choi, J.Y., R.K. Thapa, C.S. Yong, and J.O. Kim, Nanoparticle-based combination drug delivery systems for synergistic cancer treatment. *Journal of Pharmaceutical Investigation*, 2016. 46(4): p. 325-339.
- [19] Pushpalatha, R., S. Selvamuthukumar, and D. Kilimozhi, Nanocarrier mediated combination drug delivery for chemotherapy – A review. *Journal of Drug Delivery Science and Technology*, 2017. 39: p. 362-371.
- [20] Vogus, D.R., V. Krishnan, and S. Mitragotri, A review on engineering polymer drug conjugates to improve combination chemotherapy. *Current Opinion in Colloid and Interface Science*, 2017. 31: p. 75-85.
- [21] Yu, S., C. He, and X. Chen, Injectable Hydrogels as Unique Platforms for Local Chemotherapeutics-Based Combination Antitumor Therapy. *Macromolecular Bioscience*, 2018. 18(12): p. 1800240.
- [22] Huang, J., W.-J. Wang, B.-G. Li, and S. Zhu, Design and Synthesis of Poly(butyl acrylate) Networks through RAFT Polymerization with Crosslinking for Controlled-Release Applications. *Macromolecular Materials and Engineering*, 2013. 298(4): p. 391-399.
- [23] Schneible, J.D., A. Singhal, R.L. Lilova, et al., Tailoring the Chemical Modification of Chitosan Hydrogels to Fine-Tune the Release of a Synergistic Combination of Chemotherapeutics. *Biomacromolecules*, 2019. 20(8): p. 3126-3141.

- [24] Li, J., and D.J. Mooney, Designing hydrogels for controlled drug delivery. *Nature Reviews Materials*, 2016. 1(12): p. 1-17.
- [25] Dimatteo, R., N.J. Darling, and T. Segura, Designing In situ forming injectable hydrogels for drug delivery and wound repair. *Advanced Drug Delivery Reviews*, 2018. 127: p. 167-184.
- [26] Tibbitt, M.W., J.E. Dahlman, and R. Langer, Emerging Frontiers in Drug Delivery. *Journal of the American Chemical Society*, 2016. 138(3): p. 704-717.
- [27] Hamed, H., S. Moradi, S.M. Hudson, and A.E. Tonelli, Chitosan based hydrogels and their applications for drug delivery in wound dressings: A review. *Carbohydrate Polymers*, 2018. 199: p. 445-460.
- [28] Ahsan, S.M., M. Thomas, K.K. Reddy, et al., Chitosan as biomaterial in drug delivery and tissue engineering. *International Journal of Biological Macromolecules*, 2018. 110: p. 97-109.
- [29] VandeVord, P.J., H.W.T. Matthew, S.P. DeSilva, et al., Evaluation of the biocompatibility of a chitosan scaffold in mice. *Journal of Biomedical Materials Research*, 2002. 59(3): p. 585-590.
- [30] Xu, J., M. Tam, S. Samaei, et al., Mucoadhesive chitosan hydrogels as rectal drug delivery vessels to treat ulcerative colitis. *Acta Biomaterialia*, 2017. 48: p. 247-257.
- [31] Pellá M.C.G., M.K. Lima-Tenório, E.T. Tenório-Neto, et al., Chitosan-based hydrogels: From preparation to biomedical applications. *Carbohydrate Polymers*, 2018. 196: p. 233-245.
- [32] Naskar, S., S. Sharma, and K. Kuotsu, Chitosan-based nanoparticles: An overview of biomedical applications and its preparation. *Journal of Drug Delivery Science and Technology*, 2019. 49: p. 66-81.
- [33] Khan, M.A., and M. Mujahid, A review on recent advances in chitosan based composite for hemostatic dressings. *International Journal of Biological Macromolecules*, 2019. 124: p. 138-147.
- [34] Schneible, J.D., K. Shi, A.T. Young, et al., Modified graphene oxide (GO) particles in peptide hydrogels: a hybrid system enabling scheduled delivery of synergistic combinations of chemotherapeutics. *Journal of Materials Chemistry B*, 2020. 8: p. 3852-3868.
- [35] Liu, D., Y. Chen, X. Feng, et al., Micellar nanoparticles loaded with gemcitabine and doxorubicin showed synergistic effect. *Colloids and Surfaces B: Biointerfaces*, 2014. 113: p. 158-168.
- [36] Kaiser, E., R.L. Colescott, C.D. Bossinger, and P.I. Cook, Color test for detection of free terminal amino groups in the solid-phase synthesis of peptides. *Analytical Biochemistry*, 1970. 34(2): p. 595-598.

- [37] Froehlich, K., J.-D. Haeger, J. Heger, et al., Generation of Multicellular Breast Cancer Tumor Spheroids: Comparison of Different Protocols. *Journal of Mammary Gland Biology and Neoplasia*, 2016. 21(3-4): p. 89-98.
- [38] Xin, H., X. Sha, X. Jiang, et al., Anti-glioblastoma efficacy and safety of paclitaxel-loading Angiopep-conjugated dual targeting PEG-PCL nanoparticles. *Biomaterials*, 2012. 33(32): p. 8167-8176.
- [39] Wang, Y., J. Zhou, L. Qiu, et al., Cisplatin-alginate conjugate liposomes for targeted delivery to EGFR-positive ovarian cancer cells. *Biomaterials*, 2014. 35(14): p. 4297-4309.
- [40] Chou, T.-C., The mass-action law based algorithm for cost-effective approach for cancer drug discovery and development. *American Journal of Cancer Research*, 2011. 1(7): p. 925-954.
- [41] He, Y., Q. Zhu, M. Chen, et al., The changing 50% inhibitory concentration (IC₅₀) of cisplatin: a pilot study on the artifacts of the MTT assay and the precise measurement of density-dependent chemoresistance in ovarian cancer. *Oncotarget*, 2016. 7(43): p. 70803-70821.
- [42] Chou, T.-C., Drug Combination Studies and Their Synergy Quantification Using the Chou-Talalay Method. *Cancer Research*, 2010. 70(2): p. 440-446.

Figures

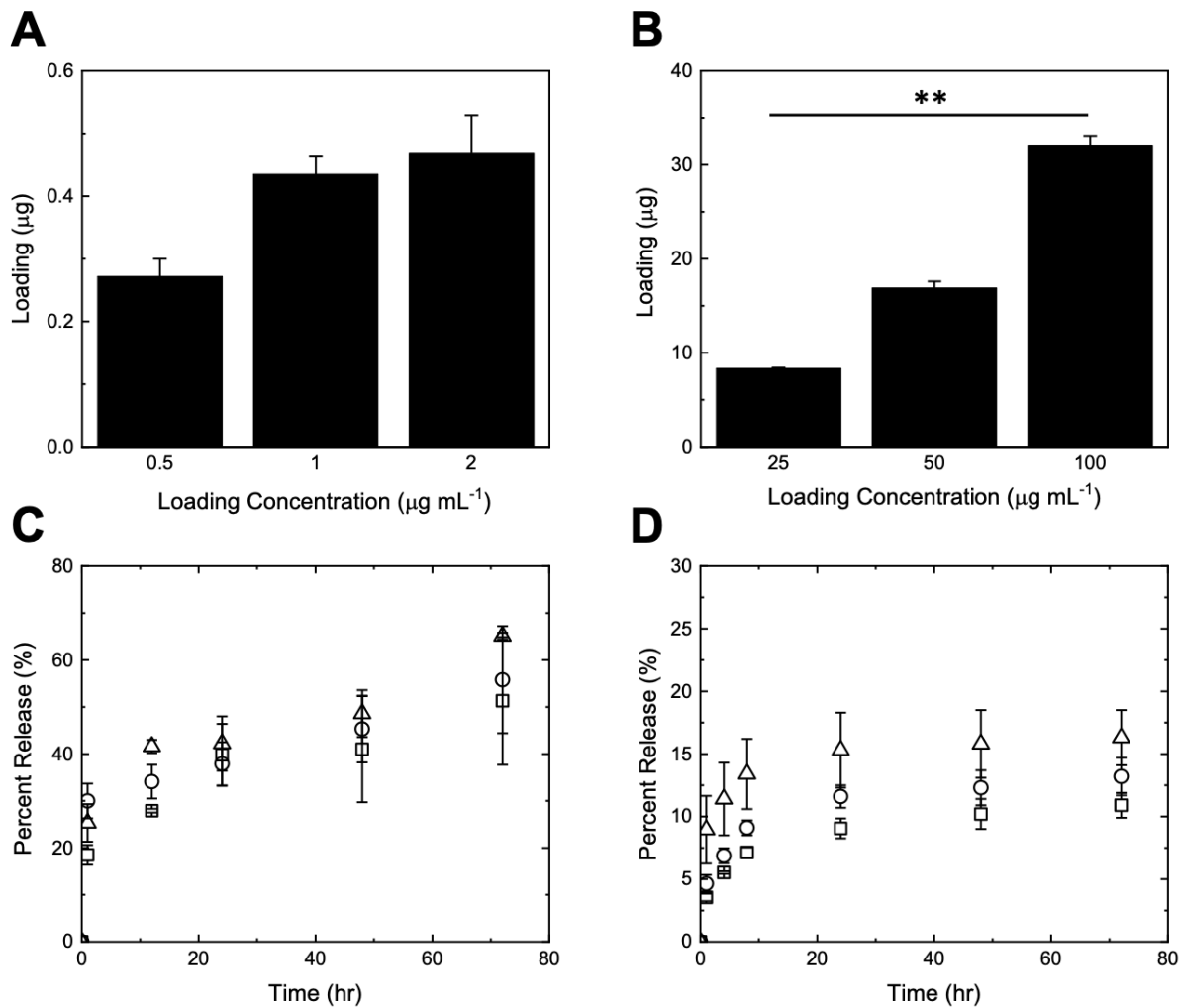


Figure 3.1 Loading of (A) DOX and (B) GEM as a function of loading concentration utilized. Release profiles for (C) DOX at various loading concentrations: $0.5 \mu\text{g mL}^{-1}$ (squares), $1 \mu\text{g mL}^{-1}$ (circles), and $2 \mu\text{g mL}^{-1}$ (triangles), and (D) GEM at various loading concentrations: $25 \mu\text{g mL}^{-1}$ (squares), $50 \mu\text{g mL}^{-1}$ (circles), and $100 \mu\text{g mL}^{-1}$ (triangles). Data are represented as mean \pm S.D. ($n \geq 3$); ** represents $p < 0.01$, as obtained from the Student's t-test.

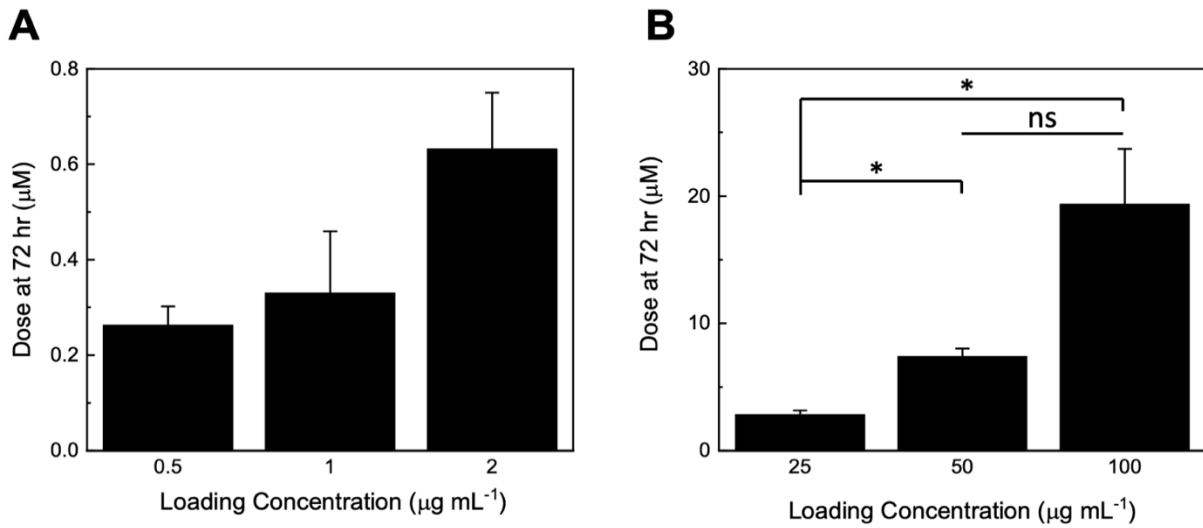


Figure 3.2 The corresponding doses from release studies for (A) DOX and (B) GEM at 72 hr. Data are represented as mean \pm S.D. ($n \geq 3$); ns and * represent no statistical significance and $p < 0.05$, respectively, as obtained from the Student's t-test.

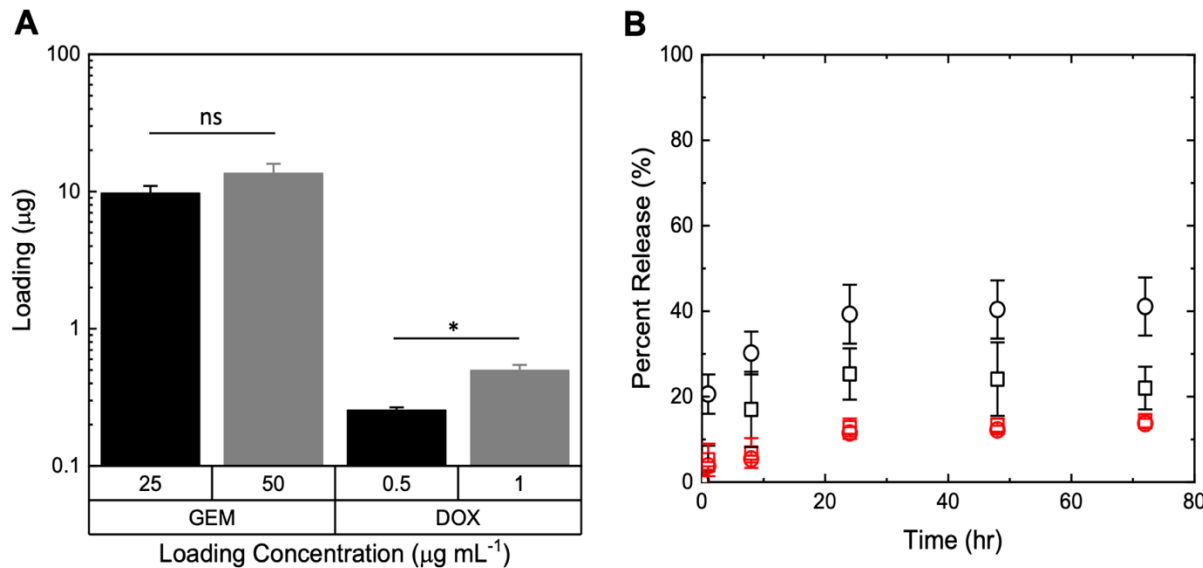


Figure 3.3 (A) Amounts of DOX and GEM loaded on ACS hydrogels using either diluted drug solutions ($25 \mu\text{g mL}^{-1}$ GEM and $0.5 \mu\text{g mL}^{-1}$ DOX, grey column) or concentrated drug solutions ($50 \mu\text{g mL}^{-1}$ GEM and $1 \mu\text{g mL}^{-1}$ DOX, black column). (B) Release profiles of DOX (red) and GEM (black) from the ACS hydrogels loaded with either concentrated (circles) or diluted (squares) drug solutions. Data are represented as mean \pm S.D. ($n \geq 3$); ns and * represent no statistical significance and $p < 0.05$, respectively, as obtained from the Student's t-test.

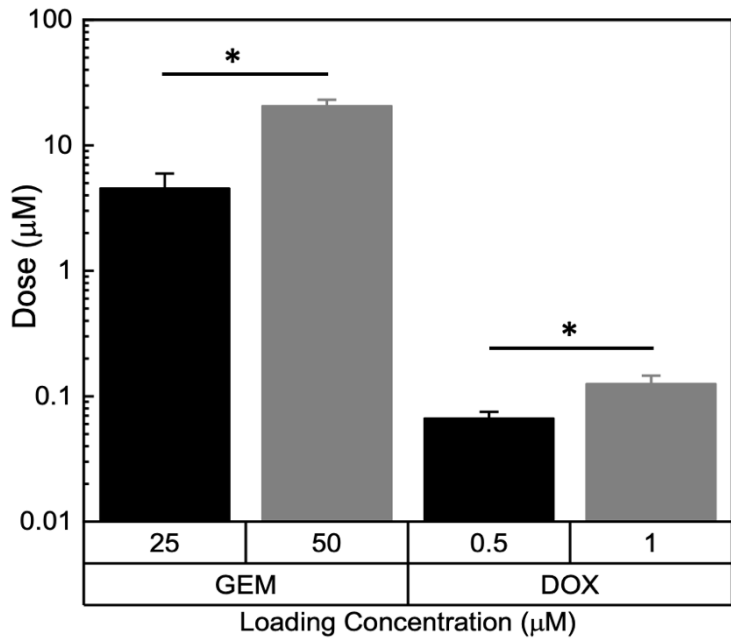


Figure 3.4 The corresponding doses from release studies for a low concentration ($25 \mu\text{g mL}^{-1}$ GEM and $0.5 \mu\text{g mL}^{-1}$ DOX) and a high concentration ($50 \mu\text{g mL}^{-1}$ GEM and $1 \mu\text{g mL}^{-1}$ DOX) at 72 hr. Data are represented as mean \pm S.D. ($n \geq 3$); * represents $p < 0.05$, as obtained from the Student's t-test.

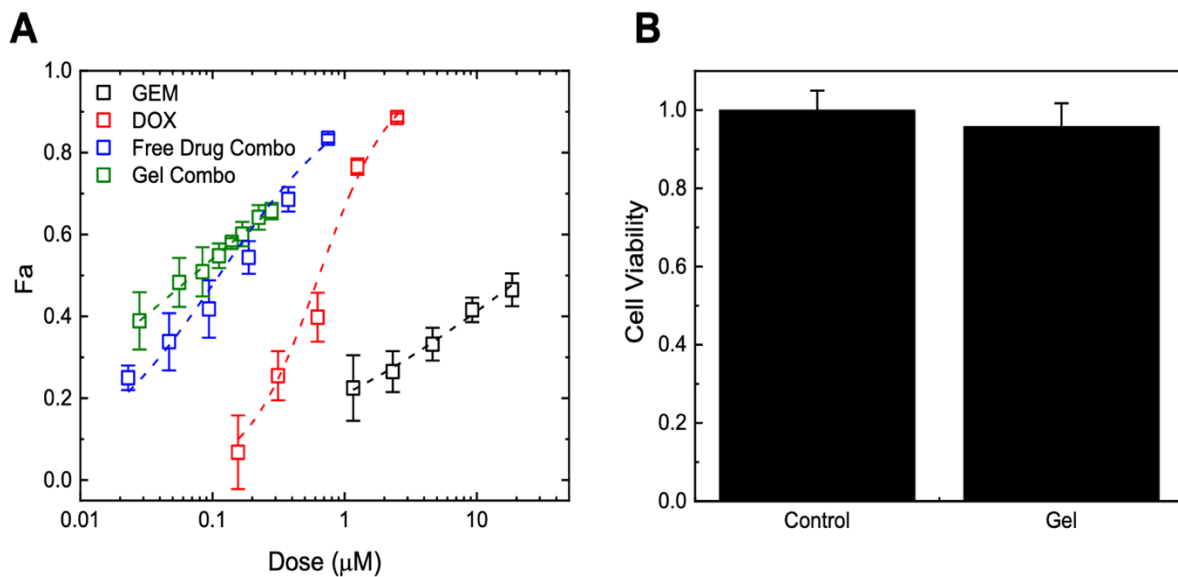


Figure 3.5 (A) Dose-response curves for free DOX (red), free GEM (black), 10:1 molar ratio free drug combination of GEM/DOX (blue), and $\geq 10:1$ molar ratio of DOX and GEM released from the ACS hydrogel; **(B)** Cytotoxicity of the ACS hydrogel relative to untreated cells (control).

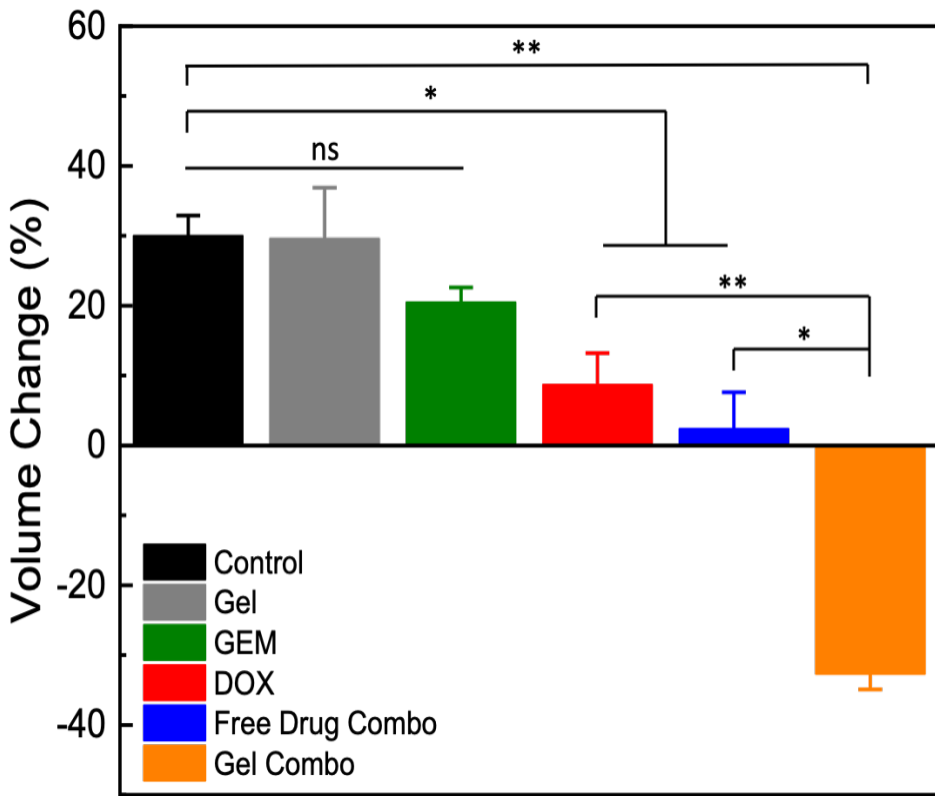


Figure 3.6 Change in volume of spheroids corresponding to a selected dose of treatment. The control (black) and ACS hydrogel (grey) represent spheroids receiving no treatment and exposure to 150 mg of unloaded hydrogel, respectively. Treatments were performed using drug concentrations of 1.67 μ M GEM (green), 2.5 μ M DOX (red), 20 μ M GEM + 2 μ M DOX as free drugs concurrently administered (blue), and 20.8 μ M GEM + 2.08 DOX μ M released from the ACS hydrogel (orange). Data are represented as mean \pm S.D. ($n \geq 3$); ns represents no statistical significance, * and ** represent $p < 0.05$, and $p < 0.01$, respectively, as obtained from the Student's t-test.

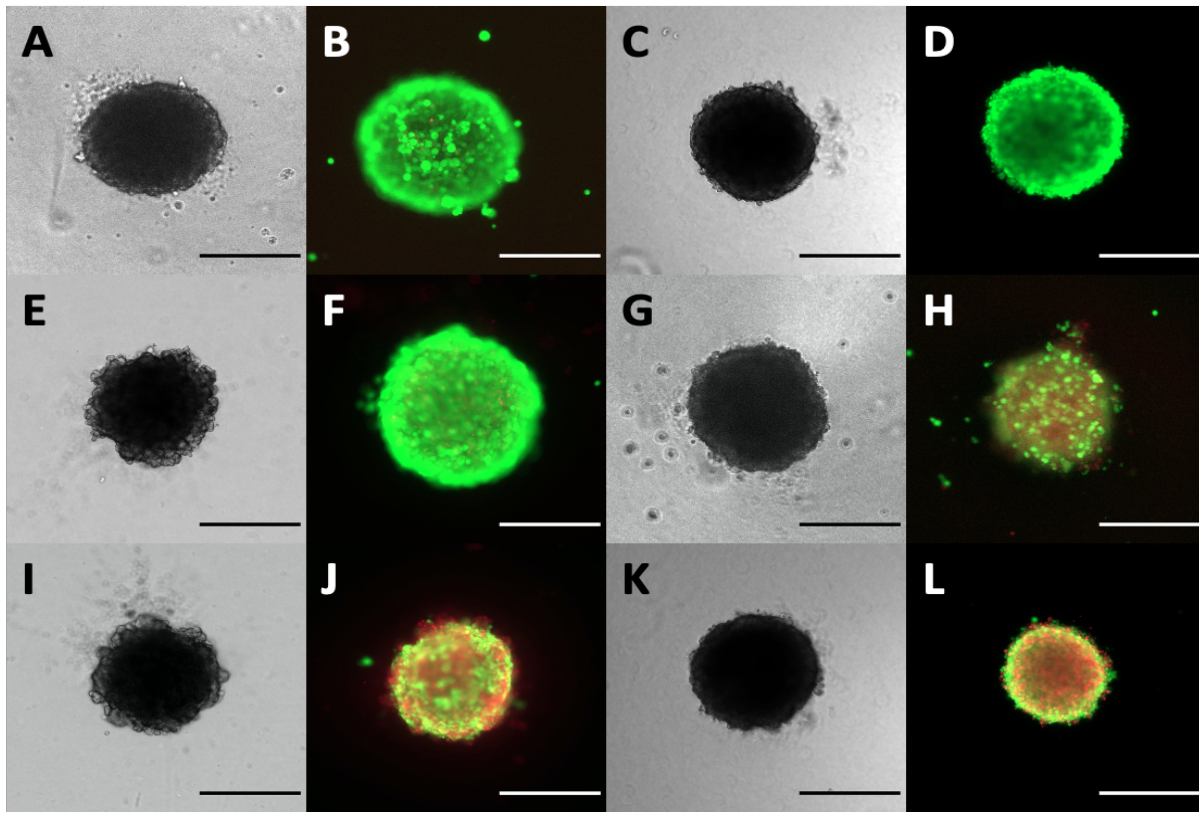


Figure 3.7 Images of spheroids corresponding to the conditions utilized in **Figure 3.6.6**; all grey-scale images represent spheroids prior to treatment and all fluorescent images represent spheroids following treatment; green and red, represent viable and non-viable cells, respectively. (A) and (B) are the control, (C) and (D) are the unloaded hydrogel, (E) and (F) represent treatment with 1.67 μM GEM, (G) and (H) represent treatment with 2.5 μM DOX, (I) and (J) represent treatment with 2.0 μM DOX and 20 μM GEM concurrently administered, and (K) and (L) represent treatment with 2.08 μM DOX and 20.8 μM GEM released from the ACS gel. The scale bar in all images is 400 μm .

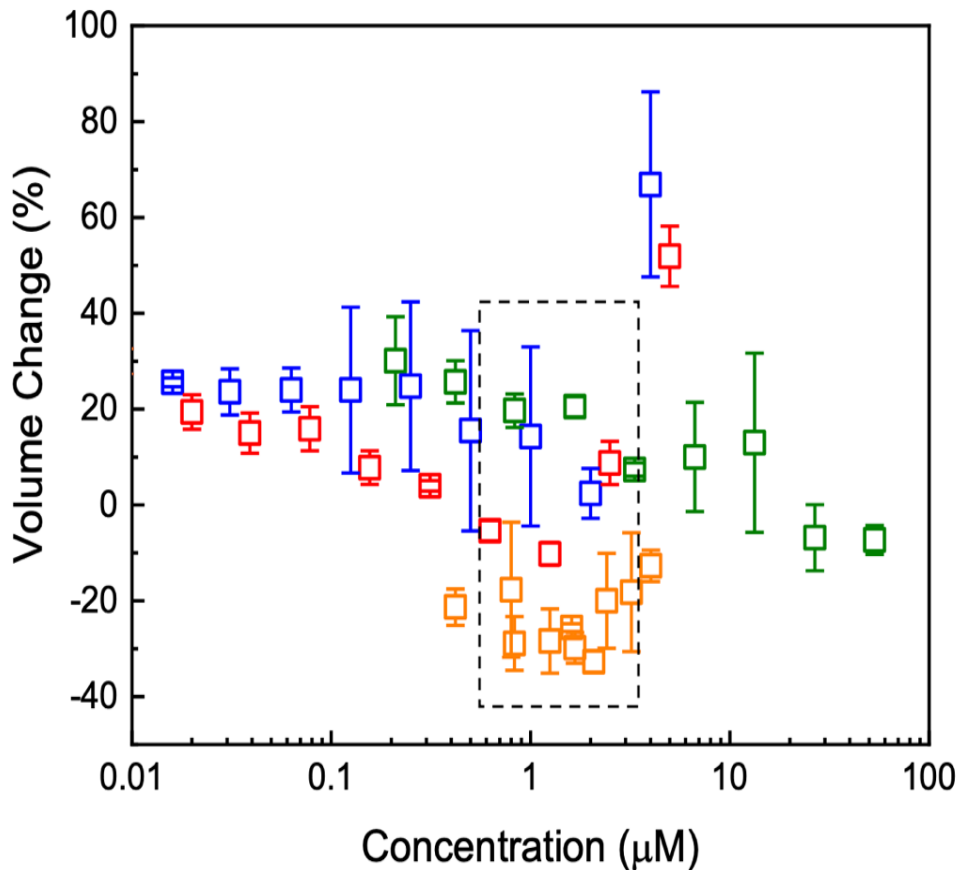


Figure 3.8 Tumor organoid volume change observed as a function of drug concentration for free GEM (green), free DOX (red), free GEM:DOX concurrently administered at a molar ratio of 10:1 (blue), and GEM:DOX released from ACS hydrogel at molar ratio $\geq 10:1$. The desired therapeutic window is indicated by the black box. Data are represented as mean \pm S.D. ($n \geq 3$).

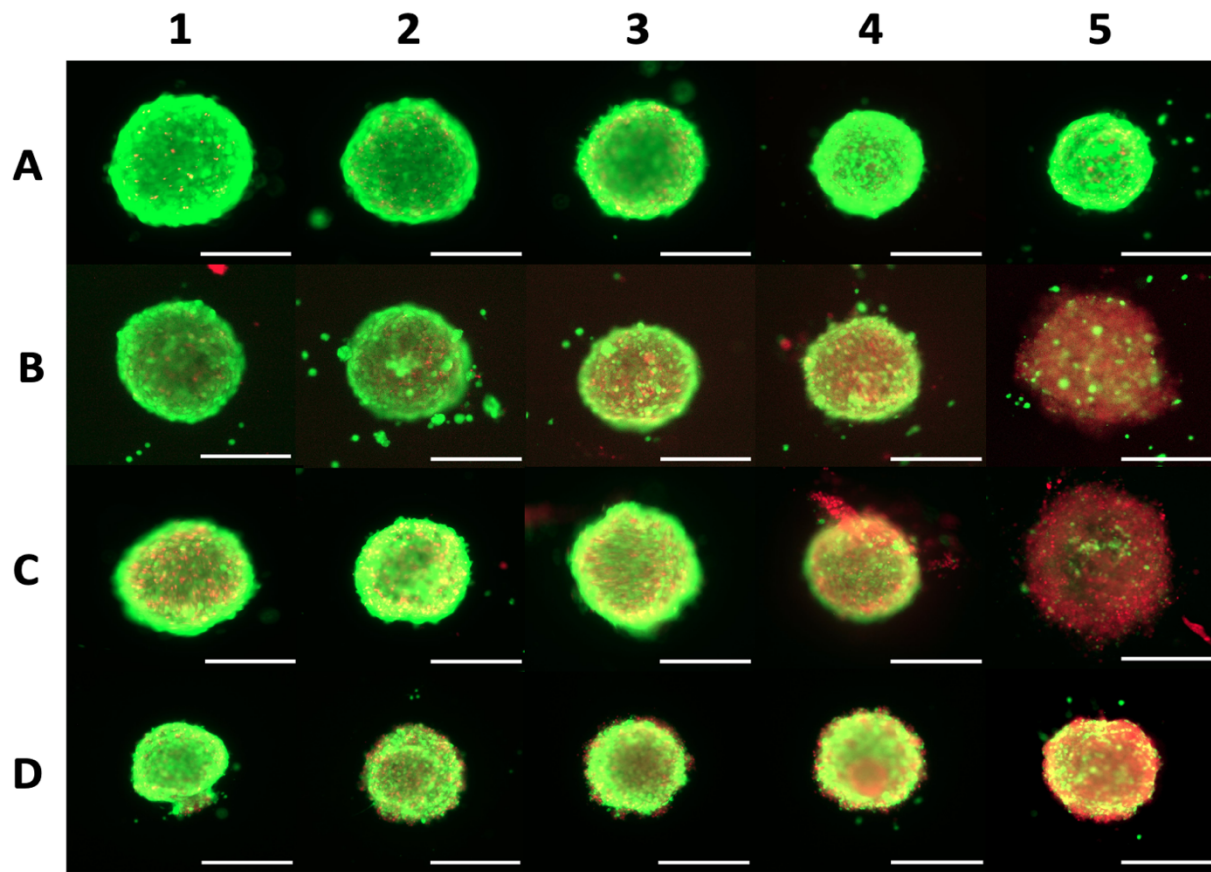


Figure 3.9 Dependence of drug concentration of spheroid volume for: **(A)** GEM (1 – 3.33 μM ; 2 – 6.67 μM ; 3 – 13.3 μM ; 4 – 26.7 μM ; 5 – 53.3 μM), **(B)** DOX (1 – 0.156 μM ; 2 – 0.313 μM ; 3 – 0.625 μM ; 4 – 1.25 μM ; 5 – 5.0 μM), **(C)** DOX and GEM free in solution (1 – 0.25 μM DOX + 2.5 μM GEM; 2 – 0.5 μM DOX + 5 μM GEM; 3 – 1.0 μM DOX + 10 μM GEM; 4 – 2.0 μM DOX + 20 μM GEM; 5 – 4.0 μM DOX + 40 μM GEM), and **(D)** DOX and GEM released from the ACS hydrogel (1 – 0.42 μM DOX + 4.2 μM GEM; 2 – 0.83 μM DOX + 8.3 μM GEM; 3 – 1.25 μM DOX + 12.5 μM GEM, 4 – 1.67 μM DOX + 16.7 μM GEM; 5 – 2.08 μM DOX + 20.8 μM GEM). The scale bar in all images is 400 μm .

CHAPTER 4

Modified Graphene Oxide (GO) Particles in Peptide Hydrogels: A Hybrid System Enabling Scheduled Delivery of Synergistic Combinations of Chemotherapeutics

John D. Schneible, Kaihang Shi, Ashlyn T. Young, Srivatsan Ramesh, Nanfei He, Clay E. Dowdey, Jean Marie Dubnansky, Radina L. Lilova, Wei Gao, Erik Santiso, Michael A. Daniele, and Stefano Menegatti

A version of this chapter has been published in Journal of Materials Chemistry B 2020, 8, 3852-3868.

Abstract

The scheduled delivery of synergistic drug combinations is increasingly recognized as highly effective against advanced solid tumors. Of particular interest are composite systems that release a sequence of drugs with defined kinetics and molar ratios to enhance therapeutic effect, while minimizing the dose to patients. In this work, we developed a homogeneous composite comprising modified graphene oxide (GO) nanoparticles embedded in a Max8 peptide hydrogel, which provides controlled kinetics and molar ratios of release of doxorubicin (DOX) and gemcitabine (GEM). First, modified GO nanoparticles (tGO) were designed to afford high DOX loading and sustained release (18.9% over 72 hr and 31.4% over 4 weeks). Molecular dynamics simulations were utilized to model the mechanism of DOX loading as a function of surface modification. In parallel, a Max8 hydrogel was developed to release GEM with faster kinetics and achieve a 10-fold molar ratio to DOX. The selected DOX/tGO nanoparticles were suspended in a GEM/Max8 hydrogel matrix, and the resulting composite was tested against a triple negative breast cancer cell line, MDA-MB-231. Notably, the composite formulation afforded a combination index of 0.093 ± 0.001 , indicating a much stronger synergism compared to the DOX-GEM combination co-administered in solution ($CI = 0.396 \pm 0.034$).

4.1. Introduction

Combination chemotherapy is currently the most widely utilized, clinically established route to fight cancer, owing to its distinct advantages over current single-drug chemotherapy. Single-drug therapies cause acquired drug resistance upon prolonged administration [1, 2], which cause non-responsiveness to therapy and the need of increased dosage [3, 4]. This results in poorer quality of life during treatment and decreased life expectancy [4-6]. Combination chemotherapy offers superior therapeutic outcomes by operating through the simultaneous disruption of multiple metabolic pathways in cancer cells; these provide three mechanistic outcomes: synergistic, additive, and potentiation [7]. Among these mechanistic outcomes, synergism, whereby the efficacy of multiple chemotherapeutics administered together is greater than the sum of individual therapies administered independently, represents the most favorable therapeutic outcome [7]. Historically, synergism has been attributed to the combination of the drugs utilized and their molar ratio in the chemotherapeutic cocktail [7, 8]. More recently, however, the administration schedule, that is the sequence and timing by which every drug is administered, has been shown to be critical – together with molar ratio – to achieve therapeutic synergism [9-11].

Recent research on the optimization of molar ratio and schedule of chemotherapeutic regimens has demonstrated that a more favorable therapeutic outcome can be achieved relative to single drug therapy. This has been well-documented in pre-clinical studies, both *in vitro* and in animal models [10, 12-18], as well as in clinical settings [19-22]. Current methods to administer scheduled combined chemotherapy rely on subsequent injections, which require prolonged patient hospitalization and extended observation by trained specialists and result in higher medical costs and discomfort for patients. It is now anticipated that next-generation treatments will rely on engineered solutions, comprising multiple biocompatible materials that (*i*) are seamlessly

integrated into stable systems and (*ii*) release the various therapeutic ingredients at tunable amounts and rates to provide the desired therapeutic sequence, ratio, and kinetics.

To this end, researchers have investigated a myriad of drug delivery systems (DDSs), ranging from nano-/micro-particles and liposomes [23, 24] to polymer conjugates (PDC's) [10, 12, 13, 18, 25, 26] and hydrogels [14, 27-29]. Among these systems, nanoparticles and hydrogels possess distinct advantages, mainly loading capacity and tenability of release [30-36]. A nanoscale carrier that has attracted considerable attention as a DDS is graphene oxide (GO). GO features a high specific surface area (up to $500 \text{ m}^2 \text{ g}^{-1}$) [37], which is ideal for loading large quantities of poorly bioavailable drugs, such as taxanes, anthracyclines, and camptothecan analogues [38-49]. Additionally, the surface of GO features an abundance of carboxylic acids, epoxides, and hydroxyl groups that can be modified to introduce stimuli-responsive behavior, enable active targeting, and prolong circulation [31, 50, 51]. Drug adsorption and release on native GO has also been studied *in silico* using model drugs doxorubicin (DOX), paclitaxel, 5-fluorouracil, and thioguanine [52-55]. These simulations have proven very helpful in designing GO-based drug delivery systems by guiding the choice of type and degree of surface modification, and the loading conditions that maximize therapeutic efficacy.

Hydrogels with shear-thinning and thixotropic behavior are also of interest in drug delivery, as they can be easily introduced by direct injection into surgical cavities to form “depots” that provide sustained drug release [34, 35]. This bypasses the pharmacokinetic limitations inherent in many chemotherapeutic agents, as well as the bio-distribution limitations of intravenously administered systemic delivery systems [34, 35, 56-58]. Owing to their flexible molecular architecture, hydrogels enable release kinetics that can easily be tuned by adjusting the polymer/water ratio in cross-linked gels [59, 60]. “Designer” peptides have received strong interest

to construct hydrogel-based DDSs. Designer peptides are inherently biocompatible, biodegradable, and feature rapid gelation via hierachal self-assembly [61]. Gelation kinetics can be tuned effectively by varying the amino acid composition of the peptide and the aqueous environment (pH, ionic strength, temperature) [62-66]. A designer peptide widely used is the Max8 sequence, constituted by VKVKVKVKV^DPPTKVEVKVKV-NH₂, wherein ^DP is D-proline. The Max8 peptide is a stimuli-responsive peptide that is stable in aqueous solutions at low ionic strength and undergoes gelation in physiological conditions by self-assembling into 3.2 nm diameter β-hairpin nanofibers [64]. At low gel fractions 0.5-2 % (w/w), the Max8 hydrogel imposes little resistance to the transport of both small and large molecules, as demonstrated by Branco *et al.* with fluorescein-dextran conjugates [63]. In the context of scheduled delivery of multiple drugs, the high permeability of the hydrogel makes it an ideal depot for the release of the first drug in a sequential system; the limited control of the relative flux of multiple diffusing drugs, however, limits the applicability of hydrogels alone for scheduled combined chemotherapy. Rather, composite systems combining drug-loaded nanocarriers suspended in a drug-loaded peptide hydrogel hold great promise for precise delivery kinetics of multiple payloads [67-70].

In this work, we demonstrate scheduled and synergistic release of combined chemotherapeutics through the development of a composite hydrogel system comprising DOX-loaded modified-GO nanoparticles suspended in a gemcitabine (GEM)-loaded Max8 hydrogel (**Figure 4.1**). The synergism of DOX and GEM has been extensively studied in terms of molar ratio and delivery kinetics [9, 10, 71-73], demonstrating that the combination is synergistic for molar ratios (GEM:DOX) > 1, and optimal synergism occurs at a ratio of 10:1, with GEM being administered prior to DOX [9, 10]. We initially investigated different types and levels of chemical modification to tune the surface charge and hydrophobicity of GO nanoparticles and evaluated the

corresponding DOX loading and release at different values of solution pH and ionic strength. Notably, GO modification with tris(2-aminoethyl) amine (TREN) achieved high loading, ranging from 0.2 – 0.6 mg DOX per mg GO, and afforded an initially rapid release of 18.9% of the loaded DOX within 72 hr followed by sustained release of 31.4% over the course of 4 weeks. To gain molecular-level insight into the phenomena governing the adsorption and release of DOX on TREN-GO, we developed a computational model that quantitatively describes the DOX: TREN-GO interaction at different modification degrees, in terms of (*i*) molarity of loading and release (*i.e.*, water/GO partition coefficient of DOX), and (*ii*) reversible formation and adsorption/desorption of DOX aggregates. Selected DOX-TREN-GO nanoparticles were then suspended in a GEM/Max8 hydrogel, and the composite formulation was evaluated on a triple negative breast cancer cell line (MDA-MB-231) demonstrating high therapeutic efficacy. Notably, the DOX-GEM-loaded composite system afforded a combination index of 0.093 ± 0.001 , considerably lower than the free drug DOX-GEM combination ($CI = 0.396 \pm 0.034$) at the same concentration and molar ratio (DOX: GEM = 1:10). This indicates that the differential release induced from the composite system provides the desired therapeutic increment above the molar-based synergism.

4.2. Materials and Methods

4.2.1. Materials

Graphite powder (4827) was sourced from Asbury Graphite Mills (Lumberton, NC). Doxorubicin hydrochloride (DOX) and Gemcitabine hydrochloride (GEM) were obtained from LC Laboratories (Woburn, MA). The Max8 peptide (VKVKVKVKV^DPPTKVEVKVKV-NH₂) [63, 74, 75], where ^DP represents D-Proline and -NH₂ indicates an amidated C-terminus, was

obtained from Genscript (Nanjing, China) at > 95% purity. 1,1-Carbonyldiimidazole (CDI), dimethylaminopyridine (DMAP), ethylenediamine (EDA), tris(2-aminoethyl) amine (TREN), acetic anhydride (Ac_2O), benzylamine (BA), succinic anhydride (SA), anhydrous tetrahydrofuran (THF), phosphate buffered saline (PBS), 4-(2-hydroxyethyl)-1-piperazineethanesulfonic acid (HEPES), potassium permanganate (KMnO_4), and hydrogen peroxide (H_2O_2) were purchased from Sigma (St. Louis, MO). Triple negative breast cancer cells MDA-MB-231 were purchased from ATCC (Manassas, VA). Dulbecco's Modified Eagle Medium (DMEM). Fetal bovine serum (FBS) was obtained from Genesee Scientific (San Diego, CA). Penicillin Streptomycin (Pen Strep) was obtained from Gibco (Gaithersburg, MD). 3-(4,5-dimethylthiazol-2-yl)-2,5-diphenyltetrazolium bromide (MTT), was purchased from Invitrogen (Carlsbad, CA). All other chemicals were of reagent grade or higher.

4.2.2. Synthesis of GO particles

GO was synthesized from pretreated graphite powder (4827) following the modified Hummers method [76, 77]. Briefly, graphite (6 g) was added into H_2SO_4 (230 mL), which was placed into a 1 L Erlenmeyer flask and cooled to < 10°C using an ice bath. Then, KMnO_4 (30 g) was added slowly to the mixture and kept stirred continually. The mixture was then allowed to react at room temperature (RT) for 2 hr. Afterwards, distilled (DI) water (460 mL) and 30% H_2O_2 (50 mL) were added slowly into the mixture, resulting in a brilliant yellow color. The mixture was allowed to settle for three days after which the clear supernatant was decanted. The remaining mixture was washed with 10% HCl (v/v) solution followed by DI water until the pH of the dispersion reached about 5. The resulting GO dispersion was dried in air, and then dispersed at 5 mg mL^{-1} in anhydrous THF and sonicated for 30 min. The GO was finally washed once with THF,

acetone, and water, lyophilized, and stored for subsequent modifications. For washing steps, the GO suspension was centrifuged at 5,000 rpm for 5 min; minor loss of GO particles was observed during washing steps (< 5% measured by weight of dry particles). The size of GO nanoparticles (**Figure 4.2**) was determined by scanning electron microscopy (SEM) using a FEI Verios 460L (Philips) on a dilute aqueous solution (< 0.1 mg mL⁻¹) drop cast on aluminum foil.

4.2.3. Surface modification of GO particles

Lyophilized GO was initially dispersed at 5 mg mL⁻¹ in anhydrous THF via sonication for 30 min. For surface modification with amines, CDI (50 mg) was added and allowed to react for 1 hr RT. The corresponding amine (0.5 eq. of TREN, EDA, or BA) was then added to the activated GO suspension and allowed to react for 1 hr at RT. To saturate unreacted groups, ethanolamine was added to the GO nanoparticles at a concentration in solution of 0.1 M and allowed to react for 1 hr at RT. The GO was then washed with THF, acetone, and water, and lyophilized. For surface acylation with anhydrides, the corresponding anhydride (0.5 eq. of Ac₂O or SA) and catalytic DMAP were added to the GO suspension and allowed to react for 24 hr at RT. To saturate unreacted groups, ethanolamine was added to the GO nanoparticles at a concentration in solution of 0.1 M and allowed to react for 1 hr at RT. The GO particles were then washed with THF, acetone, and water, and lyophilized. The resulting samples were analyzed using a Zetasizer Nano (Malvern, UK) to determine the zeta potential (ζ potential) of the modified GO particles.

4.2.4. DOX loading and Release Screening Studies

All GO samples were incubated in 0.5 mL of aqueous DOX solution (1 mg mL⁻¹) for 48 hr at RT. Following incubation, the samples were centrifuged and the concentration of DOX in the

supernatant was measured by UV-vis spectroscopy at 480 nm using a Synergy microplate reader (Biotek, Winooski, VT). The DOX-loaded GO particles were rinsed with water (to remove loosely bound DOX) and lyophilized. Release experiments were conducted utilizing a mass of particles corresponding to an equivalent mass of DOX (0.182 mg). The particles were suspended in 1mL of PBS, pH 7.4 at 37°C. At assigned time points (12, 24, 48, 72, 96, 144, 192, 288, 336, 384, 432, 504 hr), 200 μ L of supernatant was collected and replenished with fresh PBS. The samples were then analyzed by UV-vis spectroscopy at 480 nm to determine the amount of DOX released.

4.2.5. Synthesis of (tGO) particle library

Lyophilized GO was initially dispersed in anhydrous THF at 5 mg mL⁻¹ by sonication for 30 min. Aliquots of 1 mL of GO suspension were combined with 50 mg of CDI and allowed to react for 1 hr RT. A variable volume of TREN (0.25-2 eq., relative to CDI) was then added and allowed to react for 1 hr at RT to generate TREN-modified GO particles (tGO) with different surface density. To saturate unreacted groups, ethanolamine was added to the GO nanoparticles at a concentration in solution of 0.1 M and allowed to react for 1 hr at RT. The tGO particles were then washed with THF, acetone, and water, and lyophilized. The resulting samples were analyzed using a Malvern Zetasizer Nano to determine the ζ potential of the modified tGO particles, and a modified Kaiser's colorimetric test the surface density of primary amines [78]. For Kaiser's test, 100 μ L of tGO particles suspension (0.1 mg mL⁻¹ in H₂O) were combined with 30 μ L of potassium cyanide in water/pyridine and ninhydrin, and 30 μ L of 6% ninhydrin in ethanol, and incubated at 100°C for 5 min. The solutions were diluted 200-fold and analyzed by UV-vis spectroscopy at 570 nm. Aqueous ethanolamine (0.00125-0.025 mmol mL⁻¹) was used to generate the calibration curve.

Additionally, both GO and tGO particles were analyzed by Fourier Transform Infrared (FTIR) Spectroscopy using a Nicolet 6700 FTIR Spectrophotometer (ThermoFisher Scientific, Waltham, MA). First, the particles were finely ground in potassium bromide (dried in a vacuum oven for 3 hr at 60°C) and placed in the optical bench, which was purged continuously using dry air. The samples were then analyzed using the following data acquisition parameters: accumulation of 512 interferograms with a resolution of 4 cm⁻¹, wavenumber range of 4000-400 cm⁻¹. The resulting spectra were analyzed using the OMNIC Spectra Software (Thermo Scientific).

4.2.6. DOX Loading and Release from tGO Particle Library

DOX loading studies were performed on native GO and tGO in different aqueous environments, namely low ionic strength (0.1 mM at pH 4, 1 µM at pH 6, and 0.1 nM at pH 9; these values of concentration and pH were achieved by titration with aqueous HCl or NaOH), and PBS at pH 7.4. Loading solutions were prepared by dissolving DOX at 1 mg mL⁻¹ in the different aqueous solvents. The solutions (0.5 mL) were incubated with GO and the various tGO samples (0.5 mg) for 48 hr at RT. After loading, the samples were centrifuged, and the supernatants were analyzed by UV-vis spectroscopy at 480 nm, to quantify the amount of residual DOX in solution. The DOX-loaded particles were rinsed with water, and lyophilized. Release tests were conducted by incubating a mass of particles corresponding to an equivalent mass of DOX (0.1 mg) in 1 mL of 10 mM PBS, at either pH 7.4 or pH 5 at 37°C. At set time points, (72, 170, 263, 378, 500, 650 hr), 200 µL of supernatants from the various samples were collected and replenished with fresh buffer. The collected samples were analyzed by UV-vis spectroscopy at 480 nm to determine the amount of DOX released.

4.2.7. Molecular dynamics (MD) Simulations of tGO

To study the interactions between DOX molecules and the surface of native and TREN-modified GO at the molecular level, we adopted a simplified version of the constant-pH molecular dynamics (CpHMD) simulation technique by Baptista *et al.* [79]. In place of coupling with the stochastic protonation/deprotonation algorithm during the simulation, our version assigns a constant protonation or deprotonation to the titratable amine group of the daunosamine moiety of the DOX molecules throughout the entire simulation. This method has already been implemented in several studies [53, 80]. The number of protonated/deprotonated sites in GO sheet and DOX molecules was approximated using the Henderson-Hasselbalch equation [81, 82]. Assuming that the pKa values of isolated carboxyl groups (COOH) and hydroxyl groups (OH) on GO sheet are 6.6 and 9.8 [83], respectively, the number of deprotonated sites was calculated by Equation 1:

$$(1) \quad N_D = \frac{10^{pH-pKa}}{1 + 10^{pH-pKa}} N_t$$

where N_D and N_t are the number of deprotonated sites and the total number of titratable carboxyl and hydroxyl groups, respectively. For DOX molecules, by assuming that the pKa value of the amino group (-NH₂) is 8.4 [84], the number of protonated DOX molecules was calculated by Equation 2:

$$(2) \quad N_P = \frac{1}{1 + 10^{pH-pKa}} N_t$$

where N_P is the number of protonated DOX molecules. The adopted GO model has a chemical formula of C₁₀O₁(OH)₁(COOH)_{0.5} representing the standard oxidation process [85, 86]. Epoxy and hydroxyl groups are randomly distributed on the GO surface and the carboxyl groups are attached to the edge of the GO sheet. The general amber force field (GAFF) [87] implemented in the Amber18 simulation package was used in all simulations. Partial charges of DOX and

functional groups on the GO surface (*i.e.*, epoxy group, hydroxyl group, and carboxyl group) were obtained using the standard AMBER charge fitting procedure. First, the geometry optimization of the molecule was performed at the DFT/B3LYP/6-31G* level, and then at MP2/6-31G(d) level with tight convergence criteria using Gaussian 09; the partial charges were then derived by fitting to the molecular electrostatic potential (MEP) at the HF/6-31G* level using the restrained electrostatic potential (RESP) method [88] through R.E.D. server [89, 90]. For the GO sheet, all sp² carbon atoms were treated as uncharged, and atomic charges were only assigned to the atoms in a functional group and carbon atoms directly bonded to that functional group. The total charges of the molecule/fragment were set based on their protonated state in the solution. We ensured that the fitted RESP charges for the functional groups on the GO sheet agree with the AM1-BCC charges [91, 92] calculated by the AmberTool and with the scaled electrostatic potential (SESP) charges [93], which are linearly scaled to include the polarization effect in the aqueous solution; this agreement provided confidence in the current RESP charges, confirming the choice of 6-31G* basis set as sufficient to implicitly represent the polarization effect in the aqueous solution [88]. We further confirmed that partial charges of protonated DOX molecules agreed with the reported data [94], and that the DOX structure obtained from quantum mechanics (QM) geometry optimization agrees with that from molecular mechanics (MM) energy minimization in implicit solvent by using the GAFF. We assigned all atoms types using Antechamber [95] and verified that the atom types assigned matches the true chemical environment of that atom. For simplicity, we manually changed all sp² carbon atoms in the GO sheet to the “ca” type. The partial charges of the major functional groups on GO surface are summarized in **Table 4.1**.

To model the TREN-modified GO (tGO) surface, we tethered TREN moieties on the GO through carbamate bonds. While we recognized that TREN groups can be added to the surface of

the particles through other functional groups on the native GO surface (*e.g.*, hydroxyl groups and epoxy groups), we showed that our proposed scheme of TREN modification of the surface is sufficient to investigate the tGO-DOX interaction during both adsorption and release. The TREN density on the model tGO surface (molecules nm⁻²) was calculated from the experimental values measured by Kaiser's test, assuming 500 m² g⁻¹ as specific surface area for the GO particles [37]. As the surface area of our GO model is 50 nm², the number of TREN groups on the model surface ranges between 18 and 24. The pKa values of the two primary amines and the tertiary amine on TREN are 10.6 and 10.9, respectively. Under weak neutral conditions (pH = 6), all amine groups in the TREN are protonated and the TREN molecule carries a +3 charge. The initial configuration of the system was created using the PACKMOL package⁹⁶ and the simulation box was filled using the TIP3P water model [97]. Sixty-four DOX molecules were initially randomly distributed at a distance from the GO surface ranging between 0 and 45 Å. Following initial geometry optimization, the system was slowly heated from 0 K to room temperature (298 K) in an NVT ensemble for 200 ps with 2 fs time steps, while restraining the solid surface and the DOX molecules in their initial position by a harmonic spring force. The DOX molecules were then released, and an NPT simulation was performed to equilibrate the density of the system at 1 bar, 298 K for 2 ns. Throughout the simulation, the pressure was maintained constant using the Berendsen barostat with pressure relaxation time of 2 ps, while the temperature was controlled using the Langevin thermostat with collision frequency $\gamma = 1 \text{ ps}^{-1}$; the Langevin thermostat has been shown to be more efficient in system equilibration than the Berendsen temperature coupling scheme, but the Berendsen thermostat is more stable in reproducing the correct dynamics of the system [98]. Starting from the last equilibrated frame, a production NPT MD was performed wherein all TREN groups on the surface were allowed to relax while the base GO sheet was restrained using a weak

harmonic constraint of 10 kcal mol⁻¹ Å⁻². The Berendsen thermostat was used during the simulation with the temperature coupling time of 10 ps. All simulations were run over 70 ns, at which time the number of DOX molecules adsorbed on either the native GO or tGO surface reaches a plateau. At least two independent MD simulations were run for the native GO and three tGO (0.359, 0.435, and 0.491 TREN molecules nm⁻² corresponding to ζ potentials of -8.9, 10.1, and 20.7 mV, respectively) models to calculate the average number of DOX molecules adsorbed on different GO surfaces for subsequent comparison with experimental data.

4.2.8. Preparation Max8 hydrogel and tGO-Max8 Composite

All hydrogels were prepared at 2% (w/w) following published protocols [75]. Briefly, a peptide solution at 40 mg mL⁻¹ in MilliQ water was combined with an equal volume of 100 mM HEPES added with 300 mM NaCl, pH 7.4. The solution was briefly vortexed and centrifuged, and allowed to rest until gelation (inversion test). This protocol was also adapted for release of GEM by initially dissolving the peptide in an aqueous solution of GEM at desired concentration. The tGO particles, tGO-DOX particles, Max8 peptide hydrogel, tGO particles suspended in Max8 peptide hydrogel (tGO-Max8), and tGO-DOX particles suspended in Max8 peptide hydrogel (DOX/tGO-Max8) were imaged by fluorescent confocal microscopy using a Zeiss LSM 710 microscope (Carl Zeiss AG, Oberkochen, Germany) at $\lambda_{\text{ex}} = 590\text{nm}$ and $\lambda_{\text{em}} = 618\text{nm}$.

4.2.9. Dual Drug Release from tGO-Max8 Composite

Selected DOX/tGO particles comprising tGO (ζ potential = -19 mV) loaded with DOX in 10 mM PBS (pH 7.4) was utilized for all release studies under 3 conditions: free tGO-DOX particles, DOX/tGO particles embedded in a Max8 hydrogel, and DOX/tGO particles embedded

in a Max8 hydrogel loaded with GEM. All release experiments were performed utilizing a volume of DOX-loaded particles corresponding to an equivalent mass of DOX (0.1 mg), and GEM (0.0605 mg, when GEM was utilized). These values of payload were selected to obtain the projected 10:1 GEM: DOX molar ratio in solution upon release, based on the data of DOX release obtained. Samples including gels were prepared using a total gel volume of 200 μ L. All release tests were performed by contacting every system with 1 mL of 10 mM PBS at pH 5 at 37°C. At set time points (8, 16, 32, 48, and 72 hr), 200 μ L of supernatant was collected and replenished with fresh buffer. The collected samples were analyzed by liquid chromatography using a reverse-phase Aeris 3.6 μ m C18 column (50 \times 4.6mm) installed on a Waters 2690 HPLC system (Waters, Milford, MA). The chromatographic method utilized a 5-100% gradient of acetonitrile (0.1% formic acid (v/v)) in water (0.1% formic acid (v/v)) over 10 min, while monitoring the effluent at 290 nm and 480 nm to monitor GEM and DOX, respectively. The concentrations of GEM and DOX were determined by peak-area integration of the resulting 290 nm and 480 nm chromatograms relative to the respective standard curves.

4.2.10. Cell Culture

Triple negative breast cancer cells, MDA-MB-231, were cultured in DMEM supplemented with 10% (v/v) FBS and 1% (v/v) Pen Strep in a humidified incubator at 37°C and 5% CO₂.

4.2.11. Cell Viability Assay

Cells (5×10^3 cells per well) were seeded in a 96-well plate and allowed to adhere overnight. Stock solutions of DOX in pure DMSO and GEM in sterile MilliQ water were diluted in cell culture media (DMEM supplemented with 10% FBS (v/v) and 1% Pen-Strep(v/v)) such that

the maximum concentration of DMSO or water did not exceed 0.5% (v/v). For the systems containing DOX/tGO particles, the concentration of particles used was such that the concentration of DOX released after 72 hr matched the concentration of DOX utilized in cell viability studies conducted with free drug in solution. For systems containing Max8 hydrogel, the volumes of hydrogel utilized (5, 12.5, and 25 μ L) were prepared aseptically. After 72 hr of treatment, the media was aspirated, and the cells were incubated in a solution of 0.5 mg mL⁻¹ MTT in cell culture media for 4 hr at 37°C. The MTT solution was aspirated and DMSO was added to the wells and allowed to shake for 30 min to dissolve formazan crystals. Plate absorbance was measured at 540 nm using a Biotek Synergy microplate reader.

4.2.12. Statistical Analysis

Statistical significance was determined by evaluation of the Student's t-test using Microsoft Excel. Statistical significance for samples was evaluated against the control test condition, and p < 0.05 was considered significant. For analysis *, **, and *** represent p < 0.05, 0.01, 0.001, respectively.

4.3. Results and Discussion

4.3.1. Synthesis and Characterization of Modified Graphene Oxide (GO) DOX Loading and Release Screening Studies

An ensemble of GO particles was initially constructed by surface modification with different functional moieties to elucidate the effect of surface hydrophobicity (benzyl- vs. acetyl-groups) and electrostatic charge (carboxyl vs. amine groups) on the adsorption and release of DOX. Loading of DOX was proceeded over 48 hr to reach adsorption equilibrium. The resulting values

of drug loading (mg DOX per mg of modified GO particles) are summarized in **Figure 4.3A**. DOX adsorption on carbon-rich surfaces (*e.g.*, carbon nanotubes) can reach high values owing to the dense π - π interactions [99]. Benzyl-GO (ζ potential = -27.5 mV) particles provided the highest loading at 0.501 ± 0.005 mg of DOX per mg GO; the display of benzyl moieties on the GO surface through distal carboxylic acids may in fact provide additional binding sites for π - π interactions with DOX to occur. DOX loading on native GO (ζ potential = -36.5 mV) was slightly lower, reaching 0.488 ± 0.005 mg mg⁻¹ GO. Other surface modifications afforded lower DOX loading; acetyl- (ζ potential = -26.5 mV) and succinyl- (ζ potential = -27.3 mV) modified GO showed almost identical DOX binding capacity, 0.205 ± 0.001 mg mg⁻¹ GO and 0.204 ± 0.031 mg mg⁻¹ GO, respectively. Surface modification of GO particles with amines EDA and TREN increased the loading slightly to 0.255 ± 0.054 mg mg⁻¹ GO and 0.307 ± 0.040 mg mg⁻¹ GO, respectively. Such increase in DOX loading seems counterintuitive, given that DOX is a positively charged molecule and the surface charge of GO increases from -26.5 mV (acetyl-GO) to ζ potential = -18.4 mV (EDA) and ζ potential = -14.3 mV (TREN). This suggests that the interaction between DOX and modified GO does not depend solely on electrostatic interactions, but implicates other phenomena, such as steric hindrance upon adsorption, hydrogen bonding, and hydrophobic interaction, which are evaluated in detail later. The release of DOX from the modified GO particles was performed in PBS at pH 7.4 over a total collection time of 500 hr. The values of percent release (DOX released *vs.* loaded) are presented in **Figure 4.3B**; the values of percent release obtained through the initial 100 hr are presented in **Figure 4.4**. The GO particles modified with TREN and EDA returned the highest values of percent release, at both 72 hr and 500 hr. The electrostatic repulsion between DOX and TREN/EDA moieties, both of which are positively charged at pH 7.4, combined with a high concentration gradient between the GO surface and the solution phase, likely

play a predominant role in release. GO particles modified with TREN (2 primary and 1 tertiary amine), in fact, released 2.63 ± 0.3 % after 72 hr and 5.57 ± 0.3 % after 504 hr, whereas GO modified with EDA (1 primary amine) released 1.74 ± 0.2 % after 72 hr and 3.44 ± 0.2 % after 504 hr. Comparatively, at the 72 hr and 504 hr time points, native GO released 1.38 ± 0.2 % and 4.34 ± 0.4 %, acetyl-GO released 1.16 ± 0.4 % and 2.86 ± 0.2 %, succinyl-GO released 1.38 ± 0.2 % and 2.80 ± 0.2 %, and benzyl-GO released 0.8 ± 0.1 % and 2.20 ± 0.3 %. Notably, the loading of DOX on TREN-GO was only slightly lower compared to that of native GO. These results indicate that modification of GO particles with cationic moieties is essential towards ensuring both a favorable loading and high release of DOX. Accordingly, we selected TREN as the surface modification moiety in all subsequent studies.

4.3.2. TREN-modified GO (tGO) Characterization

Based on the initial screening process, we selected TREN-GO (tGO) as model particles in all subsequent studies of DOX loading and release. Prior to DOX adsorption and release studies, we investigated the correlation between the degree of TREN modification and the resulting electrostatic charge (ζ potential) at the surface. To this end, we prepared an ensemble of tGO particles, and measured the TREN surface density using a modified Kaiser's amine quantification test and the corresponding values of ζ potential. The values of TREN density and ζ potential vs. molar ratio of TREN utilized in the modification reaction are presented in **Figure 4.5**. Notably, the ensemble of tGO particles encompassed a wide range of ζ potential, from -36.5 mV to 19.9 mV. The surface chemistry of native GO and one tGO sample (ζ potential = -18.8 mV) was also investigated by Fourier Transform InfraRed (FT-IR) spectroscopy (**Figure 4.6**). The FT-IR spectrum of native GO exhibits the characteristic peaks of O-H stretching at 3450 cm^{-1} , C=O

stretching at 1736 cm^{-1} , aromatic C=C stretching at 1625 cm^{-1} , alkoxy C-O stretching at 1064 cm^{-1} , and epoxy C-O stretching at around 854 cm^{-1} [100]. In tGO, the appearance of overlapping peaks of C=O stretching and N-H bending of the amide functional group at around 1640 cm^{-1} , and the appearance of a C-N stretching peak at 1460 cm^{-1} [100] confirms the conjugation of TREN via formation of amide bonds. Furthermore, the presence of a carboxyl C=O stretch peak at 1730 cm^{-1} in native GO and the absence of this peak in tGO indicates that all distal carboxylic acids are implicated in the formation of amide bonds with TREN. At the same time, the high values of TREN surface density measured on tGO particles and the exiguity of distal carboxylic acids typical of native GO also suggests that TREN conjugation also occurs through the formation of carbamate bonds, which result from the activation of the hydroxyl groups on GO with CDI; however, because carbamate and amide bonds have the same FTIR signature and the adsorption of air moisture by tGO prevents the quantification of the hydroxyl groups converted in carbamate bonds [101], it is not possible to quantitatively distinguish the two conjugation routes. Finally, the persistence of the epoxy peak at $\sim 850\text{ cm}^{-1}$ in the tGO sample indicates that TREN reaction to epoxide groups is unlikely.

4.3.3. Experimental and *in silico* Evaluation of DOX Adsorption on tGO

The loading of DOX on the ensemble of tGO particles was evaluated at four conditions, namely low salinity at different pH (4, 6, and 9) and PBS at pH 7.4. The adoption of solutions at low ionic strength and different pH was aimed to study the effect of surface charge (ζ potential) alone on DOX loading. The comparison between neutral buffers with different ionic strengths (1 μM at pH 6 vs. 10 mM PBS at pH 7.4) was intended to investigate the effect of ionic strength, which both shields electrostatic repulsion and promotes mild hydrophobic interactions (sodium

chloride is an intermediate salt in the Hofmeister series) [102]. The resulting values of DOX loading, collated in **Figure 4.7A** and **Table 4.2**, indicated that under acidic condition native GO (ζ potential = -36.5 mV) gave the highest loading at $0.595 \pm 0.008 \text{ mg mg}^{-1}$ GO. However, as ζ potential increases to -18.8 mV (0.449 μmol TREN per mg of GO), the loading of DOX undergoes a sharp decline to $0.248 \pm 0.050 \text{ mg mg}^{-1}$ GO. As ζ potential increases to -8.9 mV (0.592 $\mu\text{mol mg}^{-1}$), the loading of DOX remains constant at $0.231 \pm 0.004 \text{ mg mg}^{-1}$ GO. As ζ potential further increases to 0 mV and 6.8 mV, the loading of DOX decreases only slightly to $0.169 \pm 0.009 \text{ mg mg}^{-1}$ GO and $0.150 \pm 0.002 \text{ mg mg}^{-1}$ GO, respectively. Lastly, the loading at ζ potential = 19.3 mV (0.789 $\mu\text{mol mg}^{-1}$) was $0.202 \pm 0.051 \text{ mg mg}^{-1}$ GO.

At low ionic strength, DOX loading at neutral and basic pH displays the same downward trend, featuring an initial sharp decrease from 0.581 ± 0.004 and $0.576 \pm 0.011 \text{ mg mg}^{-1}$ GO (ζ potential = -36.5 mV) to $0.257 \pm 0.030 \text{ mg mg}^{-1}$ GO and 0.262 ± 0.040 (ζ potential = -18.8 mV) followed by a shallowed decrease, reaching $0.163 \pm 0.012 \text{ mg mg}^{-1}$ GO and 0.176 ± 0.002 at ζ potential = 19.3 mV. At the same time, a subtle yet statistically significant increase in DOX loading at neutral and basic pH vs. acidic pH is observed on the tGO samples with ζ potential between -10 mV and + 10 mV. As the pH of the aqueous phase increases, in fact, the positive charge carried by DOX [84] and TREN is softened, and consequently DOX loading is improved.

DOX loading conducted at higher ionic strength (PBS, pH 7.4) exhibited the same trend observed in the low salt concentration regimes, but consistently at a higher magnitude. Specifically, the loading of DOX on native GO nearly doubles, reaching $1.048 \pm 0.009 \text{ mg mg}^{-1}$ GO; on tGO samples with higher ζ potential, DOX loading decreases to within a range of values between $0.613 \pm 0.015 \text{ mg mg}^{-1}$ GO and $0.367 \pm 0.104 \text{ mg mg}^{-1}$ GO.

These results collectively indicate two prominent trends. First, as the ζ potential of tGO increases with the modification level, the electrostatic repulsion inhibits the adsorption of DOX molecules onto the surface of tGO. Second, increasing the ionic strength of the loading solution partially screens DOX/tGO electrostatic repulsion and concurrently promotes DOX/tGO hydrophobic interactions, resulting in a constant upward shift in DOX loading across the entire range of TREN modification.

To visualize these phenomena at the molecular level, we performed a number of molecular dynamic (MD) simulations of DOX adsorption onto tGO model surfaces constructed by appending TREN moieties onto a flat, two-faced 4.8 nm \times 5.1 nm GO surface. Coherently with the FTIR results, the TREN moieties were appended through carbamate bonds to the hydroxyl groups on the GO surface. All MD simulations were performed at nearly neutral pH and in absence of salt, since the modeling of buffered aqueous systems is computationally complex and outside the scope of this work [103-105]. As expected, the values of DOX loading predicted by the MD simulations describe a downward trend with ζ potential (**Figure 4.7B**), caused by the electrostatic repulsion between the positively charged daunosamine moiety of DOX and the TREN moieties on tGO. On the other hand, the spacing between TREN moieties on the tGO surface is sufficient to allow adsorption of DOX molecules on surface patches of native graphene oxide (**Figure 4.8**) across the entire range of degree of modification (0.359-0.491 TREN molecules nm⁻² of tGO surface).

Notably, the values of DOX loading measured experimentally and those obtained *in silico* show excellent quantitative agreement (**Figure 4.7B**), indicating that the proposed *in silico* model portrays accurately the mechanism of DOX adsorption onto tGO particles. The simulations also indicate the formation of aggregated stacks of DOX molecules onto the tGO surface at the binding

equilibrium (**Figure 4.8**); the presence of aggregate aggregates will be functional to formulate a mechanism explaining the experimental data of DOX release presented subsequently.

4.3.4. Evaluation of DOX Release from tGO

Studies of DOX release from GO and tGO particles were performed at pH 5 and pH 7.4 to simulate cancerous and healthy cellular environments, respectively. The release profiles obtained at pH 5 are reported in **Figure 4.9**, while those obtained at pH 7.4 are reported in **Figure 4.10**.

Two time scales are of relevance in this study: (*i*) short term (72 hr), which is representative of a typical therapeutic window for *in vitro* DDS validation, and (*ii*) long term (> 600 hr), which fits the time scale of maintenance chemotherapy. The values of DOX percent release from GO and tGO particles at both pH 5 and 7.4 for 72 and 650 hr are reported in **Table 4.3** and **Table 4.4**, respectively. As anticipated, the release experiments conducted at pH 5 afforded higher values of DOX percent release compared to those at pH 7.4. The lower pH promotes the positive charge on both DOX and TREN moieties, which causes DOX-DOX and DOX-TREN repulsion thereby triggering release. Because drug release in a tumor-mimetic environment is more relevant in the context of this work, our analysis focuses on the release data generated at pH 5. The comparison of DOX release from the particles loaded at low ionic strength shows that only two tGO particles outperform the native GO particles, namely tGO with ζ potential = -18.8 mV and -8.9 mV. The former afforded a 72 hr release of $13.7 \pm 2.1\%$ (when loaded pH 4), $12.4 \pm 0.4\%$ (pH 6), and $11.4 \pm 0.8\%$ (pH 9), and a 650 hr-release of $22.7 \pm 3.2\%$ (pH 4), $19.2 \pm 4.2\%$ (pH 6), and $19.8 \pm 4.0\%$ (pH 9). The latter showed a 72 hr release of $9.0 \pm 1.1\%$ (pH 4), $9.2 \pm 0.3\%$ (pH 6), and $10.6 \pm 1.5\%$ (pH 9), and a 650 hr-release of $16.7 \pm 4.0\%$ (pH 4), $15.7 \pm 3.8\%$ (pH 6), and $19.8 \pm 3.9\%$.

(pH 9). Comparatively, the native GO released only ~6 % DOX after 72 hr and ~15% after 650 hr. On the other hand, tGO carriers with higher ζ potential afforded a lower release of DOX.

Given the negligible dependence of DOX loading upon pH at low salt concentration as well as DOX release from the resulting particles, only the DOX/GO systems loaded at neutral pH (low vs. high salt concentrations) were considered in the rest of this study. The values of DOX percent release at pH 5 for 72 hr and 650 hr plotted against the values of ζ potential of the corresponding GO and tGO particle carriers are presented in **Figure 4.11A** and **Figure 4.11B**, respectively; the analogous plots for release at pH 7.4 are presented in **Figure 4.12**.

It is immediately evident that DOX release is determined by two parameters, namely (*i*) the ionic strength of DOX solution during loading and (*ii*) the ζ potential of the particles. First, regarding the ionic strength of the loading solution, a significant increase is observed in the values of DOX percent release, which shift from a range of 1.48-12.4% (low salt loading) to 7.42-18.9% (high salt loading) for 72 hr release, and from 3.16-19.2% (low salt loading) to 19.1-31.8% (high salt loading) for 650 hr release. In this regard, the *in silico* modeling of DOX adsorption indicated the formation of DOX aggregates both in solution and onto the GO surface. The extent of aggregation is likely enhanced at high salt conditions, where electrostatic repulsion is softened and hydrophobic interactions are promoted, as observed with drug-like molecules [106]; accordingly, we hypothesize that DOX adsorbs onto the tGO surface in a predominantly mono-/di-meric form when loaded in a low ionic strength environment, and in a rather multimeric form at higher ionic strength. When exposed to pH 5, DOX aggregates are considerably less stable than monomeric DOX, due to the combination of DOX-DOX and DOX-TREN electrostatic repulsion, and are released more easily, resulting in an upward shift in percent release.

The dependence of DOX percent release on ζ potential, on the other hand, is rather counterintuitive. In place of a monotonic trend reverse to that of DOX loading (**Figure 4.7B**), in fact, concave downward curves were obtained (**Figure 4.11A** and **Figure 4.11B**). To explain this behavior, one must consider the charge environment onto the GO particles and in the layer of charges surrounding them (**Figure 4.13**). The surface of GO is inherently negatively charged, due to the numerous oxygen-containing moieties [107]; on this surface, the TREN moieties and the DOX molecules form a layer of “condensed” positive counter-ions (Stern layer), respectively covalently linked and non-covalently adsorbed. The enveloping Gouy layer, framed by the Stern plane and the slipping plane, at which the ζ potential is measured, contains a mixture of positive (*e.g.*, H⁺ and Na⁺) and negative (*e.g.*, OH⁻ and Cl⁻) counter-ions. On virgin GO, DOX molecules adsorbed at pH 6 are strongly retained by the negatively charged moieties on the surface of GO (**Figure 4.13A**); as the environment surrounding the DOX/GO particles is adjusted to pH 5, the softening of the inherent negative charge on the surface of GO and the DOX-DOX electrostatic repulsion molecules triggers release. On tGO particles with low TREN modification (ζ potential < 0), DOX molecules are adsorbed on patches of native GO between TREN moieties (**Figure 4.13B**); at pH 5, the softening of the negative charge on GO, and the combined DOX-DOX and DOX-TREN repulsion favors DOX desorption, resulting in an increment of percent release. On tGO particles with high TREN modification (ζ potential \approx or \geq 0), the higher density of TREN moieties in the Stern layer drives the accumulation of negative (OH⁻ and Cl⁻) counter-ions within the Gouy layer, resulting in the electric stabilization of the cationic DOX molecules adsorbed onto the surface of GO (note the cyan spheres representing Cl⁻ ions intercalated between DOX and TREN molecules in **Figure 4.13C** and **Figure 4.13D**); this results in a softening of DOX-TREN repulsions at pH 5, which translates in a decrease of percent release. These phenomena are evident

when DOX loading is performed at low ionic strength. When DOX loading is operated in PBS, in fact, the TREN moieties are stabilized by counter-anions prior to DOX adsorption and DOX release at pH 5 is mostly triggered by the disassembly of drug aggregates by DOX-DOX electrostatic repulsion. This makes the values of percent release much less dependent upon ζ potential. Native GO is an exception, given its complete lack of TREN modification.

4.3.5. Release of GEM and DOX from tGO-Max8 Composite

Based on the results of the DOX release studies, we selected tGO particles with ζ potential of -18.8 mV as model carrier to develop the composite drug delivery system (DDS); the high loading of DOX attained in PBS at pH 7.4 enables reducing the amount of tGO particles required to achieve therapeutic efficacy, which minimizes the risk of cytotoxic effects. To develop the hydrogel matrix, we initially sought to determine the optimal peptide concentration that affords rapid gelation and yields a homogenous gel that poses no diffusion limitations to the transport of either GEM or DOX. Peptide gel fractions of 2% (w/w) and 4% (w/w) were chosen owing to their nearly instant gelation kinetics. The release kinetics from GEM-loaded gels are presented in **Figure 4.14**. Within the first 4 hours, the 2% (w/w) hydrogel releases GEM more rapidly, reaching $60.9 \pm 6.1\%$ compared to $51.9 \pm 1.2\%$ by the 4% (w/w) hydrogel. After 16 hr, however, the amount of GEM released is independent of gel fraction, reaching ~80%. As we envision a scheduled/sequential delivery system wherein the first drug in the chemotherapy regimen (GEM) is released more rapidly, we elected to use the 2% (w/w) hydrogel as the matrix for embedding the DOX/tGO particles.

The composite DDS was prepared by dissolving Max8 peptide at 2% (w/w) in a sonicated aqueous suspension of the selected DOX/tGO particles. The instantaneous formation of the peptide

hydrogel resulted in a homogeneous dispersion of the particles. Confocal fluorescence microscopy images of the control tGO-Max8 composite (**Figure 4.15**) and DOX/tGO-Max8 composite immediately after gel formation (**Figure 4.15**) confirms the homogeneous dispersion of the tGO particles; further, **Figure 4.15** indicates DOX remains bound to the tGO particles upon gel formation.

The release kinetics of the composite tGO-Max8 systems are presented in **Figure 4.16**. It is first noted that the peptide hydrogel poses a notable resistance to the transport of DOX, resulting in a 3-fold reduction of the percent release in the aqueous phase surrounding the hydrogel, from the $19.0 \pm 0.1\%$ 72 hr-release given by free DOX/tGO particles in solution to the $6.2 \pm 0.2\%$ given by DOX/tGO particles embedded in the Max8 scaffold. This is likely caused by the cationic and amphiphilic nature of the Max8 peptide (rich in positively charged lysine and hydrophobic valine residues), which limits the partitioning of DOX – a positively charged molecule – from the tGO surface to the hydrogel phase and its migration through the hydrogel matrix, as noted in prior work [108]. We have observed that the display of hydrophobic moieties in polycationic hydrogels hinders the migration of DOX. Second, we observed a drastic change in GEM release after 72 hr, from $95.5 \pm 1.1\%$ from the GEM/Max8 hydrogel alone compared to $49.4 \pm 0.2\%$ from the composite system. This is likely caused by the interaction between GEM and the DOX/tGO nanoparticles during its diffusion pathway. Finally, the concurrent migration of the two drugs results in a further decrease of DOX release, from the $6.2 \pm 0.2\%$ given by the GEM-free composite to the $3.3 \pm 0.1\%$ given by the GEM-loaded hydrogel after 72 hr. This is attributed to DOX-GEM interactions that have been documented to occur and drastically change diffusion properties of the DOX-GEM pair through poly-cationic hydrogel matrices [108].

4.3.6. *In vitro* Characterization

To determine the efficacy of the composite system relative to free single drug and drug combination treatments, we conducted *in vitro* evaluation of drug-loaded DOX/tGO-GEM/Max8 composites using the triple negative breast cancer cell line MDA-MB-231. The results are presented as dose-response curves in **Figure 4.17A**, fit with the median-effect equation [109]. The corresponding IC₅₀ values are presented in **Figure 4.17D**. Free DOX and free GEM yielded IC₅₀ values of $0.399 \pm 0.04 \mu\text{M}$ and $> 20 \mu\text{M}$, respectively, in line with published data [9]. In testing the free DOX/tGO particles, we referred to the values of 72 hr release at pH 5 to determine the concentration of particles affording a release of DOX at a dose equivalent to that utilized in the free drug study and accounted for the possibility of uptake of the DOX/tGO particles. The range of DOX concentration utilized in this study, $0.025 \mu\text{M} - 1.6 \mu\text{M}$, translated in a dose of $0.2 - 14.2 \mu\text{g tGO mL}^{-1}$ of total release volume. The same volume of drug-free particles was also tested as a control to evaluate their basal cytotoxicity (**Figure 4.17C**). Notably, the DOX/tGO particles featured a cytotoxic activity comparable to that of free DOX, with an IC₅₀ value of $0.131 \pm 0.002 \mu\text{M}$, corresponding to $\sim 1.7 \mu\text{g}$ of DOX/tGO particles mL^{-1} (**Figure 4.17B**). At the same time, the tGO particles alone proved relatively biocompatible, yielding a cell survival rate above 90% when employed at concentrations below $14.2 \mu\text{g mL}^{-1}$. Most importantly, at the dose of $1.7 \mu\text{g mL}^{-1}$ needed for the DOX-loaded particles to match the IC₅₀ of free DOX, the tGO particles alone show a cell survival rate of $\sim 99\%$.

The cytotoxicity of the DOX-GEM combination was then evaluated at the reference GEM:DOX molar ratio for of 10:1, reported as synergistic in prior work (**Figure 4.17D**) [9]. For the free-drug combination, we observed an IC₅₀ value of $0.135 \pm 0.035 \mu\text{M}$, relative to DOX concentration. This corresponded to a combination index (CI), calculated utilizing the Chou-

Talalay method [110] of 0.396 ± 0.035 , confirming strong synergism of the drug pair, consistent with that obtained by Vogus *et al.* [9] using the same drug pair and concentration, and cancer cell line. Lastly, we sought to demonstrate that the dual-drug loaded tGO-Max8 composite system is more therapeutically efficacious than the free drug combination. Accordingly, the reference 10:1, GEM: DOX molar ratio was utilized in these release experiments. We observed an IC₅₀ value of $0.0116 \pm 0.0004 \mu\text{M}$, relative to DOX concentration, corresponding to a CI of 0.093 ± 0.001 , indicating a stronger synergism than the free drug pair. It is noted that the reported values of CI are comparable to those obtained by Vogus et al. of CI ~ 0.12 with sequential administration of this drug pair (GEM for 24 hr, then DOX for 48 hr) [9]. We attribute this further reduction in CI (higher synergism) to the ability of the composite tGO-Max8 system to control the release kinetics and achieve the postulated scheduled release, known to improve synergism [9, 10]. Notably, the IC₅₀ value of the composite system corresponds to a dose of $16 \mu\text{g mL}^{-1}$ of tGO particles and $5 \mu\text{L}$ of Max8 hydrogel, both proven to be non-cytotoxic *per se* (**Figure 4.6.17C**).

4.4. Conclusions

Scheduled delivery of synergistic combinations of chemotherapeutics is increasingly regarded as a highly effective treatment for aggressive solid tumors. The precise control of molar ratio, sequence, and rate of delivery, in fact, enhances drug synergism and enables a drastic reduction of the required therapeutic doses, while maintaining a highly efficacious outcome. To date, two main approaches to achieve scheduled delivery appear in clinical settings: portable devices that accompany the patient through therapy and inject different drugs based on a set timetable, or engineered materials featuring fine-tuned drug release kinetics. The design and optimization of the chemical functionalization and organization of composite materials as drug

delivery systems (DDS) greatly benefits from the integration of *in silico* design and experimental evaluation. By providing a deeper insight into the complex physicochemical interactions between drugs and materials, integrated computational-experimental methods enhance the quality and accelerate the process of discovery and validation of therapeutic products. This study aims to apply this concept to the design of a homogenous hydrogel-nanoparticle composite capable of delivering a recognized synergistic drug pair (DOX and GEM) with precise molar ratio and release kinetics. In this context, we resolved to (*i*) adopt materials that combine biocompatibility and affordability with chemically versatility, and (*ii*) implement scalable functionalization strategies to ensure the translational potential of the resulting DDS. GO nanoparticles and Max8 peptide hydrogel fulfill the requirements on the materials, while TREN modification of the GO surface and the tuning of the Max8/water ratio represent a scalable approach to achieve precise control over the ratio and kinetics of drug delivery. Crucial to the design and understanding of the proposed DDS has been the development of an MD model capable of describing quantitatively the DOX loading on and release from the modified GO particles. The homogeneous distribution of DOX-tGO particles and the thixotropic nature of the Max8 hydrogel matrix make the proposed formulation an exquisitely injectable one, ideal for the treatment of solid tumors through both first-line or consolidation chemotherapy. In this regard, the MDA-MB-231 triple negative breast cancer (TNBC) cell line adopted in this work represents an ideal target for the preclinical testing of the proposed DDS. Patients with metastatic TNBC, in fact, have a poor prognosis and a median overall survival of ~13 months upon treatment. In the attempt to contribute to the development of a therapeutic arsenal against TNBC, we have tailored our composite system to release GEM at 47-fold rate and a 10-fold molar ratio compared to DOX, which the literature indicates as highly synergistic. The results presented herein demonstrate the validity of our design: the composite DDS afforded a remarkable

combination index of 0.093 ± 0.001 . This value is not only lower than that provided by the DOX-GEM combination as free drugs in solution ($CI = 0.396 \pm 0.034$) but is lower than any value reported in the literature for this and similar drug combinations delivered by either microfluidic devices or engineered materials [6, 9, 10, 111]. Together with reinforcing the value of combining delivery schedule and molar ratio towards increasing therapeutic synergism, this study presents a step forward in the development of translatable (effective, affordable, and scalable) solutions enabling successful treatment of unmet oncological diseases. To this end, future work on different cell lines (*e.g.*, renal cell carcinoma Caki-2 cells or bladder carcinoma MB49 cells) will be undertaken to demonstrate the flexibility of the proposed DDS towards the treatment of different forms of cancer. Selected formulations will be characterized *in vivo* to evaluate, together with therapeutic efficacy, biodistribution and potential adverse effects; these, however, are not anticipated, given the biocompatibility of Max8 and the low amount of modified GO particles present in the formulation. With its focus on material design and understanding, this contribution lays the ground for the future optimization of novel composites targeting aggressive metastatic solid tumors that – to this day – impact the health and quality of life of millions of people worldwide.

REFERENCES

- [1] Croissant, J.G., D. Zhang, S. Alsaiari, et al., Protein-gold clusters-capped mesoporous silica nanoparticles for high drug loading, autonomous gemcitabine/doxorubicin co-delivery, and in-vivo tumor imaging. *Journal of Controlled Release*, 2016. 229: p. 183-191.
- [2] Anajafi, T., M.D. Scott, S. You, et al., Acridine Orange Conjugated Polymericosomes for Simultaneous Nuclear Delivery of Gemcitabine and Doxorubicin to Pancreatic Cancer Cells. *Bioconjugate Chemistry*, 2016. 27: p. 762-771.
- [3] Palmer, A.C., and P.K Sorger, Combination Cancer Therapy Can Confer Benefit via Patient-to-Patient Variability without Drug Additivity or Synergy. *Cell*, 2017. 171: p. 1678-1691.
- [4] Goto, K., Y. Ohe, T. Shibata, et al., Combined chemotherapy with cisplatin, etoposide, and irinotecan versus topotecan alone as second-line treatment for patients with sensitive relapsed small-cell lung cancer (JC0G0605): a multicentre, open-label, randomised phase 3 trial. *Lancet Oncology*, 2016. 17: p. 1147-1157.
- [5] Lee, Y.-G., J.H. Lee, S.-H. Kim, et al., Comparative analysis between combination and single-agent chemotherapy for elderly patients with advanced non-small cell lung cancer: A nationwide population-based outcome study. *Lung Cancer*, 2018. 122: p. 88-93.
- [6] Pusuluri, A., V. Krishnan, D. Wu, et al., Role of synergy and immunostimulation in design of chemotherapy combinations: An analysis of doxorubicin and camptothecin. *Bioengineering and Translational Medicine*, 2019. 4: p. e10129
- [7] Hu, Q., W. Sun, C. Wang, and Z. Gu, Recent advances of cocktail chemotherapy by combination drug delivery systems. *Advanced Drug Delivery Reviews*, 2016. 98: p. 19-34.
- [8] Fan, W., B. Yung, P. Huang, and X. Chen, Nanotechnology for Multimodal Synergistic Cancer Therapy. *Chemical Reviews*, 2017. 117, p. 13566-13638.
- [9] Vogus, D.R., A. Pusuluri, R. Chen, and S. Mitragotri, Schedule dependent synergy of gemcitabine and doxorubicin: Improvement of in vitro efficacy and lack of in vitro-in vivo correlation. *Bioengineering and Translational Medicine*, 2018. 3: p. 49-57.
- [10] Vogus, D.R., M.A. Evans, A. Pusuluri, et al., A hyaluronic acid conjugate engineered to synergistically and sequentially deliver gemcitabine and doxorubicin to treat triple negative breast cancer. *Journal of Controlled Release*, 2017. 267: p. 191-202.
- [11] Bao, Y.-X., X.-D. Zhao, H.-B. Deng, et al., Schedule-dependent cytotoxicity of sunitinib and TRAIL in human non-small cell lung cancer cells with or without EGFR and KRAS mutations. *Cellular Oncology*, 2016. 39: p. 343-352.

- [12] Zhang, Z., S. Liu, Y. Qi, et al., Time-programmed DCA and oxaliplatin release by multilayered nanofiber mats in prevention of local cancer recurrence following surgery. *Journal of Controlled Release*, 2016. 235: p. 125-133.
- [13] Li, X., Y. He, J. Hou, et al., A Time-Programmed Release of Dual Drugs from an Implantable Trilayer Structured Fiber Device for Synergistic Treatment of Breast Cancer. *Small*, 2020. 16(9): p. e1902262.
- [14] Wei, L., J. Chen, S. Zhao, et al., Thermo-sensitive polypeptide hydrogel for locally sequential delivery of two-pronged antitumor drugs. *Acta Biomaterialia*, 2017. 58: p. 44-53.
- [15] Wang, H., J. Wu, K. Xie, et al., Precise Engineering of Prodrug Cocktails into Single Polymeric Nanoparticles for Combination Cancer Therapy: Extended and Sequentially Controllable Drug Release. *ACS Applied Materials and Interfaces*, 2017. 9: p. 10567-10576.
- [16] Narayanan, S., U. Mony, D.K. Vijaykumar, et al., Sequential release of epigallocatechin gallate and paclitaxel from PLGA-casein core/shell nanoparticles sensitizes drug-resistant breast cancer cells. *Nanomedicine*, 2015. 11: p. 1399-1406.
- [17] Wang, T., D. Wang, J. Liu, et al., Acidity-Triggered Ligand-Presenting Nanoparticles To Overcome Sequential Drug Delivery Barriers to Tumors. *Nano Letters*, 2017. 17: p. 5429-5436.
- [18] Li, L., W. Sun, Z. Zhang, and Y. Huang, Time-staggered delivery of docetaxel and H1-S6A,F8A peptide for sequential dual-strike chemotherapy through tumor priming and nuclear targeting. *Journal of Controlled Release*, 2016. 232: p. 62-74.
- [19] Douillard, J.-Y., A. Sobrero, C. Carnaghi, et al., Metastatic colorectal cancer: integrating irinotecan into combination and sequential chemotherapy. *Annals of Oncology*, 2003. 14: p. ii7-ii12.
- [20] Simkens, L.H.J., H. van Tinteren, A. May, et al., Maintenance treatment with capecitabine and bevacizumab in metastatic colorectal cancer (CAIRO3): a phase 3 randomised controlled trial of the Dutch Colorectal Cancer Group. *Lancet*, 2015. 385: p. 1843-1852.
- [21] Ducreux, M., D. Malka, J. Mendiboure, et al., Sequential versus combination chemotherapy for the treatment of advanced colorectal cancer (FFCD 2000-05): an open-label, randomised, phase 3 trial. *Lancet Oncology*, 2011. 12: p. 1032-1044.
- [22] Cardoso, F., P.L. Bedard, E.P. Winer, et al., International guidelines for management of metastatic breast cancer: combination vs sequential single-agent chemotherapy. *Journal of the National Cancer Institute*, 2009. 101: p. 1174-1181.
- [23] Liang, X., C. Gao, L. Cui, et al., Self-Assembly of an Amphiphilic Janus Camptothecin-Floxuridine Conjugate into Liposome-Like Nanocapsules for More Efficacious Combination Chemotherapy in Cancer. *Advanced Materials*, 2017. 29: p. 1703135.

- [24] Camacho, K.M., S. Menegatti, D.R. Vogus, et al., DAFODIL: A novel liposome-encapsulated synergistic combination of doxorubicin and 5FU for low dose chemotherapy. *Journal of Controlled Release*, 2016. 229: p. 154-162.
- [25] Camacho, K.M., S. Menegatti, and S. Mitragotri, Low-molecular-weight polymer-drug conjugates for synergistic anticancer activity of camptothecin and doxorubicin combinations. *Nanomedicine*, 2016. 11: p. 1139-1151.
- [26] Camacho, K.M., S. Kumar, S. Menegatti, et al., Synergistic antitumor activity of camptothecin-doxorubicin combinations and their conjugates with hyaluronic acid. *Journal of Controlled Release*, 2015. 210: p. 198-207.
- [27] Zheng, Y., Y. Cheng, J. Chen, et al., Injectable Hydrogel-Microsphere Construct with Sequential Degradation for Locally Synergistic Chemotherapy. *ACS Applied Materials and Interfaces*, 2017. 9: p. 3487-3496.
- [28] Yavvari, P.S., S. Pal, S. Kumar, et al., Injectable, Self-Healing Chimeric Catechol-Fe(III) Hydrogel for Localized Combination Cancer Therapy. *ACS Biomaterials and Science Engineering*, 2017. 3: p. 3404-3413.
- [29] Balakrishnan, B., N. Joshi, K. Thorat, et al., A tumor responsive self healing prodrug hydrogel enables synergistic action of doxorubicin and miltefosine for focal combination chemotherapy. *Journal of Materials Chemistry B*, 2019. 7: p. 2920-2925.
- [30] Wang, Y., Q. Zhao, N. Han, et al., Mesoporous silica nanoparticles in drug delivery and biomedical applications. *Nanomedicine*, 2015. 11: p. 313-327.
- [31] Kiew, S.F., L.V. Kiew, H.B. Lee, et al., Assessing biocompatibility of graphene oxide-based nanocarriers: A review. *Journal of Controlled Release*, 2016. 226: p. 217-228.
- [32] Parveen, S., R. Misra, and S.K. Sahoo, Nanoparticles: a boon to drug delivery, therapeutics, diagnostics and imaging. *Nanomedicine*, 2012. 8: p. 147-166.
- [33] Masood, F., Polymeric nanoparticles for targeted drug delivery system for cancer therapy. *Material Science and Engineering C*, 2016. 60: p. 569-578.
- [34] Li, J., and D.J. Mooney, Designing hydrogels for controlled drug delivery. *Nature Reviews Materials*, 2016. 1: p.16071.
- [35] Dimatteo, R., N.J. Darling, and T. Segura, In situ forming injectable hydrogels for drug delivery and wound repair. *Advanced Drug Delivery Reviews*, 2018. 127: p. 167-184.
- [36] Fakhari, A., and J. Anand Subramony, Engineered in-situ depot-forming hydrogels for intratumoral drug delivery. *Journal of Controlled Release*, 2015. 220: p. 465-475.

- [37] Shen, B., D. Lu, W. Zhai, and W. Zheng, Synthesis of graphene by low-temperature exfoliation and reduction of graphite oxide under ambient atmosphere. *Journal of Materials Chemistry C*, 2013. 1: p. 50-53.
- [38] Deb, A., and R. Vimala, Camptothecin loaded graphene oxide nanoparticle functionalized with polyethylene glycol and folic acid for anticancer drug delivery. *Journal of Drug Delivery Science and Technology*, 2018. 43: p. 333-342.
- [39] Deb, A., N.G. Andrews, and V. Raghavan, Natural polymer functionalized graphene oxide for co-delivery of anticancer drugs: In-vitro and in-vivo. *International Journal of Biological Macromolecules*, 2018. 113: p. 515-525.
- [40] Tran, T.H, H.T. Nguyen, T.T. Pham, et al., Development of a Graphene Oxide Nanocarrier for Dual-Drug Chemo-phototherapy to Overcome Drug Resistance in Cancer. *ACS Applied Materials and Interfaces*, 2015. 7: p. 28647-28655.
- [41] Huang, Y.-S., Y.-J. Lu, and J.-P. Chen, Magnetic graphene oxide as a carrier for targeted delivery of chemotherapy drugs in cancer therapy. *Journal of Magnetism and Magnetic Materials*, 2017. 427: p. 34-40.
- [42] Hashemi, M., A. Yadegari, G. Yazdanpanah, et al., Functionalized R9-reduced graphene oxide as an efficient nano-carrier for hydrophobic drug delivery. *RSC Advances*, 2016. 6: p. 74072-74084.
- [43] Xu, Z., S. Zhu, M. Wang, et al., Delivery of paclitaxel using PEGylated graphene oxide as a nanocarrier. *ACS Applied Materials and Interfaces*, 2015. 7: p. 1355-1363.
- [44] Nasrollahi, F., J. Varshosaz, A.A. Khodadadi, et al., Targeted Delivery of Docetaxel by Use of Transferrin/Poly(allylamine hydrochloride)-functionalized Graphene Oxide Nanocarrier. *ACS Applied Materials and Interfaces*, 2016. 8: p. 13282-13293.
- [45] Lv, Y., L. Tao, S.W. Annie Bligh, et al., Targeted delivery and controlled release of doxorubicin into cancer cells using a multifunctional graphene oxide. *Material Science and Engineering C*, 2016. 59: p. 652-660.
- [46] He, L., S. Sarkar, A. Barras, et al., Electrochemically stimulated drug release from flexible electrodes coated electrophoretically with doxorubicin loaded reduced graphene oxide. *Chemical Communications*, 2017. 53: p. 4022-4025.
- [47] de Melo-Diogo, D., E.C. Costa, C.G. Alves, et al., POxylated graphene oxide nanomaterials for combination chemo-phototherapy of breast cancer cells. *European Journal of Pharmaceutics and Biopharmaceutics*, 2018. 131: p. 162-169.
- [48] Fong, Y.T., C.-H. Chen, and J.-P. Chen, Intratumoral Delivery of Doxorubicin on Folate-Conjugated Graphene Oxide by In-Situ Forming Thermo-Sensitive Hydrogel for Breast Cancer Therapy. *Nanomaterials*, 2017. 7: p. pii: E388.

- [49] Zhang, W., Z. Guo, D. Huang, et al., Synergistic effect of chemo-photothermal therapy using PEGylated graphene oxide. *Biomaterials*, 2011. 32: p. 8555-8561.
- [50] Yang, K., L. Feng, and Z. Liu, Stimuli responsive drug delivery systems based on nano-graphene for cancer therapy. *Advanced Drug Delivery Reviews*, 2016. 105: p. 228-241.
- [51] Zhang, Q., Z. Wu, N. Li, et al., Advanced review of graphene-based nanomaterials in drug delivery systems: Synthesis, modification, toxicity and application. *Material Science and Engineering C*, 2017. 77: p. 1363-1375.
- [52] Hasanzade, Z., and H. Raissi, Solvent/co-solvent effects on the electronic properties and adsorption mechanism of anticancer drug Thioguanine on Graphene oxide surface as a nanocarrier: Density functional theory investigation and a molecular dynamics. *Applied Surface Science*, 2017. 422: p. 1030-1041.
- [53] Mahdavi, M., F. Rahmani, and S. Nouranian, Molecular simulation of pH-dependent diffusion, loading, and release of doxorubicin in graphene and graphene oxide drug delivery systems. *Journal of Materials Chemistry B*, 2016. 4: p. 7441-7451.
- [54] Safdari, F., H. Raissi, M. Shahabi, and M. Zaboli, DFT Calculations and Molecular Dynamics Simulation Study on the Adsorption of 5-Fluorouracil Anticancer Drug on Graphene Oxide Nanosheet as a Drug Delivery Vehicle. *Journal of Inorganic and Organometallic Polymers*, 2017. 27: p. 805-817.
- [55] Hasanzade, Z., and H. Raissi, Investigation of graphene-based nanomaterial as nanocarrier for adsorption of paclitaxel anticancer drug: a molecular dynamics simulation study. *Journal of Molecular Modeling*, 2017. 23: p. 36.
- [56] Tibbitt, M.W., J.E. Dahlman, and R. Langer, Emerging Frontiers in Drug Delivery. *Journal of the American Chemical Society*, 2016. 138: p. 704-717.
- [57] Mathew, A.P., S. Uthaman, K.-H. Cho, et al., Injectable hydrogels for delivering biotherapeutic molecules. *International Journal of Biological Macromolecules*, 2018. 110: p. 17-29.
- [58] Park, K., Drug delivery of the future: Chasing the invisible gorilla. *Journal of Controlled Release*, 2016. 240: p. 2-8.
- [59] Huang, J., W.-J. Wang, B.-G. Li, and S. Zhu, Design and Synthesis of Poly(butyl acrylate) Networks through RAFT Polymerization with Crosslinking for Controlled-Release Applications. *Macromolecular Materials and Engineering*, 2013. 298: p. 391-399.
- [60] Hezaveh, H., and I.I. Muhamad, Modification and swelling kinetic study of kappa-carrageenan-based hydrogel for controlled release study. *Journal of the Taiwan Institute of Chemical Engineers*, 2013. 44: p. 182-191.

- [61] Dexter, A.F., N.L. Fletcher, R.G. Creasey, et al., Fabrication and characterization of hydrogels formed from designer coiled-coil fibril-forming peptides. *RSC Advances*, 2017. 7: p. 27260-27271.
- [62] Rajagopal, K., B. Ozbas, D.J. Pochan, and J.P. Schneider, Probing the importance of lateral hydrophobic association in self-assembling peptide hydrogelators. *European Biophysical Journal*, 2006. 35: p. 162-169.
- [63] Branco, M.C., D.J. Pochan, N.J. Wagner, and J.P. Schneider, Macromolecular diffusion and release from self-assembled beta-hairpin peptide hydrogels. *Biomaterials*, 2009. 30: p. 1339-1347.
- [64] Haines-Butterick, L., K. Rajagopal, M. Branco, et al., Controlling hydrogelation kinetics by peptide design for three-dimensional encapsulation and injectable delivery of cells. *Proceedings of the National Academy of Sciences of the United States of America*, 2007. 104: p. 7791-7796.
- [65] Chen, Y., H.X. Gan, and Y.W. Tong, pH-Controlled Hierarchical Self-Assembly of Peptide Amphiphile. *Macromolecules*, 2015. 48: p. 2647-2653.
- [66] Kumar, P., V. Pillay, G. Modi, et al., Self-Assembling Peptides: Implications for Patenting in Drug Delivery and Tissue Engineering. *Recent Patents on Drug Delivery and Formulations*, 2011. 5: p. 24-51.
- [67] Vashist, A., A. Kaushik, A. Ghosal, Nanocomposite Hydrogels: Advances in Nanofillers Used for Nanomedicine. *Gels*, 2018. 4: p. 75.
- [68] Liu, M., P. Huang, W. Wang, et al., An injectable nanocomposite hydrogel co-constructed with gold nanorods and paclitaxel-loaded nanoparticles for local chemo-photothermal synergetic cancer therapy. *Journal of Materials Chemistry B*, 2019. 7: p. 2667-2677.
- [69] Basso, J., A. Miranda, S. Nunes, et al., Hydrogel-Based Drug Delivery Nanosystems for the Treatment of Brain Tumors. *Gels*, 2018. 4: p. 62.
- [70] Constantin, M., S.-M. Bucatariu, F. Doroftei, and G. Fundueanu, Smart composite materials based on chitosan microspheres embedded in thermosensitive hydrogel for controlled delivery of drugs. *Carbohydrate Polymers*, 2017. 157: p. 493-502.
- [71] Liu, D., Y. Chen, X. Feng, et al., Micellar nanoparticles loaded with gemcitabine and doxorubicin showed synergistic effect. *Colloids and Surfaces B: Biointerfaces*, 2014. 113: p. 158-168.
- [72] Wang, C., G. Zhang, G. Liu, et al., Photo- and thermo-responsive multicompartiment hydrogels for synergistic delivery of gemcitabine and doxorubicin. *Journal of Controlled Release*, 2017. 259: p. 149-159.

- [73] Lammers, T., V. Subr, K. Ulbrich, et al., Simultaneous delivery of doxorubicin and gemcitabine to tumors *in vivo* using prototypic polymeric drug carriers. *Biomaterials*, 2009. 30: p. 3466-3475.
- [74] Leonard, S.R., A.R. Cormier, X. Pang, et al., Solid-state NMR evidence for β -hairpin structure within MAX8 designer peptide nanofibers. *Biophysical Journal*, 2013. 105: p. 222-230.
- [75] Yan, C., A. Altunbas, T. Yucel, et al., Injectable solid hydrogel: mechanism of shear-thinning and immediate recovery of injectable β -hairpin peptide hydrogels. *Soft Matter*, 2010. 6: p. 5143-5156.
- [76] Gilje, S., S. Han, M. Wang, et al., A chemical route to graphene for device applications. *Nano Letters*, 2007. 7: p. 3394-3398.
- [77] He, N., O. Yildiz, Q. Pan, et al., Pyrolytic-carbon coating in carbon nanotube foams for better performance in supercapacitors. *Journal of Power Sources*, 2017. 343: p. 492-501.
- [78] Kaiser, E., R.L. Colescott, C.D. Bossinger, and P.I. Cook, Color test for detection of free terminal amino groups in the solid-phase synthesis of peptides. *Analytical Biochemistry*, 1970. 34: p. 595-598.
- [79] Baptista, A.M., V.H. Teixeira, and C.M. Soares, Constant-pH molecular dynamics using stochastic titration. *Journal of Chemical Physics*, 2002. 117: p. 4184-4200.
- [80] Adnan, A., R. Lam, H. Chen, et al., Atomistic simulation and measurement of pH dependent cancer therapeutic interactions with nanodiamond carrier. *Molecular Pharmaceutics*, 2011. 8: p. 368-374.
- [81] Henderson, L.J., Concerning the Relationship Between the Strength of Acids and Their Capacity to Preserve Neutrality. *American Journal of Physiology*, 1908. 21: p. 173-179.
- [82] Hasselbalch, K.A., Die Berechnung der Wasserstoffzahl des Blutes aus der freien und gebundenen Kohlensäure desselben, und die Sauerstoffbindung des Blutes als Funktion der Wasserstoffzahl, 1916, Julius Springer: Berlin, Germany. p. 1-144.
- [83] Konkena, B., and S. Vasudevan, Understanding Aqueous Dispersibility of Graphene Oxide and Reduced Graphene Oxide through pKa Measurements. *The Journal of Physical Chemistry Letters*, 2012. 3: p. 867-872.
- [84] Speelmans, G., R.W.H.M. Staffhorst, B. de Kruijff, and F.A. de Wolf, Transport Studies of Doxorubicin in Model Membranes Indicate a Difference in Passive Diffusion across and Binding at the Outer and Inner Leaflet of the Plasma Membrane. *Biochemistry*, 1994. 33: p. 13761-13768.

- [85] Shih, C.-J., S. Lin, R. Sharma, et al., Understanding the pH-dependent behavior of graphene oxide aqueous solutions: a comparative experimental and molecular dynamics simulation study. *Langmuir*, 2011. 28: p. 235.
- [86] Lerf, A., H. He, M. Forster, and J. Klinowski, Structure of Graphite Oxide Revisited. *Journal of Physical Chemistry B*, 1998. 102: p. 4477-4482.
- [87] Wang, J., R.M. Wolf, J.W. Caldwell, et al., Development and testing of a general amber force field. *Journal of Computational Chemistry*, 2004. 25: p. 1157-1174.
- [88] Bayly, C.I., P. Cieplak, W. Cornell, and P.A. Kollman, A well-behaved electrostatic potential based method using charge restraints for deriving atomic charges: the RESP model. *Journal of Physical Chemistry*, 1993. 97: p. 10269-10280.
- [89] Dupradeau, F.-Y., A. Pigache, T. Zaffran, et al., The R.E.D. tools: advances in RESP and ESP charge derivation and force field library building. *Physical Chemistry Chemical Physics*, 2010. 12: p. 7821.
- [90] Vanquelef, E., S. Simon, G. Marquant, et al., R.E.D. Server: a web service for deriving RESP and ESP charges and building force field libraries for new molecules and molecular fragments. *Nucleic Acids Research*, 2011. 39: p. W511-W517.
- [91] Jakalian, A., B.L. Bush, D.B. Jack, and C.I. Bayly, Fast, efficient generation of high-quality atomic charges. AM1-BCC model: I. Method. *Journal of Computational Chemistry*, 2000. 21: p. 132-146.
- [92] Jakalian, A., D.B. Jack, and C.I. Bayly, Fast, efficient generation of high-quality atomic charges. AM1-BCC model: II. Parameterization and validation. *Journal of Computational Chemistry*, 2002. 23: p. 1623-1641.
- [93] Stauffer, D., N. Dragneva, W.B. Floriano, An atomic charge model for graphene oxide for exploring its bioadhesive properties in explicit water. *Journal of Chemical Physics*, 2014. 141: p. 044705.
- [94] Lei, H., X. Wang, and C. Wu, Early stage intercalation of doxorubicin to DNA fragments observed in molecular dynamics binding simulations. *Journal of Molecular Graphics and Modelling*, 2012. 38: p. 279-289.
- [95] Wang, J., W. Wang, P.A. Kollman, and D.A. Case, ANTECHAMBER: An accessory software package for molecular mechanical calculations. *Abstracts of Papers, American Chemical Society*, 2001. 222: p. U403.
- [96] Martínez, L., R. Andrade, E.G. Birgin, and J.M. Martínez, PACKMOL: a package for building initial configurations for molecular dynamics simulations. *Journal of Computational Chemistry*, 2009. 30: p. 2157-2164.

- [97] Jorgensen, W.L., J. Chandrasekhar, J.D. Madura, et al., Comparison of simple potential functions for simulating liquid water. *Journal of Chemical Physics*, 1983. 79: p. 926.
- [98] Basconi, J.E., and M.R. Shirts, Effects of Temperature Control Algorithms on Transport Properties and Kinetics in Molecular Dynamics Simulations. *Journal of Chemical Theory and Computation*, 2013. 9: p. 2887-2899.
- [99] Karnati, K.R., and Y. Wang, Understanding the co-loading and releasing of doxorubicin and paclitaxel using chitosan functionalized single-walled carbon nanotubes by molecular dynamics simulations. *Physical Chemistry Chemical Physics*, 2018. 20: p. 9389-9400.
- [100] Yang, A., J. Li, C. Zhang, et al., One-step amine modification of graphene oxide to get a green trifunctional metal-free catalyst. *Applied Surface Science*, 2015. 346: p. 443-450.
- [101] Szabó, T., O. Berkesi, and I. Dékány, DRIFT study of deuterium-exchanged graphite oxide. *Carbon*, 2005. 43: p. 3186-3189.
- [102] Chen, S., Y. Itoh, T. Masuda, et al., Ionic interactions. Subnanoscale hydrophobic modulation of salt bridges in aqueous media. *Science*, 2015. 348: p. 555-559.
- [103] Yue, Z., C. Li, G.A. Voth, and J.M.J. Swanson, Dynamic Protonation Dramatically Affects the Membrane Permeability of Drug-like Molecules. *Journal of the American Chemical Society*, 2019. 141: p. 13421-13433.
- [104] Hong, J., R.J. Hamers, J.A. Pedersen, and Q. Cui, A Hybrid Molecular Dynamics/Multiconformer Continuum Electrostatics (MD/MCCE) Approach for the Determination of Surface Charge of Nanomaterials. *Journal of Physical Chemistry C*, 2017. 121: p. 3584-3596.
- [105] Vatanparast, M., and Z. Shariatinia, Hexagonal boron nitride nanosheet as novel drug delivery system for anticancer drugs: Insights from DFT calculations and molecular dynamics simulations. *Journal of Molecular Graphics and Modelling*, 2019. 89: p. 50-59.
- [106] Hu, Y., T. Guo, X. Ye, et al., Dye adsorption by resins: Effect of ionic strength on hydrophobic and electrostatic interactions. *Chemical Engineering Journal*, 2013. 228: p. 392-397.
- [107] Li, M., C. Liu, Y. Xie, et al., The evolution of surface charge on graphene oxide during the reduction and its application in electroanalysis. *Carbon*, 2014. 66: p. 302-311.
- [108] Schneible, J.D., A. Singhal, R.L. Liova, et al., Tailoring the Chemical Modification of Chitosan Hydrogels to Fine-Tune the Release of a Synergistic Combination of Chemotherapeutics. *Biomacromolecules*, 2019. 20: p. 3126-3141.
- [109] Chou, T.-C., The mass-action law based algorithm for cost-effective approach for cancer drug discovery and development. *American Journal of Cancer Research*, 2011. 1: p. 925-954.

[110] Chou, T.-C., Drug combination studies and their synergy quantification using the Chou-Talalay method. *Cancer Research*, 2010. 70: p. 440-446.

[111] Budman, D.R., A. Calabro, L. Rosen, and M. Lesser, Identification of unique synergistic drug combinations associated with down expression of survivin in a preclinical breast cancer model system. *Anticancer Drugs*, 2012. 23: p. 272-279.

Tables

Table 4.1 Partial charges for major functional groups.

Functional groups	Elements	RESP charges (this work)	SESP charges[93]	AM1-BCC charges (this work) [§]
Epoxy	C (GO)	+0.1357	+0.18	+0.15
	O	-0.2714	-0.36	-0.28
Hydroxyl	C (GO)	+0.1904	+0.18	+0.30
	O	-0.5689	-0.57	-0.58
	H	+0.3785	+0.39	+0.41
Carboxyl (protonated)	C (GO)	+0.0642	--	-0.11
	C	+0.6655	--	+0.65
	O (sp ²)	-0.5649	--	-0.55
	O (sp ³)	-0.6080	--	-0.60
Carboxyl (deprotonated)	H	+0.4432	--	+0.44
	C (GO)	-0.3044	--	-0.03
	C	+0.8408	--	+0.90
	O	-0.7682	--	-0.81
	O	-0.7682	--	-0.81

[§]AM1-BCC charges were determined for the whole molecule, so the total charge of the functional group fragment is not necessarily equal to 0 (neutral state) or -1 (deprotonated state).

Table 4.2 Loading of DOX on GO and tGO particles (mg DOX mg⁻¹ GO). Error represents 99% C.I. (n ≥ 3).

Zeta Potential (mV)	Acidic	Neutral	Basic	PBS
-36.5	0.595 ± 0.008	0.581 ± 0.004	0.576 ± 0.002	1.048 ± 0.009
-18.8	0.248 ± 0.050	0.257 ± 0.030	0.262 ± 0.040	0.613 ± 0.015
-8.9	0.231 ± 0.004	0.266 ± 0.028	0.280 ± 0.017	0.570 ± 0.001
0	0.169 ± 0.009	0.257 ± 0.015	0.208 ± 0.013	0.524 ± 0.024
6.8	0.150 ± 0.002	0.221 ± 0.002	0.225 ± 0.011	0.521 ± 0.029
19.3	0.202 ± 0.051	0.163 ± 0.012	0.176 ± 0.002	0.367 ± 0.104

Table 4.3 Percent release of DOX from GO and tGO in 10 mM PBS pH 5 after 72 hr and 650 hr, for particles loaded in acidic, neutral, basic, and high ionic strength (PBS) conditions. Error represents 99% C.I. ($n \geq 3$).

ζ Potential (mV)	Acidic 72 hrs	Acidic 650 hrs	Neutral 72 hrs	Neutral 650 hrs	Basic 72 hrs	Basic 650 hrs	PBS 72 hrs	PBS 650 hrs
-36.5	6.21 ± 0.6	15.0 ± 1.7	6.47 ± 0.6	15.0 ± 0.5	6.01 ± 0.6	14.0 ± 0.1	7.42 ± 0.1	19.1 ± 0.9
-18.8	12.4 ± 0.4	19.2 ± 4.2	13.7 ± 2.1	22.7 ± 3.2	11.4 ± 0.8	19.8 ± 4.0	18.9 ± 2.0	31.4 ± 3.2
-8.9	9.14 ± 0.3	15.7 ± 3.8	8.99 ± 1.1	16.7 ± 4.0	10.6 ± 1.5	19.8 ± 3.9	18.0 ± 1.4	31.8 ± 2.8
0	2.68 ± 0.6	5.10 ± 1.0	2.11 ± 0.4	4.39 ± 0.3	3.08 ± 0.3	5.96 ± 0.2	15.3 ± 1.7	30.7 ± 4.1
6.8	3.03 ± 0.2	5.46 ± 0.01	3.11 ± 0.5	6.80 ± 1.3	3.94 ± 0.9	8.08 ± 0.9	16.1 ± 0.6	32.0 ± 1.3
19.3	1.48 ± 0.3	3.2 ± 0.4	0.68 ± 0.2	2.67 ± 0.1	2.01 ± 0.3	4.65 ± 0.1	14.3 ± 1.8	26.3 ± 4.7

Table 4.4 Percent release of DOX from GO and tGO in 10 mM PBS pH 7.4 after 72 hr and 650 hr, for particles loaded in acidic, neutral, basic, and high salt (PBS) conditions. Error represents 99% C.I. ($n \geq 3$).

ζ Potential (mV)	Acidic 72 hrs	Acidic 650 hrs	Neutral 72 hrs	Neutral 650 hrs	Basic 72 hrs	Basic 650 hrs	PBS 72 hrs	PBS 650 hrs
-36.5	0.35 ± 0.1	6.80 ± 1.1	0.21 ± 0.1	5.30 ± 0.5	0.30 ± 0.1	6.70 ± 0.8	0.56 ± 0.1	6.90 ± 0.4
-18.8	1.60 ± 0.7	7.80 ± 0.7	2.56 ± 1.4	7.78 ± 0.6	1.66 ± 0.6	7.81 ± 1.4	1.95 ± 0.4	9.48 ± 0.5
-8.9	1.20 ± 0.4	6.40 ± 0.2	1.24 ± 0.6	7.11 ± 0.8	1.34 ± 0.2	7.10 ± 1.7	1.60 ± 0.3	9.06 ± 2.0
0	0.25 ± 0.1	1.10 ± 0.4	0.10 ± 0.1	0.50 ± 0.1	0.25 ± 0.1	1.50 ± 0.5	0.30 ± 0.1	3.00 ± 0.6
6.8	0.30 ± 0.1	1.50 ± 0.3	0.76 ± 0.8	1.30 ± 1.1	0.20 ± 0.1	1.60 ± 0.8	0.56 ± 0.3	3.50 ± 0.6
19.3	0.30 ± 0.1	1.40 ± 0.2	0.10 ± 0.1	0.60 ± 2.0	0.30 ± 0.1	1.20 ± 0.4	0.35 ± 0.1	3.10 ± 0.2

Figures

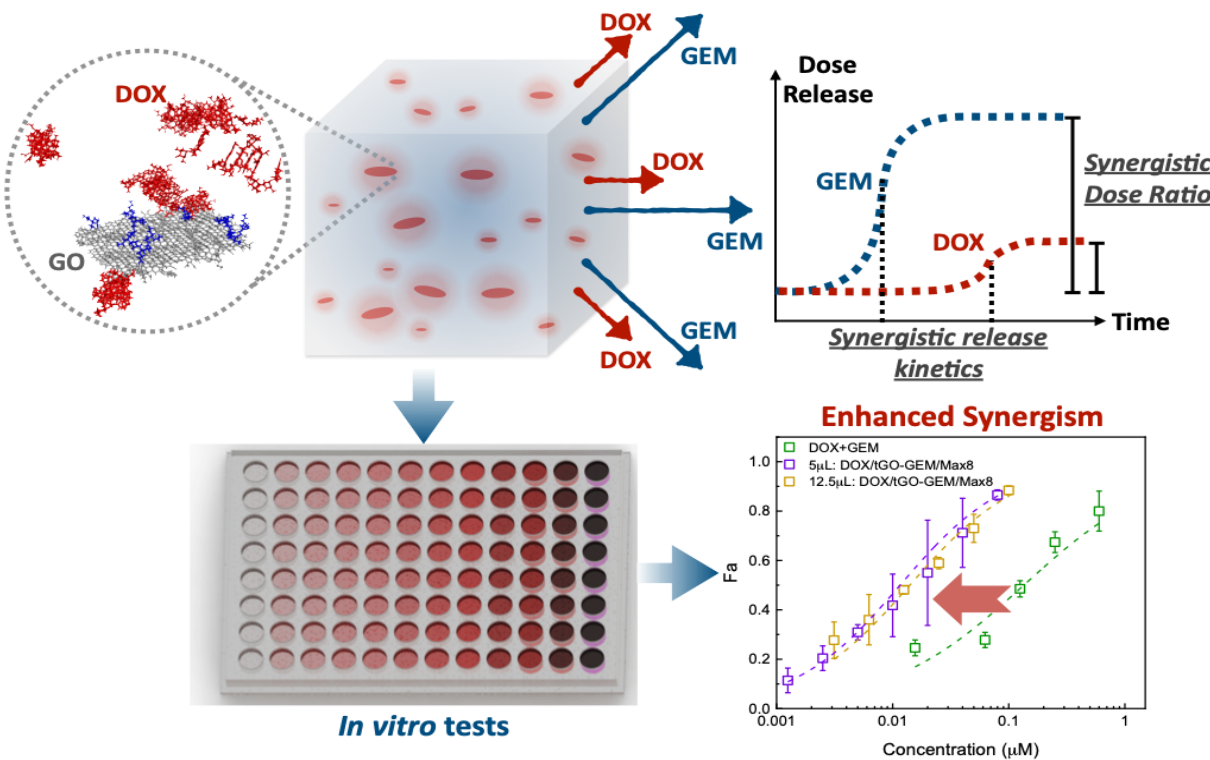


Figure 4.1 Design and proposed mechanism of dual release of DOX and GEM from the hybrid system comprising modified GO nanoparticles suspended in a Max8 hydrogel. The combination of drug release at controlled relative molar ratio and kinetics enhances the inherent synergism of DOX and GEM beyond the simple effect of codelivery.

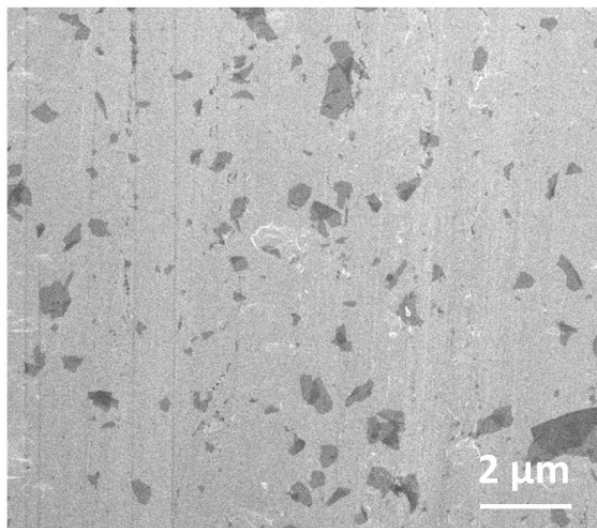


Figure 4.2 SEM of GO particles with an average size of 800 nm.

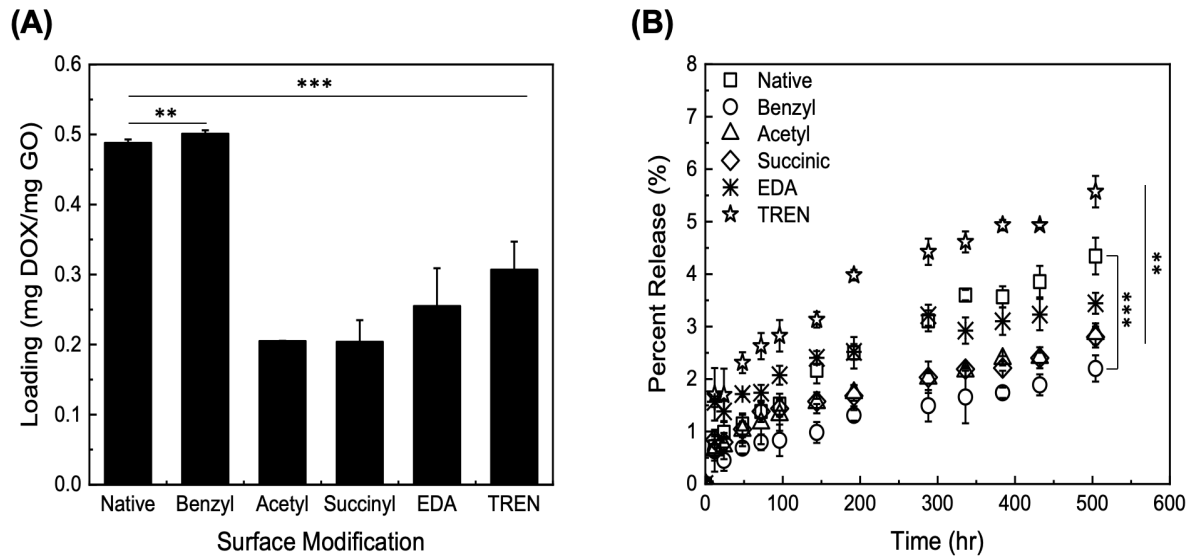


Figure 4.3 Initial screening studies of (A) DOX loading on GO particles with different chemical modifications (listed in the abscissa); (B) DOX release from modified GO particles within 500 hr. Data represent mean \pm 99% C.I. ($n \geq 3$). ** indicates $p < 0.01$, and *** indicates $p < 0.001$, as obtained from a Student's t-test.

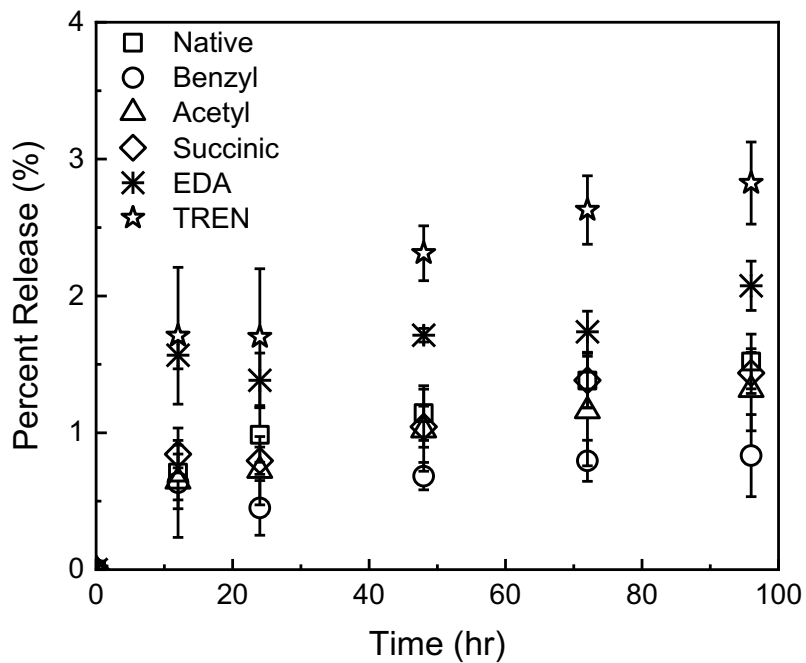


Figure 4.4 DOX release from modified GO particles within 100 hr. Data represent mean \pm 99% C.I. ($n \geq 3$).

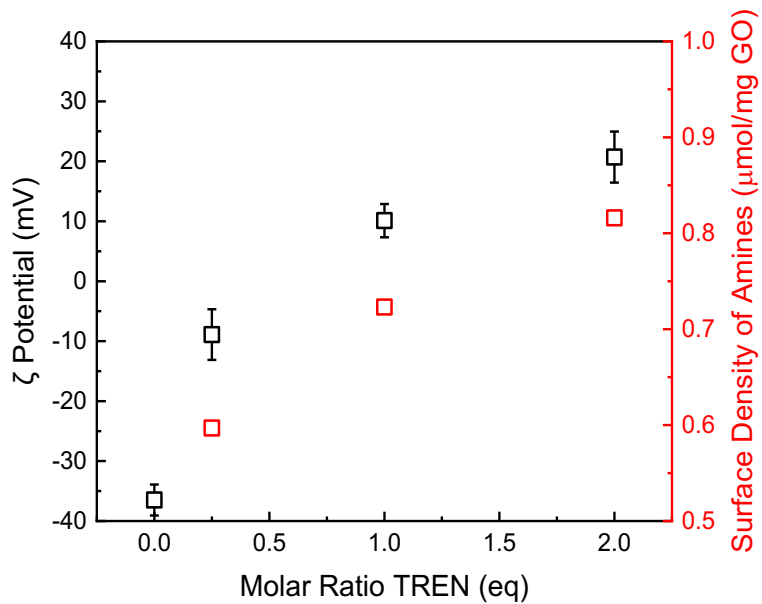


Figure 4.5 The effect of molar ratio of TREN used for tGO reactions on ζ potential (black) and the corresponding concentration of amine groups (red). Data represent mean \pm S.D. ($n \geq 3$).

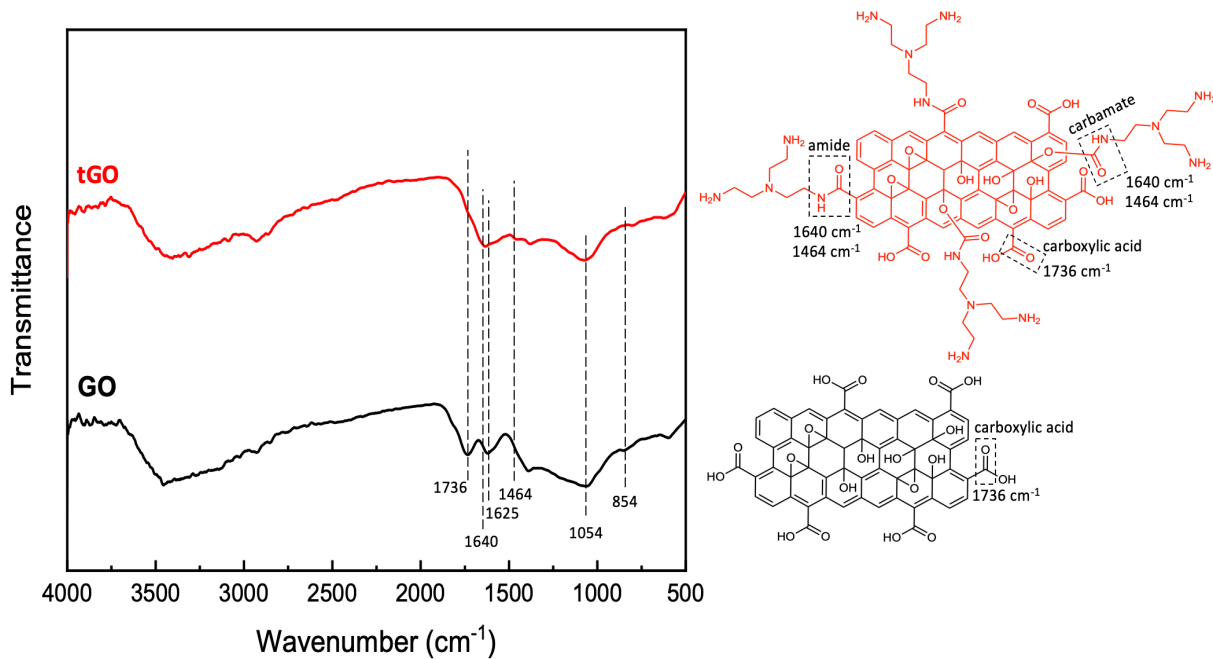


Figure 4.6 FTIR analysis of native GO and tGO particles and corresponding model structures.

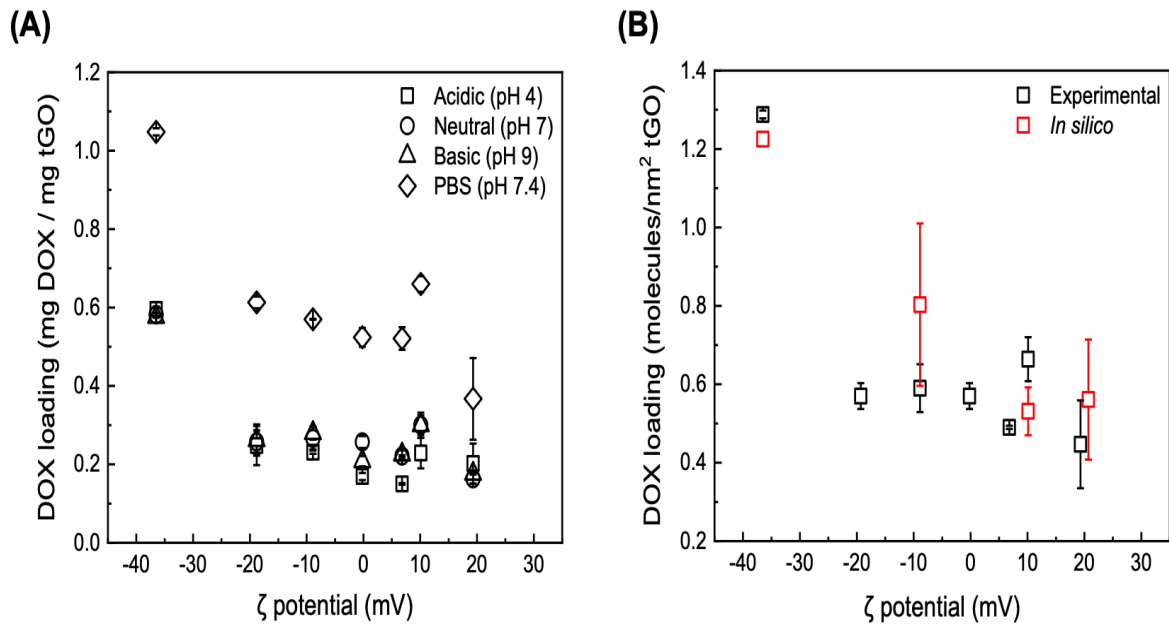


Figure 4.7 (A) Loading of DOX onto tGO particles as a function of ζ potential at different loading conditions: Milli-Q water (titrated with HCl or NaOH) at pH 4 (squares), pH 6 (circles), and pH 9 (triangles), and PBS at pH 7.4 (diamonds), where data represent mean \pm 99% C.I. ($n \geq 3$); **(B)** Comparison between the values of DOX loading measured at pH 6 (black) vs. predicted by the MD simulations at pH 6.1 (red). The experimental data is presented as mean \pm 99% C.I. ($n \geq 3$), while the data from the simulations is presented as mean \pm S.D. for $n \geq 4$ independent simulations with distinct initial configurations.

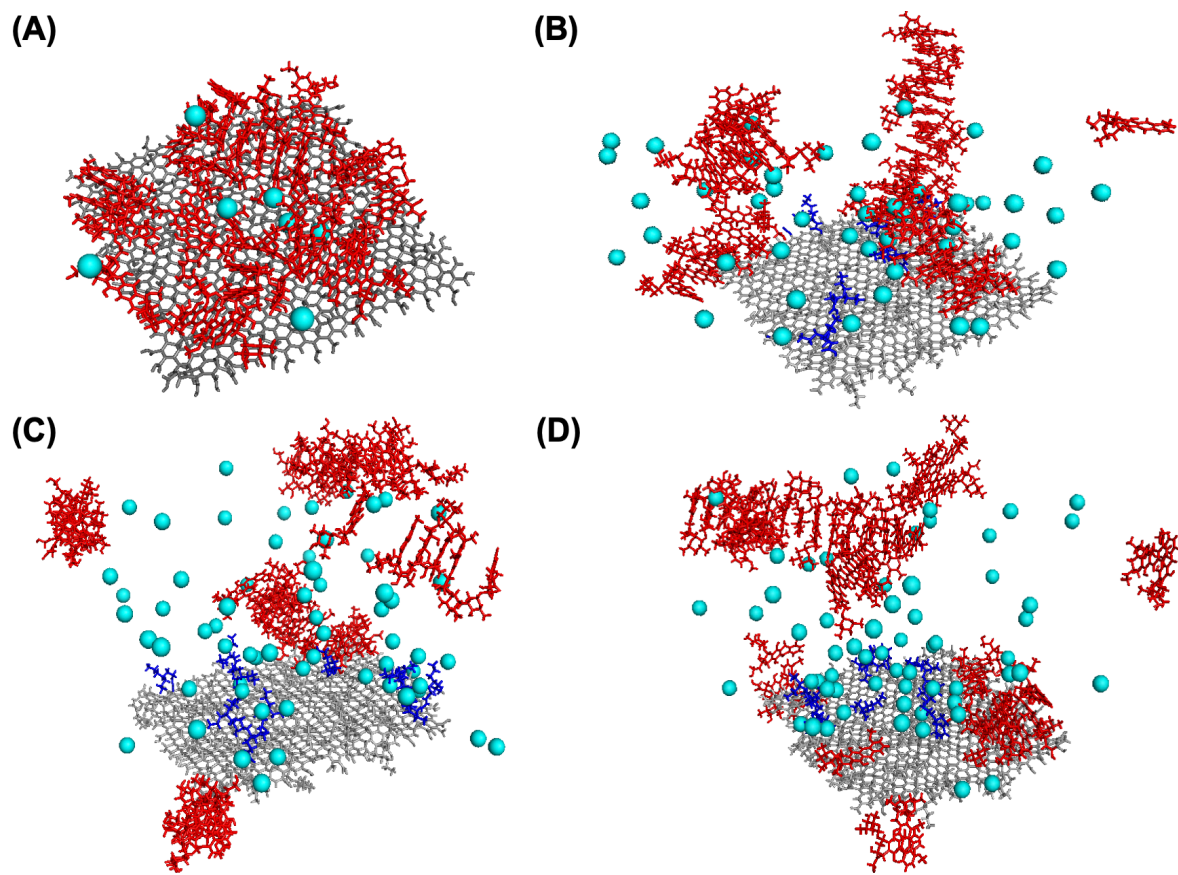


Figure 4.8 Snapshots from DOX (red frame) loading on TREN- (blue frame) modified GO (grey frame) and the dispersion of Cl^- ions (cyan balls) on (A) native GO ($\zeta = -36.5 \text{ mV}$), (B) tGO ($\zeta = -8.9 \text{ mV}$), (C) tGO ($\zeta = 10.1 \text{ mV}$), and (D) tGO ($\zeta = 20.7 \text{ mV}$).

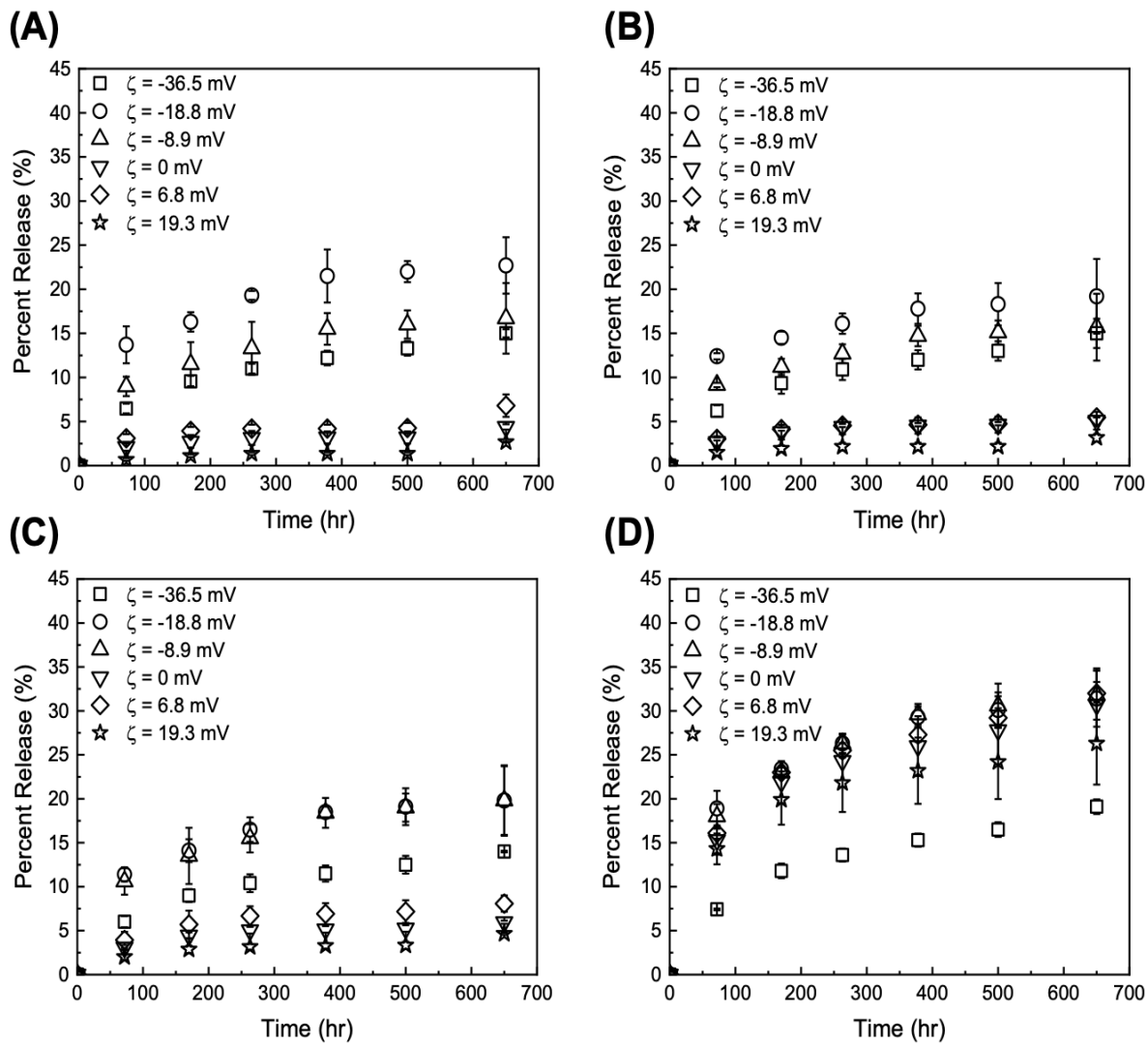


Figure 4.9 Release profiles at pH 5 from DOX/tGO particles loaded at **(A)** pH 4, **(B)** pH 6, **(C)** pH 9, and **(D)** PBS at pH 7.4. Data represent mean \pm 99% C.I. ($n \geq 3$).

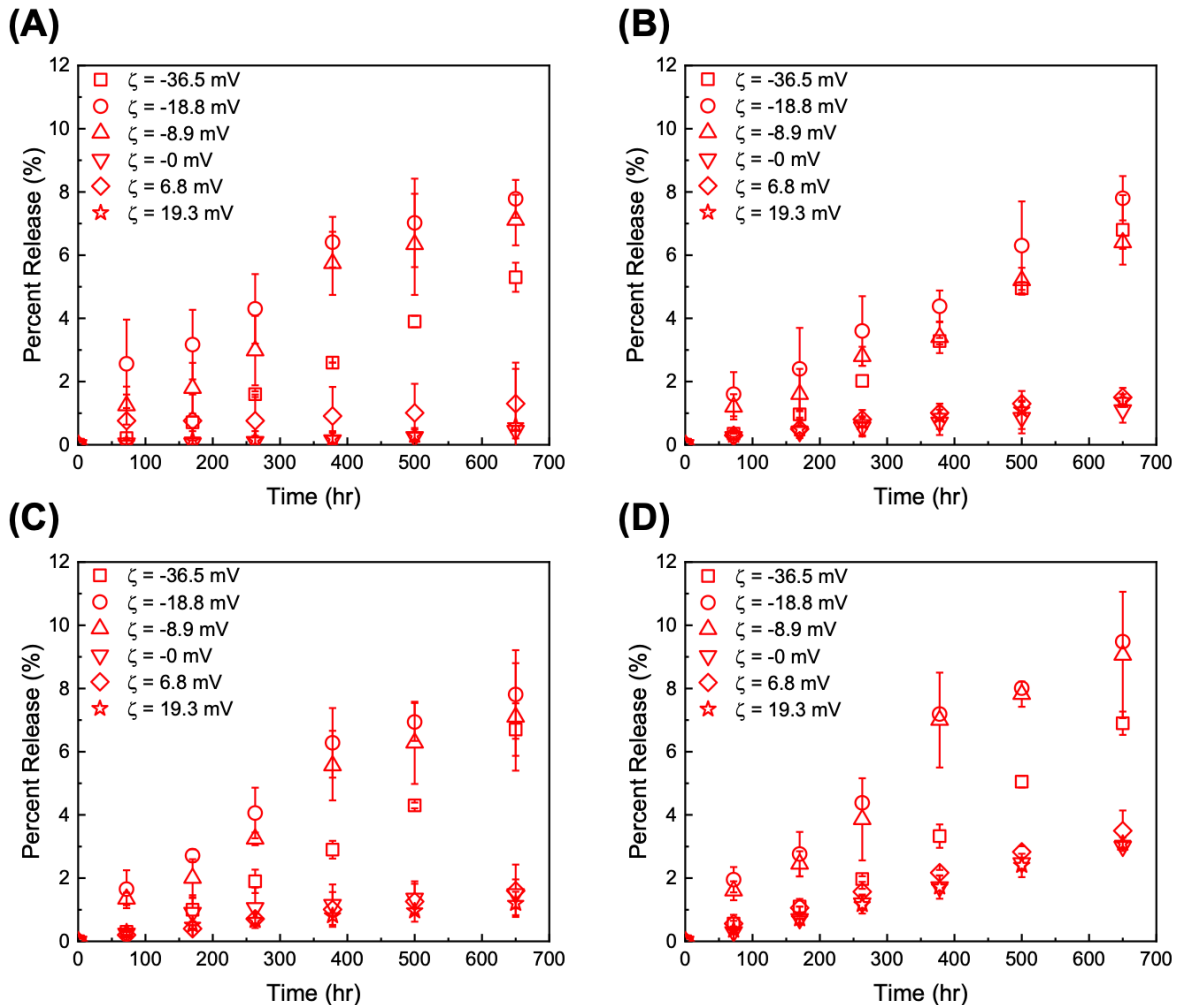


Figure 4.10 Release profiles from DOX loaded tGO at pH 7.4 for tGO loaded in **(A)** acidic (pH 4), **(B)** neutral (pH 7), **(C)** basic (pH 9), and **(D)** PBS (10 mM pH 7.4). Data represent mean \pm 99% C.I. ($n \geq 3$).

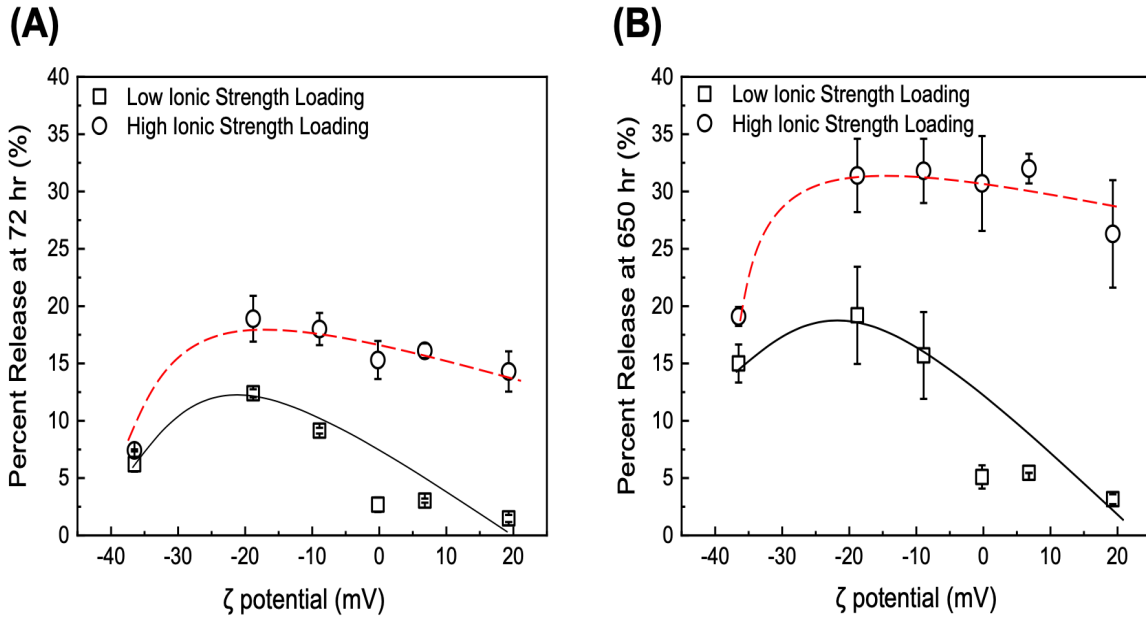


Figure 4.11 Values of DOX percent release at pH 5 after (A) 72 hr and (B) 650 hr from DOX/GO and DOX/tGO particles loaded at neutral pH and low ionic strength (squares) or high ionic strength (circles). Hashed lines are added to guide the visualization of the results. Data represent mean \pm 99% C.I. ($n \geq 3$).

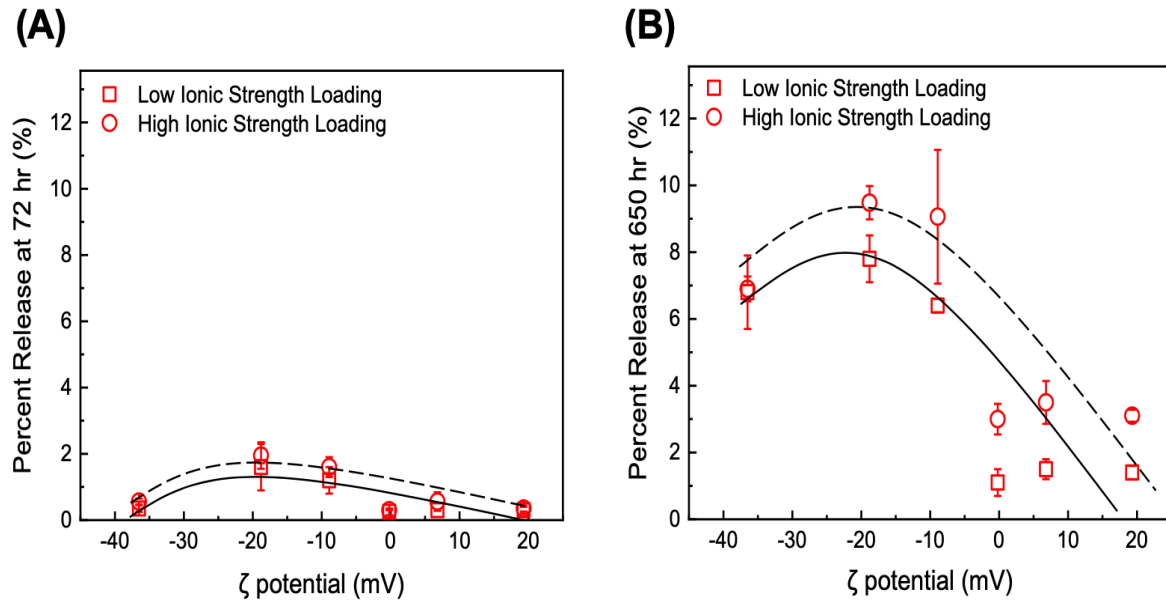


Figure 4.12 Values of DOX percent release at pH 7.4 after (A) 72 hr and (B) 650 hr from GO and tGO particles loaded at neutral pH and low ionic strength (squares) or high ionic strength (circles). Hashed lines are added to guide the visualization of the results. Data represent mean \pm 99% C.I. ($n \geq 3$).

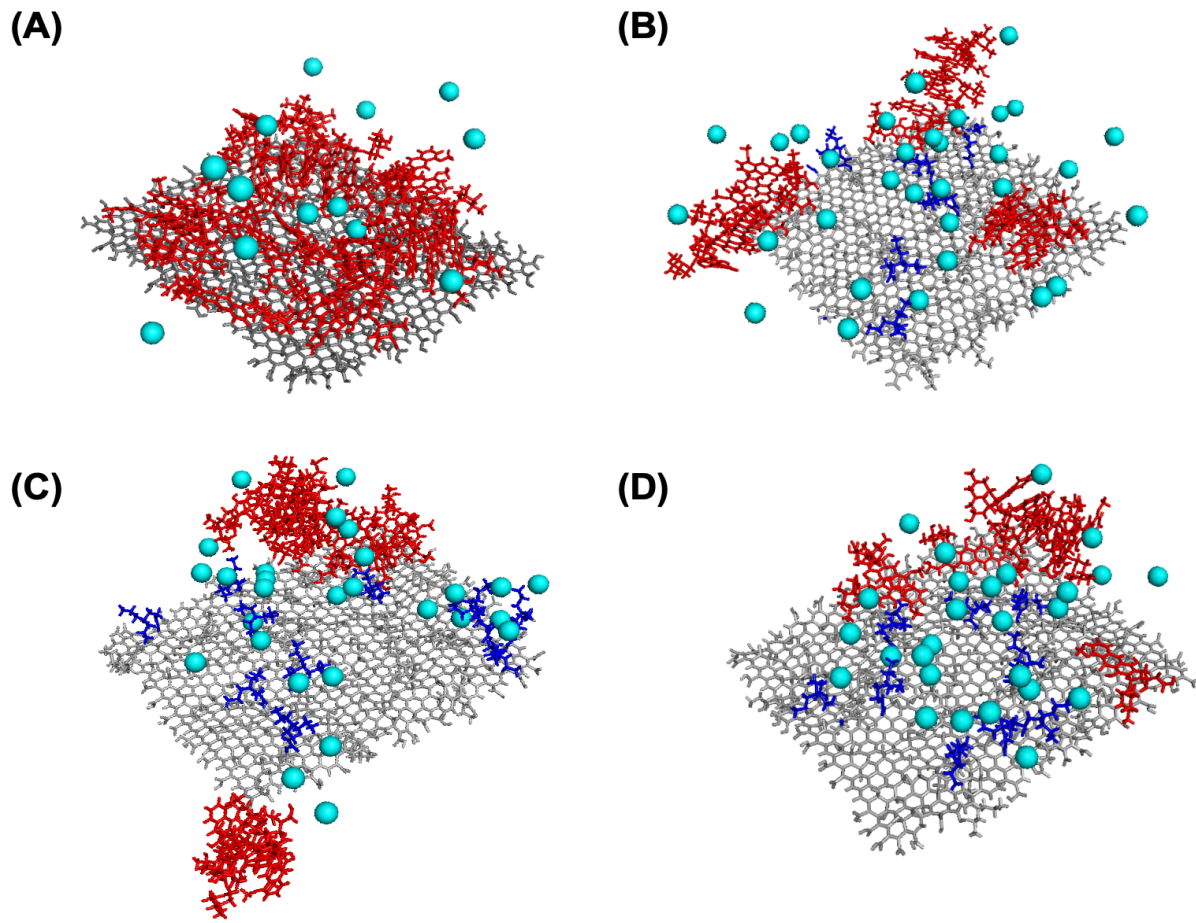


Figure 4.13 Snapshots from DOX (red frame) loading on TREN- (blue frame) modified GO (grey frame) and the dispersion of Cl⁻ ions (cyan spheres) on (A) native GO ($\zeta = -36.5$ mV), (B) tGO ($\zeta = -8.9$ mV), (C) tGO ($\zeta = 10.1$ mV), and (D) tGO ($\zeta = 20.7$ mV).

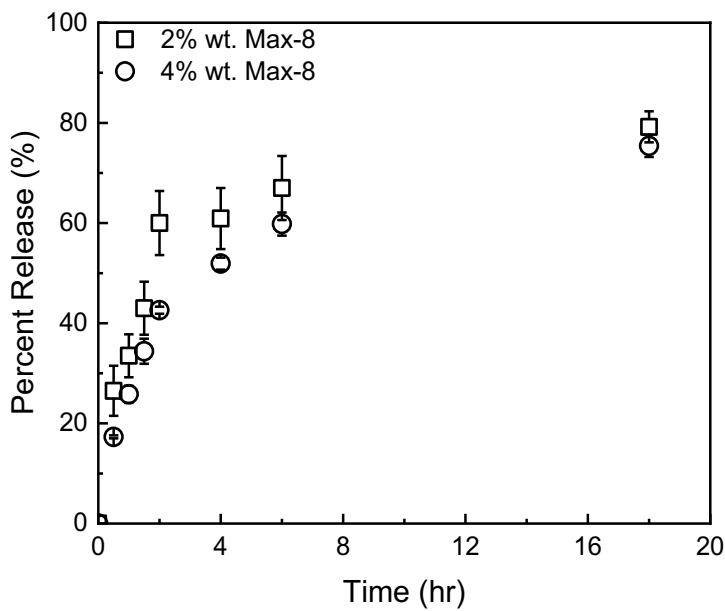


Figure 4.14 Release profiles of GEM from a Max8 hydrogel at 2% (w/w) (squares) and 4% (w/w) (circles). Data represent mean \pm 99% C.I. ($n \geq 3$).

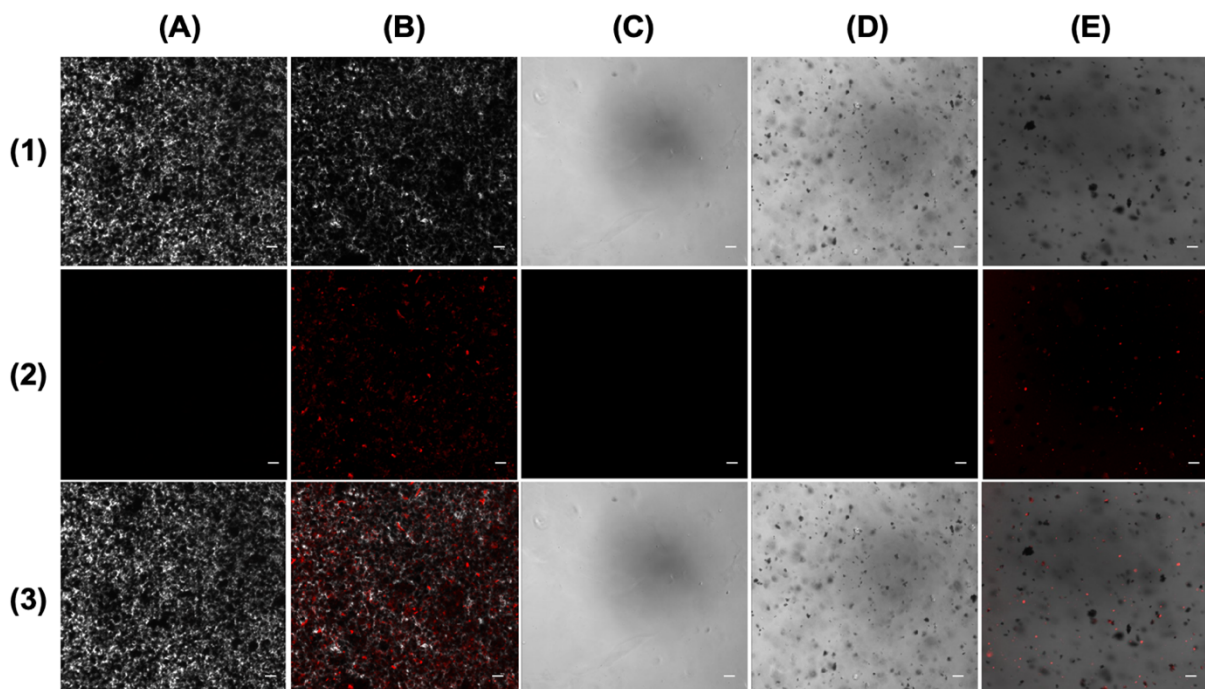


Figure 4.15 Microscopy images of (A) tGO particles, (B) DOX/tGO particles, (C) Max8 hydrogel, (D) tGO particles dispersed in Max8 hydrogel, (E) DOX/tGO particles dispersed in Max8 hydrogel; (1) brightfield, (2) fluorescence (absorption: 590 nm – emission: 617 nm), and (3) combined brightfield-fluorescence overlay. Scale bar represents 20 μm .

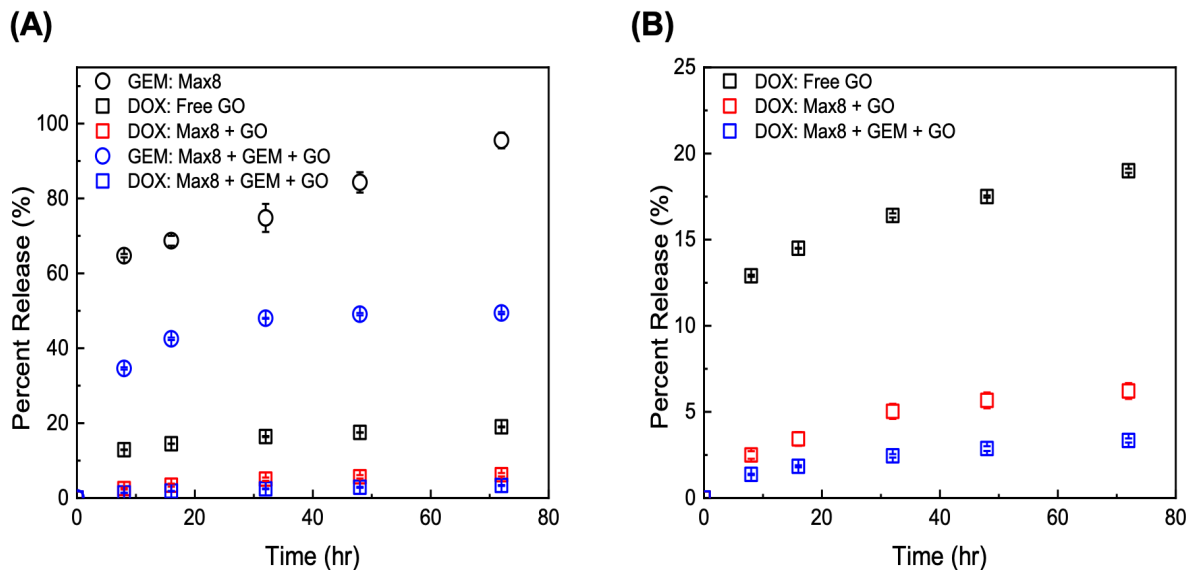


Figure 4.16 (A) Release profiles of GEM from 2% (w/w) GEM/Max8 (black circles), DOX from free DOX/tGO particles (black squares), DOX from DOX/tGO particles embedded in a 2% (w/w) Max8 hydrogel (red squares), GEM from a 2% (w/w) GEM/Max8 hydrogel loaded with tGO particles (blue circles), and DOX from DOX/tGO particles embedded in a 2% (w/w) GEM/Max8 hydrogel (blue squares); (B) release of DOX from the system listed in panel (A). Data represent mean \pm 99% CI ($n \geq 3$).

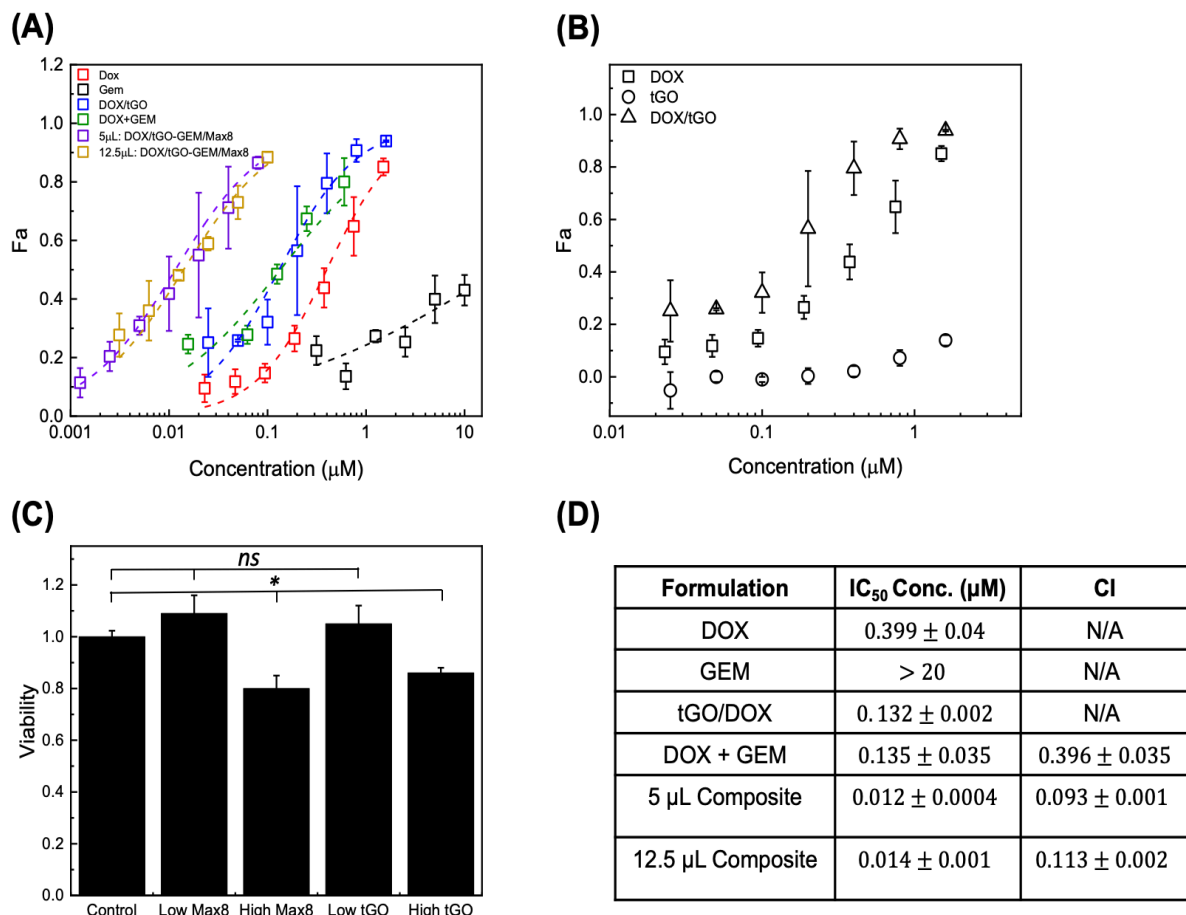


Figure 4.17 (A) Dose-response curves for free DOX (red), free GEM (black), DOX/tGO particles (blue), 10:1 molar ratio free drug combination of GEM/DOX (green), 10:1 molar ratio free drug combination of GEM/DOX from composite system with 5 μL (purple), and 12.5 μL (yellow) of DOX/tGO-GEM/Max8 composite gel; (B) Dose-response curves for DOX (squares), DOX/tGO (triangles), and tGO (circles); (C) Cytotoxicity of Max8 hydrogel (low – 5 μL and high – 12.5 μL) and tGO particles (low – 0.2 $\mu\text{g mL}^{-1}$ and high – 14.6 $\mu\text{g mL}^{-1}$) relative to untreated cells (control), and (D) calculated IC_{50} values for the various formulations and the corresponding combination index (CI). Data represent mean \pm SD. ($n \geq 3$). ns indicates no significance, and * indicates $p < 0.05$, as obtained from a Student's t-test.

CHAPTER 5

Inducible Conformation-Controlled Protein-Binding Affinity in Azobenzene-Cyclized Peptides

Kevin Day, John D. Schneible, Ashlyn T. Young, Vladimir A. Pozdin, Lewis A. Gaffney,
Raphael Prodromou, Donald O. Freytes, Michael A. Daniele, and Stefano Menegatti

An adapted version of this chapter has been published in Journal of Materials Chemistry B.

Abstract

The impact of next-generation biorecognition elements (ligands) will be determined by the ability to remotely control their binding activity for a target biomolecule in complex environments. Compared to conventional mechanisms for regulating binding affinity (pH, ionic strength, or chaotropic agents), light provides higher accuracy and rapidity, and is particularly suited for labile targets. In this study, we demonstrate a general method to develop azobenzene-cyclized peptide ligands with light-controlled affinity for target proteins. Light triggers a *cis/trans* isomerization of the azobenzene, which results in a major structural rearrangement of the cyclic peptide from a non-binding to a binding configuration. Critical to this goal are the ability to achieve efficient photo-isomerization under low light dosage and the temporal stability of both *cis* and *trans* isomers. We demonstrated our method by designing photo-switchable peptides targeting vascular cell adhesion marker 1 (VCAM1), a cell marker implicated in stem cell function. Starting from a known VCAM1-binding linear peptide, an ensemble of azobenzene-cyclized variants with selective light-controlled binding were identified by combining *in silico* design with experimental characterization via spectroscopy and surface plasmon resonance. Variant cycloAZOB[G-VHAKQHRN-K] featured rapid, light-controlled binding of VCAM1 ($K_{D,Trans}/K_{D,Cis} \sim 130$). Biotin-cycloAZOB[G-VHAKQHRN-K] was utilized to label brain microvascular endothelial cells (BMECs), showing co-localization with anti-VCAM1 antibodies in *cis* configuration and negligible binding in *trans* configuration.

5.1. Introduction

Inducible affinity interactions between ligand and target biomolecules are the underlying functions governing biological systems. The ability to design synthetic ligands whose biorecognition can be activated and controlled using remote and biocompatible stimuli is key to engineer next-generation biomimetic systems. Mainstream engineered ligands, like antibodies and aptamers [1-4], enable sensitive detection and sorting of biological targets (*e.g.*, proteins, viruses, and cells) in complex media [5, 6]. Their biorecognition activity, while strong and selective, is innate and cannot be activated on demand. Adjusting the composition, concentration, and pH of the aqueous environment provides some control over binding strength, but often at the expense of the bioactivity and viability of the target. The ability to design synthetic ligands whose affinity for a target can be activated rapidly and remotely, using external stimuli that do not adversely impact the integrity of the target, is a much sought-after goal in modern ligand engineering.

Peptides represent ideal scaffolds for developing dynamically regulated ligands, owing to their excellent biorecognition activity, modular assembly, and affordable manufacturing at large scale with no batch-to-batch variability [7]. In particular, peptides with constrained conformation (*e.g.*, cyclic peptides) feature superior target affinity and selectivity – in some instances, on par with antibodies – as well as high biochemical stability [8-10]. Furthermore, cyclic peptides can be engineered to integrate stimuli-responsive moieties that provide remote control over target-binding affinity independently of the physicochemical conditions of the environment. Of particular interest in this regard are photochromic switches, such as azobenzenes, hemithioindigos, and spiropyrans/spirooxazines, which respond to specific light wavelengths and intensities by rearranging their structure. When utilized as peptide cyclization linkers, photochromic switches can reconfigure the peptide structure upon photo-isomerization [11-18]. This mechanism can be

harnessed to remotely activate the selective binding of the peptide for a target biomolecule, resulting in adsorption on a substrate or labelling in solution.

In this study, we sought to develop a novel family of azobenzene-cyclized peptide affinity ligands that are selective, sterically inconspicuous, rapidly activated, and thermally stable (note: we adopted azobenzene as photochromic switch owing to its ease of synthesis and commercial availability to ensure the translational potential of this technology). To this end, we have developed a method for converting known linear protein-binding peptides into an azobenzene-cyclized framework (**Figure 5.1**). This comprises a protein-binding peptide segment, the azobenzene cyclization linker, connecting spacers, and a reporter (*e.g.*, a fluorescent dye or biotin). The proposed cyclization geometry provides an optimal balance between structural flexibility and rigidity, which enables rapid and high-yield photo-isomerization under moderate light intensity and ensures temporal and thermal stability of both *trans* and *cis* isomers.

To demonstrate our method, we chose the Vascular Cell Adhesion Marker 1 (VCAM1) as protein target, and the linear VCAM1-binding peptide VHPKQHR as reference sequence [19]. VCAM1 is a cell surface sialoglycoprotein implicated in directing downstream lineages of human hematopoietic progenitor cells (HPCs) [20]. VCAM1 negative (VCAM1⁻) HPCs give rise to lymphoid progenitors, while VCAM1⁺ HPCs result in myeloid progenitors, suggesting that VCAM1 expression in HPCs represents a branching point between the lymphoid and myeloid lineages [21, 22]. Sorting lineage-committed HPCs into lymphoid (VCAM1^{-/low}) and myeloid (VCAM1⁺) has the potential to enable stem cell therapies for treating leukemia, lymphoma, cardiac failure, neural disorders, autoimmune diseases, metabolic or genetic disorders. The VCAM1-binding linear peptide has been identified via phage-display screening in apolipoprotein E-deficient mice and has been utilized as a ligand for VCAM1 in numerous applications [23-26].

The design method begins with the *in silico* analysis of the crystal structure of VCAM1 (PDB IDs: 1VCA) using a “druggability” test to identify binding sites for peptide binding [27, 28]. The information on size, structure, and physicochemical properties of the putative binding sites was used to design a set of 25 peptide variants in the form cyclo_{AZOB}[G-VH(X)KQHR(Z)-K]-GSG (**Figure 5.1**) where (X) and (Z) are interchangeably A, D, N, P, or S. The structures of the azobenzene-cyclized peptides were generated by molecular dynamics (MD) [29, 30] and docked *in silico* [31, 32] on VCAM1 to identify leads with conformation dependent binding. Selected complexes were then refined by MD simulations to select azobenzene-cyclized variants with predicted high binding strength (*i.e.*, either $\Delta G_{B,Trans}$ or $\Delta G_{B,Cis} < -8 \text{ kcal mol}^{-1}$) and loss of binding upon photo-isomerization (*i.e.*, $|\Delta\Delta G_B| = |\Delta G_{B,Trans} - \Delta G_{B,Cis}| > 2.5 \text{ kcal mol}^{-1}$) [33, 34].

Three azobenzene-cyclized peptides selected from *in silico* screening were characterized to evaluate their (*i*) VCAM1 binding activity by surface plasmon resonance (SPR), (*ii*) kinetics of photo-isomerization upon exposure to light by UV/Vis spectroscopy, and (*iii*) thermal stability of the *cis* isomers. Variant cyclo_{AZOB}[G-VHAKQHRN-K] in particular showed efficient photo-isomerization and an ample affinity shift ($K_{D,Trans}/K_{D,Cis} \sim 130$), which ensured efficient light-controlled binding of VCAM1. Finally, the peptide was fused with biotin and utilized as a light-activated label for brain microvascular endothelial cells (BMECs); VCAM1 expression was induced by a synergistic treatment of Interleukin-4 (IL-4) with lipopolysaccharide (LPS) and confirmed by immunohistochemical staining and RT-qPCR. Cell imaging by fluorescence microscopy confirmed binding of VCAM1 on BMECs by the *cis* isomer of cyclo_{AZOB}[G-VHAKQHRN-K], which afforded fluorescent labelling of cells with intensity proportional to the cell surface density of VCAM1, while showing negligible binding in *trans*. These results demonstrate the effectiveness of our design and selection methods for developing peptide ligands

whose target-binding affinity can be rapidly activated via light-controlled structural reconfiguration.

5.2. Materials and Methods

5.2.1. Materials

N,N'-Dimethylformamide (DMF), dichloromethane (DCM), ethanol, HPLC-grade acetonitrile, HPLC-grade water, and endogenous biotin blocking kit were from ThermoFisher Scientific (Waltham, MA). Protected amino acids, piperidine, trifluoroacetic acid (TFA), diisopropylethylamine (DIPEA), Rink amide resin (100-200 mesh, functional density ~ 0.6 mmol g⁻¹), and Hexafluorophosphate Azabenzotriazole Tetramethyl Uronium (HATU) were purchased from ChemImpex Inc. (Wood Dale, IL). Purified cycloAZOB[G-VHAKQHRN-K]-K(Biotin) was sourced from the peptide synthesis facility at UNC Chapel Hill. Bovine serum albumin, Alexa Fluor 488-labeled streptavidin (AF488-streptavidin), DAPI nuclear stain, anti-human VCAM1 (CD106) rabbit monoclonal antibody and polyclonal goat anti-rabbit antibody, azobenzene-4,4'-dicarbonyl dichloride, glycine, glacial acetic acid, diethyl ether, triethylamine (TEA), triisopropylsilane (TIPS), ethanedithiol (EDT), Tween 20, 1M aqueous NaOH, phosphate-buffered saline (PBS) pH 7.4, acetic anhydride, Kaiser test kit, and were from Millipore Sigma (St. Louis, MO). Azido-PEG-thiol (N₃-PEG-SH, MW = 600 Da) was from Nanocs Inc. (New York, NY), while amine-PEG-thiol (NH₂-PEG-SH, MW = 2,000 Da) and hydroxyl PEG thiol (OH-PEG-SH, MW = 1,000 Da) were from Creative PEGWorks (Chapel Hill, NC). Glass sensor chips (12 × 20 × 0.5 mm) sputtered with a 50 nm gold layer were from KSV Instruments OY (Helsinki, Finland). Nitrogen gas was obtained from Airgas National Welders (Raleigh, NC). VCAM1 was obtained from SinoBiologicals (Beijing, China). Brain microvascular endothelial cells (BMECs) were obtained from ATCC (Manassas, VA).

5.2.2. Peptide Synthesis

The linear peptide precursors VHGKQHRP-K*, G-VHAKQHRN-K*-Prg, G-VHAKQHRP-K*-Prg, G-VHNKQHRP-K*-Prg, G-VHPKQHRS-K*-Prg, G-VHNKQHRS-K*-Prg, G-VHPKQHRP-K*-Prg, and VHPKQHR-GSG-Prg (Prg: propargyl-glycine) were synthesized on Rink amide polystyrene resins via Fmoc/tBu chemistry using standard protecting groups for all amino acids except K* (Fmoc-Lys(Mtt)-OH) [35-37]. All amino acid conjugations were conducted using a Biotage Alstra Initiator (Biotage, Uppsala, Sweden) by performing 3 coupling steps with protected amino acid (5 equivalents), HATU (5 eq.), and DIPEA (10 eq.) at 75°C for 5 min in DMF. Fmoc removal occurred in 20% piperidine in DMF at RT for 20 min. Upon completion of chain elongation, the Fmoc group on the N-terminus was removed, and the resin was copiously rinsed with DCM and vacuum dried. The dry resin was swollen in DCM (dried over molecular sieves), cooled to 0°C, and anhydrous TEA (1.2 eq.) and azobenzene-4,4'-dicarbonyl dichloride (1.2 eq. in anhydrous DCM) were added dropwise at 0°C over 10 min. The system was equilibrated at RT and the reaction was allowed to proceed overnight. The resin was copiously rinsed with DCM and the azobenzene conjugation was confirmed by Kaiser's test [38]. The Mtt protecting group on K* was removed by incubating the resin with 2/5/93 (TFA/TIPS/DCM) for 5 min. Completion of K* deprotection was verified by Kaiser's test. After rinsing with DCM and DMF, the peptide was cyclized through reaction of the carboxyl group on the azobenzene linker with the ε-amino group of K*, by incubating the resin with HATU (5 eq.) and DIPEA (10 eq.) in DMF for 10 min at 75°C. Completion of the cyclization reaction was verified by Kaiser's test. The resin was finally rinsed with DMF, DCM, and dried under nitrogen then incubated for 2 hr at RT 10 mL g⁻¹ of 95/2.5/2.5 (TFA/TIPS/water). The peptide was precipitated by drop-wise addition into ice-cold diethyl ether. The precipitate was copiously rinsed

with diethyl ether, dissolved in 50/50 (acetonitrile/water), and lyophilized. The crude peptide powder was purified by preparative C18 HPLC and lyophilized.

5.2.3. Peptide Photo-isomerization

All spectroscopy measurements were performed using Cary 60 spectrometer equipped with a custom cuvette holder on a Peltier stage to maintain the peptide solutions at 37°C. Orthogonal to the spectrometer beam, the peptide solution was irradiated with a BlueWave 200 lamp (Dymax, Torrington, CT) to induce photoisomerization. A volume of 700 μ L of cyclo_{AZOB}[VHGKQHRP-K*] in MilliQ water at either at 0.15 mM, 0.38 mM, or 1.5 mM was initially placed in quartz micro cuvette (Thorlabs, Newton, NJ). The cuvette was placed in the spectrometer with a 10 mm pathlength for UV-Vis spectroscopy and a 2 mm pathlength for irradiance. A UV bandpass filter (BP305-390, Thorlabs, Newton, NJ) was used to achieve *trans*-to-*cis* isomerization, whereas a 420 nm longpass (LP420, Edmund Optics, Barrington, NJ) filter was used for *cis*-to-*trans* isomerization. The incident irradiance power was calculated by measuring the output power using an Accu-Cal 50 radiometer (Dymax, Torrington, CT). The kinetics of photoisomerization was measured by monitoring the absorption at 350 nm. The absorbance vs. time data was fitted against an exponential function to derive the kinetic constant of photo-isomerization κ (s^{-1}). The values of κ were obtained for light intensities between 10 and 50 mW cm^{-2} . The rate of thermal reverse isomerization (*cis*-to-*trans*) was evaluated by monitoring the absorbance at 350 nm of a 0.15 mM solution of cyclo_{AZOB}[VHGKQHRP-K*], initially conditioned in *cis* configuration and allowed to relax in the dark over 60 hr with absorption measurements taken every 15 min.

5.2.4. Circular Dichroism

A solution of cyclo_{AZOB}[VHGKQH_P-K*] at 200 μM in PBS was placed in two 1 mL quartz micro fluorescence cuvettes (Thorlabs, Newton, NJ). The peptides in solution were conditioned to either *cis* or *trans* configuration as described in the previous section, and further diluted with PBS to reach a final concentration of 80 μM . The CD spectra of the solutions of *cis* and *trans* peptide isomer were measured on a J-715 spectropolarimeter (JASCO, Oklahoma City, OK) through the 10 mm path length of the quartz cell. The samples were scanned from 190-260 nm, at a resolution of 1.0 nm and a scanning speed of 100 nm min^{-1} . For each sample, five scans were averaged together and a 5-point moving average was applied.

5.2.5. Binding Affinity using Surface Plasmon Resonance (SPR)

Surface plasmon resonance SPR sensor chips were prepared, characterized, and utilized for affinity measures as described by Islam *et al.* [39, 40]. The sensor chips were initially coated with a PEG-based self-assembled monolayer (SAM), on which the test azobenzene-cyclized peptides and the linear precursor VHPKQHR were conjugated to the surface via azide-alkyne “click chemistry” [41]; sensor chips coated with hydroxyl-PEG-thiol only were utilized as negative controls. Three gold sensors per ligand were prepared and analyzed by variable angle spectroscopic ellipsometry (VASE, J.A. Woollam Co.) to measure ligand density. The measurements of peptide-VCAM1 dissociation constant (K_D) were performed at the UNC Macromolecular Interactions Facility [39, 40]. Briefly, sensor chips functionalized with azobenzene-cyclized peptides were initially conditioned to their *cis* or *trans* isomers and contacted with a solution of human VCAM1 at concentrations ranging between 0.01 and 1 mg mL^{-1} in PBS.

5.2.6. *In silico* Design of VCAM1-binding Peptides

The crystal structures of the extracellular domain of VCAM1 (PDB: 1VCA) [42] were subjected to standard protein preparation using Schrödinger's ProteinPrep Wizard to search for and correct missing atoms and/or entire side chains (using PRIME software), remove extra salts and non-binding ligands, add explicit hydrogens, assign tautomeric states with EPIK, optimize hydrogen-bonding networks, and minimize the protein's energy with the OPLS3e force field [43-45]. The adjusted structure was then subjected to a "druggability" study using SiteMap to identify putative binding sites capable of accommodating azobenzene-cyclized peptides [46, 47]. To this end, the SiteMap (Schrödinger, New York, NY) algorithm identifies binding pockets by placing spherical 'site points' across the protein surface. These site points are then clustered together based on (*i*) their ability to form favorable protein-ligand or protein-protein interactions, (*ii*) solvent exposure, and (*iii*) hydrophobic/philic character. Finally, regions that possess a sufficient number of site points and volume are globally scored using an S-score and D-score. The S-score represents the likelihood of the protein's surface to be a binding pocket, while the D-score provides a measure of the pocket's 'druggability.' S-score and D-score values greater than or equal to 0.7 and 0.9 respectively were considered favorable pockets for ligand binding. Herein, the SiteMap analysis was performed with the default settings and the 'detect shallow binding sites' option selected, which adjusts amino acid atomic van der Waals radii to be more accommodating for peptide binding when locating potential binding pockets.

An ensemble of 25 peptide variants of VHPKQHR in the azobenzene-cyclized form cyclo_{AZOB}[G-VH(X)KQHR(Z)-K]-GSG were designed by varying the positions (X) and (Z) using amino acids A, D, N, P, S, or R. The structures of the linear precursor VHPKQHR and the azobenzene-cyclized variants as both *cis* and *trans* isomers were initially designed using the

molecular editor Avogadro and equilibrated by molecular dynamics in the GROMACS simulation package [29, 30, 48] using the OPLS all-atom force field [49, 50] and periodic boundary conditions [51-53]. The force-field parameters for the azobenzene linker were derived from density functional theory using GAUSSIAN98 [51]. Every peptide was individually placed in a simulation box with periodic boundary conditions containing 800 water molecules (TIP3P water model). The solvated system was initially minimized by running 10,000 steps of steepest gradient descent, heated to 300 K in an NVT ensemble for 250 ps with 1 fs time steps, and equilibrated to 1 atm by running a 500-ps NPT simulation with 2 fs time steps. The production run for every peptide was performed in the NPT ensemble, at constant T = 300 K using the Nosé-Hoover thermostat [54-56] and constant P = 1 atm using the Parrinello-Rahman barostat [57, 58]. The atomic coordinates were saved every 2 ps. The leap-frog algorithm was used to integrate the equations of motion, with integration steps of 2 fs, and all of the covalent bonds were constrained by means of the LINCS algorithm [59]. The short-range electrostatic and Lennard-Jones interactions were calculated within a cutoff of 1.0 nm and 1.4 nm, respectively, whereas the particle-mesh Ewald method was utilized to treat the long-range electrostatic interactions [60, 61]. The non-bonded interaction pair-list was updated every 5 fs, using a cutoff of 1.4 nm.

The peptides were then docked *in silico* against the putative binding sites on VCAM1 using the docking software HADDOCK (High Ambiguity Driven Protein-Protein Docking, v.2.1) [31, 32]. Default HADDOCK parameters (*e.g.*, temperatures for heating/cooling steps, and number of molecular dynamics sets per stage) were used. All the residues on each binding site (solvent accessibility of 50% or greater) were defined as “active”, whereas the residues surrounding the binding sites were defined as “passive”. All variable amino acid positions on the peptide ligands were also denoted as “active”, while the GSG tripeptide spacer was defined as not being involved

in the interaction to account for the directionality of binding. Docking proceeded through a 3-stage protocol: (i) rigid, (ii) semi-flexible, and (iii) water-refined fully flexible docking. A total of 1000, 200, and 200 structures were calculated at each stage, respectively. Final structures were grouped using a minimum cluster-size of 20 (10% of the total water refined calculated structures) with a $\text{C}\alpha$ RMSD $< 7.5 \text{ \AA}$ using ProFit (<http://www.bioinf.org.uk/software/profit/>). Once the clusters were identified for each peptide-VCAM1 complex pair, FireDock and XScore were used to score the complexes [33, 34]; FireDock is an efficient method re-scoring of protein-protein docking solutions, while Xscore computes the dissociation of a protein-ligand complex using an empirical equation that considers energetic factors in a protein-ligand binding process. The selected binding poses of the peptide variants, in both their *cis* and *trans* forms, on the putative binding sites of VCAM1 were then refined via 100-ns atomistic molecular dynamics (MD) simulations using the GROMACS simulation package. The peptide-VCAM1 complexes were embedded in a cubic periodic box of 9.7 nm side lengths and solvated with 30,000 TIP3P water molecules. The MD simulations were performed at 300 K and 1 atm using the Amber99SB force field. The MM/GBSA method was used for postprocessing of the peptide-VCAM1 complexes derived from MD simulations to estimate the free energy of binding (ΔG_B) [62, 63]. If complexes had conflicting docking score or MM-GB/SA ranks, then the complex was discarded. If the two rankings agreed, then the complex was saved. The variants that possessed strong binding in either *cis* or *trans* configuration (*i.e.*, $\Delta G_{B,\text{Trans}}$ or $\Delta G_{B,\text{Cis}} < -8 \text{ kcal mol}^{-1}$) and loss of binding upon photo-isomerization (*i.e.*, $|\Delta\Delta G_B| = |\Delta G_{B,\text{Trans}} - \Delta G_{B,\text{Cis}}| > 2.5 \text{ kcal mol}^{-1}$) were selected for experimental analysis.

5.2.7. Cell Culture and VCAM1 Expression

Human brain microvascular endothelial cells (BMEC) (cAP-0002; Angioproteomie, Boston, MA, US) were cultured using Microvascular Endothelial Cell Growth Medium 2 (EGM-2 MV) (CC-3202; Lonza, Basel, Switzerland). Human dermal fibroblasts (HDFn) (PCS-201-010; ATCC, Manassas, VA, US) were cultured using Dulbecco's modified eagle's medium (DMEM) (10013CV; Corning, Corning, NY, US) supplemented with 10% fetal bovine serum (FBS) (v/v) (25-514H; Genesee Scientific, Cajon, CA, US) and 1% penicillin-streptomycin (v/v) (30-002-CI; Corning, Corning, NY, US). Human umbilical vein endothelial cells (HUVEC) (C2519A; Lonza, Basel, Switzerland) were cultured using Endothelial Cell Growth Medium 2 (EGM-2) (CC-3162; Lonza, Basel, Switzerland). Cells were cultured in an incubator maintaining an atmosphere of 5% CO₂ at 37°C and 100% humidity. A glass bottomed 96 well plate was pretreated with 50 µg of fibronectin (356008; Corning, Corning, NY, US) in deionized water for 1 hr. Fibronectin solution was aspirated and 1 × 10⁴ BMECs, HDFns, or HUVECs per well were seeded in 100 µL of EGM-2 MV media, DMEM with 10% FBS, or EGM-2 media, respectively. Cells were allowed to adhere for 24 hr. BMECs were treated with three conditions: (i) media only, (ii) 1 µg mL⁻¹ lipopolysaccharide for 24 hr, or (iii) 100 ng mL⁻¹ IL-4 for 1 hr followed by 23 hr of treatment with 1 µg mL⁻¹ lipopolysaccharide. After treatment period, cells were fixed with 4% paraformaldehyde in 1× PBS for 10 min at RT and washed twice with 1× PBS. BMECs were permeabilized with 0.1% Triton X-100 in 1× PBS for 5 min at RT and washed twice with 1× PBS. Cells were then blocked for 1 hr with 2% bovine serum albumin (BSA) (w/v) at RT.

5.2.8. RT-qPCR Quantification of VCAM1 Expression

Cells were cultured and treated as described in the previous section. To quantify gene expression, cells were lysed in TRK lysis buffer, then RNA from samples were isolated using EZNA isolation kit (Omega Bio-Tek, Norcross, GA). cDNA templates were created from the RNA samples using a Go Script reverse transcriptase kit (Promega, Madison, WI). Primers target genes were determined from PrimerBank from Harvard University and selected for specificity with the NCBI Primer BLAST tool; those primers were: AAGGTGAAGGTCGGAGTCAAC (Forward-GAPDH), GGGGTCATTGATGGCAACAATA (Reverse-GAPDH), GGGAAAGATGGTCGTGATCCTT (Forward-VCAM1), and TCTGGGGTGGTCTCGATTAA (Reverse-VCAM1). cDNA samples were analyzed using SYBR Master Mix (Applied BioSystems, Foster City, CA) with a QuantStudio 3 real time PCR machine (ThermoFisher, Waltham, MA). Relative gene expression of cell-specific genes was calculated by determining the change in VCAM1 expression relative to the housekeeping gene GAPDH, following Equation 1:

$$(1) \quad \Delta CT = 2^{-[CT_{VCAM1} - CT_{GAPDH}]}$$

where CT is the threshold cycle.

5.2.9. Cell-labelling with cyclo_{AZOB}[G-VHAKQHRN-K*]

Cells were fixed and permeabilized as described above and blocked using the endogenous biotin blocking kit (ThermoFisher, Waltham, MA). First, cells were incubated with 100 µL of the streptavidin “solution A” for 30 min at RT. The cells were then washed thrice with PBS, incubated with 100 µL of biotin solution “solution B” for 30 min RT, washed again, and stored in PBS overnight at 4°C. The cells were finally stained in three conditions; (*i*) cyclo_{AZOB}[G-VHAKQHRN-

$\text{K}^*]$ -K(Biotin) only, (ii) anti-VCAM1 antibody only, or (iii) co-localized with both peptide and antibody.

For peptide-only staining, a solution of cyclo_{AZOB}[G-VHAKQHRN-K *]-K(Biotin) at 0.1 mg mL $^{-1}$ in PBS was initially split in two pools: one was conditioned into the *cis* configuration (VCAM1-binding), while the other was conditioned into the *trans* configuration (VCAM1-nobinding), as described above. After irradiation, both peptide solutions were diluted with PBS to a final concentration of 50 $\mu\text{g mL}^{-1}$. A volume of 100 μL of peptide solution was added to the fixed cells and incubated for 2 hr at RT in dark. The fixed cells were then washed copiously with PBS, then stained with 100 μL of AF488-streptavidin (2 $\mu\text{g mL}^{-1}$) in PBS for 35 min at RT, washed with PBS, and stained with 100 μL of 300 nM DAPI in PBS for 5 min at RT.

For antibody-only staining, 100 μL solution of primary anti-VCAM1 rabbit monoclonal antibody (abcam, Cambridge, UK) at 1.75 $\mu\text{g mL}^{-1}$ in PBS was incubated with the fixed cells overnight at 4°C. After incubation, the cells were washed with 1 \times PBS and 100 μL of AF594-labeled anti-rabbit goat polyclonal antibody (Abcam, Cambridge, UK) at 4 $\mu\text{g mL}^{-1}$ was incubated with the cells for 2 hr at RT in the dark. The wells were washed with 1 \times PBS, and DAPI stained.

For co-localized staining, the fixed cells were stained with cyclo_{AZOB}[G-VHAKQHRN-K *]-K(Biotin) and subsequently with anti-VCAM1 antibody, as described above.

5.2.10. Cell Imaging

Stained cells were imaged using a Zeiss LSM 710 confocal microscope (Carl Zeiss AG, Oberkochen, Germany). The resulting images were processed using ImageJ software. The fluorescence quantification was determined by averaging the raw intensity measurement of 9 images at 20 \times magnification for each condition. Final values of relative intensity were obtained

by normalizing the averaged value to the maximum and minimum measured intensity across all conditions. Error bars are reported as standard error. Statistics were done using a 2-tailed t-test and p values < 0.05 (*) were considered statistically significant.

5.3. Results and Discussion

5.3.1. Azobenzene-cyclized Peptide Design

Azobenzene linkers have been extensively utilized to endow peptides and small proteins with the ability to reconfigure their structure reversibly upon exposure to light [64, 65]. Recently, a novel set of azobenzene linkers have been developed, which feature electron-donating/-withdrawing groups in the ortho and para position to the azo group. These modifications enable photo-isomerization under biocompatible light wavelengths (*i.e.*, red, far-red, and infrared) and tuning of the thermal *cis*-to-*trans* isomeric relaxation [66, 67]. While the structural and photokinetic properties of azobenzene-constrained peptides and proteins have been extensively studied, both experimentally [68, 69] and computationally [51-53], less effort has been dedicated to the engineering of azobenzene-peptide hybrids with light-controlled biorecognition activity [70-74]. Bellotto *et al.* have identified streptavidin-targeting light-responsive peptides by screening phage-display libraries [72]; the selected peptides exhibited a ~3-fold shift in binding strength upon light exposure, with a dissociation constant (K_D) varying between 2.2 μM (*trans* isomer) and $6.7 \pm 2 \mu\text{M}$ (*cis* isomer). Using the same peptide cyclization strategy and phage-display library technique, Jafari *et al.* identified azobenzene-cyclized peptide ligands against streptavidin [75] with a ~4.5-fold shift in K_D . Using a rational design approach, Woolley *et al.* modified a leucine zipper DNA-binding protein by crosslinking two cysteine residues using an azobenzene linker [74]; when the azobenzene is in *cis* configuration, the protein maintains its α -helical structure and

its DNA-binding activity; vice versa, when in *trans*, the azobenzene disrupts the structure of the protein, resulting in a 20-fold decrease in binding strength.

Following on this work, we sought to develop peptides that feature (*i*) rapid photoisomerization kinetics, (*ii*) a large shift in protein-binding strength between *trans* and *cis* isomers, and (*iii*) high thermal stability in *cis* configuration. To this end, we have devised an azobenzene-cyclized peptide structure (**Figure 5.1**), constructed by head-to-side-chain cyclization between the peptide N-terminal α -amine group and the ε -amine group on the C-terminal lysine using homobifunctional azobenzene-4-4'-dicarbonyl linker. The length of the protein-binding peptide segment set at 8 amino acids and cyclization through the C-terminal lysine residue were adopted to achieve a balance between chain flexibility, which increases with the number of residues and enables rapid photoisomerization, and chain rigidity, which promotes binding affinity and stability of the isomers. The observations collected in this study indicate that the proposed design indeed affords efficient photo-isomerization under moderate light dose, which translates into a remarkable shift in protein-binding affinity, and a high thermal and temporal stability of the *cis* isomer.

5.3.2. *In silico* Design of VCAM1-binding Peptides

The linear VCAM1-binding peptide VHPKQHR, discovered by phage-display screening [23-25], was adopted as precursor for the design of azobenzene-cyclized light-responsive variants. This peptide has been demonstrated to target VCAM1 with high affinity and selectivity in numerous works [25, 26]. Our method for designing light-responsive variants of VHPKQHR requires the identification of putative binding sites on VCAM1 that are compatible with the size and shape of 8-mer cyclic peptides, and the production of the crystal structure of the *trans* and *cis* isomers of the azobenzene-cyclized variants. To this end, the crystal structure of VCAM1 (PDB

ID: 1VCA) was evaluated *in silico* by performing a “druggability” analysis of the protein surface [27, 28] using Schrödinger’s SiteMap software [46, 47]. Five binding pockets (S1-S5 in **Figure 5.2**) with adequate size, shape, physicochemical properties, and solvent exposure were identified as putative binding sites for the azobenzene-cyclized peptides [76, 77]. They were ranked according to two scores, namely Site Score and Druggability Score [47]; the SiteMap outputs for sites S1-S5 are listed in **Table 5.1**. All sites are characterized by high pocket exposure (> 0.8) and low enclosure scores (< 0.4) and are relatively hydrophilic as determined by SiteMap’s balance score. Sites S1-5, with a S-score > 0.7 , were selected as putative binding pockets on VCAM1. The druggability of these sites, assessed with SiteMap’s D-score, featured a D-score > 0.8 , supporting their ability to interact with peptide ligand.

We then designed a focused library of 25 variants of the VHPKQHR precursor in the azobenzene-cyclized form cycloAZOB[GVH(X)KQHR(Z)-K]-GSG (**Figure 5.1**) by varying the positions (X) and (Z) with A, D, N, P, or S. These five amino acids were chosen to explore the effect of mild hydrophobicity (A), peptide turn (P), hydrogen bonding (N and S), and incorporation of a negative charge within a positively charged sequence (D). Aromatic amino acids were avoided to ensure water solubility of the selected peptides; sulfur-containing amino acids were also avoided to prevent formation of disulfide bonds and oxidative degradation.

The crystal structures of the linear precursor VHPKQHR and the *cis* and *trans* isomers of the azobenzene-cyclized variants were generated by molecular dynamics (MD), and evaluated to determine the values of (*i*) equivalent hydrodynamic (R_h) radius [78] and (*ii*) root-mean-square deviation of the atomic positions (RMSD) between the *cis* and *trans* isomers. These values are reported in **Table 5.2** together with representative structures of the corresponding peptides. The values of R_h , calculated using HydroPro v.10 [79, 80], resulted to be 11.7 Å for the linear

VHPKQHR precursor, and varied between $\sim 9\text{\AA}$ and $\sim 18\text{\AA}$ for the azobenzene-cyclized variants, with an average of 14.9\AA for the *trans* isomers and 12.5\AA for the *cis* isomers. Most notably, the values of atomic *cis*-to-*trans* RMSD fluctuated between $\sim 0.7\text{\AA}$ and $\sim 5.1\text{\AA}$ (average $\sim 3.1\text{\AA}$), corresponding to a 20-25% size shift upon isomerization. Substantial structural rearrangement is critical towards achieving the needed shift in binding affinity. Finally, several variants (*i.e.*, 5, 12, 13, 16, 21, and 23) featured an energy landscape considerably lower – indicating higher stability – in the *trans* configuration, whereas variant 25 showed higher stability in the *cis* configuration. These variants were deemed unable to undergo photo-isomerization and were therefore not considered for the *in silico* screening against VCAM1.

Variants 1-4, 6-11, 14, 15, 17-20, 22, and 24 were docked *in silico* against the putative binding sites S1-S5 on VCAM1 (PDB ID: 1VCA) using HADDOCK (High Ambiguity Driven Protein-Protein Docking, v.2.1) [31, 32] following the method employed in prior work [74, 81]. In particular, the GSG spacer located on the C-terminus of the peptide was marked as “inactive” to ensure its outward orientation in the peptide-VCAM1 complexes; a short peptide spacer, in fact, is utilized to link the probing moiety (*e.g.*, biotin or a fluorophore) to the peptide and should not be involved in VCAM1 binding. The resulting clusters for every peptide-VCAM1 complex were ranked using the scoring functions FireDock and XScore [33, 34]. The top binding complexes were localized mostly on putative binding sites S1, S4, and S5, and were evaluated further by atomistic MD simulations to evaluate the free energy of binding (ΔG_B). Representative examples of modeled peptide-VCAM1 complexes and the corresponding values of binding energy ($\Delta G_{B,\text{Trans}}$ and $\Delta G_{B,\text{Cis}}$) are shown in **Table 5.3**.

Variants cyclo_{AZOB}[G-VHPKQHRS-K*], cyclo_{AZOB}[G-VHAKQHRP-K*], and cyclo_{AZOB}[G-VHNKQHRP-K*] were predicted to possess strong binding in *cis* configuration

($\Delta G_{B,Cis} < -8.5$ kcal mol⁻¹, corresponding to $K_D < 0.65$ μM), while cyclo_{AZOB}[G-VHAKQHRN-K*], cyclo_{AZOB}[GVHNKQHRS-K*], and cyclo_{AZOB}[G-VHPKQHRP-K*] were predicted to possess strong binding in *trans* configuration ($\Delta G_{B,Trans} < -7.9$ kcal mol⁻¹, corresponding to $K_D < 1.5$ μM). Importantly, these variants were predicted to lose binding upon photo-isomerization ($|\Delta\Delta G_B| > 2.5$ kcal mol⁻¹, highlighted in red) and were therefore selected for experimental analysis. All other variants featured insufficient values of either ΔG_B or $|\Delta\Delta G_B|$ and were therefore abandoned.

5.3.3. Characterization of Azobenzene-cyclized Peptides

UV spectroscopy was utilized to evaluate the kinetic of photo-isomerization using sequence cyclo_{AZOB}[VHGKQHRP-K*] as model variant. The comparison of the absorption spectra of the linear precursor VHGKQHRP-K*, cyclosucc[VHGKQHRP-K*] (wherein a succinyl linker is utilized *in lieu* of the azobenzene linker), and cyclo_{AZOB}[VHGKQHRS-K*] suggests that: (i) peptide cyclization constrains the histidine residues (His), which carry aromatic imidazole rings, in a spatial orientation that produces an increase in absorbance at 254 nm (solid *vs.* dot-dash, **Figure 5.3A**); this effect was reported in a published study on the effect of spatial arrangement of histidine molecules upon their spectroscopic behavior [82]; (ii) cyclization via azobenzene linker magnifies this effect (dot-dash *vs.* dash spectra, **Figure 5.3A**, suggesting interplay between the imidazole residues and the benzene rings in the azobenzene linker; this results in a red shift in absorbance of the peptide segment and a blue shift in the azobenzene absorbance, which have been observed in other azobenzene-cyclized peptides [83]. The histidine-azobenzene interference also attenuates the difference between the spectra of the *trans* and *cis* isomers of cyclo_{AZOB}[VHGKQHRS-K*] compared to those characteristic of the *trans* and *cis* isomers of free

azobenzene. Despite the subtle difference between the spectroscopic profiles (**Figure 5.3B**), peptide photo-isomerization was detected in the 300-390 nm and 400-420 nm ranges, corresponding to the $\pi-\pi^*$ and $n-\pi^*$ bands of azobenzene, respectively. We also recorded the temporal evolution of the spectra of cyclo_{AZOB}[VHGKQHRP-K*] in solution during exposure to UV light (using a bandpass light filter BP305-390), and observed a decrease at 340 nm and an increase at 420 nm, both indicative of *trans*-to-*cis* isomerization (**Figure 5.4A** and **Figure 5.4B**); upon exposure to blue light (using a longpass light filter LP420), instead, we observed an increase at 340 nm and a decrease at 420 nm, indicative of *trans*-to-*cis* isomerization (**Figure 5.4C** and **Figure 5.4D**).

Based on the variation in absorbance at 350 nm, the kinetic constants of photo-isomerization were calculated for different values of light intensity and solution concentration (**Figure 5.4C** and **Figure 5.4D**; the data set is reported in the **Figure 5.5**). Rate constants vs. exposure intensity were fit, assuming first-order kinetics. For dilute solutions (0.15 and 0.38 mM), the rate constants of both *trans*-to-*cis* and *cis*-to-*trans* isomerization were found to be higher than the constant obtained with a 1.5 mM (**Figure 5.3C**). This deviation can be attributed to a general attenuation phenomenon occurring at high concentration, where the light absorbance by the peptide segment reduces the fraction of incident energy absorbed by the azobenzene linkers and, consequently, the isomerization rate. At the concentration of 1.5 mM, an attenuation of the excitation energy of approximately 40% is observed across the sample. This effect is illustrated by the larger difference in the rate constants of the *trans*-to-*cis* isomerization ($\lambda_{\text{ex}} = 305\text{-}390 \text{ nm}$) across the investigated concentration range (**Figure 5.3C**) compared to the difference in the rate constants of the *cis*-to-*trans* isomerization ($\lambda_{\text{ex}} = 420\text{-}500 \text{ nm}$). The effect of light intensity on the rate constant for the *trans*-to-*cis* isomerization ranges from 7.9 (0.15 and 0.38 mM) to $5.9 \text{ s}^{-1} \text{ W}^{-1}$

cm^2 (1.5 mM); for the *cis*-to-*trans* isomerization, the difference is significantly smaller (3.6 - 3.3 $\text{s}^{-1} \text{ W}^{-1} \text{ cm}^2$). This can be attributed to the fact that the absorbance of the peptide significantly decreases beyond 400 nm, which encompasses the LP420-filtered spectra used for the *cis*-to-*trans* isomerization. Notably, the isomerization rate constants of cyclo_{AZOB}[VHGKQH_RP-K*] are considerably lower than those of free azobenzene and >10-fold lower than that of azobenzene self-assembled monolayers [84, 85].

The slower kinetics are attributed to the covalent linkage of the azobenzene within the framework of the cyclic peptide structure and, potentially, to the aromatic interaction with the histidine residues in the VCAM1-binding peptide segment. It is also noted that the broad spectra used for excitation have a negligible impact on the observed kinetics, as the filtered spectra (**Figure 5.6**) used for excitation feature a narrow peak with the majority of the energy; for the BP305-390 filtered excitation the major peak is at 365 nm, and for LP420 the peak is at 437 nm. The isomerization rate constants were used to calculate the dosage required for a nearly complete ($5/\kappa$ or 99.3%) photoisomerization: 630 mJ cm^{-2} for *trans*-to-*cis* isomerization of diluted peptide solutions (0.15 mM and 0.38 mM) and 840 mJ cm^{-2} for the concentrated solution (1.5 mM); for *cis*-to-*trans* isomerization, the dosage was calculated to be 1400 mJ cm^{-2} for the diluted solutions and 1500 mJ cm^{-2} for the concentrated solution.

We finally evaluated the ability of cyclo_{AZOB}[VHGKQH_RP-K*] to undergo multiple cycles of photo-isomerization and the conformational stability of the *cis* isomer at 37°C (“thermal relaxation”). Notably, the photo-isomerization of cyclo_{AZOB}[VHGKQH_RP-K*] is completely reversible and can be cycled repeatedly (**Figure 5.7**). The thermally induced *cis*-to-*trans* isomerization was evaluated by monitoring the absorbance at 350 nm of a 0.15 mM solution of the *cis* isomer of the peptide for 60 hr at 37°C (**Figure 5.8**). The resulting half-life of ~44 hr proves

that the *trans* isomer of the peptide is thermally stable within the time span required for cell labelling and imaging without significant unbinding of the peptide. The thermal stability of cyclo_{AZOB}[VHGKQHRPK*] is coherent with the results of the MD simulations, which showed

that the energy landscape of the *trans* and *cis* isomers feature minima with similar values, respectively 1063 and 1089 kJ mol⁻¹; these, in turn, are comparable to those of the linear precursor VHPKQHR (958 kJ mol⁻¹) and the cyclic variant cyclo_{SUCC}[G-VHAKQHRN-K*] (1035 kJ mol⁻¹), later used in cell labeling.

These results are particularly remarkable considering that, unlike other azobenzene-cyclized variants, neither isomer of cyclo_{AZOB}[GVHAKQHRN-K*] features elements of secondary structure (*i.e.*, α -helix or β -sheet) known to confer stability to peptides [86-88]; both VHPKQHR and cyclo_{SUCC}[G-VHAKQHRN-K*], in fact, possess a short α -helical segment (**Figure 5.9C**), which contributes to a more favorable energetic state. The secondary structures of cyclo_{AZOB}[G-VHAKQHRN-K*], VHPKQHR, and cyclo_{SUCC}[VHGKQHRP-K*] predicted *in silico* were confirmed by circular dichroism (**Figure 5.9**).

Lastly, we have conducted a spectroscopic characterization under a broad range of UV light exposure ($\lambda_{\text{ex}} = 305\text{-}390$ nm and $\lambda_{\text{ex}} = 420\text{-}500$ nm) to address concerns of potential cytotoxicity. We note that the dose applied for nearly complete photo-isomerization of the proposed peptide has been reported to cause minimal cytotoxic effects, especially in absence of photosensitizers [89-93]; UV dosing in the range of 138-6000 mJ cm⁻² has, in fact, been shown to be viable for multiple cell processing methods [89-94]. The effects of photo-isomerization on cell activity are dependent on several factors, such as the photoisomerization reaction, wavelength, light power, exposure time, and presence of a photosensitizer. It is also noted that the proposed peptide demonstrates thermal stability, indicating that low-dose rapid pulse excitation can be

applied to achieve light-induced activation of binding activity. Future efforts should always optimize the operating conditions for each cell-type or target protein, including photoisomerization parameters, to limit cytotoxicity and off-target effects.

5.3.4. Binding Affinity by Surface Plasmon Resonance (SPR)

Efficient photo-controlled activation of biorecognition requires a strong shift in binding energy from the inactive to the binding configuration upon photo-isomerization. The *in silico* screening provided several sequences that fulfilled both conditions and were therefore tested by SPR to measure both their $\Delta G_{B,Trans}$ and $\Delta G_{B,Cis}$. The average ligand density for the SPR chips used was 0.86 molecules nm⁻², as reported in **Table 5.4**. The values of VCAM1 mass bound to the peptide sensors were fitted to a Langmuir isotherm (**Figure 5.10**), from which the values of K_D were calculated (**Table 5.5**). Variant cycloAZOB[G-VHAKQHRN-K*] showed a remarkable variation in binding strength for VCAM1 in solution between the *cis* and *trans* conformations.

5.3.5. Cell-labelling with cycloAZOB[G-VHAKQHRN-K*]

The light-activated biorecognition activity of variant cycloAZOB[G-VHAKQHRN-K*] was finally demonstrated *in vitro* via labelling of VCAM1⁺ BMECs. VCAM1 expression was induced by treating the cells with interleukin-4 (IL-4) and lipopolysaccharide (LPS); this pair has been shown to be synergistic in eliciting VCAM1 expression in endothelial cells [95-97]. VCAM1 expression by BMECs was confirmed by RT-qPCR (**Figure 5.11** and **Figure 5.12**); LPS alone also induced VCAM1 expression in BMECs, though to a lesser extent. Human umbilical vein endothelial cells (HUVECs) and human dermal fibroblasts (HDFn) were also considered, but they did not demonstrate significant changes in VCAM1 expression when treated with either condition.

VCAM1⁺ BMECs were incubated with either the *cis* or *trans* isomer of cycloAZOB[G-VHAKQHRN-K*]-biotin and stained with AlexaFluor488-Streptavidin. As anticipated, the cells labeled with the *cis* isomer demonstrated significantly higher fluorescence intensity compared to those labeled with the *trans* isomer (**Figure 5.13**). The *cis* conformation of cycloAZOB[G-VHAKQHRN-K*] also conferred significantly higher fluorescent intensity to VCAM1⁺ cells compared to VCAM1⁻ cells. To confirm selective VCAM1 binding, we also evaluated peptide co-localization with anti-VCAM1 antibodies on VCAM1⁺ BMECs. The images collected using confocal microscopy shows a clear co-localization of the *cis* isomer of cycloAZOB[G-VHAKQHRN-K*] with the VCAM1 antibody (**Figure 5.14**).

Collectively, these results demonstrate both selectivity and light-controlled VCAM1-binding activity of cycloAZOB[G-VHAKQHRN-K*], as well as adequate thermal stability for *in vitro* studies.

5.4. Conclusions

The ability to activate – remotely, efficiently, and rapidly – the binding affinity of ligands to target biomolecules will uniquely enable next-generation biotech applications. As more effective mechanisms for affinity regulation are developed, more advanced applications can be explored. To this end, we have developed and demonstrated a novel approach to design and validate azobenzene-cyclized peptide affinity ligands featuring inducible protein-binding activity via light-controlled structural reconfiguration.

Azobenzene-cyclized variants of a known VCAM1-binding peptide (VHPKQHR) were discovered *in silico* that promised isomerization-dependent binding of VCAM1. Selected variants were experimentally characterized for thermal stability, isomerization kinetics, and VCAM1

binding affinity. The selected candidate cyclo_{AZOB}[GVHAKQHRN-K*] was finally tested in vitro via light-controlled labelling of VCAM1⁺ BMEC. The peptide showed a statistically significant, conformation-dependent binding selectivity, confirming that the *in silico* and experimental characterizations. This study demonstrates a general method for developing azobenzene-cyclized peptides featuring efficient and robust light-controlled activation of protein-binding affinity. Notably, the light-responsive behavior is imparted to the ligand irrespectively of its protein-binding segment, making our design experimental methods presented herein are applicable to the design of light-responsive labels to virtually any target protein.

These results will enable future studies focusing on the aspects of on-demand, spatio-temporal control, and reversibility of cell labelling. Specifically, future efforts will evaluate (*i*) the kinetics of binding and unbinding the surface of the cells upon exposure to light at activating and de-activating wavelengths; (*ii*) the ability to direct the labelling of a subset of cells in solution via spatial control of the incident light; and (*iii*) the potential downstream effects of the peptide to the cell surface and, potentially, intracellular metabolic pathways upon binding and unbinding.

REFERENCES

- [1] Valli, H., M. Sukhwani, S. Dovey, et al., Fluorescence- and magnetic-activated cell sorting strategies to isolate and enrich human spermatogonial stem cells. *Fertility and Sterility*, 2014. 102(2): p. 566-580.
- [2] Boxall, S., and E. Jones, The use of multiparameter flow cytometry and cell sorting to characterize native human bone marrow mesenchymal stem cells (MSC). *Methods in Molecular Biology*, 2015. 1235: p. 121-130.
- [3] O'Brien, C.M., H.S. Chy, Q. Zhou, et al., New Monoclonal Antibodies to Defined Cell Surface Proteins on Human Pluripotent Stem Cells. *Stem Cells* 2017. 35(3): p. 626-640.
- [4] Schröter, C., S. Krah, J. Beck, et al., Isolation of pH-Sensitive Antibody Fragments by Fluorescence-Activated Cell Sorting and Yeast Surface Display. *Methods in Molecular Biology*, 2018. 1685: p. 311-331.
- [5] Plouffe, B.D., and S.K. Murthy, Perspective on Microfluidic Cell Separation: A Solved Problem?. *Analytical Chemistry*, 2014. 86(23): p. 11481-11488.
- [6] Gao, Y., W. Li, and D. Pappas, Recent advances in microfluidic cell separations. *Analyst*, 2013. 138(17): p. 4714-4721.
- [7] Lam, K.S., Affinity Selection and Sequencing. *Nature Chemical Biology*, 2019. 15(4): p. 320-321.
- [8] Heinis, C., and G. Winter, Encoded libraries of chemically modified peptides. *Current Opinion in Chemical Biology*, 2015. 26: p. 89-98.
- [9] Shivange, A.V., and P.S. Daugherty, De novo discovery of bioactive cyclic peptides using bacterial display and flow cytometry. *Methods in Molecular Biology*, 2015. 1248: p. 139-153.
- [10] Zorzi, A., K. Deyle, and C. Heinis, Cyclic peptide therapeutics: past, present and future. *Current Opinion in Chemical Biology*, 2017. 38: p. 24-29.
- [11] Jiang, L., and L. Wen, Photonic Sensitive Switchable Materials, in *Switchable and Responsive Surfaces and Materials for Biomedical Applications*, (ed. Z. Zhang). 2015, Woodhead Publishing: Oxford, United Kingdom. p. 93-118.
- [12] Lerch, M.M., M.J. Hansen, G.M van Dam, et al., Emerging Targets in Photopharmacology. *Angewandte Chemie*, 2016. 55(37): p. 10978-10999.
- [13] Wiedbrauk, S., and H. Dube, Hemithioindigo—an emerging photoswitch. *Tetrahedron Letters*, 2015. 56(29): p. 4266-4274.

- [14] Wiedbrauk, S., T. Bartelmann, S. Thumser, et al., Simultaneous complementary photoswitching of hemithioindigo tweezers for dynamic guest relocalization. *Nature Communications*, 2018. 9(1): p. 1-9.
- [15] Kitzig, S., M. Thilemann, T. Cordes, and K. Rück-Braun, Light-Switchable Peptides with a Hemithioindigo Unit: Peptide Design, Photochromism, and Optical Spectroscopy. *ChemPhysChem*, 2016. 17(9): p. 1252-1263.
- [16] Balmond, E.I., B.K. Tautges, A.L. Faulkner, et al., Comparative Evaluation of Substituent Effect on the Photochromic Properties of Spiropyrans and Spirooxazines. *Journal of Organic Chemistry* 2016. 81(19): p. 8744-8758.
- [17] Cardano, F., E.D. Canto, and S. Giordani, Spiropyrans for light-controlled drug delivery. *Dalton Transactions*, 2019. 48(41): p. 15537-15544.
- [18] Walkey, M.C., C.R. Peiris, S. Ciampi, et al., Chemically and Mechanically Controlled Single-Molecule Switches Using Spiropyrans. *ACS Applied Materials and Interfaces*, 2019. 11(40): p. 36886-36894.
- [19] Ailuno, G., S. Baldassari, G. Zuccari, et al., Peptide-based nanosystems for vascular cell adhesion molecule-1 targeting: a real opportunity for therapeutic and diagnostic agents in inflammation associated disorders. *Journal of Drug Delivery Science and Technology*, 2020. 55: p. 101461.
- [20] Ulyanova, T., L.M. Scott, G.V. Priestley, et al., VCAM-1 expression in adult hematopoietic and nonhematopoietic cells is controlled by tissue-inductive signals and reflects their developmental origin. *Blood*, 2005. 106(1): p. 86-94.
- [21] Kondo, M., I.L. Weissman, and K. Akashi, Identification of clonogenic common lymphoid progenitors in mouse bone marrow. *Cell*, 1997. 91(5): p. 661-672.
- [22] Lai, A.Y., and M.J. Kondo, Asymmetrical lymphoid and myeloid lineage commitment in multipotent hematopoietic progenitors. *Journal of Experimental Medicine*, 2006. 203(8): p. 1867-1873.
- [23] Liu, C., G. Bhattacharjee, W. Boisvert, et al., In vivo interrogation of the molecular display of atherosclerotic lesion surfaces. *American Journal of Pathology*, 2003. 163(5): p. 1859-1871.
- [24] Kelly, K.A., M. Nahrendorf, A.M. Yu, et al., In vivo phage display selection yields atherosclerotic plaque targeted peptides for imaging. *Molecular Imaging and Biology*, 2006. 8(4): p. 201-207.
- [25] Kuo, C.-H., L. Leon, E.J. Chung, et al., Inhibition of atherosclerosis-promoting microRNAs via targeted polyelectrolyte complex micelles. *Journal of Materials Chemistry B*, 2014. 2(46): p. 8142-8153.

- [26] Nahrendorf, M., F.A. Jaffer, K.A. Kelly, et al., Noninvasive vascular cell adhesion molecule-1 imaging identifies inflammatory activation of cells in atherosclerosis. *Circulation*, 2006. 114(14): p. 1504-1511.
- [27] Burns, V.A., B.G. Bobay, A. Basso, et al., Targeting RNA with cysteine-constrained peptides. *Bioorganic and Medicinal Chemistry Letters*, 2008. 18(2): p. 565-567.
- [28] Bobay, B.G., L.R. Butler, and J. Cavanagh, Computational Design of Cyclic Peptide Inhibitors of the Anti-Apoptotic Protein Calbindin-D28K, *Biochemistry and Pharmacology*, 2014. 03 (04): p. 1-5.
- [29] Hess, B., C. Kutzner, D. van der Spoel, and E. Lindahl, GROMACS 4: Algorithms for Highly Efficient, Load-Balanced, and Scalable Molecular Simulation. *Journal of Chemical Theory and Computation*, 2008. 4(3): p. 435-447.
- [30] Klepeis, J.L., K. Lindorff-Larsen, R.O. Dror, and D.E. Shaw, Long-timescale molecular dynamics simulations of protein structure and function. *Current Opinion in Structural Biology*, 2009. 19(2): p. 120-127.
- [31] Dominguez, C., R. Boelens, and A.M. Bonvin, HADDOCK: a protein-protein docking approach based on biochemical or biophysical information. *Journal of the American Chemical Society*, 2003. 125(7): p. 1731-1737.
- [32] de Vries, S.J., M. van Dijk, and A.M. Bonvin, The HADDOCK web server for data-driven biomolecular docking. *Nature Protocols*, 2010. 5(5): p. 883-897.
- [33] Wang, R., L. Lai, and S. Wang, Further development and validation of empirical scoring functions for structure-based binding affinity prediction. *Journal of Computer Aided Molecular Design*, 2002. 16(1): p. 11-26.
- [34] Wang, R., Y. Lu, and S. Wang, Comparative Evaluation of 11 Scoring Functions for Molecular Docking. *Journal of Medicinal Chemistry*, 2003. 46(12): p. 2287-2303.
- [35] Amblard, M., J.-A. Fehrentz, J. Martinez, and G. Subra, Methods and protocols of modern solid phase Peptide synthesis. *Molecular Biotechnology*, 2006. 33(3): p. 239-254.
- [36] Isidro-Llobet, A., M. lvarez, and F. Albericio, Amino acid-protecting groups. *Chemical Reviews*, 2009. 109(6): p. 2455-2504.
- [37] Chandra, K., T.K. Roy, D.E. Shalev, et al., A tandem *in situ* peptide cyclization through trifluoroacetic acid cleavage. *Angewandte Chemie*, 2014. 53(36): p. 9450-9455.
- [38] Kaiser, E., R.L. Colescott, C.D. Bossinger, and P.I. Cook, Color test for detection of free terminal amino groups in the solid-phase synthesis of peptides. *Analytical Biochemistry*, 1970. 34: p. 595-598.

- [39] Islam, N., P.V. Gurgel, O.J. Rojas, and R.G. Carbonell, Effects of Composition of Oligo(ethylene glycol)-Based Mixed Monolayers on Peptide Grafting and Human Immunoglobulin Detection. *Journal of Physical Chemistry C*, 2014. 118(10): p. 5361-5373.
- [40] Islam, N., F. Shen, P.V. Gurgel, et al., Dynamic and equilibrium performance of sensors based on short peptide ligands for affinity adsorption of human IgG using surface plasmon resonance. *Biosensors and Bioelectronics*, 2014. 58: p. 380-387.
- [41] von Maltzahn, G., Y. Ren, J.-H. Park, et al., In vivo tumor cell targeting with "click" nanoparticles. *Bioconjugate Chemistry*, 2008. 19(8): p. 1570-1578.
- [42] Jones, E.Y., K. Harlos, M.J. Bottomley, et al., Crystal structure of an integrin-binding fragment of vascular cell adhesion molecule-1 at 1.8 Å resolution. *Nature*, 1995. 373(6514): p. 539-544.
- [43] Sastry, G.M., M. Adzhigirey, T. Day, et al., Protein and ligand preparation: parameters, protocols, and influence on virtual screening enrichments. *Journal of Computer Aided Molecular Design*, 2013. 27(3): p. 221-234.
- [44] Jacobson, M.P., R.A. Friesner, Z. Xiang, and B. Honig, On the role of the crystal environment in determining protein side-chain conformations. *Journal of Molecular Biology*, 2002. 320(3): p. 597-608.
- [45] Shivakumar, D., J. Williams, Y. Wu, et al., Prediction of Absolute Solvation Free Energies using Molecular Dynamics Free Energy Perturbation and the OPLS Force Field. *Journal of Chemical Theory and Computation*, 2010. 6(5): p. 1509-1519.
- [46] Halgren, T.A., New method for fast and accurate binding-site identification and analysis *Chemical Biology and Drug Design*, 2007. 69(2): p. 146-148.
- [47] Halgren, T.A., Identifying and characterizing binding sites and assessing druggability. *Journal of Chemical Information and Modeling*, 2009. 49(2): p. 377-389.
- [48] Berendsen, H.J.C., D. van der Spoel, and R. van Drunen, GROMACS: A message-passing parallel molecular dynamics implementation. *Computer Physics Communications*, 1995. 91(1): p. 43-56.
- [49] Jorgensen, W.L., J. Chandrasekhar, J.D. Madura, et al., Comparison of simple potential functions for simulating liquid water. *Journal of Chemical Physics* 1983. 79(2): p. 926-935.
- [50] Jorgensen, W.L., and J. Tirado-Rives, The OPLS [optimized potentials for liquid simulations] potential functions for proteins, energy minimizations for crystals of cyclic peptides and crambin. *Journal of the American Chemical Society*, 1988. 110(6): p. 1657-1666.

- [51] Nguyen, P.H., Y. Mu, and G. Stock, Energy landscape of a small peptide revealed by dihedral angle principal component analysis. *Proteins: Structure, Function, and Bioinformatics*, 2005. 60(3): p. 485-494.
- [52] Nguyen, P.H., R.D. Gorbunov, and G. Stock, Photoinduced Conformational Dynamics of a Photoswitchable Peptide: A Nonequilibrium Molecular Dynamics Simulation Study. *Biophysical Journal*, 2006. 91(4): p. 1224-1234.
- [53] Nguyen, P.H. and G. Stock, Nonequilibrium molecular dynamics simulation of the energy transport through a peptide helix. *Journal of Chemical Physics*, 2006. 323(1): p. 36-44.
- [54] Nosé, S., A molecular dynamics method for simulations in the canonical ensemble. *Molecular Physics*, 1984. 52(2): p. 255-268.
- [55] Hoover, W.G., Canonical Dynamics: Equilibrium Phase-Space Distributions. *Physical Review A*, 1985. 31: p. 1695-1697.
- [56] Fu, J., H. Yang, and J. Wang, Computational design of the helical hairpin structure of membrane-active antibacterial peptides based on RSV glycoprotein epitope scaffold. *Computational Biology and Chemistry*, 2018. 73: p. 200-205.
- [57] Parrinello, M., and A.J. Rahman, Polymorphic transitions in single crystals: A new molecular dynamics method. *Applied Physics*, 1981. 52(12); p. 7182-7190.
- [58] Yu, H., and Y.-S. Lin, Toward structure prediction of cyclic peptides. *Physical Chemistry Chemical Physics*, 2015. 17(6): p. 4210-4219.
- [59] Hess, B., H. Bekker, H.J.C. Berendsen, and J.G.E.M. Fraaije, LINCS: A linear constraint solver for molecular simulations. *Journal of Computational Chemistry*, 1997. 18(12): p. 1463-1472.
- [60] Cheatham III., T.E., J.L. Miller, T. Fox, et al., Molecular Dynamics Simulations on Solvated Biomolecular Systems: The Particle Mesh Ewald Method Leads to Stable Trajectories of DNA, RNA, and Proteins. *Journal of the American Chemical Society*, 1995. 117(14): p. 4193-4194.
- [61] Quimbar, P., U. Malik, C.P. Sommerhoff, et al., High-affinity cyclic peptide matriptase inhibitors. *Journal of Biological Chemistry*, 2013. 288(19): p. 13885-13896.
- [62] Hou, T., J. Wang, Y. Li, and W. Wang, Assessing the performance of the MM/PBSA and MM/GBSA methods. 1. The accuracy of binding free energy calculations based on molecular dynamics simulations. *Journal of Chemical Information and Modeling*, 2011. 51(1): p. 69-82.
- [63] Genheden, S., and U. Ryde, The MM/PBSA and MM/GBSA methods to estimate ligand-binding affinities. *Expert Opinion in Drug Discovery*, 2015. 10(5): p. 449-461.

- [64] Ulysse, L., J. Cubillos, J. Chmielewski, et al., Photoregulation of cyclic peptide conformation. *Journal of the American Chemical Society*, 1995. 117(32): p. 8466-8467.
- [65] Flint, D.G., J.R. Kumita, O.S. Smart, and G.A. Woolley, Using an azobenzene cross-linker to either increase or decrease peptide helix content upon trans-to-cis photoisomerization. *Chemical Biology*, 2002. 9(3): p. 391-397.
- [66] Samanta, S., and G.A. Woolley, Bis-azobenzene cross-linkers for photo-control of peptide structure. *ChemBioChem*, 2011. 12(11): p. 1712-1723.
- [67] Dong, M., A. Babalhavaeji, S. Samanta, et al., Red-Shifting Azobenzene Photoswitches for in Vivo Use. *Accounts of Chemical Research*, 2015. 48(10): p. 2662-2670.
- [68] Yasuike, N., H. Lu, P. Xia, and G.A. Woolley, Intramolecular Cross-Linking of Proteins with Azobenzene-Based Cross-Linkers, in *Methods in Enzymology*; (ed. A. Deiters), 2019, Academic Press: Cambridge, MA, United States. p. 129-149.
- [69] Nguyen, P.H., H. Staudt, J. Wachtveitl, and G. Stock, Real Time Observation of Ultrafast Peptide Conformational Dynamics: Molecular Dynamics Simulation vs Infrared Experiment. *Journal of Physical Chemistry B*, 2011. 115(44): p. 13084-13092.
- [70] Reis, J.M., X. Xu, S. McDonald, et al., Discovering Selective Binders for Photoswitchable Proteins Using Phage Display. *ACS Synthetic Biology*, 2018. 7(10): p. 2355-2364.
- [71] Babalhavaeji, A., and G.A. Woolley, Modular design of optically controlled protein affinity reagents. *Chemical Communications*, 2018. 54(13): p. 1591-1594.
- [72] Bellotto, S., S. Chen, I. Rentero Rebollo, et al., Phage selection of photoswitchable peptide ligands. *Journal of the American Chemical Society*, 2014. 136(16): p. 5880-5883.
- [73] Guerrero, L., O.S. Smart, C.J. Weston, et al., Photochemical Regulation of DNA-Binding Specificity of MyoD. *Angewandte Chemie*, 2005. 44(47): p. 7778-7782.
- [74] Woolley, G.A., A.S.I. Jaikaran, M. Berezovski, et al., Reversible photocontrol of DNA binding by a designed GCN4-bZIP protein. *Biochemistry*, 2006. 45(19): p. 6075-6084.
- [75] Jafari, M.R., L. Deng, P.I. Kitov, et al, Discovery of Light-Responsive Ligands through Screening of a Light-Responsive Genetically Encoded Library. *ACS Chemical Biology*, 2014. 9(2): p. 443-450.
- [76] Bayó-Puxan, N., R. Rodríguez-Mias, M. Goldflam, et al., Combined Use of Oligopeptides, Fragment Libraries, and Natural Compounds: A Comprehensive Approach To Sample the Druggability of Vascular Endothelial Growth Factor. *ChemMedChem*, 2016. 11(8): p. 928-939.

- [77] Shaikh, F., and S.W.I. Siu, Identification of novel natural compound inhibitors for human complement component 5a receptor by homology modeling and virtual screening. *Medicinal Chemistry Research*, 2016. 25: p. 1564-1573.
- [78] Peirotti, M.B., M.V. Piaggio, and J.A. Deiber, Hydration, charge, size, and shape characteristics of peptides from their CZE analyses. *Journal of Separation Science*, 2008. 31(3): p. 548-554.
- [79] Armstrong, C.T., A.L. Boyle, E.H.C. Bromley, et al., Rational design of peptide-based building blocks for nanoscience and synthetic biology. *Faraday Discussions*, 2009. 143: p. 305-317; discussion 359-372.
- [80] Ortega, A., D. Amorós, and J. García de la Torre, Prediction of hydrodynamic and other solution properties of rigid proteins from atomic- and residue-level models. *Biophysical Journal*, 2011. 101(4): p. 892-898.
- [81] Kish, W.S., H. Sachi, A.D. Naik, et al., Design, selection, and development of cyclic peptide ligands for human erythropoietin. *Journal of Chromatography A*, 2017. 1500: p. 105-120.
- [82] Pal, N.K., and C.J. Kryschi, A facile UV-light mediated synthesis of l-histidine stabilized silver nanocluster for efficient photodegradation of methylene blue. *Journal of Molecular Catalysis A: Chemistry*, 2015. 404-405: p. 27-35.
- [83] Wachtveitl, J., S. Spörlein, H. Satzger, et al., Ultrafast Conformational Dynamics in Cyclic Azobenzene Peptides of Increased Flexibility. *Biophysical Journal*, 2004. 86(4): p. 2350-2362.
- [84] Krekien, N.R., M. Müller, U. Jung, et al., UV/Vis Spectroscopy Studies of the Photoisomerization Kinetics in Self-Assembled Azobenzene-Containing Adlayers. *Langmuir*, 2015. 31(30): p. 8362-8370.
- [85] Samai, S., D.J. Bradley, T.L.Y. Choi, et al., Temperature-Dependent Photoisomerization Quantum Yields for Azobenzene-Modified DNA. *Journal of Physical Chemical C*, 2017. 121(12): p. 6997-7004.
- [86] Kwok, S.C., C.T. Mant, and R.S. Hodges, Importance of secondary structural specificity determinants in protein folding: Insertion of a native β -sheet sequence into an α -helical coiled-coil. *Protein Science*, 2002. 11(6): p. 1519-1531.
- [87] Rathore, N., S.H. Gellman, and J.J de Pablo, Thermodynamic Stability of β -Peptide Helices and the Role of Cyclic Residues. *Biophysical Journal*, 2006. 91(9): p. 3425-3435.
- [88] Ji, Y.-Y., and Y.-Q. Li, The role of secondary structure in protein structure selection. *European Physical Journal E: Soft Matter*, 2010. 32(1): p. 103-107.

- [89] Bryant, S.J., C.R. Nuttelman, and K.S. Anseth, Cytocompatibility of UV and visible light photoinitiating systems on cultured NIH/3T3 fibroblasts in vitro. *Journal Biomaterials Science, Polymer Edition*, 2000. 11(5): p. 439-457.
- [90] Fedorovich, N.E., M.H. Oudshoorn, D. van Geemen, et al., The effect of photopolymerization on stem cells embedded in hydrogels. *Biomaterials*, 2009. 30(3): p. 344-353.
- [91] Mironi-Harpaz, I., D.Y. Wang, S. Venkatraman, and D. Seliktar, Photopolymerization of cell-encapsulating hydrogels: crosslinking efficiency versus cytotoxicity. *Acta Biomaterialia*, 2012. 8(5): p. 1838-1848.
- [92] Williams, C.G., A.N. Malik, T.K. Kim, et al., Variable cytocompatibility of six cell lines with photoinitiators used for polymerizing hydrogels and cell encapsulation. *Biomaterials*, 2005. 26(11): p. 1211-1218.
- [93] Wong, D.Y., T. Ranganath, and A.M. Kasko, Low-Dose, Long-Wave UV Light Does Not Affect Gene Expression of Human Mesenchymal Stem Cells. *PLoS One*, 2015. 10(9): p. 1-21.
- [94] Aubin, H., J.W. Nichol, C.B. Hutson, et al., Directed 3D cell alignment and elongation in microengineered hydrogels. *Biomaterials*, 2010. 31(27): p. 6941-6951.
- [95] Blease, K., J. Seybold, I.M. Adcock, et al., Interleukin-4 and Lipopolysaccharide Synergize to Induce Vascular Cell Adhesion Molecule-1 Expression in Human Lung Microvascular Endothelial Cells. *American Journal of Respiratory Cell and Molecular Biology*, 1998, 18(5): p. 620-630.
- [96] Lee, Y.W., H. Kühn, B. Hennig, et al., IL-4-induced Oxidative Stress Upregulates VCAM-1 Gene Expression in Human Endothelial Cells. *Journal of Molecular and Cellular Cardiology*, 2001 33(1): p. 83-94.
- [97] Wong, D., and K. Dorovini-Zis, Expression of Vascular Cell Adhesion Molecule-1 (VCAM-1) by Human Brain Microvessel Endothelial Cells in Primary Culture. *Microvascular Research*, 1995. 49(3): p. 325-339.

Tables

Table 5.1 SiteMap parameters for the top five scored potential VCAM1 binding pockets. All scores are unitless unless otherwise noted.

Property	S1	S2	S3	S4	S5
S-score	0.89	0.86	0.89	0.87	0.73
Size (points)	323.00	142.00	137.00	122.00	66.00
D-score	1.01	0.99	1.01	1.00	0.82
Volume (Å³)	192.42	77.86	84.38	73.06	35.67
Exposure	0.82	0.88	0.81	0.87	0.91
Enclosure	0.36	0.31	0.37	0.32	0.31
Contact	0.31	0.27	0.33	0.29	0.23
Phobic	0.08	0.11	0.12	0.11	0.03
Philic	0.46	0.41	0.47	0.42	0.39
Balance	0.18	0.26	0.25	0.27	0.07
Don/Acc	1.72	1.15	1.26	0.89	0.84

Table 5.2 Structure of 25 variants of the VHPKQHR precursor in the azobenzene-cyclized form cyclo_{AZO}[G-VH(X)KQHR(Z)-K]-GSG as both *cis* and *trans* isomers, and corresponding values of their hydrodynamic radius (R_h) and root mean square deviation (RMSD). Note: the GSG spacer is abstracted for clarity.

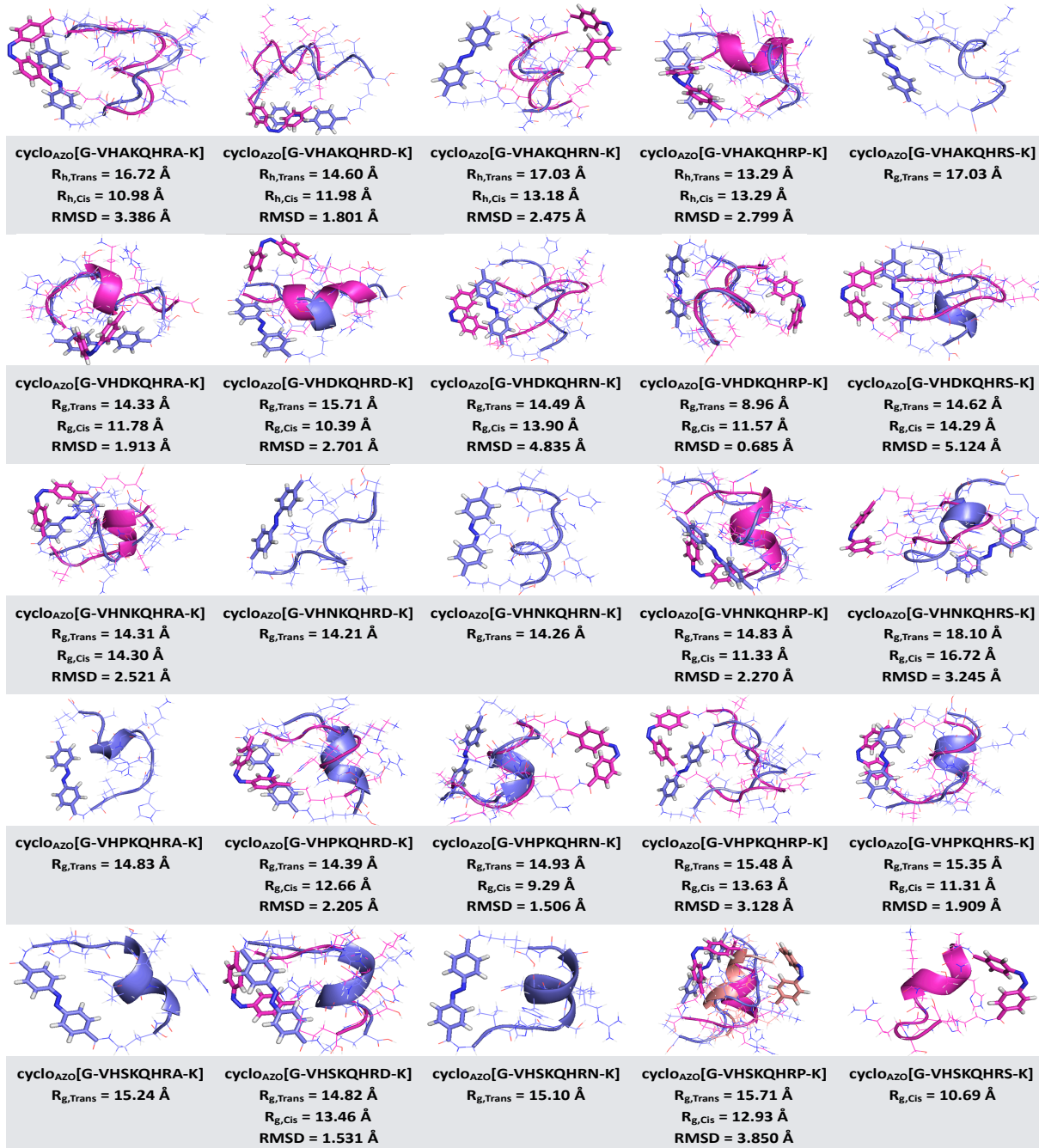


Table 5.3 Structure of the peptide-VCAM1 complexes formed by docking azobenzene-cyclized peptide variants 1-4, 6-11, 14, 15, 17-20, 22, and 24 (Table 5.1) onto the putative binding sites S1-S5 of VCAM1.

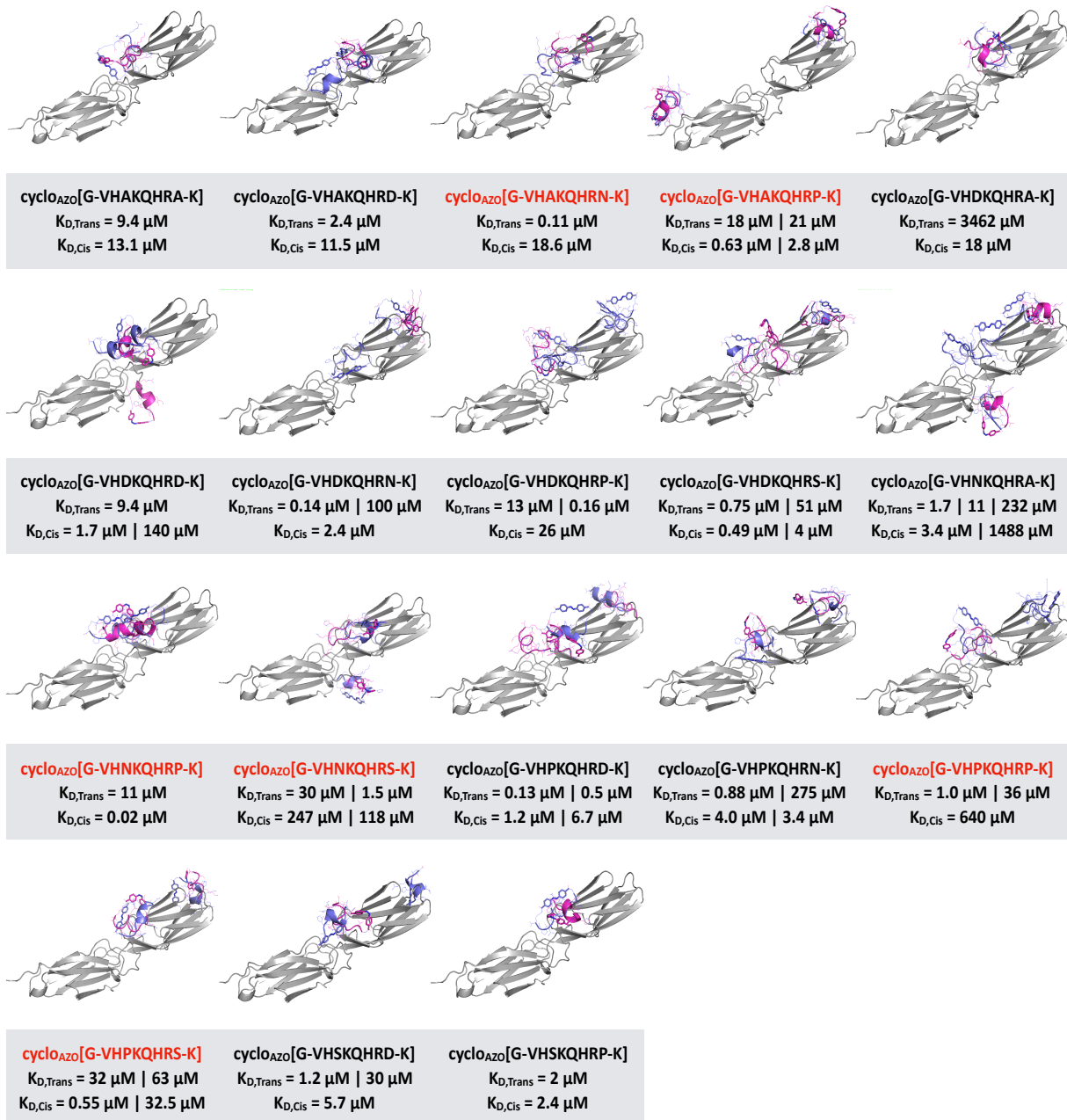


Table 5.4 Average thickness of the SAM and SAM-peptide monolayers, and corresponding peptide density determined by ellipsometry.

Sample	Thickness (Å)	Peptide density (molecules nm ⁻²)
15:85 N ₃ -PEG : HO-PEG SAM (N ₃ SAM)	20.1 ± 3.0	---
15:85 NH ₂ -PEG : HO-PEG SAM (amino SAM)	22.3 ± 1.5	---
cyclo _{AZOB} [G-VHAKQHRN-K] on N ₃ SAM	35.0 ± 2.3	0.85 ± 0.22
cyclo _{AZOB} [G-VHPKQHRS-K] on N ₃ SAM	33.7 ±	0.79 ± 0.27
cyclo _{AZOB} [G-VHAKQHRD-K] on N ₃ SAM	33.7 ±	0.93 ± 0.21
VHPKQHR-GSG on N ₃ SAM	30.5 ±	1.01 ± 0.21
Anti-VCAM1 antibody on amino SAM	68.2 ± 11.6	---

Table 5.5 Values of ΔG_{B,Trans}, ΔG_{B,Cis}, and |ΔΔG_B| of the interaction between VCAM1 and cyclo_{AZOB}[G-VHAKQHRP-K*], cyclo_{AZOB}[G-VHNKQHRP-K*], cyclo_{AZOB}[G-VHPKQHRS-K*], cyclo_{AZOB}[G-VHAKQHRN-K*], cyclo_{AZOB}[G-VHNKQHRS-K*], cyclo_{AZOB}[G-VHPKQHRP-K*], and VHPKQHR determined by fitting the VCAM1 adsorption data obtained from the SPR sensorgrams to a Langmuir isotherm. The “---” indicates that no accurate SPR reading could be obtained.

Peptide	ΔG _{B,Trans} (kcal/mol)	ΔG _{B,Cis} (kcal/mol)	ΔΔG _B
cyclo _{AZOB} [G-VHAKQHRP-K*]	---	1.09	---
cyclo _{AZOB} [G-VHNKQHRP-K*]	1.29	-0.55	1.84
cyclo _{AZOB} [G-VHPKQHRS-K*]	3.20	0.68	2.52
cyclo _{AZOB} [G-VHAKQHRN-K*]	2.86	-0.07	2.93
cyclo _{AZOB} [G-VHNKQHRS-K*]	2.14	---	---
cyclo _{AZOB} [G-VHPKQHRP-K*]	1.58	0.06	1.52
VHPKQHR		-0.93	

Figures

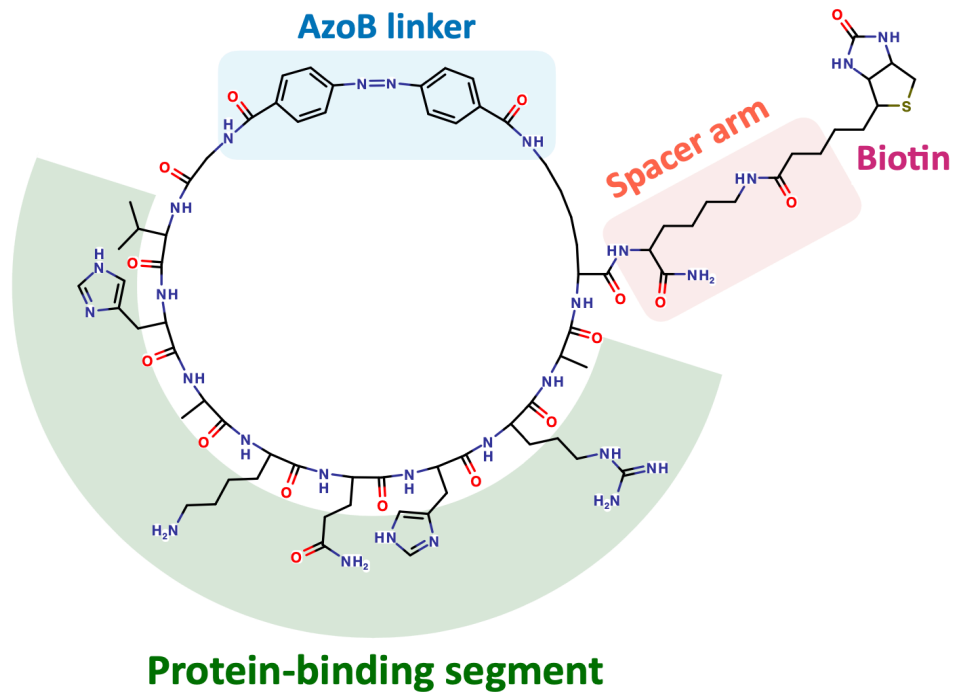


Figure 5.1 Structure of the proposed azobenzene-cyclized peptides.

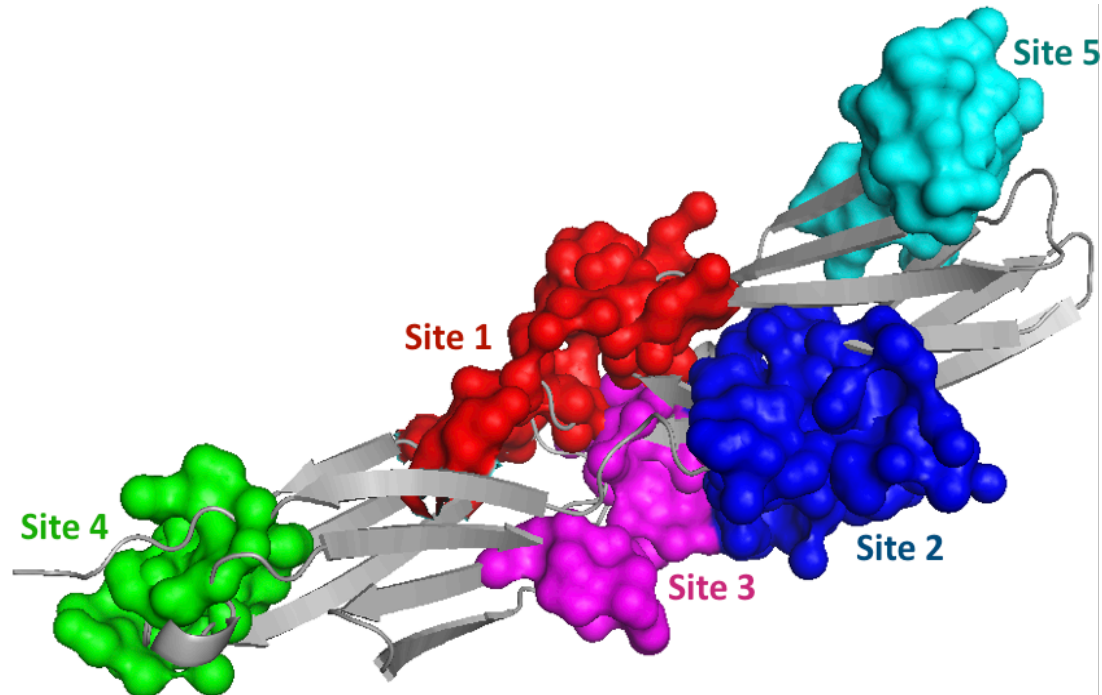


Figure 5.2 Putative peptide binding sites (S1-S5) on VCAM1 identified by performing a druggability analysis of the crystal structure of VCAM1 (PDB ID: 1VCA) using SiteMap.

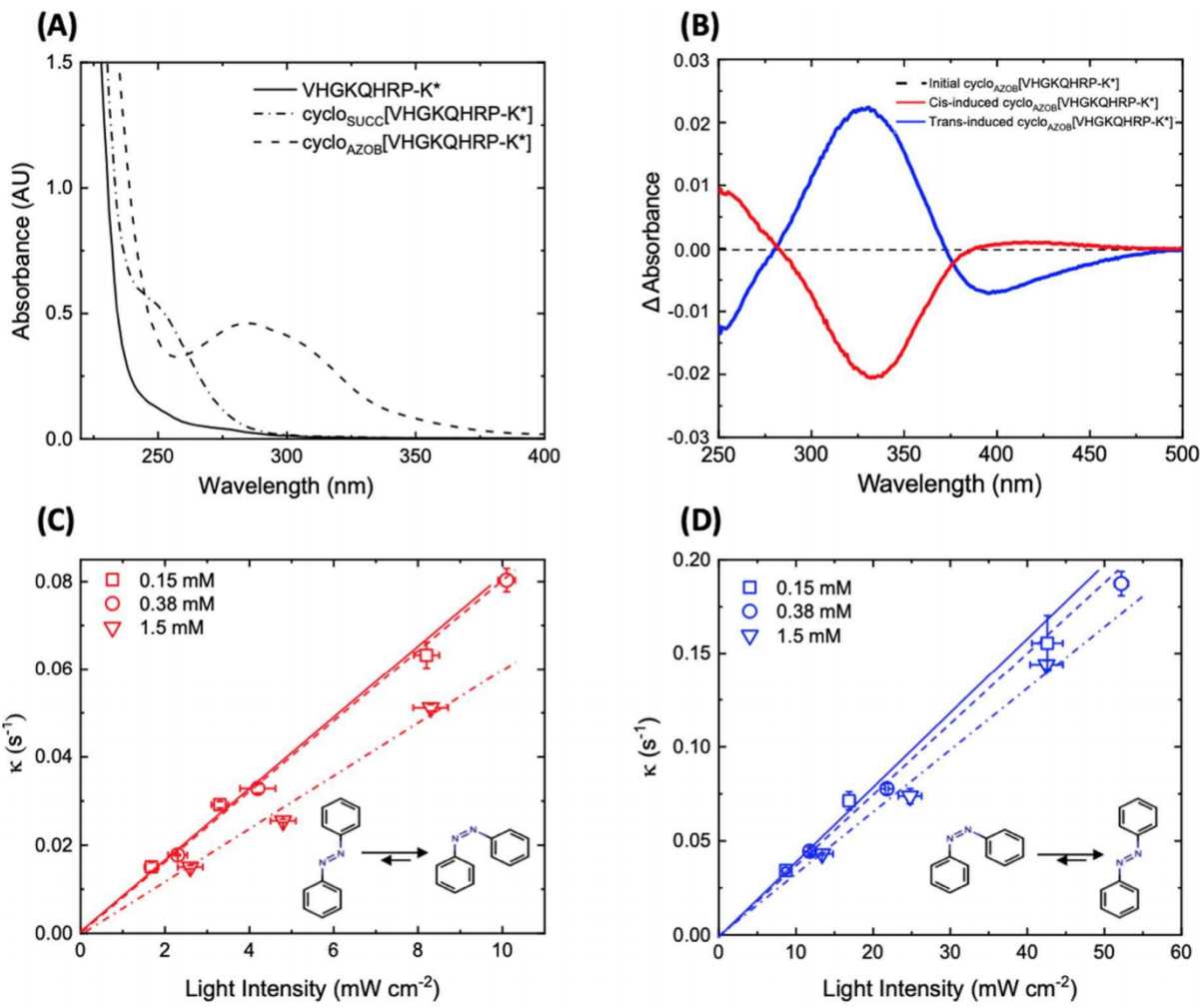


Figure 5.3 (A) UV-vis absorption spectra for VHGKQHRP-K* (solid), cyclo_{SUCC}[VHGKQHRP-K*] (dot-dash), and cyclo_{AZOB}[VHGKQHRP-K*] (dash); (B) Δ Absorbance for the *cis*-induced isomer (red) and *trans*-induced isomer (blue); (C) *trans*-to-*cis* isomerization upon exposure to UV light (305–390 nm) and (D) *cis*-to-*trans* isomerization upon exposure to visible light (> 420 nm). For (C) and (D) fitted lines are solid (squares), hash (circles), dot-hash (triangles), and data are mean \pm S.D.

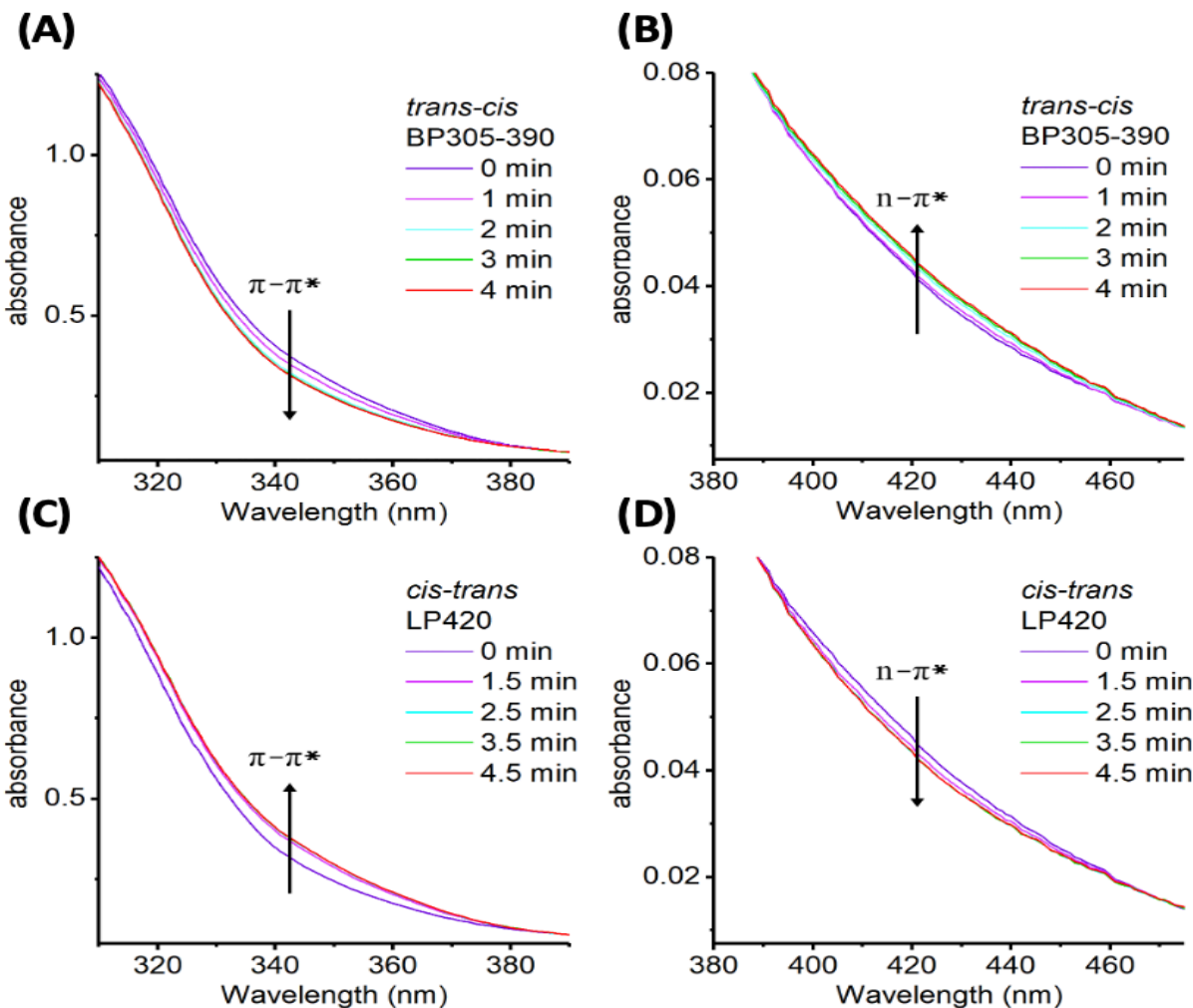


Figure 5.4 Spectral absorbance changes of a 0.38 mM solution of cyclo_{AZOB}[VHGKQHRP-K*] in MilliQ water upon exposure to UV bandpass filtered light (**A** and **B**) and subsequent LP420 filtered light (**C** and **D**). Spectra are scanned from 500 nm to 250 nm at 10 nm s⁻¹ and time indicates light exposure at the start of each scan.

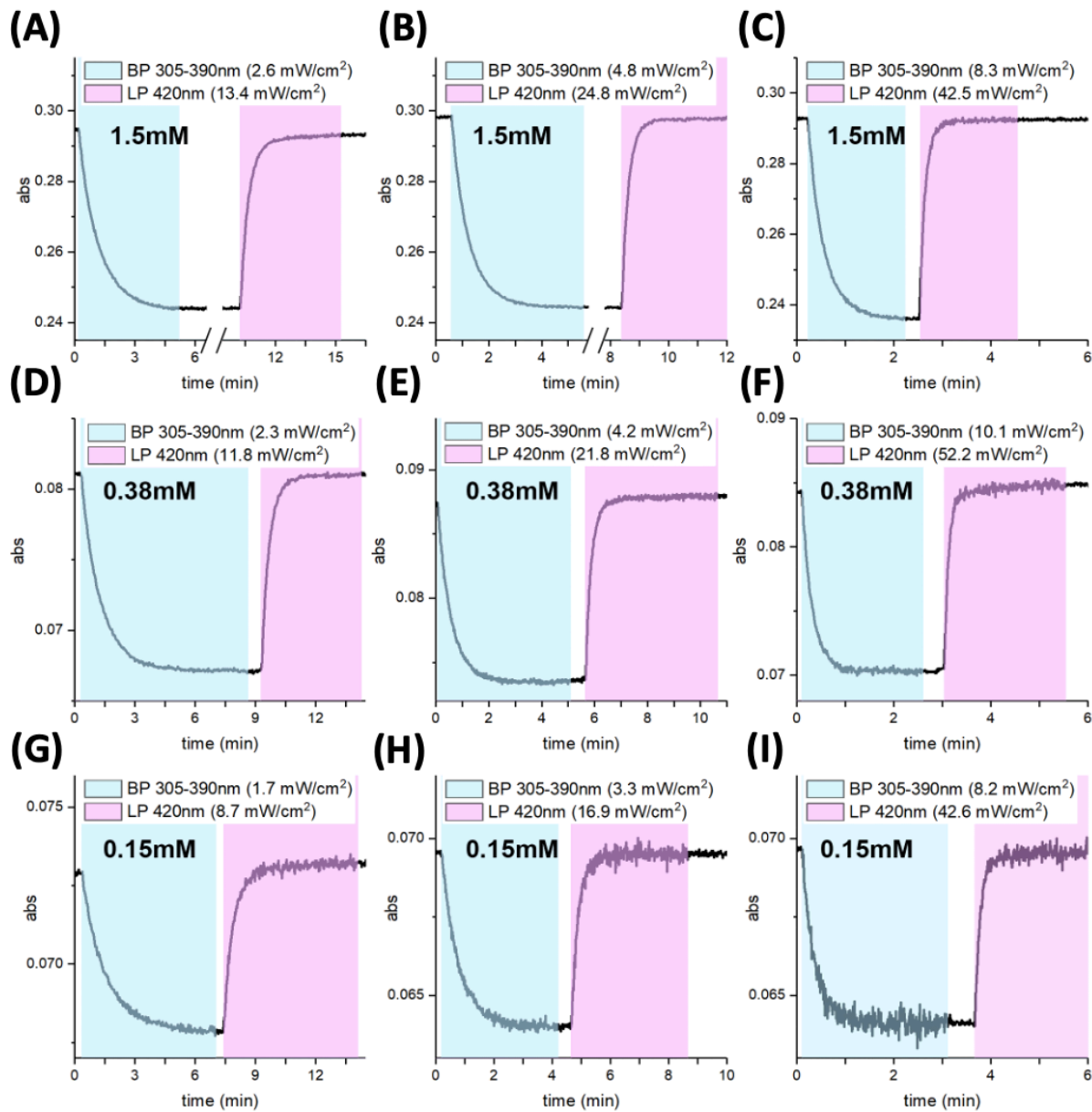


Figure 5.5 Representative changes of absorbance at 350 nm for 1.5 mM (A, B, C), 0.38 mM (D, E, F), and 0.15 mM (G, H, I) solutions of cycloAZOB[VHGKQHRP-K*] upon exposure to light filtered with UV bandpass (BP 305-390 nm) and LP420 filters at different values of light intensity.

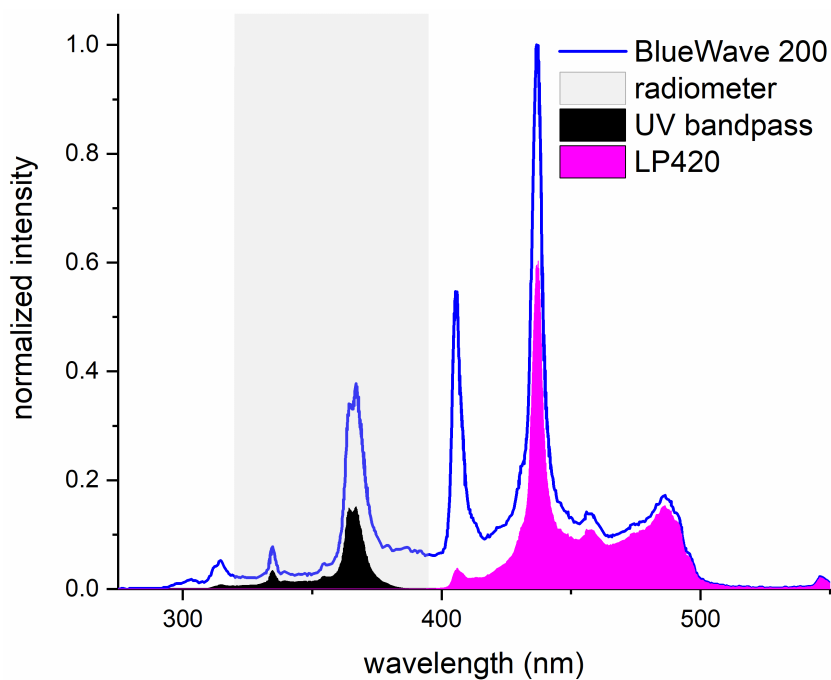


Figure 5.6 Spectra of Dymax BlueWave 200 curing lamp and corresponding filtered outputs using UV bandpass (BP305-390) and LP420 filters.

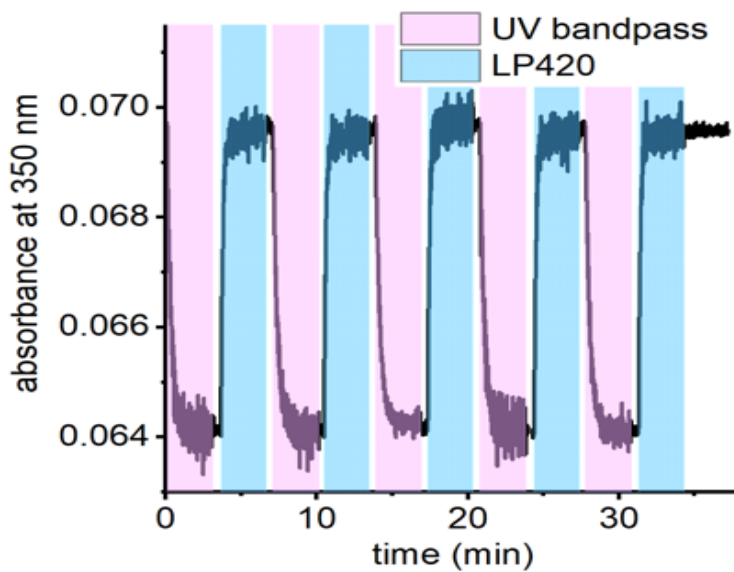


Figure 5.7 Reversible and repeatable *trans-cis* and *cis-trans* isomerization of cycloAZOB[VHGKQHRP-K*] dissolved in MilliQ water at the concentration of 0.15 mM.

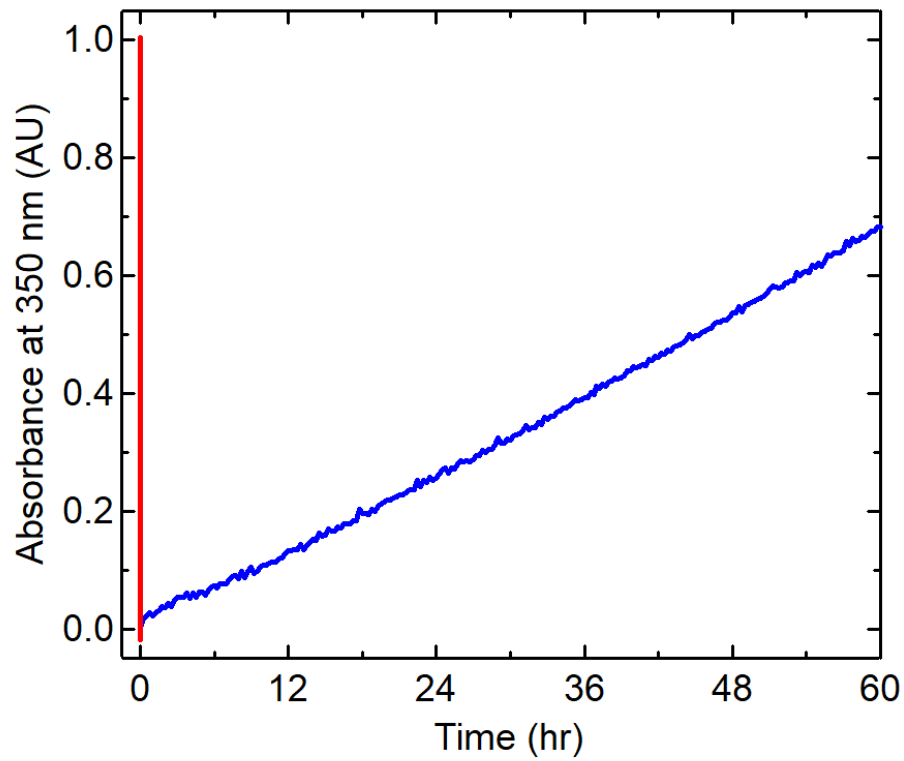


Figure 5.8 Thermal *cis*-to-*trans* isomerization (relaxation) of cycloAZOB[VHGKQHRP-K*]. The red curve represents initial induction of the peptide into the *cis* conformation and the blue curve represents the recovery of the *trans* configuration. Isomerization was monitored by recording the absorbance at 350 nm of a 0.15 mM solution of peptide in MilliQ water for 48 hr, at 37°C in the dark.

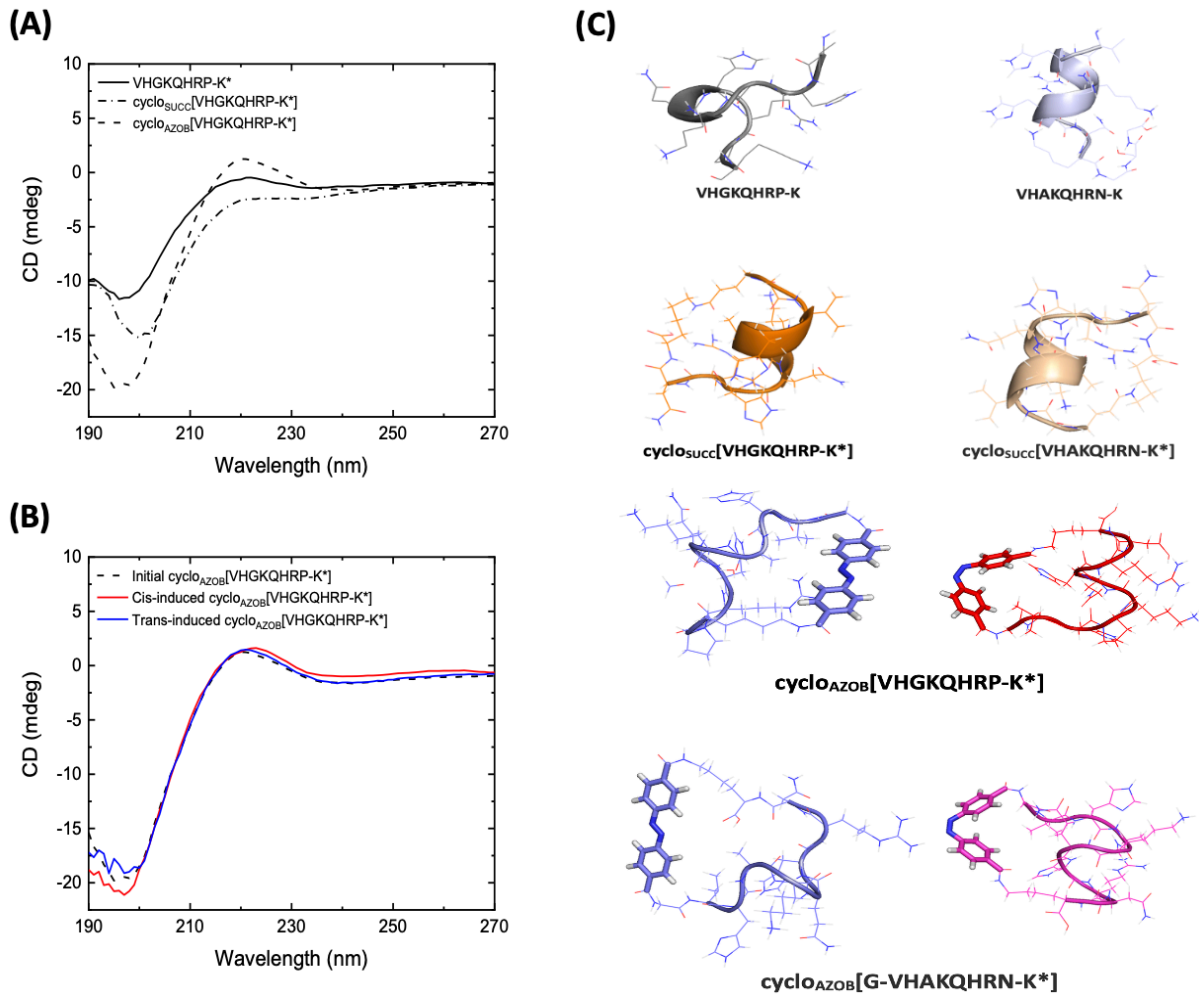


Figure 5.9 **(A)** Circular dichroism (CD) spectra of cyclo_{AZOB}[VHGKQHRP-K*] peptide upon photo-induced isomerization, indicating a random coil conformation, **(B)** CD spectra of peptide variants, indicating a random coil conformation for all peptides. **(C)** Structure of VHPKQHRS-GSG and cycloSUCC[G-VHAKQHRN-K*] peptides with an α -helix segment, and cyclo_{AZOB}[G-VHAKQHRN-K*] with random coil in both *trans* and *cis* conformation.

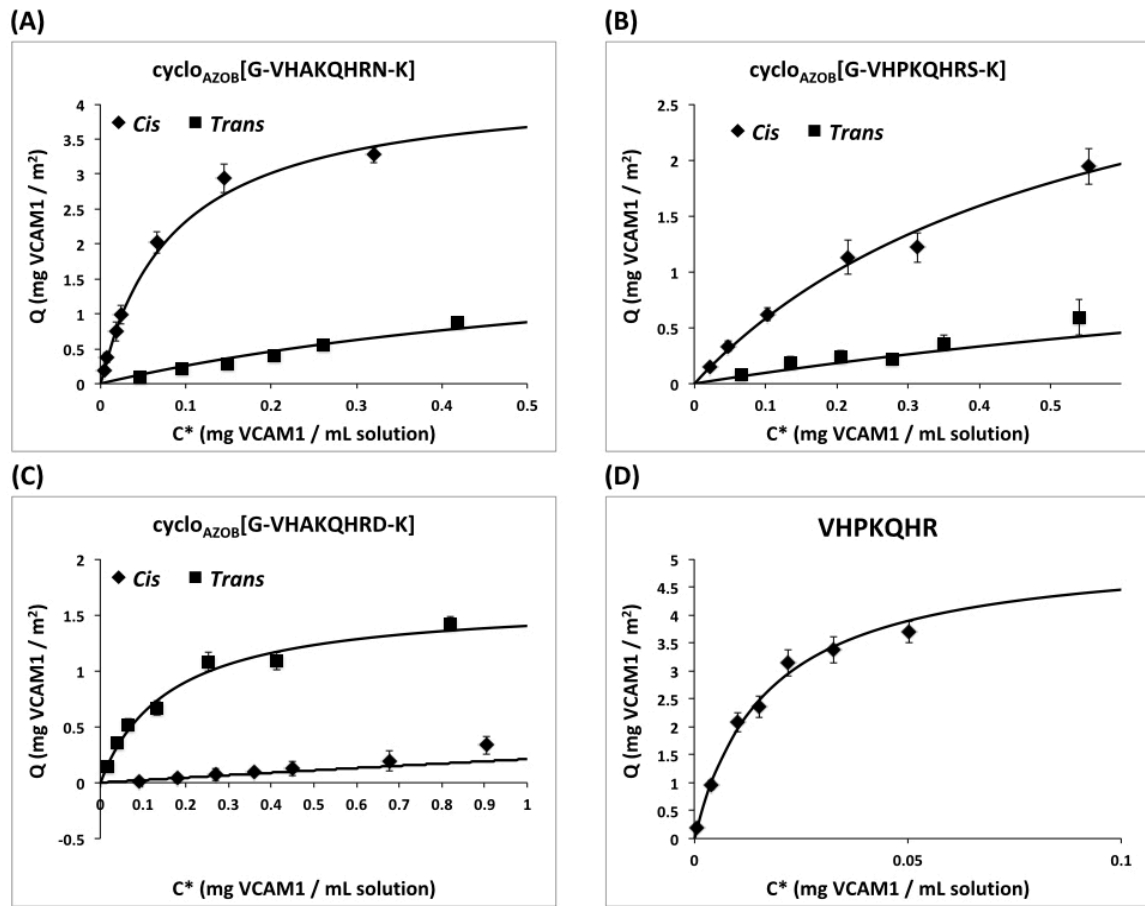


Figure 5.10 SPR measurements of VCAM1:peptide $K_{D,Trans}$ and $K_{D,Cis}$ for (A) of cyclo_{AZOB}[G-VHAKQHRN-K*]; (B) cyclo_{AZOB}[G-VHPKQHRS-K*]; (C) cyclo_{AZOB}[G-VHAKQHRD-K*]; and (D) VHPKQHR. The data points were obtained as average of triplicate readings.

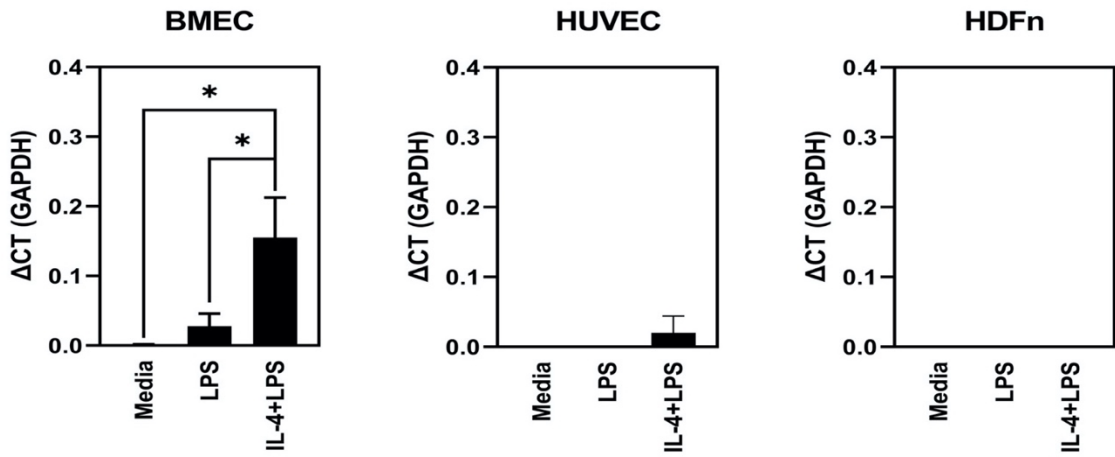


Figure 5.11 Confirmation of VCAM1 induction by LPS exposure via immunohistochemical analysis and qRT-PCR characterization. BMEC was demonstrated to express VCAM-1 when treated with IL-4, followed by LPS. LPS treatment alone showed no significant change in VCAM-1 expression. HUVEC and HDFn controls showed no increase in VCAM-1 expression with either treatment condition. Statistical analysis was performed using a 2way ANOVA with Tukey's *post hoc* comparison test with an alpha value of 0.05 (*) considered statistically significant.

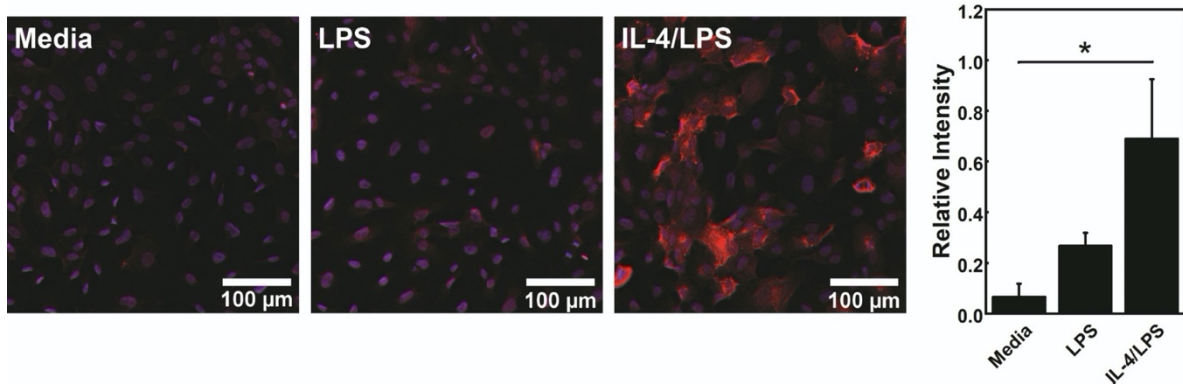


Figure 5.12 Confirmation of VCAM1 induction in BMECs by synergistic treatment with IL-4 and LPS via immunohistochemical analysis quantification. Relative intensity of tagged VCAM-1 antibody compared across different cell treatment condition agrees with RT-qPCR measurements, showing the most induction of VCAM-1 in BMECs treated with IL-4 followed by LPS. Error bars represent standard deviation. Statistical analysis was performed using a paired t-test with an alpha value of 0.05 (*) considered statistically significant.

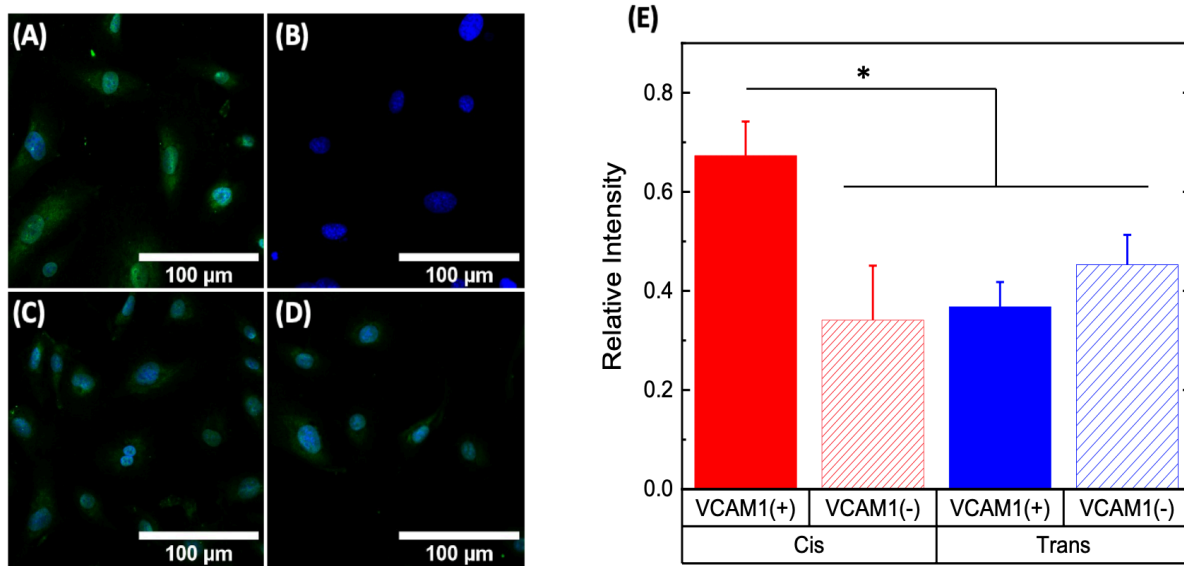


Figure 5.13 CycloAZOB[G-VHAKQHRN-K*] in the *cis* conformation incubated with cells (**A**) expressing and (**B**) not expressing VCAM-1, cycloAZOB[G-VHAKQHRN-K*] in the *trans* conformation incubated with cells; (**C**) expressing and (**D**) not expressing VCAM-1, and (**E**) the relative intensity of biotin-labelled *cis/trans* cycloAZOB[G-VHAKQHRN-K*] incubated with VCAM-1^{+/−} induced cells. Statistics were done with a 2-tailed t-test with a p value < 0.05 (*) considered statistically significant.

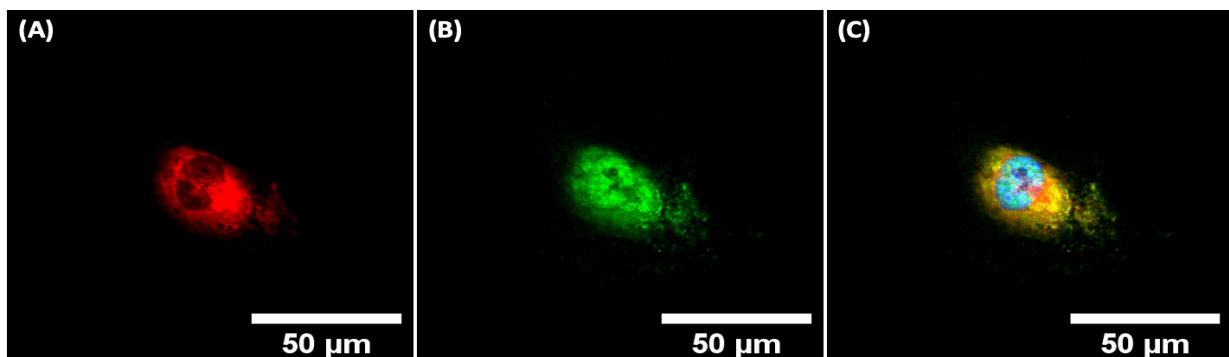


Figure 5.14 IL-4/LPS treatment induced VCAM1 expression confirmed with (**A**) antibody staining, (**B**) *cis*-cycloAZOB[G-VHAKQHRN-K*] peptide, and (**C**) the colocalization of the anti-VCAM1 antibody and *cis*-cycloAZOB[G-VHAKQHRN-K*] peptide around the nucleus of the cell.

CHAPTER 6

Synthetic Platelet Microgels Containing Fibrin knob B Mimetic Motifs Enhance Clotting

Responses

Seema Nandi, Emily Mihalko, Kimberly Nellenbach, Mario Castaneda, John D. Schneible,
Stefano Menegatti, Thomas H. Barker, and Ashley C. Brown

A version of this chapter has been submitted to Advanced Therapeutics for publication.

Abstract

Native platelets are crucial players in wound healing. Key to their role is the ability of their surface receptor GPIIb/IIIa to bind fibrin at injury sites, thereby promoting clotting. When platelet activity is impaired, as a result of traumatic injury or certain diseases, uncontrolled bleeding can result. To aid clotting and tissue repair in cases of poor platelet activity, our lab has previously developed synthetic platelet-like particles capable of promoting clotting and improving wound healing responses. These are constructed by functionalizing highly deformable hydrogel microparticles (microgels) with fibrin-binding ligands including a fibrin-specific whole antibody or a single-domain variable fragment. To improve the translational potential of these clotting materials, we explored the use of fibrin-binding peptides as cost-effective, robust, high-specificity alternatives to antibodies. Herein, we present the development and characterization of soft microgels decorated with the peptide AHRPYAAK that mimics fibrin knob ‘B’ and targets fibrin hole ‘b’. These “Fibrin-Affine Microgels with Clotting Yield” (FAMCY) were found to significantly increase clot density *in vitro* and decrease bleeding in a rodent trauma model *in vivo*. These results indicate that FAMCYs are capable of recapitulating the platelet-mimetic properties of previous designs while utilizing a less costly, more translational design.

6.1. Introduction

Wound repair is a dynamic, interconnected process involving the orchestration of numerous physiological cues and events. During normal healing, the body proceeds through several phases in order to reestablish tissue integrity, including (*i*) hemostasis; (*ii*) inflammation; (*iii*) cell migration and proliferation; and (*iv*) tissue repair and long-term tissue remodeling [1]. Platelet and fibrin(ogen) interactions are key contributors during healing. Following injury, circulating platelets become activated and marginate to the injured vasculature, and during primary hemostasis aggregate to form a platelet plug to aid in the cessation of bleeding. Additionally, secondary hemostasis occurs wherein soluble fibrinogen polymerizes into an insoluble fibrin network via cleavage of fibrinopeptides A and B from the fibrinogen molecule [2]. Cleavage of these fibrinopeptides exposes peptide sequences known as knobs ‘A’ and ‘B’, which respectively bind to holes ‘a’ and ‘b’ on neighboring fibrin and fibrinogen molecules, thereby forming an insoluble fibrin network (**Figure 6.1**) [3]. A:a binding occurs rapidly and forms strong bonds making it the primary driving force behind fibrin polymerization, whereas the rate of B:b binding increases as polymerization continues [4].

At sites of injury, activated platelets bind to nascent fibrin fibers via their surface receptor GPIIb/IIIa, which catalyzes fibrin formation and results in the formation of a platelet and fibrin rich clot [5]. Platelet-fibrin interactions are critical in both initial clot formation and on longer time scales; following initial clot formation, activated platelets contract via actin-myosin machinery, pulling on the bound fibers and bringing about clot retraction [3]. Clot retraction expels serum from the clot, decreases clot porosity, and increases clot stiffness [3]; this process stabilizes the clot and reduces its susceptibility to fibrinolysis [6, 7], allowing it to act as a provisional matrix

capable of supporting cellular infiltration and proliferation during the subsequent phases of inflammation and cell migration [3, 8, 9].

In cases of traumatic injury or disease, platelet-fibrin interactions can become dysfunctional. Uncontrolled bleeding due to traumatic injury often results in dilution of clotting agents, including platelets and fibrinogen, preventing robust clotting responses [10]. Uncontrolled bleeding is a leading cause of death for both men and women under the age of 45, with most deaths occurring in the ambulatory (pre-hospital) stage [11-13]. This poses a critical need for hemostatic treatments capable of supplementing platelet function in cases of trauma or disease. To that end, our lab has previously described the development of synthetic platelet-like particles (PLPs) that target fibrin at an injury site and exert strain upon the bound fibrin fibers thereby promoting initial clot formation and subsequent clot retraction, respectively [14]. Strong and selective fibrin binding and the ability to induce clot retraction were achieved by conjugating a full monoclonal antibody or a single domain variable fragment chain (sdFv) designed to selectively bind to fibrin over fibrinogen on highly deformable microgels comprised of poly(N-isopropylacrylamide-co-acrylic acid) (pNIPAm-*co*-AAC).

While widely utilized in the research phase, anti-fibrin antibodies may not represent an ideal biorecognition moiety for translational purposes. Their high cost of manufacturing and storage requirements pose challenges to scale-up and clinical applicability. Peptides, on the other hand, combine the binding selectivity of antibodies with higher biochemical stability and large-volume manufacturing at relatively low costs. Accordingly, in this study we explored the use of fibrin knob-mimicking peptides that target the polymerization holes of fibrin to develop a new version of platelet-like particles called “Fibrin-Affine Microgels with Clotting Yield” (FAMCY). In selecting which binding site on fibrin to target using peptide ligands – hole a or hole b – we

took into account the impact of fibrin polymerization kinetics. Particles that target hole a, in fact, would present the risk of impairing the fibrin polymerization process since A:a binding is the driving force behind polymerization [15]. B:b interactions, on the other hand, appear to be less essential to fibrin polymerization, indicating that fibrin hole b is a more appropriate candidate for peptide targeting [16]. Additionally, studies with knob B mimicking peptides have previously shown that pre-engagement of fibrin hole b prior to polymerization can result in clots with enhanced mechanics and resistance to degradation [17, 18]. Accordingly, in this work we have adopted a knob B mimicking peptide, AHRPYAAK, that targets fibrin hole b to construct FAMCYs capable of augmenting clot formation and stability and decreasing bleeding times in an *in vivo* rodent model of traumatic injury. FAMCYs were found to significantly increase clot density *in vitro* and decrease bleeding in a rodent trauma model *in vivo*. These results indicate that FAMCYs are capable of recapitulating the platelet-mimetic properties of previous designs while utilizing a less costly, more translational design.

6.2. Materials and Methods

6.2.1. Ultra-low Crosslinked (ULC) Microgel Synthesis and Characterization

Poly(N-isopropylacrylamide-*co*-acrylic acid) (pNIPAm-*co*-AAc) ULCs were synthesized via precipitation polymerization. NIPAm (Millipore Sigma, St. Louis, MO, USA) and acrylic acid (Millipore Sigma) were dissolved in 100 mL ultrapure water, pH 5.0 (18.2 MΩ resistance, Milli-Q, Darmstadt, GER) at molar composition ratios of 90:10, 85:15, or 80:20 NIPAm:AAc. NIPAm was recrystallized in hexanes prior to use, and acrylic acid was incorporated into the monomer solution 10 min prior to ammonium persulfate (APS, Millipore Sigma) initiation in order to provide charged groups on the microgel particles for future coupling of targeting motifs. Each reaction was carried out using 140 mM total monomer concentration. To study how particle size

may influence hemostatic ability, smaller particles were also created at a 90:10 NIPAm:AAc ratio by incorporating 4 mM or 2 mM sodium dodecyl sulfate (SDS, Millipore Sigma) into the monomer solution for particle sizes of approximately 150 nm and 450 nm respectively. Monomer solutions were filtered through a 0.2 μ m Steriflip® pore filter (Millipore Sigma) and added into a 500 mL round-bottom 3-neck flask containing a stir bar. The 3-neck flask was transferred to a preheated (70°C) oil bath and equilibrated at 70°C for 1 hr under nitrogen purging. Acrylic acid was added to the reaction solution after 50 min and equilibrated for 10 min prior to initiation using 1 mM APS. The reaction was carried out under a nitrogen blanket for 6 hr. Polymerization was confirmed visually following the addition of APS as the monomer solution changed from translucent to opaque. After 6 hr, the flask was taken off heat and allowed to cool overnight at RT. The monomer solution underwent constant stirring at 450 rpm for the duration of the equilibration, reaction, and cooling steps. The cooled microgel solution was filtered through glass wool and then purified via dialysis against ultrapure water for 3 days using a Spectra/Por® dialysis membrane (MWCO 1000 kDa, Spectrum Laboratories, Rancho Dominguez, CA, USA). Purified microgels were lyophilized and stored at RT prior to resuspension in ultrapure water for use in experiments.

Particle deformation was determined via atomic force microscopy (AFM) dry imaging using an Asylum MFP 3D Bio atomic force microscope (Asylum Research, Santa Barbara, CA, USA) [19, 20]. For AFM imaging, glass coverslips were cleaned through submersion in a series of solutions (alconox, water, acetone, absolute ethanol, and isopropyl alcohol) in an ultrasonic bath and dried under nitrogen. The microgel suspensions were vortexed, deposited onto cleaned coverslips, and centrifuged at 3,700 rpm for 10 min and then allowed to dry overnight prior to imaging. Silicon nitride cantilevers ($k = 42$ N ml, NanoWorld) were operated in intermittent contact mode during image acquisition. Microgel height was determined using the AFM software

(Igor Pro 15) and diameter was determined using ImageJ image analysis software (National Institutes of Health, Bethesda, MD, USA). A minimum of 30 microgels were analyzed per ULC formulation. Average height and diameter \pm standard deviation is reported for each group. Nanosight (Malvern, Westborough, MA, USA) particle tracking analysis was also utilized to determine hydrodynamic diameters of small and medium sized 90:10 NIPAm:AAc ULCs.

6.2.2. Construction of FAMCY Particles by Peptide Conjugation on ULC Microgels

Knob B mimicking peptide (AHRPYAAK, Pepceuticals Ltd., UK) or a non-targeting control peptide (GPSPFPAK, GenScript) was conjugated to the microgels by EDC-Sulfo NHS chemistry. Each reaction utilized a concentration of 5 mM of sulfo-NHS, 50 mM of EDC, and a 1:1 peptide:AAc molar ratio in HEPES buffer at pH 7.4. Microgels were first incubated in the EDC and sulfo-NHS solution for 30 min under gentle agitation, then peptide solution was added to the microgels and incubated for 4 hr with gentle agitation. Following conjugation, FAMCYs (AHRPYAAK –microgels) and control peptide FAMCYs (GPSPFPAK-microgels) were purified by dialysis against ultrapure water for 3 days. Purified microgels were lyophilized and stored at 4°C prior to resuspension in ultrapure water for use in experiments.

6.2.3. Evaluation of Fibrin Clot Structure in the presence of FAMCYs

Confocal microscopy was utilized to examine fibrin clot structure in the presence of various concentrations and formulations of FAMCYs. Clots of 50 μ L volume consisting of 2.0 mg mL⁻¹ human fibrinogen (FIB 3, Enzyme Research Laboratories, USA) and HEPES buffer (25mM HEPES, 0.15M NaCl, 5mM CaCl₂, pH 7.4) were polymerized with 0.25 U mL⁻¹ human thrombin (Enzyme Research Labs, USA) and 10 μ g mL⁻¹ Alexa-Fluor 488 labeled fibrinogen (Thermo

Fisher Scientific) for visualization. Clots were formed between a glass slide and coverslip and allowed to polymerize for a minimum of 2 hr prior to imaging [21]. A Zeiss Laser Scanning Microscope (LSM 710, Zeiss Inc., White Plains, NY, USA) at a magnification of 63x was utilized for creating 1.56 μm z-stacks. A minimum of three random z-stacks were acquired per clot. ImageJ software was used to create 8-bit 3D projections from z-stacks. Clot fiber density was determined from the ratio of black (fiber) over white (background) pixels in each binary image [14, 22].

To determine how particle concentration influenced clot structure, clots containing 1, 2, or 4 mg mL⁻¹ of FAMCYs were formed using the “large” 1 μm 90:10 NIPAm:AAc microgels. To determine how microgel formulations influenced clot structure, clots containing the optimal FAMCY concentration were formed using microgels of varied AAc concentration (90:10, 85:15, and 80:20) and varied size (~150 nm as “small”, ~450 nm as “medium”, and ~1 μm as “large”). In all studies, microgels were added prior to clot polymerization with thrombin. The optimal concentration and formulation of FAMCYs to induce clot retraction was defined as the concentration found to increase clot density to the greatest degree.

6.2.4. Determination of Fibrin Clot Polymerization and Stability in the presence of FAMCYs

Fibrin clot polymerization and degradation rates in the presence of FAMCYs across varying concentrations were evaluated using a previously described endogenous fibrinolysis assay [23], which enables monitoring of fibrin polymerization and degradation within a single assay. Clots of 100 μL volume were formed as described for confocal microscopy studies using either 1, 2, or 4 mg mL⁻¹ of the 1 μm 90:10 NIPAm:AAc FAMCYs, control peptide FAMCYs, or ULCs; to observe clot degradation in addition to polymerization, 0.29 μg mL⁻¹ human tissue plasminogen activator (tPA) (Millipore Sigma), and 10.8 μg mL⁻¹ human gluplasminogen (Thermo Fisher

Scientific, Waltham, MA, USA) were also included in all clot preparations. The clots were formed in 96 well plates, and clot absorbance at 350 nm was read on a plate reader every 30 s over a period of 3 hr. A baseline absorbance measurement was taken prior to addition of thrombin, plasminogen, and tPA to clots; this baseline absorbance was subtracted from all absorbance measurements obtained during the 3 hr polymerization and degradation time in order to remove the effect of particle absorbance on clot polymerization and degradation curves. Area under the curve was calculated for each polymerization/degradation curve.

6.2.5. Analysis of FAMCY Hemostatic Ability *in vivo*

Hemostatic efficacy of FAMCYs was evaluated *in vivo* using a murine liver laceration model [24]. All procedures were approved by the North Carolina State University IACUC. 8 week-old C57BL/6 mice were anesthetized using isoflurane (5% in oxygen) through a nose cone for the duration of the procedure. 100 μ L of treatments in saline of 90:10 FAMCYs, control peptide FAMCYs or bare ULC microgels were administered via the jugular vein and allowed to circulate for 5 min prior to injury. A range of FAMCY concentrations, 5 mg kg⁻¹ animal, 10 mg kg⁻¹ animal, 15 mg kg⁻¹ animal, 50 mg kg⁻¹ animal, were tested to determine the dose response in hemostatic ability. Control peptide FAMCYs and microgel control particles were tested at a concentration of 10 mg kg⁻¹ animal. To perform the liver laceration, the abdomen was first opened via a surgical midline approach. The liver was then mobilized, and a 10 mm scalpel cut was made through the left lobe to obtain complete dorsal and ventral laceration. Blood loss was monitored for 10 min following injury via blood collected in gauze held adjacent to the injury. Gauze was changed and blood content was weighed at 10 s intervals for the first 30 s post injury, then at 30 s intervals for t = 30 s to t = 3 min, then at one min intervals for t = 3 min to t = 10 min. Gauze was weighed

immediately following removal from wound, ensuring no evaporation. Blood loss, in grams, was quantified at each gauze exchange time point by subtracting the final weight of the gauze (after blood collection) from the initial weight of the gauze (prior to use for blood collection). Blood loss over time at each gauze exchange time point was quantified as well as total blood loss over the 10 min injury and divided by animal weight. Following blood collection and prior to sacrificing the animal, the wound section was harvested from each animal, fixed in 10% formalin for 48 hr, paraffin-embedded, and sectioned for histological analysis (5 μ m thickness).

Immunohistochemistry was performed on wound cross-sections to examine fibrin at the injury site. Here, tissue was deparaffinized and rehydrated, permeabilized in phosphate-buffered saline with 0.1% Triton X-100 (PBST), blocked with 5% goat serum in phosphate-buffered saline (v/v), labeled with monoclonal antifibrin antibody (15 μ g mL⁻¹ final concentration, UC45, GeneTex, Irvine, CA, USA) overnight at 4°C, washed and labeled with secondary antibody goat anti-mouse IgM, Alexa Fluor 594 (15 μ g mL⁻¹ final concentration) (A21044, Thermo Fisher Scientific) for 1 hr at room temperature, and then washed and mounted with Vectashield HardSet mounting medium with DAPI (Fisher Scientific). Wound cross-sections were imaged with fluorescent microscopy (EVOS FL Auto Cell Imaging System, Fisher Scientific), and quantification for fibrin deposition was evaluated using ImageJ Particle Analysis and measuring particle count as well as total area.

6.2.6. Statistical Analysis

Statistical analysis was performed using GraphPad Prism 8 (GraphPad, San Diego, CA, USA). Data for all experiments was evaluated using a one-way analysis of variance (ANOVA) with a Tukey's *post hoc* test using a 95% confidence interval.

6.3. Results

In this study, we evaluated how the fibrin B knob mimetic, hole b targeting functionality (*i.e.*, peptide conjugation and particle concentration) and the base properties of the microgels (*i.e.*, AAc content and size) determine the pro-clotting activity of FAMCYs. Our previous studies on poly(NIPAM)-based ULC microgels demonstrated that microgel deformability is critical to mimicking platelet-mediated clot retraction and improving clot stability [12, 17]. In this work, we first evaluated different concentrations of FAMCY particles fabricated from deformable ~1 μm ULC microgels conjugated to knob B mimetic peptide (AHRPYAAK) on their ability to alter fibrin clot architecture. We then evaluated whether varying the particle size or AAc/NIPAM ratio alters microgel deformability. We constructed an ensemble of FAMCYs with varying diameter between ~150 nm and ~1 μm or varying AAc content, and upon conjugating knob B mimetic peptides (AHRPYAAK), utilized them to manipulate fibrin clot architecture.

6.3.1. FAMCYs Increase Clot Density at Optimal Concentrations

We first evaluated the influence of FAMCY microgels constructed by conjugating knob B mimetic peptides (AHRPYAAK) onto ULC poly(NIPAM) microgels made from 90:10 NIPAm:AAc with diameters of ~1 μm on fibrin clot architecture. Deformability of ULC poly(NIPAM) microgels made from 90:10 NIPAm:AAc was first assessed via AFM analysis by measuring diameter and height of the particles on a glass surface. A representative AFM image and height trace is shown in **Figure 6.2** where 90:10 NIPAm:AAc microgels feature an average diameter of 1398 ± 236 nm and height of 18 ± 5 nm. Microgels were then conjugated to knob B mimetic peptides to create FAMCYs. Confocal microscopy was utilized to evaluate morphology of FAMCY containing clots and determine the concentration of FAMCYs that provide improved

fibrin clot density, thus mimicking platelet-mediated retraction. First, we evaluated how altering FAMCY dosage concentration of ~1 μm 90:10 NIPAm:AAc influenced fibrin density. Here, we observed a significant increase in clot fiber density compared to fibrin only controls or clots incorporated with 1 mg mL^{-1} 90:10 NIPAm:AAc FAMCYs when using a concentration of 2 mg mL^{-1} 90:10 NIPAm:AAc FAMCYs (**Figure 6.2**), where fiber density increased from 0.85 ± 0.02 (fibrin only controls) to 2.1 ± 0.8 black pixels; white pixels (2 mg mL^{-1} FAMCYs, $p = 0.0255$). At 4 mg mL^{-1} FAMCYs, we observed a decrease in fiber density from controls to 0.61 ± 0.2 (4 mg mL^{-1} FAMCYs) ($p = 0.0099$), indicating a potential inhibitory effect on polymerization at higher concentrations of particles. The overall biphasic relationship between particle concentration is likely due to the nature of targeting B:b interactions. At low concentrations of knob B mimicking peptide, the particles will bind to hole b without inhibiting native fibrin polymerization. As particle concentration is increased, binding to fibrin holes B is likewise increased, thereby increasing the ability of FAMCYs to increase fibrin network density. However, above a certain peptide concentration, the synthetic knob:hole interactions begin to compete for and inhibit native B knob:hole b interactions to a degree that inhibits fibrin polymerization.

6.3.2. Influence of Particle Size and Acrylic Acid Content on Fibrin Clot Density

Next, we evaluated the effect of particle size on fiber density by creating FAMCYs from ULC microgels ~150 or 450 nm in diameter while keeping AAc content and particle concentration constant at 10% and 2 mg mL^{-1} , respectively. The size of ULC microgels was altered by increasing SDS content in particle synthesis reactions while keeping monomer content at 90:10 NIPAm:AAc. Nanosight particle tracking confirmed hydrodynamic diameters of small microgels to be 147 ± 65 nm and medium particles to be 456 ± 88 nm. Representative AFM dry images and height traces of

the small, medium, and large 90:10 NIPAM:AAc ULC microgels are shown in **Figure 6.3**, where small microgels feature an average dry diameter of 121 ± 87 nm and average height of 2 ± 0.5 nm, medium microgels feature an average dry diameter of 445 ± 17 nm and average height of 8 ± 3 nm, and large microgels feature an average dry diameter of 1398 ± 236 nm and height of 18 ± 5 nm. Again, microgels were incorporated in clots to manipulate fibrin clot architecture and confocal microscopy was utilized to evaluate morphology of the resulting clots and determine the optimal FAMCY size. Particle size appeared in fact to affect the formation of fibrin clots with a trend of increasing fiber density with increasing particle size (**Figure 6.3**). A statistically significant increase in fiber density was found between small (~150 nm) and large (~1 μ m) sized FAMCYs with fiber densities of 0.82 ± 0.08 and 2.1 ± 0.8 black pixels to white pixels ratio, respectively ($p = 0.0227$), as well as fibrin control clots and large (~1 μ m) sized FAMCYs with fiber densities of 0.85 ± 0.02 and 2.1 ± 0.8 black pixels to white pixels ratio respectively ($p = 0.026$). Clots formed in the presence of small (~150 nm) and medium (~450 nm) sized FAMCYs did not demonstrate statistically different fiber densities of 0.82 ± 0.08 and 1.2 ± 0.2 black pixels:white pixels, respectively ($p = 0.6766$). Similarly, the difference in fiber density between clots with medium (~450 nm) and large (~1 μ m) FAMCYs was not statistically different, 1.2 ± 0.08 and 2.1 ± 0.8 black pixels:white pixels respectively ($p = 0.1$). The size dependent increase in fibrin network density is likely due to increased interactions between fibrin fibers and the B-knob mimicking peptides on the particles as particle size increases. Our previous studies with fibrin antibody and sdFv conjugated ULC microgels demonstrated that increased fiber density in the presence of fibrin-binding ULC microgels is dependent on the high particle deformability, which allows the particles to spread extensively within the fibrin network, binding to multiple fibrin fibers [14, 26]. Brownian motion of the particles leads to deformation of the fibrin network, and increased local

fiber density, overtime. Increased particle size would increase the extent of the particle:fibrin interactions, as larger particles would geometrically occupy more space than smaller particles and would be able to bridge more fibrin fibers than smaller particles.

Next, the acrylic acid content was varied in ULC poly(NIPAM) microgels and resulting particle deformability was assessed via AFM analysis by measuring diameter and height of the particles on a glass surface. It is noted that, since the knob B mimicking peptides are conjugated to the carboxylic acid groups of the AAc monomers, the peptide surface density is connected to the AAc ratio. Results demonstrated that particle deformability was maintained across all ULC microgel formulations tested here. Figure 4 shows representative AFM traces where 90:10 NIPAm:AAc microgels feature an average diameter of 1398 ± 236 nm and height of 18 ± 5 nm. Increasing the acrylic acid content to formulate 85:15 and 80:20 NIPAM:AAc ULC microgels resulted in an average particle diameter of 1360 ± 205 nm and height of 20 ± 5 nm, or an average diameter of 1485 ± 399 nm and height of 20 ± 6 nm, respectively. Diameter and height measurements between particle types with varying AAc content showed no statistically significant difference, indicating that altering the AAc of the particles does not influence their deformability. Using FAMCYs with varying AAc content at a concentration of 2 mg mL^{-1} , we found no differences in the fibrin density between clots formed in the presence of FAMCYs fabricated from ULC microgels with AAc content varied between 10-20% monomer composition (**Figure 6.4**). This suggests that ULC particles containing 10% AAc result in a saturating peptide density on the surface of the microgels.

6.3.3. Fibrin clot stability is increased in the presence of an optimal concentration of FAMCYs

Platelet-mediated clot retraction stabilizes the clot matrix, making it more resistant to degradation, and promotes the role of fibrin clots as a provisional matrix to support cellular infiltration during the later stages of wound healing [3, 9]. We therefore hypothesized that FAMCY-mediated clot retraction, evidenced in the confocal experiments by the increase in clot density, would likewise stabilize clots, decreasing the rates at which clot fibrinolysis would occur. An absorbance-based plate assay was utilized to assess the degradation rates of clots formed using either 1, 2, and 4 mg mL⁻¹ FAMCYs, ~1 μm in diameter with 90:10 NIPAm:AAc FAMCYs, or corresponding concentrations of control particles (control peptide FAMCYs or bare ULC microgels). At the previously identified optimal concentration of 2 mg mL⁻¹, FAMCY-containing clots showed significantly greater stability than fibrin-only clots or clots containing control particles, as measured by the integrated area of the polymerization/degradation curve of each clot type. Polymerization/degradation curves for clots formed using 2 mg mL⁻¹ FAMCYs featured an integrated area of 0.36 ± 0.2 , which was significantly larger than that obtained with the fibrin-only clot (0.13 ± 0.1 , $p = 0.0105$), the 2 mg mL⁻¹ ULC clot (0.14 ± 0.1 , $p = 0.0151$), and the 2 mg mL⁻¹ control peptide FAMCYs clot (0.16 ± 0.1 , $p = 0.03$). This indicates that incorporation of FAMCYs into clots increases clot stability in a manner reminiscent of native platelet-incorporated clots (**Figure 6.5**). These data, coupled with the increased clot density observed in the presence of 2 mg mL⁻¹ FAMCYs, indicate that targeting fibrin with the knob B mimicking peptide results in platelet-mimetic particles with functionality similar to that previously observed with antibody-functionalized particles. Furthermore, while individual antibodies have much higher affinity for

fibrin than the knob B mimicking peptides used here, these results indicate that binding strength is ensured by the multi-point FAMCY-fibrin interaction (*i.e.*, particle avidity).

6.3.4. FAMCYs Decrease Blood Loss and Increase Fibrin Incorporation at Wound Sites in a Liver Laceration Model of Traumatic Injury

We next analyzed the hemostatic ability of FAMCYs in an *in vivo* traumatic liver laceration injury in mice. Large FAMCYs (~1 μm) made with 90:10 NIPAm:AAc were adopted in this study based on their ability *in vitro* to enhance fiber density within fibrin clots. FAMCYs or control particles were injected intravenously and allowed to circulate five min prior to injury, after which blood loss was monitored over time. Total blood loss over time illustrates the amount of blood lost at specific time points following the liver laceration injury. This data shows trends of less bleeding in the animals that received 15 mg kg⁻¹ FAMCYs compared to saline, bare microgel ULCs, control peptide FAMCYs, and FAMCYs at 5 mg kg⁻¹, 10 mg kg⁻¹, and 50 mg kg⁻¹ (**Figure 6.6**). Total blood loss quantification over the course of the 10 min injury showed significantly lower total blood loss for animals that received treatment with 15 mg kg⁻¹ FAMCYs (0.0078 ± 0.003 g blood per g animal) compared to saline treated animals (0.016 ± 0.004 g blood per g animal, $p = 0.0193$) (**Figure 6.6**). Minimal differences in total blood loss were seen when comparing saline treatment to bare microgel ULCs (0.012 ± 0.004 g blood/g animal, $p = 0.7195$) and control peptide FAMCYs (0.013 ± 0.002 g blood/g animal, $p = 0.8178$). Conversely, administration of 50 mg kg⁻¹ FAMCYs in animals showed significantly higher blood loss (0.019 ± 0.005 g blood/g animal) than both 10 mg kg⁻¹ (0.010 ± 0.004 g blood/g animal, $p = 0.0123$) and 15 mg kg⁻¹ FAMCYs (0.0078 ± 0.003 g blood/g animal, $p = 0.0008$), indicating that high concentrations of FAMCYs are likely inhibiting clot formation due to direct competition with native fibrin knob:hole interactions and/or steric

hindrance of fibrin polymerization due to the presence of the microgels within the clot network. Immunohistochemistry of fibrin at the wound site shows significantly more fibrin deposition in animals treated with 15mg kg⁻¹ FAMCYs ($6305 \pm 4054 \text{ um}^2$) compared to saline ($916 \pm 1616 \text{ um}^2$, $p = 0.0079$), ULCs ($840 \pm 748 \text{ um}^2$, $p = 0.0099$), or FAMCYs ($1988 \pm 1921 \text{ um}^2$, $p = 0.0469$) (**Figure 6.7**). Higher fibrin incorporation at wound sites was quantified in both the total count of fibrin deposits in addition to the total area of fibrin at the wound site.

6.4 Discussion

The goal of this study was to evaluate the hemostatic efficacy of synthetic highly deformable platelet-like particles whose surface is functionalized with a fibrin hole b-specific peptide (FAMCYs) under both in vitro and in vivo clotting conditions. Previous designs of platelet-like particles generated by our lab have demonstrated the ability to stem bleeding and induce clot retraction by binding fibrin fibers, spreading between bound fibers, and then collapsing inwards to induce clot retraction [14, 26]. These previous studies have established that fibrin-binding affinity and microgel deformability are critical design features for obtaining this unique particle-mediated clot retraction feature. However, previous designs employed either a full-length antibody or a sdFv that respectively target the fibrin E domain or polymerized fibrin. Given the challenges of antibody biomanufacturing, fibrin-targeting peptides represent an attractive alternative to develop platelet mimetic particles with strong translation potential. Therefore, the present study focused on the development of novel Fibrin-Affine Microgels with Clotting Yield (FAMCYs) capable of retaining the hemostatic function and clot contraction abilities of previous designs while utilizing a smaller and less potentially obstructive targeting motif. The ability of FAMCYs to induce clot retraction was assessed via analysis of in vitro clot structure; furthermore, the stability

and hemostatic efficacy was evaluated *in vivo* by measuring bleeding times and total blood loss in mice treated with FAMCYs prior to undergoing a traumatic liver laceration injury. Overall, we observed significantly increased clot density *in vitro* and decrease bleeding in a rodent trauma model *in vivo*. These results indicate that surface functionalization of ULC microgels with peptides mimicking the knob B sequence of native fibrin (AHRPYAAK) endows FAMCYs with the platelet-like ability to mediate the binding of fibrin fibers of previous designs while utilizing a less costly, more translational design.

These studies explored the interplay between FAMCY size, peptide particle density, concentration and fibrin network density. Our previous studies with fibrin antibody and sdFv conjugated ULC microgels demonstrated that increased fiber density in the presence of fibrin-binding ULC microgels is dependent on the high particle deformability, which allows the particles to spread extensively within the fibrin network, binding to multiple fibrin fibers [14, 26]. Brownian motion of the particles leads to deformation of the fibrin network, and increased local fiber density, overtime. It would therefore be expected that increasing fibrin-particle interactions, either through increased particle size, peptide density or concentrations, would lead to enhancement of these effects and increased fibrin density. Such relationships are expected, because increased particle size is likely to increase the extent of the particle:fibrin interactions, as larger particles would geometrically occupy more space than smaller particles and would be able to bridge more fibrin fibers than smaller particles. Similarly, increased peptide density or increased particle concentration would increase the number of peptide:fibrin interactions. Within the particle types explored, we indeed observed that larger particles were associated with increased fibrin network density. However, increasing peptide density by increasing the AAc content on the particles between 10-20% monomer concentration, did not result in large differences in fibrin network

density. This result indicates that 10% AAc ULC particles likely result in a saturating peptide density on the surface of the microgels. Evaluation of fiber density as a function of particle concentration performed using 1 μ m particles with a 10% AAc content demonstrated a biphasic response in fibrin fiber density as a function of particle concentration, such that fiber density initially increases with increasing particle concentration but then decreases as particle concentration increases further. This biphasic relationship between particle concentration and fiber density is likely due to the nature of targeting fibrin B:b interactions. At low concentrations of knob B mimicking peptide, the particles will bind to hole b without inhibiting native fibrin polymerization. As knob B mimicking peptide surface density is increased, binding to hole b is likewise increased, thereby increasing the ability of FAMCYs to increase fibrin network density. However, above a certain peptide concentration, the synthetic knob:hole interactions will begin to compete for and inhibit native knob B: hole b interactions to a degree that inhibits fibrin polymerization. These results indicate that particle composition and concentration should be carefully considered to ensure delivery of a formulation that promotes enhanced fiber density.

Enhanced fibrin fiber density was found to correlate with enhanced clot stability, as determined via an endogenous fibrinolysis assay; clots formed from an optimal 2 mg mL⁻¹ concentration of FAMCYs exhibit greater resistance to degradation via tPA and plasminogen than controls; this is reminiscent of the decreased susceptibility to fibrinolysis observed in clots that have undergone platelet-mediated clot retraction [6]. Both the confocal and the fibrinolysis assay results indicate that clots formed using FAMCYs concentrations above or below the optimal concentration do not show these same characteristics of clot retraction; this could occur due to either a lack of sufficient fibrin-binding for concentrations below the optimal concentration or an overabundance of particles at concentrations above the optimal concentration, which could result

in steric hindrance of FAMCY-induced microcollapses and thus limit the overall degree of clot retraction observed. These data, coupled with the increased clot density observed in the presence of 2 mg mL^{-1} FAMCYs indicates that targeting fibrin with the knob B mimicking peptide results in platelet-mimetic particles with functionality similar to that previously observed with antibody based particles, demonstrating that this peptide based targeting approach is a successful alternative to antibody based targeting strategies. Furthermore, while individual antibodies have much higher affinity for fibrin than the knob B mimicking peptides used here, these results indicate that binding strength is ensured by the multi-point FAMCY-fibrin interaction (*i.e.* particle avidity).

Finally, *in vivo* analysis of FAMCY efficacy in treating bleeding after trauma again demonstrated a biphasic response wherein increasing particle dosing resulted in decreased total blood loss up to a particle dose of 15 mg kg^{-1} . Further increase in particle dosing to 50 mg kg^{-1} resulted in blood loss similar to that observed in control animals. These results are likely due to an inhibition of clot formation above a certain particle concentration. Overall, these results indicate that FAMCYs are a viable alternative to previous antibody based designs of PLPs, however, particle composition (size/peptide density) and dosing should be carefully considered to ensure delivery of a formulation that promotes enhanced fiber density and decreases bleeding when applied *in vivo*.

6.5. Conclusions

In these studies, we demonstrated the creation of hemostatic platelet-mimetic fibrin-targeting knob B particles (FAMCYs) that are capable of stemming bleeding and inducing clot contraction *in vitro* and *in vivo*. These particles have the ability to enhance clot structure and stability *in vitro* and decrease *in vivo* blood loss, indicating that they have the potential to serve as

a hemostatic therapy in traumatic injury related emergency medicine. Future work will involve mechanical assessment of clots in the presence FAMCY particles, including stiffness characterization, and *in vitro* safety assessment of the particles within models of endothelial cell proliferation, hemolysis, and thrombogenicity.

REFERENCES

- [1] Hunt, T.K., H. Hopf, and Z. Hussain, Physiology of wound healing. *Advances in Skin and Wound Care*, 2000. 13: p. 6-11.
- [2] Budzynski, A.Z., S.A. Olexa, and B.V. Pandya, Fibrin polymerization sites in fibrinogen and fibrin fragments. *Annals of the New York Academy of Sciences*, 1983. 408(1): p. 301-314.
- [3] Weisel, J.W. and R.I. Litvinov, Mechanisms of fibrin polymerization and clinical implications. *Blood*, 2013. 121(10): p. 1712-1719.
- [4] Riedel, T., J. Suttnar, E. Brynda, et al., Fibrinopeptides A and B release in the process of surface fibrin formation. *Blood*, 2011. 117(5): p. 1700-1706.
- [5] Modery-Pawlowski, C.L., L.L. Tian, V. Pan, et al., Approaches to synthetic platelet analogs. *Biomaterials*, 2013. 34(2): p. 526-541.
- [6] Tutwiler, V., A.D. Peshkova, G. Le Minh, et al., Blood clot contraction differentially modulates internal and external fibrinolysis. *Journal of Thrombosis and Haemostasis*, 2019. 17(2): p. 361-370.
- [7] Tutwiler, V., H. Wang, R.I. Litvinov, et al., Interplay of Platelet Contractility and Elasticity of Fibrin/Erythrocytes in Blood Clot Retraction *Biophysical Journal*, 2017. 112(4): p. 714-723.
- [8] Kim, O.V., R.I. Litvinov, M.S. Alber, and J.W. Weisel, Quantitative structural mechanobiology of platelet-driven blood clot contraction. *Nature Communications*, 2017. 8: p. 1274.
- [9] Cines, D.B., T. Lebedeva, C. Nagaswami, et al., Clot contraction: compression of erythrocytes into tightly packed polyhedra and redistribution of platelets and fibrin. *Blood*, 2014. 123(10): p. 1596-1603.
- [10] Rossaint, R., B. Bouillon, V. Cerny, et al., Task Force for Advanced Bleeding Care in, Management of bleeding following major trauma: an updated European guideline. *Critical Care*, 2010. 14(2): p. R52-R52.
- [11] Acosta, J.A., J.C. Yang, R.J. Winchell, et al., Lethal Injuries and Time to Death in a Level I Trauma Center. *Journal of the American College of Surgeons*, 1998. 186(5): p. 528-533.
- [12] Baker, C.C., L. Oppenheimer, B. Stephens, et al., Epidemiology of trauma deaths. *The American Journal of Surgery*, 1980. 140(1): p. 144-150.
- [13] Johnson, J., A. Wells, D. Kauvar, et al., Impact of hemorrhage on trauma outcome: An overview of epidemiology, clinical presentations, and therapeutic considerations. *Journal of Trauma and Acute Care Surgery*, 2006. 60(6): p. 3-11.

- [14] Nandi, S., E.P. Sproul, K. Nellenbach, et al., Platelet-like particles dynamically stiffen fibrin matrices and improve wound healing outcomes. *Biomaterials Science*, 2019. 7(2): p. 669-682.
- [15] Litvinov, R.I., O.V. Gorkun, S.F. Owen, et al., Polymerization of fibrin: specificity, strength, and stability of knob-hole interactions studied at the single-molecule level. *Blood*, 2005. 106(9): p. 2944-2951.
- [16] Litvinov, R.I., O.V. Gorkun, D.K. Galanakis, et al., Polymerization of fibrin: Direct observation and quantification of individual B:b knobhole interactions. *Blood*, 2007. 109(1): p. 130-138.
- [17] Brown, A.C., S.R. Baker, A.M. Douglas, et al., Molecular interference of fibrin's divalent polymerization mechanism enables modulation of multiscale material properties. *Biomaterials*, 2015. 49: p. 27-36.
- [18] Stabenfeldt, S.E., M. Gourley, L. Krishnan, et al., Engineering fibrin polymers through engagement of alternative polymerization mechanisms. *Biomaterials*, 2012. 33(2): p. 535-544.
- [19] Sproul, E.P., S. Nandi, C. Roosa, et al., Biomimetic Microgels with Controllable Deformability Improve Healing Outcomes. *Advanced Biosystems*, 2018. 0(0): p. 1800042.
- [20] Joshi, A., S. Nandi, D. Chester, et al., Study of poly (Nisopropylacrilamide-co-acrylic acid) (pNIPAM) microgel particle induced deformations of tissue mimicking phantom by ultrasound stimulation. *Langmuir*, 2017. 34(4): p. 1457-1465.
- [21] Sproul, E.P., R.T. Hannan, and A.C. Brown, Characterization of fibrin-based constructs for tissue engineering, in *Biomaterials for Tissue Engineering: Methods and Protocols, Methods in Molecular Biology* (ed. K. Chawla), 2018, Springer. p. 85-99.
- [22] Nellenbach, K., N.A. Guzzetta, and A.C. Brown, Analysis of the structural and mechanical effects of procoagulant agents on neonatal fibrin networks following cardiopulmonary bypass. *Journal of Thrombosis and Haemostasis*, 2018. 16(11): p. 2159-2167.
- [23] Sproul, E.P., R.T. Hannan, and A.C. Brown, Controlling Fibrin Network Morphology, Polymerization, and Degradation Dynamics in Fibrin Gels for Promoting Tissue Repair, in *Biomaterials for Tissue Engineering: Methods and Protocols* (ed. K. Chawla), 2018, Springer. p. 85-99
- [24] Morgan, C.E., V.S. Prakash, J.M. Vercammen, et al., Development and Validation of 4 Different Rat Models of Uncontrolled Hemorrhage. *JAMA Surgery*, 2015. 150(4): p. 316-324.
- [25] Bachman, H., A.C. Brown, K.C. Clarke, et al., Ultrasoft, highly deformable microgels. *Soft Matter*, 2015. 11(10): p. 2018-2028.
- [26] Brown, A.C., S.E. Stabenfeldt, B. Ahn, et al., Ultrasoft microgels displaying emergent platelet-like behaviours. *Nature Materials*, 2014. 13(12): p. 1108-1114.

Figures

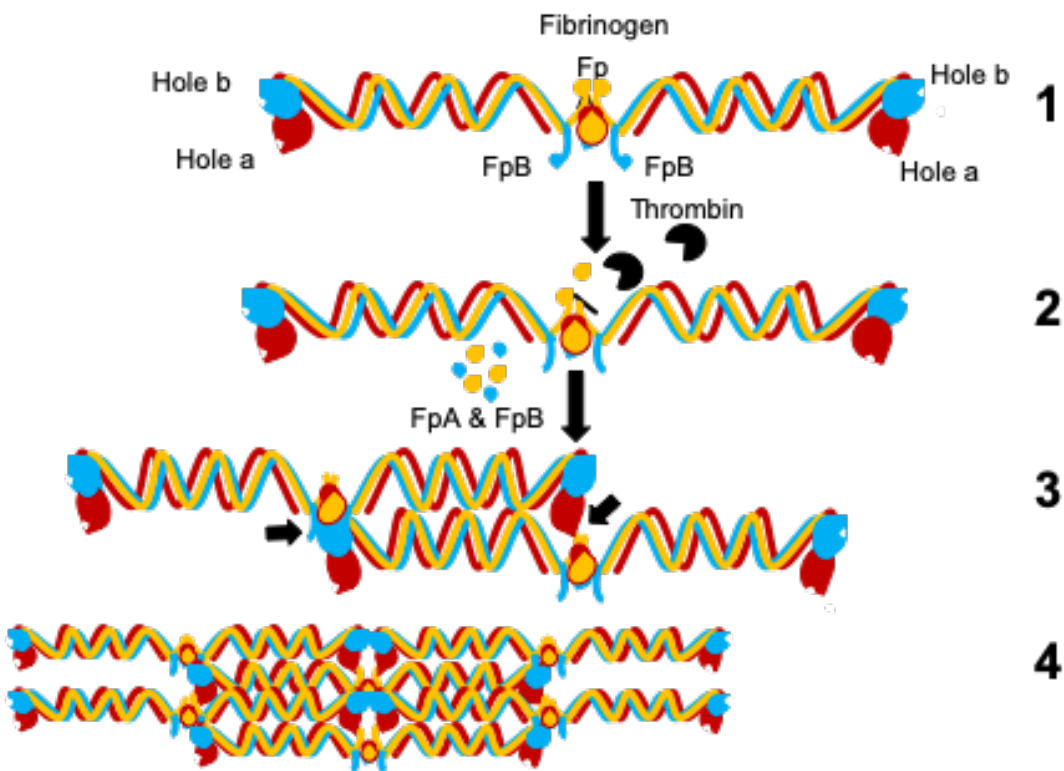


Figure 6.1 (1) Intact circulating fibrinogen; (2) Enzymatic cleavage of fibrinopeptides by thrombin activate knobs a and b; (3) Activated knobs bind to corresponding holes on adjacent proteins; (4) Fibrin network formation.

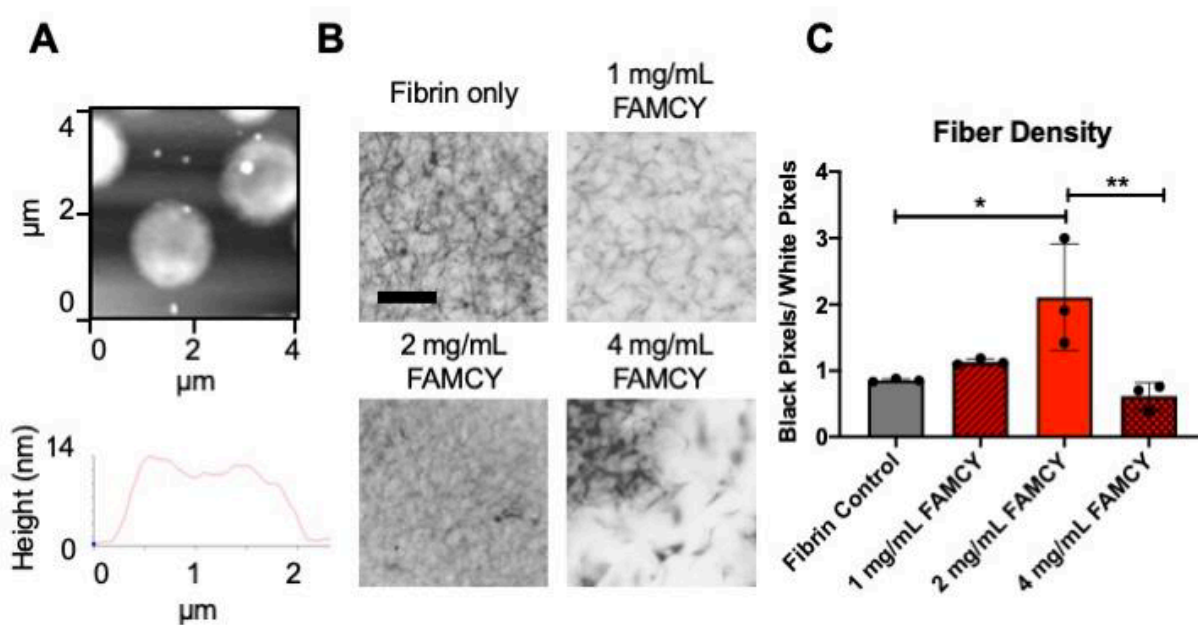


Figure 6.2 **(A)** Representative AFM image (top) and height trace (bottom) of 90:10 NIPAm:AAc ULC microgel; **(B)** Confocal microscopy images of clots formed with $\sim 1 \mu\text{m}$, 90:10 NIPAm:AAc FAMCY particles at 1, 2, or 4 mg mL^{-1} particle concentrations. **(C)** Fiber density, defined as the ratio of black pixels (fibers) to white pixels (negative space), is significantly enhanced at a concentration of 2 mg mL^{-1} relative to control clots and clots formed using higher and lower concentrations of FAMCY particles. $n = 3$ clots per group. Scale bar = 10 μm . * $p < 0.05$; ** $p < 0.01$.

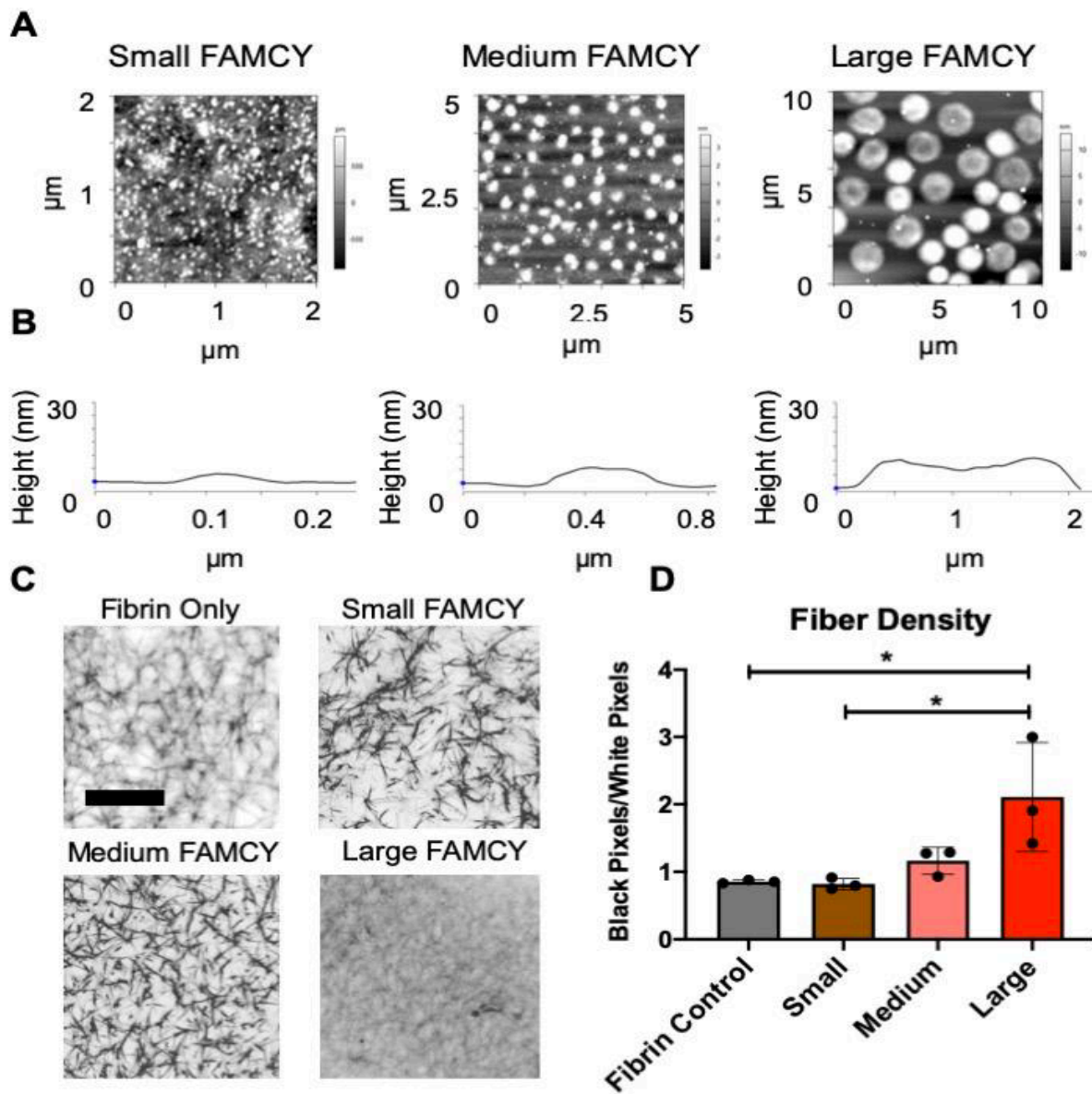


Figure 6.3 (A) Representative atomic force microscopy dry imaging and (B) height traces to confirm the creation of small ~150 nm particles and medium ~450 nm 90:10 NIPMAm:AAc particles; (C) Confocal microscopy and (D) fiber density quantification of clots formed in the presence of small, medium, and large 90:10 NIPAm:AAc FAMCYs at a concentration of 2 mg mL⁻¹. n = 3 clots per group. Scale bar = 10 μm. *p<0.05.

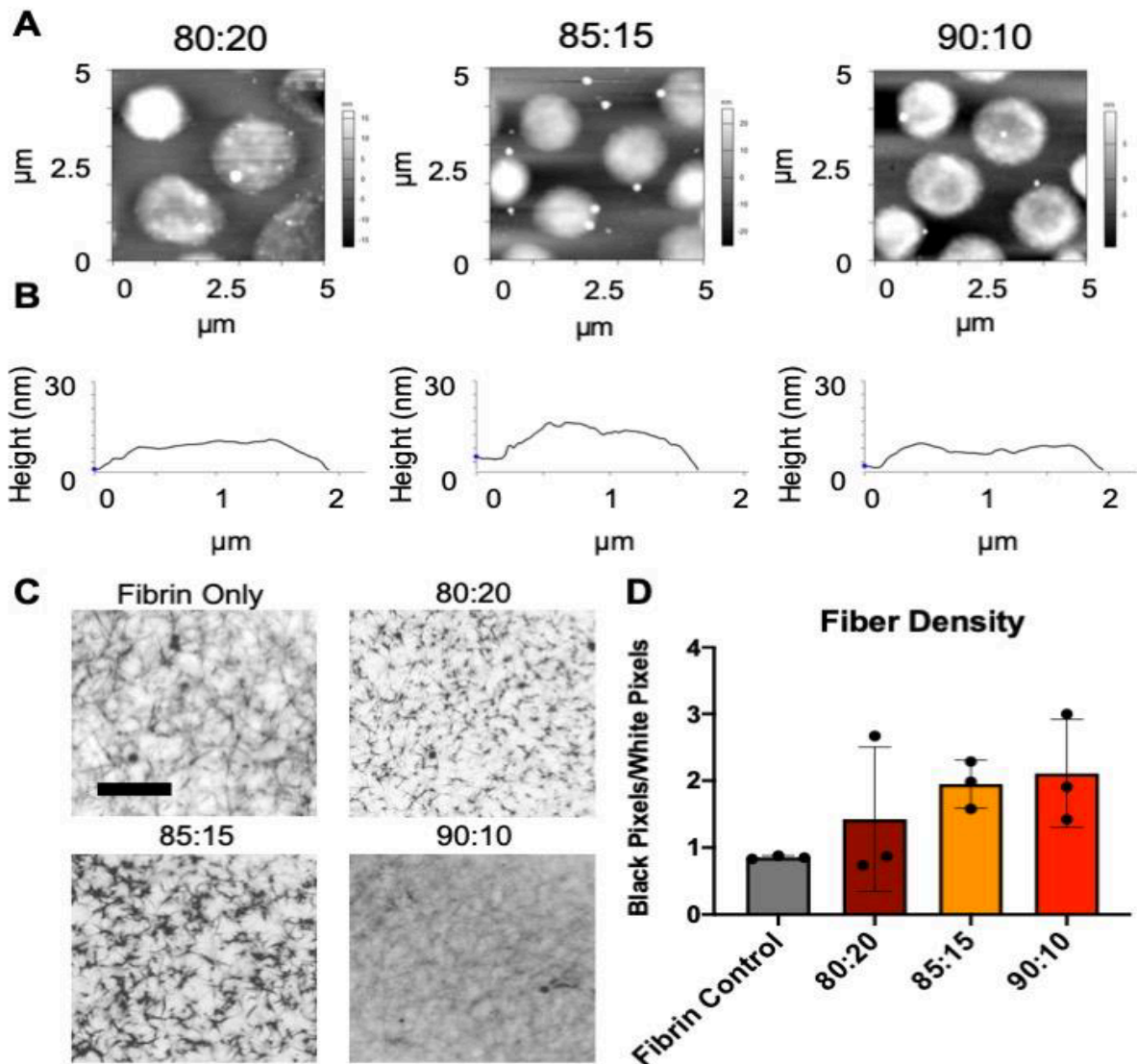


Figure 6.4 (A) Representative atomic force microscopy dry imaging and (B) height traces of 80:20, 85:15, and 90:10 NIPAm:AAc particles to determine diameter and height. Particle diameters were measured on ImageJ and particle heights calculated from max values obtained from individual height traces. No statistical difference in diameter or height was observed between particle types of varying acrylic acid content. $n \geq 30$ particles/group; (C) Confocal microscopy and (D) fiber density quantification of clots formed in the presence of $\sim 1 \mu\text{m}$, 80:20, 85:15, and 90:10 NIPAm:AAc FAMCYs at a concentration of 2 mg mL^{-1} . $n = 3$ clots per group. Scale bar = $10 \mu\text{m}$.

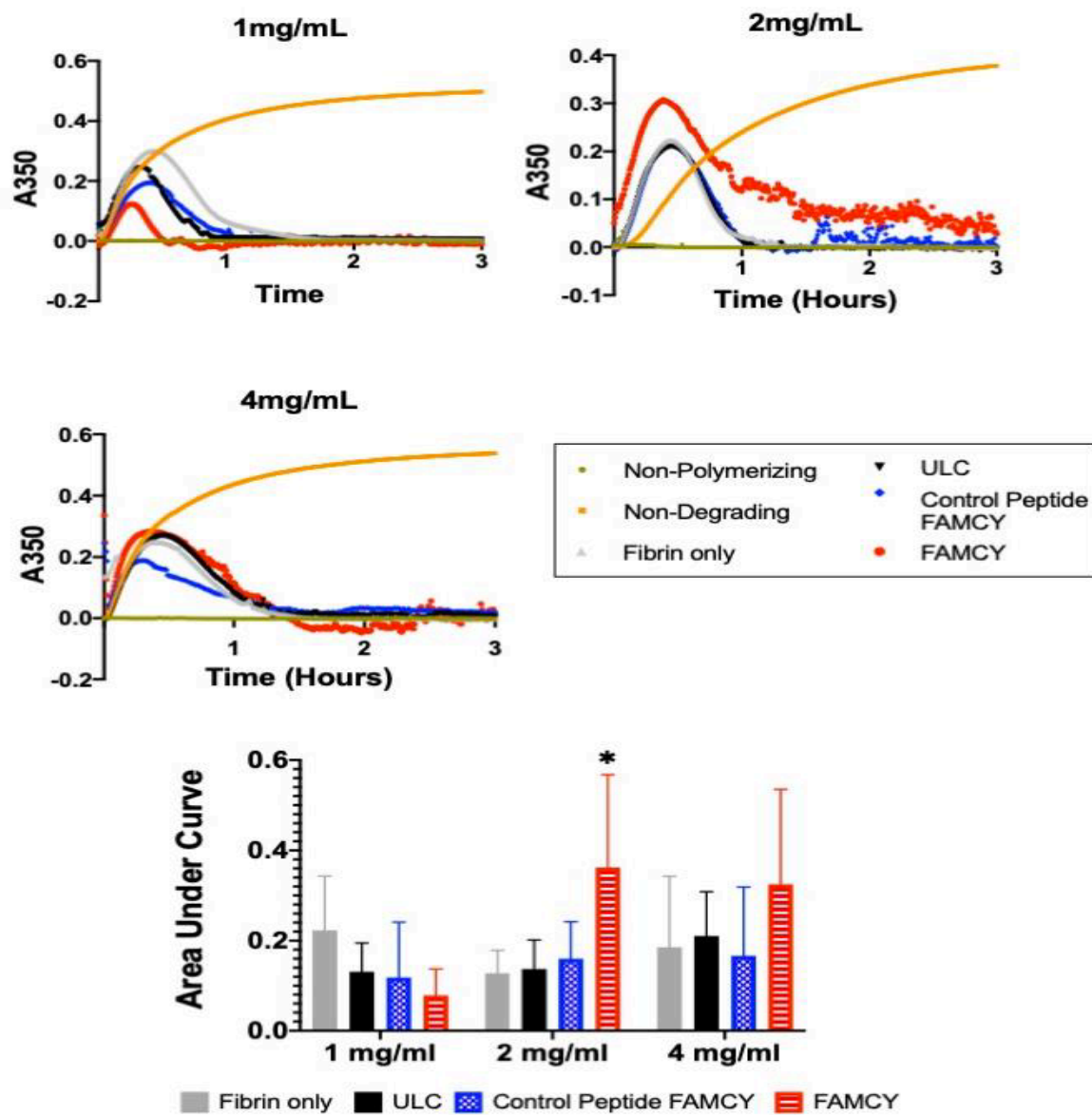


Figure 6.5 Polymerization and degradation curves for clots formed in the presence of 1, 2, or 4 mg mL^{-1} 1 μm 90:10 FAMCYs (top). At the previously discovered optimal concentration of 2 mg mL^{-1} , FAMCY clots show significantly greater maximum turbidity and resistance to fibrinolysis than control clots and clots containing control peptide FAMCYs or ULCs, as illustrated by absorbance (A350) curves of clots (top) and by quantification of the area under the curves (bottom). Clots containing control peptide FAMCYs or ULCs polymerize and degrade at rates very similar to those of control fibrin-only clots. * $p < 0.05$; $n = 3$ duplicate experiments.

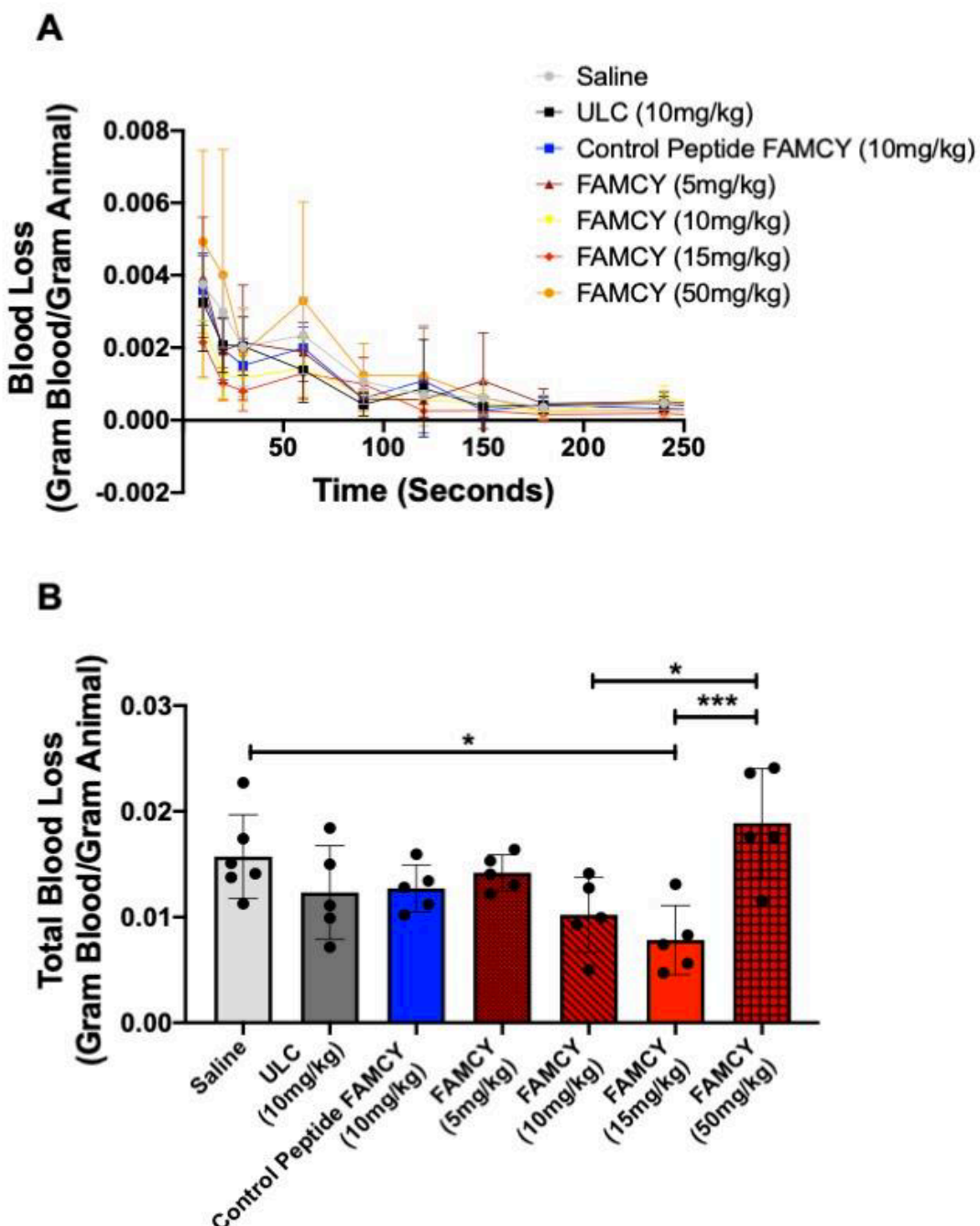


Figure 6.6 (A) Blood loss over time is decreased after treatment with an optimal dosage of FAMCYs; **(B)** Total blood loss is significantly decreased after treatment with an optimal dosage of FAMCYs relative to saline controls. Large (~1 μ m) 90:10 NIPAm:AAc FAMCYs, control peptide FAMCYs, and ULCs were examined *in vivo*. n = 6 in saline group, n = 5 in all other treatment groups; *p<0.05; ***p<0.001.

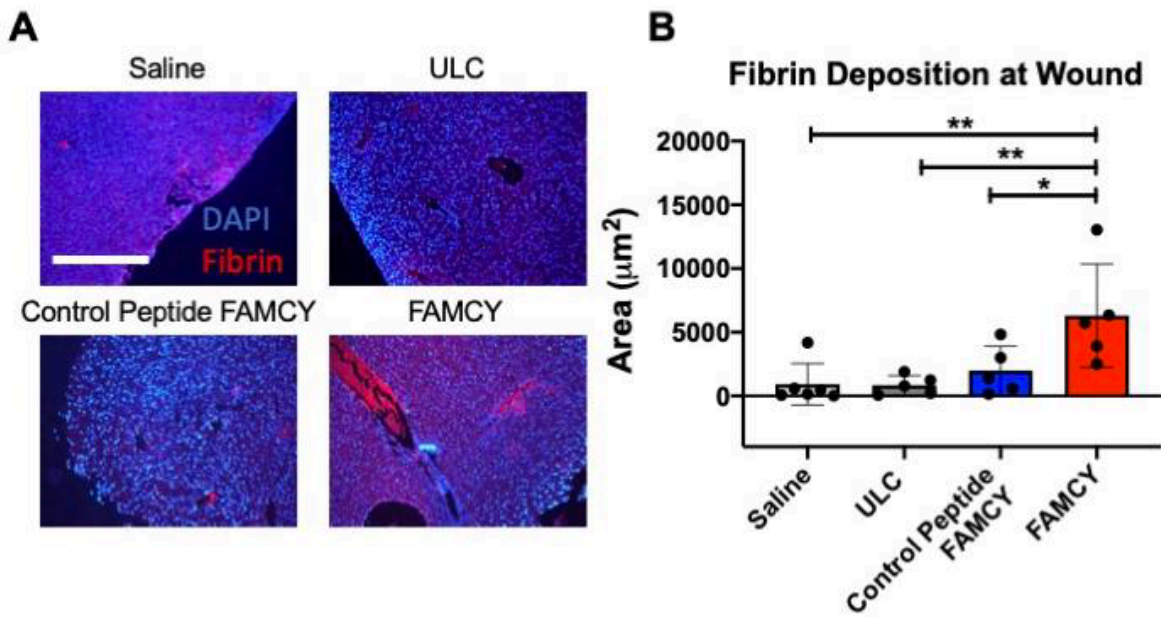


Figure 6.7 (A) Immunohistochemistry of fibrin (red) at wound sites following liver laceration injury; (B) Quantification using ImageJ Particle Analysis to determine total area (μm^2) of fibrin-positive stain shows fibrin incorporation at wound sites is increased following treatment with FAMCY particles relative to treatment with saline or control peptide FAMCYs. Scale bar = 400 μm . n = 6 in saline group, n = 5 in all other treatment groups. * $p<0.05$; ** $p<0.01$.

CHAPTER 7

Conclusions and Future Work

John D. Schneible

7.1. Summary

This work focuses on the development of material toolbox for advanced therapeutics in the fields of drug delivery, molecular diagnostics, and wound healing, comprising polysaccharide- and peptide- inspired materials. This work focused on polysaccharides and peptides owing to their biocompatibility and biodegradability, ease of chemical functionalization and processing, commercial abundance, manufacturing scalability, and low cost.

The first portion of this thesis (**Chapter 2 – Chapter 4**) reports on two hydrogel-based drug delivery systems, to deliver a synergistic combination of chemotherapeutics, doxorubicin (DOX) and gemcitabine (GEM), with a precise delivery schedule, or kinetics, that endows a maximal therapeutic synergism against an aggressive triple negative breast cancer (TNBC) cell line. In **Chapter 2**, both experimental and *in silico* studies were performed to guide the design of a hydrophobically modified-chitosan hydrogel. Within this context, a remarkable effect of alkyl chain length was observed for the transport properties of amphiphilic drug DOX, namely the tradeoff between favorable hydrophobic interactions, driving retention of DOX within the network, and a non-favorable morphological rearrangement that causes a cluster/channel morphology within the hydrogel. The work in **Chapter 3** focused on the validation of hydrogels studied in **Chapter 2**. An acetylated-modified chitosan hydrogel was selected, owing to the desirable molar ratio and scheduling of delivery kinetics for GEM and DOX discovered in **Chapter 2**; namely a molar ratio ~10 and faster GEM delivery than DOX. Further studies were undertaken to optimize the loading conditions within this gel, such that the resulting release of the dual drug combination afforded a therapeutically efficacious dose. The optimized hydrogel was evaluated in two models: (*i*) a 2-D cell monolayer, and (*ii*) a 3-D tumor spheroid. The resulting assays demonstrated the developed hydrogel released a dose that was (*i*) more synergistic than the

concurrent administration of GEM and DOX, when evaluated against the 2-D cell monolayer, and (ii) highly effective at reducing tumor volume growth in the 3-D tumor spheroid assay.

In **Chapter 4**, the focus on the drug delivery device was shifted from a homogenous hydrogel, comprising GEM and DOX co-loaded, to a heterogenous composite hydrogel, wherein the two drugs were segregated to different compartments; DOX adsorbed onto graphene oxide (GO) particles embedded within a peptide scaffold loaded with GEM. In this work, *in silico* studies were again undertaken to elucidate the underlying physicochemical factors underpinning DOX loading and release behavior from the GO particles. The composite was evaluated against the same TNBC cell line utilized in **Chapter 3**. The results demonstrated a high level of synergy when exposed to the composite, and a further improvement than what was found in **Chapter 3**.

The latter portion of this thesis focused on the development of light-responsive cyclic peptides that can selectively bind to protein biomarkers (**Chapter 5**); and the development of thermo-responsive microgel particles to improve blot clotting (**Chapter 6**). In **Chapter 5**, the development of a novel light-responsive cyclic peptide that selectively labels vascular cell adhesion marker 1 (VCAM1), a cell marker implicated in stem cell function, is reported. In this work, an *in silico* approach was adopted to identify potential cyclic peptide sequences that exhibit selective on/off binding of VCAM1 for the *cis* and *trans* isomers. A novel synthetic route was developed to make the identified cyclic peptide sequences bearing an azobenzene moiety. These sequences were subsequently characterized for photophysical behavior and screened for conformational binding affinities. **Chapter 6** reports on the development and characterization of thermo-responsive, soft microgels decorated with the peptide AHRPYAAK, a sequence that mimics fibrin knob ‘B’ and targets fibrin hole ‘b’, which are implicated in blood clotting functions. The particle-peptide construct was evaluated *in vitro*, where it was found that clot density was

increased, and *in vivo*, where the construct substantially decreased bleeding in a rodent trauma model.

7.2. Future Work

In both projects within the drug delivery purview, future work would revolve around evaluating these drug delivery systems; acetylated-chitosan hydrogel (**Chapter 2** and **Chapter 3**) and GO-peptide composite hydrogel (**Chapter 4**), in a better representative model applicable to humans. Future work would consist of screening the gels *in vivo* using a mouse model. By doing so, the drug delivery system would be tested in a system resembling the human body (*i.e.*, extracellular matrix, endogenous enzymes, tumor vasculature, etc.), and represents a necessary pre-clinical hurdle that must be cleared. Because the work in **Chapter 3** utilized 3-D tumor spheroids as a tool for validation, *in vivo* work could elucidate a connection between the results obtained *in vivo* and *ex vivo*. While previous work has demonstrated a connection between validation with a tumor spheroid and successful treatment *in vivo* [1, 2], to date, no current correlation exists for a TNBC model. Further, if such a correlation does exist, it may be reasonable to expect a paradigm shift from the mouse model to and *ex vivo* spheroid model. Such a paradigm shift would be ground-breaking, as it would greatly accelerate the development of future drug delivery systems owing to a higher throughput method of device validation. Similarly, for the composite hydrogel, presented in **Chapter 4**, the future work would consist of validation in a 3-D tumor model, and *in vivo*. In addition, future work for both delivery systems could involve validation against other pathologies. While TNBC remains a dangerous cancer, evaluation of the drug delivery systems against other types of cancer bearing higher mortality rates, such as pancreatic or colorectal cancer, would be valuable studies to undertake.

REFERENCES

- [1] Xin, H., X. Sha, X. Jiang, et al., Anti-glioblastoma efficacy and safety of paclitaxel-loading Angiopep-conjugated dual targeting PEG-PCL nanoparticles. *Biomaterials*, 2012. 33(32): p. 8167-8176.
- [2] Wang, Y., J. Zhou, L. Qiu, et al., Cisplatin-alginate conjugate liposomes for targeted delivery to EGFR-positive ovarian cancer cells. *Biomaterials*, 2014. 35(14): p. 4297-4309.